ISBN 978-82-471-3189-3 (printed ver.)
ISBN 978-82-471-3190-9 (electronic ver.)
ISSN 1503-8181

Doctoral theses at NTNU, 2011:307

Julien Cochard

Constitutive modeling of Solar-grade silicon materials

Julien Cochard

Doctoral Thesis

NTNU
Norwegian University of
Science and Technology
Thesis for the degree of
philosophiae doctor
Faculty of Engineering Sciences and Technology
Department of Structural Engineering

NTNU
Norwegian University of
Science and Technology

Doctoral theses at NTNU, 2011:307

NTNU

NTNU
Norwegian University of
Science and Technology

Julien Cochard

Constitutive modeling of Solar-grade silicon materials

Thesis for the degree of philosophiae doctor

Trondheim, December 2011

Norwegian University of
Science and Technology
Faculty of Engineering Sciences and Technology
Department of Structural Engineering

NTNU
Norwegian University of
Science and Technology

NTNU
Norwegian University of Science and Technology

Thesis for the degree of philosophiae doctor

Faculty of Engineering Sciences and Technology
Department of Structural Engineering

ISBN 978-82-471-3189-3 (printed ver.)
ISBN 978-82-471-3190-9 (electronic ver.)
ISSN 1503-8181

Doctoral Theses at NTNU, 2011:307

Printed by Tapir Uttrykk

CONSTITUTIVE MODELING OF SOLAR-GRADE SILICON MATERIALS

JULIEN COCHARD

Thesis for the degree of philosophiae doctor

Department of Structural Engineering
Faculty of Engineering Sciences and Technology (IVT)
Norwegian University of Science and Technology (NTNU)
December 2011

Julien Cochard: *Constitutive modeling of Solar-grade silicon materials*, Thesis for the degree of philosophiae doctor, © December 2011

The world's energy system is at a crossroads.
Current global trends in energy supply and consumption are patently unsustainable - environmentally, economically, socially.
But that can - and must - be altered; there's still time to change the road we're on.

It is not an exaggeration to claim that the future of human prosperity depends on how successfully we tackle the two central energy challenges facing us today: securing the supply of reliable and affordable energy; and effecting a rapid transformation to a low-carbon, efficient and environmentally benign system of energy supply.

What is needed is nothing short of an energy revolution.

— International Energy Agency, 2008

Dedicated to those who have understood that happiness and prosperity are inextricably binded to a clean and protected environment,
to those who fight for our future,
for more justice, fairness, equity and love in this world.

ABSTRACT

Residual stresses in directionally solidified silicon ingots are known to increase the likelihood of material failure, leading to unnecessary costs and material waste. These stresses develop during solidification and cooling, owing to thermal gradients, the multicrystalline nature of the materials, and its impurity content.

Silicon multicrystals (mc-Si) are simply aggregates of several, rather large single crystals. Hence, building a model for mc-Si consists in the development of accurate constitutive equations for SoG-Si monocrystals and the construction of multicrystalline aggregates by Finite Element methods.

Constitutive models for solar-grade silicon monocrystals (SoG c-Si) of various complexity are derived in this thesis. Their ultimate goal is to allow the quantification of the residual stresses in SoG-Si materials given a thermomechanical loading path.

A physical approach to modeling plasticity in semiconductors has been consistently adopted: all equations are based on the introduction of dislocation densities, carrying plastic flow and participating to material hardening with deformation. Constitutive equations are implemented into a rate-dependent crystal plasticity kinematical framework.

The benefits of this methodology are twofold: firstly, the models are perfectly useable in the temperature range where silicon behaves as a perfectly elastic material, but they excel at reproducing its particularly temperature-sensitive plastic behavior. Secondly, final dislocation densities can be predicted by the models. These are of great use for industrial applications, since regions of large dislocation contents also exhibit poor electrical performance.

Consequently, the constitutive models introduced in this Ph.D. thesis are not limited to stress calculations, but can be coupled to other physical analyses.

An exhaustive literature review has been written, covering the aspects of plastic deformation over multiple scales. It lays the foundation for analysis and improvement of existing constitutive models. Systematic identification of constitutive parameters of traditional models calls for the introduction of new internal variables, dislocations stored in dipolar structures. Accounting for these immobile dislocations enables an extension of the model of Alexander & Haasen to correctly reproduce the steady-state of deformation during uniaxial testing of silicon monocrystals oriented for single glide.

The influence of dissolved oxygen on the plastic behavior of silicon monocrystals is successfully reproduced by the introduction of an effective density of mobile dislocations. This model for extrinsic materials can be

generalized to other impurity types, provided physical parameters related to their diffusivity and dislocation locking effect are known.

Shortcomings of this extension are solved by deriving a completely new constitutive model, arguably the most accurate one available for study of covalent materials. The potentially rate-limiting dislocation motion mechanisms of jog dragging and pinning by localized obstacles are introduced in the velocity law. Dislocation populations are segmented by their character and potential mobility. An accurate dislocation multiplication law for the yield region of silicon monocrystals is introduced. The model is shown to reproduce correctly the experimentally observed steady-state of deformation, stress overshoot, and strong linear hardening rate in stage II.

The experimentally characterized flexural strength of SoG mc-Si bars can be used in the constitutive models to output the fracture probability of silicon.

Application of the extended AH model to bending cases of intrinsic and extrinsic mono- and multicrystals, to tension of a multicrystal containing hard SiC inclusions and to directional solidification of an intrinsic mc-Si ingot provide valuable information about the magnitude and various length scales over which stress heterogeneities develop in impure mc-Si materials.

Finally, some guidelines for future work are given, both on practical and theoretical aspects.

PUBLICATIONS

JOURNAL PUBLICATIONS

Constitutive modeling of intrinsic silicon monocrystals in easy glide, J. COCHARD, I. YONENAGA, S. GOUTTEBROZE, M. M'HAMDI, Z.L. ZHANG, Journal of Applied Physics, Vol. 107, No. 3, p. 033512, 2011

Constitutive modeling of intrinsic and oxygen-contaminated silicon monocrystals in easy glide, J. COCHARD, I. YONENAGA, S. GOUTTEBROZE, M. M'HAMDI, Z.L. ZHANG, Journal of Applied Physics, Vol. 108, No. 10, p. 103524, 2011

Constitutive modeling of semiconductors: the case of silicon, J. COCHARD, I. YONENAGA, M. M'HAMDI, Z.L. ZHANG, to be submitted

VISUAL PRESENTATIONS

A multicrystal model for the viscoplastic deformation of silicon at high temperature, J. COCHARD, S. GOUTTEBROZE, S. DUMOULIN, M. M'HAMDI, Z.L. ZHANG, 23rd EUPVSEC, Valencia, Spain, 2008

Mechanical modeling of impure silicon materials, J. COCHARD, S. GOUTTEBROZE, S. DUMOULIN, M. M'HAMDI, Z.L. ZHANG, 24th EUPVSEC, Hamburg, Germany, 2008

Constitutive modelling of silicon: parameters identification of classical models using crystal plasticity, J. COCHARD, I. YONENAGA, S. GOUTTEBROZE, M. M'HAMDI, Z.L. ZHANG, 3rd International Workshop on Crystalline Silicon Solar Cells (CSSC), Trondheim, Norway, 2009

ORAL PRESENTATIONS

Constitutive modelling of solar-grade silicon multicrystals at high temperatures, J. COCHARD, S. GOUTTEBROZE, M. M'HAMDI, Z.L. ZHANG, 1st Renewable Energy Research Conference, Trondheim, Norway, 2010

Mapping of stress, strain, dislocation density and fracture probability in silicon multicrystals, J. COCHARD, S. GOUTTEBROZE, M. M'HAMDI, Z.L. ZHANG, 23rd Nordic Seminar on Computational Mechanics, Stockholm, Sweden, 2010

Introduction to silicon mechanics, J. COCHARD, M. M'HAMDI, Z.L. ZHANG, 1st Nordic Workshop on mechanical issues for silicon wafer and cells, Oslo, Norway, 2010

First, I worry about climate change.
It's the only thing that I believe
has the power to fundamentally end
the march of civilization as we know it,
and make a lot of the other efforts that we're making
irrelevant and impossible.

— Bill Clinton

ACKNOWLEDGMENTS

The reason why I applied to and accepted this Ph.D. position is that I started developing an extremely strong interest for climate change and energy sustainability issues during the summer 2006, as news reports of more frequent and intense extreme weather events started to fill in the daily newsfeed.

The year after, the Intergovernmental Panel for Climate Change (IPCC) released its 4^{th} assessment report, confirming the human fingerprint on the observed increase in the global mean temperature during the late XX^{th} century, and the overwhelming threat unabated greenhouse gas emissions would mean for humanity and most of living matter on Earth. Hence, 2007 remains for me the year that triggered a committment to allocate my work capacity and offer my knowledge to those, public or private entities, that would work to mitigate climate change and pave our way to sustainability.

This is why my deepest thanks and acknowledgments go to Elkem Solar and all the staff working on the DESA project. Businesses are not created and prosper because they want to save us from environmental collapse, but because they make money at it. Therefore, any action or decision that can make these green businesses more competitive and profitable should be pursued. The decision of Elkem Solar took to invest in research while the solar PV market remains unstable is courageous and worth acknowledging. After all, they have given me my first job.

I would like to apologize to Bjørn-Rune Henriksen, Sigbjørn Berge and Ragnar Trondstad if reading my papers has caused them headaches. This thesis has not been 100 % of the "applied research" type. Meanwhile, the DESA project would have not seen the light without their work, and I am indeed thankful for their support.

From day 1, my supervisors Zhiliang Zhang and Mohammed M'Hamdi have supported me in many ways, encouraging me always to look further in my research yet keeping my results down to earth. Sylvain Gouttebroze, also on the DESA project, has been of great help all along these four years.

The contact established with Professor Ichiro Yonenaga has quickly turned out to be extremely fruitful. Prof. Yonenaga and myself have had

many interesting and challenging discussions. I would like particularly to thank him deeply for his hospitality during my stay in Sendai. His contributions have been critical to the fulfillement of this thesis.

Otto Lohne and Stephane Dumoulin have also provided with precious advice all along these four years, respectively on the physical and numerical aspects of my work. Their support is much appreciated.

The few experimental tests I did could not have been feasible without Julian (Jools) and Asle. We spent countless hours in the lab trying to fix the apparatus and deal with numerous issues; their help and patience have been very welcome. Torunn Ervik helped me preparing the samples for room-temperature experiments, and I would like to thank her for taking time for this.

Our secretaries at the Department of Structural Engineering are undoubtedly among the best, always available to help us and guide foreign Ph.D. candidates through the maze of Norwegian institutions. I have enjoyed the friendly and open atmosphere at this place, and would like to thank all my colleagues for interesting discussions through all those years.

I have spent wonderful years in Trondheim, surrounded by many good friends from all continents. There are many of them, and they will for sure recognize themselves when reading this. Thank you all for your friendship, support, the laughs we had together - you have made my time in Trondheim unforgettable.

My deepest acknowledgements go to my family, who has always supported me in my personal and professional decisions, even when it meant leaving France more than six years ago.

Last but not least, Karin has always been at my side since I moved to Trondheim. This Ph.D. thesis is also a bit hers. She is the moral support for my enterprises, giving me the strength to keep up with hard work yet knowing how to drag me out of equations and enjoy the outside world. Jag älskar dig, min älskling!

CONTENTS

NOMENCLATURE

a	lattice parameter (m)
$A_{\alpha\beta}$	long-range elastic interaction coefficient coming from mobile dislocations
$a_{\alpha\beta}$	interaction coefficient for forest interactions
b	magnitude of the Burgers vector of perfect dislocations (m)
$B_{\alpha\beta}$	long-range elastic interaction coefficient coming from immobile dislocations
b_p	magnitude of the Burgers vector of partial dislocations (m)
c_i	concentration of impurity i at the dislocation (m^{-3})
c_i^{∞}	concentration of impurity i dissolved in the bulk (m^{-3})
$c_i^{(s)}$	solubility of impurity i (m^{-3})
c_j	jog density along the dislocation line
c_k	kink concentration at thermal equilibrium (m^{-1})
d	dislocation dissociation width (m)
d_0	dislocation dissociation width at equilibrium (m)
δ_i	dislocation multiplication function for model i (m^{-1})
D_i	diffusion coefficient of the impurity i in the bulk ($m^2.s^{-1}$)
d_j	mean sessile jog spacing along a dislocation line (m)
D_{sd}	self-diffusion coefficient ($m^2.s^{-1}$)
E_i	interaction energy of impurity i with the dislocation (eV)
E_P	Peierls energy (eV)
ε	total strain (small strains approximation)
$\dot{\varepsilon}$	applied strain rate (small strains approximation) (s^{-1})
ε_e	elastic strain
ε_p	plastic strain
ε_θ	thermal strain

E_{rec}	reconstruction energy of a partial bond (eV)
η	fraction of mobile dislocations actually carrying plastic flow in extrinsic crystals
F	effective dislocation motion activation free energy (eV)
$f_{\alpha}^{(\alpha)}$	forest systems related to slip system α
F_k	single kink nucleation Helmoltz free energy (eV)
F_{km}	kink motion Helmoltz free energy, U_d or W_m (eV)
F_{kp}	kink pair interaction Helmoltz free energy (eV)
$F_{kp}^{(c)}$	critical kink pair nucleation Helmoltz free energy (eV)
F_{obs}	energy barrier for localized obstacle overcoming (eV)
F_{RD}	reconstruction defect formation Helmoltz free energy (eV)
Γ	line tension (N)
γ	resolved shear strain
$\dot{\gamma}$	total shear strain rate (s^{-1})
$\dot{\gamma}_e$	elastic shear strain rate (s^{-1})
$\dot{\gamma}_p$	plastic shear strain rate (s^{-1})
γ_{SF}	stacking fault energy ($mJ.m^{-2}$)
h	period of Peierls potential (m)
h_{max}	maximum stable dipole height (m)
h_{min}	minimum stable dipole height (m)
κ	curvature of bowed dislocation segments (m^{-1})
k_b	Boltzmann's constant ($eV.K^{-1}$)
K_i	dislocation multiplication law prefactor of model i
l_{FR}	mean free path related to dislocation multiplication by creation of Frank-Read sources (m)
l_{obs}	mean obstacle spacing (m)
l_v	mean free path of dislocations between localized obstacles (m)
m_0	stress exponent of dislocation velocity (double-kink mechanism)
μ	shear modulus ($N.m^{-2}$)

μ^*	combined machine-specimen shear modulus (N.m^{-2})
n_j	number of jogs per unit volume ($^{-3}$)
ν	Poisson's ratio
ν_D	Debye frequency (s^{-1})
ν_{eff}	effective attack frequency (s^{-1})
Ω	atomic volume (m^3)
P_{kp}	probability of kink pair nucleation (m^{-1}.s^{-1})
P_{obs}	cumulative dislocation unpinning probability from localized obstacles
r	radius of curvature of bowed dislocation segments (m)
r_0	dislocation core radius (m)
$r_{a,i}^{(\alpha)}$	effective capture radius for annihilation of immobile dislocations, α character (m)
$r_{a,m}^{(\alpha)}$	effective capture radius for annihilation of mobile dislocations, α character (m)
r_c	capture radius of mobile dislocations in the extended model of Alexander & Haasen (m)
$\rho_f^{(\alpha)}$	forest density related to slip system α (m^{-2})
ρ_i	density of immobile dislocations (m^{-2})
$\rho_{i,60}$	density of immobile dislocations of 60° character (m^{-2})
$\rho_{i,s}$	density of immobile dislocations of screw character (m^{-2})
ρ_m	density of mobile dislocations (m^{-2})
$\rho_{m,60}$	density of mobile dislocations of 60° character (m^{-2})
$\rho_{m,eff}$	effective density of mobile dislocations, accounting for impurity pinning effects (m^{-2})
$\rho_{m,s}$	density of mobile dislocations of screw character (m^{-2})
ρ_m^*	steady-state value of the mobile dislocation density (m^{-2})
ρ_{obs}	density of localized obstacles on a glide plane (m^{-2})
ρ_t	total dislocation density (m^{-2})
S	dislocation motion activation entropy (eV.K^{-1})

S_k kink nucleation activation entropy (eV.K^{-1})

S_m kink migration activation entropy (eV.K^{-1})

T temperature (K)

τ applied resolved shear stress (N.m^{-2})

τ_0 dislocation velocity normalizing stress (double-kink mechanism) (N.m^{-2})

τ_c athermal unlocking stress from a random array of forest trees (N.m^{-2})

τ_{DG-PS} Transition stress from dissociated glide to perfect shuffle dislocations (N.m^{-2})

τ_{eff} effective stress (N.m^{-2})

$\tau_{eff}^{(p)}$ effective stress acting on the partial p (N.m^{-2})

τ_{eff}^{*} steady-state value of the effective stress (N.m^{-2})

τ_l dislocation locking stress by impurity I (N.m^{-2})

τ_{II} resolved shear stress at onset of stage II (N.m^{-2})

τ_{III} resolved shear stress at onset of stage III (N.m^{-2})

τ_∞ threshold stress for uncorrelated motion of the partials (N.m^{-2})

τ_{int} internal stress (N.m^{-2})

τ_P Peierls stress (N.m^{-2})

τ_u unlocking stress to free dislocations from impurities diffused at their core (N.m^{-2})

τ_{yp} upper or lower yield stress (N.m^{-2})

T_{BDT} brittle-to-ductile transition temperature (K)

t_f dislocation free flight duration time (s)

θ_c athermal dislocation unpinning angle from localized obstacles (rad)

θ_I hardening rate in stage I

θ_{II} hardening rate in stage II

ϑ thermal expansion coefficent (K^{-1})

θ_w angle of dislocation unpinning from a localized obstacle (rad)

T_m melting temperature (K)

t_m migration time of impurities back onto the dislocation core (s)

t_w waiting time of dislocations at a pinning obstacle (s)

U effective dislocation motion activation (internal) energy (eV)

U_d activation energy for kink overcoming of obstacles during propagation (eV)

U_k kink nucleation internal energy (eV)

U_m kink migration internal energy (eV)

v dislocation velocity in free flight ($m.s^{-1}$)

v_0 dislocation velocity prefactor (double-kink mechanism) ($m.s^{-1}$)

$\overline{v}$ mean dislocation velocity in the presence of localized obstacles ($m.s^{-1}$)

v_{cl} dislocation climb velocity ($m.s^{-1}$)

v_{dk} velocity of dislocation moving by the double kink mechanism ($m.s^{-1}$)

v_{jog} velocity of dislocation controlled by jog dragging ($m.s^{-1}$)

v_k kink velocity ($m.s^{-1}$)

W_m kink migration Helmoltz free energy (eV)

W_{RD} reconstruction defect migration Helmoltz free energy (eV)

X mean free path of kinks (m)

X_c critical dislocation length for length-independent velocity (m)

X_{max} effective maximum kink mean free path (m)

INTRODUCTION

This thesis is the result of more than four years research spent at the department of structural engineering of NTNU, developing on the mechanical properties of silicon materials.

CONNECTING THE DOTS

Elkem Solar, a subsidiary of Elkem (fully owned since 2011 by China National Bluestar), developed in the 2000's a new metallurgical process for purification of silicon. In 2006, then-owner Orkla invested 2.7 bn NOK in the construction of a new plant for production of Solar-grade silicon (SoG-Si) in Kristiansand, Norway. It was to be finished in 2009.

The silicon purification process chain developed by Elkem Solar includes three steps, starting from metallurgical silicon as a raw material: slag treatment, leaching, and directional solidification. There are several advantages to the use of SoG-Si produced by Elkem Solar: less energy consumption per unit weight relative to standard purification techniques, lower GHG emissions, and lower costs; the whole without detrimental effect on the final efficiency of the solar cell.

The DESA project (standing for Design and scale-up of Solar-grade silicon production) has concentrated exclusively on the directional solidification step and aimed both at gaining an understanding of the mechanical properties of multicrystalline SoG-Si materials, and at improving the process in order to reduce the occurence of ingot breakage, hence reducing costs. Residual stresses developing during ingot solidification and cooling have been identified as potentially critical drivers behind the occurence of material fracture, and the ability to quantify them depending on the process parameters could hopefully lead to their reduction.

This goal could be achieved by tackling three aspects:

1. Model the furnace and the silicon ingot during solidification and cooling, in order to extract the temperature fields and study the behavior of the silicon melt (for impurity segregation purposes).

2. Use the temperature field in a detailed model of the ingot & mould system, to compute the shape of the solidification front, melt behavior, and stress build-up due to thermal gradients.

3. Develop a relevant and accurate constitutive model for silicon to implement in the SINTEF finite element software. Owing to the particularities of the plastic behavior of silicon and its extreme sensitivity on temperature and strain rate, standard phenomenological models

fail at providing an accurate description of the mechanical response of this material. Moreover, no research had been done on the mechanical behavior of multicrystalline aggregates and the associated stress developments.

This Ph.D. work has concentrated on the latest aspect, developing a constitutive model for SoG-Si. **Choice has been made to concentrate almost exclusively on the plastic behavior of this material**; an alternative way to proceed would have been to focus exclusively on the fracture properties of SoG-Si at room temperature.

SoG-Si is almost pure silicon, although of higher impurity content than its electronic-grade counterpart (EG-Si). Loosing on purity allows for significant cost reductions, as the marginal purification cost increases with the number of 9's after the 99.9 % purity content figure. Solar PV applications do not require EG-Si to perform well, but electronic devices could not be reliable enough were they made of SoG-Si. Indeed, developing a SoG-Si production capacity benefits both electronic chips manufacturers and the PV industry, by increasing the amount of silicon available on the market (therefore lowering its price) and creating taylor-designed materials, adapted specifically to customers' needs.

At this point, it seems important to discuss the structural properties of SoG-Si materials. Depending on the crystallization process, SoG-Si can be grown either in a monocrystalline form (c-Si), or as multicrystals (mc-Si). Polycrystals (p-Si) are of no use for PV applications: as a rule of thumb, larger grains lead to a higher solar cell efficiency because grain boundaries are detrimental to minority carrier diffusion. This rules out p-Si as a suitable material for photovoltaics. The material produced by Elkem Solar is multicrystalline.

A multicrystal is simply an aggregate of several and rather large single crystals. Each constituent grain behaves obviously as a monocrystal, albeit of potentially inhomogeneous plastic properties owing to the irregular impurity and inclusion distribution that follows from 1) the presence of grain boundaries and 2) its thermomechanical history during solidification and cooling.

This means that the mechanical properties of a multicrystal ultimately come down to the behavior of each individual monocrystal. Understanding and modeling accurately the mechanics of intrinsic and extrinsic c-Si is therefore the most important step taken during this work.

Once an adequate model has been derived for c-Si, multicrystals can be studied by means of Finite Element analyses. This is done by reproducing the different crystals (with respect to geometry, grain orientation, impurity and dislocation content, etc.), aggregating them together by imposing compatibility requirements at the grain boundaries and observing the resulting behavior.

The logic followed in this thesis is the following:

1. Analyze the scientific knowledge about silicon mechanics, be it c-Si or mc-Si of intrinsic or extrinsic nature
2. Identify the existing models for c-Si, assess their accuracy and applicability, and improve them
3. Propose an entirely new model avoiding the pitfalls of traditional ones
4. Apply such a constitutive model to mono- and multicrystals

Following this order, the thesis is made up of four Parts. Annexes provide additional information and results.

Each Part can be read independently on the others, although frequent cross-referencing allows easy jumps between sections and chapters. This choice makes it easier for the reader to start directly from the Chapter of his or her choice, but has the drawback of implying some repetitions. These have been minimized as much as possible.

OUR KNOWLEDGE ABOUT SILICON MECHANICS

The first Part, the literature review, has been written in several steps. Started during the first year, it has been enriched with time, and covers numerous aspects of silicon mechanics:

- Crystallography, nanoscale and atomistic processes responsible for dislocation motion
- Macroscopic observations of intrinsic and extrinsic silicon behavior up to very large strains for the former type
- Properties of extrinsic crystals linked to the peculiar microprocesses taking place at dislocations
- Brittle-to-ductile transition properties and the traditional models attempting to explain it, elastic and fracture properties of silicon at room temperature

This Part constitutes arguably the most complete state-of-the-art written on the subject of silicon mechanics. This also means that it includes knowledge that is not used in the rest of the book. Meanwhile, all areas covered have been deemed interesting or relevant since they provide with a holistic view of the micromechanisms responsible for the brittle and plastic behavior of silicon materials. Hopefully, this state-of-the-art will be of great help to mechanicans willing to learn about the microscopic processes leading to plastic deformation of semiconductors.

If the sole purpose of reading Part i is to get enough background to understand the work detailed in the rest of the thesis, the sections and chapters indicated by a * can be disregarded.

BUILDING EXTENSIONS OF CLASSICAL MODELS

As mentioned in Part i, several models are readily available in the literature, the oldest of which derived in the late 1960's. Interestingly, its constitutive parameters have never been tested in wide temperature and strain rate ranges. What more, no systematic attempt to assess and compare the accuracy of various constitutive models had been performed. This is why Part ii starts with such an analysis.

Two questions are raised: firstly, is there any kinematic framework allowing any general loading situation rather than limiting simulations to conveniently oriented monocrystals? Secondly, is it possible to enrich existing models in order to improve their applicability in a wide range of temperature and strain rates?

Annex A is dedicated to the introduction of the powerful rate-dependent crystal plasticity framework (RDCP) used all throughout this thesis. Chapters 6 and 7 concentrate on the extension of the oldest constitutive model for silicon crystals. The case of extrinsic crystals is investigated as well. Ultimately, **the extended model of Alexander & Haasen derived in Part ii is the most suitable one for industrial applications**, owing to its optimal compromise between accuracy and numerical cost.

Note that kinematics and constitutive equations are not necessarily coupled: the constitutive equations have for sole goal to update the stress state and internal variables upon a given kinematical loading. The equations can consequently be used in a purely scalar model, or in more complicated frameworks such as RDCP. The advantage of the latter is a more realistic representation of actual micromechanical processes taking place, in effect allowing for couplings between the several "degrees of freedom" of a single crystal through the constitutive equations.

DERIVING A NOVEL CONSTITUTIVE MODEL

Improvements brought to the model of Alexander & Haasen extend its validity and accuracy, but do not correct its most fundamental shortcomings. Although physically-based, its equations still rely on gross approximations and combinations of micromechanisms.

Part iii constitutes the most important contribution of this Ph.D. work to materials science. A novel constitutive model for semiconductors is derived in this third Part, re-investigating methodically all model components.

Dislocation motion in these materials is usually considered to proceed by the double kink mechanism. This vision is enriched by adding the effect of localized obstacles and jog dragging. It is shown that contrary to the case of fcc materials, dislocation velocity in dislocated semiconductors is not likely to be governed by pinning onto forest obstacles. A model combining jog dragging and the double-kink mechanism is derived, including the transition between these two rate-limiting processes.

Physically-based constitutive equations are then derived and calibrated. Although of high complexity, the resulting model is shown to allow a correct reproduction of the stress-strain behavior of silicon with a very limited number of unknown parameters. In particular, both the stress overshoot, existence of single slip in stage I of intrinsic crystals and strong hardening in stage II are explained by jog dragging on secondary dislocations.

APPLICATIONS TO MONO- AND MULTICRYSTALS

The last Part seeks to show some applications of the constitutive models derived in this thesis, both to mono- and multicrystals, intrinsic or oxygen-contaminated. **Modeling of various bending tests, investigation of the effects of hard inclusions in a multicrystal and simulation of an ingot casting process give a wide outlook of the insights that can be gained from advanced constitutive models**.

Multicrystals are characterized by the development of inhomogeneous stress and dislocation density distributions with deformation. It is shown that the study of such materials cannot disregard the local crystallographic properties of the specimen, because of the stress increases due to grain misorientation or the presence of inclusions.

This Ph.D. thesis covers many aspects of silicon mechanics. Several constitutive models of various complexity are proposed; finite element models of industrially-relevant problems are available for further study. It is hoped that the results introduced in this book will lead to further research into modeling of the mechanical properties of semiconductors and SoG-Si in particular, ultimately helping the PV industry improve the quality of its products.

Part I

MECHANICAL BEHAVIOR OF SILICON MATERIALS: FUNDAMENTS AND MODELING

INTRODUCTION

The more we know about a given subject, the tougher it becomes for newcomers to gain the knowledge required to dive into research and produce new results. The mechanical behavior of silicon materials is a typical example of such a case. Silicon is a semiconductor, covalent crystal, presents analogies with fcc metals and can be produced with few or no intrinsic defects; not to mention the ability we have to control the concentration of impurities in the crystals. Intensive research has therefore been done on this "ideal" material since the 1950's with the aim of understanding what the deformation mechanisms are, not only in silicon but in a broader class of materials. The understanding we have of deformation mechanisms in covalent crystals is not limited to high-temperature plasticity by means of dislocation slip. The discovery of a sharp brittle-to-ductile transition delimiting clearly the ductile and brittle domains has sparked further experimental and modeling research. Observation of dislocations in deformed silicon crystals led the researchers to study the effects of dislocation dissociation on motion and multiplication mechanisms; the question of the structure of the dislocation cores has also mobilized several scientists, and found in the last decades a renewed interest with the explosion of computational power making first principle calculations affordable. Still, in spite of our constantly increasing knowledge about silicon mechanics, many questions remain unanswered.

Modeling the mechanical behavior of silicon presents several challenges. The first one met when coming to practical applications is the temperature range to consider. Because silicon is ductile only at high temperatures, above roughly 800°C, the experimental study of this material is uneasy. Germanium has consequently been often prefered to silicon as it has a lower melting temperature. Another issue arising at high temperatures is the question of additional thermally activated mechanisms affecting the material behavior. As a consequence, each crystallization method yields silicon materials with peculiar mechanical properties, influenced among others by the crystal orientations, the impurity nature, content and distribution, the initial dislocation density, etc.

The only way to effectively understand and ultimately model such an ideal -yet very quickly complicated- material is to dive deep into material physics. Modeling silicon materials is a cross-disciplinary task, gathering results coming from different communities and bridging an old gap between material physicists and mecanicians. The advent of crystal plasticity models in the 1980's marked a turning point for these two communities as microscopic processes could be implemented into macroscopic models

with the help of an efficient mathematical framework that is reviewed in an Annex of this book.

Unfortunately, there are still many solid physicists who do not know the powerful mathematical tools offered by solid mechanics; and inversely, there are too many mecanicians who often forget the fundamental mechanisms of plasticity. The present Part has the ambition of reviewing the current knowledge about the physics of silicon mechanics, and is therefore suited to mecanicians. It has been written with one idea in mind: providing with a holistic description of deformation mechanisms in silicon, citing as many relevant references as possible for each subject touched upon that the reader can refer to if needed. The bibliography is by no means exhaustive, but covers the most popular works published in the peer-reviewed literature.

Modeling the mechanical behavior of multicrystalline aggregates, widely used for photovoltaic applications, is the primary goal of the project. Unfortunately, little has been done on the mechanics of mc-Si. Its electrical properties, as well as the impurity distribution and related effects on the solar cell or wafer performance have been extensively studied, though. The work achieved on the mechanics of mc-Si concerns principally wafers at room temperature, and mainly experimental results have been derived. The attempts to model mc-Si materials are based on a monocrystalline and isotropic representation of the material, thus neglecting the influence of grain boundaries and grain orientations. Simulations of growth of mc-Si materials using these basic models provide with good qualitative values of stress and dislocation densities, but the quantitative agreement with experimental data is quite poor [Hässler 1999, Franke 2000, Franke 2002, M'Hamdi 2005, M'Hamdi 2006, Meese 2006]. The residual stresses in the material that are critical to fracture assessment can therefore hardly be predicted with such models. The lack of accurate constitutive model for silicon materials, and more generally for semiconductors is indeed the *raison d'être* of this thesis.

Any attempt to model multicrystals must be based on a solid understanding of the mechanical behavior of its constituent single crystals. A huge work has been carried out on monocrystalline silicon (c-Si) since the early 1950's. The present Part provides the reader with this knowledge. Its use for the development of a constitutive model is the goal of the following Parts of this book.

This literature review is articulated as follows. A description of the crystallographic and physical properties of Si is given in Chapters 1 to 3. A special emphasis is put on the properties of dislocations as these structural defects are the carriers of plastic deformation and are detrimental to the efficiency of solar cells. Chapter 1 is entirely dedicated to dislocation dynamics in the diamond cubic lattice when motion takes place by the double kink mechanism.

Exposing the micromechanisms of plasticity naturally leads us to their effects on the macroscopic behavior of intrinsic crystals deformed dynamically or in creep; Chapter 2 covers both the experimental results and the

basic constitutive models for silicon single crystals. These models are based on the dislocation theory and allow a fairly good description of the plastic behavior of Si at high temperatures in the early stages of deformation. Various improvements, limitations and extensions brought to the original model of Alexander and Haasen throughout the years are also introduced.

The influence of impurities both on the dislocation motion micromechanisms and on the macroscopic behavior of extrinsic single crystals is reviewed in Chapter 3. The current ways of modeling dislocation locking at high temperatures are described as well.

Looking at fracture mechanisms in silicon towards lower temperatures leads naturally to a survey of the brittle-to-ductile transition phenomena in Chapter 4. The elastic properties of silicon and fracture mechanisms at room temperature are discussed as well. Wafering of silicon ingots relies on fracture mechanisms in the brittle range that have been explored by means of indentation and will also be described in this last Chapter of Part i.

1

DISLOCATIONS IN SILICON

This Chapter is concerned with the microscopic scale of the deformation mechanisms. An introduction to the crystallographic structure of silicon crystals and of the dislocations in Section 1.1 is followed by the study of slip at high temperatures and low stresses: both the structure of dislocation cores and the models for dislocation slip in these temperature and stress conditions will be described (Sections 1.2.1 to 1.2.4, respectively). Finally, the case of dislocations at high stresses and low temperatures will be touched upon in Section 1.3. The present work is concerned by deformation mechanisms at high temperatures, so the literature survey will be more developed for the relevant case. Available reviews related to the subjects of this Chapter are [Alexander 1968, George 1987a, George 1987b, Siethoff 1999a, Rabier 2010] among others.

1.1 CRYSTALLOGRAPHY

1.1.1 *Lattice parameter and thermal expansion*

Silicon is a covalent material, having a diamond cubic structure with a face-cubic centered (fcc) Bravais lattice and a two atom basis, which means that the structure can be understood as superposition of two fcc lattices displaced by $\frac{a}{4}$ [111], as shown in Figure 1.1. The lattice parameter is found to be roughly $a \simeq 0.543$ nm at 293 K [Hull 1999]. Temperature has an effect on the lattice through the thermal expansion coefficient ϑ, given in its isotropic form by Eq. 1.1 valid in the whole temperature range from 120 to 1500 K [Okada 1984]:

$$\vartheta(T) = 3.725 \times 10^{-6} \left(1 - \exp\left(-5.88 \times 10^{-3}(T - 124)\right)\right) + 5.548 \times 10^{-10} T \left(\mathrm{K}^{-1}\right) \tag{1.1}$$

The exponential term becomes important at temperatures below 600 K, where a marked deviation from the linear behaviour of the coefficient starts. The engineering thermal strain $\varepsilon_\theta = \Delta l / l_0$ reads:

$$\varepsilon_\theta = \int_{T_0}^{T} \vartheta(T') \mathrm{d}T' \tag{1.2}$$

1.1.2 *Phase transformations**

The diamond structure is found at standard pressure of 1 bar and up to its melting temperature of 1684 K. When the hydrostatic pressure is increased, for example under the tip of an indenter, several phase transformations are recorded. The observation of dislocations generated under indentation showed that their structure and motion mechanisms are fundamentally different than at high temperatures. Instead of screw and 60° dislocations, it is 30° and short 60° segments that are observed on the {111} planes, independently of the axis chosen for indentation. It was thought that under the indenter, the stress conditions exceed the theoretical shear strength, leading to block slip [Hill 1974]. Nanoindentation leads to high hydrostatic and shear stresses in the specimen because of the stress concentration under the indenter tip; phase transformations can take place, and the final surface state depends on the loading and unloading parameters. If the loading is strong enough, a phase transformation is recorded. Upon unloading, a layer of either amorphous silicon (a-Si) or a mix of Si-III and Si-XII phases remain on roughly 0.5 µm, depending on the loading rate (a-Si is preferred for high loading rates above 1 mm/min). A layer of Si-IV is then present underneath, and thereafter a region of plastic deformation is found, where the deformation mechanisms are the one typical for low temperature and high stress conditions: deformation takes place through slip and twinning. Annealing at high temperature after indentation is required to go back to the diamond cubic structure [Kailer 1997].

Modeling of phase transformation in monocrystalline silicon dates back to the 1990's [Pérez 1995]. This phenomenon has since then led the development of an extensive literature. A recent review covering the different plastic behaviors of silicon surfaces has been written by [Zhang 2004]. At the scale of nanoindenters, the continuum theory cannot be applied any longer and to understand the results, molecular dynamics studies are required, using interaction potentials instead of continuum elastic constants.

Plasticity is then understood in a broader sense than the generation and motion of dislocations through the material. Any rearrangement of atoms is considered as a plastic transition of the material behavior. Different loading conditions, representing the events happening during silicon wafers manufacturing, have been explored by [Zhang 2000, Zhang 2001, Zhang 2004, Vodenitcharova 2004]: indentation, scratching, grinding and polishing. These different loadings lead to different material behaviors; Table 1.1 summarizes the results available in [Zhang 2000]. The dislocations generated during scratching and grinding, typical of dislocations produced during silicon machining, are of a special character because of their nucleation at high stresses (see Section 1.3). It has to be noticed that in these experiments performed at room temperature, despite local temperature increases under loads (up to 200 K) that enhance dislocation activity, the deformations caused by dislocations and planar defects are negligible compared to plasticity induced by phase transformation. Twelve different

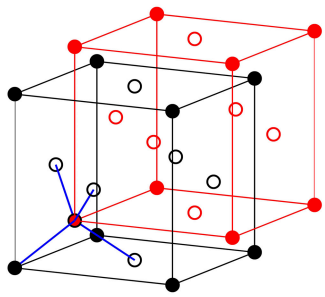

Figure 1.1: Sketch of the diamond structure. The two interpenetrating lattices are shown in black and red, respectively. Atom bonds form tetrahedrons (blue lines).

phases have been detected [Hull 1999], some of them being metastable and formed only during unloading, the loading rate being also of importance for the appearance of different phases.

The first phase transformation, from a diamond structure to an amorphous silicon, remains upon unloading after indentation only if the hydrostatic stress at full load reaches a critical threshold of 8 GPa at its maximum, and if the unloading rate is high [Kailer 1997]. The second transformation to crystalline silicon β-Sn is observed above 8 GPa, but is still found after unloading only if the hydrostatic stress reaches 15 GPa [Zhang 2004]. These results can be visualized in Figure 1.2. Molecular dynamics simulations using a Stillinger-Weber potential succeed in detecting the transformation to amorphous silicon (a-Si), but fail to model further phase transformations [Gannepalli 2001]. Only a mixed use of different potentials has recently allowed a satisfying simulation of the transformations up to β-Sn. At high stresses a mixture of different phases exist and is observed both experimentally and through simulations [Sanz-Navarro 2004]. It is doubtful whether these experiments can be used systematically for mc-Si, since they are done on oriented surfaces of a monocrystal, in controlled conditions, and without any interferences from the grain boundaries. The anisotropy effect is strong as demonstrated in [Garcia-Manyes 2005], and if the mechanisms are the same whatever the orientation of the crystal, their extent varies depending on the orientation of the surface. We concentrate in this work exclusively on the diamond cubic structure.

1.1.3 *Dislocation slip: the shuffle or glide set controversy**

Due to its analogy to the fcc structure, the primary glide planes in the diamond cubic structure are the $\{111\}$ closed-packed planes, associated to the $\langle 110 \rangle$ directions. This means that 12 primary slip systems are available for Si. The Burgers vector is of the $\frac{a}{2}\langle 110 \rangle$ type and has a magnitude of $b = 0.384\,\text{nm}$. The structure of dislocations in the diamond lattice has been

	Indentation	Scratching	Grinding	Polishing
Phase transf.	a-Si, β-Sn	a-Si	a-Si	a-Si, thin (nm)
Dislocations	no	yes	yes	no
Chemical reactions	no	no	yes	yes
Planar defects	yes	yes	no	no

Table 1.1: Characteristics of plasticity in silicon for different loading conditions [Zhang 2000].

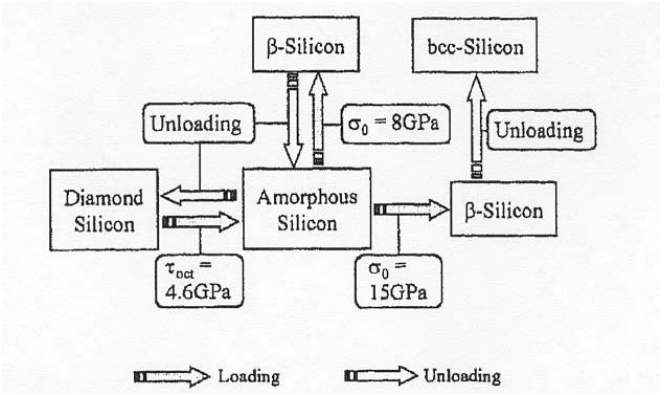

Figure 1.2: Thresholds for phase transformation and remaining phases after unloading [Zhang 2001].

discussed by [Hornstra 1958], who examined all the theoretically possible types of dislocation in this structure in addition to the classical screw and 60° dislocations often considered (see next Section).

A direct effect of the diamond structure on the close-packed planes {111} is to create a stacking sequence of the type *Aa Bb Cc*, *ABC* and *abc* being the sequences of the first and second fcc lattices respectively, see Figure 1.6. Indeed, the *aB* pairs are connected by an interplanar spacing which is one-third the one between *Aa* pairs. This means that dislocation glide *should* take place between the *Aa* planes, firstly because of the larger interplanar spacing (where the bonds are easier to break. This set is called *shuffle set*), and because dislocation motion in the shuffle set requires the breaking of one covalent bond, compared to three in the *glide set*. In which planes dislocations are located in silicon is more or less still debated, although the weight of evidence shifts the balance in favor of the glide set.

Energetic considerations [Duesbery 1996] showed that at low stresses the dislocations would lie preferentially in the glide set because the energy barrier for nucleating kink pairs on dissociated glide dislocations would be lower than the one for nucleating perfect shuffle dislocations. The difference between these two energy barriers would decrease up to $\tau_{DG-PS} \simeq 10^{-2}\mu$ where a transition from the glide to the shuffle set should take place (perfect dislocations are experimentally nucleated at 1.1-1.5 GPa at 573 K, above

the stress predicted by Duesbery & Joós [Rabier 2010]). This argument has been recently criticized in the light of experimental and theoretical results on the energy barriers for kink nucleation and migration [Pizzagalli 2008], and several alternative mechanisms have been proposed. The reason(s) for the transition from are still left unsolved. However, it is commonly assumed that dislocations at low stresses are in the glide set, whereas dislocations lie in the shuffle set at high stresses.

The case of standard stress conditions is dealt with in Section 1.2. At increasing stress, or when interactions between dislocations are weak or inexistent, dislocations lie in the Peierls valleys along the $\langle 110 \rangle$ orientations and form hexagonal loops with segments at 120° angles as shown in Figure 1.5. Two main types of perfect dislocations can be considered in such ideal conditions: screw and 60° dislocations, depending on the orientation of the dislocation line relatively to the Burgers vector [Hull 1999]. As will be seen, for energetic reasons glide dislocations are dissociated into Shockley partials following:

$$\frac{a}{2}[110] \longrightarrow \frac{a}{6}[2\bar{1}\bar{1}] + \frac{a}{6}[\bar{1}21] \tag{1.3}$$

Plasticity mechanisms vary depending on the temperature and/or stress, and several domains of dislocation motion can be identified. The next Section is devoted to the case of high temperature, low stress dislocation structure and slip.

The transition in the dislocation core structure from the glide to shuffle set occurs at much higher stresses, reachable at low temperature under confining hydrostatic pressure [Rabier 2001]. Shuffle dislocations are then observed to be perfect (non-dissociated). The prefered dislocation orientations at room temperature differ also from those observed at high temperatures. The case of low temperature, high stress deformation will be touched upon in Section 1.3.

1.2 SLIP OF DISSOCIATED DISLOCATIONS AT LOW STRESSES

We consider in this Section dislocation motion on their slip planes only. Other motion mechanisms such as climb or cross-slip, although observed in Si, are not reviewed in this Chapter.

Silicon is a covalent crystal, the bonds between atoms being strong and hard to break. Unlike in metals, the energy barrier opposing motion of a dislocation from one valley to the other requires breaking covalent bonds and is very high. Dislocation motion proceeds therefore by thermally activated nucleation and propagation of double kinks over the primary and secondary Peierls reliefs [Alexander 1968, Hirth 1992]. When internal stresses are low or inexistant, or when the applied stress is high, dislocations lie in the $\langle 110 \rangle$ oriented Peierls valleys and take the characteristic hexagonal shape mentioned above. However, the connection between each segment oriented in a $\langle 110 \rangle$ direction is not sharp, and bends can be observed at the corners of the hexagons both at rest and in motion [Gottschalk 1983a, Gottschalk 1983b], their curvature $\kappa = 1/r$ (r radius of the curvature) being determined by the line tension Γ compensating for the local stress level τ as is the case in metals:

$$\tau b = \Gamma \kappa = \frac{\Gamma}{r} \tag{1.4}$$

The line tension Γ depends on the local orientation of the dislocation segment [Hirth 1992] but is often given in the constant line tension approximation by $\Gamma = \mu b^2/2$ [Kocks 1975, Oueldennaoua 1988]. Eq. 1.4 implies that the radius of curvature of dislocation bends tends to increase as the local stress decreases, i.e. when the applied stress is low or when the internal stress strongly reduces the applied stress. At constant dislocation length this means that bowed segments take a larger fraction of the dislocation as the stress is decreased. Bowing of dislocations is indeed commonly observed in the literature (see e.g. [Alexander 1974, Nishino 1984, Oueldennaoua 1988, Yonenaga 1993]). Alexander puts forward the hypothesis that even curved dislocations follow a velocity rule similar to that valid for straight segments introduced in Section 1.2.2 [Alexander 1981a].

As will be seen in Section 1.2.4, a change in the dislocation velocity activation energy has been observed at very high temperatures, when additional diffusive mechanisms are active. The exact motion mechanisms of dislocations in Si as function of the stress and temperature are therefore somehow still subject to discussion. They vary with the deformation conditions (temperature, strain rate) and the structural state of the crystal (presence of defects such as impurities, high dislocation densities, etc.). Motion of bowed dislocations segments pinned at point defects will be described in Part II. We will consider in this Part only the case of straight dislocations.

1.2.1 *Dissociation of glide dislocations*

Stacking faults and partial dislocations

In these stress conditions glide between the *aB* planes (the glide set) allows dissociation of a dislocation into two Shockley partials separated by a stacking fault, a phenomena which cannot take place in the shuffle set under favorable energetic conditions [Ray 1971]. The Burgers vectors of the partials become of the $\frac{a}{6}\langle 112\rangle$ type, with a magnitude of $b_p = 0.222\,\text{nm}$ (see Eq. 1.3). The formation of a stacking fault can originate either from the removal of a double layer of atoms in the *Aa Bb Cc* sequence (a so-called intrinsic stacking fault), or by addition of such a double layer (the fault is then extrinsic), see Figure 1.6. The stacking fault can be thought of as a two-dimensional twin plane bounded by two one-dimensional defects, partial dislocations. A partial dislocation is however not a perfect one, its Burgers vector $\mathbf{b}_p$ not being a lattice vector.

Two or more partial dislocations can therefore combine to form a perfect dislocation. Since there is one partial on each side of the twin plane, each stacking fault is bounded by two partial dislocations separated by the stress-dependent *dissociation width*. The dissociation width at equilibrium d_0 is given by Eq. 1.5 where $A = 3.36 \times 10^{-7}\,\text{mN}$ characterizes the elastic interaction between the partials[1] [Alexander 1999], and γ_{SF} is the stacking fault energy:

$$d_0 = \frac{A}{\gamma_{SF}} \tag{1.5}$$

The ratio of the dynamic dissociation width to the equilibrium one d/d_0 depends on the applied stress, the stacking fault energy and the ration of mobilities between the partials [Wessel 1977]. In silicon, d is observed to vary[2] from 3.5 to roughly 13 nm.

The sum of the Burgers vectors of the partial dislocations gives the Burgers vector of a perfect dislocations as described above, or to the null vector (in the latter case, the result is no dislocation). Motion of a dissociated dislocation must proceed by simultaneous motion of both partials if the width of the stacking fault is to be kept constant. At low stresses the partials are hardly distinguishable from each other (Figure 1.3a). The stress acting on each partial being different because of their different Burgers vectors [Peach and Koehler 1950]. High stresses lead to a widening of the stacking fault and eventually separation of the partials, see Figure 1.3b. The threshold

1 As an approximation $A = \frac{\mu b_p^2}{2\pi}$ can be used, but the type of partials and crystal anisotropy should be accounted for.

2 Dissociation width depends on the character of the total dislocation, i.e. of its constituent partials [Ray 1971, Wessel 1977]. Using the mean dissociation width value can be found since metastable configurations exist due to the high Peierls potential in which the partials are moving. It is therefore more relevant to consider the most frequent dissociation width in the experimental distributions rather than the mean value. A discussion can be found in [Vanderschaeve 2005, Vanderschaeve 2007].

authors	γ_{SF} (mJ.m^{-2})	τ_∞ (MPa)
[Ray 1971]	51 ± 5	230
[Gottschalk 1979]	58 ± 6	260
[Föll 1979]	69 ± 7	310
[Sato 1981]	47 ± 5.7	210
[Alexander 1981b]	58 ± 6	260

Table 1.2: Intrinsic stacking fault energy of silicon measured by different authors.

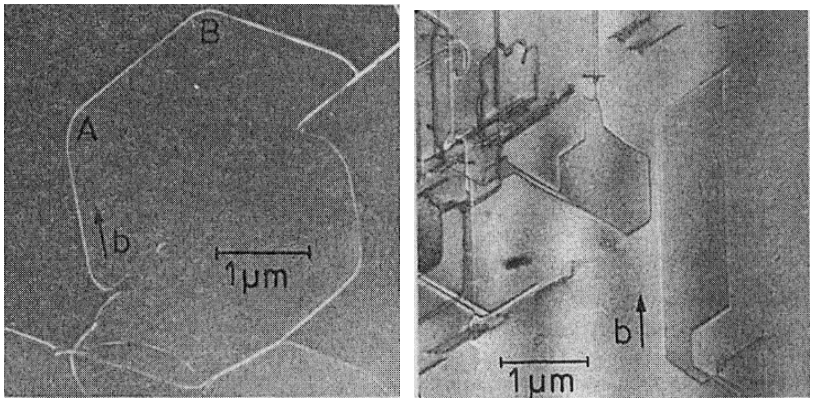

(a) Low stress, $\tau = 30$ MPa (b) High stress, $\tau = 350$ MPa $> \tau_\infty$

Figure 1.3: TEM observations of dislocation loops in Si crystals [Gottschalk 1983a].

stress delimiting those low- and high-stress ranges for separated motion of the partials is given by:

$$\tau_\infty = \frac{\gamma_{SF}}{b_p} \tag{1.6}$$

γ_{SF} being the stacking fault energy of silicon. The value obtained is $\tau_\infty \simeq 300$ MPa, see Table 1.2[3].

Although Hornstra initially assumed that screw dislocations were unlikely to dissociate into Shockley partials, it has been found that all types do (not only screw and 60° segments as discussed here, but also edge dislocations [Ray 1971, Ourmazd 1981], see Figure 1.4). In silicon the intrinsic type of stacking fault seems to be prefered, although both types can be observed on certain dislocation characters [Gomez 1975, Wessel 1977]. Dislocations have moreover been found to dissociate both at rest and when moving [Gomez 1977]. A screw dislocation dissociates in the glide set into two 30°

3 [Föll 1979]: this value is obtained from observations of stacking faults in double ribbons. Results obtained on isolated dislocations give $\gamma_{SF} = 60 \pm 10$ mJ.m^{-2}, in closer agreement with other authors. See [Alexander 1981b].
[Sato 1981]: γ_{SF} for 60° dislocations. n-type silicon crystals (doped with P) and CZ crystals exhibit lower mean stacking fault energies.

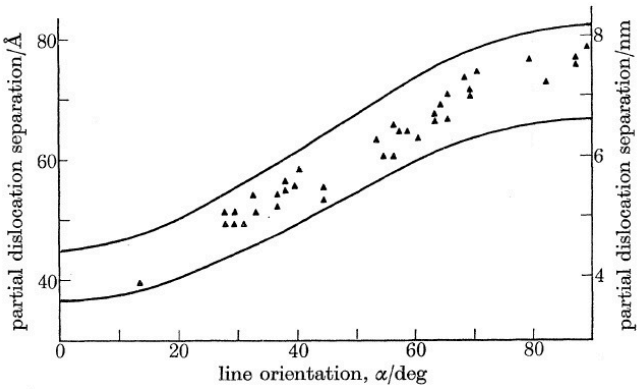

Figure 1.4: Dissocation width as a function of the dislocation line orientation [Ray 1971].

partials, whereas a 60° dislocation splits into one 30° and one 90° (edge) partial dislocation. In addition, a 60° dislocation can be decomposed either in a 30°-90° or in 90°-30° couple depending on which partial moves into the intrinsic crystal, implying two types of 60° dislocations characterized by the type of their leading and trailing partials. See Figure 1.5 for an illustration of the different types. These different partials have different mobilities due to their core configurations, affecting the velocity of the dissociated dislocations [Wessel 1977, Gottschalk 1979], see Section 1.2.3.

Constrictions are observed along the dislocation lines, where both partials merge together [Ray 1971, Gomez 1975, Gottschalk 1979]. Such constriction points might favor cross-slip of the screw dislocations during plastic deformation. Dislocations in pure crystals exhibit less constrictions than in impurity-contaminated silicon samples [Gottschalk 1979], indicating that the presence of impurities may affect the motion mechanisms. The role of electrically active impurities on the dissociation width can be understood as their effect on the partial cores, then the development of a Coulomb force would explain variations of the stacking fault energy in doped crystals [Hirsch 1980, Sato 1981, Ohno 2010].

The definition of a first stress dependency of dislocation motion stems from the evaluation of τ_∞. At applied shear stresses $\tau < \tau_\infty$ it is necessary to move both partials simultaneously (at least on a macroscopic scale) in order to set the dissociated dislocation into motion. We will call dislocation motion on its glide plane and in these stress conditions *slip at low stresses*. At $\tau > \tau_\infty$ each partial can then move independently of each other and this regime will be refered to as *slip at high stresses*. We will see later that additional stress domains for dislocation motion can be defined with the help of such stress thresholds, often conditionally reached depending on the temperature. Prior to the examination of dislocation slip, a brief review of the knowledge about the glide dislocation core structure is given.

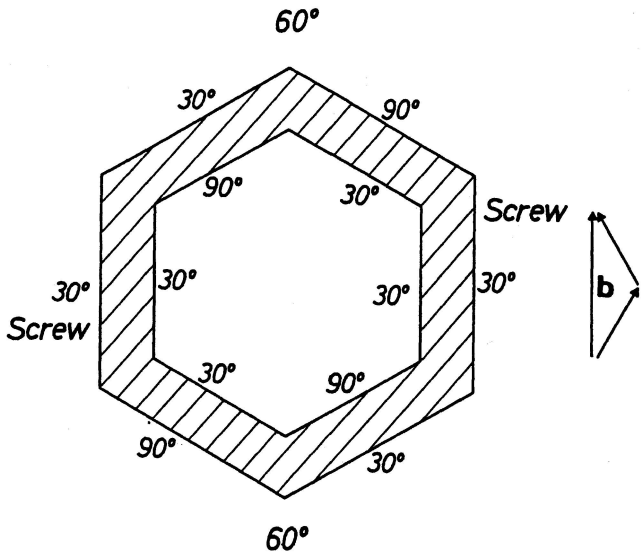

Figure 1.5: An ideal hexagonal dislocation loop in silicon, and the partials of each segment [Sumino 1999a].

*Dislocation core configuration in the glide set**

Knowledge of the core structure of dislocations in silicon is of importance for understanding several characteristics of their motion, such as the effect of doping on dislocation velocity or the influence of the secondary Peierls potential as discussed in Section 1.2. The discovery of dislocation dissociation led in the late 1970's and early 1980's to some speculations [Hirsch 1980, Marklund 1980] about the possible core structure of the partials. The advent of atomistic simulations applied to silicon has been a significant step in the understanding of dislocation motion mechanisms [Bulatov 1995]. The precise mechanisms of dislocation motion appear indeed much more complicated than initially thought. In addition to the complexity raised by the appearance of perfect shuffle dislocations at very high stresses revealed both by theoretical and experimental arguments (see Section 1.3), the case study of dissociated glide dislocations has revealed the existence of various types of core reconstructions, numerous types of kinks, reconstruction defects, etc. A brief overview of the complexity of this research area is given below. As will be seen, the calculated values of kink formation and migration energies, as well as the formation energy of defects on partials vary significantly between the groups, sometimes in clear contradiction with experimental results. These discrepancies come from the use of different modeling methods and potentials between atoms. For example the group of Nunes *et al*. uses total-energy tight binding (TETB) calculations.[Bulatov 1995] used initially a Stilling-Weber potential that was shown not to be adequate for 90° partials, and refer later [Justo 1999] to an

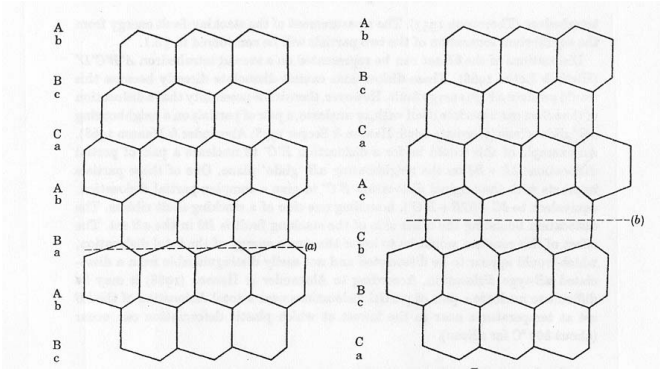

Figure 1.6: Two types of stacking faults: intrinsic fault (left), and extrinsic fault (right) [Ray 1971].

EDIP potential. See [Bulatov 2001b] for a review of the results obtained by different methods. Note that the energy barriers computed in the following paragraphs are the Helmoltz free energies at 0 K i.e. the internal energies alone; the barriers at finite temperatures must account for the entropy contribution (see e.g. Section 1.2.3).

PARTIAL RECONSTRUCTION Reconstruction of the core allows for a lowering of its energy by binding together pairs of atoms belonging to the same plane and having dangling bonds. Note that this differs from the usual binding involving one Si atom from each layer (e.g. a and A); the array of reconstructed bonds forms a one-dimensional superlattice along the core. Reconstructing a dislocation core lowers its energy and thermodynamically favors its existence, but propagating a kink in a reconstructed core is on the other hand more difficult since it requires breaking the reconstructed bonds at each interatomic distance [Bulatov 1995]. Figure 1.7 shows an example of reconstructed and unreconstructed partials. Table 1.3 summarizes the energy E_{rec} gained by reconstructing the different partials. Most of the core energy comes from the bond distortions of the reconstructed cores [Nunes 1998a]. Simulations agree on the systematic reconstruction of the 30° partial as shown in Figure 1.7. Bond reconstruction leads to a doubling of the period along the dislocation line from b to $2b$.

The case of the edge partial is more tricky as a double-period (DP) reconstruction seems energetically very close to a simpler, single-period (SP) reconstruction [Nunes 1998b, Bulatov 2001b], the small energy difference at 0 K (Table 1.3) actually increasing with temperature in favor of the DP reconstruction [Miranda 2003]. See Figure 1.8 for a schematic of the two types. The splitting of a SP into a DP structure actually means that kinks on the 90° partial are dissociated, doubling the period as in the case of the reconstructed 30° partial. In the same way that dissociation of dislocations in silicon lower their energy in the glide set, dissocation of kinks eases their propagation along the dislocation and increase the velocity of the 90°

Partial type	E_{rec} (eV.b^{-1})
30°	1.04
SP 90°	0.42
DP 90°	0.62

Table 1.3: Reconstruction energy E_{rec} for 30 and 90 partials in Si expressed in eV per bond [Bulatov 2001b].

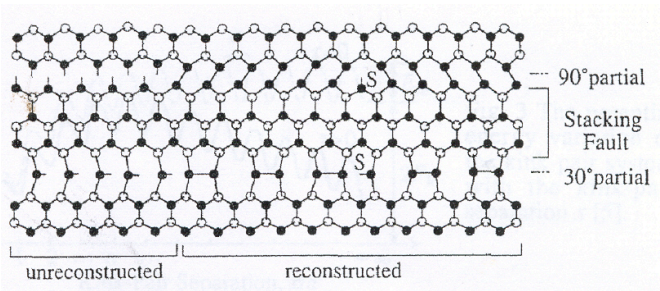

Figure 1.7: Core structure of the 30° and 90° partials in silicon, view normal to the (111) plane. Atoms above the slip plane in black, atoms below in white. No kinks are present. The cases of unreconstructed and (typical) reconstructed partials are shown for each type. Solitons on reconstruction defects (DSD on the 90° partial, PSD on the 30° one) are indicated by *S* [Maeda 1994].

partials. It is unclear whether kink dissociation on DP 90° partials actually takes place in Si [Bulatov 2001b].

RECONSTRUCTION DEFECTS Reconstruction defects[4] (RD) exist when one dangling bond is left at the otherwise reconstructed core. These sites are consequently electrically active. RDs on 30° partials are called *phase-switching defects* (PSDs) [Nunes 1998a]. By analogy to the PSDs on 30° partials, defects at the core of a SP 90° partial are called *direction-switching defects* (DSDs) because they delimit the two degenerate ground states of the SP configuration. Examples of PSDs and DSDs can be found in Figure 1.7. Both PSDs and DSDs have rather high formation energies but are found to migrate easily along the dislocation lines (see Table 1.4) [Nunes 1998a]. Recent work raises the potential importance of PSDs in generating and propagating kink pairs [Choudhury 2010]. The dynamical aspect of dislocation motion being computationally prohibitive (MD simulations require models tens of thousands of atoms large over long simulation time), most studies have until now considered only static configurations.

4 we use here the terminology of [Nunes 1998a]. Other authors [Hirsch 1980, Justo 1999] use the denomination antiphase defects (ADP), others call them solitons [Heggie 1983].

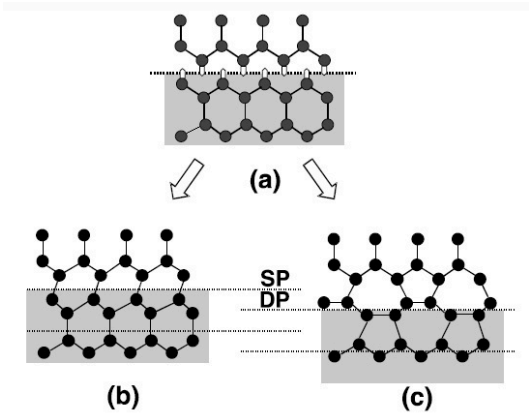

Figure 1.8: Example of core reconstructions of a 90° partial. (a) unreconstructed core (b) Single-period reconstruction (c) Double-period reconstruction [Bulatov 2001a].

RD	F_{RD}		W_{RD}
	[Nunes 1998a]	[Justo 1999]	[Nunes 1998a]
PSD	1.32	0.49	0.3
DSD	1.45	0.65	0.03

Table 1.4: Formation F_{RD} and migration W_{RD} energies (expressed in eV) of reconstruction defects in Si according to different authors.

Partial	Kink type	U_k	U_m	U_k	U_m	U_k	U_m
		[Nunes 1998a]		[Justo 1999]		[Oyama 2004]	
30°	LK	0.35	1.53	0.65	1.46	0.61	1.35
30°	RK	1.24	2.1	0.39	0.89	0.61	1.47
SP 90°	LR/RL	0.12	1.62	0.7	0.62	-	-

Table 1.5: Formation and migration energies of pure kinks in Si according to different authors (in eV). The definition of left and right kink for the SP 90° partial differs from the usual meaning, see e.g. [Nunes 1998a]. Methods employed: [Nunes 1998a] TBTE, [Justo 1999] EDIP, [Oyama 2004] DFT.

KINK TYPES Different types of kinks are present on each partial, possibly in combination with PSDs or PSDs in the case of a 30° or 90° partial[5], respectively. Each kink or kink+RD type has its own formation and migration energy (see Figure 1.9 for the simple example of pure left and right kinks). Table 1.5 summarizes the results given by various groups using different methods. It can be seen that strong disagreements can be found. Experimental results give $F_k \simeq 0.7\,\text{eV}$ and $W_m \simeq 1.2\,\text{eV}$ (see Section 1.2.4). It is interesting to note that even some methods reputed to be accurate (DFT) applied to the SP 90° partial can give values extremely far from the experimental ones, with $U_k = 0.04\,\text{eV}$ and $U_m = 1.09\,\text{eV}$ [Valladares 1998].

Kink propagation along the dislocation line proceeds in the 30° partial by an alternance between two stable configurations $2b$ away from each other, with the passage through a metastable kink configuration in between [Justo 1999, Oyama 2004], both for left and right kinks. The calculated migration energy for this process varies with the method employed but remains high because of a double bond switching. Propagation of kink+RD complexes exhibits lower energy barriers [Bulatov 2001b], high temperature and stress conditions influence considerably the dynamic properties of kink motion [Wang 2008]. A similar double bond switching mechanism can be deduced in the SP 90° partial. A recent review of the knowledge about the formation and motion of complexes on SP 90° partial can be found in [Valladares 2007].

Adding to these few points the case of the DP 90° partial, the overall picture becomes highly complex [Bulatov 2001a], and we will not go further into atomistic details of dislocation motion mechanisms. This research area is still active; of interest for the present work is the actual strong partial reconstruction that can explain the difference in partial velocities mentioned in Section 1.2.3 and the influence of dopants on dislocation motion reviewed in Section 3.2.

5 A kink+DSD complex on a 90° partial is unstable or weakly stable depending on the method, the DSD detaching from the kink very fast [Nunes 1998a, Bulatov 2001b].

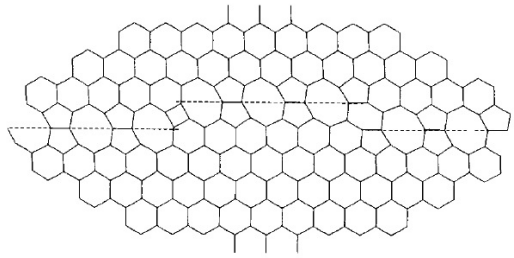

Figure 1.9: Early work did predict the existence of different types of kinks on each partial. Here the example of "pure" left and right kinks on a 30° partial [Marklund 1984] (see e.g. [Nunes 1998a] for other types associated to phase switching defects).

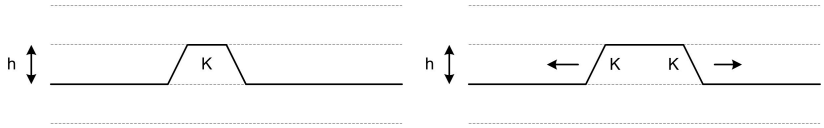

(a) Nucleation of one kink along the line (b) Propagation of two kinks along the line

Figure 1.10: Motion of a dislocation line by nucleation and propagation of kinks. h is the potential period.

1.2.2 *Motion of perfect dislocations in covalent crystals*

For more details about the kink motion mechanisms, the reader is refered to e.g. [Kocks 1975, Nagdornyi 1988, Hirth 1992, Caillard 2003]. The case of perfect, undissociated dislocations is considered first, before generalization of the model to dissociated configurations.

The double kink nucleation and propagation model

It has been long assumed and confirmed by atomic simulations that dislocation glide in semiconductors proceeds by formation of double kinks of height h, followed by their sideways migration along the dislocation line. See Figure 1.10 for a depiction of nucleation of a single or double kink in a planar view. Propagating kinks on partials have been indeed experimentally observed [Kolar 1996]. The primary *Peierls potential* that has to be overcome for nucleation $E_P(y)$ depends on the position y of the dislocation in the plane. Assuming that the potential has a sinusoidal form[6], $E_P(y)$ is given per unit length of the dislocation by:

$$E_P(y) = \frac{\tau_P b \lambda}{2\pi}\left(1 - \cos\left(\frac{2\pi}{\lambda}y\right)\right) \tag{1.7}$$

6 A sinusoidal potential is a good model for fcc metals. The Peierls potential in covalent crystals is much sharper.

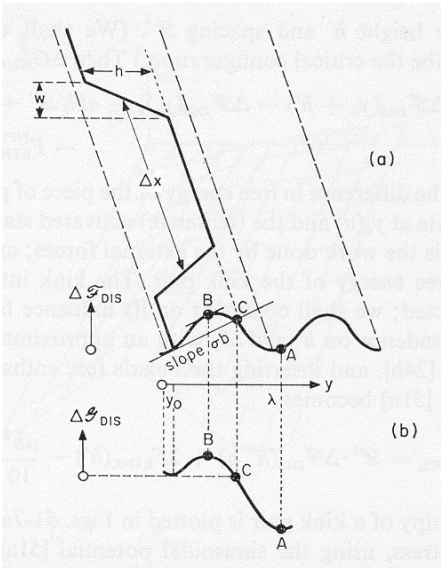

Figure 1.11: Thermally activated nucleation of a kink pair of height h and length Δx in the primary Peierls potential ($\tau < \tau_P$). The kink width w is assumed small compared to Δx [Kocks 1975].

where $\tau_P = \max\left(\frac{1}{b}\frac{\mathrm{d}E_P}{\mathrm{d}y}\right)$ is the *Peierls stress* and λ the period of the potential, taken as equal to $h = \frac{\sqrt{3}}{2}b$ in the following[7]. The *Peierls energy* is defined as the amplitude of the Peierls potential, in the case of a sinusoidal potential it is $E_P = \frac{\tau_P b \lambda}{\pi}$. Different shapes of the potential can be chosen, see e.g. [Kocks 1975]. In covalent crystals the Peierls stress is very high, of the order of $10^{-2}\mu$. This means that the transition from thermally activated motion of dislocations to a viscous mode in covalent crystals can take place only at very high stresses $\tau > \tau_P$ of the order of a couple of GPa. The viscous mode of motion is obviously not considered in this work. At low stresses, the high primary Peierls barrier can therefore be overcome only by means of thermal activation [Alexander 1968, Kocks 1975, George 1987a]. The probability P_{kp} of nucleation of a kink pair per unit dislocation length and per unit time is given by Eq. 1.8:

$$P_{kp} = \nu_D \frac{b}{x_c^2} \exp\left(-\frac{F_{kp}^{(c)}(\tau)}{k_b T}\right) \tag{1.8}$$

with ν_D is the attack frequency, usually taken equal to the Debye frequency of silicon ($1.34 \times 10^{13}\,\mathrm{s}^{-1}$ [Dolling 1966]), x_c^{-1} is the density of nucleation sites for kink pairs, $F_{kp}^{(c)}(\tau)$ is the stress-dependent critical free energy for nucleation of the kink pair and k_b is Boltzmann's constant ($8.617 \times$

7 This approximation is valid at low stresses with respect to the Peierls stress, $\tau \ll \tau_P$. For the sinusoidal potential, $h/\lambda = \sqrt{1 - \sqrt{\tau/\tau_P}}$ (see [Kocks 1975]).

10^{-5} eV.K^{-1}). Assuming the kinks have a rather low mobility once they have reached their final height h, the dislocation velocity reads:

$$v_{dk} = P_{kp} X h \tag{1.9}$$

where X is the mean free path of kink pairs before annihilation or disappearance. A single kink crosses a distance $X/2$ in a time $\Delta t = X/(2v_k)$ with v_k the kink velocity. The time for kink nucleation along this segment is $2/(P_{kp}X)$. The propagating kink will therefore annihilate by collision with another one of opposite sign if $X > X_c$ with

$$X_c = 2\sqrt{\frac{v_k}{P_{kp}}} \tag{1.10}$$

X_c is the minimum dislocation length required for the dislocation to move in the collision (or *length-independent*) mode. For $X < X_c$ the propagating kinks are stopped or disappear at the dislocation ends and the velocity is *length-dependent*. Eqs. 1.9 and 1.10 give immediately the dislocation velocity in both modes:

$$v_{dk} = \begin{cases} P_{kp} L h \text{ if } L \leq X_c \\ 2h\sqrt{P_{kp} v_k} \text{ if } L > X_c \end{cases} \tag{1.11}$$

The next step is to derive the probability for kink pair nucleation P_{kp} and the kink velocity v_k. Dislocation motion proceeds therefore by the overcoming of two barriers: nucleation and extension of a stable kink pair over the linear primary Peierls relief affecting P_{kp}, and subsequent propagation of this kink pair until it has reached a stable configuration (entering into v_k). The question of which process governs dislocation motion in silicon depends on the relative importance of the activation energies for these two steps. Two models are competing for modeling the kink mobility: either it is governed by the presence of random localized obstacles along the line, or kink diffusion in the secondary Peierls potential controls their velocity. Both models are described in the following.

Kink mobility controlled by random obstacles

If there was very early an agreement on the presence of a strong primary Peierls potential keeping the dislocation lines straight and hindering their motion, it was believed for a long time that the kink pair propagation along the Peierls valley, leading ultimately to a forward motion of the whole dislocation line, would be impeded by the presence of impurities or small obstacles of energy barrier U_d, whereas the intrinsic core structure of dislocations would not play a significant role. Figure 1.12a shows the shape of the energy of a kink pair at low stresses as function of its separation Δx. Models neglecting the secondary Peierls potential W_m have been suggested accordingly [Celli 1963, Möller 1978], other thermally surmountable obstacles such as point defects at the core of the partials (intrinsic

or impurities), jogs and constrictions along the lines impeding kink motion [Alexander 1981a]. The critical kink pair nucleation free energy $F_{kp}^{(c)}$ corresponds to the maximum of the kink pair free energy $F_{kp}(\Delta x)$. F_{kp} depends on the single kink nucleation free energy F_k, the elastic interaction energy between the kinks[8] $F_{int}(\Delta x)$ and the work done by the applied stress (Eq. 1.12).

$$F_{kp}(\Delta x) = 2F_k - \frac{\mu h^2 b^2}{8\pi\Delta x} - hb\Delta x\tau \tag{1.12}$$

Assuming that the kink separation is large compared to their width, it is possible to derive the kink concentration c_k along the dislocation line at zero stress:

$$c_k = \frac{1}{l}\exp\left(-\frac{F_k}{k_b T}\right) \tag{1.13}$$

with l the shortest crystal-symmetry repeat distance along the line [Hirth 1992]. The derivation of $\mathrm{d}F_{kp}/\mathrm{d}\Delta x = 0$ under a small[9] applied stress τ yields $F_{kp}^{(c)}$ [Caillard 2003]:

$$F_{kp}^{(c)} = 2F_k - hb\sqrt{hb\frac{\mu\tau}{2\pi}} \tag{1.14}$$

This maximum of interaction energy is reached for[10] $\Delta x = x_c = \sqrt{\frac{hb\mu}{8\pi\tau}}$ (see Figure 1.12). If the mobility of kinks were governed by random localized obstacles along the Peierls valley of strength $U_d \gg W_m$ the kink velocity would be $v_k \propto \exp\left(-\frac{U_d}{k_b T}\right)$. Inserting Eq. 1.14 into Eq. 1.8 and the result into Eq. 1.11 gives an effective activation energy for dislocation motion $F = (F_{kp}^{(c)} + U_d)/2$ in the length-independent mode and $F = F_{kp}^{(c)}$ in the length-dependent one. According to [Celli 1963] P_{kp} itself would be altered by the presence of obstacles.

If weak obstacles along the dislocation line are inexistent or have a small effect on determining dislocation velocity, the mean free path of kinks is rather controlled by the secondary Peierls potential, especially if propagation of a kink involves the breaking and reconstruction of strong covalent bonds. This is what the model of Hirth & Lothe accounts for.

The influence of the secondary Peierls potential

The thermally activated breaking of bonds at the core allowing propagation of kinks over a length l is characterized by the activation free energy W_m,

8 the corresponding term in [Hirth 1992] (in the isotropic approximation) includes the effect of Poisson's ratio on $F_{int} = -\frac{\mu h^2 b^2}{8\pi\Delta x}\frac{1+\nu}{1-\nu}$. The correction term is of the order of unity in Si (~ 1.5). We follow here the approximation of [Caillard 2003].

9 This approximation of F_{kp} is valid at small stresses in metals only for $\tau \ll \frac{\tau_p}{2\pi^2}$. At higher stresses the Coulomb interaction does not yield adequate results. [Celli 1963] assumed the kink width to be large with respect to b, the kink pair looking like a bulge rather than sharp kinks such as in Figure 1.10.

10 x_c is the kink pair width for which the kink pair energy is maximum. This is not the stable kink pair width x^* [Hirth 1992]. x^* is found by solving $F(x^*) = F^* = F_{kp}^{(c)} - k_b T$, so that the probability of kink pair shrinking by thermal fluctuations is small for $\Delta x > x^*$.

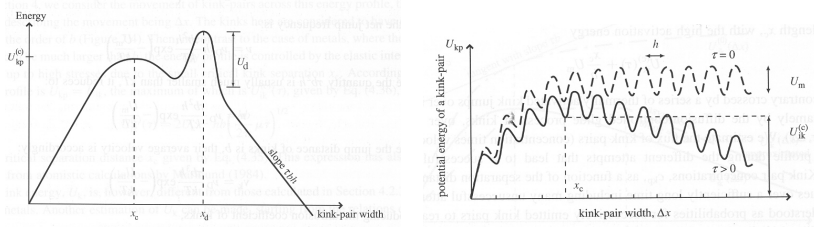

(a) Model of [Celli 1963]: presence of obstacles of height U_d.

(b) Model of [Hirth 1992]: secondary Peierls potential U_m.

Figure 1.12: Energy profiles for kink pair nucleation and propagation under stress according to different authors [Caillard 2003].

the total energy profile for kink-pair nucleation being shown in Figure 1.12b. The velocity of kinks is given by the rate of successful jumps over the barrier of height W_m under an applied stress τ providing the work τlbh during each jump of distance[11] l:

$$v_k = l\nu_D \sinh\left(\frac{\tau lbh}{k_b T}\right) \exp\left(-\frac{W_m}{k_b T}\right) \simeq \nu_D \frac{\tau l^2 bh}{k_b T} \exp\left(-\frac{W_m}{k_b T}\right) \qquad (1.15)$$

The probability for kink-pair nucleation P_{kp} is given[12] by Eq. 1.16, as derived by [Hirth 1992] or, using an alternative method, by [Caillard 2003]:

$$P_{kp} = \nu_D \frac{\tau hb}{k_b T} \exp\left(-\frac{F_{kp}^{(c)}(\tau) + W_m}{k_b T}\right) \qquad (1.16)$$

with $F_{kp}^{(c)}$ given[13] by Eq. 1.14. The two motion regimes can be distinguished depending on the length of the dislocation segment. The critical segment length X_c reads:

$$X_c = 2l \exp\left(\frac{F_{kp}^{(c)}(\tau)}{2k_b T}\right) \qquad (1.17)$$

11 This distance is the crystal periodicity along the dislocation line. It is usually considered to be equal to the magnitude of a perfect Burgers vector $l = b$. Atomistic simulations tend to show that $l = 2b$ (see Section 1.2.1).

12 Note that the derivation of P_{kp} is the trickiest part of the model. An alternative model yielding a sublinear stress dependence of v was used in [Iunin 2001], although its results do not fit the experimental data.

13 contrary to the model of [Celli 1963], in covalent crystals the kink width is of the order of the magnitude of one Burgers vector, and elastic interaction dominates the energy profile also at high stresses. F_{kp} can then be used in the whole stress domain. See e.g. [Caillard 2003].

and the velocity of a perfect dislocation in a crystal with high Peierls potential depends on its length X as follows:

$$v_{dk} = \begin{cases} \nu_D \frac{\tau h^2 b X}{k_b T} \exp\left(-\frac{F_{kp}^{(c)}(\tau)+W_m}{k_b T}\right) & \text{if } X \leq X_c \\ 2\nu_D \frac{\tau h^2 b l}{k_b T} \exp\left(-\frac{\frac{1}{2}F_{kp}^{(c)}(\tau)+W_m}{k_b T}\right) & \text{if } X > X_c \end{cases} \tag{1.18}$$

Note that these equations should include the entropy terms of the activation (Helmoltz) free energies [Hirth 1992]. $F_{kp}^{(c)}$ and W_m can be decomposed into internal energy and entropy terms, respectively $F_{kp}^{(c)} = 2(U_k - TS_k)$ (the entropy term in $F_{kp}^{(c)}$ coming solely from $2F_k$) and $W_m = U_m - TS_m$. If the activation entropies do not depend on the temperature, the temperature-dependent exponential terms in Eqs. 1.18 identified from "macroscopic" experiments do actually incorporate only U_k and U_m. The effective activation energy for dislocation motion F is equal to $\frac{1}{2}F_{kp}^{(c)} + W_m$ or $F_{kp}^{(c)} + W_m$ depending on the length regime.

This model is valid for perfect (undissociated) dislocations. The presence of a stacking fault and the elastic interaction between the partials induce additional internal stresses that must be accounted for in the derivation of the velocity of dissociated dislocations. The influence of the partial Burgers vector is also discussed in the following.

1.2.3 *Motion of dissociated dislocations in Si**

Impacts of dissociation on the double kink model

Partial dislocations have a Burgers vector of magnitude $b_p = \frac{b}{\sqrt{3}}$ and the theory for perfect dislocations introduced previously remains valid for each partial. The stress they feel is however influenced by the presence of the stacking fault ribbon between them, so an effective stress $\tau_{eff}^{(p)}$ (see below) must be substituted to τ in the equations of Section 1.2.2. This gives for the kink velocity of partials:

$$v_k^{(p)} = \nu_D \frac{\tau_{eff}^{(p)} l^{(p)2} h b_p}{k_b T} \exp\left(-\frac{W_m^{(p)}}{k_b T}\right) \tag{1.19}$$

where $l^{(p)}$ is the crystal periodicity along the partial. The kink pair nucleation probability on the partial $P_{kp}^{(p)}$ reads:

$$P_{kp}^{(p)} = \nu_D \frac{\tau_{eff}^{(p)} h b}{k_b T} \exp\left(-\frac{F_{kp}^{(c,p)}(\tau_{eff}^{(p)}) + W_m^{(p)}}{k_b T}\right) \tag{1.20}$$

The kink pair interaction energy is affected by the presence of the stacking fault. With some approximations $F_{kp}^{(p)}$ differs from F_{kp} only by a term proportional to Δx, that is, the additional term can be aggregated to the effects of the applied stress τ. The definition of the effective stress $\tau_{eff}^{(p)}$ comes from this manipulation. The critical kink pair nucleation free energy becomes

$$F_{kp}^{(c,p)} = 2F_k^{(p)} - hb\sqrt{hb\frac{\mu\tau_{eff}^{(p)}}{2\pi}} \tag{1.21}$$

and finally the partial velocity reads, depending on the length regime (h replaced by its value):

$$v_{dk}^{(p)} = \begin{cases} \nu_D \frac{3}{4} \frac{\tau_{eff}^{(p)} b^3 X}{k_b T} \exp\left(-\frac{F_{kp}^{(c,p)} + W_m^{(p)}}{k_b T}\right) & \text{if } X \leq X_c^{(p)} \\ \nu_D \frac{3^{3/4}}{2} \frac{\tau_{eff}^{(p)} b^3 l^{(p)}}{k_b T} \exp\left(-\frac{\frac{1}{2}F_{kp}^{(c,p)} + W_m^{(p)}}{k_b T}\right) & \text{if } X > X_c^{(p)} \end{cases} \tag{1.22}$$

The final step is to determine the velocity of the total dislocations given the ones of its constituent partials. Let us distinguish between the leading and trailing partials. Their velocities are noted $v_{dk}^{(l)}$ and $v_{dk}^{(t)}$ respectively. The effective stress acting on each partial depends on the resolved shear stress on each partial obtained by the Peach-Koehler law [Peach and Koehler 1950], the stacking fault energy and the elastic interaction stress τ_i:

$$\begin{aligned} \tau_{eff}^{(l)} &= \tau^{(l)} - \frac{\gamma_{SF}}{b_p} + \tau_i \\ \tau_{eff}^{(t)} &= \tau^{(t)} + \frac{\gamma_{SF}}{b_p} - \tau_i \end{aligned} \tag{1.23}$$

Imposing $v_{dk}^{(l)} = v_{dk}^{(t)}$ in the low stress regime of this Section gives an expression for $\tau_i - \frac{\gamma_{SF}}{b_p}$ and finally

$$v_{dk} = \frac{M_l M_t}{M_l + M_t}\tau b \tag{1.24}$$

with M_l and M_t the mobilities of the leading and trailing partial dislocations, that read $M_p = \frac{v^{(p)}}{b_p \tau_{eff}^{(p)}}$. Screw dislocations are constituted of two 30° partials, giving $v_{dk,screw} = \frac{1}{2} M_{30} \tau b$. On the other hand, 60° dislocations are dissociated in 30° and edge partials and the 30° one being much slower than the edge partial $v_{dk,60°} \simeq M_{30}\tau b$.

Experimental observations of moving partials

Early experimental determination of dislocation velocity revealed the different mobilities of screw and 60° dislocations [Alexander 1968]. The discrepancy has been consistently reported throughout the years whenever

dislocation velocity measurements were done by etch-pitting, X-ray topography or TEM methods [George 1972, George 1979a, Kolar 1996]. Using the lower yield point to determine dislocation velocity parameters as done by the group of Siethoff (see Chapter 2) does not allow for discrimination between both types and reveals only the activation energy for the rate-limiting dislocation character [Siethoff 1969].

Early measurements of dislocation velocities used an intermittent technique, meaning that the samples were deformed at high temperatures, analyzed by etch pitting or X-ray topography at room temperature, then heated and deformed again, etc. This method has several drawbacks and has led to the determination of approximate values for the quantitative activation energy of dislocation motion and dependence of the velocity on the stress. *In situ* X-ray topography has shed light on this issue [Imai 1983].

When dissociated dislocations move, one can distinguish the leading and trailing partials, being separated by the ribbon of stacking fault. As noticed previously, the two types of perfect dislocations present in silicon have a slightly different velocity. This difference originates from the edge partial of the 60° perfect dislocations, which has a higher mobility (three times that of 30° partials [Kolar 1996, Alexander 1999]). The difference in velocity between the partials varies with temperature and tends to fade out with increasing temperature. This difference in mobility is thought to originate from the higher energy barrier required to break a reconstructed bond at the dislocation core in the 30° partials (see below). Early models [Wessel 1977] assigned the different velocities to the influence of the stacking fault on the partial mobility.

It was originally thought that the location of the partial, leading or trailing with respect to the dislocation motion, would also influence the partial mobility, since the presence of the stacking fault induces an additional dragging force on the partials [Wessel 1977, Gottschalk 1979]. The leading partial moves in a perfect lattice, whereas the trailing one has to overcome the force induced by the stacking fault. Climb forces would then also affect the activation energy for dislocation motion, meaning that Schmid's law would not be respected in silicon. The model introduced above does not introduce any such dependency: recent investigations show that the discrepancies found in earlier experiments come either from the limited amount of measurements, not able to represent in a statistically correct way the distribution inherent to the dissociation distance; or from the misuse of a mean dissociation width [Vanderschaeve 2005, Vanderschaeve 2007]. Schmid's law is therefore applicable in silicon.

Results from atomistic simulations

It can be seen in Table 1.3 that reconstruction of a 30° partial lowers significantly more its core energy than it does for a 90° partial. The reconstruction energy per bond is equal to the energy required to break it, for example when attempting to propagate a kink along the dislocation. Breaking reconstruction bonds is therefore more difficult on the 30° partial. This explains

the lower mobility of this partial type, i.e. ultimately the one of screw dislocations compared to 60° segments; dissociation of kinks might enhance further this discrepancy between the 90° and 30° partials [Bulatov 2001b]. Dislocation mobility in silicon can be defined entirely by the evaluation of the activation energies for these thermally activated processes that depend intrically on the type of partial and of kink considered [Bulatov 1995]. Correcting the equations for dislocation velocity derived above, one should in addition have in the length-dependent regime [Nunes 1998a]:

$$v_{dk}^{(p)} = \nu_D \frac{3}{4} \frac{\tau_{eff}^{(p)} b^3 X}{k_b T} \exp\left(-\frac{F_{LK} + F_{RK}}{2 k_b T} \right) \times \frac{1}{2} \left[\exp\left(-\frac{W_m^{LK}}{k_b T} \right) + \exp\left(-\frac{W_m^{RK}}{k_b T} \right) \right] \tag{1.25}$$

A similar expression holds for the length-independent regime. Because the kink nucleation and migration energies depend both on the partial considered and the kink type ([Nunes 1998a, Justo 1999], see Table 1.5), the mesoscopic F_k and W_m derived from experiments result from the contribution of left and right kinks to the overall kink pair mobility. Obviously, being able to determine theoretically the activation energies for the different processes involved in dislocation motion, one should be able to deduce the macroscopic value, an exercise that still has not been successfully performed. Theoretical work on the partials of a screw dislocation has revealed that the entropy contribution to the activation free energy for kink migration on the 30° partial might depend on the kink type (left or right) considered, adding further to the complexity of the atomistic motion mechanisms [Jin 2010].

An additional interesting effect of the finite width of the stacking fault on dislocation mobility, already predicted by [Möller 1978], has been discussed by [Cai 2000]. Using as best estimates $F_k = 0.7\,\text{eV}$, $W_m = 1.2\,\text{eV}$ and $S = 3k_b$ allowing reproduction of the experimental data [George 1979a, Imai 1983], the authors determine[14] the existence of a nonlinear stress-dependent dislocation mobility regime below 16.8 MPa in which the partials should move in a perfectly correlated manner because of their mutual elastic interaction on the kink pair nucleation and propagation mechanisms (Figure 1.13). Note that this critical stress is of the same order of magnitude as the 20 MPa threshold of [George 1979a] and of the critical stress calculated by [Möller 1978].

This domain would be detectable only if the actual stress-dependent dissociation width were an integral multiple of the equilibrium dissociation width d_0. Stress dependence would then be enhanced at low stresses in order to set partials into a correlated motion regime. d_0 is expressed in the model of [Cai 2000] as a function of the stacking fault energy γ_{SF} and a nonglide stress acting on the dissociation width. Any variation in these parameters

14 Note that the model of [Cai 2000] does not account for the elastic interaction between kinks in a pair entering into F_{kp} (Eq. 1.12). This is justified for small stresses, but has the consequence of forcing the authors to define $x_c = 10b$ in order to limit the collapse of small kink pairs.

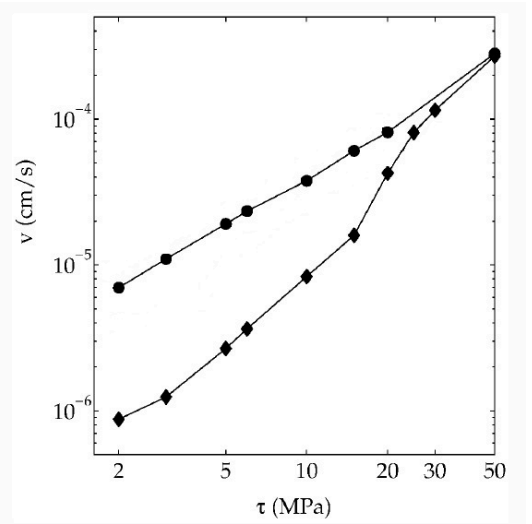

Figure 1.13: Simulated effect of dissociation width d on screw velocity at 1000 K. Circles: d is a non-integral multiple of d_0, kinks on both 30° partials can be nucleated without elastic interference and the total dislocation velocity is linear up to low stresses. Diamonds: d is an integral multiple, and partial motion must be fully correlated [Cai 2000].

(e.g. due to impurities affecting γ_{SF}, or particular stress conditions) would influence dislocation velocity at low stresses. This phenomena has not been observed experimentally yet [Jacques 2001].

The presence of a highly stress dependent dislocation velocity at low stresses was indeed justified by [Imai 1983] as the consequence of impurity pinning at the cores since the Japanese group did not observe any deviation of the velocity vs stress curve down to 1 MPa. The existence of a correlated kink pair motion regime on the partials is still unresolved.

1.2.4 *Microscopic mechanisms governing dislocation mobility*

The previous paragraphs have detailed several features of glide dislocations in silicon potentially affecting their motion mechanisms: dissociation into Shockley partials, motion in a lattice with strong covalent bonds leading to a strong lattice friction opposing dislocation motion. Some questions can be raised: firstly, concerning the mechanism limiting the propagation of kinks along the partials. Answering this question allows for discrimination between the approaches followed by [Celli 1963] (obstacles) and [Hirth 1992] (secondary Peierls potential). Secondly, in which length regime dislocation motion takes place. As seen previously, the activation energy in both domains differs by $F_{kp}^{(c,p)}/2$. Finally, one can wonder what happens at very high temperatures. These three questions will be addressed in the following.

What mechanism governs kink migration?

ACKNOWLEDGING OBSTACLES TO KINK MIGRATION Early calculations showed that the activation energy for kink pair nucleation alone would be close to the experimentally determined one [Labusch 1965]. The immediate conclusion was therefore that kink pair nucleation was the sole rate-limiting process for dislocation motion [Alexander 1968]. Some authors [Kannan 1970, George 1972, Kulkarni 1976] noted however that kink propagation -whatever the actual governing mechanism- should indeed take a large share of the total activation energy for dislocation motion, although without being able to quantify more precisely the share taken by the kink migration energy. Assuming that barriers to kink propagation were small would lead to a viscous, high velocity motion of the kinks along the Peierls valleys. Something had to prevent them from reaching this viscous mode. The models introduced above proposed respectively obstacles and the presence of a strong secondary Peierls potential as candidates. Let us call F_{km} the energy barrier to kink motion; we do not know *a priori* whether $F_{km} = W_m$ (diffusion of kinks in the secondary Peierls potential) or $F_{km} = U_d$ (obstacles along the line).

Following the view that $F_{km} \ll 1$, [Möller 1978] noted that the exact nature of weak obstacles along the line, separated by $\Delta l \simeq 1$ μm in his model with Δl temperature-dependent, could not be easily identified. Constrictions limiting the kink mean free path were tentatively designed as responsible. [Alexander 1981a], trying to find obstacles opposing sideways motion of the kinks, identified the possible influence of jogs and intrinsic point defects, constrictions being actually coalesced thermal jogs [Cockayne 1979].

In situ observations by means of Transmission Electron Microscopy [Hirsch 1981a, Louchet 1981b], as well as pulse loading experiments [Farber 1986, Nikitenko 1987] allowed for a more accurate determination of F_{km} and the formation of a consensus around $F_{km} \simeq 1.2\,\text{eV}$. It appeared that kink migration was indeed responsible for a large share, if not the majority, of the activation energy for dislocation motion $F \backsimeq 2.2\,\text{eV}$. Table 1.6 lists the values of F_{km} derived *experimentally* by several authors[15]. See Table 1.5 for theoretical determinations of U_{km}.

ATTRIBUTION TO THE SECONDARY PEIERLS POTENTIAL Once it was acknowledged that the barrier to kink migration was not negligible, the question remained to determine where such a barrier would come from. Potential obstacles such as jogs, radiation-induced defects or impurities could be ruled out [Hirsch 1981a, Louchet 1981a]. The influence of point

15 [Farber 1986, Nikitenko 1987]: consider that kink motion in the secondary Peierls potential is strongly affected by point defects.
[Yamashita 1993]: it is assumed that the value $F \simeq 2.2\,\text{eV}$ given by the authors has been corrected for the effect of the high applied stress.
[Gottschalk 1993]: the authors assume that activation energy for motion of edge segments constituted of densely packed geometrical kinks is equal to their motion activation energy. They neglect kink mutual interactions, which could explain the high value derived.

author	F_{km} (eV)	T (K)	τ (MPa)	dislocation
[Hirsch 1981a]	≤ 1.2	693	270	90° P
[Louchet 1981b]	1.2	873	90	60°
[Vanderwalker 1984]	1.2	723		90° P
[Farber 1986]	1.58	873	7	60°
[Nikitenko 1987]	1.6	873	7	60°, screw
[Gottschalk 1987]	≤ 1.2	373	200	60°
[Gottschalk 1993]	1.8	693	50	60°, screw
[Farber 1993]	1.5	873	7	edge
[Yamashita 1993]	1.2	773	300	60°
[Kolar 1996]	1.24	403	275	90° P
[Alexander 1999]	1.7	873	110	90° P
[Vanderschaeve 2000]	1.3	813	550	60°, screw

Table 1.6: Kink migration energy barrier F_{km} experimentally determined by different authors. "dislocation" precises the dislocation character on which parameter identification has been done. P: partial.

defects under electron beam irradiation is commonly reported[16] and makes it difficult to separate the intrinsic kink motion mechanism from pinning artefacts at temperatures above ~ 500 K, where kink pair nucleation can proceed by thermal activation [Gottschalk 1987]. [Kolar 1996], using HREM, could not determine if obstacles or diffusion were governing at 873 K because the moving partials were observed under beam irradiation enhancing kink nucleation (so-called REDG, Radiation Enhanced Dislocation Glide [Maeda 1996, Caillard 2003]) and promotes diffusion of point defects and impurities. In this case, the authors observed unpinning by thermal activation at obstacles of height 2.4 eV; pinning was tentatively attributed to the presence of oxygen at the reconstruction defects affected by irradiation. It is however unclear what happens without the presence of the electron beam. The same team [Alexander 1999] assign $W_m = 1.24$ eV preferentially to the secondary Peierls potential. The higher value identified at 873 K is attributed to a possible stress dependence of W_m.

Turning to atomistic simulations to help solve this issue, it seems that kink migration is limited by the presence of the secondary Peierls potential and not by obstacles. This is explained by the core reconstruction that implies bond breaking, shifting and straining as fundamental processes upon propagation of kinks [Bulatov 2001b]. The model of Hirth & Lothe (*HL model* in the following) is therefore believed to be the relevant one to consider.

16 The 90° partial is particularly affected by unidentified pinning points observed under beam irradiation at intermediate temperatures. In extreme cases, dissociated dislocations form "noses", the 90° partial lagging far behind the 30° one [Wessel 1977, Gottschalk 1987].

THE CRUCIAL ROLE OF POINT DEFECTS It must be underlined in the meantime that this *does not prevent* obstacles on the dislocation line to play a role in affecting kink nucleation or migration processes, especially at high temperatures where point defects come into play (the example of [Kolar 1996] being flagrant). The Russian group (Farber, Nikitenko, Petukhov and colleagues) developed a model in which the presence of point defects could favor kink nucleation by distorting the core, but also affect its migration [Farber 1986, Nikitenko 1989, Farber 1993]. The effective stress acting on kink would be the applied stress τ reduced by a starting stress τ_{pd} due to the inhomogeneous accumulation of point defects in the dislocation stress field and at its core, estimated to range from 1.5 to 2.5 MPa at 873 K [Farber 1993]. Such a model can explain their results obtained by intermittent loading of samples. The increase of the effective activation energy for dislocation motion observed at very high temperatures (see below) is also thought to be closely linked to the role of point defects on kink nucleation and migration processes.

A model based on locking of expanding kink pairs has also been suggested, without any precise identification of the pinning obstacles [Maeda 1989]. These obstacles would then be strong enough to block the expansion of a single kink, but weak enough to be overcome when a kink of opposite sign collides the immobilized one.

More generally, the role of point defects is often mentioned in the literature as a potential candidate for alteration of the energy barriers to the double kink mechanism. Atomistic calculations and molecular dynamics have indeed stressed the role of reconstruction defects in promoting kink migration and acting as nucleation centers for kink pairs. For example, observations of a tremendous increase of the velocity of 60° dislocation segments upon reversal of the applied stress, dependent on the heat treatment prior to backwards motion [Nikitenko 1984] were linked to the effects of point defects left by the trailing dislocation on its glide plane, enhancing the kink formation rate and diffusivity but also leading to strong pinning of the kinks at obstacles separated by $\Delta l \simeq 0.4$ μm [Farber 1989]. Whether the point defects are dragged along with the moving dislocation or left behind in its glide plane is still unclear. Overall the picture seems quite intricated and not completely solved yet.

Which length regime governs dislocation motion?

As seen previously, whatever the model chosen at small dislocation lengths the activation energy for its motion should be increased. The question is obviously what the critical length is for appearance of this motion mode. It has traditionally been assumed that dislocation segments were long enough to disregard the length-dependent regime. Early considerations gave $X_c \leq 20$ μm [George 1972]. Improvement of the experimental methods, from double etching to X-ray topography and then HVEM observation of dislocations, ultimately allowed for the observation of the length-dependent motion regime in silicon.

OBSERVATIONS OF LENGTH-DEPENDENT DISLOCATION MOTION The critical dislocation length X_c has been estimated by [Hirsch 1981a] to be roughly 0.2 μm within a factor 2 or 3 whereas [Louchet 1981a] determined independently from the former group X_c =0.4 μm at 873 K and $\tau = 90$ MPa [Louchet 1981b]. Similarly, relaxation of misfit strain in heteroepitaxial layers at 300 MPa and 773 K exhibited a length-effect for dislocation lengths below roughly 0.85 μm [Yamashita 1993]. Using jogged edge dislocations at low temperatures (693 K and 50 MPa), [Gottschalk 1993] could not observe the existence of a length-dependent velocity regime, neither for edge nor for screw or 60° segments. All in all it remained clear that the length-dependent regime was limited to very small dislocation lengths. Identification of the dislocation velocity parameters by means of macroscopic observations would indeed require the use of the velocity expressions at $X > X_c$, since all observations were done on segment lengths of several tens of microns or more [George 1972, Imai 1983].

LENGTH-INDEPENDENT REGIME: ENTROPY CONTRIBUTION If one compares the value of the preexponential factor of the dislocation velocity given by Eq. 1.18 in the length-independent regime to experimental results [Imai 1983], it appears clearly that the discrepancy of several orders of magnitude poses a problem. Either the double kink mechanism is not the actual reponsible for dislocation motion, or there might be another unknown factor. Taking a large entropy term $S \simeq 8k_b$ would bridge the gap between experiment and theory, but this high value is suspicious. Refined calculations yielded $S \simeq 5.5\,k_b$, the largest share of the entropy term coming from kink migration [Marklund 1985]. [Gottschalk 1993] derived $S_m = 3.7\,k_b$ from edge segments, and $S = 2.5\,k_b$. Although explaining the inconsistency between those two values by the effect of point defects, it is highly probable that it comes partly from the overestimation of W_m from the velocity of edge dislocations. Recent atomistic computations, in addition to approximating the entropy of kink migration on 30° partial dislocations to $\simeq 2\,k_b$ [Jin 2010], raise the question of a kink type-dependency of S_m.

REVIVAL OF THE OBSTACLE-CONTROLLED MOTION REGIME Some authors pretend that dislocations in silicon propagate in the length-dependent mode, with an apparent dislocation length of roughly 1 μm due to the presence of impurities along the lines preventing further propagation of the kinks. This has been shown by observing dislocations in epitaxial layers and computing the activation energy for dislocation motion in the two apparently distinct regimes [Yamashita 1993]. An additional argument is the closer agreement between theoretical and experimental velocity prefactors without invoking large entropy terms if one considers that motion always proceeds in the length-dependent regime. Their model of kinks stopped at obstacles overcome when an opposite kink collides [Maeda 1989] would then explain the existence of an effective dislocation length. The atomistic

computations of [Oyama 2004] support this hypothesis. The issue is still debated.

Dislocation motion at very high temperatures

Additional diffusion processes at the core are believed to become rate-controlling towards higher temperatures ($T \gtrsim 0.75\,T_m$, 1320 K in Si), as translated by an increase in the apparent activation energy of the dislocation motion at very high temperatures for 60° dislocations, from $U \simeq 2.2\,\text{eV}$ to $U \simeq 4\,\text{eV}$ [Farber 1982, Siethoff 1999a, Siethoff 2002]. The transition temperature increases as the stress is lowered, and strain rates larger than $\simeq 10^{-3}\,\text{s}^{-1}$ seem to prevent the appearance of this deformation stage. Pre-strained crystals do exhibit a different mechanical behavior with higher U only closer to the melting point than virgin samples [Siethoff 1999a]. The exponential prefactor changing as well, dislocation velocity is actually enhanced at very high temperatures. This temperature domain causes a breakdown of the double kink model, and additional diffusion-controlled mechanisms such as climb tend to govern dislocation motion. Such a change of regime has also been observed in germanium crystals, although accompanied with a *decrease* of the dislocation velocity evolution with temperature [Siethoff 2002]. Note that such a significant change in the velocity parameters has not been detected by analysis of the upper yield stress of dislocation-free intrinsic and CZ silicon crystals [Yonenaga 1996b], leaving some questions about what the conditions are for the appearance of a special motion regime at very high temperatures.

At high homologous temperatures, lattice friction tends to disappear to leave obstacles (as impurities, solute atoms, point defects...) and diffusion-controlled processes (like climb and cross-slip) control the motion mechanisms. Drag of thermally formed jogs along screw segments[17] [Kannan 1970] has been mentioned as causing local bowing of the dislocations, still without becoming rate-controlling at 1323 K. All in all, the transition from vacancy to interstitial self-diffusion is believed to cause such a large change in the dislocation activation energy [Siethoff 1999a]. These changes in microscopic processes have an influence on the macroscopic behavior of silicon crystals as will be discussed in Section 2.1.1.

Slip in these conditions is commonly modeled in the literature of fcc metals by the incorporation of a mechanical threshold acting on the stress dependence of dislocation velocity, representing the effects of the dislocation forest. The stress exponent increases also tremendously. This regime is characterized by activation volumes much higher than in the case of motion by means of kink pair nucleation and propagation [Kulkarni 1980]. A unified model exists but is not easy to implement because the expression for the dislocation motion is not available in closed-form [Dour 2002]. As

17 The jog formation energy U_j was identified by measuring the mean spacing l_j between pinning points at 1323 K (assumed to be due to thermal jogs), varying as $l_j = b\exp(U_j/k_bT)$ and $U_j = 1.2\,\text{eV}$ [Hirth 1992].

mentioned previously, there is no single dislocation motion mechanism ruling the whole temperature range from the melting point.

1.2.5 *Dislocation generation*

It is nowadays possible to produce virtually dislocation-free silicon crystals, with the help of the FZ or CZ methods. When the crystal is initially dislocation-free, surface defects act as favorable dislocation nucleation sources as cross-slip is enhanced by the free surfaces leading to local constriction of the screw segments (see e.g. [George 1973, Kirscht 1978]). Clusters of defects in the bulk can also generate dislocations. When moving, dislocations multiply through thermally activated double-cross slip mechanism, as has been demonstrated in [Vallino 2001], or through activation of Frank-Read sources that dominate at lower temperatures, or by activation of secondary slip systems towards larger strains. When the dislocation density increases in slip bands, dislocations move on to parallel planes and multiply from there. Dislocation glide and flow is generally not homogeneous at the onset of plasticity if the temperature is not close enough from the melting point or the initial dislocation density is too low. Parallel glide bands are formed that are separated by dislocation-free zones, as observed in germanium crystals [Nyilas 2004].

The question of fixed dislocation sources still remains at the onset of plastic deformation, since to form a stable source the poles have to be stabilized, and merely unstable dislocation sources have been observed. Only later can sources of the Frank-Read type be activated, although this mechanism depends strongly on the stress and temperature conditions. [Moulin 1999a] have studied extensively this type of source both for high stress plasticity and for the low stress range [Moulin 1997, Moulin 1999b]. This mechanism was already suggested by[Alexander 1968]. The role of impurities present in as-grown silicon crystals can be raised here, since they can act as pinning points for dislocations and therefore act as potential sites for nucleation of fixed and stable sources at lower strains than in intrinsic crystals. These sources must nevertheless be submitted to a critical stress in order to be activated. Dislocation multiplication mechanisms will be discussed more thoroughly in the next Part of this work, as a prerequisite to modeling the mechanical behaviour of silicon materials. The following Section is dedicated to dislocation nucleation and motion at high stresses-low temperatures.

1.3 SHUFFLE DISLOCATIONS AT HIGH STRESSES*

The study of high stress (or low temperature) plasticity in silicon is of interest for specific situations e.g. wafer cutting or bulk material machining. The plasticity mechanisms differ from high-temperature slip; for example twinning gains some importance as the temperature is lowered, although the formation of twins depends also on favorable crystallographic orientations. Whereas many different research groups studied high temperature silicon plasticity, we owe our knowledge about dislocations at low temperature only to a handful of teams, almost exclusively to the French group based at the University of Poitiers. The first articles reporting experimental results obtained under a confining hydrostatic pressure date back the the early 1980's [Castaing 1981]. Compared to the case of dislocations in the glide set, this branch of silicon plasticity is therefore rather young. A review of our knowledge of high stress plasticity in silicon is available [Rabier 2010]; the reader is refered to it for more details beyond the few points we will touch upon in the following.

1.3.1 *Low temperature plasticity under confining hydrostatic stress*

High stresses can be only conditionally reached: if the temperature is too high, silicon will yield at low stresses and stresses high enough to activate the new mechanisms will never be reached. Two methods exist for solving this issue, relying respectively on nanoindentation and the use of a high confining pressure. Results derived from the former method have been introduced in Section 1.1. Some drawbacks of using nanoindentation are the lack of knowledge of the stress tensor under the indenter tip, the very localized plastic region and the phase transitions that take place above 12 GPa. The best method to observe these mechanisms is actually to study silicon samples under high hydrostatic pressures, still below 12 GPa in order to avoid transition to a β-Sn phase, so that brittle fracture is prevented [Castaing 1981]. Increasing the confining pressure to 5 GPa, it became possible to deform plastically dislocation-free silicon samples at room temperature in the beginning of the 2000's [Rabier 2000]. Table 1.7 summarizes the temperatures and strain rates that can be reached with different pressures and sample preparations.

Core transformations: from glide dissociated to shuffle perfect and vice-versa

Prestraining of the samples at high temperatures leads to the generation of dislocations able to carry the plastic flow imposed at lower temperatures, and allows to lower further the temperature at which plasticity can be observed. Prestraining has however the drawback of leaving the imprint of high-temperature characteristics on the dislocations: these are observed to be still dissociated at high stresses, although the motion of their partials is uncorrelated [Castaing 1981, Demenet 1984].

author	T (K)	$\dot{\gamma}$ (s^{-1})	P (GPa)	sample type
[Castaing 1981]	673-873	$5 \times 10^{-5} - 5 \times 10^{-6}$	1.5	⟨100⟩ disl.free
[Castaing 1981]	548-673	5×10^{-6}	1.5	⟨100⟩ prestrained
[Demenet 1984]	660-923	2×10^{-5}	10^{-4}	⟨123⟩ prestrained
[Demenet 1987]	698	2×10^{-6}	1.5	⟨100⟩ & ⟨123⟩ disl.free
[Rabier 2000]	293-323	5×10^{-5}	5	⟨123⟩ disl. free
[Rabier 2001]	293	5×10^{-5}	5	⟨123⟩ disl. free & prestrained

Table 1.7: Evolution of the observation temperature with increase of the hydrostatic stress (P) with time. [Demenet 1984] used a three-stages deformation protocol to be able to deform samples at atmospheric pressure.

The possibility of core transformation (from dissociated generated at high temperatures to perfect when stressed at low temperature and vice-versa) has been explored [Rabier 2005]. Cross-slip and climb are two mechanisms allowing for moving a dislocation from a set to another. Since climb requires the thermally activated diffusion of point defects to the core, it is thought that at room temperature cross-slip should prevail. Cross-slip of perfect dislocations is straightforward if the applied stress on the collinear slip system is high enough; cross-slip of dissociated dislocations requires the presence of constrictions to proceed. In spite of this, it appears that no core transformation can take place. Notwithstanding the case of the applied stress widening the stacking fault up to uncorrelated motion of the partials, even a stress state bringing the partials closer to each other cannot transform a dissociated dislocation back into a perfect one [Rabier 2001]. The opposite transformation, from perfect to dissociated dislocations upon annealing at high temperatures (up to 958 K), has not shown to be likely either, glide dislocations being nucleated from crystalline defects (e.g. crack edges from the low-temperature deformation stage) [Rabier 2005] and transformation taking place locally at low rates [Rabier 2010]. Cross-slip of a perfect screw dislocation has in addition been shown by atomistic simulations to be impossible, making the transition from perfect in the shuffle set to dissociated in the glide set even harder [Rabier 2010, Rabier 2007]. Higher temperatures could help dislocation climb by enhancing point defect concentration and diffusion. These result show that the core structure of dislocations does not only depend on the applied stress/temperature but also on the thermodynamical state of the crystal prior to its deformation.

Characteristics of high stress deformation

Samples deformed at low temperatures contain microcracks, and are dislocated. Those deformed under confining pressure after prestraining contain dissociated dislocations whose partials have moved in an uncorrelated manner. Microtwins and twins are also observed in prestrained samples, provided the compressive crystallographic orientation is favorable [Castaing 1981, Demenet 1987]. A phase change to an hexagonal structure

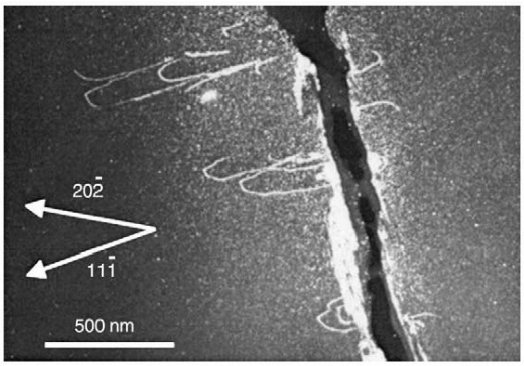

Figure 1.14: Perfect dislocation half-loops nucleated at crack edges. Deformation at room temperature, $\dot{\gamma} \simeq 5 \times 10^{-5}\,\mathrm{s}^{-1}$ and 5 GPa confining pressure [Rabier 2001].

has been reported at low hydrostatic pressures (700 MPa), and is thought to be stabilized by the presence of twins [Demenet 1987].

Perfect dislocations are emitted from microcracks that act as nucleation sources under hydrostatic stresses around 5 GPa [Rabier 2000]. Observation of the material after testing revealed the existence of perfect dislocations (assumed to be in the shuffle set), on the $\{111\}$ planes and Burgers vectors $\frac{a}{2}\langle 110\rangle$. Dislocations are aligned not only along the $\langle 110\rangle$ directions (screws) but also following Peierls valleys oriented along $\langle 112\rangle/30°$ and $\langle 123\rangle/41°$, the characteristic hexagonal shape of high-temperature dissociated dislocations being lost (see Figure 1.14). Some short 60° segments are however observed. These orientations specific to perfect dislocations are also observed at scratches made on silicon surfaces at room temperature and atmospheric pressure [Rabier 2000, Rabier 2010].

The $\langle 123\rangle/41°$ dislocations are thought to be reconstructed, made up of geometrical kinks alternating between 30° and 60° segments. The other dislocation orientations are less prone to reconstruction because the dangling bonds of perfect dislocations are oriented along the normal to the dislocation plane, a less favorable orientation for bond pairing. A direct consequence of unreconstructed core is a lower Peierls stress opposing dislocation motion. The motion of perfect dislocations has been investigated by means of atomistic simulations for the sole case of the screw segments, and very little is known about the other dislocation characters.

1.3.2 *Twinning*

In the high stresses-low temperatures domain, typically below 873 K, deformation of prestrained samples by dislocation glide progressively shifts in favor of twinning [Yasutake 1987, Vanderschaeve 2005]. The twins and microtwins detected in early confining pressure experiments are linked only to $\langle 100\rangle$ compression loading axes [Demenet 1987]; similarly twins

appear in tension provided the loading is aligned in a $\langle 110 \rangle$ direction. This means that twin planes can be formed on favorable crystallographic planes only. Stresses required to let twinning overcome dislocation slip are larger than τ_∞. This deformation mode is characterized by a velocity law similar to the standard slip deformation, but with a higher stress dependence and slightly lower activation energies. Once again, the (twinning) partials show a different velocity depending on their type.

The theoretical model of twin formation proposed by [Pirouz 1987] was confirmed by simulations to work in certain stress/temperature conditions: twin generation can take place through successive cross-slip and Frank-Read mechanisms [Moulin 1999a]. Nevertheless, this model and the related simulations imply that the partials have a different mobility depending on their location with respect to the stacking fault. As noticed previously, this might not be the case [Caillard 2003, Vanderschaeve 2005]. In addition, the model of Pirouz assumes that a dissociated screw dislocation acting as source for twin planes transforms its core from dissociated to perfect. As seen above, such a transformation is very unlikely, so the formation of twins in silicon might take place through another mechanism.

1.4 CONCLUSION ON DISLOCATION STRUCTURE AND MOTION

Intensive research on the structure and motion of dislocations in silicon has brought to light several interesting aspects. At high temperatures, plastic deformation is allowed by slip of glide dislocations that are dissociated for energetic reasons. This dissociation of dislocations in the glide set has strong consequences on the core of the partials, leading to their reconstruction and the existence of a myriad of types of kinks. The influence of reconstruction defects and other point defects on the motion of the partials is a crucial point that still needs to be explored further, as the macroscopic dislocation velocity directly depends on the microscopic mechanisms taking place at the cores. Dissociation has also an influence on the ability of dislocations to change their glide plane either by cross-slipping or climbing.

The thermally activated nucleation of kink pairs over the high primary Peierls relief and subsequent kink pair expansion by migration through the secondary potential, both due to strong covalent bonding and core reconstruction, lead to a strongly temperature-dependent and weakly stress-dependent dislocation velocity. Associated to very low as-grown dislocation densities to carry plastic flow, these factors are translated in macroscopic deformation experiments by a particular shape of the stress-strain curves taht will be described in the coming Chapters. The existence of a stress domain below roughly 20 MPa where the partials should move in a perfectly correlated manner depending on the stacking fault width has been postulated by theoretical arguments but never directly observed experimentally. Point defect diffusion to the dislocation core and formation of an atmosphere around it at low stresses has however been shown to affect dislocation mobility.

Slip of glide dislocations becomes more difficult as the temperature is lowered. The applied stresses can no longer be relieved by plastic deformation, and defects at the surface and in the bulk can act as crack nucleation sites. Unless a high confining pressure is applied, brittle fracture occurs at temperatures below the brittle-to-ductile transition, typically 873 K in standard strain rate conditions. Twinning can be observed in specimen deformed at such temperatures, provided cleavage does not occur. A change of core configuration takes place in virgin materials deformed under high hydrostatic stresses. Nucleation of perfect dislocations in the shuffle set is observed, having different characteristic segment orientations than at higher temperatures. Such a change is not observed in prestrained specimen, the high shear stresses simply widening the stacking fault until the partials move in an uncorrelated manner.

To summarize this discussion, it might be useful to gather the above-cited results into a single graph that describes the different deformation domains studied for silicon. Considering a fixed strain rate, and letting temperature and stress vary, one obtains Figure 1.15. It is important to keep in mind that the frontiers between the different domains are *not sharply defined*, especially for impurity-containing and dislocated silicon. In this case, and as will be

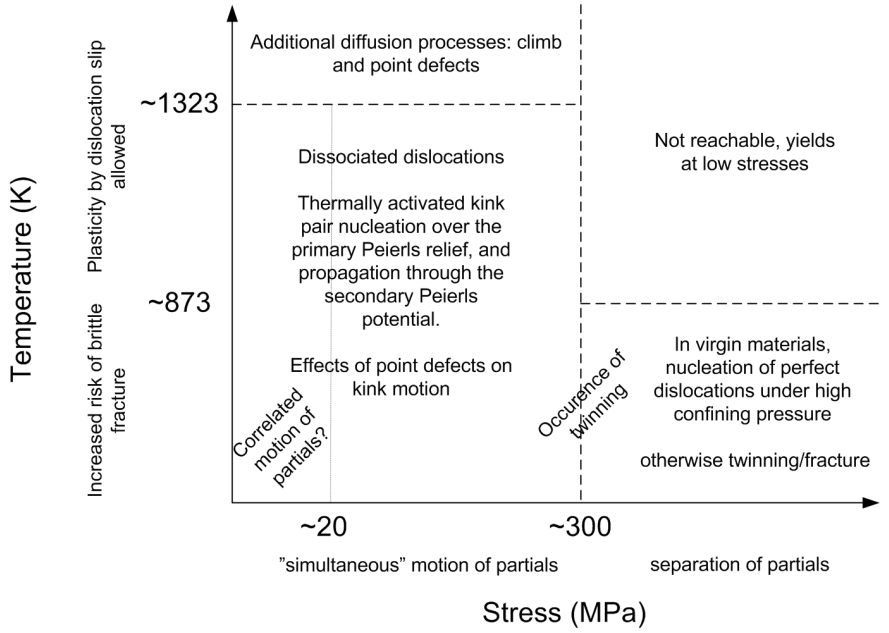

Figure 1.15: Plasticity domains of intrinsic silicon as function of shear stress on the active slip plane and temperature.

discussed later, the brittle-to-ductile transition might not be abrupt and would take place over a larger range of temperatures. The limiting stress for high-stress plasticity is linked to the critical stress for separation of the two partials bounding a stacking fault, and depends on the fault energy. Now we have surveyed the microscopic motion mechanisms of dislocations, it is high time to study their effect on the mechanical behavior of silicon monocrystals on a macroscopic level. The next Chapter introduces the experimentally recorded stress-strain curves of monocrystals deformed uniaxially and the standard physically-based constitutive model used to reproduce the characteristic behavior of as-grown crystals.

2

MACROSCOPIC BEHAVIOR OF INTRINSIC SILICON MONOCRYSTALS

This Chapter introduces the experimental results of deformation tests performed on silicon monocrystals at high temperatures, where plasticity is allowed. The material of interest here is intrinsic silicon; the case of extrinsic, impurity-containing materials is discussed in a later Chapter. The study of pure silicon relies typically on the use of Floating-Zone (FZ) single crystals that have very low concentrations of dopants and electrically inactive impurities. Dislocation motion mechanisms are similar in silicon in germanium[1]. Its lower melting temperature makes it more convenient to study, and some results obtained on germanium crystals valid for silicon will be introduced.

2.1 EXPERIMENTAL RESULTS AT SMALL STRAINS: THE YIELD REGION

2.1.1 *General observations of stage 0*

It has been very early observed that as-grown silicon single crystals deformed uniaxially at constant temperature T and strain rate $\dot{\varepsilon}$ exhibit a characteristic bell-shaped stress-strain behavior at small strains (below 10 % resolved shear strain γ) [Patel 1963]. After an apparently[2] elastic deformation stage leading to very high stresses as the temperature is lowered (and to an early fracture of the crystal if cracks eventually nucleate), a sharp drop of the flow stress happens at the upper yield stress (UYS), followed by a rapid decrease of the applied stress until it starts again to increase at the lower yield point (characterized by the lower yield stress, LYS). This deformation stage is usually refered to as *stage 0* as it is conditionally reached depending on the initial thermodynamical state of the crystal. This deformation stage is also considered to be a transition one towards the steady-state of deformation reached during stage I [Sumino 1971].

Then deformation proceeds as for FCC metals: if the specimen orientation favors single slip hardening proceeds starting from stage I; otherwise stage

1 Some differences exist however. One could for example mention the change in the temperature dependency of dislocation velocity at very high temperatures [Siethoff 1999a, Siethoff 1999b].

2 plasticity understood as dislocation glide and multiplication actually takes place very early during the initial linear stress increase, but this process does not give a macroscopic plastic deformation [Patel 1963].

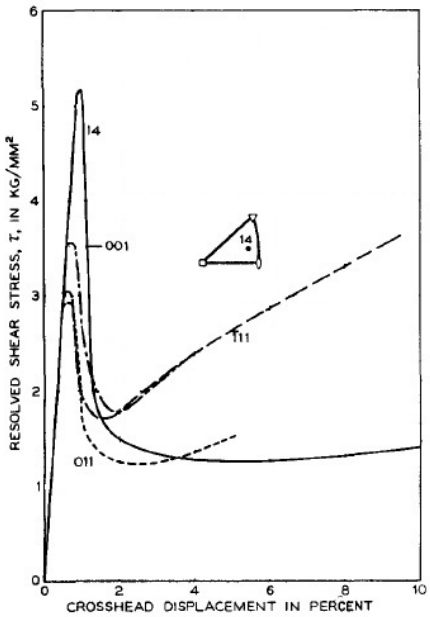

Figure 2.1: Stress-strain curves of germanium monocrystals deformed uniaxially in tension at different crystallographic orientations. $T = 788\,\mathrm{K}$, applied strain rate $\dot{\varepsilon} = 2 \times 10^{-3}\,\mathrm{s}^{-1}$ [Patel 1963]. Note the strong hardening rate taking place right after the lower yield point for "hard" orientations.

II is directly observed. Figure 2.1 shows examples of yielding behaviors for germanium crystals loaded in various crystallographic orientations.

Initially attributed to unpinning of dislocations from impurities, the yield drop was later found to depend strongly on the initial dislocation density of the specimen. This led to the conclusion, later confirmed, that such a characteristic behavior is due to the rapid multiplication of dislocations at the upper yield point and during the yield drop [Patel 1963, Alexander 1968]. The deficit of mobile dislocations able to carry plastically the applied strain rate $\dot{\varepsilon}$ in as-grown crystals, associated to their weakly stress-dependent velocity (see Chapter 1), only exacerbates a phenomenon that is *a priori* common to all materials deforming plastically by glide of dislocations [Estrin 1986]. The upper yield stress is reproducible for dislocation-free crystals only, the initial presence of dislocations leading to a strong reduction of both the UYS and of the magnitude of the yield drop. Because the origin of the yielding behavior of semiconductors lies in the dynamic properties of dislocations, several factors can influence it.

2.1.2 *The factors influencing the yield region*

Experimental observations

The parameters influencing both the magnitude of the yield stresses and the yield drop are temperature, strain rate and the amount of dislocations initially present in the crystal [Alexander 1968, Yonenaga 1978]. Figure 2.3 provides an overview of the variations of the mechanical behavior of intrinsic silicon single crystals with those three factors. Their precise influence on the magnitude of the yield points and of the yield drop, eventually with the help of mathematical models, has been discussed elsewhere [Alexander 1968, Yonenaga 1978]. Figure 2.4 shows the effect of temperature on the stress-strain behavior of dislocation-free crystals in a wide range of T. While the upper yield stress and magnitude of the yield drop depend sensitively on the initial thermodynamical state of the crystal, the magnitude of the lower yield point remains rather insensitive to the initial dislocation density as long as it can be observed [Kojima 1971]. The yield stresses τ_{yp} at the upper or lower yield points of dislocation-free crystals are experimentally observed to follow Eq. 2.1:

$$\tau_{yp} = C_{yp}\dot{\gamma}^{\frac{1}{n_{yp}}} \exp\left(\frac{U_{yp}}{k_b T}\right) \tag{2.1}$$

where C_{yp} is a constant with respect to temperature and strain rate, n_{yp} and U_{yp} are parameters depending on the yield point considered and found to be in the usual temperature range between 0.45 and $0.8\,T_m$ [Alexander 1968]:

$$\begin{cases} U_{uyp} = 1.1, & n_{uyp} = 2.1 \\ U_{lyp} = 0.8, & n_{lyp} = 2.9 \end{cases} \tag{2.2}$$

The prestrain and following heat treatment applied to virgin samples in order to introduce a dislocation density prior to a dynamic test has been observed to influence the temperature- and strain-rate dependence of the lower yield point, so that Eq. 2.1 is not always valid for predeformed crystals. The effect of trace impurities and other point-like defects is suspected to influence dislocation motion in these cases [Siethoff 1992].

The reader will notice that the slopes of the elastic parts of the stress-strain curves in Figure 2.3 seem to depend on temperature, initial dislocation density and strain rate. This has also been observed in [Patel 1963]. This effect, largely stronger than the sole temperature dependence of the shear modulus, is due to the tensile apparatus. A harder testing machine will lead to a more intense yield drop because of a sharper transition in the evolution of the density of mobile dislocations in this region, see Figure 2.2. This will be discussed in details in the next Part.

It is of interest to note that lower temperatures (or larger strain rates, or lower initial dislocation densities) extend the yield region to larger strains in addition to affecting the yield stresses [Omri 1987].

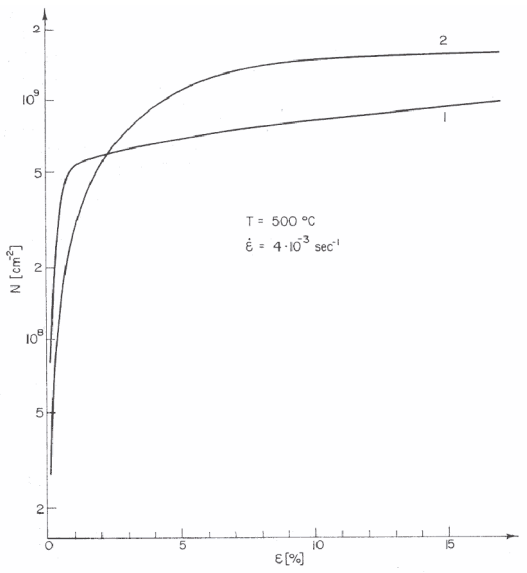

Figure 2.2: Computed dislocation density N as a function of strain in a dynamical tests of Ge ($\rho_{m,0} = 10^6\,\mathrm{m}^{-2}$, $T = 773\,\mathrm{K}$, $\dot{\gamma} = 4 \times 10^{-3}\,\mathrm{s}^{-1}$). Curve 1: hard machine, $\mu^* = \mu_{Si}$. Curve 2: usual machine $\mu^* \simeq \mu_{Si}/25$ [Alexander 1968].

Influence of temperature on the parameters governing the yield stresses

Some authors find the parameters given by Eq. 2.2 are valid in the whole temperature range up to 1573 K [Yonenaga 1996b]. Experiments by Siethoff *et al.* have shown on the contrary that these values do not always hold irrespectively of the strain rate and temperature, and a new regime of the yield points appears for low strain rates at very high temperatures in dislocation-free FZ silicon samples: from 1373 K and below $10^{-3}\,\mathrm{s}^{-1}$ for the lower yield point. The presence of as-grown dislocations and lower strain rates shifts this new regime towards higher temperatures [Siethoff 1999a]. The same pattern has been observed for the upper yield point, although it fades out above 1523 K [Yonenaga 1996b, Siethoff 2001]. See Figure 2.5 for a plot of the upper and lower yield stresses as function of the strain rate, at different temperatures and for dislocation-free intrinsic FZ silicon.

Such a change in the behavior of the yield points must be seen in parallel to the modifications in the dislocation motion mechanisms taking place at these temperature and strain rate conditions (see [Farber 1982] and Section 1.2.4), and due to a shift from vacancy to interstitial self-diffusion. Between those low- and high strain-rate regimes, another domain appears that is not fully understood yet, with an activation energy close to the one in the high-temperature regime but a strain-rate exponent where $2 + m \simeq 4$.

Omri *et al.* observed the appearance of a plateau for τ_{lyp} between 1173 and 1323 K when samples were loaded at low strain rates ($2 \times 10^{-5}\,\mathrm{s}^{-1}$). Such a plateau does not appear towards higher rates [Omri 1987]. This plateau

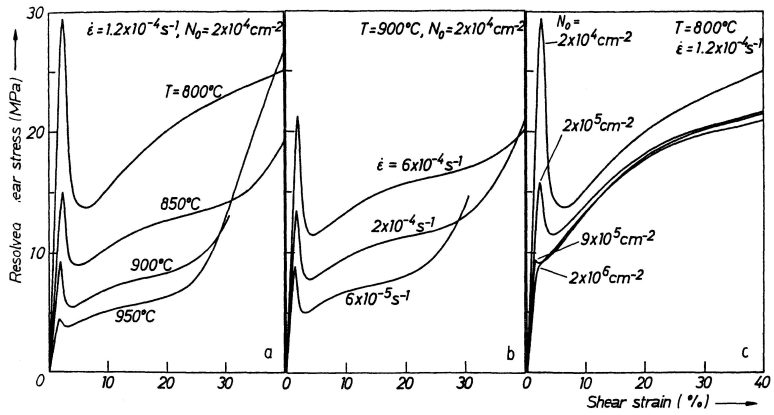

Figure 2.3: Resolved shear stress-strain curves of FZ silicon monocrystals deformed in single glide at different: (a) temperatures, (b) strain rates, (c) initial dislocation densities [Yonenaga 1978, Sumino 1999a].

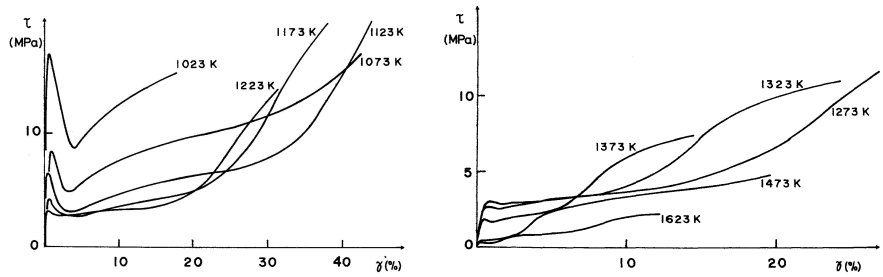

Figure 2.4: Stress-strain curves of dislocation-free silicon crystals obtained at various temperatures and a resolved shear strain rate $\dot{\gamma} = 2 \times 10^{-5}\,\mathrm{s}^{-1}$ [Omri 1987]. The appearance of a plateau of the lower yield stress at high temperatures is attributed by [Siethoff 1988] to the effect of nitrogen present in the deformation atmosphere (10 % H_2, 90 % N_2).

stemming only from internal stresses has been interpreted as the manifestation of athermal dislocation motion mechanisms, higher temperatures allowing even lower flow stresses thanks to additional diffusion processes [Oueldennaoua 1988]. Siethoff later attributed this peculiar regime of the lower yield point to the presence of nitrogen in the atmosphere on dislocation motion mechanisms (see Chapter 3 for a discussion of the effects of light impurities on the mechanical behavior of silicon crystals), insisting as well on the modifications of the shape of the yield drop with the deforming atmosphere [Siethoff 1988].

A so-called low temperature regime (between $0.45\,T_m$ and $0.65\,T_m$) of the yield points in silicon is revealed in n-type material, see Section 3.2.3 [Siethoff 2002].The results obtained in the high temperature regime can therefore be extended down to the brittle domain for intrinsic silicon, where plasticity becomes insignificant under no applied hydrostatic pressure.

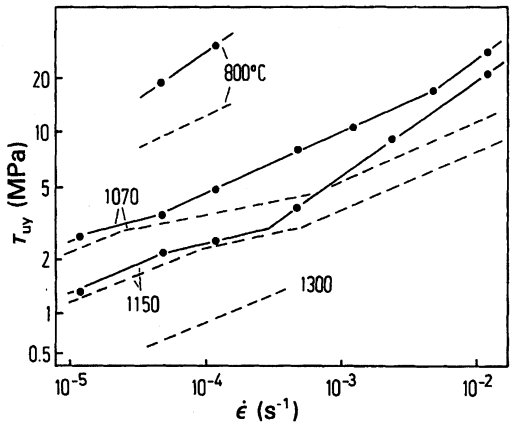

Figure 2.5: Values of the upper (plain) and lower (dashed) yield stresses at different temperatures of undoped dislocation-free FZ silicon [Siethoff 2001].

The influence of the applied stress on U identified by the yield points at temperatures between 923 and 1573 K has also been studied when τ is kept below 45 MPa [Schröter 1983, Siethoff 2002]. It appears that U is not significantly stress-dependent in intrinsic materials, see Figure 2.6.

Theoretical considerations

A straightforward method for determining which factors migh influence the yield region and the reasons for that is to consider the evolution of the applied (shear) stress τ. Considering the case of small deformations only, the total resolved shear strain rate can be decomposed into an elastic and a plastic terms: $\dot{\gamma} = \dot{\gamma}_e + \dot{\gamma}_p$. Writing μ^* the effective shear modulus, a combination of the specimen and machine stiffnesses, the rate equation for the shear stress reads:

$$\dot{\tau} = \mu^* \dot{\gamma}_e = \mu^* (\dot{\gamma} - \dot{\gamma}_p) \tag{2.3}$$

This equation is called the *machine equation* [Alexander 1968]. Orowan's law bridges the gap between the macroscopic plastic strain rate and the microscopic processes:

$$\dot{\gamma}_p = b \int_0^\infty \rho(v) v dv \tag{2.4}$$

Where the distribution of dislocation densities as a function of their velocity $\rho(v)$ is used and all dislocations have the same Burgers vector[3]. The velocity might depend among other factors on the applied stress τ and ρ itself. Here a crucial assumption is made, namely that the behavior of all dislocations

3 this assumption is true if Orowan's law is applied to dislocations belonging to a single slip system. This is in particular true in the case considered here of uniaxial tensile testing of monocrystals loaded in single glide. The more complicated cases of multiple slip require the use of a crystal plasticity framework as introduced in the next Part.

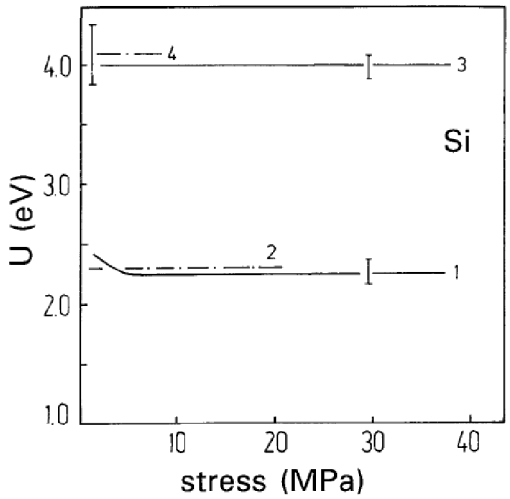

Figure 2.6: Activation energy of dislocation motion in silicon as a function of the applied stress. Curves 1 and 2: high temperature regime, from velocity measurements and lower yield point analysis respectively. Curves 3 and 4: very high temperature regime, from velocity of 60° dislocations and lower yield point analysis respectively [Siethoff 2002].

in the crystal $\int_0^\infty \rho(v)vdv$ can be replaced by the one resulting from a single population of mobile dislocations ρ_m moving at given velocity v:

$$\dot{\gamma}_p = b\rho_m v \tag{2.5}$$

with v depending on an effective stress τ_{eff} to be derived later. Supposing that the velocity of the density of mobile dislocations is similar to the velocity of a single dislocation (see Chapter 1, reminded in Eq. 2.6) one gets:

$$v = v_0 \left(\frac{\tau_{eff}}{\tau_0}\right)^{m_0} \exp\left(-\frac{U}{k_b T}\right) \tag{2.6}$$

$$\dot{\gamma}_p = b\rho_m v_0 \left(\frac{\tau_{eff}}{\tau_0}\right)^{m_0} \exp\left(-\frac{U}{k_b T}\right) \tag{2.7}$$

where v_0 is a prefactor depending on the dislocation character, $\tau_0 = 1$ MPa is a normalizing stress, m_0 is the stress exponent and U is the apparent activation energy for dislocation motion, often taken as stress-independent[4]. It has been demonstrated that the collective motion of dislocations has a similar expression than the motion of an isolated dislocation, provided that the applied stress is reduced by an internal stress τ_{int} that depends on dislocation mutual interactions, the presence of impurity atmospheres around the dislocations, long-range stress fields created by precipitates, etc.

4 the entropy contribution is aggregated into v_0. The stress independence of U is justified for the relatively low stresses reached during experiments at high temperatures.

[Sumino 1971, Sumino 1979]. The exact expression of this internal stress will be derived later. Combining Eqs. 2.3 and 2.7 yields

$$\dot{\tau} = \mu^* \left(\dot{\gamma} - b\rho_m v_0 \left(\frac{\tau - \tau_{int}}{\tau_0} \right)^{m_0} \exp\left(-\frac{U}{k_b T} \right) \right) \tag{2.8}$$

which is a differential equation of the first order in τ. Its integration is however not straigthforward since both ρ_m and τ_{int} change with time. However one sees immediately that the three extrinsic parameters influencing the magnitude and evolution of the applied stress are

1. temperature through an exponential dependence of the dislocation velocity,
2. the applied strain rate and
3. the density of mobile dislocations.

Integrating such an equation requires evolution laws for ρ_m and τ_{int}. The combination of all these equations forms the basis of the model introduced by [Alexander 1968] that has since then been widely used to model silicon materials.

A yield point is found numerically by setting $\dot{\tau} = 0$. An approximation commonly done in order to differentiate the upper from the lower yield point is to consider that $\tau_{int} \ll \tau$ at the upper yield point. The lower yield point is a minimum of $\tau(\rho_m)$ and of $\tau(\gamma)$; one needs as well a differential equation ruling the evolution of the mobile dislocation density [Alexander 1968].

2.2 CONSTITUTIVE MODELING OF THE YIELD REGION OF SILICON

For a detailed presentation of the original Alexander & Haasen model (*AH model* in the following), the reader is referred to [Alexander 1968]. This model is intended for the description of the very early stages of deformation of silicon, typically to simulate the yield drop behavior up to the lower yield point. The AH model has strongly influenced the study of dislocation mobility and modeling of plasticity in silicon since its publication in 1968. Many authors have performed experiments in order to validate or test the hypothesis of this model and compute its associated parameters. Some limitations have been established, and possible improvements are suggested. The 1980's saw the first attempts to generalize the applicability of the model to three dimensional specimen with the help of the finite elements method.

2.2.1 *Introduction to the AH model*

Assumptions of the model

First, the basic equations will be reviewed. The model is based on some assumptions, sometimes observed experimentally not to be always verified:

1. deformation proceeds homogeneously throughout the monocrystalline sample, so that the local equations remain valid for the whole specimen

2. all dislocations in the crystal are mobile, i.e. they all carry plastic flow and enter into Orowan's law. This limits the validity of the AH model to small strains. In addition the dislocations contributing the the internal stress are precisely the mobile ones. This is justified by the fact that immobilized dislocations tend to form dipoles, whose contribution to the internal stress and effective stress is lower compared to mobile dislocations.

3. the behavior of all dislocations exhibiting different mobilities and velocities can be resumed to a single population of mobile dislocations moving at the same speed

4. one single slip system is activated, and the influence of the 11 remaining ones on the primary dislocations is negligible because of the low density of forest dislocations.

5. no impurities or defects other than dislocations are present

These assumptions will be discussed in the following. At the end of the 1960's the dependence of dislocation velocity on stress and temperature had already been explored; although some uncertainty was still left on the exact value of the parameters it was clear that dislocation velocity is weakly dependent on stress, while temperature has a strong influence on this velocity. This behavior is typical of semiconductors and not limited to silicon

alone. Moreover, considering the two predominant types of dislocations, i.e. screw and 60°, one can notice that their velocities are quite the same, especially at high temperatures. This argument has been indeed refined later on, and the screw dislocations have proved to be slightly slower than the 60° ones, being therefore rate-limiting for the development of dislocation loops [Alexander 1968, Suezawa 1979].

Equations of the AH model

In addition to relying on the set of equations deriving from Orowan's law introduced previously, the AH model provides the rate equation steering dislocation multiplication:

$$\frac{\mathrm{d}\rho_m}{\mathrm{d}t} = K\rho_m v \tag{2.9}$$

where K is a function characterizing the multiplication rate. To account for results on germanium crystals, K is taken to be equal to $\delta\tau_{eff}$, with δ constant at given temperature and strain rate conditions [Berner 1967]. Note that Eq. 2.9 implies that there is no sink for the dislocation density.

Finally, the effective stress exerted on the dislocations results from the difference between the applied stress and a back stress stemming from the mutual interaction between dislocations. To determine its value, Alexander & Haasen computed the stress resulting from the interaction between N parallel edge dislocations yielding a density ρ_m, $\tau_{int} = \mu b A\sqrt{\rho_m}$, with $A = \frac{1}{2\pi(1-\nu)}$ a constant derived from the theory of dislocations and ν Poisson's ratio. The effective stress becomes:

$$\tau_{eff} = \langle \tau - \mu b A\sqrt{\rho_m} \rangle \tag{2.10}$$

where it is assumed that the effective stress is always larger than zero: $\langle x \rangle = \max(x, 0)$.

The set of equations 2.3 to 2.10 allows to solve numerically the classic stress-strain relationship either in creep ($\dot{\tau} = 0$) or dynamical tests (in which case $\dot{\gamma}$ =cst). The initial condition required by the AH model is the density of (mobile) dislocations $\rho_{m,0}$ which must be finite. The parameters of the model are those related to dislocation velocity (v_0, m_0, U), dislocation multiplication (δ) and internal stress (A). They have been measured or computed by different authors throughout the years. Table 2.1 gathers some results obtained[5]. Most of the research groups have concentrated on the parameters for dislocation velocity, and very few have worked on the determination of the parameters δ and A.

5 Some authors distinguish screws from 60° dislocation segments that have different mobilities. The data taken from [George 1972, George 1979a] is related to 60° segments only. The latter work is concerned by dislocation velocity at small stresses only, and the stress sensitivity m is found to vary with τ. For an explanation of the high values of U found at very high temperatures by [Farber 1982] or [Siethoff 1999a], see Section 1.2.4.

authors	U (eV)	m	v_o (m.s^{-1})	A (N.m^{-1})	δ (m.N^{-1})
[Chaudhuri 1962]	2.2	1.4			
[Siethoff 1969]	2.3 ± 0.1	0.9 ± 0.1			
[Kannan 1970]	1.8 ± 0.3				
[George 1972]	2.01 - 2.51	0.88 - 1.6	3.2×10^3 - 9.3×10^4		
[Kulkarni 1976]	2.1				
[Yonenaga 1978]	2.64 ± 0.26	1.3 ± 0.1			
[Suezawa 1979]	2.17	1.1	3.4×10^3	0.3	3.1×10^{-4}
[George 1979a]	2.16 - 2.43		1.1×10^5 - 4.4×10^5		
[Schröter 1983]	2.32	0.9			
[Farber 1982]	4 ± 0.1		10^{10} - 10^{12}	$T \gtrsim 1323$ K	
[Imai 1983]	2.35 or 2.2	1			
[Siethoff 1999a]	2.25 ± 0.3	1 ± 0.3		$T \lesssim 1373$ K	
[Siethoff 1999a]	4.1 ± 0.3	3.2 ± 0.3		$T \gtrsim 1373$ K	

Table 2.1: Parameters of the AH model for intrinsic silicon crystals found by different authors.

2.2.2 *Properties of the model: yield points*

This model represents pretty well the typical yielding behavior of c-Si deformed in single slip [Yonenaga 1978, Suezawa 1979]. It reproduces satisfactorily semiconductors deformed in creep conditions, and is also suited to dynamical tests. The latter are characterized by the yield points, and the model can predict their magnitude with a good accuracy [Alexander 1968]. The AH model actually yields strain rate and temperature dependencies of the yield points similar to Eq. 2.1 derived experimentally. An interesting feature of this model is that the expression of the activation energy for dislocation motion U follows the remarkable relationship:

$$U = U_{lyp} n_{lyp} \tag{2.11}$$

A numerical analysis of the AH model enables the detailed computation of the upper and lower yield stresses τ_{uyp} and τ_{lyp} and the density of (mobile) dislocations at the yield points (respectively $\rho_{m,uyp}$ and $\rho_{m,lyp}$). The upper yield point is characterized by a maximum of the stress as a function of ρ_m and an internal stress small compared to the applied one: $\mu b A \sqrt{\rho_{m,uyp}} \ll \tau_{uyp}$. The lower yield point is obtained by assuming that the applied strain rate is completely plastic ($\dot{\gamma} = \dot{\gamma}_p$) and goes through a minimum as a function of the dislocation density ($\mathrm{d}\dot{\gamma}/\mathrm{d}\rho_m = 0$):

$$\begin{cases} \tau_{lyp} = \left(1 + \frac{2}{m_0}\right) \left(\frac{\mu^2 b A^2 m_0^2 \tau_0^m}{4 v_0}\right)^{\frac{1}{m_0+2}} \dot{\gamma}^{\frac{1}{m_0+2}} \exp\left(\frac{U}{(m_0+2) k_b T}\right) \\ \rho_{m,lyp} = \left(\frac{2}{m_0+2}\right)^2 \left(\frac{\tau_{lyp}}{\mu b A}\right)^2 \end{cases} \tag{2.12}$$

The second equation can be inverted to link the lower yield stress to the internal stress:

$$\tau_{lyp} = \mu b A \sqrt{\rho_{m,lyp}} \left(1 + \frac{m_0}{2}\right) \tag{2.13}$$

With $m_0 = 1$ one gets $\tau_{lyp} = 3/2\tau_{int}$ and

$$\tau_{eff,lyp} = \tau_{lyp}/3 \tag{2.14}$$

Another characteristic of the AH model is consequently to predict that $U_{lyp} = U/(m_0 + 2)$ and $n_{lyp} = m_0 + 2$. The experimental determination of the variations of the lower yield stress with temperature and strain rate combined with Eq. 2.12 allows for the identification of U, assuming that the AH model correctly describes the yield region indeed. This methodology provides with some information about the dislocation velocity parameters without having to rely on their direct *in situ* observation. Such an approach has been followed for example by the group of Siethoff.

2.3 HARDENING AND RECOVERY STAGES

This Section aims at introducing the deformation stages that follow the yield region (stage o). Deformation of silicon to high strains, reachable at high temperatures and low strain rates, reveals the existence of five stages: after the easy glide stage (commonly named stage I) comes a first work hardening stage (stage II), followed by a couple of relaxation and hardening stages (III to V). See Figure 2.7 for a typical five-stages stress-strain curve. There are two means of reaching such high strains experimentally: either by deformation tests performed at a constant strain rate $\dot{\varepsilon}$ (dynamic experiments), or creep tests during which the applied stress is kept constant and the variations of strain are recorded.

2.3.1 *Dynamic experiments*

Stage I

The first hardening stage follows the lower yield point. Stage I is visible only in monocrystals loaded in single glide. In cases where the crystal is oriented in a "hard" direction (corners and sides of the crystallographic triangle), a yield region of lower intensity than in single slip is observed, followed immediately by stage II of hardening. If the initial dislocation density is high enough, or equivalently if the strain rate is low enough or the temperature high enough, stage o and I disappear completely. Figure 2.8 shows the effect of temperature on the stress-strain curves of silicon single crystals oriented for multiple slip. If the orientation allows for stage I to set in, a steady-state of deformation is observed [Sumino 1971, Yonenaga 1978], during which the effective stress and the density of mobile dislocations remain constant, and depend solely on temperature and the applied strain rate [Kojima 1971]. More details about stage I and the steady-state of deformation will be given in the next Part of this work.

Stage II

Stage II sets in when secondary systems are activated because of lattice rotation or simply because the sample is oriented for multiple slip right from the beginning of deformation. The dislocation structure at the onset of stage II has been described for example in [Oueldennaoua 1988]. Stage II is characterized by interactions between dislocations belonging to different slip systems and formation of sessile Lomer-Cottrell locks. [Siethoff 2004] derived an expression from experiments on intrinsic and doped Si for determination of the stress linking the first and second deformation stages (Eq. 2.15, the exponent and activation energy are valid for intrinsic silicon only).

$$\begin{cases} \tau_{II} = C_{II}\dot{\gamma}^{\frac{1}{n_{II}}} \exp\left(\frac{U_{II}}{n_{II}k_bT}\right) \\ n_{II} = 3.2,\ U_{II} = 3.0\,\text{eV} \end{cases} \tag{2.15}$$

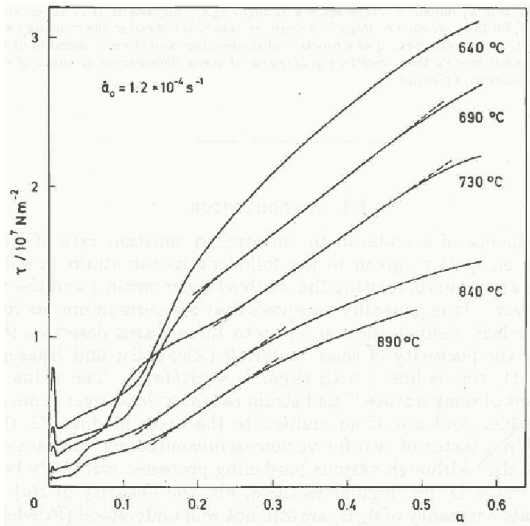

Figure 2.7: Typical stress-strain curve of semiconductors (here germanium) with ⟨123⟩ orientation [Siethoff 1991].

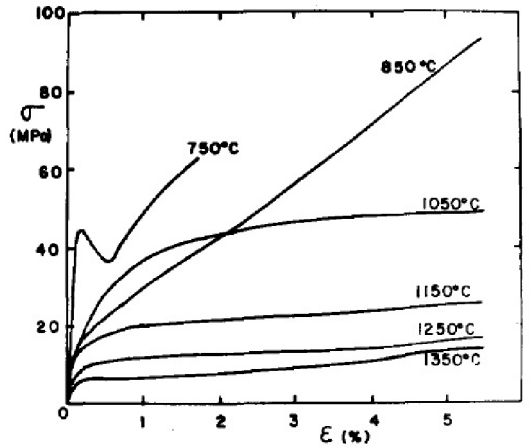

Figure 2.8: Stress-strain curves of silicon single crystals oriented for multiple slip (⟨100⟩ orientation, initially dislocation-free, strain rate $\dot{\varepsilon} = 6 \times 10^{-6}\,s^{-1}$) at different temperatures [Michel 1982].

τ_{II} exhibits different regimes depending on the temperature, the strain rate and the dopant concentration, like the lower yield stress does (see Section 2.1.2). Sumino *et al.* noticed that dislocation velocity in stage II of deformation of germanium monocrystals did not exhibit the same activation energy as during stages 0 and I [Sumino 1971]. The effect of jogs resulting from dislocation intersections has been mentioned there as additional obstacles to dislocation motion.

Stage III

The transition to the first recovery stage is governed by mechanisms that depend both on temperature and strain rate.

- At high temperatures (above 1173 K and at least up to 1573 K) the temperature dependence of the $\tau_{III}(T, \dot{\gamma})$ data (the stress defining the onset of stage III, see Figure 2.7) can be fitted to an Arrhenius law with an activation energy close to the one of monovacancy self-diffusion (3.6 eV), see [Siethoff 1978, Siethoff 1983c, Shimizu 2007]. A power law exists for determination of τ_{III} as a function of the strain rate. The precise diffusion mechanism steering recovery during stage III is believed to be climb of edge dislocations, prefered to jog dragging by screws [Siethoff 1983a]. The final relationship $\tau_{III}(T, \dot{\varepsilon})$ is expressed in eq. 2.16.

$$\begin{cases} \tau_{III} = C_{III}\dot{\gamma}^{\frac{1}{n_{III}}} \exp\left(\frac{U_{III}}{n_{III}k_bT}\right) \\ n_{III} = 3.5,\ U_{III} = 3.5\,\text{eV} \end{cases} \tag{2.16}$$

  A particularity of constant strain-rate deformation tests is that hardening mechanisms are active *before* stage III reaches a steady-state (i.e. a constant stress after recovery τ_{IIIm}). A steady-state value of stage III stress τ_{IIIm} can be extrapolated using the reduced hardening coefficient θ_{III}/μ (where $\theta = \frac{d\tau}{d\gamma}$). This method applied by Siethoff *et al.* to derive an expression for this theoretical stress equivalent to Eq. 2.16 with very close parameters $U_{IIIm} = 3.7$ eV and $n_{IIm} = 3.4$, showing that the diffusion-controlled mechanism responsible for the onset of stage III actually takes place during the whole recovery stage [Siethoff 1983a].

- At lower temperatures or higher strain rates (meaning higher stresses), deviations from the power law behavior of τ_{III} are observed. It is actually explained by a shift in the mechanisms governing stage III from a diffusion-controlled process (climb) to a cross-slip mechanism. In the latter case, a very good agreement of the experimental data with the Escaig model is reached [Siethoff 1983c, Siethoff 1984].

Therefore, two different mechanisms, either climb of edge dislocations or cross-slip of screw dislocations can be responsible for this recovery stage. The temperature and strain rate determine which one rules during this stage.

Stages IV and V

These late deformation stages were discovered in semiconductors at very high temperatures above $0.8\,T_m$ by the German group at the beginning of the 1980's [Brion 1981]. As the strain increases, the second hardening stage (stage IV) begins and the mechanism that was not active during stage III leads to the recovery stage V. Therefore, at low temperatures stage V is controlled by a diffusion mechanism, whereas at high temperatures (above 1173 K) cross-slip takes over. Note that increasing the strain rate has the same effect on the choice of governing recovery mechanism as decreasing the temperature.

These two independent mechanisms, namely cross-slip and climb, are both processes that can lead to recovery upon large deformations. Each one of them dominates only one of the two recovery stages since they do not affect the other type of dislocation.

2.3.2 *Creep experiments*

At stresses below roughly 100 MPa the creep curve of silicon crystals is made up of three parts: strain rate increase, establishment of a steady-state and finally decrease of the strain rate due to dislocation interactions and formation of subgrains. However a breakdown of this behavior is observed at stresses above 100 MPa where the creep behavior resembles the one of fcc metals, with an increase of the strain rate in the last stage, followed by sample fracture [Myshlyaev 1969]. The steady-state creep at high temperature is characterized by an activation energy much higher than the activation energy for monovacancy self-diffusion, and can be modeled[6] using:

$$\dot{\varepsilon} = \dot{\varepsilon}_0 \exp\left(-\frac{U_c - V_c\sigma}{k_b T}\right) \tag{2.17}$$

where $V_c = 2.7 \times 10^{-27}$ m^3, $U_c = 5.6$ eV is the activation energy for steady-state creep and $\dot{\varepsilon}_0$ a reference strain rate of 10^{11} s^{-1}. Observation of thin foils deformed during the steady state reveal the formation of tangles and cells impeding dislocation movement; however dislocations still multiply at a rate large enough to compensate for their immobilization, hence a constant macroscopic strain rate. During steady-state creep subgrains form, the interactions between dislocations and the subboundaries limiting their motion.

Mechanism controlling the creep steady-state

At high creep stresses, a deviation from Eq. 2.17 is observed and an activation energy of 3.7 eV is found [Myshlyaev 1969]. This reflects the same

6 the model is valid for a compression stress lower than 100 MPa and specimen loaded in a $\langle 111 \rangle$ direction.

	$T \lesssim 1173\,\mathrm{K}$	$T \gtrsim 1173\,\mathrm{K}$
stage III	cross-slip	climb
stage V	climb	cross-slip
creep	climb	cross-slip

Table 2.2: Mechanisms governing stage III, stage V and steady-state creep in semiconductors as a function of temperature. Note that the effect of increasing temperature is similar to decreasing the strain rate in dynamical experiments, or to decrease the applied stress in creep tests.

phenomena as described previously in the case of constant strain rate experiments: for high creep stresses climb of edge dislocations governs the steady-state strain rate.

The underlying mechanism all along this dynamic recovery stage at temperatures above 1173 K is believed to be cross-slip of screw dislocations, and is reproduced correctly by the Escaig model [Siethoff 1983b]. It is interesting to notice that the activation energy for steady-state creep is very close to the one for self-diffusion at temperatures above $\sim$ 1200 K (5.6 eV for an interstitial mechanism according to [Wu 1977], although more recent results point to an activation energy for diffusion of self-interstitals of 4.95 eV, see [Shimizu 2007]), hence a confusion about the mechanism actually responsible prior to the analysis of Siethoff.

More generally and independently on the temperature, the mechanism governing creep steady-state is the one responsible for stage V hardening in constant strain-rate experiments. An hypothesis is that no steady-state of deformation can be reached before both edge and screw dislocations have been affected, neither in dynamic experiments nor in creep. The steady-state observed in creep would then be the last mechanism affecting dislocations in dynamic experiments, i.e. the same as in stage V [Siethoff 1984]. Note that this cross-over of recovery mechanisms is also valid for germanium [Siethoff 1984, Siethoff 1986]. Table 2.2 summarizes the results exposed in this Section.

2.3.3 *Modeling recovery stages**

These late deformation stages cannot be described using a physically based formalism, since short-range interactions between dislocations as well as non-Schmid effects gain importance and dislocation structures that cannot be described by equations begin to form (subgrains, dislocation walls, etc.). Closely linked to these interactions are the immobilization and annihilation mechanisms responsible for the significant increase of the density of immobile dislocations that is absent in the model of Alexander & Haasen (see below) and never accounted for in the mechanical modeling of silicon crystals. Alternative models exist though, but these are not connected to

the dislocation density (for example, it is possible to use the creep law described above) [Moon 2002].

Constitutive models for silicon materials are therefore limited to the very first stage of deformation, the yield region described in Section 2.1. The reason for this limited modeling capacity lies in the practical needs of the silicon industry in the second half of the XX^{th} century: materials produced could be dislocated but large strains were never reached in single crystals actually used. The case of monocrystals deformed in "hard" crystallographic orientations is atypical: although relevant no attempt to model their mechanical behavior has seen the light until now. Next Section introduces the constitutive model that has traditionally been used for any type of silicon material, in spite of its simplicity.

2.4 LIMITATIONS AND IMPROVEMENTS OF THE AH MODEL

2.4.1 *Assumptions of the model*

The various explicit or implicit assumptions of the AH model are discussed in light of experimental observations. The main critics concern deformation homogeneity (assumption nr. 1), the assimilation of all dislocations to the mobile ones (nr. 2) and the activation of a single slip system (nr. 4).

Deformation homogeneity

The first hypothesis of the AH model, namely that deformation is homogeneous throughout the sample, is far from always being valid. Inhomogeneities appear macroscopically by the propagation of Lüders bands in the yield region, starting from the specimen end faces and propagating inwards and associated to slip on the coplanar slip system at the propagation front. Widening of the bands is believed to proceed by cross-slip of screw dislocations located at the boundaries [Mahajan 1979]. The bands form preferentially at regions submitted to higher stresses such as the ends of a tensile specimen kept between the grips of the testing apparatus, where multiple glide can be observed as well [Alexander 1968]. Figure 2.9a shows etch pits of dislocation-free germanium crystals deformed at small strains: in addition to inhomogeneous distribution of the dislocations several slip systems are active.

Inhomogeneous plastic deformation is observed preferentially in dislocation free crystals or crystals containing very little dislocations, sometimes even at temperatures close to the melting point as discussed by [Yonenaga 1996b, Siethoff 2001]. The propagation of Lüders bands in dislocation-free crystals leads to the development of Lüders strain in CZ materials, the case of FZ crystals being unclear. High temperature annealing solves the issue, indicating that impurities might play a role in the preferential development of plastic inhomogeneities by pinning of the dislocation sources [Mahajan 1979]. Doping favors the development of plastic inhomogeneities: Figure 2.10 shows the macroscopic effects of the formation of Lüders bands depending on the orientation of their propagation front with respect to the primary glide plane [Siethoff 1973].

Prestrained crystals deform homogeneously on a macroscopic level (Fig. 2.9b) [Yonenaga 1978]. Heat treated dislocation-free CZ crystals exhibit similarly slip at a much finer scale than otherwise [Mahajan 1979]. Homogeneity at the lower yield point is nevertheless not straightforward at a microscopic scale, especially at high temperatures (see, e.g., [Oueldennaoua 1988]). Low stresses tend to leave dislocations inhomogeneously distributed on a microscale, with bundles of edge character separated by 10 to 50 μm depending on the temperature and strain rate, connected with each other by superjogs. Deformation at lower temperatures leads to a more homogeneous distribution of the dislocations, even at the microscale. Finally, homogeneity at such a small scale in the yield region of prestrained samples is not

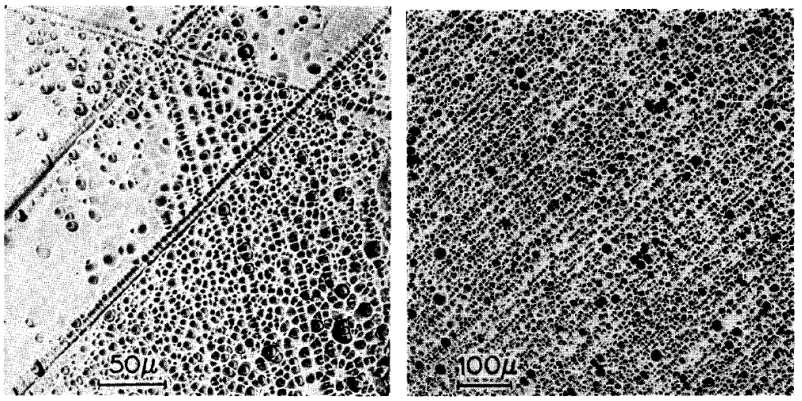

(a) Dislocation-free crystal. (b) Prestrained crystal, $\rho_{m,0} = 5 \times 10^9\ \mathrm{m}^{-2}$.

Figure 2.9: Etch pit observations of germanium crystals deformed at small strains ($\sim 0.1\,\%$) [Patel 1963].

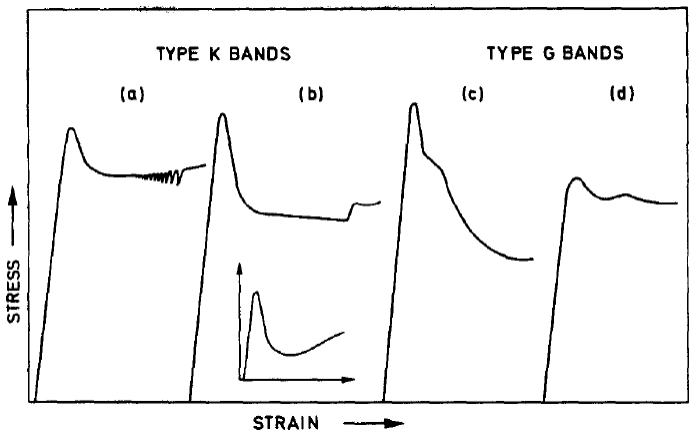

Figure 2.10: Stress-strain curves of heavily doped FZ silicon crystals. Type K bands: propagation front of the Lüders bands perpendicular to the primary plane. Type K: band front parallel to the primary plane. The insert shows the mechanical behavior of undoped material [Siethoff 1973].

guaranteed before the upper yield point [Allem 1989]. The consequences of dislocation pinning by impurities such as oxygen will be discussed later.

Dislocation multiplication at the onset of plasticity

Closely linked to the homogeneity of plastic deformation is the location and efficiency of dislocation sources in dislocation-free material. If these sources are inhomogeneously distributed then odds are high that deformation will localize in the yield region while the crystal is not yet filled with dislocations. The question of what and where the sources are in intrinsic crystals[7] has been investigated by several authors [George 1973, George 1975, Kirscht 1978, Vallino 2001]. The surfaces and edges of dislocation-free samples are preferential nucleation sites since polishing and sample preparation cannot provide with atomically flat surfaces [Kirscht 1978]. A dislocation nucleated at the surface can climb or cross-slip with the eventual help of image forces. Cross-slipping can then results in dislocation multiplication by the formation of a spiral Frank-Read source [George 1973]. Double cross-slip at the surface or in the bulk allows dislocations to spread onto parallel slip planes after their generation [George 1975, Vallino 2001]. These multiplication mechanisms take place preferentially at surface defects and can therefore lead to inhomogeneous plastic deformation by strain localization. Multiple slip is also observed at surface defects [Vallino 2001]. A detailed discussion about the dislocation multiplication mechanisms is available in the next Part of this work.

Presence of immobile and forest dislocations

The assumption that all dislocations are mobile in as-grown crystals of low dislocation densities is experimentally verified prior to deformation, as long as the material is intrinsic. Measurements of the effective stress at the lower yield point combined with experimental determination of the total dislocation density and the use of Orowan's law allows for the determination of the share of mobile dislocations, whereas etch pitting on different planes gives the density of the eventual forest dislocations generated during deformation.

Dislocation-free samples always deform on multiple slip systems, especially as the upper yield stress is enhanced by low temperatures or high strain rates [Patel 1963, Alexander 1968]. The activation of secondary slip systems is dampened by prestraining and annealing of the samples [Yonenaga 1978]. The density of forest dislocations is one order of magnitude lower than the total density at the lower yield point. The fraction of mobile dislocations depends on the deformation conditions and can reach several tens percent [Sumino 1974a, Yonenaga 1978]. These observations call indeed for adaptations of the AH model to real crystals.

The influence of a high initial dislocation density on the mechanical behavior of silicon crystals has been extensively studied by the Nancy group

7 the case of dislocation generation in extrinsic crystals is discussed in Chapter 3.

[Omri 1987, Oueldennaoua 1988, Allem 1989] that worked on samples prestrained at 1323 K up to the end of the easy glide stage and subsequently deformed at lower temperatures. Such a treatment leads to the buildup of a population of immobile dislocations and shows that the AH model is not valid for prestrained crystal.

Effective stress at the lower yield point

The prediction made by the AH model of an effective stress at the lower yield point equal to one-third of the applied stress has been shown not to hold in prestrained samples [Oueldennaoua 1988, Allem 1989]. The effective stress is then experimentally found to be almost equal to the lower yield stress. It is noticed that the total dislocation density increases significantly beyond the upper yield point, and that the density of mobile dislocations becomes preponderant as the temperature is lowered. As a consequence, at low temperatures and at the lower yield point the back stress is effectively expressed as a sole function of the density of mobile dislocations, while this becomes unclear at higher temperatures. The AH model fails hereby to predict the accurate internal stress and overestimates it by predicting a high density of mobile dislocations that is not found experimentally. On the other hand, using the AH model to compute the lower yield stress still yields satisfying results. The authors distinguish therefore two stress regimes, temperature and strain rate deciding which one to be relevant:

- For $\tau_{lyp} \gtrsim 10$ MPa, the effective stress at the lower yield point is an important fraction of the applied stress, and the mobile dislocation density is a weak function of the deformation conditions. A steady-state of the density of mobile dislocation density and of the effective stress are observed after the upper yield point while the total dislocation density still increases, also in agreement with the observations of [Suezawa 1979]:
$$\tau_{eff,lyp} \gtrsim 0.75\,\tau_{lyp} \tag{2.18}$$
- For $\tau_{lyp} \lesssim 10$ MPa, the preferred <110> dislocation orientations disappear, the mobile dislocation density becomes a small fraction of the total dislocation density and the effective stress might be lower than the lower yield stress. The relative lack of knowledge of the conditions at high temperatures comes mainly from the increasing difficulty of distinguishing mobile from immobile dislocations as they loose their clearly defined shape and start to condense in tangles. Note that this stress threshold actually depends on the microstructure and its associated internal stress. A different prestraining would affect the value of 10 MPa mentioned here.

2.4.2 *Equations of the AH model*

There are two ways of analyzing the AH model: either by assuming that its characteristic equations (Eqs. 2.9 and 2.10) are right and checking the

accuracy of its predictions, in which case the weaknesses of the simplifications done to build the model can be highlighted; or by questioning the very expressions for dislocation multiplication and internal stresses.

Predictions of the yield stresses

PLASTIC STRAIN RATE VARIATIONS AT THE LOWER YIELD POINT The condition used by Alexander and Haasen for analytical determination of the lower yield point (Eq. 2.12) is two-fold: the derivative of the plastic strain rate with respect to the dislocation density has to be zero, and the total strain rate at the lower yield point is equal to the plastic strain rate, $\dot{\gamma} = \dot{\gamma}_p$. Sumino and Yonenaga have questioned this assumption and showed that the condition for lower yield point is different when taking into account the variations of the plastic strain rate with the total strain in the yield region [Suezawa 1979]. The appropriate condition would then be Eq. 2.19:

$$\tau_{yp} = \mu b A \sqrt{\rho_{m,yp}} \left(1 + \frac{m_0}{2} \frac{1}{1 - \left(\frac{\partial \ln \dot{\gamma}_p}{\partial \ln \rho_m} \right)_{yp}} \right) \tag{2.19}$$

to compare to Eq. 2.13. Formally, Alexander & Haasen's method of computation is consequently not valid; nevertheless the numerical results yielded by Eq. 2.13 are quite similar to those obtained using the correction of Eq. 2.19. This is due to the fact that computation of the density of dislocations at the lower yield point $\rho_{m,yp}$ in the alternative model of Suezawa leads to a slightly higher value than using the original approximation of the AH model. Those two combined effects compensate each other and the same numerical value is found.

INFLUENCE OF INITIAL DISLOCATION DENSITY AND FOREST DISLOCATIONS Some concerns have been emitted about the accuracy of the equations derived from the AH model which do not take into account the initial dislocation density [Yonenaga 1978]. Siethoff showed that the lower yield stress actually depends on the as-grown dislocation density of the sample and the quality of the pre-deformation if applied [Siethoff 1992], in agreement with the previous authors. This flaw leads to some discrepancies between theoretical and experimental results of τ_{yp} at low initial dislocation densities. An expression alternative to Eq. 2.2 has been suggested to relate the yield stresses to the initial dislocation density:

$$\tau_{yp} = C_1 \ln \frac{\rho_{m,0}}{C_2} \tag{2.20}$$

This equation is valid for $\rho_{m,0} < \rho_{0,max} \simeq 10^9$ m^{-2}. C_1, C_2 as well as the critical density $\rho_{0,max}$ are dependent on the temperature and the strain rate [Suezawa 1979].

The magnitude of the lower yield point is influenced by the presence of forest dislocations introduced during yielding: a higher magnitude of the

upper yield point due to a small initial dislocation density causes activation of secondary slip systems and indeed a higher lower yield point caused by latent hardening. This contribution of secondary slip systems can be neglected at high initial dislocation densities, though. The incorporation of forest dislocations into the predicted yield stresses is simply done by adding to Eq. 2.19 the internal stress they create.

Internal stress

The expression for the back stress exerted by the pile-ups initially used by Alexander & Haasen has been found not to be accurate, as the value of β has been identified by best fit both to experimental stress-strain curves [Suezawa 1979] and to simulations [Moulin 1999b]. Sumino and Yonenaga also mention the need for accounting for the contribution to the flow stress of immobile dislocations, even at the yield points. This implies some additional terms in the expression of the internal stress, Eq. 2.21.

$$\begin{cases} \tau_{int}^{i} = \tau^{0}\sqrt{\gamma - \gamma_{0}} \\ \tau^{0} = \tau^{0}\left(T, \dot{\gamma}\right) \end{cases} \tag{2.21}$$

The observation of a steady state of deformation, where the density of mobile dislocations and the effective stress reach constant values depending on the deformation conditions, leads to results describing effectively the behavior of silicon crystals after the lower yield point during the easy glide stage [Sumino 1971]. The description of the steady-state cannot be done without the introduction of the additional hardening term given by Eq. 2.21 coming from the presence of immobile dislocations and the increasing short-range interactions taking place in the crystal [Sumino 1974b, Suezawa 1979].

It has been observed more recently that the stress state at the lower yield point is likely not to follow these assumptions: the effective stress at the lower yield point of prestrained crystals seems to be closer to the applied one. The flow stress into stage I at high temperatures is even recorded to be much smaller than the addition of contributions from mobile dislocations $\mu b A\sqrt{\rho_m}$ and immobile ones τ_{int}^{i} [Oueldennaoua 1988]. This indicates a change from an athermal mode of dislocation motion over the barriers to a thermally activated one, that cannot be described by the current constitutive models.

Multiplication law

INFLUENCE OF FOREST DISLOCATIONS The multiplication law proportional to the effective stress is questionable as it is purely empirical. Forests dislocations have also been found to play a significant role in the yield region, influencing the lower yield stress behavior and being able to act as dislocation sources as is commonly observed in FCC metals. Generation of dislocations from forest dislocations could explain partly the dependence of the lower yield stress on the initial dislocation density up to a critical

value [George 1987b]. [Suezawa 1979] indicate that the constant δ steering dislocation multiplication (Eq. 2.9) should be dependent on the initial dislocation density in order to represent correctly the yielding behavior of silicon, a correction that could translate the additional dislocation density nucleated by interaction of the primary dislocation with the trees of the forest. It has actually been demonstrated on germanium single crystals that an appropriate dislocation multiplication law should consider δ as a free parameter that depends on the sample tested, and would translate the influence of varying conditions such as inhomogeneity of the deformation [Fikar 2005, Fikar 2006].

All experiments performed in the literature have been performed with perfectly controlled crystal orientations, most often chosen so that only one primary glide system was activated. In the case of multicrystals or polycrystals, no such control is allowed *a priori*, and applying a strain on a random orientation of a sample can lead to activation of several slip systems. The mathematical formulation of this problem will be dealt in the second Part; here we will concentrate on the model already existing. Some discrepancies between experiments and simulations can be solved through the adoption of a multiple slip formulation: both the multiplication rates and expressions of effective stresses are affected [Sumino 1993]. The evolution of dislocations on the slip system α reads:

$$\begin{cases} \dot{\rho}_m^{(\alpha)} = \tau_{eff}^{(\alpha)} \rho_m^{(\alpha)} v^{(\alpha)} \left(\delta + \delta^* \sum_{\beta \neq \alpha} \rho_m^{(\beta)} \right) \\ \tau_{eff}^{(\alpha)} = \tau^{(\alpha)} - \mu b \left(A \sqrt{\rho_m^{(\alpha)}} + A^* \sum_{\beta \neq \alpha} \sqrt{\rho_m^{(\beta)}} \right) \end{cases} \tag{2.22}$$

$$\dot{\gamma}_p^{(\alpha)} = b \rho_m^{(\alpha)} v^{(\alpha)} + b \sum_{\beta \neq \alpha} s_\beta \rho_m^{(\beta)} v^{(\beta)} \tag{2.23}$$

where the superscripts refer to the slip system. The parameters δ^* and A^* are experimentally found to be 4×10^{-8} MPa^{-1}m^{-1} and 0.45, respectively. They translate the influence of secondary dislocations on the multiplication process (δ^*) and internal stress (A^*) on the primary system. The s_β's are coefficients related to the Schmid factors, relative to the primary slip system and associated to the different slip systems β. This modification of the model yields excellent results, in agreement with the experimental observations.

ALTERNATIVE MULTIPLICATION LAWS [Moulin 1999b] have proposed another multiplication law based on mesoscale simulations of dislocation multiplication. They consider that there is no physical justification for the stress dependence, as the law was determined to fit creep experiments on germanium, and some doubts could be emitted about its validity. Their simulations show that a multiplication law proportional to the swept area is not adequate either and leads to errors of representation of the multiplica-

tion rate at the upper yield point. They suggest instead to use to following equation to model the multiplication rate:

$$\frac{\mathrm{d}\rho_m}{\mathrm{d}t} = \delta_M \sqrt{\tau_{eff}\rho_m} v \exp\left(-\frac{\rho_m}{\rho_s}\right) \tag{2.24}$$

where δ_M is a constant analogous to δ in the AH model and ρ_s is a saturation term depending on the temperature and applied strain rate. The exponential term is added to take into account the size effect due to saturation of the simulated specimen. For an infinite crystal, this term can be considered to be unity.

However, such a law has been derived for a constant number of dislocation sources and planar glide only, the authors emphasizing that cross-slip mechanisms have not been accounted for[8]. In addition, this law is valid for temperatures between 800 and 1200 K, where the dislocation motion mechanism is assumed to be governed by Peierls forces. The temperature domain influenced by point defects is therefore excluded from the discussion.

In addition to this generation term, it might be relevant to raise the possibility of an annihilation or immobilization term, since the AH model deals only with mobile dislocations although experiments point to the buildup of a population of immobile dislocations already at the lower yield point. Several models exist for these terms, but for covalent crystals only one group has conducted extensive research in this direction by performing transient tests on germanium single crystals [Fikar 2002, Fikar 2005, Fikar 2006]. Several immobilization laws have been tested and fitted to experimental results. Disappearance of mobile dislocations at the surface of the samples has also been modelled. The model accounting for dislocation immobilization (Eq. 2.25) considers however single slip only:

$$\dot{\rho}_i = \delta_{imm}(\rho_m b v)\rho_t \tag{2.25}$$

where ρ_i and ρ_t are the density of immobile dislocations and total dislocation density, respectively.

2.4.3 *3D-modeling*

The need to simulate industrial processes has been investigated by several authors for different semiconductors [Dillon 1986, Kim 1987, Tsai 1992, Maroudas 1999], and a modification of the classical one-dimensional model for its generalization to three dimensions has therefore been derived. Since dislocation generation is reactive to shear stresses, a J_2 plasticity formulation is chosen (Eqs. 2.26 and 2.27). Fundamental assumptions related to such a choice are that plasticity is isotropic and that only one fictious slip system can be activated.

$$\begin{cases} \dot{\boldsymbol{\varepsilon}} = f\boldsymbol{S} \\ \boldsymbol{S} = \boldsymbol{\sigma} - \frac{1}{3}\mathrm{tr}\boldsymbol{\sigma}\boldsymbol{I} \end{cases} \tag{2.26}$$

8 cross-slip mechanisms in the bulk are not fully understood yet, and never modelled directly in the equations of the reviewed papers.

$$\begin{cases} f = \frac{\rho_m v b}{\sqrt{J_2}} \\ J_2 = \frac{1}{2}\boldsymbol{S} : \boldsymbol{S} \end{cases} \tag{2.27}$$

and the equations for the effective stress and dislocation multiplication are similar to those of the AH model:

$$\sigma_{eff} = \sqrt{J_2} - \mu b A \sqrt{\rho_m} \tag{2.28}$$

$$\dot{\rho}_m = \delta \sigma_{eff} \rho_m v = \delta \sigma_{eff}^{m_0+1} \rho_m \frac{v_0}{\tau_0} \exp\left(-\frac{U}{k_b T}\right) \tag{2.29}$$

Such a model has several drawbacks coming from the choice of the plastic yield surface but give qualitatively good results for monocrystals or polycrystals.

2.5 CONCLUSION ON THE MACROSCOPIC BEHAVIOR OF INTRINSIC SILICON MONOCRYSTALS

More than thirty years after the pioneering review of Alexander & Haasen, Siethoff *et al*. confirmed the validity of the expression for dislocation velocity in FZ-grown silicon for temperatures up to 1573 K under certain conditions of strain rate and initial dislocation density. To the knowledge of the author, the additional velocity regimes at very high (or low) temperatures and low strain rates have never been considered in simulations of silicon mechanical behavior. This might be due to an appearance of these regimes that is not clearly defined and depends on several factors such as the initial dislocation density, temperature, strain rate, and other contributions from point defects that are still not fully understood.

It can be concluded that the formalism of the AH model can be applied to the modeling of the yield region of silicon crystals throughout the whole temperature range 723-1323 K, and eventually up to 1573 K if the variations of the velocity parameters are accounted for in the low strain-rate range (lower than 10^{-3} s^{-1} for an initially dislocation-free material). The dislocation multiplication law must be adapted to account for thermally activated immobilization and annihilation processes taking place at high temperatures, and for the role played by forest dislocations on both multiplication mechanisms and the internal stress. A high initial dislocation density must be carefully examined as well since the influence of immobile dislocations and of the microscopic dislocation structure might lead to a different mechanical behavior. The next Chapter deals with the effects of impurities and other extrinsic species on the mechanical behavior of silicon materials.

3

IMPURITIES AND DEFECTS IN SILICON MATERIALS

The presence of impurities and defects in silicon directly influence the macroscopic behavior of the bulk material by affecting the microscopic mechanisms of plasticity, namely motion and multiplication of dislocations. Section 3.1 introduces the major impurities and defects found in silicon materials of electronic and solar grades. Oxygen precipitates have special effects on plasticity that will be described there. The macroscopic effects of dissolved impurities will be discussed in Section 3.2. Finally, models for dislocation pinning and formation of atmospheres around the dislocations will be surveyed in Section 3.3. The literature about impurities in EG-Si is very abundant and this Chapter aims only at giving a snapshot of the complexity of this research field. In addition to the impurity type, content and distribution that depends on the crystal growth technology, one must account for the influence of thermal treatments on impurity precipitation and the multiple interactions that can take place between the contaminants. The case of the hydrogen impurity has not been reviewed.

3.1 DEFECTS IN EXTRINSIC SILICON MATERIALS

3.1.1 *Semiconductor-grade Si (EG-Si)*

Impurities

The major impurities that can be found in EG-Si are oxygen, nitrogen and carbon. Electronic applications require the use of monocrystalline materials, therefore EG-Si is always found as single crystals (c-Si). EG-Si has very low impurity contents and these can be controlled. Therefore such a material is ideal for experimental investigation of the effects of given impurities on the mechanical behavior of silicon materials. Undoped FZ crystals are usually taken as representative of the intrinsic material.

The typical impurity content will vary depending on the method chosen for crystal growth, Czochralski or Float-Zone (CZ or FZ, respectively). For example, oxygen concentration in CZ silicon crystals is usually two to three orders of magnitude higher than in FZ crystals. These impurities can lead to varying macroscopic mechanical strengths of dislocated silicon crystals, see next Section. Some other impurities are found, B and P being of interest since they are used for doping. Electrically active impurities such

as dopants affect the activation energy for dislocation motion by affecting the core structure of the dislocations. As a matter of fact, there are very few impurities to consider in EG-Si, apart from the three electrically inactive ones mentioned above and as long as this feedstock material is not used for production of multicrystalline ingots, in which case additional impurities must be considered (see below). This explains why literature about impurity-related defects in silicon earlier than the 1990's has concentrated almost exclusively on oxygen and dopants, and to a less extent on nitrogen and carbon.

CZ crystals doped with high boron concentrations are prone to the formation of boron-oxygen complexes that form under illumination and degrade the efficiency of the solar cell with time and ultimately determine the lifetime of minority carriers in materials virtually free from metallic impurities and other recombination centers. These defects result from the complexation of interstitial oxygen dimers O_{2i} and substitutional boron B_s and the stable cell efficiency is reached in up to a few days at low B concentrations [Bothe 2005].

Planar and extended defects: oxygen precipitates

Closely related to the impurity content in CZ-Si, oxygen precipitates (SiO_2) are observed to form in the bulk material that create a complex strain field around them [Yonemura 1999], which in turn leads to the formation of interstitial defects [Bolotov 1993] and can act as gettering centers for other metallic impurities [Hielsmair 1998]. The solubility of O in silicon is given by Eq. 3.1 [Mikkelsen 1986]:

$$c_O^{(s)} = 9 \times 10^{22} \exp\left(-\frac{1.52}{k_b T}\right) \text{ cm}^{-3} \tag{3.1}$$

A very high supersaturation is required in defect-free crystals to nucleate oxygen precipitates. The presence of dislocations or other extended defects eases significantly the formation of precipitates [Freeland 1977]. Nitrogen is also believed to enhance their formation [Yang 2003]. The density and size of oxygen precipitates depends on the annealing temperature and time. Three precipitation stages can be observed at different temperatures given an annealing time; actually the three different morphologies result from diffusion kinetics only as the ones observed at high annealing temperatures can also be obtained by a long intermediate temperature annealing [Sumino 1999b]. Below 923 K small spheres of diameter 2 nm are formed. At intermediate temperatures between 1123 and 1273 K, square-shaped platelets are obtained. Finally between 1373 and 1473 K octahedrons form, eventually surrounded by extrinsic stacking faults. The formation of these precipitates requires nucleation sites and high concentrations of dissolved oxygen seem to increase their number, resulting in enhanced precipitation in such crystals [Yonenaga 1984a].

Prismatic loops gathering impurities are actually punched out from the square-shaped precipitates [Tan 1976, Tan 1977]. These loops can act in turn

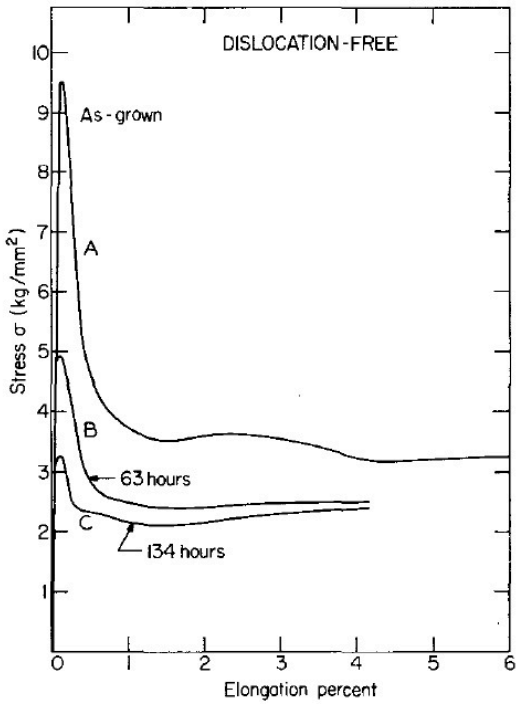

Figure 3.1: Effect of heat-treatment-induced oxygen precipitation on the mechanical behavior of dislocation-free silicon monocrystals. (A) as-grown material (B) 63 hours annealing at 1273 K (C) 134 hours annealign at 1273 K. Deformation at 1073 K [Patel 1962].

as dislocation sources and enhance a homogeneous dislocation generation in the crystal; the larger the precipitate the lower the required stress to generate dislocations. Oxygen precipitates larger than 200 μm are therefore favorable nucleation sites for dislocations, with the consequence of lowering the yield stress of heat treated silicon materials in which oxygen precipitation occurs (see Figure 3.1) [Yonenaga 1984a]. This softening phenomena has been reported very early in research on semiconductors [Patel 1962]. This is the reason why heat treated CZ crystals do deform homogeneously without Lüders bands [Mahajan 1979].

Such precipitates can also pin dislocations if they are small enough [Yang 2003], and oxygen atoms that have not precipitated during the heat treatment also act as strong pinning agents (see Section 3.2.2), so a competition exists between their ability to act as dislocation nucleation centers on the one hand and as dislocation stoppers on the other hand [Yasutake 1980, Yonenaga 1984a]. The resulting net effect of precipitates when dissolved oxygen concentration is low is generally a softening of the material, because large amounts of dislocations generated at large precipitates cannot be pinned at the smaller ones unless the latter are present in sufficiently large numbers [Nishino 1982]. As mentioned earlier, the

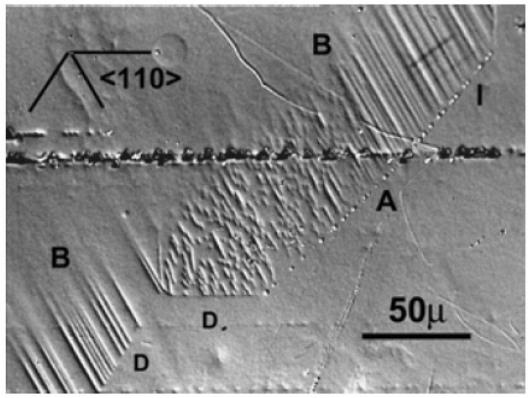

Figure 3.2: Optical image of silicon deformed at 900 K and etched to reveal trailing extended defects (TED). AB correspond to the TED positions. Note the TEDs starting exactly at the dislocation line (D) [Eremenko 2009].

heat treatment decides the size and distribution of these defects in the bulk. Oxygen precipitates that form at the dislocation cores have different atomic structures than those found in the silicon matrix [Sumino 1992] (see Section 3.2).

Other planar and extended defects

Other planar defects are of course stacking faults, surrounded by the dislocation partials, stacking faults generated by oxygen precipitates, Frank partials. Deformation itself creates defects that behave differently with temperature and annealing time, as well as with the extent of deformation: dislocations, dislocation dipoles, small loops of dislocations, faulted dipoles, point defects, etc. These are described and studied in [Yonenaga 1993]. Moving dislocations themselves leave in their trail electrically active extended defects as revealed by EBIC measurements [Eremenko 2007]. These defects are generated from 60° dislocations only at very regular intervals along the lines (1-5 μm) and form ridges aligned along a screw orientation as seen at the surface of the etched crystal (see Figure 3.2) [Eremenko 2009]. Their exact origin is not known yet. The atmosphere in which deformation takes place is known to affect the mechanical behavior of silicon crystals as well. For example, nitrogen present in forming gas has been mentioned to develop a Si_3N_4 coating at the sample surface between 1273 and 1473 K, affecting the properties of the stress-strain curve in the yield region [Siethoff 1988]; crack healing is observed in oxygen-containing atmospheres (see Section 4.3.3).

3.1.2 *Solar-grade Si (SoG-Si) and multicrystals (mc-Si)*

Solar-grade silicon materials are used exclusively by the photovoltaic industry, hence their name. The impurity requirements for PV applications

are lower than in the case of electronics, so that it becomes cost-effective to purify raw metallurgical-grade silicon by means of ingot casting. Such a process has the drawback of forming multicrystals (mc-Si) instead of monocrystals, in addition to being less effective at purification than other classical CZ or FZ methods.

Multicrystals differ from single crystals by the presence of grain boundaries that have particularly strong effects on the impurity and defect segregation. When reading the literature it is easy to forget the fundamental difference between the feedstock (SoG-Si) and the topology of the materials (mc-Si): it is possible to produce mc-Si from EG-Si feedstock and vice-versa. For example one should notice that some wafer providers use SoG-Si feedstock to grow large monocrystals using the CZ technology for the PV market. Monocrystalline solar cells have indeed a higher efficiency than their multicrystalline counterparts since no grain boundary and less dislocations are present to trap minority carriers. In the following we will concentrate on the defects and impurities traced in SoG-Si and in mc-Si materials crystallized from such a feedstock. A review of the impurities in SoG-Si is available [Macdonald 2007].

Oxygen, carbon and nitrogen

Oxygen, carbon and nitrogen are the main impurities in mc-Si, and their distribution as well as interaction have been studied for example by the groups of Möller and Yang [Möller 1999, Möller 2002, Yang 2002]. Oxygen impurities come mainly from the crucible and its coating [Kvande 2005]. Oxygen can occupy interstitial sites, where it does not alter the performance of the solar cell, but oxygen precipitates affect both cell efficiency and mechanical strength. This is thought to be caused by impurity gettering at precipitates that act as recombination centers. Oxygen can form a variety of defects: clusters of a few atoms, SiO_2 precipitates and donors that affect the solar cell efficiency [Hässler 2000].

Which oxygen-related defect is preferably formed depends on the thermal history of the material and on the presence of other impurities [Möller 1999, Hässler 2000]. Depending on the temperature, plate-like defects or spherical precipitates can be detected in the bulk, the critical temperature for transition between the two shapes being 1323 K (See Figure 3.3). Their formation in the bulk[1] requires a concentration of interstitial oxygen larger than $3 \times 10^{17}\,\mathrm{cm}^{-3}$ and is enhanced in the presence of high carbon concentrations. In the latter case, oxygen and carbon co-precipitate. Precipitation of oxygen occurs mostly in the temperature range from 1073 to 1473 K, and annealing at 1530 K for 1 hour dissolves all precipitates in as-grown mc-Si wafers [Möller 1999].

Precipitation occurs during crystal growth and is enhanced at grain boundaries and dislocations, although these intrinsic defects do not affect

1 precipitation at lower concentrations is possible at the dislocations by formation of clusters [Möller 2002].

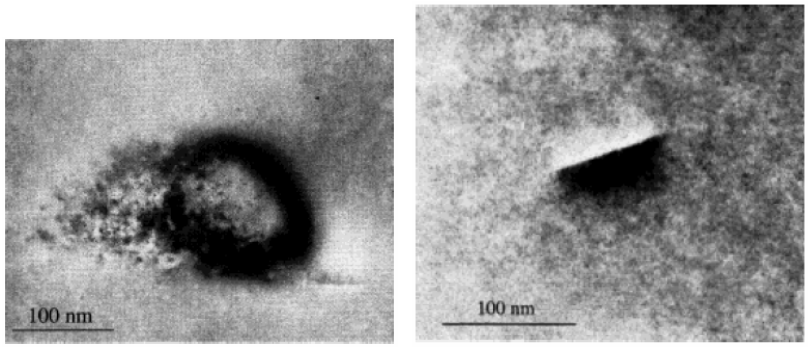

(a) Spherical precipitate of amorphous nature.

(b) Plate-like SiO_2 precipitate. High-resolution microscopy reveals that defects are attached to the plate.

Figure 3.3: TEM images of oxygen precipitates in mc-Si material [Möller 1999].

the precipitation process. The decoration of most of the dislocations by oxygen is of interest for dislocation mobility, as will be discussed later [Möller 2002]. Dislocations can hence be used for impurity gettering, which explains by the way why they act as recombination centers in the solar cells in spite of their low intrinsic electrical activity due to their core reconstruction (Chapter 1).

Carbon originates from from insulation and heating elements of the furnace [Kvande 2005]. It has a strong influence on the precipitation of O at temperatures below 1123 K, because of its associated lattice contraction when dissolved in the bulk as a substitutional atom, providing effective precipitate nucleation centers. At higher temperatures, carbon diffuses to the oxygen precipitates without enhancing their promotion. The enhanced oxygen precipitation in presence of high carbon concentrations is not affected by grain boundaries or dislocations [Yang 2002]. C can also precipitate as SiC when its concentration exceeds the solubility limit, but its precipitation is more dependent on its diffusion than on its supersaturation because of its low diffusivity. Another source of SiC particles comes from their formation in the melt and subsequent incorporation into the solidified silicon matrix [Liu 2008].

Nitrogen introduced by the crucible coating Si_3N_4 forms N-O complexes that are are electrically active and can be avoided by high temperature heat treatments. They form preferentially in the bottom region of the ingot and near its edges [Yang 1996].

Metallic contaminants

Metallic contaminants are also commonly found in concentrations in the range 10^{10} to 10^{15} cm^{-3}: Fe, Ni, Cu, Cr, Co, Mo, and to a lesser extent Mn, Ti, Zn and V. Some species are present in the feedstock but some also come

from the crucible [Macdonald 2007]. These atoms tend to be located at the top of the mc-Si ingot because of segregation during crystallization, but a backward solid diffusion occurs during the cooling time, leading to a larger spreading of these impurities [Matinuzzi 2007]. Grain boundaries and dislocations act as precipitation centers for these metals, reducing the carrier lifetime and being hereby detrimental to the solar cell efficiency. Fast diffusers Ni, Cu and Co almost always precipitate when their concentration exceeds the solubility limit. Observation of the location of precipitation of metallic impurities at grain boundaries reveals that they are likely to precipitate on boundaries with low atomic coincidence (high Σ) [Buonassisi 2006], which is explained by the low level of bound distortions found in low-Σ boundaries. Here, it might be interesting to increase the content of low-Σ grain boundaries so as to decrease the sinks for metallic impurities, as pointed out in [Buonassisi 2006].

Metallic impurities (e.g. iron and copper) have been much less studied than dopants, principally because of their limited presence in silicon single crystals. The extensive use of ingot casting in the last decades has led to an increased interest in the field. Dislocations acting as gettering centers for impurities, their decoration by metallic contaminants has an extremely harmful effect on the solar cell efficiency as they act as recombination centers.

Fe atoms diffuse to the dislocation cores where they aggregate without forming precipitates as oxygen atoms do [Sumino 1999b]. Nickel can precipitate in dislocation-free silicon by forming $NiSi_2$ platelets on the {111} planes. Its precipitation at dislocation leads to the formation of tetrahedra and octahedra as is the case for oxygen precipitates in the intermediate temperature range [Seibt 2005]. Cu gettering at dislocations was used very early to observe dislocation loops in bulk silicon [Dash 1956]. Copper precipitation depends on its concentration at high temperature and the cooling rate. Dislocations in the crystal act as nucleation centers for Cu precipitates, which then emit interstitials because of the strong lattice distortion following their buildup, provoking climb of the dislocation segments and further development of precipitates [Seibt 2005, Sumino 1999b].

Inclusions

Inclusions of SiC (Figure 3.4) and Si_3N_4 are also found in multicrystalline silicon ingots. Both species are found as single particles or together as clusters, although in an inhomogeneous distribution through the ingot. It seems that Si_3N_4 particles act as nucleation centers for SiC. It is consequently common to find both species at the same location (Figure 3.5). The large size of these inclusions, found to lie usually between 75 and 385 µm, makes them important from a mechanical point of view, for example when considering fracture and the wafering phase (see Section 4.3.4) [Søiland 2004]. Like oxygen precipitates, SiC particles are not directly detrimental to the solar

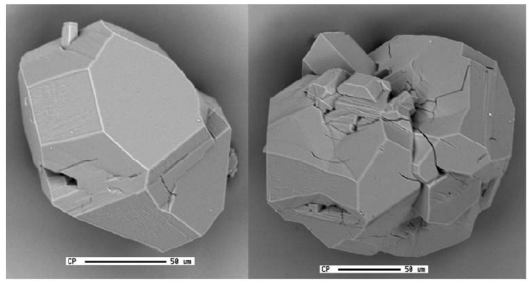

Figure 3.4: SEM of β-SiC particles [Søiland 2004].

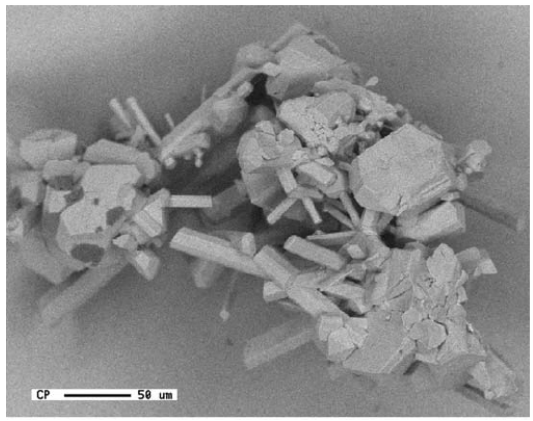

Figure 3.5: SEM of clusters of β-SiC and β-Si_3N_4 particles [Søiland 2004].

cell efficiency but the accumulation of other impurities around them makes them harmful for the minority carrier lifetime.

Grain boundaries and dislocations

These extended defects are fingerprints of mc-Si materials. They act as segregation sites, especially for oxygen, and as such are generally detrimental to solar cell efficiency, although grain boundaries are less dangerous than dislocations in this respect [Hässler 2000]. Diffusion of impurities to the grain boundaries creates denuded zones free from contaminants and leading to large minority carrier lifetimes, as shown in Figure 3.6. Regions of high dislocation densities have been known for a long time to be harmful to the solar cell efficiency [Pizzini 1988]. While individual dislocations can act as gettering centers, clusters of dislocations are believed to cause serious efficiency losses [Sopori 2005].

Distribution of impurities and inclusions in the ingots

The distribution of impurities in as-grown directionally solidified ingots is not homogeneous and depends on two factors: segregation and diffusion.

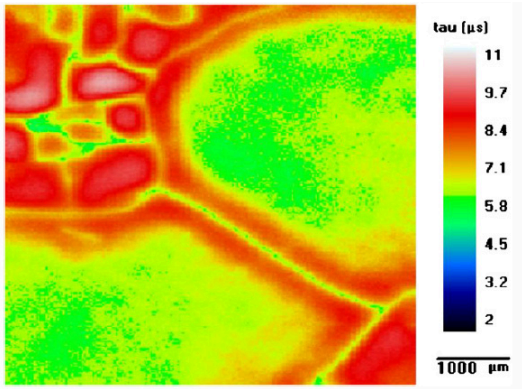

Figure 3.6: Minority carrier lifetime scan map in a mc-Si wafer. Note the denuded zones along the grain boundaries exhibiting larger lifetimes [Matinuzzi 2007].

Most impurities have low segregation coefficients, meaning that they are more soluble in the liquid than in the solid phase. During ingot crystallization these impurities are consequently pulled out from the solid/liquid interface until they finally incorporate the solid phase when little melt is left, i.e. at the top of the ingot. Diffusion is responsible for the appearance of oxygen at the bottom and the edges of the ingots as it diffuses from the crucible walls. Backward solid-state diffusion of the seggregated impurites deeper into the crystal during the cooling phase of the ingot is also observed and results in the extension of the "contaminated" region of the ingots that must be discarded.

Vertically speaking, oxygen is therefore found preferably at the bottom of the ingot, whereas the concentration of carbon and other impurities increases from the bottom to the top [Möller 1999, Kvande 2005]. High concentrations of dissolved interstitial oxygen favor its precipitation, and more oxygen precipitates are observed at the bottom of the ingots and at the ingot edges [Yang 2000, Möller 2002]. Although the oxygen content of mc-Si materials is similar to the one of CZ monocrystals, the concentration of interstitial oxygen O_i in the former varies a lot with the position in the ingot and can be lower than in CZ Si by one order of magnitude. This is due to enhanced oxygen precipitation in mc-Si. This particularity of mc-Si materials limits the development of boron-oxygen complexes compared to the case of CZ crystals, and implies that the minority carrier lifetime is limited in mc-Si by other species than these complexes [Bothe 2005].

It has been found that the concentration of dissolved oxygen decreases with increasing dislocation density, since they have the ability to act as precipitate nucleation sites. Moreover, less dissolved oxygen precipitates per dislocation length with increasing dislocation density, because of increased competition between dislocation segments for the available interstitial oxygen [Möller 2002]. See also Section 3.3.

The horizontal distribution of impurities stems directly from the temperature gradients during ingot solidification and the curvature of the solid/liquid interface. It is widely known that the edges of the ingots exhibit low minority carrier lifetimes due to high concentrations of impurities and other structural defects. Because the solubility limits are reached, higher precipitation of oxygen is noticed in these regions as well [Rossberg 2005].

3.2 INFLUENCE OF IMPURITIES ON PLASTICITY

We concentrate in this Section on the mechanical properties of silicon crystals containing dissolved impurities only. The case of precipitates and inclusions in the bulk has already been touched upon previously. Several reviews have been published dealing with the complex subject of interaction between impurities and dislocations [Sumino 1983b, Sumino 1992, Sumino 1999b, Sumino 2002]. This Section will expose the main results of this research field.

Roughly speaking, one could say that dissolved impurities affect the macroscopic behavior of dislocated crystals homogeneously whereas inclusions and precipitates have more local effects[2]. The formation of precipitates at the dislocations is of course possible, as will be seen below for the case of oxygen.

3.2.1 *Impurity gettering by dislocations*

There are two ways for impurities to interact with dislocations: either by forming a Cottrell atmosphere around the dislocation core (elastic binding), or by diffusing directly to the core (chemical binding). Impurities segregate around a dislocation or more generally at an extended defect because of their associated strain fields, in which case the interaction energy between an impurity and an extended defect is elastic in nature. The formation of an impurity atmosphere requires additional stress to keep the dislocation into motion as the atmosphere must be dragged along. Diffusion of impurities at the core will be seen in the next Section to have a starker effect on dislocation motion, resulting in an effective local pinning of the dislocation as its velocity is lowered. This pinning effect can result in the complete immobilization of the dislocation by dynamic ageing, ultimately preventing the dislocation from carrying plastic flow and thereby enhancing elastic deformation above the plastic one. Once impurities are segregated at the dislocation core, precipitates can form by diffusion of the atoms along the line.

Energetic considerations associated to the theoretical probability of formation of a Cottrell atmosphere lead to the conclusion that in semiconductors with impurity concentrations of 10 ppm or less, the formation of such atmospheres at high temperatures where dislocation locking is observed is not possible (see Figure 3.7). Interaction energies E_i larger than 1.5 eV are required at concentrations of 1 ppm to lead to the formation of an atmosphere at 973 K, where the majority of impurities diffuse significantly. However the maximum E_i is believed to be lower than 0.5 eV [Sumino 1992]. Therefore, impurities gettered by dislocations usually *do not* form Cottrell atmospheres at high temperatures, but are rather diffused to the cores.

2 the case of oxygen precipitates obtained by annealing is different since they are more homogeneously distributed throughout the wafers

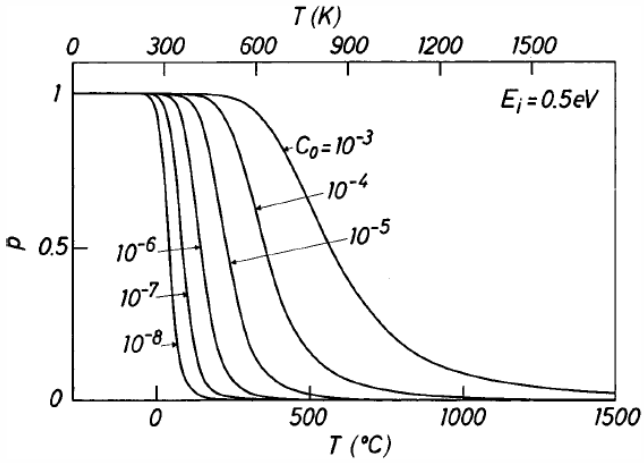

Figure 3.7: Occupation probability p in thermal equilibrium of an impurity at a site with interaction energy $E_i = 0.5\,\text{eV}$ for various impurity concentrations c_0 (per atomic site) [Sumino 1999b].

The gettering efficiency at defects depends on several factors: defect type (e.g. partial type), species and diffusion properties of the impurity, its concentration in the matrix, morphology of the impurities already gettered at the cores and temperature.

Impurities can affect dislocation motion, hence plasticity, by two means: the first possibility is to affect their core structure, thereby modifying the very process of double kink nucleation and propagation by effectively changing the activation energy for dislocation motion. The second option is to pin dislocations and preventing their motion by creating an additional energy barrier to motion. We will distinguish in the following light from electrically active impurities: the former pin dislocations whereas the latter can both pin dislocations and influence their motion properties.

3.2.2 *Light impurities*

The qualitative macroscale effects of O, N and C have been studied experimentally by Sumino *et al.* in the 1980's and onwards at temperatures up to 1073 K. More recently, Senkader *et al.* took on the challenge of studying in more details the locking phenomena by O and N. Their results will be summarized here.

Oxygen

The influence of dissolved oxygen atoms on the stress-strain curve of Si crystals was carefully determined in the early 1980's, and could explain the higher mechanical strength of dislocated CZ crystals compared to the pure FZ materials [Sumino 1980, Yonenaga 1984a]. The early stage of

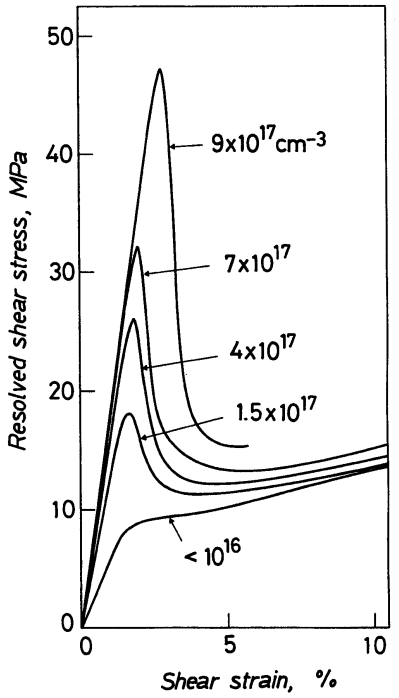

Figure 3.8: Influence of dissolved oxygen concentration $[O_i]$ on the mechanical behavior of dislocated silicon single crystals [Yonenaga 1984a]. $T = 1073\,\mathrm{K}$, $\dot{\gamma} = 1.1 \times 10^{-4}\,\mathrm{s}^{-1}$, $\rho_{m,0} \simeq 10^{10}\,\mathrm{m}^{-2}$.

deformation of as-grown silicon is characterized to the appearance of an upper yield point followed by a sharp yield drop due an intensive dislocation multiplication following their motion under high stresses (see Chapter 2). Preventing this multiplication process leads indeed to higher upper yield points, i.e. materials less prone to plastic deformation. Figure 3.8 gives an example of the measured influence of the oxygen concentration on the mechanical behavior of dislocated crystals. The pinning effect is observed to stronger as $[O_i]$ is raised.

No difference in the upper yield stresses can be detected when the crystals are originally dislocation-free (Fig. 3.9) and no dislocation motion is observed in prestrained CZ crystals unless very high stresses are applied: this points out the pinning effect of oxygen atoms, preventing dislocation multiplication by hindering their motion [Sumino 1980, Sumino 1981, Yonenaga 1984a]. Significant effects of dissolved oxygen on dislocation multiplication are observed for concentrations $[O_i]$ larger than $\sim 10^{16}\,\mathrm{cm}^{-3}$.

Oxygen diffusion at the dislocation cores does *not* affect dislocation velocity when these are moving under high stresses, that is, when dislocations cores are not affected by the presence of impurities. The activation energy

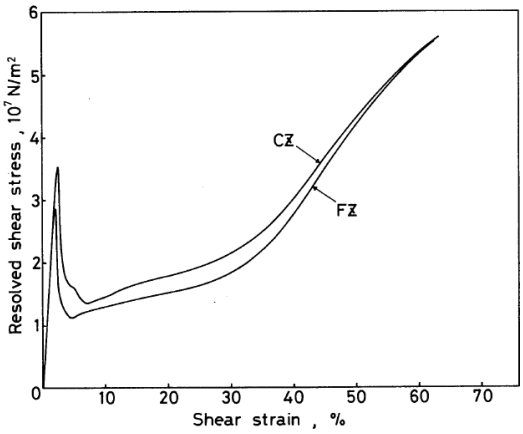

Figure 3.9: Influence of dissolved oxygen concentration $[O_i]$ on the mechanical behavior of dislocation-free silicon single crystals [Sumino 1980]. $T = 1173\,\mathrm{K}$, $\dot{\gamma} = 1.2 \times 10^{-4}\,\mathrm{s}^{-1}$.

for dislocation motion is then similar to the one in pure materials and the same effective stress is found in the steady-state of deformation in stage I (see Section 2.3.1) [Sumino 1980]. However, a divergence from the linear stress-velocity relationship (Eq. 2.6) is detected as the stress is lowered, simultaneoulsy as irregularities are observed in the shape of the intially straight dislocation lines (see Figure 3.10). This is due to the local pinning of dislocations by impurities and reflects the local phenomena taking place along the dislocation line. Line tension still frees dislocations from the impurity atoms provided that the applied stress is high enough to counter the effect of impurities. If the stress is lowered further, dislocations are immobilized at a locking stress τ_l that increases with $[O_i]$ (Figure 3.11) [Imai 1983]. τ_l depends as well on the diffusion kinetics, that is, on the temperature at which locking takes place.

Immobilized dislocations see their core progressively contaminated by an increasing amount of oxygen atoms, until the oxygen concentration at the core is in thermodynamical equilibrium: as many atoms are transported to the core as are emitted by thermal excitation. The presence of impurities increases the stress needed to free dislocations from the contaminants and set them back into motion, called the unlocking stress τ_u. When the core is saturated, τ_u reaches a plateau, the magnitude of which decreases with increasing temperature [Senkader 2000]. Precipitates form at the core by pipe diffusion. Their size and separation increase with time and affect the unlocking stress required to free dislocations from their impurity decoration. τ_u depends again on the ageing time, because it is associated to the formation of these aggregates of varying size and distribution [Sumino 1983a, Yonenaga 1996a].

Precipitates on dislocations form in their very early stage preferentially on the 90° partial and therefore affect firstly the 60° dislocations, although

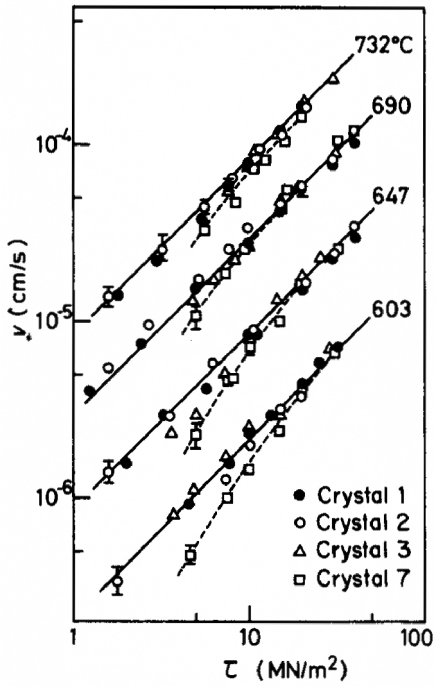

Figure 3.10: *in situ* determined velocity of 60° dislocations in crystals containing different light impurity contents and at different temperatures as a function of the applied stress. Crystal 1: intrinsic FZ. Crystal 2: FZ doped at $[C_s] = 10^{17}\,\mathrm{cm}^{-3}$. Crystal 3: FZ doped at $[N_s] = 5.4 \times 10^{15}\,\mathrm{cm}^{-3}$. Crystal 7: CZ with $[O_i] = 7.4 \times 10^{17}\,\mathrm{cm}^{-3}$ [Imai 1983].

their subsequent development takes place both at 60° and screw dislocations [Sumino 1999b]. The shape, size and separation of precipitates formed on dislocations depend on temperature and annealing time, as it does in the matrix (see Section 3.1.1). Figure 3.12 shows the evolution of the morphology of oxygen precipitates on a screw dislocation as a function of annealing time. Note the helical shape taken by the dislocation after long annealing. A prolonged annealing time leads ultimately to the appearance of five different locking strength regimes (numbers refer to the stages represented in Figure 3.13): after an initial rise and plateau due to diffusion of individual atoms to the dislocation described previously (1-2), precipitates start to form and increase in size, increasing the unlocking stress (3) until a second plateau (4) leads to a final decrease of τ_u (5) due to separation of the precipitates from the dislocations [Yonenaga 1996a, Senkader 2001a]. Dislocations act therefore as nucleation centers for oxygen precipitates, provided the annealing time is long enough to allow for their growth and separation from the dislocations.

Pinning of dislocations by dissolved oxygen atoms results in a lowering of their cross-slip ability, limiting the dislocation multiplication process

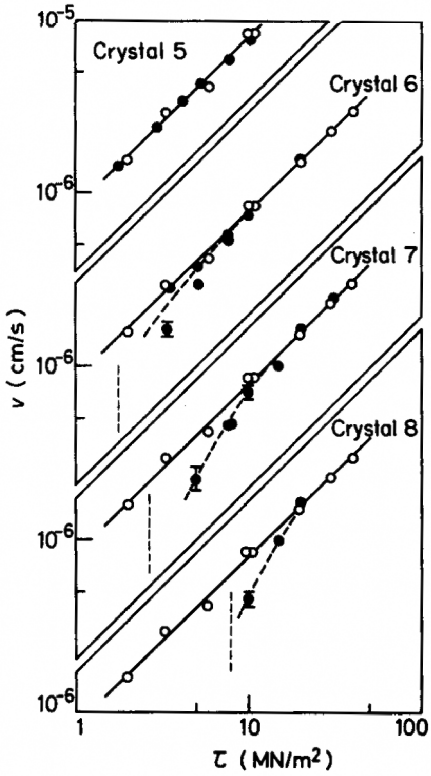

Figure 3.11: *in situ* determined velocity of 60° dislocations in CZ crystals of various $[O_i]$ and at $T = 920\,\mathrm{K}$ as a function of stress. The immobilization stresses are indicated by vertical dashed lines when detected. Crystal 5: $[O_i] = 1.5 \times 10^{17}\,\mathrm{cm}^{-3}$. Crystal 6: $[O_i] = 2.5 \times 10^{17}\,\mathrm{cm}^{-3}$. Crystal 7: $[O_i] = 7.4 \times 10^{17}\,\mathrm{cm}^{-3}$. Crystal 8: $[O_i] = 9.2 \times 10^{17}\,\mathrm{cm}^{-3}$ [Imai 1983].

and therefore a less homogeneous deformation of the samples in the yield region (see Figure 3.9 and Section 2.4.1). This is associated to a higher lower yield stress and different dislocation microstruture at the lower yield point in dislocation-free CZ crystals compared to their FZ counterparts [Doerschel 1981, Yonenaga 1984a].

Nitrogen

Nitrogen has the same pinning effect on dislocations as oxygen, meaning that it locks dislocations when these are at rest or slowly moving by diffusing to the dislocation cores, and does not affect dislocation motion at high stresses (see Figure 3.10) [Giannattasio 2003]. As previously, this results in an increase of the upper yield point of dislocated crystals and no significant difference when the crystals are dislocation-free [Sumino 1983c]. A difference with oxygen is that high N diffusivity leads to an almost complete disappearance of the intermediate dislocation velocity regime due

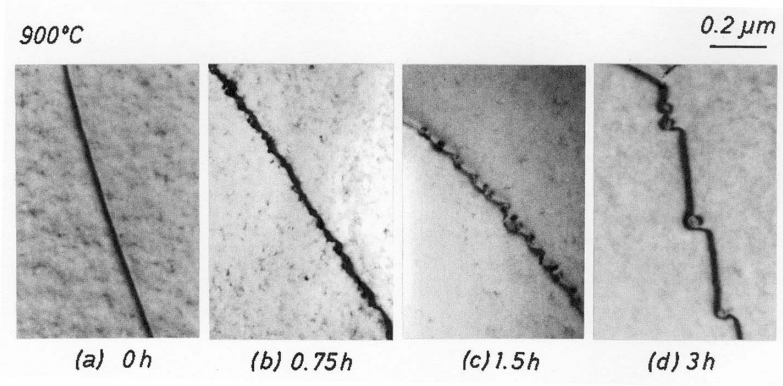

Figure 3.12: Formation of oxygen precipitates along a screw dislocation during ageing [Yonenaga 1996a].

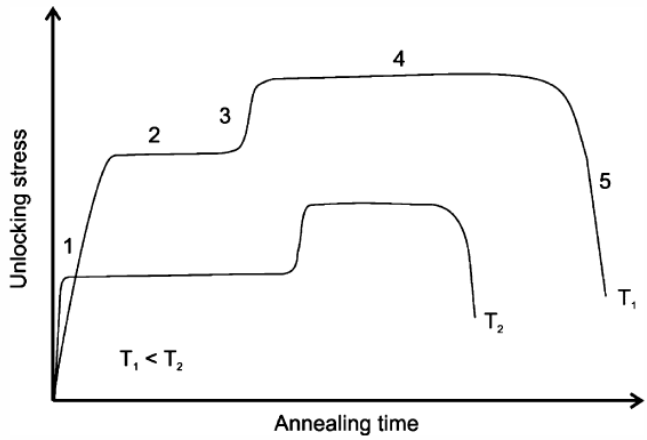

Figure 3.13: Schematic evolution of the dislocation unlocking stress with annealing time at two different temperatures T_1 and T_2 [Murphy 2006a].

to the progressive diffusion of impurities to the core: compare Figures 3.11 and 3.14 [Imai 1983, Sumino 1983a]. The absence of a mixed velocity regime results in a reduced difference of the lower yield stresses between intrinsic and nitrogen-doped FZ crystals compared to oxygen doping. In crystals containing both dissolved O and N atoms, the mixed velocity mode is due solely to the pinning effect of oxygen on the dislocations [Yonenaga 2005]. Finally, there is no formation of nitrogen precipitates in the bulk by annealing at very high temperatures, unlike in the case of oxygen contaminants (see Section 3.1.1) [Sumino 1983c].

Dislocation ageing by additional diffusion of N to the core and formation of nitrogen aggregates has the same effect as in the case of O, but no more than two stages of the unlocking stress have been observed [Alpass 2009]. It has been observed in nitrogen-doped FZ-Si that N is able to lock firmly

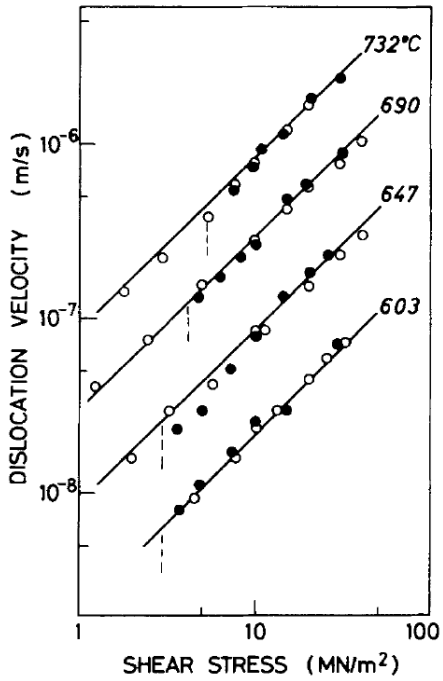

Figure 3.14: *in situ* determined velocity of 60° dislocations in N-doped FZ crystals (solid circles) and intrinsic Si (open circles) at different temperatures as a function of stress. The immobilization stresses are indicated by vertical dashed lines when detected. $[N_i] = 5.4 \times 10^{15}\,\mathrm{cm}^{-3}$ [Sumino 1983c].

dislocations in the whole range of temperature 973-1473 K, whereas O is not able to attain such a locking capacity at high temperatures. At equal concentrations, nitrogen has in addition a much stronger locking effect than oxygen [Sumino 1983a]. This point to different chemical reactions between the light impurities N and O and dislocation cores.

Rapid diffusion of N at the dislocation core[3] creates a preferential site for segregation of O: the co-presence of N and O impurities in dislocated silicon crystals results in enhanced dislocation locking between 923 and 1173 K and a decreased locking capacity beyond 1173 K [Yonenaga 2005]. Incorporation of nitrogen in CZ crystals allows moreover a homogeneous distribution of SiO_2 precipitates by favoring oxygen precipitation at dislocations as described above.

Carbon

Carbon in substitutional form does not affect the mobility of moving dislocations, unlike O and N, and plays a little dislocation locking role by itself. Carbon atoms at $[C_s] \gtrsim 10^{17}\,\mathrm{cm}^{-3}$ actually play an important role when in

3 N diffuses more rapidly than O in silicon, see next Section.

presence with atoms of oxygen $[O_i] \gtrsim 5 \times 10^{17}\,\mathrm{cm}^{-3}$ in dislocated crystals between 1073 and 1173 K by favoring diffusion of oxygen at the dislocation core and strengthening dislocation locking. An increase of the upper yield stress is then detected linearly dependent on $[C_s]$, whereas the lower yield stress is not affected, as is the case for nitrogen [Yonenaga 1984b].

It is found that at low temperatures interstitial carbon atoms tend to bind with substitutional immobile carbon atoms, suggesting a possible mechanism for growth of carbon aggregates and probably to SiC precipitates. At higher temperatures on the contrary, carbon is mobile and these aggregates disappear. C is considered to be present as a substitutional species during crystal growth, its diffusion taking then place under an interstitial form. Very high concentrations of dissolved carbon, above $10^{19}\,\mathrm{cm}^{-3}$, affects the diffusivity of other species such as boron by affecting the amount of intrinsic point defects in the bulk [Pinacho 2002].

3.2.3 *Effects of electrically active impurities*

The case of electrically active impurities (e.g. dopants) is more complex than the previous one, because the dislocation pinning and locking effect can be superimposed to a modification of the core structure of the dislocations and an alteration of the activation energy for dislocation motion. This Section is concerned by the influence of dopants onto dislocation motion. The case of metallic impurities is dealt with in the following Section.

Silicon belongs to the 14^{th} column[4] of the periodic table of elements, and has consequently four valence electrons usually used to build the covalent bonds with its four Si neighbours in the intrinsic crystal. Insertion of impurities belonging to one of the neighbouring columns in concentrations large enough to affect the electrical properties of intrinsic Si is called doping, and affects the concentration of holes or electrons (charge carriers) in the material. Very high doping ends up making intrinsic semiconductors conductors.

- *n*-type doping[5] (*n* for negative) implies the use of donor species on the 15^{th} column such as phosphorus (P), arsenic (As), and less commonly antimony (Sb). These atoms have one more valence electron available than Si and increase therefore the concentration of negative charges in *n*-doped Si: four of their electrons are shared to make covalent bonds while the fifth remains available to increase the conductivity of the doped material by increasing the amount of electrons in the conduction band. The dominant carriers in *n*-doped Si are consequently electrons.

4 it is also common to refer to the groups III, IV and V instead of groups 14, 15 and 16. This has the advantage of indicating directly how many valence electrons the species have.

5 the name n^+ (resp. p^+) doping is also used to mean that the concentration of negative (resp. positive) carriers is increased.

- *p*-type dopants belonging to the 13th column of the periodic table are acceptors and possess on the contrary one valence electron less than Si. Their insertion in the silicon matrix leads to the formation of a broken bond (a *hole*) coming from an unpaired electron of an Si atom, which is then available for conduction. *p*-type doping increases consequently the hole concentration, which become dominant carriers. Commonly used *p* dopants are boron (B), and gallium (Ga) to a lesser extent.

When *n*- and *p*-type dopants are in equal concentrations in a semiconductor, the resulting effect is no change in the electrical properties of intrinsic Si since holes and electrons combine with each other. Compensation can be done by injecting more of one doping species but has the drawback of reducing the free carrier mobility, steered by the total concentration of dopants and not the net doping concentration. Compensation is commonly done in SoG-Si materials because of the high concentrations of (often unwanted) electrically active impurities in as-grown materials. As we will see in the following, doping not only affects the electrical properties of silicon but also its mechanical behavior. In addition, the effect of dopants on the activation energy for dislocation motion, that is on the mechanism of double kink nucleation and propagation, does not depend on the exact dopant species but solely on the group it belongs to (acceptor or donor), as long as the locking effects are negligible [George 1979b].

Evolution of the stress-strain curve

Use of Eq. 2.1 at large strain rates shows that doping does not affect the stress sensitivity of dislocation velocity m. The activation energy U is reduced by *n*-doping and unaffected by *p*-doping at temperatures above 873 K. Low strain rates associated to high temperatures lead however to the saturation of the yield points, a phenomena exacerbated as the doping concentration (*n*-type or *p*-type) increases.

The lower yield stress seems then to be independent on the strain rate but still to vary exponentially with temperature[6] and linearly with the dopant concentration[7]: the saturation of the lower yield stress is observed e.g. at $\dot{\gamma} \lesssim 10^{-3}$ s^{-1} at 1473 K and $[B] \simeq 10^{20}$ cm^{-3}, saturation being observed generally above dopant concentrations larger than 5×10^{19} cm^{-3} independently on the dopant [Siethoff 2001]. This has been understood as the lower yield stress being the unlocking stress necessary to free dislocations from the impurities gathered at the core. Eq. 3.2, based on the interaction between dislocations and a short-range cloud of impurities around its core, has been

6 the lower yield point of boron-doped crystals becomes independent on temperature as well provided its concentration is large enough [Siethoff 2003].

7 precipitation of boron affects the stabilization of the lower yield stress and its linear dependence on $[B]$ because of its low solubility [Siethoff 2003].

found to correctly describe the temperature- and $[P]$-dependency of τ_{lyp} in highly doped Si crystals [Brion 1971, Siethoff 2003]:

$$\tau_{lyp} \propto [P] \frac{k_b T}{b^3} \exp\left(\frac{U_P}{k_b T}\right) \tag{3.2}$$

Such an equation does not fit results obtained on B-doped crystals, indicating that the long-range elastic interaction between B atoms and dislocations might influence impurity segregation as well [Siethoff 2003].

The upper yield stress seems less affected by high dopant concentrations than the lower yield point does [Siethoff 1970, Siethoff 2001].

The deformation proceeds as propagation of Lüders bands when starting from very low dislocation densities, especially at very high dopant concentrations. These Lüders bands can give rise to serrations in the stress-strain curve or to the appearance of secondary yield peaks. Dynamic strain ageing (Portevin-LeChatelier effect) is also observed in the region beyond the lower yield point [Siethoff 1970, Siethoff 1973]. The presence of dopants is otherwise found to homogenize slip [George 1987b].

Motion of individual dislocations: change in dislocation motion parameters

Dislocation velocity studied by etch pitting methods has revealed that it is affected only at dopant concentrations larger than the intrinsic carrier concentration, meaning that higher dopant concentrations are required as the temperature is raised to affect dislocation motion. No change in the stress dependency is detected for both doping types, but the disturbance from straight dislocation lines and existence of starting stresses for dislocation motion in doped crystals shows that electrically active impurities do also diffuse to the dislocation cores and have a pinning ability, in agreement with the deductions from the behavior of the lower yield stress mentioned above [Kulkarni 1976, George 1979b].

A consensus has been formed that *n*-doping increases dislocation velocity no matter the temperature[8] and the dislocation character by affecting U, an effect detectable at dopant concentrations larger than $\sim 10^{18}\,\mathrm{cm}^{-3}$ and increasing with the dopant concentration [Alexander 1968, Erofeev 1969, Patel 1976, George 1979b]. A stress dependence of U for 60° dislocations in P-doped Si observed in [George 1979b] is not detected by analysis of the lower yield point through Eq. 2.1 [Siethoff 2002]. The velocity prefactor v_0 is also affected to guarantee continuity at the frontier between the standard and enhanced velocity regimes. The case of *p*-doping has led to several controversies:

- some authors pretend that acceptor dopants do *not* affect dislocation velocity at high temperatures (see e.g. Figure 3.15), whereas an *accelerating* regime would exist below $\sim 873\,\mathrm{K}$, where *p*-type dopants would also ease dislocation motion (Figure 3.16) [Patel 1976].

8 as long as the dopant concentration is high enough compared to the intrinsic carrier concentration. Dislocation velocity is the same as in intrinsic crystals otherwise [George 1979b].

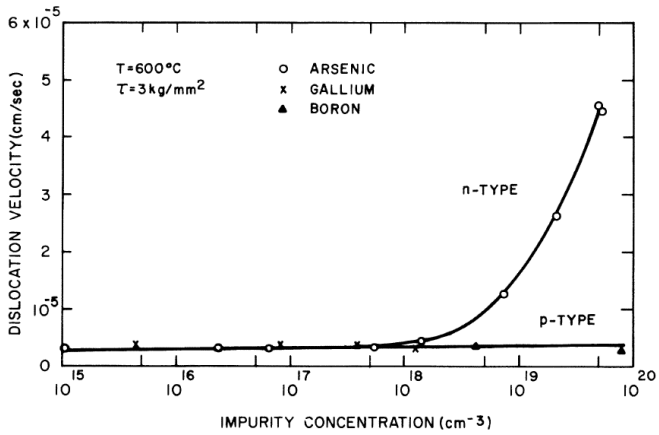

Figure 3.15: Velocity of screw dislocations as a function of dopant concentration in n-type and p-type silicon, at high temperatures ($T = 873\,\mathrm{K}$) and under a stress $\tau = 3\,\mathrm{MPa}$ [Patel 1976].

- the French research group in Nancy signals on the contrary a slight *decelerating* effect of boron on 60° dislocations only below $\sim 973\,\mathrm{K}$ and no effect on dislocation velocity otherwise [George 1979b].
- others researchers detected *accelerating* effects in p-doped Si in all the investigated temperature range [Erofeev 1969, Kulkarni 1976, Yonenaga 2001].

It seems that acceptor impurities slightly increase U at intermediate concentrations $\sim 5 \times 10^{17}\,\mathrm{cm}^{-3}$ before effectively reducing the activation energy until accelerating effects are detected at concentrations larger than $\sim 5 \times 10^{18}\,\mathrm{cm}^{-3}$ [George 1979b]. The effect of p dopants on dislocation motion (accelerating or decelerating) is however one order of magnitude lower than in n-doped materials, showing that acceptor impurities are much less effective at affecting dislocation motion than donors are [Patel 1976, George 1979b].

The influence of doping impurities on dislocation velocity and dislocation pinning at low stresses have been investigated by Sumino and his group with *in-situ* X-ray topography and allowed to clarify the previous observations [Imai 1983, Sumino 1983a]. As previously, it was found that doping by phosphorus atoms strongly enhances the velocity of moving dislocations by lowering their activation energy, this effect increasing with $[P]$. It can be seen in Figure 3.17 that B has little or no influence on the velocity of dislocations at the considered concentration and temperatures ($1.4 \times 10^{19}\,\mathrm{cm}^{-3}$ below 973 K). If anything, doping by acceptors slightly reduces the activation energy. It has been long assumed that the accelerating effect of dopants depends only on their concentration and not on the exact species [Sumino 2002], but recent results question this [Yonenaga 2001], indicating that the elastic interactions between dissolved dopants and dislocations might also influence dislocation velocity under high stresses. Figure 3.18

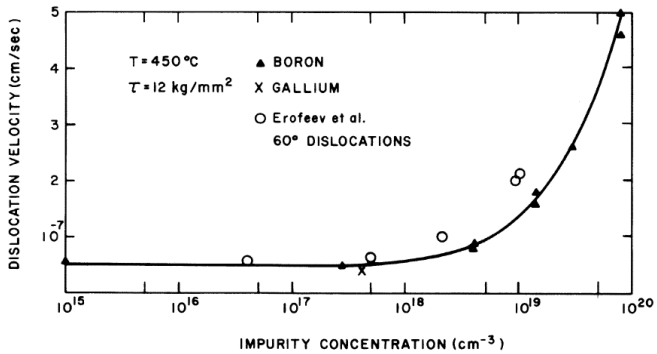

Figure 3.16: Velocity of screw dislocations (full symbols) and 60° dislocations (open circles) as a function of dopant concentration in p-type silicon, at low temperatures ($T = 723\,\mathrm{K}$) and under a stress $\tau = 12\,\mathrm{MPa}$ [Patel 1976]. Note the different magnitude of dislocation acceleration by dopants compared to the case of n-doping (Figure 3.15).

summarizes the results obtained for n-type and p-type dopants. Finally, it can be noted that interstitial Cu enhances dislocation motion as dopants do [Vanderwalker 1984].

*Atomic explanations of the doping effect**

The reasons for the modification of activation energy for dislocation motion have been quickly identified as coming from the electrical properties of dislocations. [Hirsch 1981b] proposes a review of the models developed by the early 1980's.

Patel *et al.* proposed a model based on two assumptions: firstly, that kinks are nucleated at charged dislocation sites, and secondly that the dislocation velocity enhancement by doping is proportional to the concentration of charged sites along the dislocation line. Dislocations would be acceptors in n-type materials and donors would then increase the kink concentration by lowering the kink *nucleation* energy barrier F_k and thereby reduce the activation energy for dislocation motion. Dislocations in p-type materials would then be donors to explain the experimental observations. A fundamental result of their model is that the change in activation energy is equal to the change of Fermi level induced by doping. This way, increasing the dopant concentration would initially decrease U until saturation [Patel 1976].

[Kulkarni 1976] suggested on the contrary that kink *migration* would be affected by the changes in the electronic state of the crystal and controlled by electrically active impurities. They affect $F_{km} = 1.3\,\mathrm{eV}$ to Auger recombination and generation at the dislocation core, but do not distinguish between the effects of n- and p-doping, in disagreement with results provided by other authors [George 1979b].

Atomistic simulations have provided a deeper understanding of the reasons behind dislocation velocity enhancement in doped silicon. Dislocation

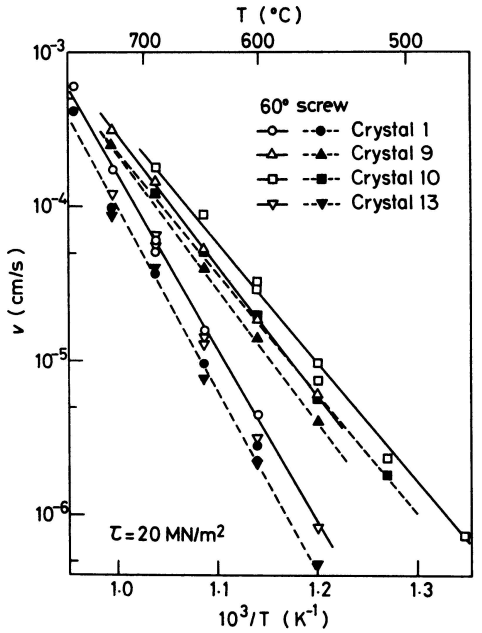

Figure 3.17: Influence of electrically active impurities on the dislocation velocity dependence temperature for both types of dislocations. Crystal 1: intrinsic. Crystal 9: CZ, $[P] = 6.2 \times 10^{18}\,\mathrm{cm}^{-3}$. Crystal 10: CZ, $[P] = 1.5 \times 10^{19}\,\mathrm{cm}^{-3}$. Crystal 13: CZ, $[B] = 1.4 \times 10^{19}\,\mathrm{cm}^{-3}$ [Imai 1983].

motion proceeding by double kink nucleation and migration necessitates the breaking and reconstruction of covalent bonds at the core: the stronger the reconstruction, the higher the activation free energy F. It has been mentioned in Chapter 1 that the bond reconstruction energy is actually the fundamental quantity determining the activation energy [Bulatov 2001b]. First-principle simulations have shown that the reconstructed cores of the neutral 30° and 90° partials remain stable in p-type material, whereas the negatively charged cores gain in stability in an n-type environment. Bond reconstruction energy is however smaller in doped materials with respect to intrinsic silicon, meaning that doping could ease bond breaking, hence kink nucleation and propagation [de Araújo 2004].

The case study of phosphorus doping on a 90° partial revealed that P most likely takes the place of solitons along the dislocation core (see Section 1.2.1), as a threefold coordination there leads to a more stable configuration than a fourfold one, with a binding energy of 1.5 eV. Its presence at a reconstructed site of the core leads to the breaking of the reconstruction bond, so that both the P and Si atoms take a threefold coordination. The presence of an additional P atom gives a stable structure when a P pair forms at opposite core sites with broken a bond, leaving the core once again electrically active in the valence band and a stable configuration at a binding energy of 2.3 eV [Heggie 1991]. The presence of these broken bonds at the core would then

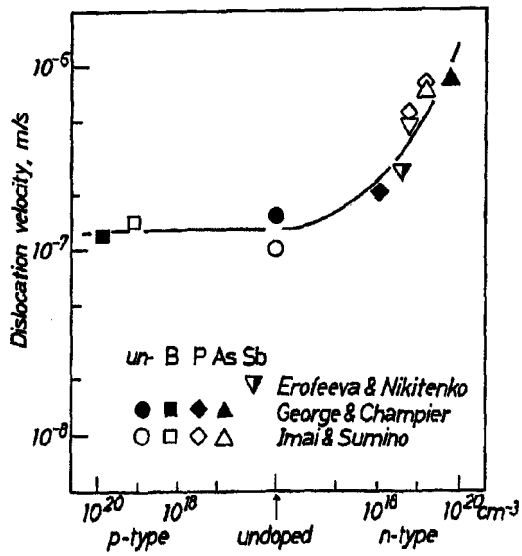

Figure 3.18: Variation of the activation energy with the dopant concentration [Sumino 2002].

enhance kink propagation by avoiding the need for bond braking and reconstruction during their migration.

Dislocation pinning by electrically active impurities

Dopants can diffuse at the dislocation cores and immobilize dislocations by preferential segregation as light impurities do. This ability leads to the appearance of a highly stress-sensitive dislocation velocity regime at low stresses (see Figure 3.19), followed upon stress reduction by dislocation immobilization and inhibition of their multiplication. Dislocation ageing increases the unlocking stress required to set dislocations back into motion.

The discovery of a saturation of the lower yield point at high temperatures, low strain rates and high dopant concentrations has been readily attributed to the existence of an unlocking stress in extrinsic crystals doped with B or P impurities [Siethoff 1970, Siethoff 2003]. [Erofeev 1969, Kulkarni 1976] observed the existence of starting stresses in crystals doped with B, P, As and Sb species. [George 1979b] observed pinning of dislocations by both dopant types as well, as did the Japanese group, which however noticed a weaker locking ability of boron compared to phosphorus [Imai 1983].

B, P, Sb and As alone have been found to prohibit the generation of dislocations when at concentrations as high as 10^{19} cm^{-3}, this effect increasing with increasing concentrations of electrically active impurities. Dislocation locking at lower concentrations is thought to come from the presence of dissolved oxygen in the crystal. Ge does not seem to have such a strong

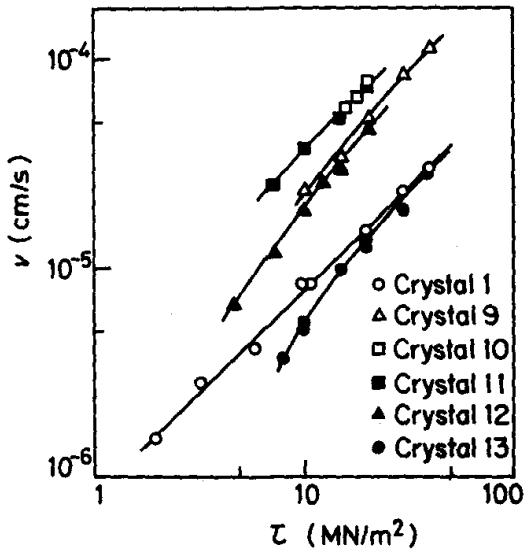

Figure 3.19: *in situ* measured velocity of 60° dislocations in intrinsic and extrinsic crystals at low stresses as a function of stress. $T = 920\,\mathrm{K}$. Crystal 11: CZ, $[As] = 1.5 \times 10^{19}\,\mathrm{cm}^{-3}$. Crystal 12: CZ, $[Sb] = 6.5 \times 10^{18}\,\mathrm{cm}^{-3}$. Other crystals, see Figure 3.17 [Imai 1983].

suppression effect [Yonenaga 2002]. The origin of the strong interaction of P with dislocations was initially thought to come from the electrical properties of dopants, since the elastic misfit between phosphorus and silicon is rather small [Sumino 1983a], but further investigations have ruled out the possibility of electrostatic interactions, pinning being now supposed to come from condensation of P at the dislocation cores as light impurities do [Siethoff 2003].

The effects of other impurities (B, As, Sb) have been studied for concentrations up to $2.5 \times 10^{20}\ \mathrm{cm}^{-3}$ [Erofeev 1969, Yonenaga 2002]. The common feature of dopants is indeed to induce a critical stress for generation of dislocations, especially when in presence of high concentration of oxygen. B interacts with oxygen by enhancing its transport through the lattice, whereas the other electrical impurities have not been found to. This oxygen diffusion enhancement is thought to originate in the electronic effects between B and O [Murphy 2006a]. A model for incorporation of the locking effects generated by impurities into the AH model is exposed in Section 3.3.

3.3 MODELING DISLOCATION LOCKING BY IMPURITIES

At the origin of both change in dislocation velocity parameters and dislocation locking are diffusion and drift processes of impurities to the dislocations. Slowly diffusing impurities can remain dissolved in the bulk, posing no special problem for solar cell efficiency if these are not electrically active; however fast diffusing species such as metals can affect dislocations and precipitation in a wide range of temperatures. The concentration c_i of an impurity i at an immobile dislocation is obtained by solving a macroscopic diffusion problem as given by Eq. 3.3 [Sumino 1983a] valid at a distance $r > r_0$:

$$\begin{cases} \frac{\partial c_i}{\partial t} = D_i \nabla \left(\nabla c_i + \frac{c_i}{k_b T} \nabla \left(\Delta G_i \right) \right) \\ \Delta G_i(r \geq r_0, \theta) = \left(\Delta H_i^{max} - T \Delta S_i \right) \frac{b \sin \theta}{r} \end{cases} \tag{3.3}$$

where r_0 is the core radius (of the order of a following [Maroudas 1991a, Senkader 2000]), D_i is the diffusion coefficient of the impurity in the silicon lattice, ΔG_i is the interaction potential between the impurity and the dislocation (the change in Gibbs free energy due to the presence of the dislocation). ΔH_i^{max} and ΔS_i are respectively the maximum binding enthalpy and binding entropy, depending on the impurity. The first term on the right-hand side of Eq. 3.3a is due to diffusion, whereas the second one is linked to drift of the impurities in the presence of a dislocation. The latter can have purely mechanical origins (interactions between the strain fields) or electrostatic ones (if the impurity and dislocation are charged).

The diffusion problem is there simplified to the case of a cylindrical geometry, which is appropriate at the usual dislocation densities met in silicon materials [Maroudas 1991a]. Such an equation associated to boundary conditions (the impurity concentrations respectively at the core radius and at the outer boundary of the studied cylinder, equal to the concentration in the bulk c_i^∞) must be solved numerically with the help of e.g. finite elements. The boundary condition at the dislocation core ($r = r_0$) depends on the authors. At high temperatures the formation of a Cottrell atmosphere is very unlikely, and assuming that $c_i(r_0) = c_i^\infty$ is then a valid assumption. At temperatures below 873 K impurity seggregation at dislocations takes on a larger importance, and the boundary condition must be determined with the help of numerical methods.

Section 3.3.1 is concerned with diffusivity of impurities, whereas Section 3.3.2 deals with the locking strength of impurities, steered by the ΔG_i term.

3.3.1 *Diffusion of impurities and formation of an impurity atmosphere*

Oxygen

The case of oxygen diffusion has been widely studied, both experimentally and numerically. See [Murphy 2006a] for a review.

STATIC DIFFUSION Equation 3.3 has been solved by [Sumino 1983a] in the case of static ageing of dislocations, that is for the first stage of evolution of the dislocation unlocking stress, when impurities still diffuse to the dislocation core and equilibrium is not reached (see Figure 3.13). The concentration of oxygen atoms along the dislocation line c_O is then found numerically to evolve as:

$$c_O \propto c_O^{\infty} \left(D_O t\right)^{0.787} \tag{3.4}$$

a result close to the experimental results and almost linearly time-dependent. [Sumino 1983a] solved Eq. 3.3 considering that dislocations are a perfect sink for impurities, neglecting the thermally activated emission from the core. [Senkader 2000] included on the other hand the emission term, equal for each impurity atom at the core to the probability of overcoming the energy barrier of height $\Delta G(r_0, \theta)$.

The diffusivity of oxygen has been measured by several authors and depends on the diffusing species: monomers, dimers or trimers. Which species dominates depends on the temperature as demonstrated by Senkader *et al*. Diffusion of dissolved oxygen as monomers O_i has been found to take place at high temperatures (973-1473 K), whereas at lower temperatures (623-973 K) the dimer O_{2i} takes over [Senkader 2001b].

- At high temperatures $T \geq 973\,K$, interstitial oxygen diffuses as a monomer and $D_{O_i} = 0.13 \exp\left(-\frac{2.53}{k_b T}\right)$ cm^2.s^{-1} [Mikkelsen 1986, Senkader 2000]. Ab initio calculations find an activation energy for diffusion between 623 and 1473 K of 2.59 eV, in agreement with the experimental results in the high temperature regime [Gusakov 2005].
- below 973 K the effective diffusivity in cm^2.s^{-1} depends on the oxygen content in the matrix [Senkader 2001b, Senkader 2002]:
  - $[O_i] = 2.6 \times 10^{17}$ cm^{-3}: $D_{O,eff} = 2.04 \times 10^{-7} \exp\left(-\frac{1.51}{k_b T}\right)$
  - $[O_i] = 6.3 \times 10^{17}$ cm^{-3}: $D_{O,eff} = 7.33 \times 10^{-7} \exp\left(-\frac{1.52}{k_b T}\right)$
  - $[O_i] = 10.4 \times 10^{17}$ cm^{-3}: $D_{O,eff} = 2.16 \times 10^{-6} \exp\left(-\frac{1.55}{k_b T}\right)$

The presence of dopants influences oxygen diffusivity at low temperatures. The case of boron doping between 623 and 823 K has been investigated by [Murphy 2006b] and has shown that the effective diffusion coefficient of oxygen is extremely enhanced in the presence of *p*-type dopants. Its activation energy is hardly affected whereas the prefactor is increased by a factor 60. Sb does not show any similar influence, leaving $D_{O,eff}$ unchanged. The trimer species O_{3i} is thought to become preponderant in the presence of boron dopants [Murphy 2006a, Murphy 2006b]. Cluster formation when the dislocations are at rest is not taken into account by any static ageing model.

DYNAMIC DIFFUSION Based on a model of point-defect migration in cubic lattices, Maroudas & Brown derived the anisotropic diffusion tensor of interstitials under stress in silicon and applied it to oxygen interstitials to study the drag force of the impurity atmosphere on a moving dislocation [Maroudas 1991a, Maroudas 1991b]. Their model assumes that oxygen diffuses as a monomer and is consequently valid at high temperatures only. Their early work disregards the mechanical effect of impurity segregation at the dislocation core and is concerned solely by the influence of the Cottrell atmosphere on dislocation drag. Using an elastic interaction energy of 0.5 eV (that is actually shown not to lead to the buildup of any significant atmosphere at the relevant temperatures, see Section 3.2.1), they determined a critical dislocation velocity v_c at which the dislocation-atmosphere interaction would reach its maximum, close to Cottrell's approximation that reads:

$$v_c = \frac{4k_b T D_{O_i}}{\Delta H^{max} b} \tag{3.5}$$

where D_{O_i} is the isotropic diffusion coefficient of oxygen interstitials, and $\Delta H^{max} \simeq 0.5\,\text{eV}$ defines the interaction potential (see Section 3.3.2 for a better estimate). Coupling of their model to the AH constitutive model (Chapter 2) qualitatively reproduces the alteration of dislocation velocity at low stresses observed by [Imai 1983] (see Figure 3.10), but does not lead to the appearance of a locking stress. The slowing effect of the atmosphere is simulated to significantly reduce dislocation velocity at stresses of the order of $\sim 0.5\,\text{MPa}$ in the conditions of high oxygen contents considered by the Japanese group, leaving some doubts about the importance of the drag of an impurity atmosphere if ever present in real crystals. The incorporation of oxygen atoms segregated at the core and their associated drag stress allowed however to find back the experimental results and the hysteresis characterizing the locking-unlocking process [Maroudas 1991c].

Another author that has developed a numerical model for dynamic diffusion of impurities to dislocations and incorporated it to the AH model is Petukhov [Petukhov 1990, Petukhov 2002]. The variation of the impurity concentration at the dislocation core results from the competing processes of oxygen gettering under motion and unlocking from the atmosphere (first and second terms in the right-hand side of Eq. 3.6, respectively).

$$\frac{\partial c_i}{\partial t} = \frac{v}{a}\left(\frac{r_t}{a} c_i^{\infty} - c_i \exp\left(-\frac{a}{v t_m}\right)\right) \tag{3.6}$$

where $\frac{a}{v}$ is the time required for the dislocation line to overcome the Peierls barrier[9], r_t the radius of trapping of impurities, and t_m is the time of migration of impurities within the core[10]. An assumption of his model is

9 following Chapter 1, the period of the Peierls potential should rather be $\frac{\sqrt{3}}{2}b$.

10 t_m is proportional to $\frac{a^2}{D_O}\exp\left(\frac{\Delta G_O}{kT}\right)$, where D_O is the diffusion coefficient of oxygen in silicon and ΔG_O the difference in binding energy between an oxygen atom on a dislocation compared to as an interstitial species in the bulk [Petukhov 1990].

that the impurity concentration next to the dislocation core is equal to the bulk concentration c_i^{∞}.

Nitrogen

The diffusivity of interstitial N is five orders of magnitude higher than its dimer form and the binding energy of nitrogen atoms to each other is very high (between 3.67 and 4.3 eV). It is therefore expected that all interstitial N atoms are paired (as interstitial N_{2i}), complexed, or substituted really fast [Stoddard 2005]. The diffusivity of nitrogen depends on the temperature as the very diffusion mechanism (as monomer, dimer, etc.) depend on T [Giannattasio 2003, Alpass 2009]. The effects of intrinsic point defects on the diffusivity of nitrogen has been mentioned by [Fujita 2005] and could lower the activation energy.

- Between 773 and 1023 K, [Alpass 2009] found from dislocation locking experiments $D_{N,eff} = 2 \times 10^5 \exp\left(-\frac{3.24}{k_b T}\right)$ cm^2s^{-1}. The diffusivity of the monomer species is estimated to exhibit an activation energy of roughly 1.4 eV.
- At higher temperatures and up to 1473 K, an activation energy around 2.8 eV is found, and $D_{N,eff} = 2.7 \times 10^3 \exp\left(-\frac{2.8}{k_b T}\right) cm^2s^{-1}$ [Itoh 1988].
- *Ab initio* calculations yield for the dimer species $D_{N_2} = 67 \exp\left(-\frac{2.38}{k_b T}\right)$ cm^2s^{-1} between 1073 and 1673 K, or $117 \exp\left(-\frac{2.42}{k_b T}\right)$ cm^2s^{-1} between 573 and 973 K [Stoddard 2005]. The diffusivity of the monomer is assumed to be very high, with an activation energy of 0.56 eV.

Other impurities

- carbon: $D_{C,eff} = 0.95 \times 10^{-4} \exp\left(-\frac{3.04}{k_b T}\right)$ cm^2s^{-1} from 1173 K up to the melting temperature [Roller 1989], with dissolved atoms as substitutionals.
- phosphorus: $D_P = 0.39 \exp\left(-\frac{3.12}{k_b T}\right)$ cm^2s^{-1} (1223-1473 K) following [Makris 1973],
  or $D_P = 1.245 \exp\left(-\frac{3.5}{k_b T}\right)$ cm^2s^{-1} (723-823 K) [Morinetti 1984].

3.3.2 *Dislocation locking and unlocking processes*

BINDING ENERGY TO THE DISLOCATIONS Dislocation locking by diffused impurities is due to the strength of the dislocation-impurity binding:

the transported impurities exert on the dislocation a force equal in magnitude to the one the dislocation exert on the impurities. This interaction can be conveniently represented by a potential in which the impurity atoms evolve, which expression depends ultimately on the nature of the interaction [Hirth 1992]. Dislocations and impurities can interact by means of e.g. chemical, electronic, elastic potentials. In the case of oxygen, the elastic term is thought to dominate because of the interstitial nature of dissolved oxygen atoms leading to strong strain fields, and a usually considered expression for the potential is [Sumino 1983a, Senkader 2001a]:

$$\Delta H_O(r,\theta) = \Delta H_O^{max} \frac{b \sin\theta}{r} \tag{3.7}$$

Resolution of the diffusion equation (Eq. 3.3) with a boundary condition at the core radius incorporating impurity emission as well as absorption, two temperature regimes for the binding enthalpy have been determined [Senkader 2001a, Senkader 2002, Senkader 2004] that translate the change in the diffusing oxygen species taking place around 973 K:

- $\Delta H_O^{max} = 0.74\,\text{eV}$ at $T \geq 923\,\text{K}$
- $\Delta H_O^{max} = 0.23\,\text{eV}$ at $T \leq 923\,\text{K}$

The binding entropy is calculated to be close to the Boltzmann's constant, $\Delta S_O \simeq k_b$.

The case of binding by nitrogen atoms is more complicated, with a locking strength measured at 823 K peaking after annealing at around 900 K and vanishing beyond 1273 K [Alpass 2009]. This can be interpreted in different binding energies for the species diffusing to the dislocation cores.

DEPENDENCIES OF THE UNLOCKING STRESS ON T AND c_o Modeling the locking effect of impurities at dislocations through equations is traced back to Sumino and the observations his group made in situ in impurity-containing silicon crystals [Sumino 1983a]. The authors calculated the thermally activated overcoming of the energy barrier created by individual oxygen atoms dispersed regularly along the dislocation line. The unlocking stress is then given by:

$$\tau_u = (\Delta G_i^{max} - \lambda_{1i} k_b T) \frac{\pi c_i r_0^2}{b^2} \tag{3.8}$$

In this equation λ_i is a prefactor logarithmically depending on c_i. Such an equation gives linear dependencies of the unlocking stress on temperature and impurity concentration. This model is valid only up to saturation of the locking stress (stages 1 and 2 of Figure 3.13) and is also satisfied experimentally [Senkader 2004].

As has been described in Section 3.2.2, oxygen atoms tend to aggregate in clusters along the dislocation with time, forming groups of n atoms. This

can be modeled by using an alternative expression for the locking stress (Eq. 3.9), which is found to increase rapidly with n.

$$\tau_u(n) = \left(n\Delta G_i^{max} - (\lambda_i - \ln n)\, k_b T\right) \frac{\pi c_i r_0^2}{nb^2} \tag{3.9}$$

Values of n and ΔG_i^{max} are givend for B, P, Ge and O in [Yonenaga 2002], for N in [Yonenaga 2005]. Dislocation locking by oxygen is not very efficient at temperatures larger than 1073 K; above this temperature N is more likely to efficiently lock dislocations. Dissolved N actually exhibits a strong locking ability up to 1473 K [Murphy 2006c].

The unlocking stress is almost proportional to the concentration of impurities at the core, therefore a traditional way of writing τ_u is

$$\tau_u = f(T) c_i \tag{3.10}$$

where $f(T)$ is a prefactor depending linearly on temperature as long as the impurity atoms are not aggregated along the dislocation line.

DISLOCATION LOCKING AND THE AH MODEL Implementation of the locking stress into the AH model is relatively straightforward if the internal stresses are assumed additive. Then the internal stress stemming from impurity diffusion consists in two terms, the first one due to the Cottrell atmosphere and being essentially elastic in nature, the second one due to the chemical binding of the impurities at the core [Maroudas 1991a]. Comparison of both terms shows that the elastic drag is negligible compared to the chemical component τ_u [Maroudas 1991c]. The applied stress τ is then considered to be reduced by the "dry friction" component τ_u linearly proportional to the concentration of impurities at the dislocation core. The effective stress of the AH model (Eq. 2.10) becomes:

$$\tau_{eff} = \langle \tau - \mu b A \sqrt{\rho_m} - \tau_u \rangle \tag{3.11}$$

What is important is that the contribution of each dislocation to the total plastic deformation depends on its velocity through Orowan's law, meaning the effective stress acting on it, that is controlled by the concentration of impurities at the core, which in turn depends on the age of the dislocation.

The final model succeeds in representing the unlocking stress observed in experiments, and a new expression for the yield stresses is found to depend on the stress rate. Cluster formation when the dislocations are at rest is not taken into account and could be the object of a further improvement of the model (this would principally affect the value of the dry friction coefficient). For early stages of deformation, one neglects the backstress coming from mutual interaction between dislocations τ_{int}. Solving these equations for a steady state leads to two branches, representing either the dislocation slowly moving and accumulating impurities, or its motion free from an atmosphere, both regimes being limited by a critical shear stress τ_s. If one assumes that in the early deformation stages, where locking occurs, $\tau = E\varepsilon$,

and $\varepsilon = \dot{\varepsilon}t$ (constant strain rate), then the critical stress is directly connected to a critical time t_s.

- For $\tau \leq \tau_s$, aging takes place through drag of impurities, and $\frac{\partial c}{\partial t} = \frac{v}{a^2} r c_0 = \frac{B(T)(\tau - fc)}{a^2} r c_0$.
- For $\tau \geq \tau_s$, the impurity drag can be disregarded.

The equations of the original model have then to be modified in order to reflect the age of each dislocation. For large stresses, the dislocations move without interference with the impurities, and the material behaves as an intrinsic one, described by the classical equations of Alexander and Haasen. As was noticed by Sumino *et al.*, increasing impurity concentration has the same effect as reducing the initial dislocation density; this phenomena is directly translated in this model, and the whole problem can be reduced to solving the classical equations with a modified initial dislocation density

$$\rho_{0i} = \rho_0 \exp\left(-\frac{2frc_0}{a^2} B_s + \frac{2}{3} \frac{B(T)}{\mu \dot{\varepsilon} \sqrt{\delta}} \left(\frac{2frc_0}{a^2} \right)^{\frac{3}{2}} \right) \tag{3.12}$$

A nice feature of the resulting model is that an analytical expression for the updated upper yield stress is deduced. If the upper yield stress is reached before the critical stress, then the impurities still affect dislocation motion after yielding, and the equations have still to take into account the modifications above-cited.

A limitation of this model is that the updated upper yield stress is not *systematically* dependent on the temperature. This has also been demonstrated in [Petukhov 2005], where it was shown that according to this model, the applied stress becomes:

$$\tau = \tau_{int} + \sqrt{\frac{2frc_0}{\delta a^2}} \tag{3.13}$$

and the temperature dependence disappears. This might be true for low-mobile impurities, but as noticed earlier, oxygen and nitrogen diffuse fast in silicon, especially at high temperatures, so the incorporation of diffusion to the dislocations might be relevant. The work of Maroudas and Brown [Maroudas 1991a, Maroudas 1991b, Maroudas 1991c] might be useful there, although the implementation of such a model becomes increasingly more complicated.

Secondly, pipe diffusion of impurities along the dislocation line is not correctly reproduced. Following this model, their concentration would simply increase linearly with time without formation of clusters. The resulting modulation of the locking stress that eventually *weakens* after some dislocation aging time is therefore not represented.

3.3.3 *The case of electrically active impurities*

Electrically active impurities diffusing to dislocations can pin the segments in a similar way as for light impurities. However, their electrical charge

affects the activation energy for dislocation motion.
Accounting for this effect on dislocation velocity could be done simply by using the results introduced in Figures 3.15 and 3.16.

3.4 CONCLUSION ON THE MECHANICAL PROPERTIES OF EXTRINSIC SILICON MATERIALS

Extrinsic silicon materials are characterized by their inclusion and impurity contents, the latter being either dissolved in the bulk as interstitial/substitutional atoms or as precipitates.

Inclusions have a significant effect on the fracture properties of silicon materials because of their relatively large size associated to their thermal expansion properties that differ from those of the silicon matrix. At high temperatures inclusions are potential dislocation sources; however as the brittle-to-ductile transition is crossed the elastic mismatch is likely to increase the risk of fracture.

The properties of precipitates on plasticity in semiconductors are more subject to discussion, as their size and concentration determine their net effect on dislocation motion: large amounts of small precipitates likely act as locking agents whereas larger precipitates can both act as dislocation sources and stoppers. The overcoming of precipitates by dislocation climb is a mechanism allowed at very high temperatures and affects indeed the net effect of these extended defects on the mechanical properties of covalent crystals.

Impurites affect the mechanical properties of silicon materials because of the influence they have on dislocation mobility. All impurities have the ability to diffuse to the dislocation core or to gather around it, forming a Cottrell atmosphere, because of the lattice distortion associated with the presence of the dislocation. Such aggregation locks the dislocation in place and prevents its motion; this results macroscopically in the extension of the elastic region. It has been demonstrated that the formation of Cottrell atmospheres is thermodynamically improbable at temperatures where plastic deformation by dislocation glide is intrinsically allowed. At high temperatures, the only significant locking mechanism is therefore due to the diffusion of impurities directly at the dislocation core.

Which impurity will lock dislocations and to which extent depends both on its diffusivity (how fast it diffuses to the core), its concentration in the bulk and its intrinsic locking ability per atom at the core (its binding energy to the dislocation). This explains why N has a stronger locking effect than O even at bulk concentrations several orders of magnitude lower: its high diffusivity is associated to a high binding energy, and few dissolved atoms are necessary to effectively lock dislocations in place.

Two types of impurities can be distinguished, depending on their electrical activity. Light impurities, or electrically inactive impurities, namely O, N and C, have no effect on the dislocation core configuration, and do not affect the velocity of dislocations already in motion. On the contrary, electrically active impurities such as dopants modify the electronic state of the dislocation core and alter the energy barriers for double kink nucleation and propagation.

Both the locking effect and alteration of the activation energy by dissolved impurities can be modeled. Coupling with the model of Alexander & Haasen has allowed some authors to successfully reproduce the stark increase of the upper yield point at high concentrations.

As temperature is lowered dislocation glide looses its ability to relieve the elastic stresses. Ultimately, the mechanical behavior of silicon crystals become entirely brittle. The next Chapter is concerned with the study and modeling of the transition between the ductile and brittle fracture mechanisms, very marked in covalent crystals.

4

THE BRITTLE-TO-DUCTILE TRANSITION IN SILICON

Silicon has the property of having its brittle-to-ductile (BDT) transition temperature high enough to behave as a brittle material at room temperature, which can pose some problems for example when silicon is sliced into wafers that break without noticeable plastic deformation. Silicon is a ductile material when grown from the melt, as has been exposed in last Sections. Indeed, the brittle-to-ductile transition of silicon has received a lot of attention, and it might be interesting to present some major results obtained, and the established theories. Since the kink generation and migration mechanism that rules dislocation mobility below $0.6T_m$ is thermally activated, reaching too low temperatures leads to the occurrence of a competition between the time required to generate mobile dislocations able to sustain plastic flow, and the increase of stress that can lead to breakage.

4.1 BDT IN SILICON: EXPERIMENTS AND MODELING*

4.1.1 *Basic principles of the BDT in intrinsic materials*

ARGON exposed recently the physical principles behind the BDT in intrinsically ductile and intrinsically brittle materials [Argon 2001]. Since silicon can exhibit brittle behavior at low temperatures and high strain rates, it belongs to the latter category. There exist large energy barriers to dislocation emission from the crack tip, but temperature can help these barriers to be overcome, which explains why silicon becomes ductile at higher temperatures. It appears that the key element to the transition involves atomic processes at the core of the dislocation: as noticed in Chapter 1, the motion of dislocations in silicon is due to the generation of kink pairs, which has to be followed by motion of these pairs along the dislocation line; energy barriers also oppose this propagation (for example, coming from interaction with defects or impurities). Indeed, ductile behavior would basically be controlled by the mobility of dislocations moving away from the crack tip. When the loading rate results in a higher rate of stress increase in the crack tip than the rate of stress relaxation resulting from dislocation activity, then brittle fracture occurs. Experiments made on high purity single crys-

tals, initially dislocation-free, yield the following expression for the BDT temperature:

$$T_{BDT} = T_0 / \ln\left(\frac{\dot{K}_0}{\dot{K}_I}\right) \tag{4.1}$$

with T_0 equal to 2.78×10^4 K and $\dot{K}_0$ equal to 1.42×10^{12} MPa.m$^{1/2}$.s^{-1}. In reality, the BDT temperature is found to be lower than the one given by the equation; this comes from the type of silicon used for these experiments and the impurity content of the samples, among other factors that will be exposed in the following.

Basically two experimental methods exist: tests performed on tapered double-cantilever beams, and by the means of four-point bending tests. The former method has been chosen by several research groups [Michot 1986, Brede 1988] since the early work of [St John 1975], while the research group of Hirsch in Oxford chose the indentation-four point bending method [Hirsch 1987, Hirsch 1989a, Hirsch 1989b]. The results obtained by the latter are qualitatively good, but have been criticized by Brede on the basis of the discrepancies observed between the different testing methods. Since each experimental method has lead to a singular model for brittle-to-ductile transition, both will be exposed here. A third model for the BDT, proposed by Khantha *et al.*, was later analyzed by Hirsch and Roberts and shown not to be relevant for silicon [Hirsch 1996]. It will therefore not be exposed in this report.

4.1.2 *Characteristics of the BDT in initially dislocation-free silicon*

Experiments clearly show a sharp transition from the brittle to the ductile deformation regimes, both in cantilever-like experiments and with indentation-created crack tips. The transition occurs in a very narrow temperature range, typically less than 10 K.

Dynamic experiments

Given a loading rate, the specimen behaves as brittle below the critical temperature T_c, and no dislocations are observed on the fracture plane. At the transition temperature, the specimen still breaks in a brittle manner, but at a critical stress intensity factor that is 5 to 7 times higher than in the perfectly brittle range; moreover some dislocation activity is revealed by etch pit above a stress intensity factor close to the critical one. Above the transition temperature, the specimen becomes ductile, and can be deformed plastically before it breaks. In this case, its behavior is the same as samples tested in compression or tension, meaning that it exhibits an upper and lower yield stresses. The resulting curve of the critical stress intensity factor vs the temperature is found in Figure 4.2 for an ideal case. The critical temperature for transition T_c increases with the applied loading rate $\dot{K}_{\mathrm{Ia}}$, following a thermally activated law that has an activation

energy approximately equal to the one for dislocation motion (2.2 eV, equation 4.2), suggesting that the BDT is governed by dislocation velocity. In this equation, A translates the effects of the crack geometry and the activity of the dislocation nucleation sources; it varies a lot with the experimental method used. The activation energy is lowered by doping.

$$\dot{K}_{\mathrm{Ia}} = A \exp\left(-\frac{U_{BDT}}{k_b T_{bc}}\right) \tag{4.2}$$

Static experiments

In static (creep) experiments at temperatures favorable to dislocation motion, dislocation activity is observed at the crack tip for a loading between K_{In}=0.25 and 0.3 MPa.m$^{1/2}$, as reported by Michot and George above 973 K [Michot 1986, George 1993]. This threshold might depend on the temperature as noticed by Xin and Hsia [Xin 1996] who found it to be 0.394 MPa.m$^{1/2}$ at 773 K. It was already observed in [Michot 1986] that increasing the temperature would slightly lower the critical stress intensity factor for dislocation nucleation at or close to the crack tip. Generation and propagation of dislocations leads to the formation of a plastic zone ahead of the crack tip, whose size grows up to a steady-state value (due to the non-singular terms of the stress far from the crack tip) that increases with the applied stress intensity factor but does not depend on the temperature; see Figure 4.1 for an example at 1073 K.

Brede and Haasen in Germany, as well as Michot *et al*. in France, found a critical stress intensity factor of $K_{\mathrm{Ico}} \simeq$0.9 MPa.m$^{1/2}$ for propagation of cracks at room temperature on double-cantilever beams on a (111) plane [Michot 1982, Brede 1988]. See Section 4.3 for more details about fracture toughness and propagation along other planes. From room temperature and below the BDT temperature for propagation on a {111} plane, fracture occurs between $K_{\mathrm{Ic}} = K_{\mathrm{Ico}}$ and 2.5 K_{Ico}, increasing with temperature and reaching a plateau before the BDT temperature. This is due to the development of a plastic zone at the crack tip that shields it and increases its fracture resistance. It has been observed that the development of a plastic zone can be enhanced by a crack jump that always occurs at K_{Ico} [Brede 1988].

4.1.3 *The model of Brede and Haasen*

In the original model of Brede and Haasen [Brede 1988], the transition from perfectly brittle to partially ductile fracture was explained through the idea of a "saturation zone" that dislocations emitted from the crack tip would fill up. This zone is limited by the contour of the lowest stress required for dislocation mobility (cf. the AH model, Eq. 2.10), itself depending on the back stress acting on dislocations and of possible locking effects coming

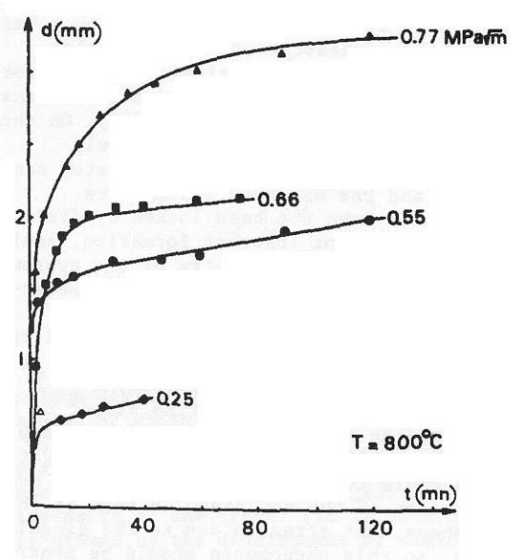

Figure 4.1: Evolution of the size of the plastic zone with time in double cantilever beams, for various applied stress intensity factors (creep conditions). The temperature is 1073 K and the crack plane {111} [Michot 1986].

from impurities of dopants. The formation of such a plastic zone is possible only when dislocations can be moved out from the tip, meaning when the stress intensity factor at the tip is larger than K_{In}. As noted above, the size of the plastic zone does not depend on the temperature, although this claim is based on observations performed in a restricted temperature range (typically 100 K wide).

As temperature increases dislocations move faster and can reach the far end of this zone, effectively shielding as much as possible the crack. When the temperature is high enough to allow full saturation of the zone, then the critical stress intensity factor does not depend any longer on the temperature, thereby creating a plateau in the observed K_{Ic}. At the transition temperature and in dynamic experiments, the size of the plastic zone increases with the load and is found to be a linear function of the applied loading rate. When a dislocation is emitted, it goes through a dislocation-free zone where stresses are high enough to enable dislocation motion, whatever the structure of the plastic zone might be.

Brede and Haasen explain the transition from brittle to ductile as follows: if the dislocation velocity is too low to accommodate for the increase in the applied stress intensity factor, then the maximum tensile stress achieved at the crack tip becomes larger than the cohesive stress, and fracture occurs. At the BDT temperature, dislocation motion compensates exactly the applied $\dot{K}_{\mathrm{I}}$, and σ_{max} stays below its critical value. It is therefore assumed that dislocations are nucleated at the crack tip since the early beginning of testing as observed experimentally (for a stress intensity factor at the tip

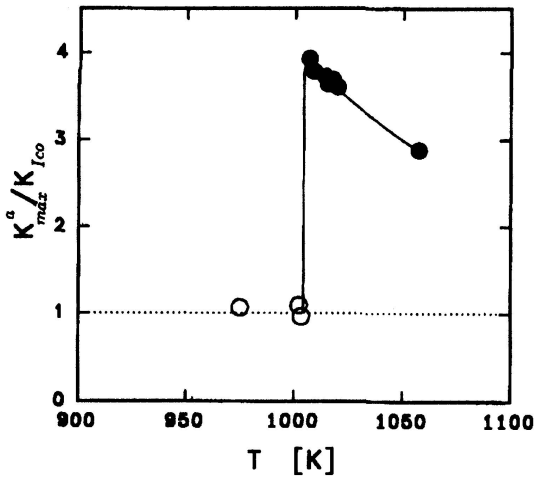

Figure 4.2: Perfect brittle-to-ductile transition [Brede 1993]. The sample tested was an FZ-grown crystal, $[B] = 5.2 \times 10^{14}$ cm^{-3}, $[O] \leq 10^{15}$ cm^{-3}. Loading rate 4583 MPa$\sqrt{m}$.s^{-1}, T$_c$=1004 K.

above K_{In}), and that the existence of a critical shear stress for dislocation propagation exists below T_c. Once this shear stress is reached, the formation of a zone that is conditionally saturated begins, allowing an increase in toughness up to a maximum value under the brittle-ductile transition temperature. The thermally activated dislocation motion competes with the stress intensity factor increase rate, and nucleation of dislocations is determined merely by the speed of dislocations moving away from the tip, thereby decreasing the back stress on the emitter. The principal equation of the model [Brede 1988] is introduced below.

It is assumed that in mode I loading, dislocations emitted from the crack tip and moving it this plane shield the tensile stress only through the "vertical" component of their Burgers vector, perpendicular to the crack plane. The spacing between each dislocation is taken as constant and written Δ. The plastic zone has a length d. When filled up with screw dislocations, the effective stress intensity factor at the tip becomes, when applying a stress intensity factor K_{Ia}:

$$K_{tip} = K_{\mathrm{Ia}} \frac{3}{2\pi} \left(\frac{\Delta}{d}\right)^{\frac{1}{2}} \left[\ln \frac{4d}{\Delta} + \frac{4}{3}\right] \tag{4.3}$$

and the normal stress at the tip $\sigma = \frac{2K_{tip}}{\sqrt{\pi r}}$, r being the radius of the tip, whose growth rate is directly linked to the velocity of the emitted dislocations. Using Eq. 2.6 for the dislocation velocity, it follows an equation linking the BDT temperature to the strain rate (speed of the cantilever beam).

This model contains several flaws [Haasen 1991, Hirsch 1991]. First, the spacing between dislocations is certainly not constant since they interact

with each other. This is clearly shown in experiments, where the shape of the plastic zone is an inverted pile-up from the crack tip [Hirsch 1987, Hirsch 1989a, Warren 1989]. Therefore, the number of dislocations in the plastic zone, and the size of the plastic zone, are not proportional to each other. Secondly, the assumption that the plateau corresponds to a constant resolved shear stress in the plastic zone is not consistent with the fact that dislocations interact with each other and feel a different shear stress depending on their location in the pile-up. Finally, the shear stress in the dislocation-free zone is not equal to the starting stress. All these results were obtained by simulation in [Brede 1993], which allowed furthermore to provide more insights into the BDT:

- The semi-brittle transition observed, leading to a plateau, comes directly from the mutual interactions between dislocations in the pile-up. It becomes temperature-independent because the local shear stress is no longer determined by dislocation velocity, but by the forces dislocations generate.
- The resolved shear stress is found to be lowest at the outer boundary of the dislocation-free zone, meaning in the inner part of the plastic zone. It is controlled by the starting stress.
- Applying an initial load higher than K_{Ico} leads to the emission of a single dislocation ahead of the plastic zone later created, because prior to shielding the local shear stress is rather high in the considered slip system. This has no influence on the final results, as is observed experimentally.
- Mode II and III are activated by the different components of the Burgers vectors of the dislocations, leading to activation of several slip systems. The additional shielding coming from these slip systems could lead to the sharp transition.

4.1.4 *The model of Hirsch, Roberts and Samuels*

[Warren 1989] showed tn indented specimens prepared for 4-point bending testing that reducing the amount of dislocations close to the crack tip prior to testing was leading to a less effective crack shielding (higher BDT temperature), proving that the dislocations close from the crack tip before deformation play a critical role in the transition process. His results are correctly reproduced by the model of [Hirsch 1987] that explains the sharp transition observed in silicon by the existence of a critical stress intensity factor for a dislocation nucleation event at the crack tip, taking place at K_o that is close to K_{Ico} (approximately 95 %) when the initial dislocation density is low in the vincinity of the tip. The stress intensity factor for dislocation generation once this threshold has been reached is nevertheless significantly lower ($K_{In} = 0.25\,K_{Ioc}$, in accordance with Brede and Haasen): once K_o is reached, dislocations are emitted in large numbers from the tip,

effectively shielding it and raising the effective K_{Ic} far above its theoretical value.

This is in contradiction with the model of Brede and Haasen, who suppose that dislocations are emitted from the crack tip without another threshold than overcoming the critical shear stress for dislocation motion, considered temperature-independent. Indeed, the four-point bending test method used by the Oxford group has been severely criticized by Brede, as will be seen later.

The mathematical model proposed by Hirsch, Roberts and Samuels (HRS model) succeeds in providing with a potential explanation to the BDT, and some emphasis will be put on it here. It was first introduced in [Hirsch 1987], and used in a beautiful and elegant manner a couple of years later [Hirsch 1989a, Hirsch 1989b]. A presentation of the generalized model to line crack tips (called HR model) is found in [Hirsch 1991]; reviews are available in [Hirsch 1996, Hirsch 1997]. In the following the variant for indented cracks is introduced.

The HRS model is physically based on the emission of dislocations from sources located close to the crack tip, at precise locations that are favorable for cross-slip of screw dislocations, allowing their multiplication: along a circular tip, four such locations exist, that can be found where the tangent to the crack tip is parallel to one of the three <110> glide directions in the {111} glide plane, taken as the plane of the crack in the experiments, see Figure 4.3. On the other hand, computing the stress intensity factor along such a geometry leads to the determination of the weakest point Z where fracture should start, see Figure 4.4.

The HR model assumes a discrete distribution of nucleation sites along the crack tip (this assumption agrees with the observations of different research groups [George 1993, Xin 1996]). For simplicity of modeling, mode III is assumed instead of mode I in the HRS model, and the curved crack tip is represented as a line. The effective stress acting on a dislocation situated at $x_i$is given by 4.4. The more general case (HR model) is given by equation 4.5:

$$\tau_{x_i} = \frac{K}{\sqrt{2\pi x_i}} - \frac{\alpha\mu b}{x_i} - \frac{\mu b}{2\pi}\sum_{x_j}\left(\frac{x_j}{x_i}\right)^{\frac{1}{2}}\frac{1}{x_j - x_i} \tag{4.4}$$

$$\tau_{x_i} = f\frac{K}{\sqrt{2\pi x_i}} - \frac{\alpha\mu b}{x_i} - \sum_{j\neq i}\tau_{ij} \tag{4.5}$$

The first term comes from the crack tip stress field, the second one represents the image stress acting on the dislocation, and the third one arises from the stress field created by the other dislocations. α is found to be 0.1 in silicon [Hirsch 1996], f is a geometrical factor, μ is the shear modulus, b the Burgers vector. Expressing the velocity as a function of the effective stress and considering the ratio $\frac{\dot{K}}{v_0/\tau_0 \exp(-U/k_bT)}$ independent of the temperature,

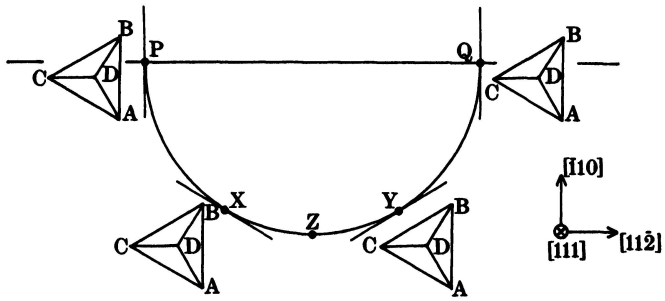

Figure 4.3: Location of the nucleation sites along the crack tip [Hirsch 1989b].

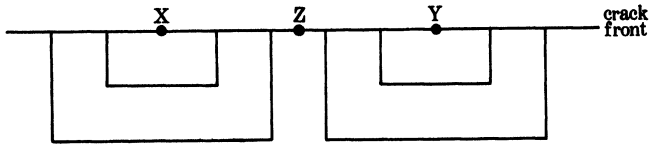

Figure 4.4: Idealization of the crack tip. X and Y are the active dislocation sources, Z is the point to shield to prevent fracture [Hirsch 1989b].

it is possible to simulate the successive generation of dislocations from a source, given the stress intensity factor.

Nucleation proceeds as follows: when the shear stress at the source (ahead of the tip, so the stress field can be computed from the stress intensity factor at the tip) for motion is reached, a dislocation can move out of the source, and shields it, preventing it from propagating another dislocation. The distance between the source and the tip is adjusted so that the first emission occurs at $K_{tip} = K_{\mathrm{In}}$, in agreement with the experiments. As the dislocation moves further away from the tip, its backstress acting on the tip diminishes, the stress intensity factor at the tip increases with time and reaches once again K_{In}, until the source can act and emit a second dislocation, which in turn shields the source, etc... The process results in an inverted pile-up, see Figure 4.5 and the creation of a dislocation-free zone (DFZ) that is due to the stress fluctuations with distance from the crack tip: the effective stress acting on dislocations stems from the crack tip stress and the backstress of the dislocation pile-up ahead of the tip. [Michot 1994] computed for example the evolution of the dislocation density and effective stress from etch-pit observations, see Figure 4.6. These results are correctly represented in the HRS model. Nucleation conditions are critical parameters for the effectiveness of the model [Roberts 1994].

Dislocations are considered to shield the critical point on the tip Z only when they have passed it. Therefore, the effective stress intensity factor acting on Z is

$$K_{eZ} = K - \sum_{j, x_j \geq x_Z} \frac{\mu b}{\sqrt{2\pi x_j}} \tag{4.6}$$

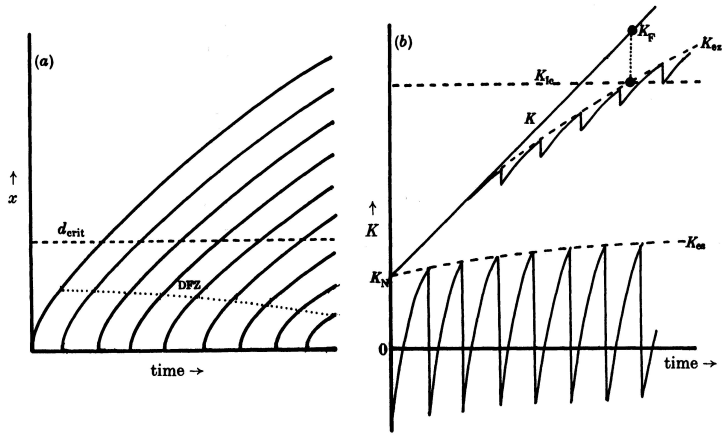

Figure 4.5: (a) Computation of the pile-up created at the sources. (b) Stress intensity factors at the sources, modulated by the shielding of emitted dislocations, and emitting a new one once the effective stress intensity factor reaches K_{In}; the stress intensity factor at Z reaches conditionally K_{Ic0} if shielding is not efficient enough to compensate the applied K [Hirsch 1989b].

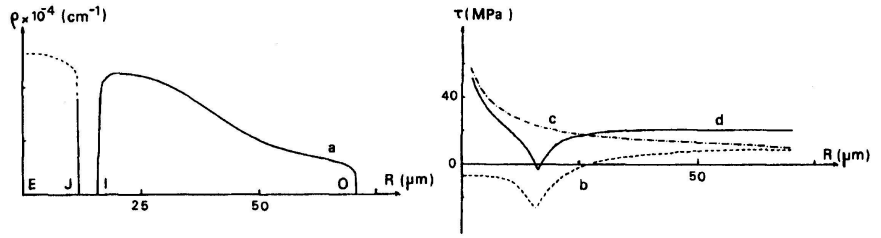

Figure 4.6: Evolution of dislocation density (left), and of stresses (right) ahead of the crack tip: curve (b) internal stress, (c) applied stress and (d) effective stress [Michot 1994].

and this point is shielded if enough dislocations can reach it on time, before $K_{eZ} \geq K_{Ic0}$.

Simulating the crack behavior at constant loading rates with different values of K_0 for the first emission of a dislocation, Hirsch *et al*. have shown that the BDT is sharp only when K_0 is close from K_{Ic0}. Therefore, the idea of a critical nucleation event that has to be independent on temperature, or of the same dependence as the dislocation velocity, governs the HRS model. Once K_0 is reached, the source emits dislocations, and continues to operate at $K_{In} \ll K_0$, resulting in an avalanche of dislocations shielding the crack.

When dislocations are initially present in the vincinity of the crack tip (a situation that is not obvious in silicon), their multiplication proceeds by successive cross-slip events only when they reach the crack tip, since cross-slipping is not an easy process in the bulk. If dislocations are already present in large numbers close from the tip, then the transition is not sharp

(meaning lower values of K_0) and follows the same pattern as observed in the experiments.

The model agrees also on the size effect observed: the BDT temperature increases with the crack size, since dislocations have to travel a longer distance in order to shield the crack. The detailed experimental methods and mathematical model are found in [Hirsch 1989a] and [Hirsch 1989b], respectively. See the mentioned articles for a complete description.

The HR model assumes furthermore that dislocations emitted from the initial source trigger the activation of new sources as they propagate along the crack tip, they . The transition from ductile to brittle follows from a competition between the rising stress intensity factor at the weakest Z points along the tip on the one hand, and the shielding provided by the dislocations emitted from the initial sources on the other hand. If dislocations propagate fast enough and reach Z before K_{Ic0} is attained, then the weakest point is shielded and ductile behavior results: the transition temperature is reached. The role of the secondary sources is to govern the sharpness of the transition; they are activated at a given stress intensity factor K_0. Close to T_c, the secondary source is activated at K_0 ; between this source and Z is a dislocation-free zone of width d^f_{crit}. If the width is too large, the resulting shielding will be weak and fracture may occur at a stress lower than the macroscopic yield stress. The shorter this distance, the sharper the transition.

These models are effective at predicting the BDT temperature and material behavior, provided that the configuration (localization, type) of the dislocation sources are known. Their critical assumptions are twofold: first, the dislocation sources have to be discrete along the crack tip (verified experimentally); second, there has to exist a threshold stress intensity factor close to the critical one for activation of the sources that will ultimately provoke the effective crack shielding (also observed in dynamical experiments). They nevertheless suffer from their monodimensional aspect: improvements would include full 3-dimensional and multislip modeling. These dynamical models are discussed in [Roberts 1993, Roberts 1994].

4.2 FACTORS CONTROLLING THE BDT*

The most important result is that the transition to a ductile behavior is not only governed by the kinetics of dislocation nucleation at the crack tip, but also by the mobility of the dislocations, be it either to act as sources or to move away from the crack tip. This was observed for example by [Michot 1986] and justified by the observed activation energy of the stress intensity factor rate, similar to the activation energy for dislocation motion (see Section 4.1.2). The role of dislocation nucleation was studied later by the same authors [George 1993]. Given a loading rate, several parameters modulate the recorded transition temperature. They are described below.

4.2.1 *Crack plane and nucleation conditions*

It is emphasized by [Brede 1988] that the different orientations of the glide systems at the crack tip could have an influence on the dislocation nucleation, so the competition for dislocation motion/stress increase at the crack tip might induce different results depending on the crack propagation plane, even though the crack propagation always tends to happen on {111} planes in macroscopic samples, as will be discussed later. It appears moreover that cleavage on {110} planes is cleaner than on {111} slip planes as the crack misorientation with respect to the <110> direction is reduced, because of the absence of disruptive ledges along the tip in this case [Michot 1988]. [Brede 1993] noticed indeed in his simulations that dislocation generation did not happen symmetrically on the same slip system if not on the same lobe, and attributed this discrepancy to different resolved shear stresses. The activation of several slip systems is critical to obtain a sharp transition, as shown by simulations [Ferney 1999]. This is a feature that the HR/HRS models do not take into account, these models finding the origin of the sharp transition in other nucleation events. Indeed, activating several glide systems allows for a more effective shielding at the tip, and is observed experimentally.

The nucleation conditions are important to explain the sharp transition observed, and using different crystallographic orientations leads to different results coming from the nucleation and loop propagation conditions on this plane. Nevertheless, the computation of the resolved shear stresses acting on the slip planes is not sufficient to predict where propagation actually occurs [George 1993], because activation of nucleation sources is critical for further development of plasticity on a slip system.

Nucleation can happen on the free surfaces of the specimen, especially when loaded at high rates. When nucleation occurs in the bulk, then it is observed to be on a few sources along the crack tip only, and at rather low loading rates. Ledges present at the crack tip are believed to be enhanced nucleation centers, although in their experiments, [George 1993] observed nucleation sometimes at sites where no ledge was visible, whereas the presence of a ledge did not guarantee an active dislocation source. Microdefects

are obviously preferential nucleation sites, although these are not relevant for FZ-grown crystals. Using AFM, they however observed that shallow ledges are always present on the cleavage plane, sometimes a few ngströms high only. Theoretical analysis shows that activation energies for dislocation nucleation are realistic only at cleavage ledges, below the critical fracture threshold, so they might be the preferential sites for dislocation nucleation at low loading rates, free surfaces of the sample being the preferential nucleation sites at high loading rates as pointed out above. These ledges are likely to be the very reason for the existence of an increase in the toughness observed below the transition temperature: static experiments done on perfect crack tips have shown that no plastic activity at all is observed (and indeed, fracture occurs always at K_{Ic0} below T_c), even after several hours at a constant load [Scandian 1999].

4.2.2 *Specimen and crack geometry*

The dependence on the specimen type and test method has been cited previously, and a large scatter of BDT temperatures results [Hull 1999]. This structure dependence has also been noticed and modelled by [Hirsch 1989a, Hirsch 1989b], and can explain discrepancies between different authors for given testing conditions, but using different crack shapes or sizes. Their HRS model reflects this size dependence on the transition temperature: the pre-existing dislocations need to travel varying distances before they reach the crack and can multiply from there for further shielding.

Brede criticized strongly the four-points bending method used by Hirsch *et al.*: among other factors, it was emphasized that indentation at room temperature leads to residual dislocations at the vincinity of the indentation mark, that do not disappear effectively upon annealing. This leads to residual stresses that disturb the results, resulting for example in a higher measured K_{Ic0}. Furthermore, when the intially semi-circular or ellipsoidal crack propagates, it does not keep its initial shape and the stress distribution in the sample is modified consequently, preventing from easy analysis. Therefore, if this testing method allows for demonstration of the geometry effect on the BDT, it might not be relevant to obtain intrinsic values of the material fracture behavior [Brede 1993].

The presence of free surfaces in both sample types inevitably leads to stress concentrations. These are lower in the case of tapered double-cantilever beams, although it has been observed that for high loading rates, dislocation nucleation takes place preferentially at the free surfaces in these specimens. Ledges at the crack tip and imperfect sample preparation (crack healing, crack tip not orthogonal to the free surfaces) lead to biased results and a large scatter in the measured BDT temperatures results [George 1993]. Nevertheless, double-cantilever beams tend to reduce these errors, compared to four-point bending samples. All these factors lead to the conclusion that such specimens are more suitable for testing and further numerical modeling of the BDT.

4.2.3 *Impurities*

In n-doped silicon for example, the dislocation mobility is enhanced (Section 3.2) and the transition occurs at lower temperatures[1] than for intrinsic silicon, although for low loading rates, a starting stress for dislocation motion related to dislocation locking by the doping impurities perturbs this motion enhancement. Indeed, dissolved oxygen increases the BDT temperature by dislocation locking and lowering of dislocation mobility [Michot 1986, Scandian 1999]. Precipitated oxygen in silicon has no clearly-defined influence. It can lower the BDT temperature by allowing higher generation of dislocations at the extended defects, but also raise it by locking dislocations. SiO_2 platelets have in particular been noticed for their effect on the BDT temperature, since the extrinsic stacking faults that are connected to them act as dislocation sources [Behrensmeier 1987].

The inevitable presence of impurities also creates a "semi-brittle" temperature domain, below the usual transition temperature, and where the critical stress intensity factor for brittle fracture is higher than the one found at room temperature (K_{Ic0}=0.9 MPa.m$^{1/2}$, relatively independent on the doping). In this case, a crack jump is observed at K_{Ic0} and plastic activity is revealed on the fractured specimen. Above a certain temperature, a plateau effect is observed, as described in Section 4.1.3. Figure 4.7 gives an example of such a semi-brittle behavior. This progressive change can begin 673 K below the observed BDT, this behavior being thought to come partly from the locking effect of impurities.

4.2.4 *Pre-existing dislocations and grain boundaries*

The singular characteristic of the brittle-to-ductile transition in intrinsic silicon is that it occurs suddenly over a few degrees: the stress intensity factor to fracture rises sharply in this interval. Nevertheless it is worth noting that this result is valid only for initially *dislocation-free* silicon, as pre-straining leads to smoother brittle-ductile transitions over a larger range of temperatures. One of the first publications about the macroscopic mechanical behavior of silicon single crystals already noticed the existence of a brittle-to-ductile transition depending on the initial dislocation density [Patel 1963]. Indeed, dislocation shielding is very effective to raise the critical intensity factor because of crack shielding [Hirsch 1987, Warren 1989]. When comparing the results obtained by the different testing methods, Brede pointed out that the lower critical stress intensity factors found by the Oxford group were due to pre-existing dislocations in the sample [Brede 1993]. It has been noticed that grain boundaries help to prevent brittle fracture, by stopping the cleavage for a certain time, allowing dislo-

1 The authors in [Brede 1988] cite a 30% decrease in the BDT temperature in n-doped silicon. More generally, the decrease in activation energy for dislocation mobility results in a lower BDT temperature that is unlikely to exceed 100°C compared to the intrinsic material [Hirsch 1989a].

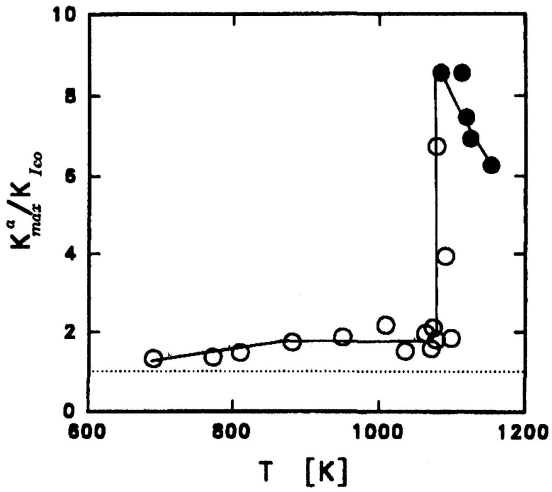

Figure 4.7: Semibrittle behavior observed in As-doped CZ sample [Brede 1993]. $[As] = 2.9 \times 10^{19}$ cm^{-3}, $[O] = 6.7 \times 10^{17}$ cm^{-3}, loading rate 384 MPa$\sqrt{m}$.s^{-1}, T_c=1077 K.

cations to propagate and relieve the high stresses in the vicinity of the crack tip. This particular aspect will be dealt with in another report.

4.3 SILICON AS A BRITTLE MATERIAL

The fracture of silicon wafers is mentioned here, since it provides results on the propagation behavior of cracks at room temperature. Indentation tests and indentation fracture mechanics will also be discussed here, since this might be of interest in the case of wafering of silicon ingots, as shown in Section 4.3.4. A review of the mechanical properties of silicon is available in [Hull 1999].

4.3.1 *Elastic properties of silicon*

Silicon is an anisotropic material with a cubic structure, defined by three elastic constant parameters as follows, at atmospheric pressure. These coefficients vary linearly with temperature above 673 K up to 1273 K [Burenkov 1974]:

$$\begin{cases} C_{11}(T) = (16.552 - 0.0015\,T) \times 10^{10}\,\text{Pa} \\ C_{12}(T) = (6.383 - 0.0006\,T) \times 10^{10}\,\text{Pa} \\ C_{44}(T) = (8.1986 - 0.0006\,T) \times 10^{10}\,\text{Pa} \end{cases}$$

and the stiffness tensor can be written:

$$\left[\underline{\underline{C}}\right] = \begin{bmatrix} C_{11} & C_{12} & C_{12} & 0 & 0 & 0 \\ C_{12} & C_{11} & C_{12} & 0 & 0 & 0 \\ C_{12} & C_{12} & C_{11} & 0 & 0 & 0 \\ 0 & 0 & 0 & C_{44} & 0 & 0 \\ 0 & 0 & 0 & 0 & C_{44} & 0 \\ 0 & 0 & 0 & 0 & 0 & C_{44} \end{bmatrix}$$

Compliances, as well as the bulk modulus can be obtained from the elastic constants. In the isotropic approximation, one can obtain the shear modulus μ, Poisson's ratio ν and Young's modulus E at room temperature and standard atmosphere:

$$\begin{cases} \mu = 6.8 \times 10^{10}\,\text{Pa} \\ \nu = 0.218 \\ E = 16.56 \times 10^{10}\,\text{Pa} \end{cases}$$

4.3.2 *Indentation mechanics of ceramics*

The mechanics of indentation of ceramics have been presented in [Lawn 1980, Marshall 1982]. The pattern common to all ceramic materials is the formation of a median/radial crack system upon indentation, and possibly the appearance of a lateral crack, parallel to the surface, which can reach the surface and cause chipping of the material. This is the mechanism used for wafering as will be seen Section 4.3.4.

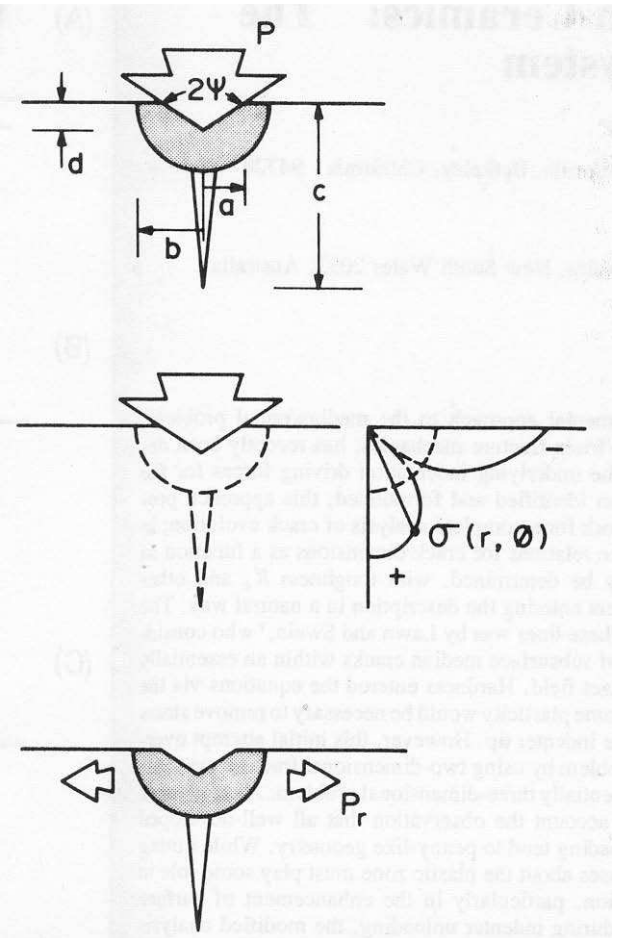

Figure 4.8: The median/radial cracks [Lawn 1980].

The median/radial crack system

When studying the effects of indentation on ceramics, it is important to consider both loading and unloading phases, since the progressive relaxation of the applied load can give freedom to the plastic zone beneath the indenter to cause further crack opening and propagation in the material. The basic model considers the superposition of two fields: a far field of an ideally elastic material, and a residual field beneath the indenter, see Figure 4.8. This results in a total stress intensity factor coming from contributions of the two fields, and it appears that the radial crack continues its growth until full unloading, whereas the median one reaches its full length at full loading.

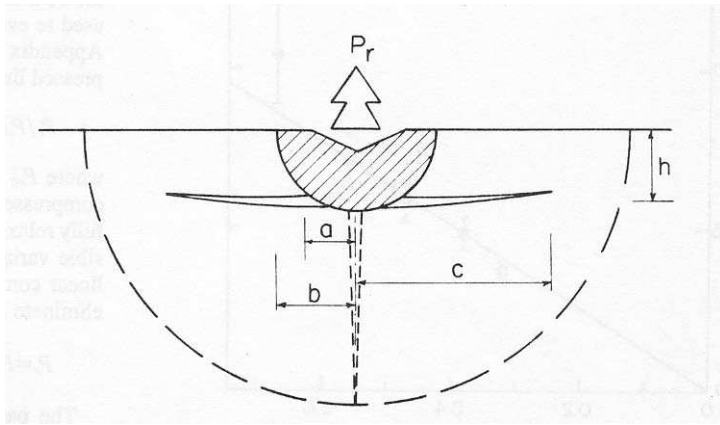

Figure 4.9: Picture of the lateral crack system [Marshall 1982].

The lateral crack system

The lateral crack initiates near the base of the plastic deformation zone, and spreads out on a plane parallel to the surface. Its growth occurs during the unloading phase, and the residual stresses are thus identified as the primary drivers. The cracks are modelled with the help of the plate theory since they are located close to the surface, see Figure 4.9.

Measurement of fracture toughness

Two methods exist for evaluation of fracture toughness after indentation: the direct observation of the indented surface, and the indirect one. The former relies on measurement of the size of the crack systems, and assumes that the crack is in equilibrium both during and after the event, which is not always the case, since slow crack growth can take place after removal of the indenter, even when oil is used to slow down this process. Moreover, if the grain size is of the same order of magnitude as the cracks (100 µm), then the fracture pattern is not useful to obtain a correct description of the properties of the material [Anstis 1981]. In order to work, this method requires in addition the pre-knowledge of E and H, Young's modulus and the hardness of the material, but these parameters can be obtained from experiments with a good accuracy, see Eq. 4.7, where a is defined in Figure 4.8. Drawbacks of this direct method are the need for a well-defined radial/median system, with a deep radial crack. That means that loads high enough to generate such a crack system are required; while too high loads might lead to the formation of a lateral crack system which is to avoid.

$$\begin{cases} H = \frac{P}{\alpha_0 a^2} \\ P \text{ peak load} \\ \alpha_0 \text{ constant} \end{cases} \tag{4.7}$$

The second method [Chantikul 1981] has the positive aspect not to require accurate crack measurements, and it is moreover relatively insensitive to slow crack growth effects, as compared to the direct method described above. The theory is based upon a decomposition of the stress field into an elastic and plastic part, leading to the expression of the concentration factor in eq. 4.8. There, σ_a is the stress associated to the load P_r, shown as well as c and P in Figure 4.8. ω_c is a parameter defining the crack geometry, χ_r a constant depending on E and H. Using the relationship $K = K_c$ and $\frac{d\sigma_a}{dc} = 0$ for crack growth give the maximum stress $\sigma_a = \sigma_m$ and crack length c_m for a full indentation. From these equations the toughness is extracted. A limitation is that failure must occur under equilibrium conditions so as to determine the right stress and load values at this point.

$$K = K_e + K_r = \sigma_a \sqrt{\pi \omega_c} + \chi_r \frac{P}{c^{\frac{3}{2}}} \tag{4.8}$$

Indeed, this method is attractive for several reasons: no crack measurement is needed, the crack size is replaced by the indentation load for determination of the toughness; but it is necessary to establish that the crack evolution is well behaved prior to identification of K_c.

4.3.3 *Crack healing and toughness at room temperature*

It has been observed that annealing of a cracked silicon surface in an atmosphere containing oxygen leads to crack healing [Yasutake 1986]. This is not caused by rebonding between the Si atoms, but by formation of SiO_2 at the crack tip, which induces a compressive stress and spreading of the formation of such molecules through the whole crack length. Healing is not homogeneous and is detrimental to a further controlled and regular spreading of the crack during fracture experiments. Therefore, to prevent healing, it is required to keep the specimen under load prior to experimentation.

Fracture tests have been performed both on crystalline and multicrystalline silicon crystals by [Chen 1980, Chen 1982]. In the crystalline material, it appears that the flaw always deviates towards a {111} plane, which has been found to have a fracture toughness of 0.93 MPa.m$^{1/2}$, in accordance with the results presented in Section 4. Table 4.1 summarizes the results obtained by different authors at room temperature[2]. The results on mc-Si are consistent with single crystal data, with a toughness of 0.82-0.93 MPa.m$^{1/2}$. This is due to the flaw size, smaller than the grain size. Since fracture occurs within grains, the influence of grain boundaries and other defects is minimized. These tests have been performed by means of 4-points bending tests, after introduction of a flaw by Knoop indentation. Consequently, the observed fracture mechanism in mc-Si might not be representative of the situation in the bulk material, where fracture could also occur between or close to the grains, where impurities and inclusions tend to segregate.

2 This relatively high fracture toughness of [Warren 1989] is due to residual stresses at the crack tip created during indentation and not efficiently removed by annealing.

Source	K_{Ic0} (MPa.m$^{1/2}$)	cleavage plane	method
[St John 1975]	0.96	{111}	DCB
[Brede 1988]	0.9±0.1	{111}	DCB
[Michot 1982]	0.93	{111}	DCB
[Warren 1989]	1.12	{111}	4PB
[Chen 1980]	0.93	{111}	4PB
[Xin 1996]	0.95±0.07	{110}	4PB
[Michot 1988]	0.89±0.04	{110}	DCB
[Yasutake 1986]	0.91±0.09	{110}	4PB
[Yasutake 1986]	0.95±0.1	{100}	4PB

Table 4.1: Critical stress intensity factors in mode I loading at room temperature as found by various authors. DCB: double-cantilever beam, 4PB: 4-point bending test.

4.3.4 *Application of brittle fracture to wire-sawing*

The process of wafering silicon crystals with the help of saws has been described and modelled in the recent years [Möller 2004, Möller 2006], and some issues such as the defects induced by the presence of inclusions in the bulk have been described [Du 2007]. For a detailed description of the sawing mechanism, the reader is advised to look at the above references. Basically, the sawing process relies on the creation of microcracks at the surface of the crystal, by interaction between particles of SiC and the crystal ("rolling-indenting model"). The material is progressively chipped away by the formation of lateral cracks (see Section 4.3).

The sawing rate and the different detrimental effects (uneven sawing for example) are determined by the combination of a mechanical model (interaction slurry-crystal) and a hydrodynamic model, taking into account the movement of the wire and flow of slurry between the wire and the ingot surface. Uneven surfaces are partly due to the bowing of the wire caused by the edges of the ingot; which leads in turn to varying slurry film thickness and pressure along the wire. Hard inclusions (of SiC) have the drawback of leading to unusable wafers, which have to be discarded, and might induce an extra tensile stress in the wire, possibly leading to breakage.

Surface damage created by the wafering process has to be removed in order to increase wafer strength [Möller 2005]. It is due to the presence of the radial and median cracks at the surface of the wafer of depth typically in the 10-15 µm range. This layer has to be removed by etching before further processing [Stefancich 2001, Borchet 2006]. It increases both wafer strength and its electrical properties.

CONCLUSION

The more research goes the more we know and the more we realize that things aren't that simple. [Jones 2000] entitled its publication "do we really understand dislocations in semiconductors?". After more than 60 years of intense research the answer to this question still seems to be negative. Although we have learnt a lot on the quantitative aspects of dislocation motion since the first dislocation velocity measurements it still remains unclear what the very fundamental mechanisms of dislocation mobility are, even in such an ideal material as silicon.

Silicon presents several features making it an attractive mechanical material to study. The possibility to produce virtually dislocation-free silicon ingots enables the exploration of the multiplication mechanisms at the onset of plasticity at intermediate and high temperatures. As typical for covalent crystal, dislocations are sensitive to the testing temperature and strain rate, resulting in a characteristic yield drop phenomena that increases in strength as temperature is lowered, due to the explosion of the dislocation density on the stressed slip system. Pursuing mechanical testing towards lower temperatures reveals a sharp and almost perfect brittle-to-ductile transition thermally governed both by dislocation nucleation and motion close to the crack tip. We have examined the physical and atomistic mechanisms underlying dislocation motion both in the low- and high-stress regimes, and showed that velocity is affected by the presence of impurities, be them electrically active (typically dopants) or not (oxygen being the most common impurity).

The model commonly used to describe the material behavior of silicon in its early deformation stage is based on the 40-years old work of Alexander and Haasen relying on Orowan's law to compute the plastic flow rate. Empirical laws steer the dislocation velocity and multiplication. If the former has been experimentally confirmed and refined during the following decades, it has been shown that the latter can be improved with the help of dislocation dynamics simulations. Limitations to this model exist though, since it is limited in its nature to single slip deformation cases, with no account taken for the effects of the various impurities that are most likely to be present in the multicrystals used in the photovoltaic industry. In addition, the model and its variations are not able to describe the hardening and recovery stages following the lower yield point, when interactions between dislocations lead to the immobilization of mobile dislocations and eventually to the formation of substructures governed by diffusion mechanisms that are absent in the original equations.

As perfectly brittle at room temperature, silicon has also been found to be an ideal material for exploration of the brittle-to-ductile transition. The leading HRS model explains the transition by the competition between

increase of the stress intensity factor at the crack tip on the one hand, and of the shielding provided by the stress fields of moving dislocations. These have to reach a critical zone prior to multiplication in order to effectively allow ductile fracture to occur. The nucleation and growth of cracks upon indentation, that can rip off material from the surface, is commonly used in wire-sawing techniques, although other mechanisms such as grinding lead to other types of damage that can be of interest.

The way towards modeling of silicon multicrystals is almost already paved. Crystal plasticity is a field that has been widely studied the last two decades, due to a tremendous increase in available computational power. The single crystal model needs further improvement in order to account for interactions between dislocations on various slip systems. Incorporating the influence of grain boundaries on dislocation motion and multiplication is the last step prior to the establishment of a complete mechanical model for silicon multicrystals and implementation in a commercial finite element code. Only then is it possible to study accurately the effects of inclusions and impurities on the internal stress build-up, as well as fracture mechanisms in multicrystals, a subject still left unexplored in the literature.

BIBLIOGRAPHY

[Alexander 1968] *Dislocations and plastic flow in the diamond structure*, H. Alexander, P. Haasen, Solid State Physics, Vol. 22, pp. 27-158, 1968

[Alexander 1974] *Dissociation and plasticity of covalent crystals*, H. Alexander, Journal de Physique Colloque, Vol. 35, No. 12, pp. C7/173-180, 1974

[Alexander 1981a] *New results on dislocation motion in Silicon and Germanium*, H. Alexander, Crystal Research and Technology, Vol. 16, No. 2, pp. 231-238, 1981

[Alexander 1981b] *TEM of dislocations under high stress in germanium and doped silicon*, H. Alexander, H. Eppenstein, H. Gottschalk, S. Wendler, Journal of Microscopy, Vol. 118, No. 1, pp. 13-21, 1981

[Alexander 1987] *On the stress dependence of dislocation velocity in silicon*, H. Alexander, C. Kisielowski-Kemmerich, A.T. Swalski, Physica Status Solidi (a), Vol. 104, pp. 183-192, 1987

[Alexander 1999] *Kinks on partials of 60°dislocations in silicon as revealed by a novel TEM technique*, H. Alexander, H.R. Kolar, J.C.H. Spence, Physica Status Solidi (a), Vol. 171, pp. 5-16, 1999

[Allem 1989] *On the yield point of floating-zone silicon single crystals III. The evolution of the dislocation structure through the yield point at low temperature*, R. Allem, J.-P. Michel, A. George, Philosophical Magazine A, Vol. 59, No. 2, pp. 273-302, 1989

[Anstis 1981] *A critical evaluation of indentation techniques for measuring fracture toughness: I. Direct crack measurements*, G.R. Anstis, P. Chantikul, B.R. Lawn, D.B. Marshall, Journal of the American Ceramic Society, Vol. 64, No. 9, pp. 533-538, 1981

[Alpass 2009] *Nitrogen diffusion and interaction with dislocations in single-crystal silicon*, C.R. Alpass, J.D. Murphy, R.J. Falster, P.R. Wilshaw, Journal of Applied Physics, Vol. 105, No. 1, pp. 013519/1-6, 2009

[Argon 2001] *Mechanics and physics of brittle to ductile transitions in fracture*, A.S. Argon, Journal of Engineering Materials and Technology, Vol. 123, pp. 1-11, 2001

[Behrensmeier 1987] *The influence of precipitated oxygen on the brittle-ductile transition of silicon*, R. Behrensmeier, M. Brede, P. Haasen, Scripta Metallurgica, Vol. 21, pp. 1581-1585, 1987

[Berner 1967] *Dislocation density and local slip in germanium single crystals*, K. Berner, H. Alexander, Acta Metallurgica, Vol. 15, iss. 5, pp. 933-941, 1967

[Bolotov 1993] *Raman study of mechanical stresses in processes of oxygen precipitation in silicon*, V.V. Bolotov, M.D. Efremov, I. Babanskaya, K. Schmalz, Materials Science and Engineering B, Vol. 21, pp. 49-54, 1993

[Borchet 2006] *Influence of the thermal treatment during the saw damage etching process on the mechanical stability of multicrystalline silicon wafers*, D. Borchet, S. Riepe, R. Kübler, J. Beinert, T. Kraft, G. Kleer, S. Petri, Conference Record of the 2006 IEEE 4^{th} World Conference on Photovoltaic Energy Conversion, WCPEC-4, Vol. 1, p 1085-1087, 2007

[Bothe 2005] *Fundamental Boron-Oxygen related carrier lifetime limit in mono- and multicrystalline silicon*, K. Bothe, R. Sinton, J. Schmidt, Progress in Photovoltaics: Research and Applications, Vol. 13, No. 4, pp. 287-296, 2005

[Brion 1981] *New stages in stress-strain curves of germanium at high temperatures*, H.G. Brion, H. Siethoff, W. Schröter, Philosophical Magazine A, Vol. 43, No. 6, pp. 1505-1513, 1981

[Brede 1988] *The brittle-to-ductile transition in doped silicon as a model substance*, M. Brede, P. Haasen, Acta Metallurgica, Vol. 36, iss. 8, pp. 2003-2018, 1988

[Brede 1993] *The brittle-to-ductile transition in silicon*, M. Brede, Acta Metallurgica, Vol. 41, No. 1, pp. 211-228, 1993

[Brion 1971] *The yield point of highly-doped germanium*, H.G. Brion, P. Haasen, H. Siethoff, Acta Metallurgica, Vol. 19, No. 4, pp. 283-290, 1971

[Bulatov 1995] *Atomic modes of dislocation mobility in silicon*, V.V. Bulatov, S. Yip, A.S. Argon, Philosophical Magazine A, Vol. 72, No. 2, pp. 453-496, 1995

[Bulatov 2001a] *Bottomless complexity of core structure and kink mechanisms of dislocation motion in silicon*, V.V. Bulatov, Scripta Materialia, Vol. 45, No. 11, pp. 1247-1252, 2001

[Bulatov 2001b] *Parameter-free modeling of dislocation motion: the case of silicon*, V.V. Bulatov, J.F. Justo, W. Cai, S. Yip, A.S. Argon, T. Lenosky, M. De Koning, T. Diaz de la Rubia, Philosophical Magazine A, Vol. 81, No. 5, pp. 1257-1281, 2001

[Buonassisi 2006] *Metal precipitation at grain boundaries in silicon: Dependence on grain boundary character and dislocation decoration*, T. Buonassisi, M.D. Pickett, A.A. Istratov, M.A. Marcus, T.F. Ciszek, E.R. Weber, Applied Physics Letters, Vol. 89, 2006

[Burenkov 1974] *Temperature dependence of the elastic constants of silicon*, Y.A. Burenkov, S.P. Nikaronov, Soviet Physics - Solid State, Vol. 16, No. 5, pp. 963-964, 1974

[Cai 2000] *Intrinsic mobility of a dissociated dislocation in silicon*, W. Cai, V.V. Bulatov, J.F. Justo, A.S. Argon, S. Yip, Physical Review Letters, Vol. 84, No. 15, pp. 3346-3349, 2000

[Caillard 2003] *Thermally activated mechanisms in crystal plasticity*, D. Caillard, J.-L. Martin (ed. R.W. Cahn), 2003, Pergamon Materials Series, Pergamon

[Castaing 1981] *The plastic deformation of silicon between 300°C and 600°C*, J. Castaing, P. Veyssière, L.P. Kubin, J. Rabier, Philosophical Magazine A, Vol. 44, No. 6, pp. 1407-1413, 1981

[Celli 1963] *Theory of dislocation mobility in semiconductors*, V. Celli, M. Kabler, T. Ninomiya, R. Thomson, Physical Review, Vol. 131, No. 1, pp. 58-72, 1963

[Chantikul 1981] *A critical evaluation of indentation techniques for measuring fracture toughness: II. Strength method*, P. Chantikul, G.R. Anstis, B.R. Lawn, D.B. Marshall, Journal of the American Ceramic Society, Vol. 64, No. 9, pp. 539-543, 1981

[Chaudhuri 1962] *Velocities and densities of dislocations in germanium and other semiconductor crystals*, A.R. Chaudhuri, J.R. Patel, L.G. Rubin, Journal of Applied Physics, Vol. 33, No. 9, pp. 2736-2746, 1962

[Chen 1980] *Fracture toughness of silicon*, C.P. Chen, M.H. Leipold, American Ceramic Society bulletin, Vol. 59, No. 4, pp. 469-472, 1980

[Chen 1982] *Fracture of directionally solidified mc-Si*, C.P. Chen, M.H. Leipold, Journal of the American Ceramic Society, Vol. 65, No. 4, pp. C49, 1982

[Choudhury 2010] *Molecular dynamics studies of the dissociated screw dislocation in silicon*, R. Choudhury, C. Gattinoni, G. Makov, A. De Vita, Journal of Physics: Condensed Matter, Vol. 22, pp. 074210-1/8, 2010

[Cockayne 1979] *Dislocations in semiconductors as studied by weak-beam electron microscopy*, D.J.H. Cockayne, A. Hons, Journal de Physique Colloque, Vol. 40, No. 6, pp. C6-11/18, 1979

[Dash 1956] *Copper precipitation on dislocations in silicon*, W.C. Dash, Journal of Applied Physics, Vol. 27, No. 10, pp. 1193-1195, 1956

[de Araújo 2004] *Electronic charge effects on dislocation cores in silicon*, M.M. de Araújo, J.F. Justo, R.W. Nunes, Applied Physics Letters, Vol. 85, No. 23, pp. 5610-5612, 2004

[Demenet 1984] *On the plasticity of silicon below 650°C*, J.L. Demenet, J.C. Desoyer, J. Rabier, P. Veyssière, Scripta Metallurgica, Vol. 18, pp. 41-45, 1984

[Demenet 1987] *TEM observations of silicon deformed under an hydrostatic pressure*, J.L. Demenet, J. Rabier, H. Garem, Proceedings of the Institute of Physics Conference on Microscopy of Semiconducting Materials, pp. 355-360, 1987

[Dillon 1986] *Dislocation dynamics during the growth of silicon ribbon*, O.W. Dillon, C.T. Tsai, R.J. De Angelis, Journal of Applied Physics, Vol. 60, No. 5, pp. 1784-1792, 1986

[Doerschel 1981] *Differences in plastic deformation behaviour of CZ- and FZ-grown silicon crystals*, J. Doerschel, F.G. Kirscht, Physica Status Solidi (a), Vol. 64, pp. K85-88, 1981

[Dolling 1966] *The thermodynamic and optical properties of germanium, silicon, diamond and gallium arsenide*, G. Dolling, R.A. Cowley, Proceedings of the Physical Society, Vol. 88, pp. 463-494, 1966

[Dour 2002] *Dislocation motion in crystals with a high Peierls relief: a unified model incorporating the lattice friction and localized obstacles*, G. Dour, Y. Estrin, Journal of Engineering Materials and Technology, Vol. 124, pp. 7-12, 2002

[Du 2007] *Hard inclusions and their detrimental effects on the wire sawing process of multicrystalline silicon*, G. Du, L. Zhou, P. Rossetto, Y. Wan, Solar Energy Materials & Solar Cells, Vol. 91, No. 18, pp. 1743-1748, 2007

[Duesbery 1996] *Dislocation motion in silicon: the shuffle-glide controversy*, M.S. Duesbery, B. Joos, Philosophical Magazine Letters, Vol. 74, No. 4, pp. 253-258, 1996

[Eremenko 2007] *Structure and recombination properties of extended defects in the dislocation slip plane in silicon*, V. Eremenko, E. Yakimov, N. Abrosimov, Physica Status Solidi (c), Vol. 4, No. 8, pp. 3100-3104, 2007

[Eremenko 2009] *Extended defects generated in the slip plane by moving dislocation in diamond lattice crystals: morphology and properties*, V. Eremenko, J.L. Demenet, J. Rabier, Physica Status Solidi (c), Vol. 6, No. 8, pp. 1801-1806, 2009

[Erofeev 1969] *Effect of impurities on the individual dislocation mobility in silicon*, V.N. Erofeev, V.I. Nikitenko, V.B. Osvenskii, Physica Status Solidi, Vol. 35, pp. 79-88, 1969

[Estrin 1986] *Local strain hardening and nonuniformity of plastic deformation*, Y. ESTRIN, L.P. KUBIN, Acta Metallurgica, Vol. 34, No. 12, pp. 2455-2464, 1986

[Farber 1982] *Change of dislocation mobility characteristics in Si single crystals at elevated temperatures*, B.YA FARBER, V.I. NIKITENKO, Physica Status Solidi (a), Vol. 73, pp. K141-143, 1982

[Farber 1986] *Experimental study of the double kink formation kinetics and kink mobility on the dislocation line in Si single crystals*, B.YA. FARBER, YU.L. IUNIN, V.I. NIKITENKO, Physica Status Solidi (a), Vol. 97, pp. 469-478, 1986

[Farber 1989] *On the nature of the asymmetry effect in dislocation mobility in Si single crystals*, B.YA. FARBER, YU.L. IUNIN, Proceedings of the 6th International Symposium on Structure and Properties of Dislocations in Semiconductors, pp. 297-302, 1989

[Farber 1993] *Barriers for the kink motion on dislocations in Si*, B. YA. FARBER, Y.L. IUNIN, V.I. NIKITENKO, V.I. ORLOV, H. ALEXANDER, H. GOTTSCHALK, P. SPECHT, Physica Status Solidi (a), Vol. 138, pp. 557-571, 1993

[Ferney 1999] *The influence of multiple slip systems on the brittle-ductile transition in silicon*, B.D. FERNEY, K.J. HSIA, Materials Science and Engineering A, Vol. 272, pp. 422-430, 1999

[Fikar 2002] *Searching for the proper law of dislocation multiplication law in covalent crystals*, J. FIKAR, B. VIGUIER, T. KRUML, C. DUPAS, Journal of Physics: Condensed Matter, Vol. 14, pp. 12887-12895, 2002

[Fikar 2005] *Dislocation multiplication rate in the early stage of germanium plasticity*, J. FIKAR, C. DUPAS, T. KRUML, A. JACQUES, J.-L. MARTIN, Materials Science and Engineering A, Vol. 400-401, pp. 431-434, 2005

[Fikar 2006] *A critical assessment of dislocation multiplication laws in germanium*, T. KRUML, C. DUPAS, J.-L. MARTIN, Acta Materialia, Vol. 54, pp. 4721-4729, 2006

[Franke 2000] *Change of dislocation density in silicon wafers during thermal processing*, D. FRANKE, M. APEL, Conference Record of the 28th IEEE Photovoltaic Specialists Conference - 2000, pp. 237-40, 2000

[Franke 2002] *Silicon ingot casting: process development by numerical simulations*, D. FRANKE, T. RETTELBACH, C. HÄSSLER, W. KOCH, A. MÖLLER, Solar Energy Materials & Solar Cells, Vol. 72, pp. 83-92, 2002

[Freeland 1977] *Precipitation of oxygen in silicon*, P.E. FREELAND, K.A. JACKSON, C.W. LOWE, J.R. PATEL, Applied Physics Letters, Vol. 30, No. 1, p. 31-33, 1977

[Fujita 2005] *Diffusion of nitrogen in silicon*, N. Fujita, R. Jones, J.P. Goss, P.R. Briddon, T. Frauenheim, S. Öberg, Applied Physics Letters, Vol. 87, No. 2, pp. 021902-1/3, 2005

[Föll 1979] *Direct TEM determination of intrinsic and extrinsic stacking fault energies of silicon*, H. Föll, C.B. Carter, Philosophical Magazine A, Vol. 40, No. 4, pp. 497-510, 1979

[Gannepalli 2001] *Molecular dynamics studies of plastic deformation during silicon nanoindentation*, A. Gannepalli, S.K. Mallapragada, Nanotechnology, Vol. 12, pp. 250-257, 2001

[Garcia-Manyes 2005] *Nanomechanics of silicon surfaces with atomic force microscopy: an insight to the first stages of plastic deformation*, S. Garcia-Manyes, A.G. Güell, P. Gorostiza, F. Sanz, Journal of Chemical Physics, Vol. 123, pp. 692-697, 2005

[George 1972] *Velocities of screw and 60°dislocations in silicon*, A. George, C. Escaravage, G. Champier, W. Schröter, Physica Status Solidi (b), Vol. 53, pp. 483-496, 1972

[George 1973] *X-ray topographic observation of single dislocation mobility in silicon*, A. George, C. Escaravage, W. Schröter, G. Champier, Crystal Lattice Defects, Vol. 4, pp. 29-36, 1973

[George 1975] *Double cross-slip in silicon*, A. George, G. Champier, Philosophical Magazine, Vol. 31, No. 4, pp. 961-967, 1975

[George 1979a] *Measurements of the dislocation velocities in silicon*, A. George, Journal de Physique Colloque, Vol. 40, No. 6, pp. C6/133-137, 1979

[George 1979b] *Velocities of screw and 60°dislocations in n- and p-type silicon*, A. George, G. Champier, Physica Status Solidi (a), Vol. 53, pp. 529-540, 1979

[George 1987a] *Dislocations and plasticity in semiconductors. I. Dislocation structures and dynamics*, A. George, J. Rabier, Revue de physique appliquée: supplément au Journal de Physique, Vol. 22, No. 9, pp. 941-966, 1987

[George 1987b] *Dislocations and plasticity in semiconductors. II. Relation between dislocation dynamics and plastic deformation*, A. George, Revue de physique appliquée: supplément au Journal de Physique, Vol. 22, No. 11, pp. 1327-1351, 1987

[George 1993] *Dislocation loops at crack tips: nucleation and growth-an experimental study in silicon*, A. George, G. Michot, Materials Science and Engineering A, Vol. 164, pp. 118-134, 1993

[Giannattasio 2003] *Dislocation locking by nitrogen impurities in FZ-silicon*, A. Giannattasio, S. Senkader, R.J. Falster, P.R. Wilshaw, Physica B, Vols. 340-342, pp. 996-1000, 2003

[Gomez 1975] *Dissociation of near-screw dislocations in germanium and silicon*, A. Gomez, D.J.H. Cockayne, P.B. Hirsch, V. Vitek, Philosophical Magazine, Vol. 31, No. 1, pp. 105-113, 1975

[Gomez 1977] *On the mobility of dislocations in germanium and silicon*, A.M. Gomez, P.B. Hirsch, Philosophical Magazine, Vol. 36, No. 1, pp. 169-179, 1977

[Gottschalk 1979] *Motion of partial dislocations*, H. Gottschalk, Journal de Physique Colloque, Vol. 40, No. 6, pp. C6/127-131, 1979

[Gottschalk 1983a] *Dislocation bends in high stress deformed silicon crystals*, H. Gottschalk, Journal de Physique Colloque, Vol. 44, No. 9, pp. C4/69-74, 1983

[Gottschalk 1983b] *On the motion of dislocation bends in terms of the kink model*, H. Gottschalk, Journal de Physique Colloque, Vol. 44, No. 9, pp. C4/475-477, 1983

[Gottschalk 1987] *The fine structure of dislocations in silicon*, H. Gottschalk, H. Alexander, V. Dietz, Proceedings of the 5^{th} Oxford Conference on Microscopy of Semiconducting Materials, pp. 339-347, 1987

[Gottschalk 1993] *Constricted dislocations and their use for TEM measurements of the velocities of edge and 60°dislocations in silicon*, H. Gottschalk, N. Hiller, S. Sauerland, P. Specht, H. Alexander, Physica Status Solidi (a), Vol. 138, pp. 547-555, 1993

[Gusakov 2005] *Unified model of diffusion of interstitial oxygen in silicon and germanium crystals*, V. Gusakov, Journal of Physics: Condensed Matter, Vol. 17, pp. S2285-S2291, 2005

[Haasen 1991] *Brittle-to-ductile transition in silicon as a model for intermetallics*, P. Haasen, Materials Science and Engineering, A137, pp. 105-110, 1991

[Heggie 1983] *Solitons and the electrical and mobility properties of dislocations in silicon*, M. Heggie, R. Jones, Philosophical Magazine B, Vol. 48, No. 4, pp. 365-377, 1983

[Heggie 1991] *Interaction of impurities with dislocation cores in silicon*, M. Heggie, R. Jones, A. Umerski, Philosophical Magazine A, Vol. 63, No. 3, pp. 571-584, 1991

[Hielsmair 1998] *Gettering of iron by oxygen precipitates*, H. Hielsmair, A.A. Istratov, S.A. McHugo, C. Flink, T. Heiser, E.R. Weber, Applied Physics Letters, Vol. 72, No. 12, pp. 1460-1462, 1998

[Hill 1974] *Deformation of silicon at low temperatures*, M.J. Hill, D.J. Rowcliffe, Journal of Materials Science, Vol. 9, pp. 1569-1576, 1974

[Hirsch 1980] *The structure and electrical properties of dislocations in semiconductors*, P.B. Hirsch, Journal of Microscopy, Vol. 118, No. 1, pp. 3-12, 1980

[Hirsch 1981a] *Relaxation of dislocations in deformed silicon*, P.B. Hirsch, A. Ourmazd, P. Pirouz, Proceedings of the 2nd Oxford Conference on Microscopy of Semiconducting Materials, pp. 29-34, 1981

[Hirsch 1981b] *Electronic and mechanical properties of dislocations in semiconductors*, P.B. Hirsch, in Defects in Semiconductors. Proceedings of the Materials Research Society Annual Meeting, pp. 257-71, 1981

[Hirsch 1987] *The dynamics of dislocation generation at crack tips and the ductile-brittle transition*, P.B. Hirsch, S.G. Roberts, J. Samuels, Scripta Metallurgica, Vol. 21, No. 11, pp. 1523-1528, 1987

[Hirsch 1989a] *The brittle-ductile transition in silicon. I. Experiments*, J. Samuels, S.G. Roberts, Proceedings of the Royal Society of London, Series A, Vol. 421, pp. 1-23, 1989

[Hirsch 1989b] *The brittle-ductile transition in silicon. II. Interpretation*, P.B. Hirsch, S.G. Roberts, J. Samuels, Proceedings of the Royal Society of London, Series A, Vol. 421, pp. 25-53, 1989

[Hirsch 1991] *The brittle-ductile transition in silicon*, P.B. Hirsch, S.G. Roberts, Philosophical Magazine A, Vol. 64, No. 1, pp. 55-80, 1991

[Hirsch 1996] *Comment on the brittle-to-ductile transition: a cooperative dislocation generation instability; dislocation dynamics and the strain-rate dependence of the transition temperature*, P.B. Hirsch, S.G. Roberts, Acta Materialia, Vol. 44, No. 6, pp. 2361-2371, 1996

[Hirsch 1997] *Modeling plastic zones and the brittle-ductile transition*, P.B. Hirsch, S.G. Roberts, Philosophical Transactions of the Royal Society of London A, Vol. 355, pp. 1991-2002, 1997

[Hirth 1992] *Theory of dislocations (second edition)*, J.P. Hirth, J. Lothe, Wiley, New York, 1992

[Hornstra 1958] *Dislocations in the diamond lattice*, J. Hornstra, Journal of the Physics and Chemistry of Solids, Vol. 5, Nos.1-2, pp. 129-141, 1958

[Hull 1999] in *Properties of Crystalline Silicon*, R. Hull (ed), pp. 89-148, 1999

[Hässler 1999] *Low dislocation density multicrystalline silicon for photovoltaic applications*, C. Hässler, E.-U. Reisner, W. Koch, A. Möller, D. Franke, T. Rettelbach, Solid State Phenomena, Vol. 67-68, pp. 447-452, 1999

[Hässler 2000] *Formation and annihilation of oxygen donors in multicrystalline silicon for solar cells*, C. Hässler, H.-U. Höfs, W. Koch, G. Stollwerck, A. Möller, D. Karg, G. Pensi, Materials Science and Engineering B71, pp. 39-46, 2000

[Imai 1983] *In situ X-ray topographic study of the dislocation mobility in high-purity and impurity-doped silicon crystals*, M. Imai, K. Sumino, Philosophical Magazine A, Vol. 47; No. 4, pp. 599-621, 1983

[Itoh 1988] *Diffusion coefficient of a pair of nitrogen atoms in float-zone silicon*, T. Itoh, T. Abe, Applied Physics Letters, Vol. 53, No. 1, pp. 39-41, 1988

[Iunin 2001] *Modes of kink motion on dislocations in semiconductors*, Yu.L. Iunin, V.I. Nikitenko, Scripta Materialia, Vol. 45, pp. 1239-1246, 2001

[Jacques 2001] *Ideal and possible experiments for further progress on dislocation mobility in silicon*, A. Jacques, A. George, Scripta Materialia, Vol. 45, pp. 1279-1285, 2001

[Jin 2010] *Computing transition rates of thermally activated events in dislocation dynamics*, C. Jin, W. Ren, Y. Xiang, Scripta Materialia, Vol. 62, pp. 206-209, 2010

[Jones 2000] *Do we really understand dislocations in semiconductors?*, R. Jones, Materials Science and Engineering B, Vol. 71, pp. 24-29, 2000

[Justo 1999] *Dislocation core reconstruction and its effect on dislocation mobility in silicon*, J.F. Justo, V.V. Bulatov, S. Yip, Journal of Applied Physics, Vol. 86, No. 8, pp. 4249-4257, 1999

[Kailer 1997] *Phase transformations of silicon caused by contact loading*, A. Kailer, Y.G. Gogotsi, K.G. Nickel, Journal of Applied Physics, Vol. 81, No. 7, pp. 3057-3063, 1997

[Kannan 1970] *Direct dislocation velocity measurement in silicon by X-ray topography*, V.C. Kannan, J. Washburn, Journal of Applied Physics, Vol. 41, No. 9, pp. 3589-3597, 1970

[Kim 1987] *Dislocation motion and multiplication during the growth of silicon ribbon*, Y.K. Kim, R.J. De Angelis, C.T. Tsai, O.W. Dillon, Acta Metallurgica, Vol. 35, No. 8, pp. 2091-2099, 1987

[Kirscht 1978] *Some observations concerning the initial stage of plastic flow in silicon*, F.G. Kirscht, J. Doerschel, C. Hansch, Physica Status Solidi (a), Vol. 47, No. 1, pp. K17-20, 1978

[Kocks 1975] *Thermodynamics and kinetics of slip*, U.F. Kocks, A.S. Argon, M.F. Ashby, Progress in Materials Science, Vol. 19, 1975, Pergamon Press, Oxford

[Kojima 1971] *Strain rate and temperature dependence of mechanical behaviour in germanium crystals*, K.I. Kojima, K. Sumino, Crystal Lattice Defects, Vol. 2, pp. 147-158, 1971

[Kolar 1996] *Observation of moving dislocation kinks and unpinning*, H.R. Kolar, J.C.H. Spence, H. Alexander, Physical Review Letters, Vol. 77, No. 19, pp. 4031-4034, 1996

[Kulkarni 1976] *Dislocation velocities and electronic doping in silicon*, S.B. Kulkarni, W.S. Williams, Journal of Applied Physics, Vol. 47, No. 10, pp. 4318-4324, 1976

[Kulkarni 1980] *The deformation of silicon at high temperatures and strain rates*, S.B. Kulkarni, C. Lall, D.P. Pope, C.D. Graham Jr., Metallurgical Transactions A, Vol. 11A, No. 11, pp. 1869-1876, 1980

[Kvande 2005] *Growth rate and impurity distribution in multicrystalline silicon for solar cells*, R. Kvande, Ø. Mjøs, B. Ryningen, Materials Science and Engineering A, Vol. 413-414, pp. 545-549, 2005

[Labusch 1965] *Calculation of Peierls potentials in diamond lattice*, R. Labusch, Physica Status Solidi, Vol. 10, No. 2, pp. 645-658, 1965

[Lawn 1980] *Elastic/plastic indentation damage in ceramics: the median/radial crack system*, B.R. Lawn, A.G. Evans, D.B. Marshall, Journal of the American Ceramic Society, Vol. 63, No. 9-10, pp. 574-581, 1980

[Liu 2008] *Carbon concentration and particle precipitation during directional solidification of multicrystalline silicon for solar cells*, L. Liu, S. Nakano, K. Kakimoto, Journal of Crystal Growth, Vol. 310, No. 7-9, pp. 2192-2197, 2008

[Louchet 1981a] *On the mobility of dislocations in silicon by in situ straining in a high-voltage electron microscope*, F. Louchet, Philosophical Magazine A, Vol. 43, No. 5, pp. 1289-1297, 1981

[Louchet 1981b] *Evidence of a transition in glide mechanisms of dislocations in silicon by weak-beam in situ straining experiments*, F. Louchet, Proceedings of the 2nd Oxford Conference on Microscopy of Semiconducting Materials, pp. 35-38, 1981

[Macdonald 2007] *Impurities in solar-grade silicon*, D. Macdonald, J. Tan, Proceedings of the SPIE - The International Society for Optical Engineering, Vol. 6800, pp. 68000X-1/7, 2007

[Maeda 1989] *Kink formation and migration in covalent crystals*, K. Maeda, Y. Yamashita, Proceedings of the 6th International Symposium on Structure and Properties of Dislocations in Semiconductors, pp. 269-280, 1989

[Maeda 1994] *The fundamental process of dislocation motion and non-metallurgical effects in covalent crystals*, K. MAEDA, Fundamental Physical Aspects of the Strength of Crystalline Materials. Proceedings of the 10th International Conference on the Strength of Materials, pp. 79-86, 1994

[Maeda 1996] *Enhancement of dislocation mobility in semiconducting crystals by electronic excitation*, K. MAEDA, S. TAKEUCHI, in Dislocations in Solids Vol. 10 (Eds.: F.R.N. NABARRO & M.S. DUEBERRY), Elsevier Science, Amsterdam, 1996

[Mahajan 1979] *Lüders bands in deformed silicon crystals*, S. MAHAJAN, D. BRASEN, P. HAASEN, Acta Metallurgica, Vol. 27, No. 7, pp. 1165-1173, 1979

[Makris 1973] *Phosphorus isoconcentration diffusion studies in silicon*, J.S. MAKRIS, B.J. MASTERS, Journal of the Electrochemical Society, Vol. 120, No. 9, pp. 1252-1255, 1973

[Marklund 1980] *On the core structure of the glide-set 90°and 30°partial dislocations in silicon*, S. MARKLUND, Physica Status Solidi (b), Vol. 100, pp. 77-85, 1980

[Marklund 1984] *A note on double kink interaction and formation energies in silicon*, S. MARKLUND, Solid State Communications, Vol. 50, No. 2, pp. 185-187, 1984

[Marklund 1985] *The entropy factor involved in the Hirth and Lothe theory of dislocation velocity in silicon*, S. MARKLUND, Solid State Communications, Vol. 54, No. 6, pp. 555-558, 1985

[Maroudas 1991a] *Analysis of the effects of oxygen migration on dislocation motion in silicon*, D. MAROUDAS, R.A. BROWN, Journal of Applied Physics, Vol. 69, No. 7, pp. 3865-3877, 1991

[Maroudas 1991b] *Analysis of point-defect diffusion and drift in cubic-type lattices: Constitutive modeling*, D. MAROUDAS, R.A. BROWN, Physical Review B, Vol. 44, No. 6, pp. 2567-2581, 1991

[Maroudas 1991c] *Model for dislocation locking by oxygen gettering in silicon crystals*, D. MAROUDAS, R.A. BROWN, Applied Physics Letters, Vol. 58, No. 17, pp. 1842-1844, 1991

[Maroudas 1999] *On the prediction of dislocation formation in semiconductors grown from the melt: analysis of the Haasen model for plastic deformation dynamics*, D. MAROUDAS, R.A. BROWN, Journal of Crystal Growth, Vol. 108, pp. 399-415, 1999

[Marshall 1982] *Elastic/plastic indentation damage in ceramics: the lateral crack system*, D.B. MARSHALL, B.R. LAWN, A.G. EVANS, Journal of the American Ceramic Society, Vol. 65, No. 11, pp. 561-566, 1982

[Matinuzzi 2007] *Segregation phenomena in large-size cast multicrystalline Si ingots*, S. Martinuzzi, I. Périchaud, O. Palais, Solar Energy Materials & Solar Cells, Vol. 91, 2007

[Meese 2006] *Modeling of directional crystallization of silicon ingots-heat transfer and experimental validation*, E.A. Meese, E.J. Øvrelid, H. Laux, M. M'Hamdi

[M'Hamdi 2005] *Analysis of dislocation multiplication during multicrystalline silicon ingot casting*, M. M'Hamdi, E. Olsen, Proceedings of the 21st European Photovoltaic Solar Energy Conference, Dresden, 2005

[M'Hamdi 2006] *Thermo-mechanical analysis of directional crystallisation of multi-crystalline silicon ingots*, M. M'Hamdi, E.A. Meese, H. Laux, E.J. Øvrelid, Materials Science Forum, Vol. 508, pp. 597-602, 2006

[Michel 1982] *Plastic deformation and surface investigations of <100> oriented silicon single crystals*, J.P. Michel, M. Omri, A. Oueldennaoua, A. George, Scripta Metallurgica, Vol. 16, pp. 677-682, 1982

[Michot 1982] *In situ observation by X-ray synchrotron topography of the growth of plastically deformed regions around crack tips in silicon under creep conditions*, G. Michot, A. George, Scripta Metallurgica, Vol. 16, No. 5, pp. 519-524, 1982

[Michot 1986] *Dislocation emission from cracks-Observations by X-ray topography in silicon*, G. Michot, A. George, Scripta Metallurgica, Vol. 20, No. 11, pp. 1495-1500, 1986

[Michot 1988] *Fundamentals of silicon fracture*, G. Michot, Crystal Properties & Preparation, Vols. 17 & 18, pp. 55-98, 1988

[Michot 1994] *Dislocation loops at crack tips: control and analysis of sources in silicon*, G. Michot, M. Angela Loyola de Oliveira, A. George, Materials Science and Engineering A, Vol. 176, pp. 99-109, 1994

[Mikkelsen 1986] *The diffusivity and solubility of oxygen in silicon*, J.C. Mikkelsen Jr., in *Oxygen, Carbon, Hydrogen and Nitrogen in Crystalline Silicon*, Materials Research Society Symposia Proceedings, Vol. 59, pp. 19-30, 1986

[Miranda 2003] *Temperature effects on dislocation core energies in silicon and germanium*, C.R. Miranda, R.W. Nunes, A. Antonelli, Physical Review B, Vol. 67, No. 23, pp. 235201-1/8, 2003

[Mitchell 2003] *Nucleation of kink pairs on partial dislocations: a new model for solution hardening and softening*, T.E. Mitchell, P.M. Anderson, M.I. Baskes, S.P. Chen, R.G. Hoagland, A. Misra, Philosophical Magazine, Vol. 83, No. 11, pp. 1329-1346, 2003

[Moon 2002] *A constitutive model for the mechanical behavior of single crystal silicon at elevated temperature*, H.-S. MOON, L. ANAND, S.M. SPEARING, Proceedings of the 4th Symposium on Materials Science of MEMS Devices, Vol. 687, pp. 279-284, 2002

[Moulin 1997] *Simulation of Frank-Read sources in silicon*, A. MOULIN, M. CONDAT, Materials Science and Engineering A234-236, pp. 406-409, 1997

[Moulin 1999a] *Perfect and partial Frank-Read sources in silicon: a simulation*, A. MOULIN, M. CONDAT, Philosophical Magazine A, Vol. 79, No. 8, pp. 1995-2011, 1999

[Moulin 1999b] *Mesoscale modeling of the yield point properties of silicon crystals*, A. MOULIN, M. CONDAT, L.P. KUBIN, Acta Materialia, Vol. 47, iss. 10, pp. 2879-2888, 1999

[Morinetti 1984] *Low temperature diffusivity and precipitation of phosphorus in silicon*, L. MORINETTI, D. NOBILI, Materials Chemistry and Physics, Vol. 10, pp. 21-30, 1984

[Murphy 2006a] *Oxygen transportation in Czochralski silicon investigated by dislocation locking experiments*, J.D. MURPHY, S. SENDAKER, R.J. FALSTER, P.R. WILSHAW, Materials Science and Engineering B, Vol. 134, pp. 176-184, 2006

[Murphy 2006b] *Enhanced oxygen diffusion in highly doped p-type Czochralski silicon*, J.D. MURPHY, P.R. WILSHAW, B.C. PYGALL, S. SENKADER, Journal of Applied Physics, Vol. 100, No. 10, pp. 103531-6, 2006

[Murphy 2006c] *Nitrogen in silicon: transport and mechanical properties*, J.D. MURPHY, C.R. ALPASS, A. GIANNATTASIO, S. SENKADER, R.J. FALSTER, P.R. WILSHAW, Nuclear instruments and Methods in Physics Research B, Vol. 253, pp. 113-117, 2006

[Myshlyaev 1969] *Dislocation structure and macroscopic characteristics of plastic deformation at creep of silicon crystals*, M.M. MYSHLYAEV, V.I. NIKITENKO, V.I. NESTERENKO, Physica Status Solidi (a), Vol. 36, pp. 89-96, 1969

[Möller 1978] *The movement of dissociated dislocations in the diamond-cubic structure*, H.J. MÖLLER, Acta Metallurgica, Vol. 26, No. 6, pp. 963-973, 1978

[Möller 1999] *Oxygen and carbon precipitation in Multicrystalline Solar Silicon*, H.J. MÖLLER, L. LONG, M. WERNER, D. YANG, Physica Status Solidi (a), Vol. 171, No. 1, pp. 175-189, 1999

[Möller 2002] *Oxygen and lattice distortions in multicrystalline silicon*, H.J. MÖLLER, C. FUNKE, A. LAWERENZ, S. RIEDEL, M. WERNER, Solar Energy Materials & Science, Vol. 72, pp. 403-416, 2002

[Möller 2004] *Basic mechanisms and models of multi-wire sawing*, H.J. Möller, Advanced Engineering Materials, Vol. 6, no. 7, 2004

[Möller 2005] *Multicrystalline silicon for solar cells*, H.J. Möller, C. Funke, M. Rinio, S. Scholz, Thin Solid Films, Vol. 487, pp. 179-187, 2005

[Möller 2006] *Wafering of silicon crystals*, H.J. Möller, Physica Status Solidi (a), Vol. 203, no. 4, pp. 659-669, 2006

[Nagdornyi 1988] *Dislocation dynamics and mechanical properties of crystals*, E. Nagdornyi, Progress in Materials Science, Vol. 31, pp. 1-530, 1988

[Nikitenko 1984] *Asymmetry of isolated dislocation mobility in silicon single crystals*, V.I. Nikitenko, B.Ya. Farber, E.B. Yakimov, Crystal Research and Technology, Vol. 19, No. 3, pp. 295-302, 1984

[Nikitenko 1987] *Experimental investigation of the dynamics of kinks of dislocation lines in semiconductor single crystals*, V.I. Nikitenko, B.Ya. Farber, Yu.L. Iunin, Soviet Physics - JETP, Vol. 66, No. 4, pp. 738-746, 1987

[Nikitenko 1989] *Experimental investigation of kink motion in a field of random forces*, V.I. Nikitenko, B.Ya. Farber, Proceedings of the 6th International Symposium on Structure and Properties of Dislocations in Semiconductors, pp. 257-268, 1989

[Nishino 1982] *Generation process of dislocations in precipitate-containing silicon crystals*, Y. Nishino, T. Imura, Physica Status Solidi (a), Vol. 73, pp. 173-182, 1982

[Nishino 1984] *Temperature dependence of friction force acting on dislocations in silicon crystals*, Y. Nishino, H. Saka, T. Imura, Journal of Materials Science, Vol. 19, pp. 245-253, 1984

[Nunes 1998a] *Atomic structure of dislocation kinks in silicon*, R.W. Nunes, J. Bennetto, D. Venderbilt, Physical Review B, Vol. 57, No. 17, pp. 10388-10397, 1998

[Nunes 1998b] *Core reconstruction of the 90°partial dislocation in nonpolar semiconductors*, R.W. Nunes, J. Bennetto, D. Venderbilt, Physical Review B, Vol. 58, No. 19, pp. 12563-12566, 1998

[Nyilas 2004] *Dislocation structures and mechanical behavior of Ge single crystals deformed by compression*, K. Nyilas, C. Dupas, T. Kruml, L. Zsoldos, T. Ungár, J.L. Martin, Materials Science and Engineering A, Vol. 387-389, pp. 25-28, 2004

[Ohno 2010] *Interaction of dopant atoms with stacking faults in silicon crystals*, Y. Ohno, T. Taishi, Y. Tokumoto, I. Yonenaga, Journal of Applied Physics, Vol. 108, pp. 073514-1/4, 2010

[Okada 1984] *Precise determination of the lattice parameter and thermal expansion coefficient of silicon between 300 and 1500 K*, Y. Okada, Y. Tokumaru, Journal of Applied Physics, Vol. 56, No. 2, pp. 314-320, 1984

[Omri 1987] *On the yield point of floating-zone silicon single crystals I. Yield stresses and activation parameters*, M. Omri, C. Tete, J.-P. Michel, A. George, Philosophical Magazine A, Vol. 55, No. 5, pp. 601-616, 1987

[Oueldennaoua 1988] *On the yield point of floating-zone silicon single crystals II. A quantitative analysis of the dislocation structure at the lower yield point*, A. Oueldennaoua, R. Allem, A. George, J.-P. Michel, Philosophical Magazine A, Vol. 57, No. 1, pp. 51-77, 1988

[Ourmazd 1981] *The climb of dissociated dislocations in semiconductors*, A. Ourmazd, D. Cherns, P.B. Hirsch, Proceedings of the 2nd Oxford Conference on Microscopy of Semiconducting Materials, pp. 39-44, 1981

[Oyama 2004] *Migration processes of the 30°partial dislocation in silicon*, N. Oyama, T. Ohno, Physical review Letters, Vol. 93, No. 19, pp. 195502-1/4, 2004

[Patel 1962] *Oxygen precipitation effects on the deformation of dislocation-free silicon*, J.R. Patel, A.R. Chaudhuri, Journal of Applied Physics, Vol. 33, No. 7, pp. 2223-2224, 1962

[Patel 1963] *Macroscopic plastic properties of dislocation-free germanium and other semiconductor crystals. I. Yield behavior*, J.R. Patel, A.R. Chaudhuri, Journal of Applied Physics, Vol. 34, No. 9, pp. 2788-2799, 1963

[Patel 1976] *Electronic effects on dislocation velocities in heavily doped silicon*, J.R. Patel, L.R. Testardi, P.E. Freeland, Physical Review B, Vol. 13, No. 8, 1976

[Peach and Koehler 1950] *The forces exerted on dislocations and the stress fields produced by them*, M. Peach, J.S. Koehler, Physical Review, Vol. 80, pp. 436-439, 1950

[Pérez 1995] *First principles simulations of silicon nanoindentation*, R. Pérez, M.C. Payne, Physical Review Letters, Vol. 75, iss. 26, pp. 4748-4751, 1995

[Petukhov 1990] *The threshold for dislocation motion in impure semiconductors*, B.V. Petukhov, Soviet Physics - Technical Physics, Vol. 35, No. 10, pp. 1150-1153, 1990

[Petukhov 2002] *Effect of dynamic aging of dislocations on the deformation behavior of extrinsic semiconductors*, B.V. Petukhov, Semiconductors, Vo. 36, No. 2, pp. 121-125, 2002

[Petukhov 2003] *Hardening of crystals caused by dynamic aging of dislocations*, B.V. Petukhov, Crystallography Reports, Vol. 48, No. 5, pp. 813-818, 2003

[Petukhov 2004a] *A theory of the effect of impurities on the yield stress of silicon crystals*, B.V. Petukhov, Semiconductors, Vol. 38, iss. 4, pp. 369-375, 2004

[Petukhov 2004b] *Effect of dynamic aging of dislocations on the deformation behavior of extrinsic semiconductors*, B.V. Petukhov, Solid State Phenomena, Vol. 95-96, pp. 459-464, 2004

[Petukhov 2005] *Hardening of semiconductor crystals caused by the dynamic aging of dislocations*, B.V. Petukhov, Physica Status Solidi (c), Vol. 2, No. 6, pp. 1864-1868, 2005

[Pinacho 2002] *Carbon in silicon: modeling of diffusion and clustering mechanisms*, R. Pinacho, P. Castrillo, M. Jaraiz, I. Martin-Bragado, J. Barbolla, H.-J. Gossmann, G.-H. Gilmer, J.-L. Benton, Journal of Applied Physics, Vol. 92, No. 3, pp. 1582-1587, 2002

[Pizzagalli 2008] *Dislocation motion in silicon: the shuffle-glide controversy revisited*, L. Pizzagalli, P. Beauchamp, Philosophical Magazine Letters, Vol. 88, No. 6, pp. 421-427, 2008

[Pirouz 1987] *Deformation mode in silicon, slip or twinning?*, P. Pirouz, Scripta Metallurgica, Vol. 21, No. 11, pp. 1463-1468, 1987

[Pizzini 1988] *Influence of extended defects and native impurities on the electrical properties of directionally solidified polycrystalline silicon*, S. Pizzini, A. Sandrinelli, M. Beghi, D. Narducci, F. Allegretti, S. Torchio, G. Fabbri, G.P. Ottaviani, F. Demartin, A. Fusi, Journal of the Electrochemical Society, Vol. 135, No. 1, pp. 155-165, 1988

[Rabier 2000] *Dislocation microstructures in Si plastically deformed at RT*, J. Rabier, P. Cordier, T. Tondellier, J.L. Demenet, H. Garem, Journal of Physics: Condensed Matter, Vol. 12, pp. 10059-10064, 2000

[Rabier 2001] *On a change in deformation mechanism in silicon at very high stress: new evidences*, J. Rabier, J.L. Demenet, Scripta Materialia, Vol. 45, No. 11, pp. 1259-1265, 2001

[Rabier 2005] *On the nucleation of shuffle dislocations in Si*, J. Rabier, J.L. Demenet, Physica Status Solidi (a), Vol. 202, No. 5, pp. 944-948, 2005

[Rabier 2007] *High-stress plasticity and the core structures of dislocations in silicon*, J. Rabier, Physica Status Solidi (a), Vol. 204, No. 7, pp. 2248-2255, 2007

[Rabier 2010] *Dislocations in silicon at high stresses*, J. RABIER, L. PIZZAGALLI, J.L. DEMENET, in Dislocations in Solids (Eds.: J.P. HIRTH, L.KUBIN), Vol. 16, Chp. 93, pp. 47-108, 2010

[Ray 1971] *The dissociation of dislocations in silicon*, I.L.F. RAY, D.J.H. COCKAYNE, Proceedings of the Royal Society of London A, Vol. 325, pp. 543-554, 1971

[Roberts 1993] *Dislocation dynamics and brittle-to-ductile transitions*, S.G. ROBERTS, M. ELLIS, P.B. HIRSCH, Materials Science and Engineering A, Vol. 164, pp. 135-140, 1993

[Roberts 1994] *Dislocation activity and brittle-ductile transitions in single crystals*, S.G. ROBERTS, A.S. BOOTH, P.B. HIRSCH, Materials Science and Engineering A, Vol. 176, pp. 91-98, 1994

[Roller 1989] *Diffusion of carbon-14 in silicon*, F. ROLLERT, N.A. STOLWIJK, H. MEHRER, Materials Science Forum, Vol. 38-41, pt. 2, pp. 753-758, 1989

[Rossberg 2005] *Investigation of defects in the edge region of multicrystalline solar silicon ingots*, M. ROSSBERG, M. NAUMANN, K. IRMSHER, U. JUDA, A. LÜDGE, M. GOSH, A. MÖLLER, Solid State Phenomena, Vol. 108-109, pp. 531-536, 2005

[Sanz-Navarro 2004] *Atomistic simulations of structural transformations of silicon surfaces under nanoindentation*, C.F. SANZ-NAVARRO, S.D. KENNY, R. SMITH, Nanotechnology, Vol. 15, pp. 692-697, 2004

[Sato 1981] *Impurity effect in stacking fault energy of silicon crystals studied by high resolution electron microscopy*, M. SATO, K. SUMINO, K. HIRAGA, Physica Status Solidi (a), Vol. 68, pp. 567-577, 1981

[Scandian 1999] *Dislocation nucleation and multiplication at crack tips in silicon*, C. SCANDIAN, H. AZZOUZI, N. MALOUFI, G. MICHOT, A. GEORGE, Physica Status Solidi (a), Vol. 171, pp. 67-82, 1999

[Schröter 1983] *Yield point and dislocation mobility in silicon and germanium*, W. SCHRÖTER, H.G. BRION, H. SIETHOFF, Journal of Applied Physics, Vol. 54, No. 4, pp. 1816-1820, 1983

[Seibt 2005] *Structural and electrical properties of metal impurities at dislocations in silicon*, M. SEIBT, V. KVEDER, W. SCHRÖTER, O. VOSS, Physica Status Solidi (a), Vol. 202, No. 5, pp. 911-920, 2005

[Senkader 2000] *A study of oxygen dislocation interactions in CZ-Si*, S. SENKADER, K. JURKSCHAT, P.R. WILSHAW, R.J. FALSTER, Materials Science and Engineering B, Vol. 73, pp. 111-115, 2000

[Senkader 2001a] *On the locking of dislocations by oxygen in silicon*, S. SENKADER, K. JURKSCHAT, D. GAMBARO, R.J. FALSTER, P.R. WILSHAW, Philosophical Magazine A, Vol. 81, No. 3, pp. 759-775, 2001

[Senkader 2001b] *Oxygen-dislocation interactions in silicon at temperatures below 700°C: dislocation locking and oxygen diffusion*, S. Senkader, P.R. Wilshaw, R.J. Falster, Journal of Applied Physics, Vol. 89, No. 9, 2001

[Senkader 2002] *On the dislocation-oxygen interactions in Czochralski-grown Si: oxygen diffusion and binding at low temperatures*, S. Senkader, A. Giannattasio, R.J. Falster, P.R. Wilshaw, Journal of Physics: Condensed Matter, Vol. 14, pp. 13141-13145, 2002

[Senkader 2004] *Dislocation locking in silicon by oxygen and oxygen transport at low temperatures*, S. Senkader, A. Giannattasio, R.J. Falster, P.R. Wilshaw, Solid State Phenomena, Vols. 95-96, pp. 43-52, 2004

[Shimizu 2007] *Experimental evidence of the vacancy-mediated silicon self-diffusion in single-crystalline silicon*, Y. Shimizu, M. Uematsu, K.M. Itoh, Physical Review Letters, Vol. 98, No. 9, pp. 095901-1/4, 2007

[Siethoff 1969] *Yield points of Si and Si-Ge solid solutions*, H. Siethoff, Material Science and Engineering, Vol. 4, No. 2-3, pp. 155-62, 1969

[Siethoff 1970] *The effect of charged impurities on the yied point of silicon*, H. Siethoff, Physica Status Solidi, Vol. 40, pp. 153-161, 1970

[Siethoff 1973] *Lüders bands in heavily doped silicon single crystals*, H. Siethoff, Acta Metallurgica, Vol. 21, pp. 1523-1531, 1973

[Siethoff 1978] *Dynamical recovery and self-diffusion in silicon*, H. Siethoff, W. Schröter, Philosophical Magazine A, Vol. 37, No. 6, pp. 711-718, 1978

[Siethoff 1983a] *Work hardening and dynamical recovery in silicon and germanium at high temperatures and comparison with fcc crystals*, H. Siethoff, W. Schröter, Scripta Metallurgica, Vol. 17, pp. 393-398, 1983

[Siethoff 1983b] *Cross-slip in the high-temperature deformation of germanium, silicon and indium antimonide*, H. Siethoff, Philosophical Magazine A, Vol. 47, No. 5, pp. 657-669, 1983

[Siethoff 1983c] *Recovery processes in the high-temperature deformation of germanium, silicon and indium antimonide*, H. Siethoff, Journal de Physique Colloque, Vol. 44, No. 6, pp. C4/217-225, 1983

[Siethoff 1984] *Two independent mechanisms of dynamical recovery in the high-temperature deformation of silicon and germanium*, H. Siethoff, K. Ahlborn, W. Schröter, Philosophical Magazine A, Vol. 50, No. 1, pp. L1-L6, 1984

[Siethoff 1986] *Dynamical recovery of <111> germanium*, H. Siethoff, H.G. Brion, K. Ahlborn, W. Schröter, Physica Status Solidi (a), Vol. 97, pp. 153-162, 1986

[Siethoff 1988] *The effect of a nitrogen atmosphere on the lower yield point of silicon*, H. SIETHOFF, Philosophical Magazine Letters, Vol. 58, No. 3, pp. 129-133, 1988

[Siethoff 1991] *The effect of solutes on the dynamical recovery of silicon and germanium*, H. SIETHOFF, K. AHLBORN, H.G. BRION, Acta Metallurgica, Vol. 39, No. 6, pp. 1133-1140, 1991

[Siethoff 1992] *The yield point of as-grown and pre-deformed semiconductors*, H. SIETHOFF, Philosophical Magazine Letters, Vol. 66, No. 1, pp. 1-7, 1992

[Siethoff 1999a] *A regime of the yield point of silicon at high temperatures*, H. SIETHOFF, H.G. BRION, W. SCHRÖTER, Applied Physics Letters, Vol. 75, iss. 9, 1999

[Siethoff 1999b] *New analysis of the yield point of germanium*, H. SIETHOFF, K. AHLBORN, W. SCHRÖTER, Physica Status Solidi (a), Vol. 175, pp. 205-212, 1999

[Siethoff 2001] *The deformation regimes of the yield point of silicon*, H. SIETHOFF, H.G. BRION, Philosophical Magazine A, Vol. 81, No. 1, pp. 145-152, 2001

[Siethoff 2002] *Yield point and dislocation velocity of diamond and zincblende semiconductors in different temperature regimes*, H. SIETHOFF, Philosophical Magazine A, Vol. 82, No. 7, pp. 1299-1316, 2002

[Siethoff 2003] *The interaction of boron and phosphorus with dislocations in silicon*, H. SIETHOFF, H.G. BRION, Materials Science and Engineering, Vol. A355, pp. 311-314, 2003

[Siethoff 2004] *The onset of secondary slip in the plastic deformation of tetrahedrally bound semiconductors*, H. SIETHOFF, Materials Science and Engineering A, Vol. 386, pp. 68-74, 2004

[Sopori 2005] *Efficiency limitations of multicrystalline silicon solar cells due to defect clusters*, B. SOPORI, C. LI, S. NARAYANAN, D. CARLSON, Materials Research Society Symposium Proceedings, Vol. 864, pp. 233-240, 2005

[Stefancich 2001] *Mechanical effects of chemical etchings on monocrystalline silicon for photovoltaic use*, M. STEFANCICH, M. BUTTURI, D. VINCENZI, G. MARTINELLI, Solar Energy Materials & Solar Cells, Vol. 69, pp. 371-377, 2001

[St John 1975] *Brittle-to-ductile transition in pre-cleaved silicon single crystals*, C. ST. JOHN, Philosophical Magazine, Vol. 32, No. 6, pp. 1193-1212, 1975

[Suezawa 1979] *Dislocation dynamics in the plastic deformation of silicon crystals. II. Theoretical analysis of experimental results*, M. SUEZAWA, K. SUMINO, I. YONENAGA, Physica Status Solidi (a), Vol. 51, pp. 217-226, 1979

[Stoddard 2005] *Ab Initio identification of the nitrogen diffusion mechanism in silicon*, N. Stoddard, P. Pichler, G. Duscher, W. Windl, Physical Review Letters, Vol. 95, iss. 2, pp. 025901/1-4, 2005

[Sumino 1971] *Microdynamics of dislocations in plastic deformation of germanium crystals*, K. Sumino, K.I. Kojima, Crystal Lattice Defects, Vol. 2, pp. 159-170, 1971

[Sumino 1974a] *Dynamical state of dislocations in germanium crystals during deformation*, K. Sumino, S. Kodaka, K.I. Kojima, Materials Science and Engineering, Vol. 13, pp. 263-268, 1974

[Sumino 1974b] *A model for the dynamical state of dislocations in crystals during deformation*, K. Sumino, Materials Science and Engineering, Vol. 13, pp. 269-275, 1974

[Sumino 1979] *Dislocation mobility and mechanical behaviour of Si crystals*, K. Sumino, Journal de Physique Colloque, Vol. 40, No. 6, pp. C6/147-150, 1979

[Sumino 1980] *The origin of the difference in the mechanical strengths of Czochralski-grown silicon and Float-zone-grown silicon*, K. Sumino, H. Harada and I. Yonenaga, Japanese Journal of Applied Physics, Vol. 19, No. 1, pp. L49-52, 1980

[Sumino 1981] *Difference in the mechanical strengths of dislocation-free crystals of Czochralski silicon and float-zone silicon*, K. Sumino, I. Yonenaga, Japanese Journal of Applied Physics, Vol. 20, No. 9, pp. L685-688, 1981

[Sumino 1983a] *Interactions of dislocations with impurities in silicon crystals studied by in situ X-ray topography*, K. Sumino, M. Imai, Philosophical Magazine A, Vol. 47, No. 5, pp. 753-766, 1983

[Sumino 1983b] *Interactions between dislocations and impurities in silicon*, K. Sumino, Journal de Physique Colloque, Vol. 44, No. 9, pp. C4/195-205, 1983

[Sumino 1983c] *Effects of nitrogen on dislocation behavior and mechanical strength in silicon crystals*, K. Sumino, I. Yonenaga, M. Imai, Journal of Applied Physics, Vol. 54, iss. 9, pp. 5016-5020, 1983

[Sumino 1992] *Current problems of defects in semiconductors - interaction of defects with impurities*, K. Sumino, Materials Science Forum, Vols. 105-110, pp. 139-160, 1992

[Sumino 1993] *Dislocation dynamics and mechanical behavior of elemental and compound semiconductors*, K. Sumino, I. Yonenaga, Physica Status Solidi (a), Vol. 138, pp. 573-581, 1993

[Sumino 1999a] *Deformation behavior of silicon*, K. SUMINO, Metallurgical and Materials Transactions A, Vol. 30A, pp. 1465-1479, 1999

[Sumino 1999b] *Impurity reaction with dislocations in semiconductors*, K. SUMINO, Physica Status Solidi (a), Vol. 171, pp. 111-122, 1999

[Sumino 2002] *Interactions of impurities with dislocations: mechanical effects*, K. SUMINO, I. YONENAGA, Solid State Phenomena, Vols. 85-86, pp. 145-176, 2002

[Søiland 2004] *SiC and Si_3N_4 inclusions in multicrystalline silicon ingots*, A.K. SØILAND, E.J. ØVRELID, T.A. ENGH, O. LOHNE, J.K. TUSET, Ø. GJERSTAD, Materials Science in Semiconductor processing, Vol. 7, pp. 39-43, 2004

[Tan 1976] *Oxygen precipitation and the generation of dislocations in silicon*, T.Y. TAN, W.K. TICE, Philosophical Magazine, Vol. 34, No. 4, pp. 615-631, 1976

[Tan 1977] *Intrinsic gettering by oxide precipitate induced dislocations in Czochralski Si*, T.Y. TAN, E.E. GARDNER, W.K. TICE, Applied Physics Letters, Vol. 30, No. 4, pp. 175-176, 1977

[Tsai 1992] *Prediction of dislocation generation during Bridgman growth of GaAs crystals*, C.T. TSAI, M.W. YAO, A. CHAIT, Journal of Crystal Growth, Vol. 125, pp. 69-80, 1992

[Valladares 1998] *First principles simulations of the structure, formation, and migration energies of kinks on the 90°partial dislocation in silicon*, A. VALLADARES, J.A. WHITE, A.P. SIMON, Physical Review Letters, Vol. 81, No. 22, pp. 4903-4906, 1998

[Valladares 2007] *First principles simulations of kink defects on the SP 90°partial dislocation in silicon*, A. VALLADARES, A.P. SUTTON, Progress in Materials Science, Vol. 52, pp. 421-463, 2007

[Vallino 2001] *Dislocation multiplication during the very first stages of plastic deformation in silicon observed by X-ray topography*, F. VALLINO, J.-P. CHÂTEAU, A. JACQUES, A. GEORGE, Materials Science and Engineering A, Vol. 319-321, pp. 152-155, 2001

[Vanderschaeve 2000] *Transmission electron microscopy in situ investigation of dislocation mobility in semiconductors*, G. VANDERSCHAEVE, C. LEVADE, D. CAILLARD, Journal of Physics: Condensed Matter, Vol. 12, pp. 10093-10103, 2000

[Vanderschaeve 2005] *Dissociation of dislocations and the mobility of partial dislocations in elemental semiconductors*, G. VANDERSCHAEVE, D. CAILLARD, Physica Status Solidi (a), Vol. 202, No. 5, pp. 939-943, 2005

[Vanderschaeve 2007] *On the mobility of dislocations in semiconductors crystals*, G. VANDERSCHAEVE, D. CAILLARD, Materials Science and Engineering A, Vol. 462, pp. 418-421, 2007

[Vanderwalker 1984] *The influence of Cu on dislocation motion in Si*, D.M. VANDERWALKER, Physica Status Solidi (a), Vol. 82, pp. 93-99, 1984

[Vodenitcharova 2004] *A new constitutive model for the phase transformations in monocrystalline silicon*, T. VODENITCHAROVA, L.C. ZHANG, International Journal of Solids and Structures, Vol. 41, pp. 5411-5424, 2004

[Wang 2008] *Atomic simulations of the dynamic properties of the 30°partial dislocation in Si crystal*, C.Y. WANG, Q.Y. MENG, K.Y. ZHONG, Z.F. YANG, Physical Review B, Vol. 77, pp. 205209-1/5, 2008

[Warren 1989] *The brittle-ductile transition in silicon: the influence of pre-existing dislocation arrangements*, P.D. WARREN, Scripta Metallurgica, Vol. 23, No. 11, pp. 637-642, 1989

[Wessel 1977] *On the mobility of partial dislocations in silicon*, K. WESSEL, H. ALEXANDER, Philosophical Magazine, Vol. 35, iss. 6, pp. 1523-1536, 1977

[Wu 1977] *On the shrinkage of rod-shaped defects in boron-ion implanted silicon*, W.K. WU, J. WASHBURN, Journal of Applied Physics, Vol. 48, No. 9, pp. 3742-3746, 1977

[Xin 1996] *A technique to generate straight through thickness surface cracks and its application to studying dislocation nucleation in Si*, Y.-B. XIN, K.J. HSIA, Acta Materialia, Vol. 44, No. 3, pp. 845-853, 1996

[Yamashita 1993] *Dislocation glide motion in heteroepitaxial thin films of $Si_{1-x}Ge_x/Si(100)$*, Y. YAMASHITA, K. MAEDA, K. FUJITA, N. USAMI, K. SUZUKI, S. FUKATSU, Y. MERA, Y. SHIRAKI, Philosophical Magazine Letters, Vol. 67, No. 3, pp. 165-171, 1993

[Yang 1996] *Effect of nitrogen–oxygen complex on electrical properties of Czochralski silicon*, D. YANG, R. FAN, L. LI, K. SUMINO, Applied Physics Letters, Vol. 68, No. 4, pp. 487-489, 1996

[Yang 2000] *Oxygen-related centers in multicrystalline silicon*, D. YANG, L. LI, X. MA, R. FAN, D. QUE, H.J. MÖLLER, Solar Energy Materials & Solar Cells, Vol. 62, pp. 37-42, 2000

[Yang 2002] *Effect of heat treatment on carbon in multicrystalline silicon*, D. YANG, H.J. MÖLLER, Solar Energy Materials & Solar Cells, Vol. 72, pp. 541-549, 2002

[Yang 2003] *Influence of oxygen precipitates on the warpage of annealed silicon wafers*, D. YANG, G. WANG, J. XU, D. LI, D. QUE, C. FUNKE, H.J. MÖLLER, Microelectronic Engineering, Vol. 66, No. 1-4, pp. 345-351, 2003

[Yasutake 1980] *Mechanical properties of heat-treated Czochralski-grown silicon crystals*, K. YASUTAKE, M. UMENO, H. KAWABE, Applied Physics Letters, Vol. 37, No. 9, pp. 789-791, 1980

[Yasutake 1986] *Crack healing and fracture strength of silicon crystals*, K. YASUTAKE, M. IWATA, K. YOSHII, M. UMENO, H. KAWABE, Journal of Materials Science, Vol. 21, pp. 2185-2192, 1986

[Yasutake 1987] *Velocity of twinning partial dislocations in silicon*, K. YASUTAKE, S. SHIMIZU, M. UMENO, H. KAWABE, Journal of Applied Physics, Vol. 61, No. 3, pp. 940-946, 1987

[Yonemura 1999] *Analysis of local lattice strain around oxygen precipitates in Czochralski-grown silicon wafers using convergent beam electron diffraction*, M. YONEMURA, K. SUEOKA, K. KAMEI, Japanese Journal of Applied Physics, Vol. 38, No. 6, pp. 3440-3447, 1999

[Yonenaga 1978] *Dislocation dynamics in the plastic deformation of silicon crystals. I. Experiments*, I. YONENAGA, K. SUMINO, Physica Status Solidi (a), Vol. 50, pp. 685-693, 1978

[Yonenaga 1984a] *Mechanical strength of silicon crystals as a function of the oxygen concentration*, I. YONENAGA, K. SUMINO, K. HOSHI, Journal of Applied Physics, Vol. 56, No. 8, pp. 2346-2350, 1984

[Yonenaga 1984b] *Role of carbon in the strenghtening of silicon crystals*, I. YONENAGA, K. SUMINO, Japanese Journal of Applied Physics, Vol. 23, No. 8, pp. L590-592, 1984

[Yonenaga 1993] *Deformation-induced defects and their thermal stability in silicon*, I. YONENAGA, K. SUMINO, Physica Status Solidi (a), Vol. 137, pp. 611-617, 1993

[Yonenaga 1996a] *Influence of oxygen precipitation along dislocations on the strength of silicon crystals*, I. YONENAGA, K. SUMINO, Journal of Applied Physics, Vol. 80, No. 2, pp. 734-738, 1996

[Yonenaga 1996b] *Upper yield stress of Si crystals at high temperatures*, I. YONENAGA, Journal of the Electrochemical Society, Vol. 143, No. 8, pp. L176-L178, 1996

[Yonenaga 2001] *Dislocation behavior in heavily impurity doped Si*, I. YONENAGA, Scripta Materialia, Vol. 45, No. 11, pp. 1267-1272, 2001

[Yonenaga 2002] *Impurity effects on dislocation activities in Si*, I. YONENAGA, Journal of Physics: Condensed Matter, Vol. 14, pp. 13179-13183, 2002

[Yonenaga 2005] *Nitrogen effects on generation and velocity of dislocations in Czochralski-grown silicon*, I. YONENAGA, Journal of Applied Physics, Vol. 98, No. 2, p. 023517, 2005

[Zhang 2000] *Plasticity in mono-crystalline silicon under complex loading conditions*, L. ZHANG, I. ZARUDI, Key Engineering Materials, Vol. 177-180, pp. 121-128, 2000

[Zhang 2001] *Towards a deeper understanding of plastic deformation in monocrystalline silicon*, L. ZHANG, I. ZARUDI, International Journal of Mechanical Sciences, Vol. 43, pp. 1985-1996, 2001

[Zhang 2004] *Plasticity in monocrystalline silicon: experiment and modeling*, L. ZHANG, Key Engineering Materials, Vol. 274-276, pp. 1-10, 2004

Part II

BUILDING ON THE LEGACY OF ALEXANDER & HAASEN

INTRODUCTION

MOTIVATIONS

The mechanical behavior of multicrystalline solar-grade silicon materials is a complex subject. From a local perspective, the material is expected to behave like a common, albeit impure, monocrystal. Modeling the mechanical behaviour of a silicon single crystal (c-Si) subjected to random thermomechanical loadings is in itself problematic due to the limited validity of the constitutive models available in the literature. The loading cases that can be studied with the existing numerical tools are very limited: small window of temperatures and strain rates, controlled crystallographic orientation, small strains and single glide.

This work is concerned with modeling the mechanics of silicon materials. In other words, it aims at deriving a model, *a set of equations whose solution provides an approximation of reality*, linking stresses to strains. Ultimately, we want to know what the stress tensor is given the strain tensor history. Every additional information provided by the model is icing on the cake. Because of the particular interest the industry has in knowing the dislocation density in solar cells, basing the model on these physical quantities is the ideal case.

An easy way of modeling the mc-Si aggregates would be to assume the amount of grains to be large enough, and their respective crystallographic orientations sufficiently varied to guarantee an isotropic -averaged- material behaviour. This problem is known as homogeneization: bridging the scales from micro to macro using averaging techniques that smoothen the local variations. Unfortunately, the relatively large size of the grains typically encountered in solar-grade silicon materials (SoG-Si), of the order of the mm, would require a representative volume element, i.e. a representative amount of grains, too large to be manageable. Crystal growth methods might also lead favorite crystallographic orientations of columnar grains, limiting the pertinence of an -isotropic- homogeneization.

A detailed description of the grain topology is consequently required to study mc-Si, and modeling these materials comes down to the definition of an adequate constitutive model for their constituent single crystals. The role of grain boundaries during deformation is an issue to model as well. Whatever the method chosen to develop the model, we need first to understand how stresses develop in materials. Let us consider the case of a multicrystal submitted to a given thermal field history.

Let us at first consider monocrystals only. We know that any temperature variation leads to the development of *isotropic* thermal *strains*, the magnitude of which depends on the temperature itself since the thermal expansion coefficient is not constant. The "macroscopic" *stresses* that arise

from such a field are however *anisotropic* since the stiffness matrix of silicon presents a cubic symmetry. The extent of thermally-induced Von Mises stresses in this ideal single crystal is very limited. Simulations of directional solidification have shown that from the melting point down to room temperature a stress of the order of 10 MPa can be calculated, depending on the boundary conditions imposed.

Thermal stresses are completely hydrostatic. In this case no plastic flow should set in, since the latter is produced by shear stresses. However, any kinematic compatibility requirement develops the stress tensor further, very likely with a finite non-hydrostatic component. The existence of thermal gradients owing to the non-planarity of the solidification front in cast ingots is a typical example of such a situation.

These conditions are also particularly relevant in the case of multicrystals, where grain misorientations add kinematic constraints at the boundaries that affect -likely increase- the stress level. This is why we expect larger dislocation contents close to the grain boundaries. We can call these stresses "mesoscopic" as their extent is limited by the shape and orientation of the grains constituting a multicrystal. They are dependent on the topology of the multicrystal (size, shape and crystallographic orientation of its grains).

On a microscopic scale, additional stress sources in SoG-Si are a large number of impurities and inclusions. The former are known to influence the dislocation behaviour by altering the activation energy for their motion (either easing plastic flow or hardening it) or by locking them (in which case plasticity is hindered). The latter are sources of strong stress concentrations that might lead to increased dislocation generation and increased stress concentrations depending on the temperature; dislocation locking by inclusions is also possible under certain size requirements.

It is therefore of importance to quantify the respective magnitude of the following stresses:

- macroscopic stresses (on the scale of the whole ingot, or whole wafer), thermally induced by thermal gradients or mechanical loads during processing,
- mesoscopic stresses, typically on a length scale of the mm or the average grain size, coming from the peculiar geometrical and crystallographic arrangement of grains. Their relative size, shape and orientation impose kinematic constraints that might lead to additional stress concentrations.
- microscopic stresses, due to the very chemistry of the material. The nature and size of hard inclusions, concentration of dopants (B, P,...) and light impurities such as N and O, metallic contaminants (Fe, Ni,...) affect dislocation generation and motion.

The combined effect of impurities, inclusions and of grain boundaries likely leads to complex situations where the stress and strain fields strongly differ from the ones predicted by traditional constitutive models. Modeling

the mechanical behavior of SoG-Si materials would allow us to study the effects of various thermomechanical loading paths (e.g., a solidification and cooling process, or a bending test representative of mechanical loadings applied on a solar cell during its processing) on the micromechanical and structural state of the solids. This is of high relevance for the PV industry. If stresses are to be avoided, then it is preferable to relieve them by plastic flow (meaning, dislocation generation and multiplication) at high temperatures. On the other hand, the dislocations thus generated are detrimental to the solar cell efficiency and some other engineers might prioritize low dislocation densities rather than stress relief.

At low temperatures, plasticity is not allowed any longer and any strain leads to the development of elastic stresses that can ultimately lead to brittle fracture of the material if stress concentrators are present. Such losses are costly to the industry and ultimately to the consumer. Indeed, the knowledge of the maximum stress induced by a given process step allows for its validation upon comparison with the experimentally derived material strength. A model able to quantitatively predict the mechanical state of the crystals would help the industry achieve its quality goals and improve cost efficiency. However, today's models are not developed enough to give us insightful results on the mechanical behavior of SoG-Si materials. This work hopes to fill in that knowledge gap.

METHODOLOGY

From this preliminary discussion, we can already infer that an advanced constitutive model for pure silicon single crystals (c-Si) is required prior to its extension to extrinsic materials. This task is done in the present Part, taking as a starting point the work of Alexander & Haasen. Although powerful, we show that the relevance of this model, even extended, is limited to easy glide conditions, when one slip system only is active. Hence, a model solving this issue is derived in the next Part of this thesis. Application of such constitutive models to multicrystals represents the ultimate step of this work.

Macroscopic stresses could be estimated by considering a mc-Si aggregate as a monocrystal. As mentionned above, this approximation could yield acceptable results owing to the large size of the grains encountered in such a material: far from the grain boundaries, the loading most likely leads to the activation of a single slip system.

The previous state-of-the-art has briefly described different ways of modeling the mechanical behaviour of silicon single crystals in uniaxial tension experiments. All models follow the assumptions made by Alexander & Haasen, and differ by their choice of dislocation multiplication law. Chapter 5 analyses the abilities and limitations of the classical models in the yield region. We show that their constitutive parameters obtained by best fit to experimental data are functions of temperature and strain rate, implying physical processes badly accounted for by the models.

Their basic assumptions, namely that all dislocations are mobile and that only one slip system is active, are no longer valid as is experimentally observed. Annex A is a companion to this Part and introduces a novel kinematic framework allowing the application of any physically-based constitutive model to random and potentially complex loading conditions. The abilities of a RDCP framework are demonstrated there by the study of the yield region of silicon crystals deformed in single glide using the standard constitutive equations. Comparison with the results yielded by a J_2 formulation highlights the advantages of the RDCP framework.

The kinematics being established, two choices are left to improve the accuracy and validity of the traditional models: either extending them, or deriving a wholly new model. Chapter 6 starts with a review of the knowledge we have of the different hardening and recovery stages, and the physical mechanisms responsible for them. Dislocation motion mechanisms and internal stresses will be dealt with. Building upon the existing multiplication laws and the assumption of deformation in single glide only, extentions of the model of Alexander & Haasen to a broad range of temperature and strain rate conditions are introduced thereafter.

The influence of impurities on dislocations in semiconductors has been extensively studied in the literature and reviewed in Part i. The implementation of additional equations into the constitutive model enables the study of extrinsic crystals. Because all light impurities basically have the same qualitative effect on dislocation motion, only oxygen is considered in this work. This limitation is justified by the large amounts of oxygen found in SoG-Si materials and the exhaustive literature available.

Extending the AH model will prove interesting by providing a physical justification to the variations of its constitutive parameters. In the meantime, many intrinsic limitations cannot be avoided by the choice of such simple equations. Therefore, a novel physically-based constitutive model allowing the study ov c-Si samples in the most general case will be derived in Part iii, keeping in mind the knowledge gained through the Chapters of the present one.

5

ANALYSIS OF TRADITIONAL MODELS

Traditional constitutive models for modeling the mechanical behavior of silicon monocrystals loaded in single glide in the yield region are introduced. We identify their parameters by best fit to experimental data obtained on FZ-Si at different temperatures and strain rates. Strong variations are shown to result. It is shown that all models can reproduce accurately the stress-strain curves. They differ by their prediction of the dislocation density evolution through deformation. It is concluded that improvements to the classical models must provide with a physical explanation to the variations of the constitutive parameters, in addition to allowing for more general loading conditions.

5.1 INTRODUCTION

Some results introduced in this Chapter have been presented in [Cochard 2009].

5.1.1 *Mathematical background*

The existing models differ mainly by two features: the expression of the internal stress and the law used for dislocation multiplication. All assume that dislocation motion is thermally activated and follows an Arrhenius-like law, given in Eq. 5.1:

$$v = v_0 \left(\frac{\tau_{eff}}{\tau_0} \right)^{m_0} \exp\left(-\frac{U}{k_b T} \right) \tag{5.1}$$

Adopting such a law implies that no distinction is made between the screw and 60° dislocations, although these have different velocities because of the different partials they are constituted of ([Bulatov 2001]). From a macroscopic point of view, the slowest dislocation segment will set a limit to the velocity of the whole loop. Therefore, the standard method is to use the parameters corresponding to the motion of screw dislocations in Eq. 5.1. These have been identified accurately by [Imai 1983], and are valid for pure

silicon crystals in the temperature range from 873 to 1050 K and at effective stresses from 1.2 to 40 MPa:

$$\begin{cases} m_0 = 1 \\ v_0 \tau_0^{-1} = 3.5 \times 10^{-2}\,\mathrm{N^{-1}.m^3.s^{-1}} \\ U = 2.35\,\mathrm{eV} \end{cases} \tag{5.2}$$

These parameters are adopted in the following. The activation energy has been found valid at temperatures up to 1323 K by [Siethoff 2001]. By continuity the velocity prefactor is kept the same in the whole temperature range. The stress dependency of U is neglected in our case, since the stresses considered in our work remain small enough (see [Siethoff 2002]). A direct limitation of this choice of parameters is the case of very high temperatures (VHT, above 1323 K) where dislocation motion mechanisms differ, see Part I. Nonetheless, it was found that in crystals containing as-grown dislocations, this VHT regime is shifted towards higher temperatures. In the following, the crystals we are modeling all have non-zero initial dislocation densities and this VHT domain will be excluded from our discussions.

We will in addition assume that these parameters are valid for any effective stress. Since we are first aiming at modeling pure, FZ-grown silicon crystals, the impurity atmosphere and segregation at the dislocation cores will be disregarded here. The effects of dissolved oxygen on dislocation motion and plasticity of silicon crystals will be modeled and discussed in Chapter 6.

The scalar models have been established to represent uniaxial straining of silicon monocrystals activated in single slip; usually the tensile axis is a $\langle 123 \rangle$ direction that favors such a deformation mode. Therefore, it is possible to extract the shear stress-shear strain curves from the experimental stress-strain data. This is achieved by projecting the stress and deformation onto the active slip system. A small strains approximation is traditionally chosen to study the yield region. Note that only one slip system is assumed to be active in this Chapter, so that no distinction is done between the twelve systems. This allows a relatively easy integration of the constitutive equations. The classical *machine equation* linking the resolved shear stress τ to the elastic shear strain γ_e reads in rate form:

$$\dot{\tau} = \mu^* \dot{\gamma}_e = \mu^* \left(\dot{\gamma} - \dot{\gamma}_p \right) \tag{5.3}$$

$$\dot{\gamma}_p = \rho_m b v \tag{5.4}$$

Where μ^* is the effective shear modulus accounting for the effect of the testing machine[1]. The plastic shear strain rate $\dot{\gamma}_p$ is given by Orowan's law (Eq. 5.4) valid on any slip system [Orowan 1940]. The model is completed by the expression of the effective stress and a differential equation describing the evolution of the dislocation density:

$$\tau_{eff} = \tau - \tau_{int} \tag{5.5}$$

1 Adopting an effective shear modulus implies that the effective strain rate acting on silicon $\dot{\gamma}$ is constant. This will be discussed in the following.

$$\dot{\rho}_m = K\left(\rho_m, v, \tau_{eff}\right) \tag{5.6}$$

All models exposed in the following adopt the same expression for the average internal stress τ_{int}, given as a function of the total dislocation density assumed to be equal to the density of mobile dislocations: $\rho = \rho_m$. It is also assumed that interactions between dislocations were only caused by long-range internal stresses, since their density was too low to generate significant short-range elastic interactions. The internal stress is calculated here as the stress caused by a density of mobile edge dislocations ρ_m, considered to be infinitely long:

$$\tau_{int} = \frac{\mu b}{2\pi(1-\nu)}\sqrt{\rho_m} \tag{5.7}$$

Further investigations have shown that this approximation can be refined by using a multiplicative parameter A, usually found to lie between 0.1 and 1 (see, e.g., [Alexander 1968, Suezawa 1979, Moulin 1997a] and Part I):

$$\tau_{int} = A\mu b\sqrt{\rho_m} \propto \frac{\mu b}{2\pi(1-\nu)}\sqrt{\rho_m} \tag{5.8}$$

All models introduced in this Chapter consider Eq 5.8 as valid. The shear modulus is computed using the geometrical average (Eq. 5.9) and the data for temperature dependence of the elastic constants (Eq. 5.10, from [Burenkov 1974]). The set of Eq. 5.10 is valid from 673 to 1273 K, but we assume here that its validity extends to the whole temperature range.

$$\mu = \sqrt{\frac{C_{44}(C_{11}-C_{12})}{2}} \tag{5.9}$$

$$\begin{cases} C_{11}(T) = (16.552 - 0.0015\,T) \times 10^{10}\,\mathrm{N.m^{-2}} \\ C_{12}(T) = (6.383 - 0.0006\,T) \times 10^{10}\,\mathrm{N.m^{-2}} \\ C_{44}(T) = (8.1986 - 0.0006\,T) \times 10^{10}\,\mathrm{N.m^{-2}} \end{cases} \tag{5.10}$$

Note that the density of dislocations used is the total density of dislocations in the whole crystal, not only the one on the activated slip system. In as-grown silicon of low initial dislocation density, this approximation is justified because the density of (mobile) dislocations on the active primary system (α) is by far larger than the density on the latent systems (β) after small amounts of plastic strain as discussed by [Yonenaga 1978]. In the case of dislocation-free crystals deformed uniaxially, only a small fraction of the total dislocation density after straining in the yield region is found on secondary systems, typically 10 % as mentioned by [Oueldennaoua 1988]:

$$\rho_m^{(\alpha)} \gg \rho_m^{(\beta)},\ \beta \neq \alpha$$

The models analyzed here differ by their choice of dislocation multiplication law. For the sake of simplicity, they will be numbered instead of being called by their name.

5.1.2 *Methodology*

Experimental data

The models are fitted to experimental data coming from the work of [Yonenaga 1978]. This choice is justified by the quality of the experiments performed in controlled conditions, and because of the special care that was taken to master the initial dislocation density of the samples prior to deformation. Taking experimental results from other authors would also have been possible, but most often the crystals were initially dislocation-free, a case that the models cannot account for. An equivalent initial dislocation density that represents the nucleation sources (such as Frank-Read sources as was done by [Moulin 1997a, Moulin 1999]) could be taken, but its value is generally unknown. Another factor favoring this choice of data set is the large range of testing conditions explored by the Japanese group, allowing for determination of the influence of each factor on the mechanical behaviour of silicon.

A first issue noticed when gathering experimental data is the discrepancy observed between two stress-strain curves recorded for the same temperature, strain rate and initial dislocation density conditions and published in two different articles (Figures 1 in [Yonenaga 1978] and 1 in [Sumino 1993]). After correspondence with Professor Yonenaga it appeared that the discrepancy comes from the brittleness of silicon even at temperatures as high as 1073 K. The higher upper yield point reported in [Sumino 1993] is actually believed to be more representative of the ideal response of silicon in these deformation conditions. The stress-strain curves available in this work have therefore been scanned and sampled at a number of points sufficient to ensure a good quality of the reproduced data. No error margin has been published. It must be kept in mind however that the upper yield point is very much more sensitive to the initial dislocation density than the lower yield point is. The range of strains considered is limited to the yield region only. In practice, the points considered for the fitting procedure are those sampled up to the lower yield point. Fig. 5.1 shows the original data, whereas Fig. 5.2 is a plot of the sampled data that is used in the present work. Fig. 5.3 introduces the experimental data relied upon to study the effect of oxygen on the yield region, as detailed in the next Chapter.

The *reference conditions* used in the following are defined as a temperature of 1073 K, a shear strain rate of $1.2 \times 10^{-4}\,\mathrm{s}^{-1}$ and an initial dislocation density of $2 \times 10^{8}\,\mathrm{m}^{-2}$.

Actual strain rate

It is quite difficult to estimate what the real shear strain rate (or resolved shear strain rate) the silicon crystal is subjected to in the early stages of deformation when plasticity is not fully developped in the specimen: at low strains the experimental setup does not guarantee a fully fixed specimen. Measuring displacements (or strains, or strain rate) at the cross-head is

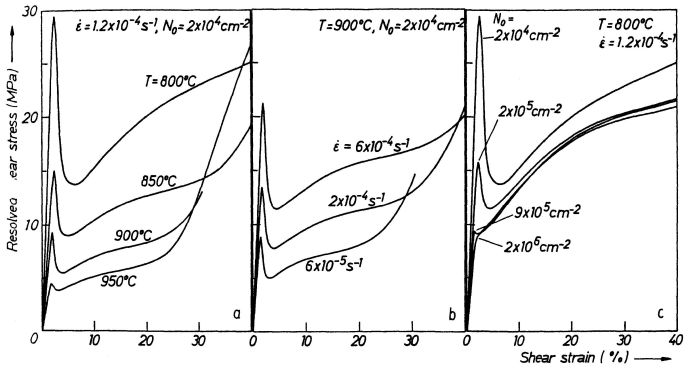

Figure 5.1: Experimental data used for parameter identification on intrinsic crystals, from [Sumino 1993].

a potential source of errors since it does not record the actual specimen deformation. This is translated in the recorded stress- strain results by an initial slope that is well below the actual Young's modulus (or shear modulus) of the material. In [Yonenaga 1978, Suezawa 1979] this effect is refered to as the "relaxation at the contact between the specimen and the machine". Further issues of strain rate stem from the softening taking place in the yield region, as will be discussed below.

For fitting procedures such an effect is usually dealt with by ignoring the elastic part of the experiment. The plastic part is then translated towards lower strains, the initial modulus being corrected (see Fig. 5.4 for an idealized example). Once plasticity sets in, deformation is considered to develop entirely by means of plastic dissipation in the specimen. Two issues arise in the case of silicon. First, it is tricky to determine when plasticity actually is significant enough to consider the further results as relevant. In a strict way one could argue that plasticity sets in extremely early in silicon crystals, although the macroscopic effects are detectable only beyond the upper yield point (see Part i). Still, the transition between those local and macroscopic dimensions of plasticity is not clearly defined, leaving the question of the cut-off strain unanswered[2].

Elastic region

The obvious issue is the actual strain rate acting on the silicon specimen in the "elastic" (in the macroscopic sense) domain. Since strain measurements are deduced from the cross-head displacement of the tensile equipment, the actual strain rate acting on the silicon sample is not known and a contribution from the remaining parts of the tensile apparatus cannot be

2 In particular, the question of what happens during the yield drop is worth mentioning. This "mixed" or transition region is clearly dominated by silicon plasticity but the elastic deformation of the tensile equipment could still play a non-negligible role. To be rigorous one should consider the lower yield point as the relevant limit. Unfortunately the yield region is precisely what we are interested in here.

excluded. It is easily conceivable that the effective strain rate acting on the specimen during its elastic loading is lower than the measured one, the elastic deformation of the machine components accounting for the remaining deformation. This could mean that the upper yield point is reached at lower stresses than what would be attained if a constant strain rate was applied all throughout the experiment.

The classical approach that considers an effective shear modulus in place of the actual one is indeed questionable, as this method is not physically right (especially when used in addition to Orowan's law). Considering *only the silicon specimen*, one can write in a general rate form:

$$\dot{\tau} = \mu_{Si}(\dot{\gamma} - \dot{\gamma}_p) \tag{5.11}$$

Considering the macroscopically elastic region (before the upper yield point), plastic strain can be neglected and Eq. 5.11 reads:

$$\dot{\tau} = \mu_{Si}\dot{\gamma} \tag{5.12}$$

and the resolved shear strain rate acting on the primary slip system can be calculated by inversion of the relation. Applying this formula to the reference stress-strain results, the resolved shear strain rate the specimen is subjected to before yielding is found to be of the order of $10^{-11}\,\mathrm{s}^{-1}$, extremely far from the assumed $10^{-4}\,\mathrm{s}^{-1}$. The assumption of constant strain rate during the experiment is consequently not verified. If the model parameters are rate-dependent, their identification might be tedious because of such variations in the yield region.

Yield region

A yield point is defined by $\dot{\tau} = 0$, or $\dot{\gamma} = \dot{\gamma}_p = \rho_m b v$. At the upper yield point we can assume in addition that the internal stress is small compared to the applied stress: $\tau|_{uyp} \simeq \tau_{eff}\Big|_{uyp}$. Combining Eqs. 5.3 to 5.7 in the case of a constant strain rate at the upper yield point gives:

$$\dot{\gamma} = \rho_{m,uyp} b v_0 \left(\frac{\tau_{uyp}}{\tau_0}\right)^{m_0} \exp\left(-\frac{U}{k_b T}\right) \tag{5.13}$$

Eq. 5.13 can be used to determine a range of actual shear strain rates at the upper yield point, given the upper yield stress and the measured dislocation densities. Using the shear strain/shear stress results in the case of deformation at 1073 K at an *apparent* shear strain rate of $1.2 \times 10^{-4}\,\mathrm{s}^{-1}$ on samples of initial dislocation densities of $2 \times 10^8\,\mathrm{m}^{-2}$ [Yonenaga 1978], the acceptable strain rates are $\left[2 \times 10^{-4},\, 5.6 \times 10^{-4}\,\mathrm{s}^{-1}\right]$ with a mean at $3.9 \times 10^{-4}\,\mathrm{s}^{-1}$. The standard deviations of the measured dislocation density at the upper yield point [Yonenaga 1978] have been used here. Note that the discrepancy might come from an approximative measurement of the dislocation density at the upper yield point, due to the dynamical state of deformation. The orders of magnitude are in agreement with each other.

Discussion - Variations of the resolved shear strain rate

A possible scenario is as follows:

- During elastic deformation of the specimen of high Young's modulus ($\sim 160\,\text{GPa}$) some machine components also deform elastically. The strain rate is measured at the cross-head, and therefore accounts for deformation of both the machine and silicon. The actual strain rate acting on the specimen is much lower than the overall one in the elastic region.
- As plasticity leads to material softening, the deformation concentrates on the specimen. This provokes a relaxation of the machine components that behave like springs and tend to go back to their initial undeformed shape. This plastic softening accompanied by the springback effect of the components locally affects the applied strain rate, consequently composed of the overall measured one and the additional effects of the fixing components.
- As the yield region is passed deformation concentrates exclusively on the tensile specimen and no additional disturbing effects can be noticed.

A consequence of these remarks is that the (resolved) strain rate acting on the specimen is not constant before the lower yield point, and of the order of the applied strain rate at the upper yield point (from dislocation density measurements). Silicon mechanical behaviour being significantly dependent on the strain rate, the measured dislocation densities at the upper yield point are the result of a strain rate history we do not know. It is indeed tricky to guess the intrinsic upper yield stress given a *constant* strain rate and an initial dislocation density. Only simulations would give the relevant values, provided that model parameters can be identified correctly. These ones should be calibrated using the plastic region of the stress-strain experiments only, provided that the dislocation density at the upper yield point (initial conditions for simulations) is known[3].

A solution to this problem would be to perform either tensile tests but measuring the specimen displacements instead of the cross-head ones. Alternatively, compression tests would be a viable option, provided that sufficent lubrication is guaranteed by the experimental setup to exclude disturbing friction at the sample ends.

In spite of these remarks and because of the lack of experimental data covering such a wide range of testing conditions, we will assume in this Chapter that the strain rate is constant throughout the whole duration of the experiments. The actual strain rate variations and parameter identification as a function of strain rate will be derived with the help of a Finite Elements model in Chapter 6.4.

3 If the cut-off for relevant data is the lower yield point as noted above then the study of the yield region with the present experimental data does not make sense.

ds1	1073 K	1123 K	1173 K	1223 K
μ^* (10^9 N.m^{-2})	3.25	1.55	1.09	0.61
ds2	6×10^{-5} s^{-1}	2×10^{-4} s^{-1}	6×10^{-4} s^{-1}	
μ^* (10^9 N.m^{-2})	1.3	1.65	2.22	
ds3	2×10^9 m^{-2}	9×10^9 m^{-2}	2×10^{10} m^{-2}	
μ^* (10^9 N.m^{-2})	1.63	1.38	not used	

Table 5.1: Equivalent shear moduli μ^* determined by best fit in different temperature, strain rate and initial dislocation density conditions.

Algorithm

The algorithm employed for integrating Eqs. 5.1 to 5.6 is based on small strains assumptions and implemented into MATLAB and FORTRAN. In addition, the internal stress is assumed to come solely from dislocations on the primary slip plane, and no influence of the secondary slip systems is accounted for. The integration procedure is purely explicit, the time step being chosen small enough to guarantee convergence of the results. In practice a time step of the order of 10^{-2} s was found to be sufficient. Implementation in a FORTRAN routine guarantees extremely fast execution of the program and easy coupling to the fitting algorithm as described below.

Fitting procedure

For simplicity and unless specified otherwise, each model is fitted to one set of reference experimental conditions. We consider that the announced initial dislocation density is the one on the primary system. We adopt as reference conditions the same set that was chosen by [Suezawa 1979] in 1979 to fit the model of Alexander & Haasen, so this choice allows for a comparison of the parameters we find with the ones that have traditionally been used in the literature. The effective shear modulus μ^* entering into Eqs. 5.3 is determined by best fit as well using the initial linear hardening slope of the experimental data.

The program used for identification of the model parameters is an adapted version of PIKATCHOU [Castelnau 2003]. The method chosen has always been a simulated annealing, to ensure that local minima are avoided as much as possible. When an initial set of parameters close to the actual solution was known, a Powell method was prefered, for computation time reasons.

This program uses optimization methods that do not require the computation of the gradient of the cost function `cost` to minimize. This somehow simplifies the numerical procedure, but requires larger computation times than the gradient alternative. The cost function is given by Eq. 5.14, where the sums are performed on all the *comparisons* of all *experiments* (trials).

Comparisons for a given experiment can be, for example, the data describing the evolution of the stress *and* the dislocation density with the strain. Thus, comparisons are the evolutions of different observable variables within a given trial. *Trials* are experiments performed in different conditions. For example, trials would be the experimental data obtained from uniaxial stressing of identical silicon crystals but at various temperatures, strain rates or initial dislocation densities. The cost function of each comparison is given by Eq. 5.15. y_M is the maximum of the N_p experimental data points y_{exp}, $\left(\frac{y_M}{\sigma_c}\right)^2$ the user-defined weight of the comparison, and y_{model} the points computed by the model to calibrate. The model results are interpolated by a first-order polynom in order to provide with the same points as the experimental ones[4]. Constraints on the parameters to fit are applied by giving the cost function an extremely high value if a solution violates the restrictions imposed by the user. For example, if the optimization program returns a negative value for a distance then the iteration step is severely weighted in order to be disregarded by the algorithm.

$$\texttt{cost} = 1 + \sum_{trials} \sum_{comparisons} f_c \tag{5.14}$$

$$f_c = \left(\frac{y_M}{\sigma_c}\right)^2 \frac{1}{N_p} \sum_{points} \frac{\left(y_{model} - y_{exp}\right)^2}{y_M^2} \tag{5.15}$$

The equivalent shear modulus μ^* are determined by considering the initial linear slope of the stress-strain curves only. They are given in Table 5.1.

4 A second order interpolation is available but was found to often lead to crashes. Using a high number of output points counterbalances the use of a linear interpolation.

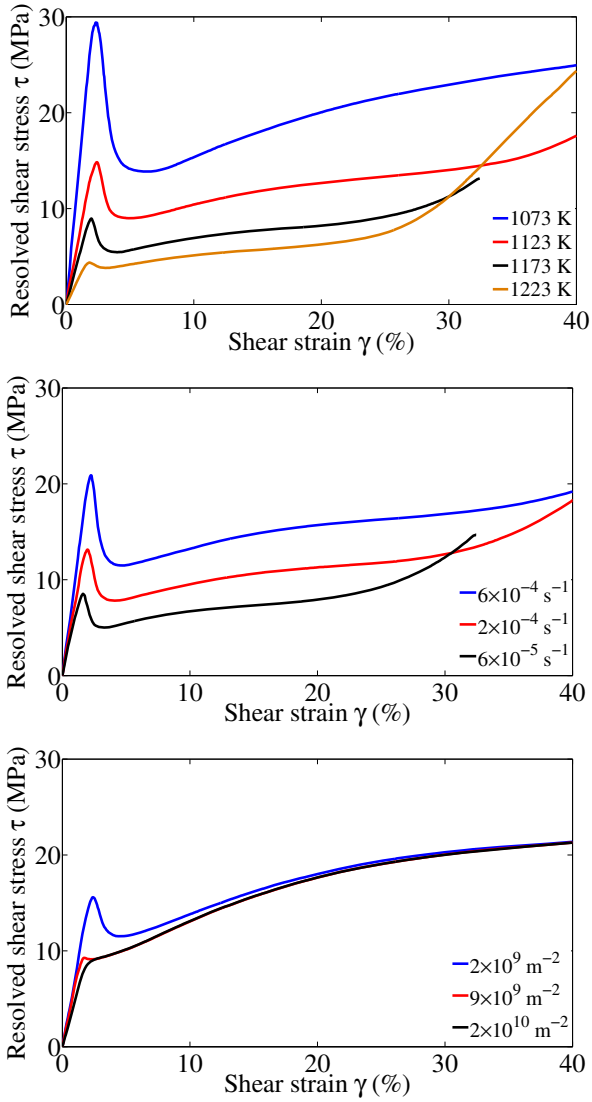

Figure 5.2: Sampled data sets (*ds1* to *ds3*, intrinsic crystals) used for the fitting procedures. Varying parameter from top to bottom: (1) temperature T, (2) shear strain rate $\dot{\gamma}$ and (3) initial dislocation density ρ_0. The other conditions are set by default respectively as (1) $\dot{\gamma} = 1.2 \times 10^{-4}\,\mathrm{s}^{-1}$ and $\rho_0 = 2 \times 10^{8}\,\mathrm{m}^{-2}$, (2) $T = 1173\,\mathrm{K}$ and $\rho_0 = 2 \times 10^{8}\,\mathrm{m}^{-2}$, (3) $T = 1073\,\mathrm{K}$ and $\dot{\gamma} = 1.2 \times 10^{-4}\,\mathrm{s}^{-1}$.

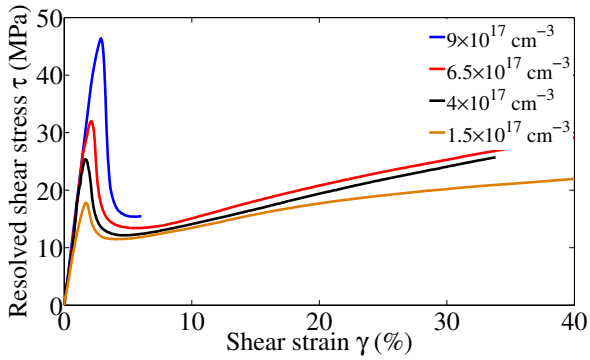

Figure 5.3: Sampled data set (*ds4*, extrinsic crystals) used for model parameter calibration. The thermodynamic conditions are set as $T = 1073\,\mathrm{K}$, $\dot{\gamma} = 1.1 \times 10^{-4}\,\mathrm{s}^{-1}$ and $\rho_0 = 10^{10}\,\mathrm{m}^{-2}$. From [Yonenaga 1984].

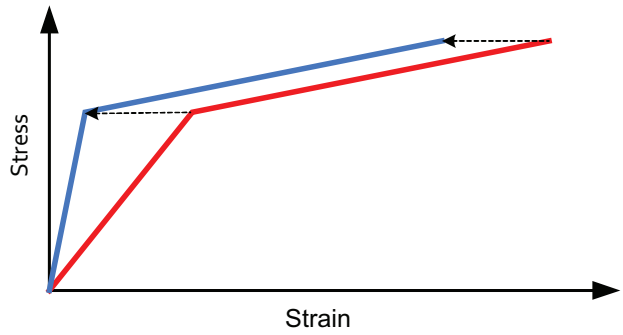

Figure 5.4: Correction of the elastic slope of experimental data. In red, the raw data recorded. The elastic part is suppressed and replaced by the material intrinsic one, the plastic part translated (in blue, the final curve).

5.2 THE MODEL OF ALEXANDER & HAASEN (MODEL 1)

This model relies on an empirical law for dislocation multiplication, found to be valid for germanium crystals and derived by [Berner 1967]. The multiplication law depends on one parameter δ_{AH} only:

$$\dot{\rho}_m = \delta_{AH} \tau_{eff} \rho_m v \tag{5.16}$$

Eq. 5.16 has been extended by [Suezawa 1979] who added one parameter, the effective stress exponent λ_{AH} (see Part I. $\lambda_{AH} = 1$ in the original model):

$$\dot{\rho}_m = \delta_{AH} \tau_{eff}^{\lambda_{AH}} \rho_m v \tag{5.17}$$

5.2.1 *Reference conditions*

Fitting the model parameters δ_{AH}, λ_{AH} and A_{AH} (see Eq. 5.8) to the reference curve yields the parameters introduced in Table 5.2. Since it makes more sense to take $\lambda_{AH} = 1$ (at least from a historical point of view), another fit has been executed, setting this parameter to unity. The results are presented besides the former ones.

The cost discrepancy between the two sets of parameters is quite significant. The model is sensible to slight changes in the parameters. As seen here, varying the stress exponent by 5 % leads to a variation of δ_{AH} of a factor two. This will be discussed in Section 5.5. The results of the fitting procedure are plotted in Figure 5.5 for $\lambda_{AH} = 1$ only since there is no remarkable difference between both cases.

δ_{AH}	1.11×10^{-4}	2.46×10^{-4}
λ_{AH}	1.05	1
A_{AH}	9.23×10^{-1}	9.18×10^{-1}
Cost	10.6	10.8

Table 5.2: Parameters of model 1 obtained by best fit in the reference conditions. λ_{AH} is set to be an independent parameter in the second case. δ_{AH} is expressed in $\mathrm{m}^{2\lambda_{AH}-1}.\mathrm{N}^{-\lambda_{AH}}$. The equivalent shear modulus $\mu*$ is found to be 1.36×10^9 N.m^{-2}.

5.2.2 *Parameters dependency on the testing conditions*

Individual fits

Individual fits have been performed for each experimental curve available, letting λ_{AH} be a free parameter. All results point out to $\lambda_{AH} \approx 1$ (see Table 5.3 for various temperatures) and a strong dependency of the dislocation multiplication prefactor δ_{AH} on λ_{AH} is noticed. Letting the (resolved)

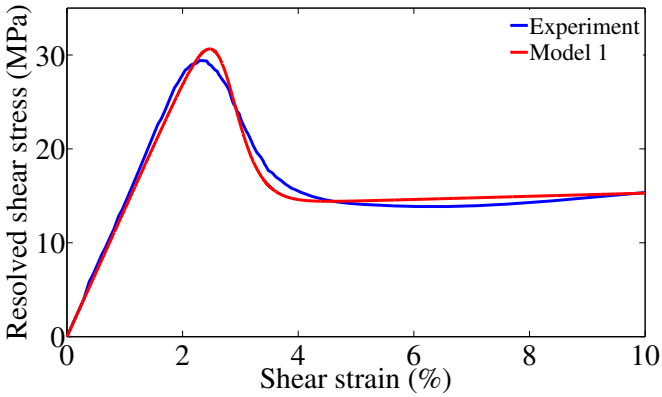

Figure 5.5: Fit of model 1 to the reference conditions (1073 K, resolved shear strain rate $1.2 \times 10^{-4}\,s^{-1}$, initial dislocation density $2 \times 10^{8}\,m^{-2}$). The stress exponent $\lambda_{AH} = 1$ is an independent parameter.

shear strain rate and initial dislocation vary, we get the results of Tables 5.4 and 5.5 with $\lambda_{AH} = 1$ set as an independent parameter.

A_{AH} seems to decrease with increasing temperature and increasing initial dislocation density, but not to depend on the strain rate. If the internal stress is assumed to come from long-range elastic interactions between dislocations, no dependence on the temperature should be found other than through the weak variations of μ_{Si}. The influence of the initial dislocation density on A_{AH} could be explained as more homogeneous dislocation patterns that smoothen the density gradient and therefore reduce the internal stress acting on individual dislocations (see next Chapter for a discussion). Another possibility is that the total dislocation density is not equal to the one on the primary slip system and that the secondary systems have non-zero initial densities. A decrease of A_{AH} at higher ρ_0 would compensate for an overestimation of the dislocation density on the principal slip system.

A suggestion is that dislocation immobilization favored by high temperatures enhances the formation of dipoles and multipoles in the yield region at high temperatures or low strain rates. These microstructures having no long-range elastic stress fields, they do not enter the internal stress expression and lead to a decrease of its magnitude through A_{AH}.

The significant increase of δ_{AH} with the initial dislocation density is ought to translate the increasing importance of forest dislocations on the multiplication mechanisms. Its variations with temperature point to the thermally activated nature of multiplication processes such as double cross slip events.

Simultaneous optimization

The software PIKATCHOU (see [Castelnau 2003]) allows for simultaneous comparison of a model to several experimental curves. It is therefore pos-

T (K)	1123	1173	1223
δ_{AH}	1.41×10^{-4}	1.34×10^{-4}	1.24×10^{-4}
λ_{AH}	1.05	1.07	1.12
A_{AH}	7.91×10^{-1}	6.39×10^{-1}	5.87×10^{-1}
Cost	1	0.5	0.5

T (K)	1123	1173	1223
δ_{AH}	3.37×10^{-4}	3.83×10^{-4}	7.42×10^{-4}
λ_{AH}	1	1	1
A_{AH}	7.9×10^{-1}	6.37×10^{-1}	5.82×10^{-1}
Cost	1.2	0.6	0.7

Table 5.3: Best fits at $\dot{\gamma} = 1.2 \times 10^{-4}\,\mathrm{s}^{-1}$ and $\rho_0 = 2 \times 10^{8}\,\mathrm{m}^{-2}$. δ_{AH} is expressed in $\mathrm{m}^{2\lambda_{AH}-1}.\mathrm{N}^{-\lambda_{AH}}$.

$\dot{\gamma}$ (s^{-1})	6×10^{-5}	1.2×10^{-4}	2×10^{-4}	6×10^{-4}
δ_{AH}	2.06×10^{-4}	3.83×10^{-4}	2.8×10^{-4}	3.43×10^{-4}
λ_{AH}	1	1	1	1
A_{AH}	8.08×10^{-1}	6.37×10^{-1}	8.49×10^{-1}	8.79×10^{-1}
Cost	4.1	0.6	1.6	1.3

Table 5.4: Best fits for different resolved shear strain rates at $T = 1173\,\mathrm{K}$ and $\rho_0 = 2 \times 10^{8}\,\mathrm{m}^{-2}$. δ_{AH} is expressed in $\mathrm{m}^{2\lambda_{AH}-1}.\mathrm{N}^{-\lambda_{AH}}$. λ_{AH} is set to unity.

ρ_0 (m^{-2})	2×10^{8}	2×10^{9}	9×10^{9}
δ_{AH}	2.46×10^{-4}	8.29×10^{-4}	3.91×10^{-3}
λ_{AH}	1	1	1
A_{AH}	9.18×10^{-1}	6.44×10^{-1}	4.63×10^{-1}
Cost	10.8	0.9	0.6

Table 5.5: Best fits at $T = 1073\,\mathrm{K}$ and $\dot{\gamma} = 1.2 \times 10^{-4}\,\mathrm{s}^{-1}$. δ_{AH} is expressed in $\mathrm{m}^{2\lambda_{AH}-1}.\mathrm{N}^{-\lambda_{AH}}$. λ_{AH} is set to unity. No fit was performed for $\rho_0 = 2 \times 10^{10}\,\mathrm{m}^{-2}$ since no yield drop is correctly observed.

δ_{AH}	3.58×10^{-4}
λ_{AH}	1
A_{AH}	6.78×10^{-1}
Cost (total)	493

Table 5.6: Simultaneous optimization of the parameters (δ_{AH}, A_{AH}) of model 1, for various temperatures and at $\dot{\gamma} = 1.2 \times 10^{-4}\,\mathrm{s}^{-1}$ and $\rho_0 = 2 \times 10\,\mathrm{m}^{-2}$. Assumption of constant parameters.

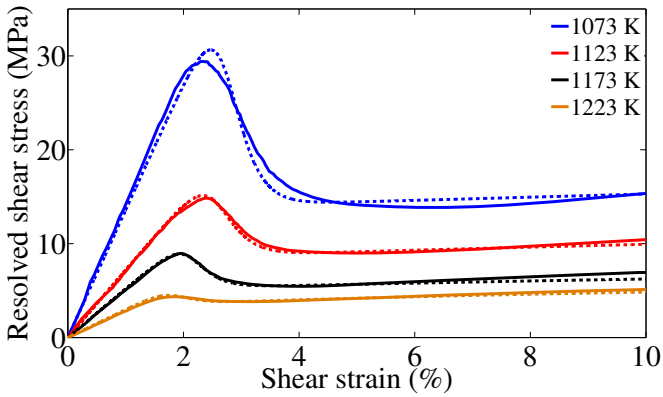

Figure 5.6: Comparison of experimental data *ds1* (full curves) with model 1 (dashed curves), using the parameters $A_{AH}(T)$ and $\delta_{AH}(T)$ as given by Eq. 5.19 at different temperatures.

sible to optimize the set of parameters to, for example, the experimental results obtained at different temperatures. In this case, the four total cost of each fitting attempt is the sum of the costs of the individual simulations. The software then optimizes the set of parameters (δ_{AH}, A_{AH}), λ_{AH} being set to unity. Considering these parameters as constants independent on the temperature does not yield satisfying results, as their variations are quite large considering the results shown in Table 5.3. Table 5.6 gives the detailed results of this fitting procedure, rejected because giving a too large total cost.

Another trial has been done, using this time a linear variation of the internal stress prefactor A_{AH} with temperature: a linear regression of the data of Table 5.3 gives:

$$A_{AH}(T) = 3.4 - 2.3 \times 10^{-3} T \tag{5.18}$$

which is indeed valid up to 1473 K only because of its linear form. In this case $\delta_{AH} = 3.86 \times 10^{-4}$ yields the best result but still leads to a large aggregated cost of the objective function (245), affecting mainly the results at the lowest temperature (1073 K).

The last option left is to account for the temperature variations of the dislocation multiplication prefactor δ_{AH}. Assuming that a thermally activated process enhances dislocation multiplication at high temperatures (for example, double cross-slipping events), a law of the form $\delta_{AH} = \delta_1 \exp\left(-\frac{U_{AH}}{k_b T}\right)$ gives $\delta_1 = 1.77$ and $U_{AH} = 0.83$.

Such an approach yields excellent results, with a total cost of 44 as depicted in Figure 5.6 for a comparison between the experimental results and the predictions of the model. Note that the underlying assumption of a linear variation of A_{AH} with the temperature is not physically justified and should be used with caution in a limited temperature range. Note also that these parameters are valid for a resolved shear strain rate of $1.2 \times 10^{-4}\,\mathrm{s}^{-1}$ only. A strain rate dependence of δ_{AH} can be expected for example.

The analysis of experimental data at temperatures from 1073 to 1223 K yields the following model parameters, obtained by best fit and valid for an initial dislocation density of $2 \times 10^8\,\mathrm{m}^{-2}$ and a resolved shear strain rate of $1.2 \times 10^{-4}\,\mathrm{s}^{-1}$:

$$\begin{cases} A_{AH}(T) = 3.4 - 2.3 \times 10^{-3} T \\ \delta_{AH}(T) = 1.77 \exp\left(-\frac{0.83}{k_b T}\right) \end{cases} \tag{5.19}$$

5.3 THE MODEL OF MOULIN (MODEL 2)

[Moulin 1999] has studied the yield points of silicon crystal using dislocation dynamics simulations. It has been found that the dislocation multiplication law suggested in model 1 would not fit correctly to the computed evolution of the dislocation density with time. An improved law has been derived from the dislocation dynamics simulations, given in Eq. 5.20 where ρ_S is a saturation density that models the size effect of their fictious small crystal. For real crystals this density should tend to infinity; this has been checked during the fitting experiments:

$$\dot{\rho}_m = \delta_M \sqrt{\rho_m \tau_{eff}} v \exp\left(-\frac{\rho_m}{\rho_S}\right) \tag{5.20}$$

Using the reference conditions only, it was possible either to consider the same value for the effective shear modulus as determined previously ($\mu^* = 1.36 \times 10^9$ N.m^{-2}), or to set it as a free parameter. Allowing this extra degree of freedom improves the quality of the fit but does not have any physical meaning as the effective shear modulus is uniquely determined by the slope of the stress-strain curve at the origin. The discrepancy between both slopes is nonetheless small.

The resulting sets are shown in Table 5.7. The computed stress-strain curve for $\mu^* = 1.36 \times 10^9$ N.m^{-2} is shown in Figure 5.7. The position of the lower yield point is not affected significantly by setting the effective shear modulus as a free parameter, whereas the upper yield point strongly depends on the choice of the parameter set. It is interesting to note that the internal stress prefactor A_M is very close to the one obtained with model 1.

δ_M(m^{-1}.N$^{-1/2}$)	9.53×10^4	1.06×10^5
A_M	8.17×10^{-1}	8.04×10^{-1}
μ^*(N.m^{-2})	1.57×10^9	1.36×10^9
Cost	7.3	23.4

Table 5.7: Parameters of model 2 obtained by best fit in the reference conditions. μ^* is an independent parameter in the second case (right hand side column). δ_M is expressed in m^{-1}.N$^{-1/2}$.

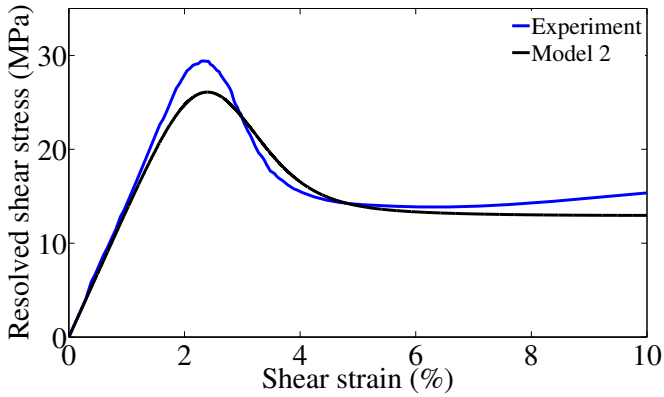

Figure 5.7: Best fit of model 2 parameters to the projection of the experimental data (reference conditions) onto the primary slip system.

5.4 THE CLASSICAL MODEL (MODEL 3)

The choice of a dislocation multiplication law depending on τ_{eff} is typical of covalent crystal, and has not found any physical justification yet. [Moulin 1997a] has mentioned the possible effect of cross-slip at the surface of the specimen that would enhance dislocation multiplication and lead to a surface-to-volume dependency of the evolution law. The effective stress term entering into the dislocation multiplication law would disappear for infinitely large specimen. Nevertheless, this hypothesis has never been tested out, but we can consider the case where this assumption is actually right. This yields Eq. 5.21 for the dislocation multiplication law, classical for fcc metals. It derives from a Johnston-Gilman hardening mechanism that assumes dislocation multiplication by double cross-slip events ([Johnston 1959, Gilman 1960]).

It simply expresses that the increase in dislocation density is proportional to the area swept by a dislocation loop during a small time interval and corresponds to dislocation multiplication by cross-slip breeding. Note that this case is similar to model 1 with $\lambda_{AH} = 0$. The results are given in Table 5.8 and the corresponding simulated curve compared to the sampled experimental one in Figure 5.8. Although the upper yield point is correctly represented, the sharp yield drop that follows leads to an early lower yield point and further hardening.

$$\dot{\rho}_m = \delta_{JG} \rho_m v \tag{5.21}$$

δ_{JG}	4.87×10^3
A_{JG}	7.64×10^{-1}
Cost	26.6

Table 5.8: Parameters of model 3 obtained by best fit in the reference conditions. δ_{JG} is expressed in m^{-1}.

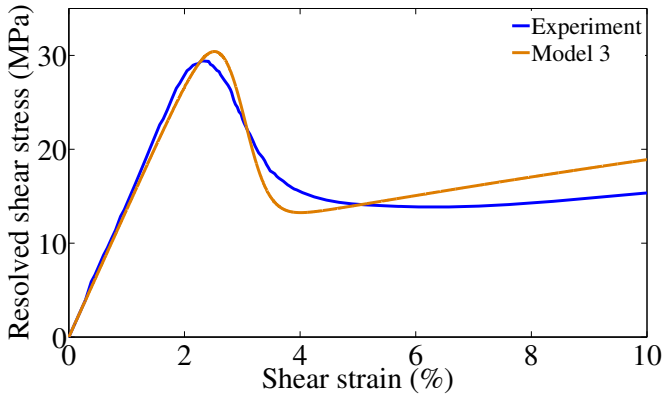

Figure 5.8: Best fit of model 3 with the experimental curve in the reference conditions.

5.5 GENERIC MODEL (MODEL 4)

Model 1 has been established on an experimental basis, but fails to be generalized to a wide range of testing conditions with constant constitutive parameters, although taken individually it is possible to adequately fit every single experimental data set analyzed here. Model 2 is justified by dislocation dynamics simulations but still weakly describes the yield drop in our reference case. Model 3 has the advantage of being widely used and to have a physical meaning, but its validity is limited to the yield drop region and it poorly represents the smooth transition from the yield region to stage I. Based on these observations, one can draw three main conclusions:

- There does not seem to be any dislocation multiplication law with *constant parameters* that describes accurately the yield region in all deformation conditions considered here.
- The internal stress prefactor A depends on the model considered, but remains of the same order of magnitude.

We proposed in this Section a dislocation multiplication law for the yield region that depends on three free parameters δ_F, λ_F and β_F and written as:

$$\dot{\rho}_m = \delta_F \rho_m^{\beta_F} \tau_{eff}^{\lambda_F} v \tag{5.22}$$

The expression of the internal stress is kept as previously. Such an approach has already been applied by [Fikar 2005] on germanium. Their results show that these parameters depend strongly on the specimen considered. From this expression we can find back model 1 ($\beta_F = 1$ and $\lambda_F = 1$), model 2 ($\beta_F = \lambda_F = 0.5$) and model 3 ($\beta_F = 1$ and $\lambda_F = 0$).

It has been verified that the optimal parameters vary strongly with the deformation conditions and that no general law could be drawn from the fitting procedures. In the following only the reference experimental data is considered. The main feature differenciating the previous models is the value of the stress exponent λ_F. Therefore, several fits have been performed using the Equation 5.22 with $\lambda_F \in [0, 5]$. For each value of λ_F set as an independent parameter the optimal set of free parameters (δ_F, β_F, A_F) that minimizes the cost function is computed. The results are shown in Figure 5.9.

An interesting feature is the perfect logarithmic variation of the parameter δ_F with λ_F, given by Eq. 5.23. The parameter β_F remains approximately constantly between 0.7 and 0.8 in all simulations, whereas A_F depends slightly on λ_F but stays in the $[0.7, 0.9]$ interval. The region of low costs (best fits) is quite extended. This is translated graphically by simulated stress-strain curves that all fit well the experimental curve, see Figure 5.10 for some examples. Due to the approximate scan of the experimental data and the inevitable uncertainty that comes with the experiment, it is not possible to decide which set is closest to the actual behaviour of silicon. It

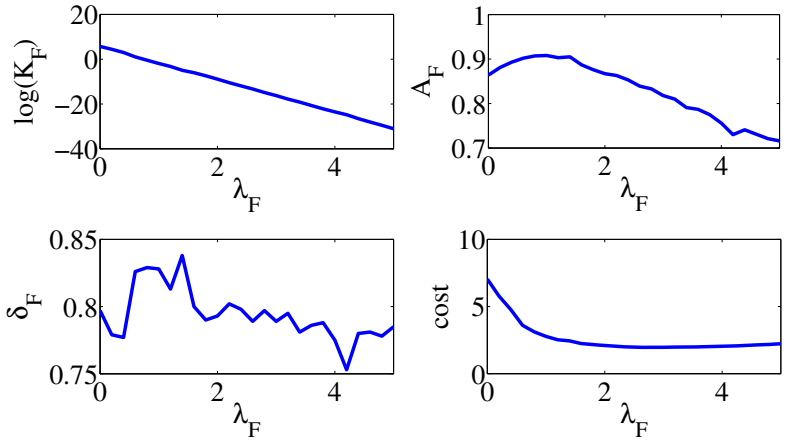

Figure 5.9: Variations of the set of optimal parameters of model 4 in the reference conditions (δ_F, β_F, A_F) with the stress exponent λ_F.

δ_F	5×10^{-16}
λ_F	2.87
β_F	7.89×10^{-1}
A_F	8.24×10^{-1}
Cost	1.96

Table 5.9: Parameters of model 4, obtained by best fit of the experimental data at the reference conditions. δ_F is expressed in $\mathrm{m}^{2(\lambda_F+\beta_F)-3}.\mathrm{N}^{-\lambda_F}$.

could hence be assumed *a priori* (without any consideration of the physical relevance of the parameters) that any of those sets represents satisfactorily the actual mechanical behaviour of silicon.

Larger discrepancies are observed when it comes to the evolution of the dislocation density, as depicted in Figure 5.11. None of the sets can actually reach the experimentally measured dislocation density at the lower yield point, reported to be approximately $6 \times 10^{11}\,\mathrm{m}^{-2}$ by [Yonenaga 1978]. This leads to the conclusion that such a model *cannot accomodate for both the stress and the dislocation density data simultaneously*. Reaching higher densities at the lower yield point requires low values of λ_F that do not fit with the stress data.

It seems nevertheless from this numerical experiment that almost any choice of λ_F can give a satisfying fit of the stress-strain data, the parameter δ_F balancing the evolution of the dislocation density. The dislocation densities predicted by the models are of the same order of magnitude as the experimental value. Adopting $\lambda_F = 2.87$ yields the best results as given

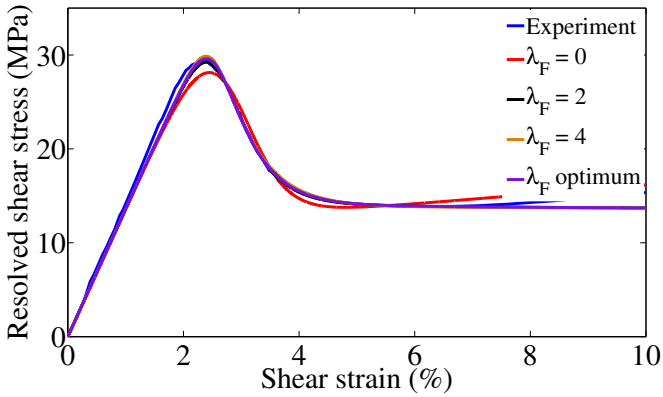

Figure 5.10: Stress-strain curves obtained by model 4 in the reference conditions.

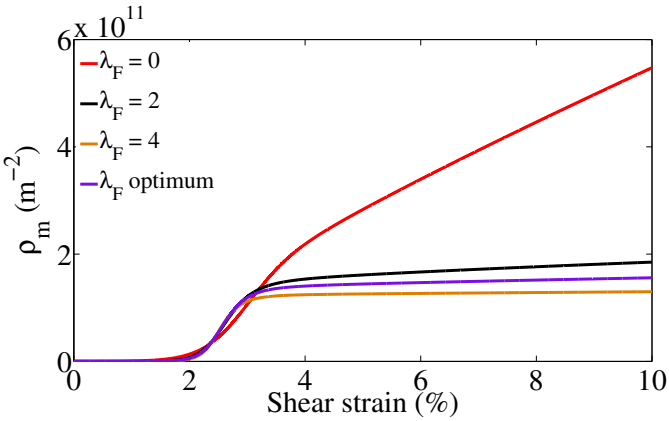

Figure 5.11: Evolution of the density of mobile dislocations for different values of λ_F (model 4). The experimental value measured at the lower yield point is $6 \times 10^{11}\,\mathrm{m}^{-2}$ [Yonenaga 1978].

in Table 5.9. Such a set has no physical meaning but represents almost perfectly the yield drop up to the lower yield point.

$$\log(\delta_F) = -7.31 \times \lambda_F + 5.61 \tag{5.23}$$

Note that these results are valid only for the reference conditions (1073 K, resolved shear strain rate $1.2 \times 10^{-4}\,\mathrm{s}^{-1}$, initial dislocation density $2 \times 10^{8}\,\mathrm{m}^{-2}$) and depend strongly on them.

5.6 DISCUSSION

Using these models beyond the lower yield point is in general not recommended since they rely on assumptions that are not verified towards large strains. Firstly, considering that the total dislocation density is equal to the density of mobile dislocations is wrong in stage I of deformation. It is known from observations in silicon that trapping of mobile dislocations, formation of dipoles or multipoles, multiplication of dislocations by forest interactions, as well as annihilation of screw segments by cross-slip are active processes responsible for the hardening in easy glide (see [Oueldennaoua 1988] and Chapter 6). The current models do not incorporate any density of such immobile dislocations. This is also a reason for the simulated dislocation density being too low at the lower yield point, where a non-negligible share of the total measured density is bound to be immobile.

Secondly, long-range elastic stress fields created by the dislocations stored in dipolar and multipolar structures does contribute to the flow stress. Therefore the internal stress should account for such interactions. In particular, a steady-state of the internal stress and a saturation of the density of mobile dislocations have been observed beyond the lower yield point (see [Yonenaga 1978, Oueldennaoua 1988]). Models 1 to 3 consider this density to increase with further deformation (see Fig. 5.13 for the evolution of the density of mobile dislocations predicted by the models), a fact disproven experimentally. Model 4 yields such a steady state after the upper yield point, but at a value significantly below the actual one. Figure 5.12 shows the predictions of the stress-strain curves by the different models introduced in this Chapter up to 10 % deformation. None is able to represent the first hardening stage, even less on a physical basis[5]. From this discussion it remains unclear which constitutive equations are best suited to study the yield region.

- If model evaluation is based solely on the best fit to experimental stress-strain curves and disregards the physical meaning of the evolution laws, thenthe model of Alexander & Haasen or a generic model allow for the best approximation of the yield drop. Care must anyway be taken to fit the parameters to the experimental conditions (temperature, strain rate and initial dislocation density). The accuracy and applicability of such a standard model is anyway very limited by the thermodynamical state of deformation.

- If a physical basis is prefered to a pure perfect fit of the experimental data, the model of Moulin seems to be the most appropriate for silicon, although it stems from numerical simulations only and has not been observed to fit the experimental data. Model 3 is valid for fcc metals and could be a good candidate for silicon crystals, provided

5 The accuracy of the predictions by the models is limited by the small deformations framework implemented in the routine, so care should be taken when analyzing the stress-strain curves and other outputs from these models at large strains.

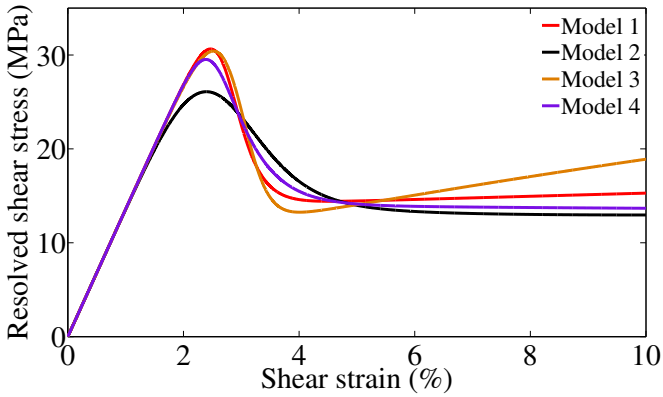

Figure 5.12: Simulations of the stress-strain behaviour of silicon at 1073 K, a resolved shear strain rate of $1.2 \times 10^{-4}\,s^{-1}$ and an initial dislocation density of $2 \times 10^{8}\,m^{-2}$, by models 1 to 4.

its accuracy could be improved in the yield region. This could be achieved by accounting for the possible strain rate dependency of its parameters, or by including additional multiplication sources such as forest dislocations.

- All models will have a tendency to fail towards very high temperatures, where dislocation velocity is not ruled by the same equation parameters as introduced previously. They will also be less accurate and loose their physical basis as the initial dislocation density is increased. Indeed, studying highly predeformed silicon samples with such models has no meaning since dislocation patterns are observed when deformation progresses in stage I. No formulation introduced here can predict the activation of secondary slip systems and the (slight) evolution of the dislocation densities on these ones, as observed experimentally for low initial densities by [Yonenaga 1978].

- Most importantly, no constant set of parameters valid in all the investigated temperature and strain rate ranges seems to be reachable from the results of the different fitting procedures performed in this Chapter. The parameters depend strongly on the experimental conditions and may vary as deformation proceeds. As has already been mentionned in the literature ([Fikar 2005]), these parameters might as well vary during deformation and with the sample considered.

- The constitutive parameters derived in this Chapter differ from what is gathered in the literature, although remain at the same order of magnitude. The most surprising discrepancy is the values fitted for the internal stress prefactor A, found here to be much higher than the usually reported one (≈ 0.3). Setting this parameter as independent could not give satisfying results. Remarkable is the redundancy of

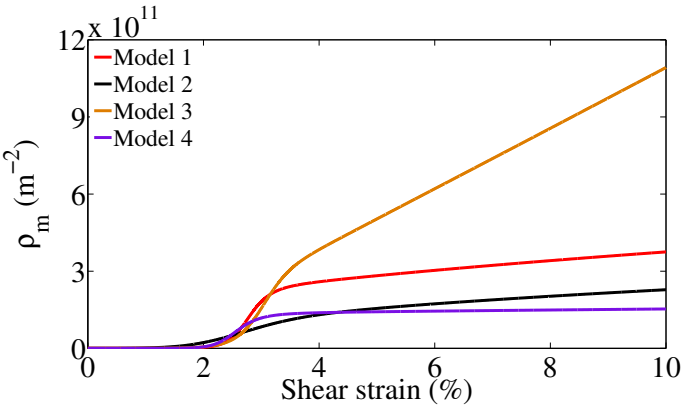

Figure 5.13: Simulations of the evolution of the density of mobile dislocations at 1073 K, a resolved shear strain rate of $1.2 \times 10^{-4}\,s^{-1}$ and an initial dislocation density of $2 \times 10^{8}\,m^{-2}$, by models 1 to 4.

this discrepancy with the four different models. Fits of different experimental curves (see Tables 5.3, 5.4 and 5.5) are consistent with this observation. The following explanation is suggested.

- dislocation interactions stem from long-range interactions coming from both mobile and immobile dislocations. As the dislocation density increases, some dislocations are stored. The effect of the predeformation in the experiments with high initial densities might has been to create a (relatively) high density of immobile dislocations that have more local stress fields and do not contribute strongly to the long-range stresses individually. Their high number would however lead to a significant contribution to the flow stress. It is also possible that higher dislocation densities mean a more homogeneous distribution of dislocations on the microscopic scale that ends up in lower density gradients and therefore lower internal stresses.
- The unphysical decrease of A with increasing temperature (see Table 5.3) could be also ascribed to the development of another dislocation population enhanced at high temperatures.

These attempts point out to limitations of these simple models that cannot account for high initial dislocation densities and high temperatures. Modeling the yield region should be done in a holistic manner, accounting for the mechanisms that are visible only in the subsequent deformation stages. The results obtained by these models might differ when immobilization and annihilation of dislocations are taken into account. However, before deriving a new physically-based constitutive model based on the equations of Alexander & Haasen in Chapter 6, a mathematical framework allowing its implementation in Finite Elements package is required. Annex A introduces such a framework allowing a more realistic simulation of the mechanical

behavior of silicon crystals by generalizing the pointwise models of this Chapter to a three-dimensional case. This way, complex loadings can be accounted for, freeing us from the limitation to the very special case of uniaxial tensile testing of single crystals.

6

EXTENSIONS OF THE MODEL OF ALEXANDER & HAASEN

Based on the results from the analysis of the traditional models and using a RDCP framework, a constitutive model for intrinsic silicon crystals is derived based on the equations of Alexander & Haasen. The physical processes responsible for the mechanical behavior of silicon crystals through the different hardening stages are reviewed first. Constitutive equations are derived on physical arguments. A model for extrinsic crystals is suggested, taking oxygen as a reference impurity.

6.1 INTRODUCTION

It has always been argued that interactions between dislocations in silicon monocrystals during the early stage of deformation are due to their long-range elastic stress fields only [Alexander 1968, Alexander 1986]. This is justified by several theoretical and experimental observations. The theoretical argument considers that the low dislocation densities of silicon crystals prevent from the dominance of any short-range interactions. In silicon crystals of low dislocation densities, the dislocations are observed to be widely separated from each other. No dipole or multipole that have short-range stress fields are found. Experimentally, it is observed that structures similar to pile-ups were forming in deformed crystals, and the expression for the resulting stress acting on the leading dislocation has been computed using the standard elastic theory, although considering an ideal case of infinite edge dislocations [Alexander 1968]. The study of dislocation curvatures also allows for computation of the internal stress, and such an analysis clearly yielded stresses emanating from long-range stresses only, at least in silicon crystals of low dislocation densities (see [Nishino 1984, Alexander 1986] and references therein). Indeed, the hexagonal shape of dislocation loops at low temperatures and/or high stresses is a proof that internal stress fields in weakly deformed crystals are not always strong enough to overtake the Peierls potential.

All these observations consider the case of crystals with low dislocation contents, most often deformed in single slip and with -if present- extremely low densities on the secondary slip systems. Therefore, all dislocations can be considered to be mobile and present on the primary slip system. This is

based on these premices that Alexander and Haasen derived their constitutive model introduced in the previous Part of this thesis and analyzed in Chapter 5 of the present one. The core of their model is the dislocation multiplication law, and we have seen that its parameters must be adapted to the temperature and strain rate considered in order to correctly fot to the experimental data.

It can be argued that the sole originality of the AH model is the dislocation multiplication law, along with its rather limiting assumptions. The remaining model equations (namely, Orowan's law and the definition of the internal stress) are classical and have been used independently by many other authors.

The interaction mechanisms beyond the yield region of covalent crystals differ from the particular case of stage 0, and can give us some hints about the physical mechanisms responsible for the variations of the constitutive parameters of the AH model. In the following a complementary view of dislocation interactions is given, that is helpful to model the large strain behaviour of silicon crystals and allows to partially relieve the limitations of the AH model in the yield region.

A distinction is done between so-called *mobile* and *immobile* dislocations. The former are the dislocations that are free to move under a sufficently high applied stress but remain at rest otherwise. In other words, mobile dislocations are those carrying plastic flow under a finite effective stress. The immobile or stored dislocations are those that have been trapped in dipoles, multipoles or tangles, and that exhibit mainly short-range elastic stress fields. Their mobility is negligible compared to mobile dislocations, and it is considered in this work that stored dislocations do not carry plastic flow. The distinction consequently does not refer to the actual velocity of dislocations, but to the *ability* dislocations have to move. A single dislocation can and will in practice change its status several times during deformation, but we consider here averaged behaviours only.

Section 6.2 is concerned with the micromechanisms responsible for the mechanical behavior of single crystals in different deformation stages relevant for this work. It provides with a complementary view of Part i, by using results from the literature about f.c.c. crystals. Based on these physics, an extension of the constitutive model of Alexander & Haasen is proposed in Section 6.3, where its ability to correctly reproduce the stress-strain behavior of intrinsic silicon monocrystals in a wide range of temperature and strain rate is demonstrated.

Dislocation locking by impurities is a well-known phenomena reviewed in Part i. Oxygen is taken in Section 6.4 as a model impurity and its progressive effect on preventing plastic flow as its concentration is increased in the bulk is successfully modeled.

Definitions and notations

The total dislocation density on the slip system α is noted $\rho_t^{(\alpha)}$ and is decomposed into a density of mobile $\rho_m^{(\alpha)}$ and immobile $\rho_i^{(\alpha)}$ dislocations:

$$\rho_t^{(\alpha)} = \rho_m^{(\alpha)} + \rho_i^{(\alpha)}$$

The forest density is the density of dislocations that cut the plane of a given slip system; it is the sum of the total dislocation densities on all slip systems located on the remaining slip planes (in the case of silicon or fcc crystals, there are 9 systems constituting a forest). The dislocations belonging to the forest are called trees. Mathematically, a dislocation belonging to the forest of a given slip system α has a non-coplanar Burgers vector. Writing f_α the forest and $\rho_t^{(\beta)}$ the dislocations belonging to a slip system β characterized by a plane normal $\mathbf{n}_\beta$, one can write:

$$f_\alpha = \left\{ \rho_t^{(\beta)},\ \mathbf{n}_\beta \wedge \mathbf{n}_\alpha \neq \overrightarrow{0} \right\}$$

$$\rho_f^{(\alpha)} = \sum_{\beta \in f_\alpha} \rho_t^{(\beta)}$$

6.2 PHYSICS OF HARDENING STAGES

Silicon has often been compared to fcc metals because of the similarity of its deformation mechanisms with such materials, at least at intermediate and high temperatures. The twelve slip systems of silicon at standard pressure are actually the same as those of fcc metals, identified by the four {111} planes and their associated <110> directions (see Part i, Fig. A.1 and Annex A). Understanding the physics of the hardening and recovery stages following the initial yield peak of silicon crystals can be done by looking at the extended literature on fcc metals. In the following, the case of a uniaxial tensile test performed on a single crystal is considered to describe the successive hardening mechanisms. Experiments in double slip allow for the exploration of hardening mechanisms due to short-range dislocation interactions (junction formation and unzipping). Note that this section considers hardening mechanisms valid in the temperature range below $0.8\,T_m$, since diffusional mechanisms (e.g. overcoming of obstacles by climb and point defects migration) tend to gain in importance above this threshold [Aseev 1975, Farber 1982].

6.2.1 *The yield region*

Dislocation multiplication and forest interactions

THE YIELDING PHENOMENA The presence of a stage 0 of hardening, the yield region of silicon studied in Chapter 5, is not typical of covalent crystals but could be theoretically observed in any type of material that plastically deforms by means of nucleation and multiplication of slip dislocations[1]. [Estrin 1986] predicted the existence of such an instability in materials presenting a deficit of mobile dislocations in the very early stages of deformation. The lack of mobile dislocations prevents the material from accomodating smoothly the imposed deformation rate, and an intense multiplication follows. Once the number of mobile dislocations is sufficient to ensure normal plastic flow, the classical hardening stages can set in. Of importance is that this softening behaviour does *not* depend on the availability of fixed dislocations, but on the relative initial density of mobile dislocations compared to their saturation density, which in turn depends on the total dislocation density, linked to the density of dislocation sources. Of course, deformation conditions (temperature, strain rate) influence the saturation density as well.

DISLOCATION MULTIPLICATION The very early deformation stage of as-grown silicon crystals presenting extremely low dislocation densities is characterized by an intense multiplication that proceeds mainly by activation of

1 The strong dependence of the yield stresses and yield drop on temperature and strain rate is nonetheless a characteristic of covalent crystals, due to the highly thermally activated dislocation velocity combined to its low stress sensitivity.

Frank-Read sources and to a much lesser extent by double cross-slip in the bulk. The former mechanism has been observed for a long time [Dash 1956] and modeled by [Moulin 1997a, Moulin 1997b]. The latter mechanism has been observed *in situ* by X-ray topography, especially at the surfaces where image forces are thought to enhance stress-assisted cross-slip events (see [Siethoff 1973, Kirscht 1978a]). Pioneering articles also mentionned this possibility [Alexander 1968]. The question of whether cross-slip actually takes place in bulk material of low (or no) forest density posed by [Michel 1986] has been solved by X-ray observations of [Vallino 2001] that confirmed it is the case. Increasing temperature eventually eases the cross-slip probability as postulated [Aseev 1975] and confirmed by the dislocation dynamics simulations of [Moulin 1997a]. However at the intermediate temperatures considered in this Chapter, [Moulin 1997a] has shown that dislocation multiplication by double cross-slip is a rather limited phenomenon.

FOREST OBSTACLES The influence of forest dislocations on the yield region has been noticed by [Suezawa 1979]. Higher values of the lower yield stresses in crystals containing lower initial dislocation densities can be explained by the activation of secondary slip systems at low strains. Dislocations would hence multiply on these systems and increase the flow stress of the primary system. This process is known as *latent hardening* and is introduced in Section 6.3.2.

In addition to the effect of forest dislocations on the flow stress, their contribution to *multiplication* of primary dislocations has been mentioned and modelled later by [Sumino 1993, Sumino 1999]. Point-like obstacles such as jogs or forest trees can act as anchoring points for the creation of Frank-Read sources. Dislocation multiplication from forest trees and superjogs has actually been observed in silicon by [Louchet 1980].

In spite of the different dislocation motion mechanisms at very high temperatures, the yield phenomena is still observed by [Yonenaga 1996] in pure dislocation-free silicon crystals up to 1573 K deformed uniaxially. The initial presence of dislocations leads to the disappearance of the upper yield point, in agreement with observations at lower temperatures.

Stored dislocations

The dislocation dynamics (DD) simulations of [Moulin 1997a] point to a building-up of a density of immobile, stored dislocations on the primary slip plane in the yield region, although this phenomena has been deemed by simulations to be quite marginal and noticeable only in the vincinity of the lower yield point. His simulations nevertheless considered crystals of very low initial densities (7.5×10^7 m^{-2}) and no multiple slip was accounted for, so that the phenomena suggested by [Suezawa 1979] could not take place and no effect of the forest could be studied.

Of interest is that self-interaction between dislocations on the primary system is actually responsible for the appearance of immobile dislocations. Trapping of dislocations into dipoles or multipoles described next can be

an explanation. The presence of a forest would definitely enhance this evolution by creation of sessile junctions and other dislocation reactions.

The fraction of immobile dislocations at the lower yield point and beyond seems to be quite high from experimental results. Compression of prestrained silicon samples shows that the density of mobile dislocations at the lower yield point is weakly dependent on the deformation conditions, suggesting that it reaches a steady state value upon the initial loading of virgin samples [Omri 1987]. Observations in germanium indicate a rather low percentage of mobile dislocations at the lower yield point [Sumino 1974]. This is in agreement with the TEM observations in silicon of [Oueldennaoua 1988], with less than 15 % mobile dislocations at the end of stage I.

6.2.2 *Hardening stage I*

The yield region is characterized by high flow stresses enhanced by low temperatures or high strain rates. In conjunction with the intrinsic low dislocation densities of silicon crystals preventing the existence of short-range interactions, this leads to dislocation loops having their characteristic hexagonal shape, with segments having a screw or 60° character and lying in Peierls valleys. The junction between those straigth segments is actually curved and made up of an accumulation of geometrical kinks; the effective stress acting on dislocations can be deduced from the curvature as discussed by [Louchet 1980, Gottschalk 1983a, Gottschalk 1983b].

As the flow stress diminishes beyond the upper yield point and the total dislocation density increases, dislocation interactions gain in importance and the hexagonal shape disappears to let a more classical, edge-dominated dislocation population develop [Alexander 1968, Aseev 1975]. Figs. 6.1 and 6.2 show TEM images of dislocations in germanium deformed at 520°C at the upper and lower yield points respectively ([Alexander 1986]). This transition between hexagonal and curved dislocations is enhanced by high temperatures and high forest densities [Wagatsuma 1971]. From the beginning of stage I, dislocation interactions and hardening mechanisms resemble those of fcc metals ([Alexander 1986] and references therein). See also [Allem 1989] for observations of dislocation structure in the yield region of silicon and [Omri 1987] for numerous foil observations at the end of stage I that confirm the analogy between both material classes. The literature related to fcc crystals is indeed a valuable source of knowledge.

Evolution of dislocation densities

DIPOLE FORMATION Two dislocation segments belonging to the *same* slip system but gliding on parallel planes and having opposite Burgers vectors can trap each other if they get close enough to allow their stress fields to lock them. The formation of such a dipole structure is a first source of storage of previously mobile dislocations. Dislocations trapped in dipoles

tend to rotate in order to minimize the dipole energy [Amodeo 1990]; dipoles of mixed nature (that is neither edge nor screw) rotate towards an edge orientation for the same reason [Hoc 2004]. The maximum edge dipole height $h_{max,e}$ depends on the effective stress and reads [Hähner 1996]:

$$h_{max,e} = \frac{\mu b}{8\pi (1-\nu) \tau_{eff}} \tag{6.1}$$

Such an expression can be found for screw dipoles as well, replacing $8\pi(1-\nu)$ by 4π and yielding $h_{max,s}$.

DISLOCATION ANNIHILATION The components of a dipole can annihilate each other by cross-slip climb, depending on their nature. A newly formed dipole can either be destroyed by the application of a larger stress, strenghtened by the insertion of a new dislocation in between the two original ones, or disappear if its components are close enough to annihilate.

Screw segments eventually annihilate by cross-slip much easier than edge segments do by climb, which explains the edge-dominated dislocation population in stage I. These evolutions are also observed in silicon and germanium crystals [Kojima 1971, Aseev 1975, Yonenaga 1993].

JUNCTION FORMATION We now concentrate on short-range interactions between dislocations belonging to *different* slip systems. It has been long observed that forest dislocations contribute significantly to the flow stress by formation of junctions [Schoeck 1972]. In addition, dislocation pinning on forest obstacles can lead to the formation of additional dislocation sources by a Frank-Read mechanism. Consequently, forest dislocations play a significant role both on the flow stress and dislocation multiplication mechanisms.

Short-range interactions between dislocations come mainly from two contributions: the core interaction at their junction and the local elastic stress fields created by the lattice defaults. Core interactions are actually negligible compared to the strength of the elastic fields [Devincre 2001]. A property of the latter is *not* to depend sensitively on the temperature, except for the variations of the shear modulus.

Two intersecting dislocations can either attract or push back each other, depending on their elastic stress fields. When the attractive forces are high enough, a junction forms at the intersection and creates a "third" dislocation segment, common to the first two. The nature of this junction segment (its Burgers vector) is defined by its parents and defines whether the junction is sessile or glissile. In order to destroy the junction, a stress high enough to "unzip" it must be applied on its parents, leaving atomic jogs on them. Fig. 6.3 shows such a junction formation for perfect dislocations; the case of dissociated dislocations complicates slightly the picture [Rodney 1999].

Latent hardening experiments performed on copper and aluminium crystals by [Franciosi 1982a, Franciosi 1982b] have revealed the importance of

	A2	A3	A6	B2	B4	B5	C1	C3	C5	D1	D4	D6
A2	SH	Co	Co	CS	GJ	GJ	HL	GJ	LC	HL	LC	GJ
A3	Co	SH	Co	GJ	HL	LC	GJ	CS	GJ	LC	HL	GJ
A6	Co	Co	SH	GJ	LC	HL	LC	GJ	HL	GJ	GJ	CS
B2	CS	GJ	GJ	SH	Co	Co	HL	LC	GJ	HL	GJ	LC
B4	GJ	HL	LC	Co	SH	Co	LC	HL	GJ	GJ	CS	GJ
B5	GJ	LC	HL	Co	Co	SH	GJ	GJ	CS	LC	GJ	HL
C1	HL	GJ	LC	HL	LC	GJ	SH	Co	Co	CS	GJ	GJ
C3	GJ	CS	GJ	LC	HL	GJ	Co	SH	Co	GJ	HL	LC
C5	LC	GJ	HL	GJ	GJ	CS	Co	Co	SH	GJ	LC	HL
D1	HL	LC	GJ	HL	GJ	LC	CS	GJ	GJ	SH	Co	Co
D4	LC	HL	GJ	GJ	CS	GJ	GJ	HL	LC	Co	SH	Co
D6	GJ	GJ	CS	LC	GJ	HL	GJ	LC	HL	Co	Co	SH

Table 6.1: Types of interactions between dislocations on different slip systems. SH: self-hardening; Co: coplanar systems; GJ: glissile junction; LC: Lomer-Cottrell locks; HL: Hirth locks; CS: collinear systems. From [Franciosi 1982a].

the *type* of interaction between different slip systems. Two intersecting dislocations can interact in different ways, depending on the relative geometrical orientation their respective slip systems and leading to different dislocation reactions and junction types. The six possible types of interactions are: self-interaction, coplanar interaction, collinear interaction between a system and its cross-slip counterpart. In the case of forest interactions, the reactions can lead to formation of glissile junctions, of Lomer-Cottrell locks and of Hirth locks. Some of these interactions have indeed been observed in silicon crystals [Kirscht 1978b]. Out of these only the last four are reactions, the first two being dipolar interactions. Table 6.1 gives the type of interaction between two given systems, using Schmid & Boas notation.

The relative strength of these interactions was initially measured by latent hardening experiments [Franciosi 1982a, Franciosi 1982b, Franciosi 1985, Wu 1991, Bassani 1991]. This method has however several drawbacks as it requires backward extrapolation of the flow stress in order to define the beginning of the hardening stage as discussed in [Nemat-Nasser 2004]. It has been also suggested by [Franciosi 1986] that the anisotropy of the interaction coefficients matrix depends on the stacking fault energy of the material. Literature on covalent crystals is extremely sparce, apart from proceedings published by the Nancy research group [Michel 1986] and experimental results obtained on germanium crystals [Alexander 2000].

More recently, the development of dislocation dynamics (DD) simulations allowed for a detailed and quantitative description of the influence of each interaction type. See for example [Kubin 1998, Devincre 2001] for a

presentation of the method. In particular, the critical role of the collinear interaction in hardening behaviour of fcc metals has been demonstrated by [Madec 2003, Devincre 2005]. The strength of dislocation reactions is governed by the junction length: the longer the unzipping arm the weakest the junction [Devincre 2006]. This explains the strong collinear interaction and the weak Hirth lock.

The formation of junctions with forest dislocations also immobilizes primary dislocations. Although this mechanism was thought to dominate hardening during stage I (the particular role of the Lomer lock being emphasized), DD simulations have recently shown that the collinear interaction is a much better candidate to explain the hardening behaviour of fcc crystals in easy glide [Madec 2003, Devincre 2005]. It allows for creation of a three-dimensional microstructure, and when combined with annihilation of screws leads to the creation of superjogs in the collinear system that have a strong interaction force with primary glide dislocations. This also explains stage I hardening in crystals with no forest density such as as-grown semiconductors. These collinear segments control the transition from stage I to II of hardening [Devincre 2005]. If the forest density is significant, other types of junctions can form and lead to further storage of dislocations. The influence of jogs on gliding dislocations in silicon crystals has been mentioned in [Sumino 1971, Aseev 1975].

DISLOCATION MULTIPLICATION AND STORAGE Stress- or thermally assisted double cross-slip allows for multiplication of dislocations from a parallel slip plane, and creates dipolar loops having segments in the collinear system as well [Hirth 1982]. Cross-slip can be enhanced by the stress field of locked dislocations on parallel slip planes. Mobile dislocation loops create this way other mobile loops as they expand. This phenomena has been observed and modeled, and is known as the Johnston-Gilman hardening model [Johnston 1959, Gilman 1960, Li 1961].

As mobile dislocations multiply, the probability of formation of dipoles or other dislocation structures increases, leading to the appearance of a "sink" for mobile dislocations. A density of stored dislocations builds up. This eventually allows for a steady state of the density of mobile dislocations, as observed for example by [Sumino 1971, Yonenaga 1978, Oueldennaoua 1988, Moulin 1997a] in silicon, and commonly in fcc crystals. A consequence is the decrease of the relative density of mobile dislocations, while the total density keeps on growing. Note that the total dislocation density increases quite slowly during stage I, as translated by the relatively low hardening coefficient of the stress-strain curves and confirmed experimentally [Kojima 1971].

Internal stress

NATURE OF THE INTERNAL STRESS Stage I differs from stage 0 by the presence of short-range elastic interactions due to junction formation that

overwhelm progressively the long-range elastic stresses. Trapping of dislocations and formation of edge dipoles or multipoles, as well as intersection of dislocations with the trees of the forest and creation of debris on the cross-slip system create strong short-range interactions that hinder further dislocation movement and increase hardening of the crystal. It has been calculated that short-range interactions are responsible for roughly 80 % of the flow stress in fcc crystals, independently of temperature and strain rate [Devincre 2001, Kubin 2008a].

Meanwhile, the stress sensitivity of dislocation velocity in fcc crystals is much higher than in as-grown covalent crystals. Consequently, at the relatively low dislocation densities observed in stage I of semiconductors, short-range interactions are expected to influence less the flow stress than they do in fcc crystals. This is not expected to be true in stage II of hardening, where dislocation densities are much higher and Lomer locks are observed to form.

LONG-RANGE INTERNAL STRESSES Considering dislocation motion to proceed in one direction only, some authors have tried to determine the nature of long-range elastic interactions. The motion of dislocation segments is affected by the presence of internal stresses and the applied stress τ is reduced by the athermal internal stress field τ_{int}, leading to the definition of a *local* effective stress $\tau_{eff} = \tau - \tau_{int}$. The effective stress is usually fluctuating along a given dislocation line and between dislocations, as the wavelength of the microscopic internal stress ought to be much shorter than the one of the macroscopic applied stress. Locally only, the dislocation velocity in silicon is proportional to the effective stress $v \propto \tau - \tau_{int}$ because of its linear stress sensitivity. The use of a mean velocity $\overline{v}$ for macroscopic applications requires the definition of the mean effective stress $\overline{\tau}_{eff}$.

Considering a dislocation moving one-dimensionally under an athermal internal stress $\tau_{int}(x)$ between two obstacles separated by a distance l_v (see [Kocks 1975]) the mean velocity reads:

$$\overline{v} = \frac{l_v}{\int_0^{l_v} \frac{\mathrm{d}x}{v(x)}} \tag{6.2}$$

where $\int_0^{l_v} \frac{\mathrm{d}x}{v(x)}$ is the time required for the dislocation to move between the obstacles. Solving this equation requires the knowledge of the one-dimensional spatial variations of the internal stress. A usual assumption is that:

$$\tau_{int}(x) = \tau_b + \tau_{max} \sin\left(2\pi x / l_v\right) \tag{6.3}$$

The internal stress is additively decomposed into a constant component τ_b and a quickly fluctuating one $\tau_{max} \sin\left(2\pi x / l_v\right)$. Neglecting the stress dependency of the activation energy, Eq. 6.2 leads to $\overline{v} \propto \overline{\tau}_{eff}$ with $\overline{\tau}_{eff} = \sqrt{(\tau - \tau_b)^2 - \tau_{max}^2}$.

Dislocation motion requires that $\tau > \tau_b + \tau_{max}$; the effective stress and mean velocity are null otherwise. In the absence of forest dislocations and

using experimental results obtained on germanium crystals, [Sumino 1971, Sumino 1974] demonstrated that in a dynamical state $\tau_{max} \ll \tau_b$. This yields $\overline{\tau}_{eff} = \tau - \tau_b$. The elastic, long-range interactions between dislocations in easy glide are consequently constant along the slip plane.

The low curvatures of mobile dislocation lines observed in silicon by [Oueldennaoua 1988] have led these authors to conclude that the mean effective stress acting on dislocations at the lower yield point and beyond in predeformed specimen is very close to the applied stress. They conclude hereby that $\tau_b \ll \tau_{max}$, in disagreement with the results obtained by the Japanese group. This applies to isolated dislocations, located between tangles and in regions suitable for observations. This apparent contradiction can be solved by remembering that the French group has studied pre-deformed samples in which the density of immobile dislocations is not negligible. It is therefore possible that short-range interactions take on a larger role than long-range elastic stress fields screened by high dislocation densities. In a dynamical state, the results of [Sumino 1971, Sumino 1974] should hold.

6.2.3 *Late deformation stages*

As deformation proceeds the lattice rotates with respect to the tensile axis and the projections of the applied stress on the slip systems change. These variations of the Schmid factors eventually lead to the activation of previously latent systems. A multislip deformation mode sets in. Junctions and interactions between the different slip systems are generated during stage II. Its athermal nature is translated in fcc crystals by an almost constant strain hardening rate $\theta = d\tau/d\gamma \simeq \mu/250$ [Kocks 2003]. This is also valid in semiconductors [Kojima 1971, Siethoff 1978]. Long-range interactions progressively gain importance because of the formation of pile-ups from the junctions and the development of an early spatial structure.

A complex dislocation network progressively builds up until stage III sets in, when the applied stresses become high enough to overcome the long-range internal stresses and allow cross-slip or climb to relax the local stress peaks and form dislocation patterns [Louchet 1988, Kocks 2003] . Internal stress peaks are noticed in complex dislocation structures (walls) and locally enhance cross-slip and annihilation of dislocation segments in a thermal manner. The collinear interaction assists athermally this dynamic recovery by allowing for annihilation of segments of all natures [Madec 2002b, Devincre 2005]. This late recovery stage and its followers (stages IV and V) have been described in Part i of this book for the case of silicon. Note that dynamic recovery is a process that is depending on the stacking fault energy of the material and is therefore intimately related to core properties of dislocations.

It must be noted that in the cases where multiple slip is active straight from the beginning of deformation, dislocation interactions and patterning similar to the stage II described above are observed immediately. Such

situations arise either because of complex loading conditions or because the tensile axis (in the case of uniaxial tensile testing) is on a high-symmetrical orientation. Indeed in multi- or polycrystals the geometrical configurations and compatibility between grains might lead frequently to multislip deformation.

6.2.4 *Very high temperatures (T>0.8 T_m)*

The case of very high temperature deformation is worth mentioning, as solidification of silicon ingots proceeds from the melting temperature. Dislocation velocity has been observed to be thermally activated even at very high temperatures, a transition operating above 1323 K in pure, dislocation-free crystals[2] [Farber 1982, Siethoff 2001]. Apart from the change of the activation energy for dislocation mobility detected above this limit, climb of dislocation segments allows for relaxation of the sources of internal stress. Short range obstacles are easily overcome and a significantly less marked spatial structure is observed [Aseev 1975]. The formation of subgrain walls and subcells is actually active in silicon crystals after only 50 minutes of creep at 20 MPa.

As mentioned previously, some experiments in uniaxial tension of silicon monocrystals conclude on similar deformation mechanisms at very high and high temperatures [Yonenaga 1996]. This does not exclude quantitative variations in the velocity parameters and does not give detailed information about the hardening mechanisms beyond the yield region.

6.2.5 *Model requirements*

The model we are about to develop does *not* aim at describing the hardening and recovery stages beyond stage III, characterized by strong dislocation patterning that continuum models cannot represent. It should describe accurately the yield region and stage I, as well as activation of secondary systems during stage II and the *transition* into stage III. In addition to these qualitative features, it should as well be able to represent correctly the variation of the mechanical behaviour of silicon crystals with temperature and strain rate. The model should indeed be based on physical principles, namely the generation, multiplication, storage and annihilation of dislocations responsible for plastic flow. The activation of several slip systems and their mutual interactions leading to enhanced hardening should be accounted for.

These requirements pose problems. An example is the extremely wide temperature (or equivalently, strain rate) range that we want to cover. It is believed that nucleation and propagation of double kinks along the dislocation line is the main mechanism steering dislocation motion below

2 This transition temperature applies at relatively high applied (or effective) stresses, above 10 MPa. Lower stresses shift this transition to higher temperatures.

temperatures of approximately 0.8 T_m, that is 1200 K. [Moulin 1997a] actually points out the limits of his model beyond such a temperature. This is unfortunately the temperature range where most experiments have been performed, so the equations founding the models used until now (see Chapter 5) might not be relevant at very high temperatures. With lattice friction disappearing forest hardening might play an important role, bringing the mechanical behaviour of covalent crystals close to the one of fcc metals. The existence of a mixed mode, where lattice friction and other internal stress sources have the same magnitude, is bound to complicate our task. We disregard in this work the case of very high temperature hardening mechanisms.

Dislocation velocity

As for dislocation velocities, all expressions introduced until now in the literature consider isolated dislocations moving in a perfect lattice, exempt from forest trees or impeding obstacles.

On the other hand, it can be easily conceived that when the forest density builds up the *averaged* dislocation velocity might differ from Eq. 5.1 which represents the ideal case of *free flight of dislocations moving by the double kink mechanism*. In the presence of localized obstacles the movement of a dislocation line would be a succession of "stop-and-go" events between the trees or point obstacles. [Sumino 1971] noticed for example a change of the dislocation velocity activation energy in stage II of deformation of germanium crystals. Note that this mode of motion is similar to what is commonly observed in fcc crystals and therefore relies on the absence of any strong lattice friction that would govern dislocation velocity. See Figure 6.4 for a brief outlook of the various domains to cover.

Internal stresses

The nature of obstacles to dislocation motion is closely linked to the derivation of dislocation velocity. Each obstacle affects dislocation motion either in an athermal way, e.g. by the long-range stress fields it generates, or by creating thermally overcomable barriers. The former type of internal stress should enter directly into the definition of the effective stress: dislocation motion is simply impossible if the applied stress is lower than the internal stress. On the other hand, thermally activated barriers can be overcome with the help of temperature and the application of a finite stress. Example of such obstacles are small precipitates, junctions, etc.

Evolution of dislocation densities

At low densities, typically in as-grown crystals, multiplication of dislocations is found to follow a law given by one of the models introduced in Chapter 5. Keeping in mind that these laws have been experimentally verified at temperatures below 1273 K and low dislocation densities, one

immediately notices that their validity might be severly compromised even in the case of such intermediate temperatures but high dislocation densities (that is, when forest interactions ought to increase the dislocation density by creation of new Frank-Read sources, as exemplified by a percolation model [Cuitiño 1992, Kocks 2003]). A model that covers both low and high densities should account for all mechanisms and possibly discriminate between domains where the occurence of one is more likely than the other. The case of bcc crystals has once again emphasized the difficulty of accurately modeling hardening mechanisms in the thermal range [Tang 1999].

Storage of dislocations into tangles or multipoles that have short-range elastic stress fields, annihilation of screw segments by cross-slip should also be taken into account. The influence of temperature (or strain rate) is double-fold: it first enhances storage of dislocations and increases the occurence of thermally activated recovery mechanisms such as climb or cross-slip. In practice this should be translated by a dependence of some coefficients of the model with the deformation conditions.

Conclusions

All requirements introduced above cannot be easily fulfilled by a simple model as derived in this Part. Some aspects must consequently be left aside.

Building on the work of [Alexander 1968], we neglect the possible influence of secondary dislocations on dislocation multiplication. Next Section details extensions brought to the original model enhancing its accuracy and physical validity to a broad range of temperatures and strain rates. As will be seen, some simplifications are done to the internal stress and dislocation velocity, in order to keep the constitutive model light and numerically efficient.

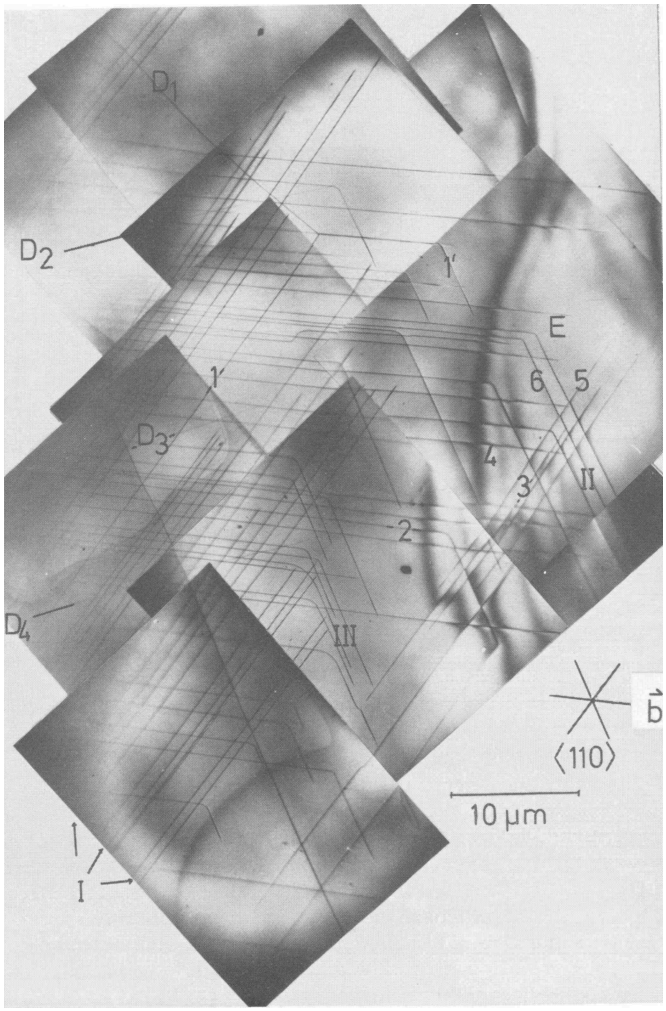

Figure 6.1: TEM of the primary slip plane of germanium deformed at 520°C at the upper yield point ($\tau = 40\,\mathrm{MPa}$) [Alexander 1986].

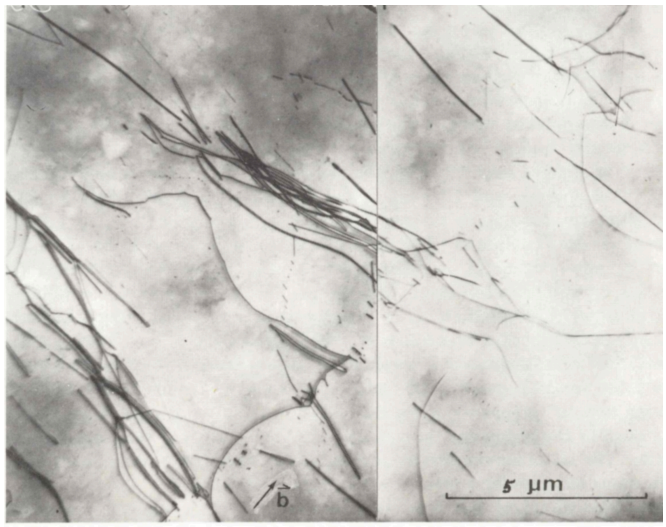

Figure 6.2: TEM of the primary slip plane of germanium deformed at 520 °C at the lower yield point ($\tau = 6.9\,\mathrm{MPa}$) [Alexander 1986].

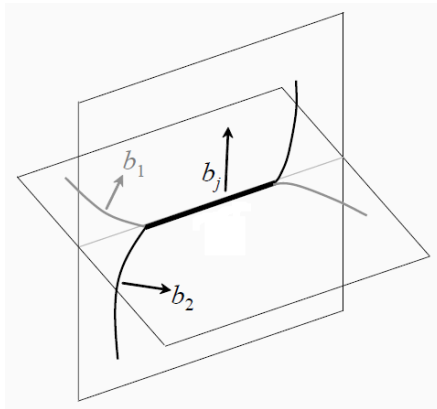

Figure 6.3: Formation of a junction of Burger's vector $\mathbf{b}_j$ after intersection of two dislocations of respective Burger's vectors $\mathbf{b}_1$ and $\mathbf{b}_2$.

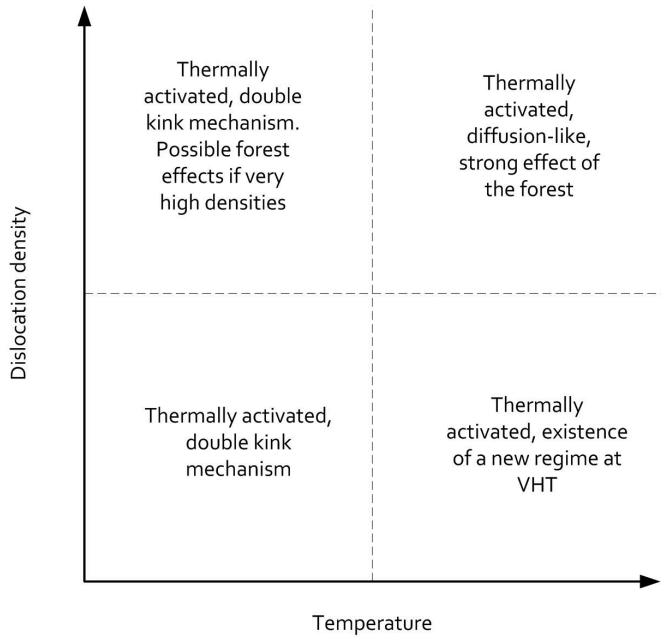

Figure 6.4: Different motion mechanisms as a function of temperature and dislocation density. Motion is always thermally activated because of the (low) stress level considered in this work, see Part i for details.

6.3 CONSTITUTIVE EQUATIONS FOR INTRINSIC CRYSTALS

We introduce in this Section the equations of a constitutive model for silicon, assuming that the dislocation multiplication law of [Berner 1967, Alexander 1968] is valid into stage I of deformation. As seen previously, any constitutive model requires expressions of the dislocation velocity, internal stress and the laws that rule the evolution of the dislocation densities. The dislocation velocity law being at the heart of the definition of the plastic behavior of a material, it is introduced first. The results of this Section and the following ones have been published in [Cochard 2010a, Cochard 2010b].

6.3.1 *Average dislocation velocity*

Theoretical aspects

A fundamental issue that prevents from a straightforward determination of dislocation velocity is the nature of motion mechanisms. It is widely accepted that at rather low temperatures (below 0.6 to 0.75 T_m) dislocation motion in covalent crystals having a strong Peierls potential proceeds by means of nucleation and propagation of double kinks along the dislocation line [Alexander 1968, Hirth 1982, Iunin 2001]. The existence of a stress-dependent regime due to the dissociation of dislocations modelled by [Möller 1978] has been ruled out by [Imai 1983] who observed no appearance of a new regime towards low applied stresses (of the order of 1 MPa). Hence, we disregard the possible existence of this low-stress regime.

Experimental results

The collective velocity of screw dislocations in an intrinsic silicon crystal is experimentally given by Eq. 6.4, with $v_0 = 3.5 \times 10^4\,\mathrm{m.s^{-1}}$, $m_0 = 1$, $\tau_0 = 1\,\mathrm{MPa}$, and $U = 2.35\,\mathrm{eV}$ ([Imai 1983]). The effective stress $\tau_{eff}^{(\alpha)}$ on a slip system α is the difference between the resolved shear stress and the back stress $\tau_{int}^{(\alpha)}$ which can also be assimilated to a kinematic hardening term: $\tau_{eff}^{(\alpha)} = \left\langle \left| \tau^{(\alpha)} \right| - \tau_{int}^{(\alpha)} \right\rangle$, where $\langle x \rangle = 0$ if $x \leq 0$ and $\langle x \rangle = x$ otherwise. In practice, this back stress is the long-range elastic stress field acting on moving dislocations.

$$v^{(\alpha)} = v_0 \left(\frac{\tau_{eff}^{(\alpha)}}{\tau_0} \right)^{m_0} \exp\left(-\frac{U}{k_b T} \right) \tag{6.4}$$

Double kink model - comparison of theory to experimental results

In Eq. 6.4 U is the apparent activation regime equal to $U_{kp} + U_m$ in the low stress approximation (see Part I and [Caillard 2003]). The velocity

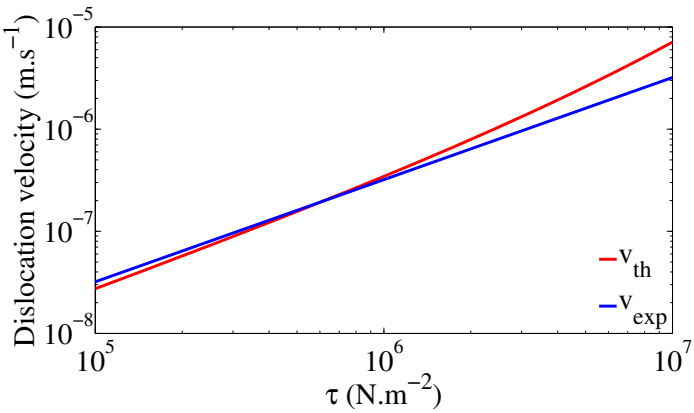

Figure 6.5: Velocity of screw dislocations in silicon using the experimental law (Eq. 6.4, law 1) [Imai 1983] and the double-kink theory (Eq. 6.5, law 2) [Hirth 1982, Caillard 2003], as a function of effective shear stress at a temperature of 1073 K. $X_c = 0.7\,\mu m$.

expression stemming from the double kink theory is given by Eq. 6.5, where $X_c = 1\,\mu m$ according to [Caillard 2003]:

$$v^{(\alpha)} = \left(\frac{\frac{3}{4}\nu_D b^3 X_c}{k_b T} \right) \tau_{eff}^{(\alpha)} \exp\left(\frac{-U + \frac{b^3}{4}\sqrt{\frac{\mu \tau_{eff}^{(\alpha)}}{\pi}}}{k_b T} \right) \tag{6.5}$$

Figs. 6.5 and 6.6 show the velocities obtained from Eqs. 6.4 and 6.5 as a function of effective stress and temperature, respectively. No significant difference can be noticed between the two formulations in the temperature and stress range of interest. The double kink theory using an apparent dislocation segment $X_c = 1\,\mu m$ predicts too high velocities. This discrepancy arises from the value of the apparent length that is not clearly defined; using $X_c = 0.7\,\mu m$ instead yields better agreement, as seen in the Figures.

Dislocation velocity at very high temperatures

What happens beyond 1200 K is not clear enough. X-ray topography has allowed for observation of dislocations in bulk specimen at temperatures as high as 1273 K, and the activation energy was calculated to be of 2.2 eV or 2.4 eV for 60° and screw dislocations respectively [Nishino 1984], the same as at lower temperatures. Diffusion-like mechanisms are believed to progressively become the rate-limiting motion mechanism, translated by an increased activation energy observed in dislocation-free crystals [Farber 1982, Siethoff 2002]. Since the presence of as-grown dislocations shifts this very high temperature regime towards even higher homologous temperatures, we ignore it here and assume that Eq. 6.4 is valid up to the melting point.

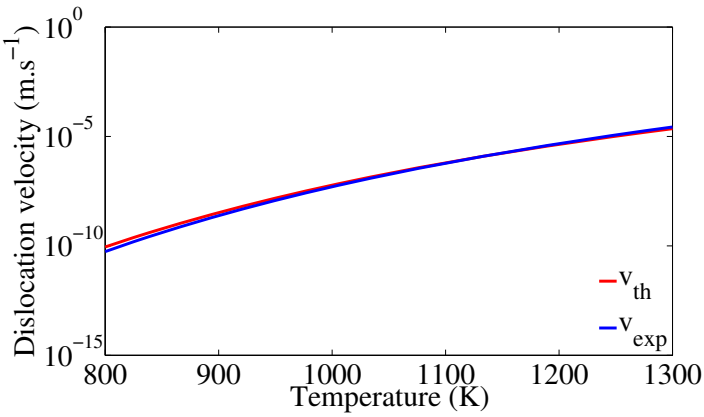

Figure 6.6: Velocity of screw dislocations in silicon using the experimental law (Eq. 6.4, law 1) [Imai 1983] and the double-kink theory (Eq. 6.5, law 2) [Hirth 1982, Caillard 2003], as a function of temperature and under an effective shear stress of 1 MPa and $X_c = 0.7\,\mu m$.

Influence of forest dislocations on the mean dislocation velocity

The influence of forest dislocations has never been taken into account in constitutive models for covalent crystals, and traditionally excluded from the quantitative discussions on dislocation velocity in silicon crystals. The reason is probably that the motivation for research has been its applications in the semiconductor industry requiring virtually dislocation-free crystals. Silicon deformed beyond stage 0 would not appeal the modeling sense of physicians. As mecanicians dealing with solar-grade materials we must find a way to fill this gap.

At large forest densities, dislocation motion is hindered by the presence of short-range obstacles along the dislocation lines and is similar to motion in fcc crystals, as discussed above. Motion is then a succession of pinning and unpinning events, dislocations moving freely between the anchoring points (junctions at the trees). The average velocity of dislocations can be written using the formalism of thermally activated glide [Kocks 1975, Nemat-Nasser 2004]:

$$\overline{v} = l_v \nu_{eff} \exp\left(-\frac{\Delta G(\tau_{eff}, T)}{k_b T}\right) \tag{6.6}$$

with l_v the average distance that dislocations move on the slip plane between consecutive barriers, and ν_{eff} the effective frequency of attempts to overcome short-range barriers of height ΔG. In the case of forest hardening, the mean free path l_v is roughly given by the inverse of the square root of the forest density.

$$l_v \propto \frac{1}{\sqrt{\rho_f}} \tag{6.7}$$

The expression of the mean free path of dislocations is nevertheless more complicated to calculate and should incorporate the effects of self-interaction and coplanar interactions as well, see [Kubin 2008b] for more details.

Simple models for dislocation velocity in fcc metals assume $\overline{v}$ to be highly stress-sensitive, motion setting in only at effective stresses close to the unlocking stress τ_c (see next Section):

$$\overline{v} \propto \left(\frac{\tau_{eff}}{\tau_c} \right)^m \tag{6.8}$$

with $m \gg 1$. Such an approximation stemming from a Taylor development of Eq. 6.6 close to τ_c is not directly applicable to silicon, as the influence of the double kink mechanism must be accounted for. This will be done in the next Part.

Conclusion: dislocation velocity expression

Two aspects seem clear from the previous discussion.

- First, motion of isolated dislocations in silicon is a thermally activated process characterized by an (almost) linear effective stress dependency and an apparent activation energy of roughly 2.3 eV in the whole temperature range where plasticity is macroscopically observed. The case of very high temperatures and diffusion-like motion mechanisms is ruled out from our model.
- Secondly, the influence of forest dislocations, impurities or other defects interacting with moving dislocations has a direct effect on their mobility by reducing their mean free path, increasing the internal stress and ultimately changing the rate-limiting motion mechanism.

Given that we develop a constitutive model for silicon based on the work of Alexander & Haasen we adopt in this Chapter the classical velocity expression given by Eq. 6.4. Additional effects such as the influence of thermally overcomable localized obstacles on the slip plane will be considered in the next Part of this work. As a simplification, forest obstacles are considered in the present Chapter to be athermal in nature and included in the expression of the internal stress (see next Section).

The activation energy for 60° dislocations $U = 2.2\,\text{eV}$ is chosen in the following instead of the one related to screw segments because we do not limit the applicability of the model to stage 0. In stage I the density of screw dislocations is observed to be reduced as they can annihilate easily by cross-slip; the majority of segments exhibit an edge character.

A simple model for edge dislocations can be derived by considering the projection of the *velocity vector* of a 60° segment onto the edge orientation, yielding a factor 1/2. As an approximation we can take $v_0 = 0.5 \times 10^4 \text{m.s}^{-1}$.

The exact value of v_0 is actually not important. Considering Orowan's law, at a given plastic strain rate the mobile dislocation density will adapt to v_0 in order for $\rho_m b v$ to equal $\dot{\gamma}$. Incidentally, $v_0 = 5 \times 10^3\,\text{m.s}^{-1}$ and

$U = 2.2\,\text{eV}$ are values very close to the ones chosen by [Suezawa 1979] to identify the constitutive parameters of the classical AH model. This allows a direct comparison of our results with theirs, see Section 7.3.

6.3.2 *Flow stress and internal stress*

The flow stress τ is the stress required to apply on the specimen to keep deforming it at given thermodynamic conditions. The flow stress usually increases with deformation, this phenomena being called strain hardening. In the athermal regime τ is made of the internal stress only. The latter can be divided into two components, as in Eq. 6.9. The former term (τ_{lr}) is related to long-range stress fields characterized by a slow spatial decay proportional to r^{-1}. The second term aims at representing other sources of internal stress exhibiting short-range behaviors ($\propto r^{-2}$, τ_{sr}).

$$\tau_{int} = \tau_{lr} + \tau_{sr} \tag{6.9}$$

Using the athermal and thermal parts of the flow stress gives Eq. 6.10. τ_{int} is the internal stress above-mentioned, whereas τ_{eff} is the effective stress, required to overcome the thermal barriers, e.g., formation of double kinks and their subsequent propagation. It is sometimes written τ^* in the literature, and assimilated to the thermal part of the flow stress that depends on temperature and strain rate. The goal of this Section is to determine the expression for the internal stress.

$$\tau = \tau_{eff} + \tau_{int} \tag{6.10}$$

Long-range internal stress

The classical approach for silicon crystals has always been to consider that only mobile dislocations contribute to the internal stress, because their stress field vanishes proportionally to the inverse of the distance compared to a quadratic dependence for dipoles [Alexander 1968, Hirth 1982]. Dipoles or multipoles are characterized by an elastic stress field of shorter range than the one created by mobile segments. Consequently, we consider immobile dislocations not to participate to the expression of the long-range elastic stress as is usually done.

The traditional way of describing the long-range elastic stresses stemming from dislocations is to use a proportionality of the critical resolved shear stress to the square root of the dislocation density, Eq. 6.11 being commonly chosen in constitutive models of silicon crystals [Alexander 1968, Suezawa 1979, Alexander 1986, Dillon 1986] (see Chapter 5). No distinction is made between the different slip systems, as this equation is valid for uniaxial deformation of as-grown crystals that have low densities on the secondary systems.

Note that this equation is extremely similar to the Taylor formula commonly used for fcc metals, that relates the critical resolved shear stress

to the square root of the *forest* density $\tau_c = \mu b A \sqrt{\rho_f}$, with a prefactor $A \simeq 0.35 \pm 0.1$. It is important to keep in mind that in the case of pure silicon crystals in the early stages of deformation the forest is virtually absent and that a Taylor expression would hence not be relevant.

$$\tau_{int} = \mu b A \sqrt{\rho_m} \tag{6.11}$$

A more advanced model, accounting for the presence of dislocations on the secondary systems, has suggested an additivity of the stresses stemming from the densities on the different systems (see [Sumino 1993] who adopted Eq. 6.12):

$$\tau_{int}^{(\alpha)} = \mu b A_\alpha \sqrt{\rho_m^{(\alpha)}} + \mu b A_f \sqrt{\rho_f^{(\alpha)}} \tag{6.12}$$

If one chooses to add up the contributions of the secondary slip systems to the internal stress, then it is not mathematically right to aggregate their densities into a single one, since $\sum_i \sqrt{x_i} \neq \sqrt{\sum_i x_i}$. One could argue that the discrepancy is reduced when the x_i are small, but we are looking for a general law that could account for the case of large densities on the secondary systems. Adopting such a law requires the computation of the interaction coefficients, that are *a priori* geometrically determined *only by the relative orientation of the different slip systems*. A more realistic expression would then be Eq. 6.13, where the interaction coefficients $\left(A_{\alpha\beta}\right)_{\alpha,\beta=1,12}$ are geometrically determined:

$$\tau_{int}^{(\alpha)} = \mu b \sum_{\beta=1}^{12} A_{\alpha\beta} \sqrt{\rho_m^{(\beta)}} \tag{6.13}$$

The $A_{\alpha\beta}$ coefficients are derived based on the mean square of the stress fields generated by a random array of dislocations. This method is prefered to a standard averaging because the latter would yield a null mean stress at any point in space. The set of Eq. 6.14 has been obtained by [Zarka 1972]:

$$\begin{cases} A_{\alpha\beta} = \frac{1}{8} \text{ if } \alpha = \beta \\ A_{\alpha\beta} = \frac{1}{16} \text{ for coplanar systems} \\ A_{\alpha\beta} = \frac{1}{20} \text{ for colinear systems} \\ A_{\alpha\beta} = \frac{1}{12} \text{ for remaining systems} \end{cases} \tag{6.14}$$

Latent hardening stemming from long-range elastic stress fields, that is the increase of the critical resolved shear stress on secondary systems due to dislocations on the primary one, cannot exceed self-hardening. This is justified by the lower interaction coefficients for $\alpha \neq \beta$. This fact is verified experimentally on various fcc metals (see for example [Wu 1991, Bassani 1991] for copper single crystals, and discussion in [Nemat-Nasser 2004]).

This expression models a back stress acting on mobile dislocations. It must be understood that the back stress is considered in the present model to be due to long-range elastic stress fields emanating from *mobile* dislocations only. It determines the effective stress acting on dislocations as they

move in the lattice, in the absence of other internal stress sources. This back stress is also the starting stress for dislocations to move, and can be enriched by other stress sources such as clouds of impurities (see Section 6.4) or junction formation.

Short-range interactions

The long-range stress fields introduced previously depend on temperature only through its influence on the shear modulus μ. In the case of short-range interactions, thermal activation allows the incoming dislocation lines to overcome more easily the short-range barriers. This explains the disappearance of the thermal part of the flow stress above a critical temperature [Nemat-Nasser 2004].

The following formulation of the critical stress required for unzipping the junctions is taken from the work of [Madec 2003, Hoc 2004, Devincre 2006, Kubin 2008b]. Simulations have allowed for determination of the strength of the six different interaction mechanisms active in fcc crystals . The critical stress reads:

$$\tau_c^{(\alpha)} = \mu b \sqrt{\sum_{\beta=1}^{12} a_{\alpha\beta} \rho_t^{(\beta)}} \tag{6.15}$$

where the $a_{\alpha\beta}$ coefficients related to junction formation depend non-linearly on the dislocation density as they are made up of a long-range term and a second one due to line tension effects:

$$a_{\alpha\beta} = \left(0.2 + 0.8 \frac{\ln\left(b\sqrt{a_{\alpha\beta}^{(ref)} \rho_t^{(\beta)}} \right)}{\ln\left(b\sqrt{a_{\alpha\beta}^{(ref)} \rho_{ref}} \right)} \right)^2 a_{\alpha\beta}^{(ref)} \tag{6.16}$$

The reference interaction coefficients $a_{\alpha\beta}^{(ref)}$ taken from [Devincre 2006, Kubin 2008b] are related to $a_{\alpha\beta}$ at a reference dislocation density $\rho_{ref} = 10^{12}\,\mathrm{m}^{-2}$:

$$\begin{cases} a_{SH} = 6.4 \times 10^{-3}\ (0.123) \\ a_{Copl} = 6.4 \times 10^{-3}\ (0.123) \\ a_{HL} = 0.07 \\ a_{GJ} = 0.137 \\ a_{LL} = 0.123 \\ a_{CS} = 0.625 \end{cases} \tag{6.17}$$

Hardening in single slip is not due to the pure self-interaction but to the generation of a density of dislocation debris in the cross-slip system that raises the self-interaction and coplanar coefficients significantly up to 0.123. The nonlinearity of the coefficients [Madec 2002a, Devincre 2006] leads to a difference of a factor two between the actual interaction strengths compared

to the use of linear ones, at low forest densities. The logarithmic variation of the coefficients is valid only for forest interactions and is due to line tension effects[3]. The densities entering into Eq. 6.15 are the *total* densities on the slip systems, no difference being done between mobile or immobile dislocations.

High temperatures minimize the influence of the forest by allowing the dislocations to overcoming the obstacles by cross-slip or climb [Louchet 1988]. More generally, thermal activation eases the unzipping process and the critical stress defined in Eq. 6.15 should be considered as the one required for passing the barriers at null temperature. Traditionally, such thermally overcomable obstacles are accounted for by introducing τ_c into the velocity law, as a normalizer to τ_{eff} (see, e.g., [Kocks 1975, Nemat-Nasser 2004] and the previous Section). Forest obstacles are then assumed to govern dislocation mobility. High stress sensitivity of the dislocation velocity in f.c.c. crystals guarantees that significant motion takes place at $\tau_{eff} \simeq \tau_c$ only, the latter playing therefore the role of a threshold stress.

Dislocation motion in covalent crystals almost free from forst dislocations is however controlled by the double kink mechanism, and the normalizing stress τ_0 in Eq. 6.4 remains constant. A model for dislocation motion accounting for both forest interactions and lattice friction is derived in the next Part. For simplicity we assume in the following that forest interactions constitute an *athermal* barrier to dislocation motion and consequently that τ_c can be added to τ_{int}:

$$\tau^{(\alpha)} = \tau_{eff}^{(\alpha)} + \mu b \sum_{\beta=1}^{12} A_{\alpha\beta} \sqrt{\rho_m^{(\beta)}} + \mu b \sqrt{\sum_{\beta=1}^{12} a_{\alpha\beta} \rho_t^{(\beta)}} \tag{6.18}$$

6.3.3 *Dislocation evolution laws*

All dislocations are assumed to be mobile when their density is low. It increases as dislocation loops expand, screw segments double cross-slip and Frank-Read sources are activated, the latter saturating quite rapidly [Alexander 1968, Moulin 1997a, Vallino 2001]. These mechanisms that take place mainly on the primary slip system are valid up to the lower yield point and as long as the density is low enough to prevent any significant interaction between dislocations. As the density of mobile dislocations increases they eventually interact with each other by forming dipoles or multipoles. The increase in dislocation density on the secondary systems also gives rise to forest hardening, that is storage of dislocations by forest interactions. Therefore, the generation mechanisms are supplemented by the trapping of mobile dislocations, leading to the creation of dipoles tangles and other structures made of realtively immobile dislocations. The

3 Line tension effects have also been mentionned for the case of bcc crystals [Tang 1999] as critical for the correct expression of the forest hardening at low temperatures. The same remark is valid for silicon crystals at low homologous temperatures and with relatively low forest densities, when the Peierls valleys are strong enough to compete with dislocation reactions.

immobile dislocations can annihilate by cross-slip or through the collinear interaction.

We distinguish primarily two types of dislocations, namely the "mobile" and "immobile" ones. The evolution rate of the former is governed by two terms, corresponding to generation and disappearance of mobile dislocations. At this stage, we consider that mobile dislocations can become immobile through formation of dipoles only. The density of immobile dislocations increases as mobile dislocations are stored.

Mobile dislocation multiplication

Since we base the model on the equations of Alexander & Haasen we obviously adopt the same dislocation multiplication law as their model, and assume it to be valid on each slip system:

$$\dot{\rho}_m^{(\alpha)} = \delta \tau_{eff}^{(\alpha)} \frac{\dot{\gamma}^{(\alpha)}}{b} \tag{6.19}$$

Storage of mobile dislocations: dipole formation

We assume that trapping of dislocations leading to the formation of dipoles occurs when two segments belonging to the same system but located on parallel planes cross each other and are separated by a distance smaller that a capture diameter $2r_c$:

$$\dot{\rho}_m^{(\alpha)} = -\left(2r_c \rho_m^{(\alpha)}\right) \frac{\dot{\gamma}^{(\alpha)}}{b} \tag{6.20}$$

The capture radius should depend on the temperature and strain rate, as noticed in [Oueldennaoua 1988] and already modeled in [Ashmawi 2000]. Its order of magnitude should be of some tenths of micron [Oueldennaoua 1988, Amodeo 1990]. The trapping of mobile dislocations is equivalent to their storage and the build-up of a density of immobile dislocations.

$$\dot{\rho}_i^{(\alpha)} = \left(2r_c \rho_m^{(\alpha)}\right) \frac{\dot{\gamma}^{(\alpha)}}{b} \tag{6.21}$$

Annihilation of dislocations

Two dislocations having opposed Burgers vectors coming close enough from each other can annihilate. The occurence of cross-slip, be it by thermal activation or because the resolved shear stress on the collinear system is finite, allows for annihilation of screw segments initially mobile or stored as screw dipoles. Annihilation of segments that are not screws is also possible by, e.g., climb, but the capture radius is actually found to be much smaller: screw annihilation takes place on distances of the order of micrometers [Amodeo 1990] while edge components cross only a couple of nanometers by climb. Dynamic recovery is neglected in this model for simplicity.

6.3.4 *Summary*

Constitutive Equations

The model we have set up is a simple extension of the equations of [Alexander 1968] to all slip systems of silicon and accounting for the build-up of a population of immobile dislocations. The internal stress is enriched as well and incorporates short-range interactions. The basic equation bridging the gap between the microscopic and macroscopic levels is Orowan's law (Eq. 6.22). It implies in turn a velocity law (Eq. 6.23) and an evolution equation for mobile dislocations (set of Eqs. 6.24). These two last components lead naturally to the question of the internal stress influencing dislocation motion, multiplication and storage. It is given in Eq. 6.25. Note that the definition of the internal stress assumes the additivity of both short-range and long-range components.

- Orowan's law

$$\dot{\gamma}_p^{(\alpha)} = \rho_m^{(\alpha)} b \overline{v}^{(\alpha)} \tag{6.22}$$

- Dislocation velocity

$$\overline{v}^{(\alpha)} = v_0 \left\langle \frac{\left|\tau^{(\alpha)}\right| - \tau_{int}^{(\alpha)}}{\tau_0} \right\rangle^m \exp\left(-\frac{U}{kT}\right) \tag{6.23}$$

- Dislocation densities

$$\begin{cases} \dot{\rho}_m^{(\alpha)} = \left(\delta\tau_{eff}^{(\alpha)} - 2r_c\rho_m^{(\alpha)}\right)\frac{\dot{\gamma}^{(\alpha)}}{b} \\ \dot{\rho}_i^{(\alpha)} = 2r_c\rho_m^{(\alpha)}\frac{\dot{\gamma}^{(\alpha)}}{b} \end{cases} \tag{6.24}$$

- Effective and internal stress

$$\begin{cases} \tau_{eff}^{(\alpha)} = \left\langle \left|\tau^{(\alpha)}\right| - \tau_{int}^{(\alpha)} \right\rangle \\ \tau_{int}^{(\alpha)} = \mu b \sum_\beta A_{\alpha\beta}\sqrt{\rho_m^{(\beta)}} + \mu b\sqrt{\sum_\beta a_{\alpha\beta}\rho_t^{(\beta)}} \end{cases} \tag{6.25}$$

Remarks and limits of the model

This model considers that plastic deformation takes place by means of dislocation generation and glide on their slip systems only. Deformation mechanisms such as twinning, or high temperatures allowing easy climb or cross-slip are also ruled out. Diffusion-like mechanisms are excluded from our formalism.

The definition of the internal stress relies on the additivity of contributions from both athermal and thermal obstacles. This is obviously not in agreement with the standard theory of thermally activated glide (see, e.g., [Kocks 1975]), as the component stemming from junction formation should be considered as a critical stress that needs not be reached before

dislocations unzip. This choice is due to the simple dislocation velocity law chosen in this work. Eq. 6.23 intrinsically assumes that no forest obstacles are present and adding the critical stress τ_c (Eq. 6.15) to τ_{int} is equivalent to assuming that thermal excitation does not help obstacle overcoming at all. Note that such an approach has already been used in the literature for modeling the effects of dissolved impurities at the core: instead of modifying the velocity law, the internal stress is simply reduced further.

The evolution of the total dislocation density $\rho_t^{(\alpha)}$ is exactly equal to the multiplication law of Alexander & Haasen: $\dot{\rho}_t^{(\alpha)} = \delta\rho_m^{(\alpha)}\tau_{eff}^{(\alpha)}v^{(\alpha)}$. Consequently our model should yield similar results than the original one in the yield region and as long as $\rho_i^{(\alpha)} \ll \rho_m^{(\alpha)}$. At larger strains, the present model should predict a steady-state of deformation defined by $\dot{\rho}_m^{(\alpha)} = 0$, the density of immobile dislocations still increasing as is experimentally observed.

This similarity also implies that the multiplication mechanisms are assumed to generate as many dislocations in the yield region as beyond. Such an assumption will be shown as fundamentally limiting the validity of our constitutive model, as it underestimates the generation rate at intermediate to large strains, or in multiple slip conditions.

More developed models of dislocation multiplication have been published recently, based on the analysis of the different dislocation segments constituting the loops [Arsenlis 2002, Cheong 2004]. The analysis leads to multiplication laws that involve terms similar to the ones of Eqs. 6.24, specialized to each type of dislocation on a given slip system (for example, different laws exist for screw and edge dislocations). The present model does not distinguish between the different dislocation characters.

Finally, it might be interesting to note that this model can be simplified if one is interested by uniaxial straining of single crystals involving one slip system only. The computational framework has not been fixed yet: it is still left to the user to decide whether a scalar formulation as done in Chapter 5 satisfies his needs. Adopting a crystal plasticity formulation as introduced in Annex A increases the computation time and requires more implementing efforts.

6.4 MODELING OXYGEN-CONTAMINATED SILICON CRYSTALS

Let us now concentrate on modeling the dislocation locking effect that dissolved impurities have. Oxygen has been the subject of extended research as it is the main contaminant in CZ crystals (see Part i of this thesis for more details). Consequently, this impurity only is considered in this Section. Application of the model to other impurities is straightforward, provided the many physical parameters it is based on are known.

Oxygen is a light impurity and therefore does not affect the activation energy of moving dislocations. As shown by [Sumino 1999], the formation of a Cottrell atmosphere at temperatures where a plastic deformation is significant is very unlikely, as the binding energy of individual impurity atoms to dislocations is quite low. The additional back stress created by such an atmosphere and the evolution of the impurity cloud around a moving dislocation (see [Maroudas 1991a, Maroudas 1991b]) are consequently neglected in the following. Furthermore, only the first two stages of the dislocation locking stress evolution are considered. Impurity aggregation and cluster formation by pipe diffusion is neglected.

6.4.1 *Internal stress*

Diffusion of light impurities to the dislocation core has the effect of tremendously raising the upper yield stress. Dislocated CZ crystals exhibit a behavior in the yield region that reminds of dislocation-free FZ crystals. The presence of oxygen actually prevents dislocations from moving and results in keeping crystals apparently virgin from dislocations. A traditional way of modeling the locking effect has been to add a back stress τ_O to τ_{int}, eventually proportional to the concentration of oxygen that has diffused to the impurity core by a factor dependent on temperature [Sumino 1983]:

$$\tau_O^{(\alpha)} = f(T)\, c_O^{(\alpha)} \tag{6.26}$$

Such an approach is far from sufficient if one aims at reproducing the increase of the upper yield stress, as a large fraction of τ_{uy} is made up of the effective stress (see, e.g., [Kalan 2001, Miyazaki 2007]). An additional enhancement of the constitutive model for extrinsic crystals is to consider that in average, only a fraction of the density of mobile dislocations is in motion.

6.4.2 *Effective density of mobile dislocations*

Both experimental observations and theoretical considerations show that only a minor fraction $\rho_{m,eff}$ of the mobile dislocation density ρ_m is actually carrying plastic flow in the yield region - where the density of immobile dislocations ρ_i can be neglected anyway and $\rho_t \simeq \rho_m$. [Petukhov 2004] has shown that this is due to dynamic ageing of dislocations as the impurity

concentration on "old" segments increases, while newly generated dislocations can move free from locking agents for a while. The averaged behavior of the dislocation population can be retraced by considering the initial dislocation density to be reduced by a factor which is a function of the locking stress τ_O.

The model derived by [Petukhov 2004] assumes that the crystal is deformed at a constant strain rate, allowing him to derive an analytical expression for $\rho_{m,eff}$. In the most general case however no analytical expression can be derived. A simple way of modeling the effect of oxygen is to replace $\rho_m^{(\alpha)}$ by $\rho_{m,eff}^{(\alpha)}$ in Eqs. 6.22 and 6.24, with

$$\rho_{m,eff}^{(\alpha)} = \eta\left(\tau_O^{(\alpha)}\right)\rho_m^{(\alpha)} \tag{6.27}$$

and $\eta\left(\tau_O\right) \leq 1$ a function left to derive.

6.4.3 *Dislocation multiplication*

[Maroudas 1991c] consider that impurities at the dislocation core hinder their multiplication by adding an additional energy barrier to overcome prior to cross-slip events. The dislocation multiplication prefactor δ (see Eq. 6.24) becomes δ_O:

$$\delta_O = \delta \exp\left(-\frac{\tau_O^{(\alpha)} b^2 l}{k_b T}\right) \tag{6.28}$$

Where l is a mean jog spacing, taken as constant and equal to 10^{-7} m.

6.4.4 *Diffusion of impurities to and from the dislocation cores*

Finally, the knowledge of $c_O^{(\alpha)}$ is required as $\tau_O^{(\alpha)}$ and ultimately $\rho_{m,eff}^{(\alpha)}$ depend on this variable. Let us consider first the case of a dislocation at rest. Neglecting the presence of a Cottrell atmosphere and setting the core radius $r_0 = a$, then the concentration of oxygen outside the core is constant and equals the bulk dissolved concentration c_O^{∞}. The diffusion problem is extremely simplified and reads:

$$\dot{c}_O^{(\alpha)}\Big|_{\overline{v}^{(\alpha)}=0} = \frac{D_O}{2\pi r_0 b}\left[c_O^{\infty} - c_O^{(\alpha)} \exp\left(-\frac{\Delta G_O}{k_b T}\right)\right] \tag{6.29}$$

where D_O is the effective diffusion coefficient in the bulk and ΔG_O the binding energy of oxygen to dislocations. The former depends both on temperature and the oxygen concentration (see [Senkader 2001, Murphy 2006]). We consider in this work the case of high temperatures only, which yields:

$$D_O = 0.13 \times 10^{-4} \exp\left(-\frac{2.53}{k_b T}\right) \tag{6.30}$$

ΔG_O can be expressed as a function of the enthalpy change ΔH_O and entropy change ΔS_O, as $\Delta G_O = \Delta H_O - T\Delta S_O$. Experimental observations give $\Delta S_O \simeq k_b$ and $\Delta H_O = 0.74\,\text{eV}$ above 923 K (see [Senkader 2002, Murphy 2006]).

The case of a moving dislocation has been investigated by [Petukhov 1990, Petukhov 2004], who derived Eq.6.31:

$$\dot{c}_O^{(\alpha)}\Big|_{\overline{v}^{(\alpha)}>0} = \dot{c}_O^{(\alpha)}\Big|_{\overline{v}^{(\alpha)}=0} + \frac{\overline{v}^{(\alpha)}}{a}\left[\frac{r_0}{a}c_O^{\infty} - c_O^{(\alpha)}\exp\left(-\frac{a}{\overline{v}^{(\alpha)}t_m}\right)\right] \tag{6.31}$$

with $t_m = \lambda_O \frac{a^2}{D_O}\exp\left(-\Delta G_O/k_bT\right)$ the time of oxygen migration from the bulk back onto the dislocation core. The factor $\lambda_O > 1$ translates the effect of the lattice distortion close to the dislocation core on the impurity diffusivity. Its influence is discussed later.

6.5 CONCLUSION: THE EXTENDED AH MODEL

Constitutive equations for intrinsic silicon materials have been introduced, based on the model of Alexander & Haasen. Attempts to account for physical mechanisms taking place during deformation have been done:

- The dislocation velocity law does not account for short-range interactions, and dislocations are assumed to move by the double kink mechanism
- Short-range interactions are voluntarily overestimated by their integration in the critical stress for dislocation motion. Latent hardening is also included in the model
- The total dislocation population on each slip system is decomposed into mobile and immobile segments. The former are inserted into Orowan's law, whereas the latter only contribute to the internal stress buildup
- Mobile segments are stored into the immobile population by the use of an effective capture radius

The case of intrinsic materials has also been considered. Dissolved oxygen is taken as a basis for derivation of the related equations, given its significant contents in SoG-Si on the one hand, and the extensive knowledge we have on this species on the other. It is suggested that oxygen atoms diffused at the dislocation core have three different effects:

- They increase the internal stress opposing the applied stress, owing to the dragging effect of pinning impurities
- Oxygen atoms hinder dislocation multiplication by creating an additional barrier to cross-slip
- When contaminated dislocations are set into motion, only a fraction η of the total population actually carries plastic flow, owing to dynamic ageing. The η function depends on the maximum impurity concentration reached at the core.

This extended AH model is calibrated and discussed in the next Chapter.

7

CALIBRATION OF THE EXTENDED AH MODEL AND DISCUSSION

The physically-based extended AH model can explain to some extent the temperature and strain rate sensitivity of the stress-strain curves in the yield region. The existence and unicity of the steady state of deformation in stage I is guaranteed by the extended model for intrinsic materials. Its generalization to oxygen-contaminated crystals extends further its applicability to extrinsic silicon. Derivation of the consistent tangent moduli for implementation of the model for intrinsic materials in implicit finite element codes is proposed. The limitations of constitutive models based on the dislocation multiplication law of Alexander & Haasen are discussed.

7.1 IMPLEMENTATION INTO A FINITE ELEMENT SOFTWARE

The constitutive equations derived in Chapter 6 can be implemented both into a stand-alone routine, where a single integration point is considered, or into a finite element software. Kinematics must be choosen either way; we use the RDCP framework as its ability to account for several slip systems surpasses a J_2 formulation (see Annex A).

The kinematics of large deformations have been described in Section A.3, based on the multiplicative decomposition of the deformation gradient. The constitutive model introduced above is implemented in a user subroutine called VUMAT. ABAQUS/EXPLICIT works in the corotational system, rotating with the material point, and only details specific to this particular formulation are given in the following.

7.1.1 *Implementation into* ABAQUS/EXPLICIT

Working in the corotational system means that the Cauchy stress must be updated and rotated into this system at each time increment. Care must also be taken to account correctly for the rotation of the material point caused by plastic shearing, as discussed by [Amirkhizi 2007]. Although leaving the lattice undeformed, the application of $\mathbf{F}^p$ induces a rotation $\mathbf{R}^p$ that can be obtained by polar decomposition $\mathbf{F}^p = \mathbf{R}^p\mathbf{U}^p$, where $\mathbf{U}^p$ is the plastic stretch gradient. [Amirkhizi 2007] update the rotational part of the plastic deformation gradient with an incremental scheme. Instead of this

approximation, we use the (exact) polar decomposition of the updated $\mathbf{F}^p$ to obtain $\mathbf{R}^p$ at each time increment.

Calling $\mathbf{Q}_t$ the matrix allowing the coordinate transformation from the MECS to the CACS at the time t (see Section A.3), a tensor $\boldsymbol{T}$ written in MECS can be expressed into CACS as follows:

$$\widetilde{\mathbf{T}} = \mathbf{Q}_t \mathbf{T} \mathbf{Q}_t^T \tag{7.1}$$

Tensors and vectors expressed in the CACS are written with a $\widetilde{}$ superscript. $\mathbf{Q}$ needs to be updated upon plastic deformation as $\mathbf{R}^p$ induces a rotation of the material element: writing $\mathbf{Q}_0 = \mathbf{Q}(t=0)$ then $\mathbf{Q}_{t+\Delta t} = \mathbf{R}^p_{t+\Delta t} \mathbf{Q}_0$. The initial relative orientation of CACS with respect to MECS can be defined by three successive rotations associated to three Euler angles (ψ, θ, ϕ) as defined in Fig. A.4, $\mathbf{Q}_0$ being given by Eq. A.43. The Euler angles at $t + \Delta t$ are extracted from $\widetilde{\mathbf{R}}_{t+\Delta t} \mathbf{Q}_{t+\Delta t}$, with $\mathbf{R}_{t+\Delta t}$ obtained from the polar decomposition $\mathbf{F} = \mathbf{R}\mathbf{U}$ at the end of the time increment.

7.1.2 *Derivation of the consistent tangent moduli for* Abaqus/Standard

The advantage of Abaqus/explicit is that it does not iterate at each time increment in order to find the solution to the BVP. Small time increments are required in order to keep the solution stable and accurate. On the contrary, relying on an implicit solver for the boundary value problem adds in accuracy and stability, but is computationally more expensive because potentially large time increments lead to an iterative process in order to reach equilibrium. The convergence speed of these iterations is at best quadratic and depends on the accuracy of the consistent tangent moduli $\boldsymbol{\mathcal{C}}_{ep}$ (CTM) defined as:

$$\boldsymbol{\mathcal{C}}_{ep} = \frac{\partial \Delta \boldsymbol{\sigma}}{\partial \Delta \boldsymbol{\varepsilon}} \tag{7.2}$$

Using a vector notation for $\Delta\boldsymbol{\sigma}$ and $\Delta\boldsymbol{\varepsilon}$ allows for writing this fourth-order tensor as a 6x6 matrix with components $C_{ij} = \partial \Delta\sigma_i / \partial \Delta\varepsilon_j$. This CTM must be derived at each integration point each time the user-defined constitutive model routine (UMAT) is called. A critical issue is that the CTM depends directly on the constitutive model chosen, and each modification brought to any of the consitutive equations introduced previously has a direct effect on $\boldsymbol{\mathcal{C}}_{ep}$ and therefore the convergence speed. An example of derivation is given in Annex B, where the extended AH model with temperature-dependent parameters is considered only. Unless stated otherwise only Abaqus/Explicit is used in this work.

7.1.3 *Finite element model*

The finite element model used for parameter identification aims at reproducing the silicon specimen attached to the tensile apparatus as used by [Yonenaga 1978] to obtain the experimental data. The tensile apparatus

strongly affects the yield region as the combined stiffness of the specimen and machine differs from the one of the silicon sample alone and varies with the testing conditions. Such an effect is usually accounted for in scalar models by the use of the machine equation including an equivalent shear modulus such as done by [Alexander 1968, Suezawa 1979] and introduced in Chapter 5. However, this approach disregards the strong variations of the strain rate in the tensile specimen upon loading as discussed in [Cochard 2010a].

In the linear elastic region the very low machine stiffness leads to a concentration of deformation in the tensile apparatus. [Yonenaga 1978] mention the relaxation at the grips. The onset of plastic flow during the yield drop results in the localization of deformation and a local increase of the strain rate in the silicon sample as softening proceeds. Overall, the strain rate acting on the gauge section of the specimen exhibits strong variations in the yield region, thereby requiring the modeling of the whole apparatus for parameter calibration. This makes the identification of a possible strain rate dependency of the constitutive parameters difficult as even tests performed at constant cross-head speed do not lead to a constant strain rate in the gauge (see [Cochard 2010b] and Section 7.2).

The whole finite element model includes the actual silicon sample of gauge dimensions of $3 \times 2 \times 30\,\mathrm{m}^3$. It is bounded by two isotropic elastic blocks representing the effect of the tensile apparatus (see Fig. 7.1). A total of 888 C3D8R elements are used for the mesh. This mesh size is sufficient to obtain converged results with $\lambda_O = 10^2$ (see [Cochard 2010b] in case λ_O is taken smaller).

The material behaviour of the specimen is defined by the VUMAT. The initial conditions required are the dislocation densities, the crystallographic orientation of the tensile specimen and its dissolved oxygen content. The apparatus elastic blocks have a Poisson's ratio of 0.3 and a Young's modulus E_{blocks} set as a free parameter for optimization in each experimental curve. E_{blocks} is found by fitting its value to the initial elastic slope of the experimental curves. Elastic blocks of low stiffness E_{blocks} are used to fit the parameters affecting the yield region only.

The experimentally determined dislocation density $\rho_{0,\mathrm{exp}}$ is assumed entirely mobile and located on the primary slip system D4. The initial mobile dislocation density on each secondary system is assumed equal to $0.01 \times \rho_{0,\mathrm{exp}}$. On all systems $\rho_i = 0$ at the beginning of the simulations.

When present, dissolved oxygen is assumed to have diffused to dislocation cores and reached its maximum allowed value prior to deformation: $c_O^{(\alpha)} = c_O^{\infty} \exp\left(\Delta G_O / k_b T\right)$.

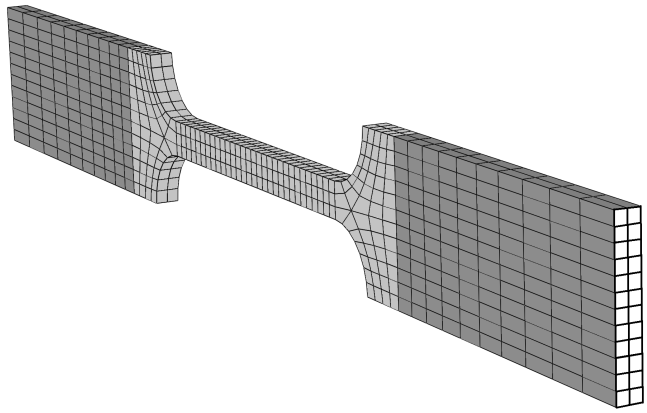

Figure 7.1: Finite element mesh used for parameter identification. The silicon sample is in light grey, the elastic bounding blocks modeling the tensile machine in dark grey. The force at the nodes of the white elements is used for comparison of the model output with the experimental data.

7.2 MODEL CALIBRATION

7.2.1 *Preliminary discussion*

The (α) superscripts are dropped here for readability.

DEFINITION OF THE STEADY-STATE OF DEFORMATION It is commonly observed that both ρ_m and τ_{eff} reach steady-state values in stage I (resp. ρ_m^* and τ_{eff}^*) [Yonenaga 1978, Sumino 1979, Oueldennaoua 1988]. Assuming the extended model correctly describes the dislocation evolution in silicon, Eq. 6.24a yields for $\dot{\rho}_m = 0$:

$$\rho_m^* = \frac{\delta \tau_{eff}^*}{2r_c} \tag{7.3}$$

Experimental results obtained at temperatures from 983 to 1273 K by [Yonenaga 1978, Yonenaga 1981] give:

$$\frac{\rho_m^*}{\tau_{eff}^*} = \frac{\delta}{2r_c} \simeq 548.6\, \dot{\gamma}^{0.26} \exp\left(\frac{0.76}{k_b T}\right) \tag{7.4}$$

The combined use of Orowan's law and Eq. 7.3 at the steady-state of deformation (i.e. at a constant resolved shear strain rate) yields:

$$(\rho_m^*)^2 \propto \frac{\delta}{r_c} \exp\left(\frac{U}{k_b T}\right) \tag{7.5}$$

It can similarly be found that $\left(\tau_{eff}^*\right)^2 \propto \frac{r_c}{\delta} \exp\left(\frac{U}{k_b T}\right)$. This shows that the steady state of deformation is entirely defined as soon as the extended model is adopted, whatever the value assigned to $\frac{\delta}{r_c}$. Fixing this ratio to, e.g., its experimental value as given in Eq. 7.4 actually ensures that the simulated steady-state is similar to the experimental one[1]. In other words, *the extended AH model guarantees the existence and unicity of the steady state variables*.

TEMPERATURE DEPENDENCY OF PARAMETERS Experiments yield for $\dot{\gamma} = 1.2 \times 10^{-4}\,\mathrm{s}^{-1}$ at steady-state:

$$\tau_{eff}^* = 1.13 \times 10^3 \exp\left(\frac{0.72}{k_b T}\right) \tag{7.6}$$

The applied strain rate being temperature-independent, insertion of the dislocation velocity law into Orowan's law implies that $\rho_m^* \propto \exp\left((U - 0.72)/k_b T\right)$ with U activation energy for dislocation motion. Insertion of this relationship into Eq. 7.6 and use of the velocity parameters given by [Suezawa 1979] yields Eq. 7.7 for the temperature dependency of ρ_m^*:

$$\rho_m^* = 5.93 \times 10^4 \exp\left(\frac{1.48}{k_b T}\right) \tag{7.7}$$

1 This remark is valid only of the velocity parameters v_0 and U used to analyze the experimental data are similar to those of the numerical model.

Assuming the steady-state of deformation and neglecting the dislocations on the secondary slip systems in stage I, the flow stress evolution reads:

$$\dot{\tau} = \dot{\tau}_{int} = \frac{\mu b}{2}\sqrt{\frac{a_{\alpha\alpha}}{\rho_t}}\dot{\rho}_t \tag{7.8}$$

with $\dot{\rho}_t = \delta\tau^*_{eff}\dot{\gamma}/b$ and $\rho_t = \rho_t^0 + \delta\tau^*_{eff}\left(\gamma - \gamma_0\right)/b$ with ρ_t^0 total dislocation density at γ_0. Taking γ_0 large enough so we can assume $\dot{\rho}_t \Delta t \ll \rho_t^0$ and noting the athermal nature of the hardening rate in stage I ($\frac{\partial}{\partial T}\left(\frac{\mathrm{d}\tau}{\mathrm{d}\gamma}\right)_I \simeq 0$) gives:

$$\delta \propto \left(\tau^*_{eff}\right)^{-1} \tag{7.9}$$

This second relationship leads to the complete description of the variations of δ and r_c with temperature:

$$\begin{cases} \delta \propto \exp\left(-\frac{0.72}{k_b T}\right) \\ r_c \propto \exp\left(-\frac{1.48}{k_b T}\right) \end{cases} \tag{7.10}$$

Agreement between the constitutive model and experimental data should therefore be reached with the help of two independent parameters only: the self-interaction coefficient for long-range elastic interactions $A_{\alpha\alpha}$ and either δ or r_c, the temperature dependency of the two last ones being readily known. This relationship implies that the two constitutive parameters δ and r_c are dependent and simplifies their identification.

THE CASE OF STRAIN RATE PARAMETER DEPENDENCY A limitation of this model is the absence of dependency of the constitutive parameters on the strain rate. It is experimentally observed that doubling the strain rate results in a significantly different mechanical response of silicon monocrystals. Considering solely temperature-dependent parameters is an approximation made for the sake of simplicity. The large variations of the strain rate in the yield region are bound to influence the values of δ and r_c. A complementary approach is obviously to consider the general case of strain-rate dependent parameters using Eq. 7.4.

Assuming that $\delta = \beta(\dot{\gamma}_p/\dot{\gamma}_0)^\theta$ with $\dot{\gamma}_0 = 1\,\mathrm{s}^{-1}$, then following Eq. 7.4 $r_c \propto \dot{\gamma}_p^{\theta-0.26}$ and $\theta \leq 0.26$. The sign of θ determines the sharpness of the yield drop. An accelerating plastic strain rate leads to an increased dislocation generation if $\theta > 0$, precipitating the occurence of the lower yield point and sharpening the yield drop. On the other hand, a negative θ tends to smooth the yield region by slowing down the dislocation generation as the plastic strain rate increases. Because the plastic strain rate in the yield region is not constant (see below) the choice of θ influences the representation of the yielding phenomena.

Both approaches are considered next, either setting $\theta = 0$ and considering that only temperature influences δ and r_c, or by inserting a strain rate dependency.

7.2.2 *Variations of the shear strain rate in the yield region*

The influence of the tensile apparatus is visible at low strains. It is translated in the experimental stress-strain results by an initial slope that is well below the actual Young's modulus (or shear modulus) of the material. The shear strain rate acting on the silicon specimen during the initial linear loading in the reference conditions, $\dot{\gamma}_e = \dot{\tau}/\mu_{Si} \backsimeq 10^{-11}\,\mathrm{s}^{-1}$, is then several orders of magnitude lower than the announced values.

At the upper yield point, the relation $\dot{\tau} = 0$, or $\dot{\gamma} = \dot{\gamma}_p = \rho_m b v$ holds and it can be assume that the internal stress is small compared to the applied stress: $\tau|_{uyp} \simeq \tau_{eff}\Big|_{uyp}$ [Alexander 1968, Suezawa 1979]. Combining Orowan's law and the dislocation velocity expression gives:

$$\dot{\gamma}_{uyp} = \rho_m|_{uyp}\, b \frac{v_0}{\tau_0} \exp\left(-\frac{U}{k_b T}\right) \tau|_{uyp} \tag{7.11}$$

Eq. 7.11 can be used to calculate the resolved strain rate at the upper yield point given the upper yield stress and the measured dislocation density. Using the experimental data in the reference conditions $\rho_m|_{uyp} \simeq 1.5 \times 10^{11}\,\mathrm{m}^{-2}$ and $\tau|_{uyp} = 30\,\mathrm{MPa}$ [Yonenaga 1978], the shear strain rate at the upper yield point is found to be roughly $5 \times 10^{-4}\,\mathrm{s}^{-1}$. This value is of the same order of magnitude as the $1.2 \times 10^{-4}\,\mathrm{s}^{-1}$ refered to. The discrepancy might come from an over-estimation of the dislocation density in such a dynamical state.

These observations point towards a variable effective strain rate in the yield region due to the tensile apparatus. The output from the FE model confirms this discussion and indicates a higher shear strain rate during the yield drop, before its value stabilizes at $1.2 \times 10^{-4}\,\mathrm{s}^{-1}$ beyond the lower yield point as shown in Fig. 7.2. Such a phenomena leads to a sharper yield drop than if a constant strain rate were applied throughout the yield region. In spite of this variable strain rate, the resolved shear strain in the following Figures assumes a perfect proportionality between time and strain to facilitate the readability of the results.

7.2.3 *Parameter identification - intrinsic crystals*

Temperature-dependent parameters

The constitutive parameters obtained by individual best fits of the yield region[2] in Table 7.1, where the relations derived in Section 7.2.1 are temporarily ignored. The self-interaction coefficient $A_{\alpha\alpha}$ is fixed in this first approach and equal to its value given by [Zarka 1972]. δ increases with temperature, but one can note that the ratio $\delta/2r_c$ follows the opposite evolution with temperature than the requirement of Eq. 7.4.

2 It must be kept in mind that these best fits are obtained over the *whole* yield region and as such are not best fits of the *upper yield stresses*.

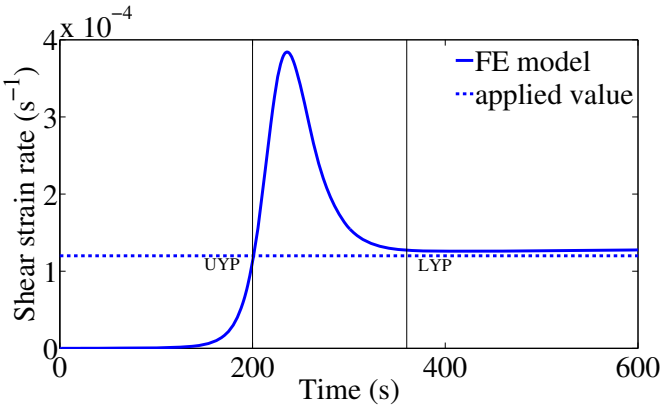

Figure 7.2: Plastic shear strain rate acting on the tensile specimen output by the FE model at 1073 K and a theoretical shear strain rate $\dot{\gamma} = 1.2 \times 10^{-4}\,\mathrm{s}^{-1}$. The positions of yield points are indicated.

Parameter	1073K	1123K	1173K	1223K
$\delta\ (10^{-4}\,\mathrm{m.N}^{-1})$	3	5	6.5	14
$r_c\ (10^{-8}\,\mathrm{m})$	0.8	1.1	0.6	0.4
$\frac{\delta}{2r_c}\ (10^{4}\,\mathrm{N}^{-1})$	1.9	2.3	5.4	17.5
$A_{\alpha\alpha}$	0.125			

Table 7.1: Best fitted parameters of the extended AH model (no strain rate dependency).

The activation energies for r_c and δ are now set dependent following Eqs. 7.4 and 7.10. As mentioned previously, the simultaneous use of these equations guarantees that the steady-state of deformation derived from experimental data is reproduced by the constitutive model.

Long-range stresses from self-interactions are modulated by the free parameter $A_{\alpha\alpha}$. Being the only free parameter affecting the magnitude of the flow stress, it defines the value of the lower yield stress.

The sum of the cost functions for all four experimental data is then minimized for the following values:

$$\begin{cases} A_{\alpha\alpha} = 0.21 \\ \delta(T) = 7.6 \times 10^{-1} \exp\left(-\frac{0.72}{k_b T}\right) \\ r_c(T) = 7.2 \times 10^{-3} \exp\left(-\frac{1.48}{k_b T}\right) \end{cases} \tag{7.12}$$

where δ is expressed in $\mathrm{m.N}^{-1}$ and r_c in meters. The resulting simulated stress-strain curves are plotted in Fig. 7.3. Note that although the parameters have been identified using the yield region only, the simulated mechanical behaviour is in quite good agreement with the experimental one throughout

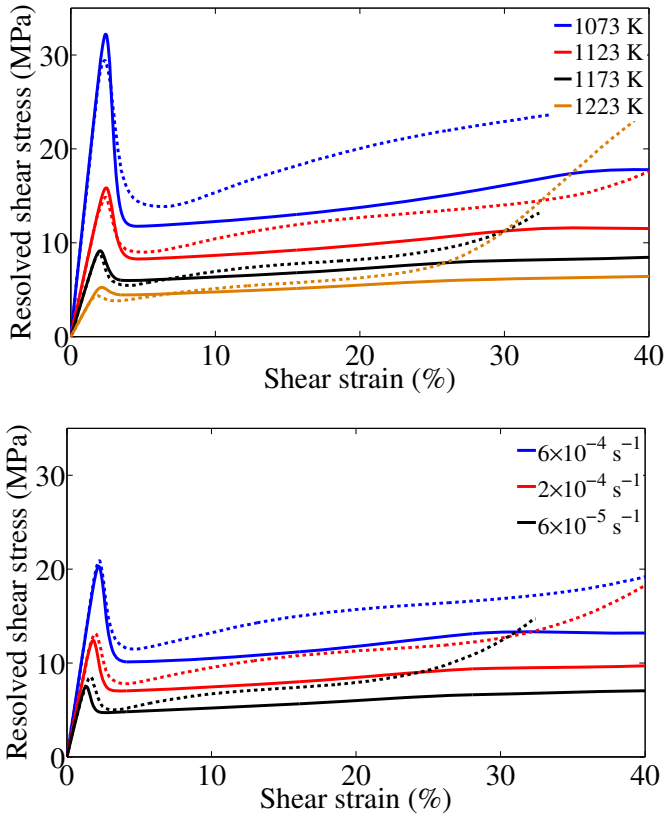

Figure 7.3: Comparison of experimental (dashed) and simulated (plain) stress response of FZ silicon tensile specimen deformed at (top) various temperatures and $\dot{\gamma} = 1.2 \times 10^{-4}\,\mathrm{s}^{-1}$, (bottom) various strain rates and T=1173 K. Temperature-dependent constitutive parameters (Eq. 7.12).

stage I of deformation. This shows that the physical micromechanisms modeled by Eqs. 6.19 and 6.21 explain to a certain extent the hardening behavior of silicon in stage I.

The model predicts an absence of strong hardening when secondary systems are activated and is consequently not appropriate for stage II or multiple slip conditions. This could be foreseen by the absence of dislocation storage on the forest in the dislocation evolution laws. The simulated stress-strain curves become more accurate as temperature is increased.

The yield region at various strain rates is still well described by these constitutive parameters, although the hardening rate in stage I remains well below its experimental value.

	$\dot{\gamma}\,(\mathrm{s}^{-1})$	6×10^{-5}	2×10^{-4}	6×10^{-4}
$\theta=-0.22$	$\beta\,(10^{-5}\,\mathrm{m.N}^{-1})$	2.7	4.3	5.6
$\theta=0$	$\beta\,(10^{-4}\,\mathrm{m.N}^{-1})$	3.8	4.7	5.2
$\theta=0.26$	$\beta\,(10^{-3}\,\mathrm{m.N}^{-1})$	9	9	9

Table 7.2: Best fitted values of β at 1173 K, using the relationship $\delta=\beta(\dot{\gamma}_p/\dot{\gamma}_0)^\theta$ to retrieve the experimental upper yield stresses.

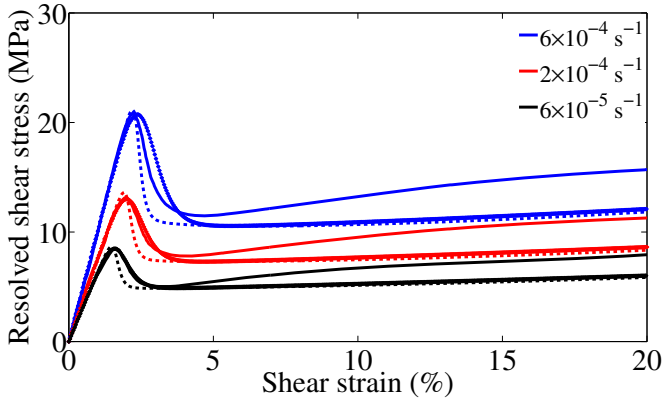

Figure 7.4: Experimental (plain lines) and simulated stress-strain curves of silicon crystals from *ds2*, with $\theta=-0.22$ (dotted) or $\theta=0.26$ (dashed).

Insertion of strain rate dependency

The yield region of the experimental data *ds2* can be reproduced very well by the constitutive model using $\theta=-0.22$. This value gives simulated yield drops of the same intensity as the experimental ones (see Fig. 7.4).

However, the main drawback of choosing $\theta\leq 0$ is that the optimum[3] θ varies with temperature, its value increasing with T and likely translating additional hardening mechanisms the model does not account for. At a given temperature but various strain rates, β must be scaled for each sample in order for the simulated upper yield points to coincide with the experimental ones, see Table 7.2.

Setting $\theta=0.26$ sharpens the simulated yield drop but has the advantage of requiring a unique β to reproduce accurately the upper yield stresses of *ds2* (Table 7.2). The hardening rate into stage I is not significantly affected by the value chosen for θ (see Fig. 7.4). $\theta=-0.26$ is consequently used in the following. Accuracy in the yield region is therefore compromised for the sake of generality.

As will be seen in the next Part, these compromises can be avoided by adopting another multiplication law than the one of Alexander & Haasen for the yield region.

3 That is, the θ value that reproduces best the slope of the yield drop.

The experimental upper yield stresses obtained at various temperatures are best fitted by setting $\delta \propto \exp(-0.42/k_bT)$. Using these relationships we obtain:

$$\begin{cases} \delta(T,\dot{\gamma}_p) = \zeta_{sp}\,(\dot{\gamma}_p/\dot{\gamma}_0)^{0.26}\,\exp\left(\frac{-0.42}{k_bT}\right) \\ r_c(T,\dot{\gamma}_p) = 9.11\times10^{-4}\,\zeta_{sp}\,\exp\left(-\frac{1.18}{k_bT}\right) \end{cases} \tag{7.13}$$

where ζ_{sp} is a constant specific to the specimen set considered. It is identified for FZ-crystals by fitting Eqs. 7.13 to the experimental data, ζ_{sp} determining the magnitude of the upper yield stress.

For the experimental data set *ds1* $\zeta_{sp} = 0.93$ provides the best fit, whereas $\zeta_{sp} = 0.56$ yields better results for the set *ds2* of specimen strained at 1173 K and different strain rates, see Fig. 7.5 where the respective optimum ζ_{sp} values have been used.

The role of forest dislocations on multiplication and storage mechanisms, absent in the present constitutive model, is believed to explain most of the variations of ζ_{sp} with respect to the set of samples considered. The discrepancy could also come from different concentrations of trace impurities in the sample sets, increasing the upper yield stresses of *ds2*.

7.2.4 *Parameter identification - extrinsic crystals*

It is always assume in simulations that oxygen has diffused to the dislocations up to c_O^{max} prior to testing, so that $c_{O,t=0}^{(\alpha)} = c_O^{max}$ on all slip systems. The initial condition is therefore $\rho_{m,eff}^{(\alpha)}\Big|_{t=0} = \eta(\tau_O(c_O^{max}))\;\rho_m^{(\alpha)}\Big|_{t=0}$. The case $\dot{c}_O^{(\alpha)} > 0$ does not occur before the upper yield point as dislocations move fast enough to be free from oxygen contaminants, and η can be identified by best fit.

Identification of the parameter ζ_{sp}

Identification of the parameter η characteristic of extrinsic crystals requires the prior knowledge of ζ_{sp}. The latter depends on the specimen and might be influenced by several factors mentioned previously. ζ_{sp} is identified for FZ-crystals by fitting the simulated stress-strain curves to the yield region. Different methods suitable for CZ crystals, whose intrinsic upper yield point is unknown, are suggested and assessed in the following.

- ζ_{sp} could be identified relying on the hardening rate in stage I, since δ_O directly affects the slope of the stress-strain curve in the steady-state of deformation (see [Cochard 2010b]). The present constitutive model predicts in the meantime a systematically too low hardening rate for us to rely on this identification method.

- Considering the lower yield stress τ_{lyp} only, since at this point most impurities should have left dislocations. It is usually considered

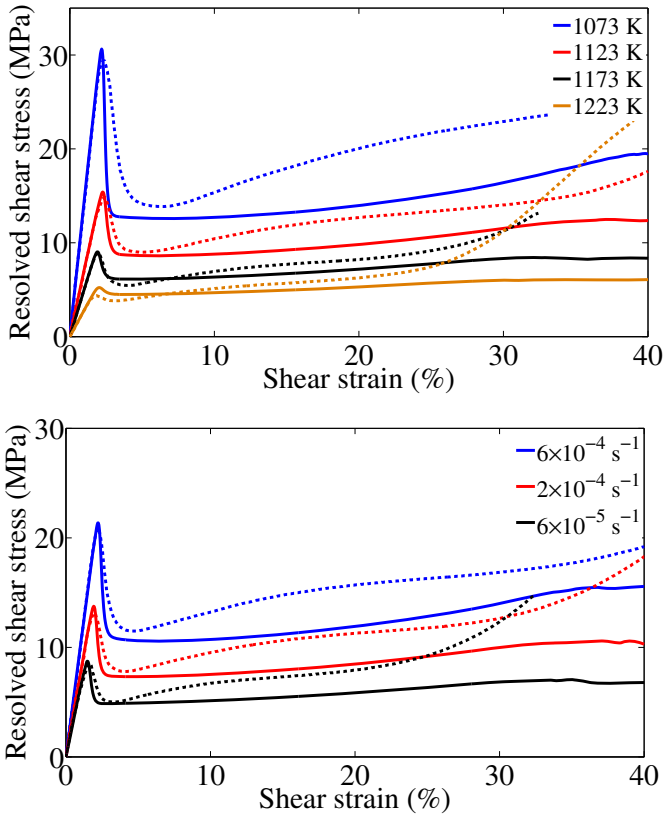

Figure 7.5: Comparison of experimental (dashed) and simulated (plain) stress-strain curves of FZ-crystals ($c_O^\infty = 0$) deformed at (top) various temperatures and $\dot{\gamma} = 1.2 \times 10^{-4}\,\mathrm{s}^{-1}$, (bottom) various strain rates and T=1173 K. Temperature- and strain-rate dependent constitutive parameters (Eq. 7.13).

that in the absence of a significant forest density τ_{lyp} should depend only on the deformation conditions (see, e.g., [Alexander 1968, Suezawa 1979]). As seen later in this Chapter, large impurity concentrations do indeed affect slightly the value of the lower yield stress, all other conditions being equal. This is partly because forest systems are expected to be more activated at intense yield drops, exacerbated by high c_O. However, this method cannot discriminate definitely between different values of ζ_{sp}, as τ_{lyp} is not significantly dependent on this parameter (see Fig. 7.6).

- Experimental observations by [Yonenaga 1984] point to a fraction of effectively mobile dislocations at $c_O^\infty = 1.5 \times 10^{17}\,\mathrm{cm}^{-3}$ of 20%. Using this information allows us to set $\eta = 0.2$ and identify ζ_{sp} in these conditions.

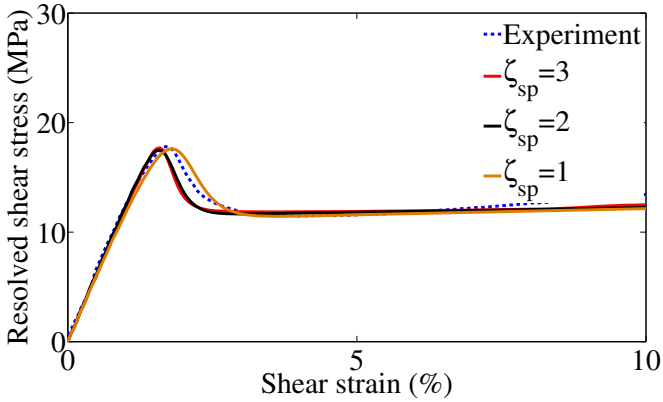

Figure 7.6: Stress-strain curves of uniaxial tension of a CZ-crystal in the reference conditions ($c_O^\infty = 1.5 \times 10^{17}\,\mathrm{cm}^{-3}$) using different values for ζ_{sp}.

$c_{O,t=0}$ ($10^{20}\,\mathrm{cm}^{-3}$)	1.65	4.4	7.15	9.9
$\tau_{O,t=0}$ (MPa)	3.6	9.6	15.5	21.5
η	2×10^{-1}	3×10^{-2}	6×10^{-3}	1.5×10^{-4}

Table 7.3: Optimum values of η for $\zeta_{sp} = 2.4$ and $T = 1073\,\mathrm{K}$.

Fig. 7.6 shows results from simulations considering the CZ-crystal with $c_O^\infty = 1.5 \times 10^{17}\,\mathrm{cm}^{-3}$ and various values of ζ_{sp}. Setting it to 1 as for *ds2* provides with an estimation of the lower yield stress very close to its experimental value. For the corresponding δ_O, it is found that $\eta = 1$ provides with the best fit of the upper yield stress. Namely, the identification method relying solely on the best estimate of τ_{lyp} indicates that impurities do not affect the mechanical behavior of silicon at $c_O^\infty = 1.5 \times 10^{17}\,\mathrm{cm}^{-3}$. This is in disagreement with the experimental data of [Yonenaga 1984] and shows that relying solely on τ_{lyp} to identify ζ_{sp} is not sufficient. On the other hand, setting $\eta = 0.2$, the upper yield stress is retrieved for $\zeta_{sp} = 2.4$, the lower yield stress still being correctly retrieved.

Determination of $\eta(\tau_O)$

The optimum η reproducing the upper yield stresses of *ds3* are given in Table 7.3. The sample with $c_O^\infty = 9 \times 10^{17}\,\mathrm{cm}^{-3}$ is representative of very highly contaminated crystals in which inhomogeneity of the oxygen distribution leads to an additional increase of the upper yield stress. Inhomogeneous distribution of the oxygen atoms along the dislocation line enhances the formation of aggregates that increase further the unlocking stress [Yonenaga 1984]. Since this nonlinear regime of the unlocking stress is not considered in the present work we disregard the result obtained at

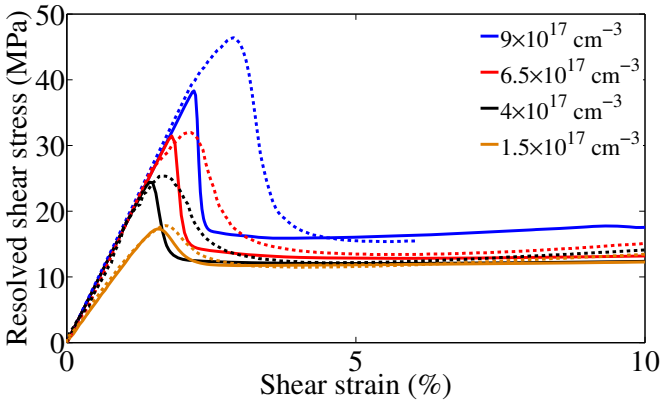

Figure 7.7: Simulated (full lines) and experimental (dashed lines) stress-strain curves of extrinsic silicon monocrystals deformed in the reference conditions and different c_O^∞.

$9 \times 10^{17}\,\mathrm{cm}^{-3}$. Enforcing $\eta(0) = 1$, the results of Table 7.3 can be approximated fairly well by Eq. 7.14.

$$\eta\left(\tau_O^{(\alpha)}\right) = \exp\left(-\frac{\tau_O^{(\alpha)}}{\tau_O^{ref}}\right) \tag{7.14}$$

where $\tau_O^{ref} = 2.91\,\mathrm{MPa}$ is a reference stress. Simulated stress-strain curves are compared to the experimental results in Fig. 7.7. The simulated yield drop is sharper than the experimentally observed one, owing to the strain rate variations in the yield region and the choice of $\theta > 0$ (see previous Section).

7.3 DISCUSSION

7.3.1 *Model parameters*

Internal stress and steady-state of deformation

$A_{\alpha\alpha} = 0.21$ found by best fit of the model to the stress-strain curves of the whole yield region is a value is of the same order of magnitude as the 0.3 usually mentioned in the literature by, e.g., [Suezawa 1979, Moulin 1997a].

As mentioned in Section 7.2.1, the steady-state of deformation in stage I is entirely defined by the adoption of the extended AH model. An excellent agreement is indeed observed between the experimental and predicted steady-state variables, independently of the parameter set chosen, either with or without the introduction of a strain rate dependency. Figure 7.8 shows the simulated ρ_m^* and τ_{eff}^* at various temperatures and strain rates if only a temperature dependency is introduced in the constitutive parameters (set of Eqs. 7.12). Figure 7.9 shows the steady-state obtained by inserting a strain rate dependency into δ and r_c and using Eqs. 7.13.

It must be reminded here that the *only* experimentally measurable variable is the effective stress τ_{eff}^* by means of strain rate changes during uniaxial tensile deformation. From Orowan's law and knowing the dislocation motion expression and parameters, the corresponding density of mobile dislocation can be deduced. Therefore the agreement with experimental data reached by the model on both τ_{eff}^* and ρ_m^* is due to the numerical values adopted in the velocity law (see Section 6.3.1), very close to those chosen by [Suezawa 1979].

Another point worth mentioning is that there is no perfect steady state of deformation corresponding to a constant shear strain rate. Namely, rotation of the crystal lattice with respect to the tensile axis owing to plastic flow affects the projected $\dot{\gamma}$ throughout stage I. Figure 7.10 shows the evolution of $\dot{\gamma}$ with strain[4]for various applied strain rates. A slight increase of the strain rate is noticed as stage I proceeds. This affects obviously both τ_{eff} and ρ_m in the "steady-state", so that the simulation data plotted in Figs. 7.8 and 7.9 actually are the τ_{eff} and ρ_m observed in the *middle* of stage I and can be considered representative of their value through stage I at $\pm 10\%$. Interestingly, the dislocation density is more affected by strain rate changes during stage I than the effective stress is. The marked decrease of $\dot{\gamma}$ at large strains is due to the activation of secondary systems.

Dislocation multiplication

The numerical values of δ given by Eq. 7.12 are very close to the ones introduced in Table 7.1. This was expected since this parameter determines the magnitude of the upper yield point.

4 As in the rest of this work, the shear strain γ is assumed here proportional to time and $\gamma = \dot{\gamma}_{th} \times t$, with $\dot{\gamma}_{th}$ the theoretically constant applied shear strain rate. Discussions both here and in Section 7.2.2 show that this relationship is not valid as the actual $\dot{\gamma}$ does vary with time.

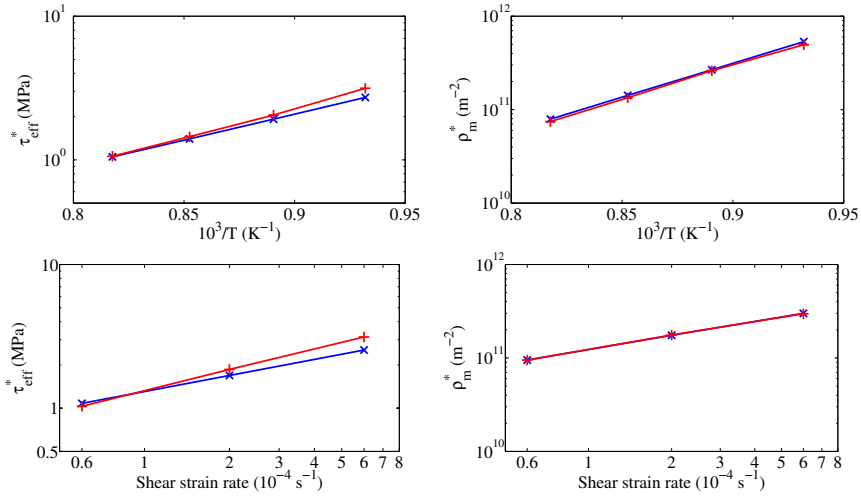

Figure 7.8: Steady-state values of τ^*_{eff} and ρ^*_m on the primary system as experimentally found and from simulations. Temperature-dependent parameters only (Eq. 7.12). Top: various temperatures at $\dot{\gamma} = 1.2 \times 10^{-4}\,s^{-1}$. Bottom: various strain rates at 1173 K.

The strain rate dependent constitutive parameters given by Eq. 7.13 allow for a good representation of the mechanical behavior of silicon monocrystals deformed in single glide. ζ_{sp} is then the only parameter that needs adjustments given a silicon specimen. Its variations with respect to the set of samples might be due to e.g. approximations of the initial dislocation density measurements, or to the influence of small impurity concentrations in the bulk. Its large increase in the case of crystals containing an inital dislocation density of $10^{10}\,m^{-2}$ shows that the variations of ζ_{sp} most likely betray the effects of forest dislocations on the multiplication and storage mechanisms that the constitutive model does not allow to represent explicitely.

Dislocation storage

Observations of thin foils from silicon samples deformed at the end of stage I at 1073 K by [Oueldennaoua 1988] yield for the maximum value of the dipole half-width $r_c^{max} = 6 \times 10^{-7}$ m. r_c is an effective dipole half-width and can be approximated *via* the average square dipole width [Hähner 1996]:

$$r_c = \sqrt{(e-1)\, r_c^{max} r_a} \tag{7.15}$$

where r_a is the critical half-width for dipole annihilation, typically a couple of Burgers vectors. Taking at 1073 K $r_a = 10^{-9}$ m gives $r_c = 3.2 \times 10^{-8}$ m, one order of magnitude larger than the result given by Eq. 7.12 but comparable to the individual best fits (Table 7.1). The capture radius found by simultaneous fit of the extended model to experimental data is conse-

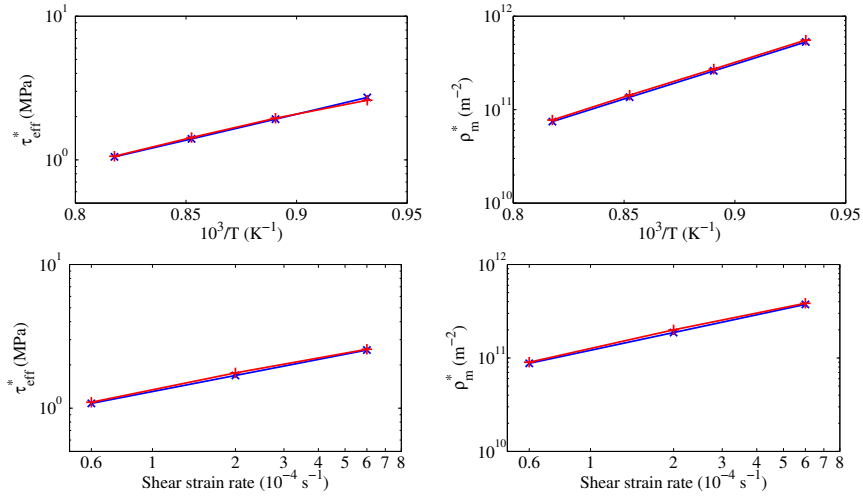

Figure 7.9: Steady-state values of τ^*_{eff} and ρ^*_m on the primary system as experimentally found and from simulations. Temperature and strain rate dependent parameters (Eq. 7.13). Top: various temperatures at $\dot{\gamma} = 1.2 \times 10^{-4}\,s^{-1}$. Bottom: various strain rates at 1173 K.

quently much lower than its empirical values when the correct steady-state of deformation is imposed through Eqs. 7.4 and 7.10. This has two main consequences:

- Firstly, the ratio $\frac{\rho_m}{\rho_t}$ is overestimated, as way too few dislocations are stored. This leads to disagreements with the experimental observations at the lower yield point (see below).
- Secondly, since not enough dislocations are stored there is no need to generate more throughout deformation in order to maintain a steady plastic flow. This results in a too low net generation rate, translated in the stress-strain curves by a too low hardening rate in stage I.

The constitutive model introduced in this work cannot allow a correct representation of both the yield region and the evolution of the flow stress beyond the lower yield point. This most likely betrays additional dislocation multiplication and storage mechanisms active from the lower yield point, such as the influence of forest dislocations generated during yielding.

Strain rate dependency

The strain rate variations of the silicon specimen in the yield region during experiments are not known. Simulations indicate that they depend strongly on the stiffness of the machine E_{blocks}, itself varying with the specimen considered. This leads to large uncertainties concerning the identification of the parameter θ governing the strain rate dependency of the constitutive parameters δ and r_c.

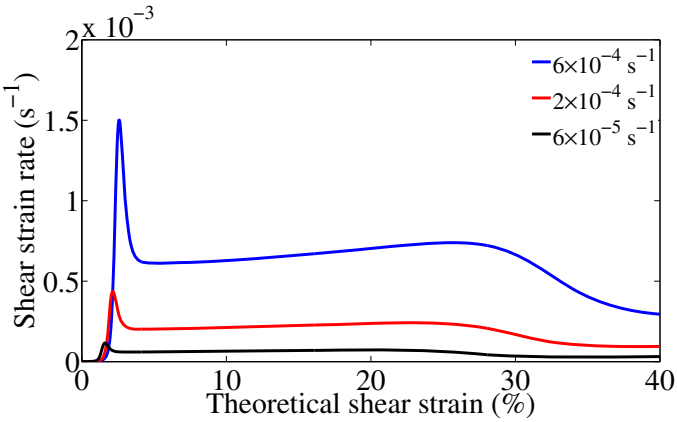

Figure 7.10: Evolution of the shear strain rate $\dot{\gamma}$ on the primary system throughout deformation.

All dependency has been transfered on the dislocation multiplication factor only, which leads to simulated yield drops sharper than the experimental ones but yields an accurate hardening behaviour throughout stage I.

Choosing the optimal θ so that the yield region is correctly represented raises questions both about its temperature dependency, and the variations of the optimum ζ_{sp} with the deformation conditions.

It will be seen in the next Part that an alternative dislocation multiplication law for the yield region can mitigate all these issues.

Stress and strain distribution

Deformation proceeds rather homogeneously throughout the sample gauge. The crystallographic orientation of the sample has a direct influence on the strain contours, as can be seen by development of plastic deformation from two localization zones close to the sample fillets, as shown in Fig. 7.11. The deformation isolines then propagate inwards and meet at the gauge center.

This localization phenomena is much less visible on the stress distribution (see Fig. 7.12).

7.3.2 *Influence of secondary slip systems and large ρ_0*

No dislocation multiplication or storage due to mutual interaction between slip systems is introduced in the constitutive model. The only way for secondary dislocations to be generated in simulations is by overcoming the critical resolved shear stress for setting them into motion and fulfilling the relation $\left|\tau^{(\alpha)}\right| \geqslant \tau_i^{(\alpha)} + \tau_b^{(\alpha)}$. This condition is realized mainly before the lower yield point.

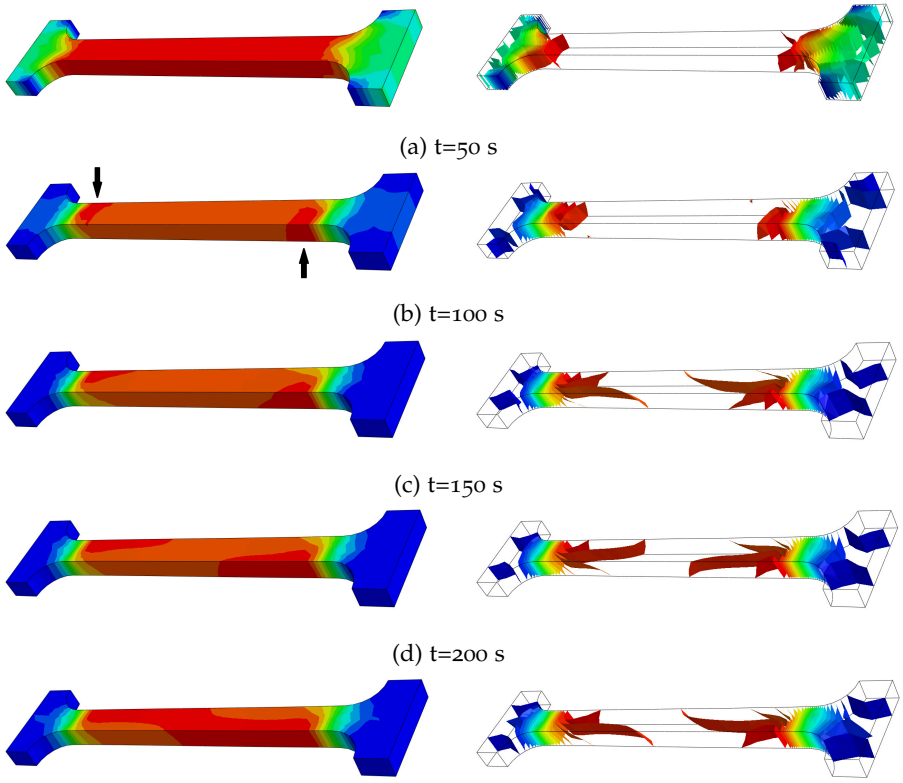

(a) t=50 s

(b) t=100 s

(c) t=150 s

(d) t=200 s

(e) t=250 s

Figure 7.11: (left hand side) Maximum principal strain distribution and (right hand side) isosurfaces in the silicon sample deformed at $\dot{\gamma} = 2 \times 10^{-4}\,\mathrm{s}^{-1}$ and T=1173 K. The scale is recomputed for each figure. The localization zones are indicated by arrows in figure b.

(a) t=50 s

(b) t=100 s

(c) t=150 s

(d) t=200 s

(e) t=250 s

Figure 7.12: Von Mises stress distribution in the silicon sample deformed at $\dot{\gamma} = 2 \times 10^{-4}\,\mathrm{s}^{-1}$ and T=1173 K. The scale is recomputed for each figure.

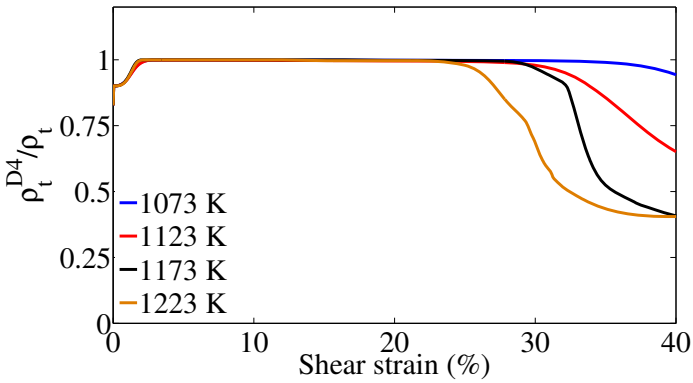

Figure 7.13: Fraction of ρ_t present on the primary slip system, D4 using the Schmid & Boas notation. Temperature-dependent parameters.

General remarks

Let us consider monocrystals oriented for single glide. As mentioned above, several slip systems are activated in the yield region owing to the large effective stress applied there. The secondary dislocation density continues to grow beyond the lower yield point, but at a slow pace, remaining two to three orders of magnitude below the primary density during stage I (see Fig. 7.13).

It follows that virtually all dislocations are present on the primary slip system throughout deformation. Secondary systems become active as the lattice rotates with deformation around $\gamma = 30\,\%$. The constitutive model looses its validity at this point.

It is experimentally observed at 1073 K that 10 % of the total dislocation density is on secondary systems at the lower yield point, this fraction diminishing as temperature is highened (see [Yonenaga 1978]). The extended models introduced in this Chapter cannot represent this phenomena.

Influence of large initial ρ_m

Turning to the case of large initial dislocation densities, Fig. 7.14 compares the model outputs to the experimental data set *ds3*.

Although a progressive disappearance of the upper yield stress with increasing ρ_0 is predicted, a strong quantitative disagreement can be observed between numerical and experimental results. This reveals a limitation of the extended AH model, not able to accurately account for the enhanced dislocation multiplication rate at larger initial densities.

Influence of sample orientation

All specimen considered until now are oriented for uniaxial tension along a [123] axis. Let us compare the predicted behavior for orientations along

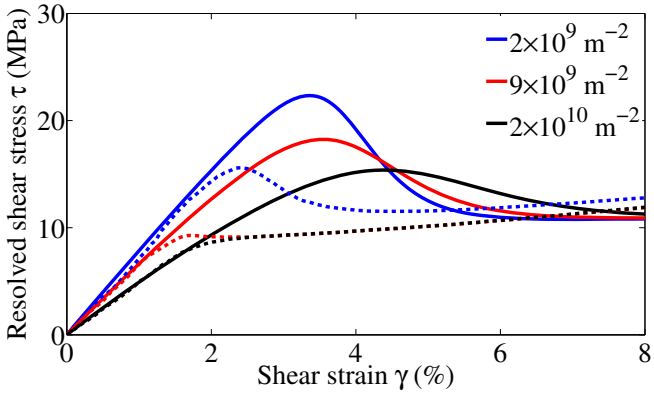

Figure 7.14: Comparison of experimental (dashed) and simulated (plain) stress response of FZ silicon tensile specimen deformed at various ρ_0, with $\dot{\gamma} = 1.2 \times 10^{-4}\,\mathrm{s}^{-1}$ and T=1073 K. Temperature-dependent constitutive parameters (Eq. 7.12).

[112], [110], [100] and [111]. The experimental results shown in Fig. 2.1 are then used as reference.

The initial density is set to $\rho_0 = 10^{10}\,\mathrm{m}^{-2}$, equally distributed among the 12 slip systems. The applied strain rate is $\dot{\varepsilon} = 2 \times 10^{-3}\,\mathrm{s}^{-1}$ and the temperature T=1095 K, the equivalent for Si[5] to the conditions used by [Patel 1963]. Fig. 7.15 is then obtained.

Two remarks can be made:

1. The ordering of the upper yield stresses does not follow the experimental one (see Fig. 2.1). Loading along symmetrical orientations should lead to a lower τ_{uy}; simulations predict on the other hand an increased τ_{uy}

2. No strong hardening rate is predicted beyond the lower yield point, even in orientations such as [111] activating 8 slip systems

The first remark is potentially due to two factors: the effective stress dependency of the multiplication law K on the one hand, and the absence of dislocation generation following from forest interactions on the other.

The latter factor is also bound to explain the lack of strong hardening rate beyond the lower yield point in symmetrical orientations.

Conclusions: dislocation generation rate

Adding a dislocation generation term proportional to the mean free path of dislocations on their glide plane could improve the model outputs at large dislocation densities. It could provide with answers to several questions

5 These experiments were obtained on Germanium crystals at a nominal temperature $T/T_m = 0.65$. This ratio gives for Si T=1095 K.

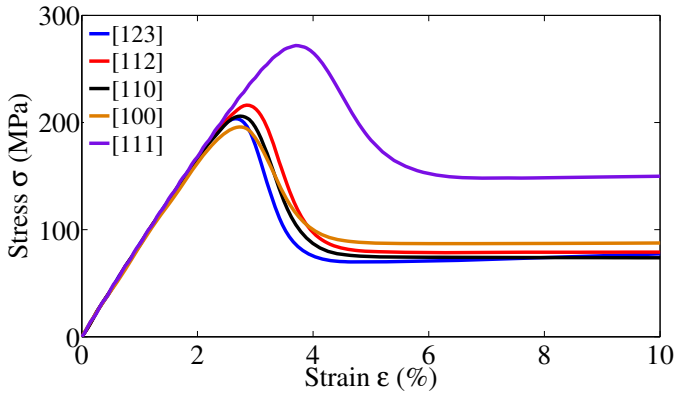

Figure 7.15: Stress-strain curves yielded by the extended AH model (temperature-dependent parameters only) for samples of various initial crystallographic orientations. See text for details.

raised throughout this Chapter, indicating that dislocation multiplication and storage mechanisms on the forest trees are active in silicon crystals even at low densities.

The additional hardening provided by such a small percentage of forest dislocations could also explain the discrepancy between the simulated and experimental flow stresses at lower temperatures (Fig. 7.3), as well as improving the hardening rate through stage I.

Another hint that additional generation mechanisms are active from the yield drop is the the optimal capture radius obtained by best fit, way too low compared to experimental observations. Increasing it to physically more acceptable values would lead to an increased steady-state effective stress if the dislocation generation rate were not increased accordingly.

7.3.3 *Mechanical state at the lower yield point*

Comparison of the model outputs with additional experimental data [Yonenaga 1981] shows that it predicts successfully the effective resolved shear stress at the lower yield point.

The model parameters nonetheless overestimate the fraction of mobile dislocations $\left.\frac{\rho_m}{\rho_t}\right|_{uyp}$. Actually, given the too low storage radius r_c stemming from Eqs. 7.12 and 7.13, almost all dislocations are mobile through deformation. [Yonenaga 1981] reports in the reference conditions fractions of 35-40 % in silicon.

A direct consequence of these remarks is that the extended model based on the empirical generation law suggested by Alexander & Haasen cannot guarantee full agreement between experimental data and simulations. Increasing r_c by one order of magnitude or more to bring its value closer

to physical ones and to reduce $\left.\frac{\rho_m}{\rho_t}\right|_{uyp}$ results, if Eq. 7.4 is to be strictly enforced, in a multiplication prefactor too high to correctly represent any yield phenomena. The multiplication law of Alexander & Haasen cannot yield accurately mobile dislocation densities and the steady-state of deformation simultaneously, if the experimental stress-strain curves are to be correctly represented.

7.3.4 *Extrinsic crystals*

The introduction of an effective density of mobile dislocations $\rho_{m,eff} \leq \rho_m$ combined with an alteration of the dislocation multiplication rate $\delta_O \leq \delta$ increases the upper yield stress of extrinsic crystals. The fraction of effectively mobile dislocations η is imposed by the constitutive model only when oxygen diffuses to the dislocations. An exponential decay of η with τ_O correctly reproduces the experimental results. The simulated stress-strain behavior of extrinsic crystals is consistent with experimental observations. The case of highly contaminated crystals in which the oxygen distribution is no longer homogeneous cannot be correctly accounted for by the constitutive model, resulting in an underestimation of the upper yield stress when oxygen clusters form along the dislocation lines.

Relative contributions of model modifications

A closer look is taken at the relative contribution of both modifications to the simulated mechanical behavior of extrinsic crystals. To achieve this, each feature is disabled and a simulation launched while keeping the remaining active. A CZ crystal is loaded at 1173 K, $\dot{\gamma} = 1.1 \times 10^{-4}\,\mathrm{s}^{-1}$, with an initial primary dislocation density of $\rho_{m,0}^{(D4)} = 10^{10}\,\mathrm{m}^{-2}$ and bounded by elastic blocks characterized by $E_{blocks} = 4 \times 10^9\,\mathrm{N.m}^{-2}$. Fig. 7.16 compares the base result with stress-strain curves obtained after either an alteration of δ or a reduction of the effective dislocation density.

Clearly setting $\delta_O = \delta$ does not lead to significant divergences in the results (red curve). On the other hand, using an effective mobile dislocation density is a necessary modification of the present model for intrinsic crystals, if the increase of the upper yield stress is to be reproduced.

Uncertainties on $\eta(\tau_O)$

Any variation of ζ_{sp} affects the upper yield stress, and η must be adapted accordingly to compensate for this drift under the constraint $\eta \leq 1$. Based on experimental observations on the CZ-crystal with $c_O^\infty = 1.5 \times 10^{17}\,\mathrm{cm}^{-3}$ we have set $\zeta_{sp} = 2.4$ to identify the variations of $\eta(\tau_O)$. Given that the constitutive model cannot reproduce the hardening rate in stage I, no other reliable option is available to identify ζ_{sp}.

An additional source of uncertainty in the identification of η is the dependency of ζ_{sp} on the initial dislocation density. The latter is set to

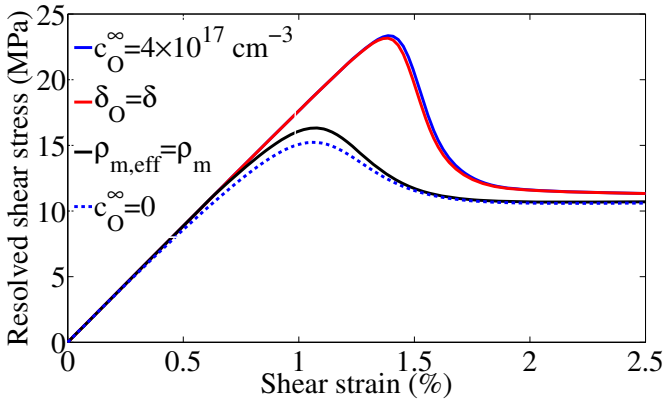

Figure 7.16: Influence of the modifications brought to the model for intrinsic crystals. Base cases in blue (with or without oxygen), with both the dislocation multiplication pre-factor δ and the effective density of mobile dislocations $\rho_{m,eff}$ affected.

$10^{10}\,\mathrm{m}^{-2}$ on the primary system, but the actual one might differ from this value by a factor two as mentioned by [Yonenaga 1984]. The individual values for η given in Table 7.3 are however in excellent agreement with experimental observations yielding at 1073 K $\eta(c_O = 4.4 \times 10^{20}\,\mathrm{cm}^{-3}) \simeq 4\,\%$ and $\eta(c_O = 6.5 \times 10^{20}\,\mathrm{cm}^{-3}) \simeq 1\,\%$ (see Fig. 3 in [Yonenaga 1984]). Determining $\eta(\tau_O)$ from these three cases alone does not give $\eta = 1$ in intrinsic crystals, therefore Eq. 7.14 only approximates the individual best fits.

Inhomogeneous distribution of oxygen at high c_O^∞ leads to the formation of impurity clusters along the dislocation line that increase significantly the unlocking stress and reduce further the fraction of effectively mobile dislocations. The present constitutive model cannot account for this phenomena and underestimate the upper yield stress in highly contaminated silicon crystals. A better determination of τ_O in the presence of oxygen aggregates would improve this aspect.

Validation of the constitutive model for extrinsic crystals

The variations of the resolved upper yield stress τ_{uy} with c_O^∞, temperature and initial dislocation density are studied. The dependency of τ_{uy} on the stiffness of the machine limits the exploitability of the simulated results. However, it is interesting to compare the trends from experiments from [Yonenaga 1984] and simulations. The Young's modulus of the elastic blocks are set to $E_{blocks} = 4 \times 10^9\,\mathrm{N.m}^{-2}$. The dislocation multiplication prefactor is set to $\zeta_{sp} = 2.4$, a choice appropriate for $\rho_{m,t=0}^{(D4)} = 10^{10}\,\mathrm{m}^{-2}$ but decreasing the upper yield stress of samples with an initial dislocation density $\rho_{m,t=0}^{(D4)} = 2 \times 10^9\,\mathrm{m}^{-2}$.

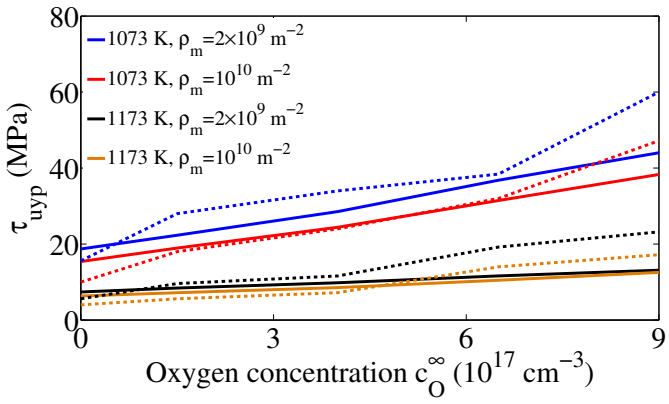

Figure 7.17: Variations of the upper yield stress with T, $\rho_{m,t=0}^{(prim)}$ and c_O^∞. Experimental data in dashed curves, simulations in full lines.

Figure 7.17 shows the values of τ_{uy} as a function of c_O^∞, at different temperatures and initial dislocation densities. The upper yield stresses of FZ-crystals are represented as well. The agreement between the experimental results and the model outputs is quite good given the many unknowns and approximations. Overall, the constitutive model is able to reproduce correctly the mechanical behaviour of oxygen-contaminated silicon crystals.

Influence of t_m and mesh sensitivity

CZ-crystals deformed in the reference conditions are considered in the following, with an oxygen content $c_O^\infty = 9 \times 10^{17}\,\mathrm{cm}^{-3}$. The material parameter $t_m \propto \lambda_O$ has a strong influence on the mechanical behavior of extrinsic silicon crystals by influencing the preference for impurities to leave the dislocation cores. Competition between dislocation velocity v and the "backjumping speed" a/t_m determines whether impurities tend to leave the core or not. Impurity drag dominates if $a/t_m > v$ (see Eq. 6.31). Using the expressions of t_m, D_O and $v(\tau_{eff})$, this inequality can be reduced to a simple condition for impurity drag to govern dislocation motion:

$$\lambda_O \lesssim \frac{1.76 \times 10^6}{\tau_{eff}} \exp\left(\frac{0.41}{k_b T}\right) \tag{7.16}$$

Eq. 7.16 can be used to determine the values of λ_O influencing the stress-strain behaviour of silicon crystals deformed at 1073 K and $\dot{\gamma} = 1.1 \times 10^{-4}\,\mathrm{s}^{-1}$ in stage I. The latter is experimentally characterized by $\tau^*_{eff}(T, \dot{\gamma})$, and $\lambda_O \lesssim 50$ is obtained. The effects of λ_O on CZ-crystals are visible in Fig. 7.18, where the behavior of a FZ-crystal is plotted for comparison. The case $\lambda_O = 10$ affects significantly the mechanical behaviour in stage I, whereas this is not the case for $\lambda_O = 100$, in agreement with our discussion.

The irregular hardening slope of extrinsic crystals beyond the lower yield point does *not* come from oxygen atoms migrating to the dislocation core in

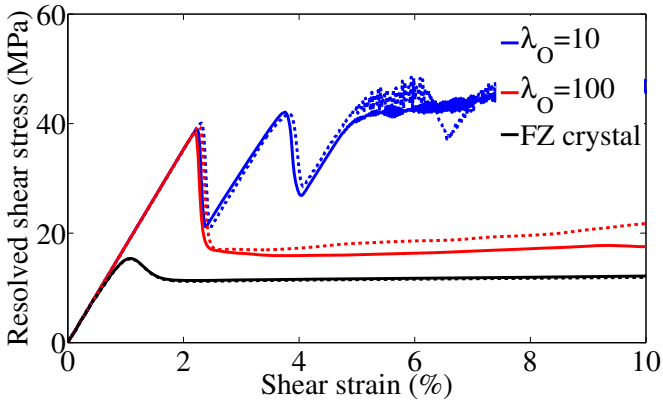

Figure 7.18: Influence of λ_O on the mechanical behavior of silicon. Full lines: standard mesh. Dashed lines: refined mesh.

the central elements used to plot the stress-strain curves. The locking effect takes place inhomogeneously through the entire silicon specimen gauge and leads to a slight mesh size dependency due to localization phenomena. Fig. 7.18 shows the simulated behavior for the standard mesh introduced in Sec. 7.1 and a refined one containing 8 times more elements. The mesh sensitivity influences the simulated stress-strain behavior only into stage I, and does not affect the validity of the results derived in this work. It increases as λ_O is decreased or c_O^∞ increases. The actual magnitude of λ_O is not known . Setting $\lambda_O = 100$ gives satisfying results while limiting the mesh sensitivity.

CONCLUSION

This part has concentrated on analyzing and improving the constitutive models available in the literature for the study of the yield region of silicon crystals.

ANALYSIS OF TRADITIONAL MODELS

We took in Chapter 5 a purely pragmatic approach and found the best fits of each available model to experimental data obtained at various temperatures. This has revealed that a temperature dependency of the constitutive parameters, physically justified or not, must be introduced if the mechanical behavior of silicon is to be reproduced accurately. A generic model for the yield region, from which all three models formerly derived by various research groups can be retrieved, has been proposed. Although without any physical basis, such a model can be used to fit the yield region with a very good accuracy.

From this preliminary study providing for the first time accurate parameters for the yield region of silicon in various thermodynamic conditions, it has been concluded that the assessment of a given model should be done *on its predictive abilities both for the stress-strain and the mobile dislocation density evolutions*. Table 7.4 gives an overview of the conclusions drawn from Chapter 5.

Some limitations of the traditional models have been exposed. We suggest that they can be overcome by working on two fronts:

- Improving the kinematics used to model silicon monocrystals to allow random loading situations
- In particular, the intrinsic elastic and plastic anisotropies must be accounted for if monocrystals or aggregates of large single crystals are to be studied
- Developing further the constitutive equations for the yield region to provide with a physical basis to the temperature and strain rate variations of the constitutive parameters.

Annex A details the rate-dependent crystal plasticity (RDCP) framework, that accounts for the anisotropic nature of plastic deformation and provides with a powerful numerical tool to explore the mechanical behavior of crystalline aggregates. Its abilities are compared to the standard J_2 framework. Although computationally less expensive, the latter barely accounts for elastic anisotropy and limits the physics of crystal plasticity to a single slip system.

	Asset	Limitation
Kinematics		scalar
Cost	cheap	
Yield region	very good	
Stage I		not valid
Multiple slip		no
Extrinsic crystals		no
Physical basis		little, if any
Parameters		variable

Table 7.4: Overview of the abilities of traditional models (Chapter 5) to represent the mechanical behavior of silicon monocrystals.

IMPROVEMENTS OF THE AH MODEL

Improving the constitutive equations on a physical basis supposes to have the knowledge of the very processes taking place during deformation. Chapter 6 starts therefore with a review of the physical processes leading to hardening and recovery during a uniaxial tensile test of a monocrystal.

Intrinsic crystals

Based on this information, a density of immobile dislocations is introduced in the model of Alexander & Haasen. The evolution of this population is assumed to stem from the storage of mobile dislocations as dipoles - dislocation annihilation is ignored. This simple extension guarantees the existence and unicity of the steady-state of deformation in stage I.

Two variations of this extended model have been introduced, accounting either only for the sole effect of temperature on the steady-state or adapted to the more general case of varying strain rate and temperature.

It follows significant improvements to the traditional model of Alexander & Haasen:

- The variations of the yield stresses with temperature and strain rate are correctly reproduced
- Insertion of experimental characterization of the steady-state allows the model to retrieve the same observable values

However, enforcing the correct description of the steady-state leads to a disagreement between the experimental and modeled magnitudes of the dislocation storage parameter r_c. The extended model does not predict enough transfer of dislocation densities from the mobile to the immobile populations owing to a small r_c. This results in an overwhelming majority

of mobile dislocations throughout deformation and a too low hardening rate in steady-state.

- If the capture radius is to be increased closer to its experimental estimations, the dislocation generation rate must be increased accordingly

The extended AH model also fails to reproduce quantitatively the experimental disappearance of the upper yield point with increasing initial dislocation density. Study of its outputs at various crystallographic orientations reveals additional discrepancies with experimental data:

- The extended AH model predicts a sensible increase of τ_{uy} upon uniaxial loading in symmetrical orientations and no subsequent significant hardening beyond the lower yield point

It can be concluded from these observations that *the extended AH model lacks a mobile dislocation generation term, likely to be active in the presence of forest obstacles, that could allow a larger r_c and correct the shortcomings identified in multiple slip and at large dislocation densities*. The effect of dislocation generaton from Frank-Read sources on the forest is investigated in the next Part.

Extrinsic crystals: dislocation locking

Based on experimental observations and theoretical arguments, an effective density of mobile dislocations actually carrying plastic flow when dissolved impurities are present in the crystal is introduced. It is shown that this enables the correct reproduction of the increased upper yield stress at large dissolved oxygen contents.

On the other hand, a reduction of the dislocation multiplication parameter δ as done by [Maroudas 1991c] has no significant effec on the quantitative evolution of the upper yield stress at high oxygen contents.

Table 7.5 summarizes shortly the present discussion. Note that the limitation induced by the expensive cost of kinematics can be reduced by implementing a small strain approximation of the RDCP framework.

Model applicability and limitations

What fundamentally defines the model of Alexander & Haasen and the other ones introduced in this work is their dislocation multiplication law. We have seen that these induce an inherent limitation to single glide, since no effect of the forest on dislocation multiplication or storage is introduced. A lack of dislocation generation at the lower yield point and beyond actually leads to the underestimation of the dislocation capture radius in stage I, and to a pathologic simulated behavior when two slip systems or more are activated.

	Asset	Limitation
Kinematics	powerful	
Cost		expensive
Yield region	very good	
Stage I	steady-state	flow stress, hardening rate
Multiple slip		no
Extrinsic crystals	very good	
Physical basis	yes	not enough
Parameters	closed-form	disagreement exp/sim

Table 7.5: Overview of the abilities of the extended AH model (Chapter 6) to represent the mechanical behavior of silicon monocrystals.

However, as long as used in single slip loading conditions, the constitutive equations introduced in this Part bring significant improvements to the simulated mechanical behavior of silicon materials. Their implementation into a cheap J_2 framework is actually fully acceptable when used in easy glide conditions.

The next Part aims at deriving a wholly new constitutive model for semiconductors, putting the classical multiplication laws aside. This lifts the limitations of the present extended model, and gives further insights into the processes taking place during deformation of silicon crystals.

BIBLIOGRAPHY

[Alexander 1968] *Dislocations and plastic flow in the diamond structure*, H. Alexander, P. Haasen, Solid State Physics, Vol. 22, pp. 27-158, 1968

[Alexander 1986] *Dislocations in covalent crystals*, H. Alexander, in: Dislocations in Solids, Nabarro (ed.), Vol. 7, pp. 114-234, 1986

[Alexander 2000] *Latent hardening of germanium crystals*, H. Alexander, J.L. Crawford, Phys. Stat. Sol. (b), Vol. 22, pp. 41-49, 2000

[Allem 1989] *On the yield point of floating-zone silicon single crystals III. The evolution of the dislocation structure through the yield point at low temperature*, R. Allem, J.P. Michel, A. George, Philosophical Magazine A, Vol. 59, No. 2, pp. 273-302, 1989

[Amirkhizi 2007] *A framework for numerical integration of crystal elasto-plastic constitutive equations compatible with explicit finite element codes*, A.V. Amirkhizi, S. Nemat-Nasser, International Journal of Plasticity, Vol. 23, pp. 1918-1937, 2007

[Amodeo 1990] *Dislocation dynamics. I. A proposed methodology for deformation micromechanics*, R.J. Amodeo, N.M. Ghoniem, Physical Review B, Vol. 41, No. 10, pp. 6958-6967, 1990

[Arsenlis 2002] *Modeling the evolution of crystallographic dislocation density in crystal plasticity*, A. Arsenlis, D.M. Parks, Journal of the Mechanics and Physics of Solids, Vol. 50, pp. 1979-2009, 2002

[Aseev 1975] *Dislocation processes during plastic deformation of Si and Ge in the range 0.50 to 0.95 of the melting temperature*, A.L. Aseev, Yu. N. Golobokov, S.I. Stenin, Phys. Stat. Sol. (a), Vol. 28, pp. 355-364, 1975

[Ashmawi 2000] *Microstructurally induced ductile deformation mechanisms and grain-boundary effects in polycrystalline aggregates*, W.M. Ashmawi, M.A. Zikry, Materials Research Society Proceedings, Vol. 578, pp. 339-344, 2000

[Bassani 1991] *Latent hardening in single crystals. II. Analytical characterization and predictions*, J.L. Bassani, T.-Y. Wu, Proceedings of the Royal Society of London A, Vol. 435, pp. 21-41, 1991

[Berner 1967] *Dislocation density and local slip in germanium single crystals*, K. Berner, H. Alexander, Acta Metallurgica, Vol. 15, No. 5, pp. 933-941, 1967

[Bulatov 2001] *Parameter-free modeling of dislocation motion: the case of silicon*, V.V. Bulatov, J.F. Justo, W. Cai, S. Yip, A.S. Argon, T. Lenosky, M. De Koning, T. Diaz De La Rubia, Philosophical Magazine A, Vol. 81, No. 5, pp. 1257-1281, 2001

[Burenkov 1974] *Temperature dependence of elastic constants of silicon*, Y.A. Burenkov, S.P. Nikanorov, Soviet Physics of Solid State, Vol. 16, No. 5, pp. 963-964, 1974

[Caillard 2003] *Thermally activated mechanisms in crystal plasticity*, D. Caillard, J.-L. Martin (ed. R.W. Cahn), 2003, Pergamon Materials Series, Pergamon

[Castelnau 2003] *Minimisation de fonctions et optimisation de paramètres avec* Pikatchou*, User's manual*, O. Castelnau, 2003

[Cheong 2004] *Discrete dislocation density modelling of single phase FCC polycrystal aggregates*, K.-S. Cheong, E.P. Busso, Acta Materialia, Vol. 52, pp. 5665-5675, 2004

[Cochard 2009] *Constitutive modelling of silicon using crystal plasticity*, J. Cochard, I. Yonenaga, S. Gouttebroze, M. M'Hamdi, Z.L. Zhang, 3rd Workshop on Crystalline Silicon Solar Cells (CSSC), Trondheim, Norway, 2009

[Cochard 2010a] *Constitutive modeling of intrinsic silicon monocrystals in easy glide*, J. Cochard, I. Yonenaga, S. Gouttebroze, M. M'Hamdi, Z.L. Zhang, Journal of Applied Physics, Vol. 107, No. 3, pp. 033512-1/10, 2010

[Cochard 2010b] *Constitutive modeling of intrinsic and oxygen-contaminated silicon monocrystals in easy glide*, J. Cochard, I. Yonenaga, S. Gouttebroze, M. M'Hamdi, Z.L. Zhang, Journal of Applied Physics, Vol. 108, No. 10, pp. 103524-1/10, 2010

[Cuitiño 1992] *Computational modelling of single crystals*, A.M. Cuitiño, M. Ortiz, Modelling Simul. Mater. Sci. Eng., Vol. 1, pp. 225-263, 1992

[Dash 1956] *Copper precipitation on dislocations in silicon*, W.C. Dash, Journal of Applied Physics, Vol. 27, No. 10, pp. 1193-1195, 1956

[Devincre 2001] *Mesoscopic simulations of plastic deformation*, B. Devincre, L.P. Kubin, C. Lemarchand, R. Madec, Materials Science and Engineering A, Vol. A309-310, pp. 211-219, 2001

[Devincre 2005] *Collinear interactions of dislocations and slip systems*, B. Devincre, T. Hoc, L.P. Kubin, Materials Science and Engineering A, Vol. 400-401, pp. 182-185, 2005

[Devincre 2006] *Physical analyses of crystal plasticity by DD simulations*, B. Devincre, L. Kubin, T. Hoc, Scripta Materialia, Vol. 54, pp. 741-746, 2006

[Dillon 1986] *Dislocation dynamics during the growth of silicon ribbon*, O.W. Dillon, C.T. Tsai, R.J. De Angelis, Journal of Applied Physics, Vol. 60, No. 5, pp. 1784-1792, 1986

[Estrin 1986] *Local strain hardening and nonuniformity of plastic deformation*, Y. Estrin, L.P. Kubin, Acta Metallurgica, Vol. 34, No. 12, pp. 2455-2464, 1986

[Farber 1982] *Change of dislocation mobility characteristics in Si single crystals at elevated temperatures*, Y.A. Farber, V.I. Nikitenko, Phys. Stat. sol. (a), Vol. 73, pp. K141-143, 1982

[Fikar 2005] *Dislocation multiplication rate in the early stage of germanium plasticity*, J. Fikar, C. Dupas, T. Kruml, A. Jacques, J.L. Martin, Materials Science and Engineering A, Vol. 400-401, pp. 431-434, 2005

[Franciosi 1982a] *Multislip in FCC crystals: a theoretical approach compared to experimental data*, P. Franciosi, A. Zaoui, Acta Metallurgica, Vol. 30, pp. 1627-1637, 1982

[Franciosi 1982b] *Multislip tests on copper crystals: a junctions hardening effect*, P. Franciosi, A. Zaoui, Acta Metallurgica, Vol. 30, pp. 2141-2151, 1982

[Franciosi 1985] *The concept of latent hardening and strain hardening in metallic single crystals*, P. Franciosi, Acta Metallurgica, Vol. 33, No. 9, pp. 1601-1612, 1985

[Franciosi 1986] *FCC single crystals hardening and stacking fault energy*, P. Franciosi, Proceedings of the 7^{th} ICSMA, Vol. 1, pp. 281-286, 1986

[Gilman 1960] *Behavior of individual dislocations in strain-hardenend LiF crystals*, J.J. Gilman, W.G. Johnston, Journal of Applied Physics, Vol. 31, No. 4, pp. 687-692, 1960

[Gottschalk 1983a] *Dislocation bends in high stress deformed silicon crystals*, H. Gottschalk, Journal de Physique Colloque, Vol. 44, No. 9, pp. C4/69-74, 1983

[Gottschalk 1983b] *On the motion of dislocation bends in terms of the kink model*, H. Gottschalk, Journal de Physique Colloque, Vol. 44, No. 9, pp. C4/475-477, 1983

[Hirth 1982] *Theory of dislocations (second edition)*, J.P. Hirth, J. Lothe, Wiley, New York, 1982

[Hoc 2004] *Deformation stage I of FCC crystals: constitutive modelling*, T. Hoc, B. Devincre, L.P. Kubin, in: C. Gundlach, et al. (Eds), Evolution of deformation microstructures in 3D (Rise 25th Int. Symposium), Rise Natl. Lab., Denmark, pp. 43-59, 2004

[Hähner 1996] *The dynamics of dislocation dipoles during single glide*, P. Hähner, Scripta Materialia, Vol. 34, No. 3, pp. 435-441, 1996

[Imai 1983] *In situ X-ray topography of the dislocation mobility in high-purity and impurity-doped silicon crystals*, M. Imai, K. Sumino, Philosophical Magazine, Vol. 47, No. 4, pp. 599-621, 1983

[Iunin 2001] *Modes of kink motion on dislocations in semiconductors*, Y.L. Iunin, V.I. Nikitenko, Scripta Materialla, Vol. 45, pp. 1239-1246, 2001

[Johnston 1959] *Dislocation velocities, dislocation densities, and plastic flow in lithium fluoride crystals*, W.G. Johnston, J.J. Gilman, Journal of Applied Physics, Vol. 30, No. 2, pp. 129-144, 1959

[Kalan 2001] *Micromechanical based constitutive relations for modeling the bulk growth of single crystal InP*, R.J. Kalan, A.M. Maniatty, Journal of Crystal Growth, Vol. 233, No. 4, pp. 645-659, 2001

[Kirscht 1978a] *Some observations concerning the initial stage of plastic flow in silicon*, F.-G. Kirscht, J. Doerschel, C. Hansch, Phys. Stat. Sol. (a), Vol. 47, pp. K17-K20, 1978

[Kirscht 1978b] *Dislocation reactions in plastically deformed silicon observed by X-ray topography*, F.-G. Kirscht, C. Hansch, J. Doerschel, Phys. Stat. Sol (a), Vol. 48, pp. K11-K14, 1978

[Kocks 1975] *Thermodynamics and kinetics of slip*, U.F. Kocks, A.S. Argon, M.F. Ashby, Progress in Materials Science, Vol. 19, 1975

[Kocks 2003] *Physics and phenomenology of strain hardening: the FCC case*, U.F. Kocks, H. Mecking, Progress in Materials Science, Vol. 48, pp. 171-273, 2003

[Kojima 1971] *Strain-rate and temperature dependence of mechanical behaviour in germanium crystals*, K.-I. Kojima, K. Sumino, Crystal Lattice Defects, Vol. 2, pp. 147-158, 1971

[Kubin 1998] *Mesoscopic modelling and simulation of plasticity in fcc and bcc crystals: dislocation intersections and mobility*, L.P. Kubin, B. Devincre, M. Tang, Journal of Computer-Aided Materials Design, Vol. 5, No. 1, pp. 31-54, 1998

[Kubin 2008a] *Toward a physical model for strain hardening of fcc crystals*, L. Kubin, B. Devincre, T. Hoc, Materials Science and Engineering A, Vol. 483-484, pp. 19-24, 2008

[Kubin 2008b] *Modeling dislocation storage rates and mean free paths in face-centered cubic crystals*, L. KUBIN, B. DEVINCRE, T. HOC, Acta Materialia, Vol. 56, pp. 6040-6049, 2008

[Li 1961] *Cross slip and cross climb of dislocations induced by a locked dislocation*, J.C.M. LI, Journal of Applied Physics, Vol. 32, No. 4, pp. 593-599, 1961

[Louchet 1980] *Thermally activated dislocation sources in silicon*, F. LOUCHET, Journal of Physics C: Solid State Physics, Vol. 13, pp. L847-849, 1980

[Louchet 1988] *Dislocation patterning in uniaxial deformation*, F. LOUCHET, Y. BRECHET, Solid State Phenomena, Vol. 3-4, pp. 335-346, 1988

[Madec 2002a] *From dislocation junction to forest hardening*, R. MADEC, B. DEVINCRE, L.P. KUBIN, Physical Review Letters, Vol. 89, No. 25, pp. 255508-1/4, 2002

[Madec 2002b] *Simulation of dislocation patterns in multislip*, R. MADEC, B. DEVINCRE, L.P. KUBIN, Scripta Materialia, Vol. 47, pp. 689-695, 2002

[Madec 2003] *The role of collinear interaction in dislocation-induced hardening*, R. MADEC, B. DEVINCRE, L. KUBIN, T. HOC, D. RODNEY, Science, Vol. 301, pp. 1879-1882, 2003

[Maroudas 1991a] *Analysis of the effects of oxygen migration on dislocation motion in silicon*, D. MAROUDAS, R.A. BROWN, Journal of Applied Physics, Vol. 69, No. 7, pp. 3865-3877, 1991

[Maroudas 1991b] *Model for dislocation locking by oxygen gettering in silicon crystals*, D. MAROUDAS, R.A. BROWN, Applied Physics Letters, Vol. 58, No. 17, pp. 1842-1844, 1991

[Maroudas 1991c] *Constitutive modeling of the effects of oxygen on the deformation behavior of silicon*, D. MAROUDAS, R.A. BROWN, Journal of Materials Research, Vol. 6, No. 11, pp. 2337-2352, 1991

[Michel 1986] *Cross slip and latent hardening in silicon single crystals*, J.P. MICHEL, R. ALLEM, A. GEORGE, Proceedings of the 7th ICSMA, Vol. 1, pp. 69-74, 1986

[Miyazaki 2007] *Dislocation density evaluation using dislocation kinetics model*, N. MIYAZAKI, Journal of Crystal Growth, Vol. 303, No. 1, pp. 302-309, 2007

[Moulin 1997a] *Etude de la plasticité du silicium à une échelle mésoscopique par simulation numérique tridimensionnelle*, A. MOULIN, PhD Thesis, Universite Paris XI, 1997

[Moulin 1997b] *Simulation of Frank-Read sources in silicon*, A. Moulin, M. Condat, L.P. Kubin, Acta Materialia, Vol. 45, No. 6, pp. 2339-2348, 1997

[Moulin 1999] *Mesoscale modelling of the yield point properties of silicon crystals*, A. Moulin, M. Condat, L.P. Kubin, Acta Materialia, Vol. 47, No. 10, pp. 2879-2888, 1999

[Murphy 2006] *Oxygen transportation in Czochralski silicon investigated by dislocation locking experiments*, J.D. Murphy, S. Sendaker, R.J. Falster, P.R. Wilshaw, Materials Science and Engineering B, Vol. 134, pp. 176-184, 2006

[Möller 1978] *The movement of dissociated dislocations in the diamond-cubic structure*, H.-J. Möller, Acta Metallurgica, Vol. 26, No. 6, pp. 963-973, 1978

[Nemat-Nasser 2004] *Plasticity: a treatise on finite deformation of heterogeneous inelastic materials*, Sia Nemat-Nasser, Cambridge Monographs on Mechanics, pp. 440-501, 2004

[Nishino 1984] *Temperature dependence of friction force acting on dislocations in silicon crystals*, Y. Nishino, H. Saka, T. Imura, Journal of Materials Science, Vol. 19, pp. 245-253, 1984

[Omri 1987] *On the yield point of floating-zone silicon single crystals. I. Yield stresses and activation parameters*, M. Omri, C. Tete, J.-P. Michel, A. George, Philosophical Magazine A, Vol. 55, No. 5, pp. 601-616, 1987

[Orowan 1940] *Problems of plastic gliding*, E. Orowan, Philosophical Transactions of the Royal Society of London A, Vol. 52, No. 289, pp. 8-22, 1940

[Oueldennaoua 1988] *On the yield point of floating-zone silicon single crystals II. A quantitative analysis of the dislocation structure at the lower yield point*, A. Oueldennaoua, R. Allem, A. George, J.P. Michel, Philosophical Magazine A, Vol. 57, No. 1, pp. 51-77, 1988

[Patel 1963] *Macroscopic plastic properties of dislocation-free germanium and other semiconductor crystals. I. Yield behavior*, J.R. Patel, A.R. Chaudhuri, Journal of Applied Physics, Vol. 34, No. 9, pp. 2788-2799, 1963

[Petukhov 1990] *The threshold for dislocation motion in impure semiconductors*, B.V. Petukhov, Soviet Physics - Technical Physics, Vol. 35, No. 10, pp. 1150-1153, 1990

[Petukhov 2004] *A theory of the effect of impurities on the yield stress of silicon crystals*, B.V. Petukhov, Semiconductors, Vol. 38, No. 4, pp. 369-375, 2004

[Rodney 1999] *Structure and strength of dislocation junctions: an atomic level analysis*, D. RODNEY, R. PHILLIPS, Physical Review Letters, Vol. 82, No. 8, pp. 1704-1708, 1999

[Schoeck 1972] *The contribution of the dislocation forest to the flow stress*, G. SHOECK, R. FRYDMAN, Phys. Stat. Sol. (b), Vol. 53, pp. 661-673, 1972

[Senkader 2001] *Oxygen-dislocation interactions in silicon at temperatures below 700°C: dislocation locking and oxygen diffusion*, S. SENKADER, P.R. WILSHAW, R.J. FALSTER, Journal of Applied Physics, Vol. 89, No. 9, pp. 4803, 2001

[Senkader 2002] *On the dislocation-oxygen interactions in Czochralski-grown Si: oxygen diffusion and binding at low temperatures*, S. SENKADER, A. GIANNATTASIO, R.J. FALSTER, P.R. WILSHAW, Journal of Physics: Condensed Matter, Vol. 14, pp. 13141-13145, 2002

[Siethoff 1973] *Lüders bands in heavily doped silicon single crystals*, H. SIETHOFF, Acta Metallurgica, Vol. 21, pp. 1523-1531, 1973

[Siethoff 1978] *Dynamical recovery and self-diffusion in silicon*, H. SIETHOFF, W. SCHRÖTER, Philosophical Magazine A, Vol. 37, No. 6, pp. 711-718, 1978

[Siethoff 2001] *The deformation regimes of the yield point of silicon*, H. SIETHOFF, H.G. BRION, Philosophical Magazine A, Vol. 81, No. 1, pp. 145-152, 2001

[Siethoff 2002] *Yield point and dislocation velocity of diamond and zincblende semiconductors in different temperature regimes*, H. SIETHOFF, Philosophical Magazine A, Vol. 82, No. 7, pp. 1299-1316, 2002

[Stroh 1953] *The mean shear stress in an array of dislocations and latent hardening*, A.N. STROH, Proceedings of the Physical Society Section B, Vol. 66, pp. 2-6, 1953

[Suezawa 1979] *Dislocation dynamics in the plastic deformation of silicon crystals. II. Theoretical analysis of experimental results*, M. SUEZAWA, K. SUMINO, I. YONENAGA, Physica Status Solidi (a), Vol. 51, pp. 217-226, 1979

[Sumino 1971] *Microdynamics of dislocations in plastic deformation of germanium crystals*, K. SUMINO, K. KOJIMA, Crystal Lattice Defects, Vol. 2, No. 3, pp. 159-170, 1971

[Sumino 1974] *Dynamical state of dislocations in germanium crystals during deformation*, K. SUMINO, S. KODAKA, K. KOJIMA, Materials Science and Engineering, Vol. 13, pp. 263-268, 1974

[Sumino 1979] *Dislocation mobility and mechanical behaviour of Si crystals*, K. SUMINO, Journal de Physique Colloque, Vol. 40, pp. C6-147, 1979

[Sumino 1983] *Interaction of dislocations with impurities in silicon crystals studied by in situ X-ray topography*, K. Sumino. M. Imai, Philosophical Magazine A, Vol. 47, No. 5, pp. 753-766, 1983

[Sumino 1993] *Dislocation dynamics and mechanical behaviour of elemental and compound semiconductors*, K. Sumino, I. Yonenaga, Phys. Stat. Sol (a), Vol. 138, pp. 573-581, 1993

[Sumino 1999] *Impurity reaction with dislocations in semiconductors*, K. Sumino, Physica Status Solidi (a), Vol. 171, No. 1, pp. 111-122, 1999

[Tang 1999] *Simulation and modelling of forest hardening in body centre cubic crystals at low temperature*, M. Tang, B. Devincre, L.P. Kubin, Modelling and Simulation in Materials Science and Engineering, Vol. 7, No. 5, pp. 893-908, 1999

[Vallino 2001] *Dislocation multiplication during the very first stages of plastic deformation in silicon observed by X-ray topography*, F. Vallino, J.P. Château, A. Jacques, A. George, Materials Science and Engineering A, Vol. 319-321, pp. 152-155, 2001

[Wagatsuma 1971] *Dislocation configurations in the pre-yield stage of Germanium crystals*, R. Wagatsuma, K. Kojima, K. Sumino, Journal of Applied Physics, Vol. 42, No. 2, pp. 867-869, 1971

[Wallin 2008] *Multi-scale plasticity modeling: coupled discrete dislocation and continuum crystal plasticity*, M. Wallin, W.A. Curtin, M. Ristinmaa. A. Needleman, Journal of Mechanics and Physics of Solids, No. 20, pp. 179-195, Vol. 56, No. 11, pp. 3167-3180, 2008

[Wu 1991] *Latent hardening in single crystals. I. Theory and experiments*, T.-Y. Wu, J.L. Bassani, C. Laird, Proceedings of the Royal Society of London A, Vol. 435, pp. 1-19, 1991

[Yonenaga 1978] *Dislocation dynamics in the plastic deformation of silicon crystals I. Experiments*, I. Yonenaga, K. Sumino, Phys. Stat. Sol (a), Vol. 50, pp. 685-93, 1978

[Yonenaga 1981] I. Yonenaga, PhD Thesis, Tohoku University, 1981

[Yonenaga 1984] *Mechanical strength of silicon crystals as a function of the oxygen concentration*, I. Yonenaga, K. Sumino, K. Hoshi, Journal of Applied Physics, Vol. 56, No. 8, pp. 2346-2350, 1984

[Yonenaga 1993] *Deformation-induced defects and their thermal stability in silicon*, I. Yonenaga, K. Sumino, Phys. stat. sol. (a), Vol. 137, pp. 611-617, 1993

[Yonenaga 1996] *Upper yield stress of Si crystals at high temperatures*, I. Yonenaga, Journal of the Electrochemical Society, Vol. 143, No. 8, pp. L176-L178, 1996

[Zarka 1972] *Généralisation de la théorie du potentiel plastique multiple en viscoplasticité*, P. ZARKA, Journal of the Mechanics and Physics of Solids, Vol. 20, No. 3, pp. 179-195, 1972

Part III

A HOLISTIC APPROACH TO CONSTITUTIVE MODELING OF SILICON

INTRODUCTION

The applicability of the models introduced and derived in the previous Part has been shown limited to the case of easy glide conditions - with only one active slip system - and indeed to cases where the dislocation density on secondary systems is small enough not to play a significant role on dislocation generation mechanisms. These limitations are potentially important, since three dimensional loadings of a silicon monocrystal ought to require the activation of several slip systems in order for the imposed deformation to be accomodated by the material. Such a situation also appears when a single crystal is loaded along a symmetrical direction right from the beginning of deformation.

More importantly, deriving a model for multiple slip conditions is required in order to study multicrystals. Enforcement of kinematic compatibility at the grain boundaries associated to grain-to-grain misorientation leads to complex loading cases that very likely require several slip systems to be active. Strong hardening can be expected in these cases. As discussed in the introduction of the previous Part, estimating the "mesoscopic", or intergranular, stresses supposes a constitutive model able to account correctly for all loading situations.

The extensions brought to the original model of Alexander & Haasen do not fulfill this condition. As mentioned in Section 7.3, a "missing" dislocation generation term causes an underestimation of the capture radius with respect to its theoretical value. In addition, no dislocation annihilation has been accounted for although this phenomena is experimentally observed, especially on screw dislocations as their mutual annihilation by cross-slip can take place over relatively large distances.

The *only* characteristic of the model of Alexander & Haasen, besides its many assumptions, is its dislocation evolution law. Reliance on Orowan's law to link a microstructural parameter (the density of mobile dislocations) to the plastic strain rate is made possible by the knowledge of the dislocation velocity law as a function of both stress and temperature and is common practice in the literature.

The definition of the internal stress adopted by Alexander & Haasen is, again, a standard one. Ultimately, what makes their model powerful is their choice of dislocation multiplication law. As seen in Chapter 5, several different laws could yield similar stress-strain behaviors in the yield region, albeit associated to different mobile dislocation density evolutions. Their common drawback comes from the strain rate and temperature dependency of their constitutive parameters, that limit their applicability to restricted thermodynamic conditions if accuracy is to be guaranteed.

- We propose in this Part a dislocation multiplication law that accurately reproduces the yield region of silicon crystals in the whole range of strain rate and temperature experimentally covered with the help of a single constant parameter.

The mechanical behavior of covalent crystals strained uniaxially beyond the yield region is very similar to the one of fcc crystals. Dislocations move then under lower stresses and loose their hexagonal shape: short-range dislocation interactions tend to dominate the Peierls potential and dislocation motion at large strains presents several common features with dislocation dynamics in fcc crystals. After a stage of easy glide (stage I), whose extent varies strongly with temperature and strain rate, secondary systems are activated owing to lattice rotation. Strong short-range dislocation interations lead to a strong and linear hardening rate in stage II. Additional recovery and hardening stages have been observed beyond this, but these are not of relevance for this work.

- The conflict that arose in the previous Part between the magnitude of the best fitted constitutive parameter for dislocation storage and the experimentally estimated ones is solved in the following. It is shown that dislocation generation from the forest trees is indeed significant in stage I and largely overwhelms the generation law active in the yield region. Moreover, dislocation storage and annihilation laws are derived on purely physical basis and do not require additional calibration.

In crystals exhibiting large dislocation contents on a single slip system, the applied stress τ is reduced by an internal stress τ_{int} stemming from the long-range elastic strain fields of the dislocations. This internal stress is *a priori* not constant on the slip plane.

[Sumino 1971, Sumino 1974a] have shown that the internal stress on the slip plane is almost constant in a dynamical state throughout stage I of hardening. Consequently, the velocity law derived for individual dislocations can still be applied in stage I. Determination of the effective stress during dynamic straining allows the derivation of the mean dislocation velocity and ultimately the calculation of the density of mobile dislocations by inverting Orowan's law. This way the steady-state of deformation in stage I has been characterized both for silicon and germanium crystals by [Kojima 1971, Sumino 1974a, Yonenaga 1978, Yonenaga 1981].

The case of highly dislocated crystals is less studied. Semiconductors have been historically used as virgin materials or with very low dislocation densities, and high dislocation densities were not of practical interest. Multicrystals contain large dislocation densities because of the combination of thermal gradients during solidification and the presence of several grains exhibiting different crystallographic orientations. Dislocations move on their slip plane through an array of obstacles such as impurity clusters, small precipitates, or forest dislocations. The creation of jogs during forest cutting

processes affect the velocity of dislocations as well. The effect of secondary dislocations on the velocity law has indeed received little attention in the literature. The mean dislocation velocity might therefore differ significantly from the standard law the traditional models rely on. In particular, the effect of jog dragging on dislocation motion, suggested as possible rate-limiting mechanism in stage II, has never been modeled for semiconductors.

- A dislocation velocity law generalizing their motion to glide in an array of localized obstacles is derived. The influence of jog dragging is explicitely modeled, and we show that the transition between the double kink mechanism and jog-controlled motion is delayed in covalent crystals exhibiting a high μb^3 energy.

We distinguish explicitely the evolution of both screw and 60° dislocation populations in this Part. Although complicating the constitutive model, such an approach has several advantages *a fortiori*:

- Storage by formation of dipoles and dislocation annihilation by cross-slip and climb can be explicitely accounted for for each dislocation character: screws canot climb and we consider that 60° segments behave like edges, that is, they cannot cross-slip. Each population evolves following similar, albeit adapted, laws.
- The relative evolution of the dislocation characters can be studied in detail. It is experimentally observed that most dislocations have an edge character in stage I and beyond; our model can give an estimation of the density ratio.

The particular case of extension of any model to SoG-Si materials deserves a discussion. The difference between such materials and, say, crystals grown from an EG-Si feedstock lies in their impurity and/or inclusion content. How to account in a macroscopic model for the particular microscopic characteristics of an inclusion content? How to model the macroscopic effects of a given inclusion distribution that ought to change with the location in the ingot? This is where experimentally determined fracture strength of SoG-Si multicrystals can be used, translating in macroscopic terms the microscopic -local- effects of the defects. Incorporation of the expression of the cumulative fracture probability in the constitutive model allows us to map this variable of high interest.

- The constitutive model outputs the cumulative fracture probability at each point, based on experimental characterization of the material considered.

Chapter 9 introduces a model for computation of the mean dislocation velocity in dislocated crystals. The holistic constitutive model for extrinsic silicon monocrystals is detailed and calibrated in Chapter 10 where the internal stresses and dislocation evolution laws are derived. Chapter 11 suggests an adaptation of the constitutive model to Solar-grade silicon materials and includes experimental results.

8

MODELING DISLOCATION VELOCITY IN REAL SEMICONDUCTORS

For historical reasons, models of the dislocation motion in semiconductors have most often been based on the double kink mechanism. A quick review of this motion mode is followed by the derivation of a holistic model for dislocation motion in dislocated, extrinsic crystals. Both the cases of dislocation unpinning from localized obstacles (forest trees) and jog dragging are modeled. Numerical aspects are exposed and discussed. It is shown that the former mechanism is very unlikely to be rate-limiting in dislocated crystals with usual forest densities, as the time spent overcoming the obstacles is negligible compared to the time of free-flight. The latter can be determined either by the standard double kink theory, or by accounting for the effects of jogs on dislocation velocity. In particular, we investigate the motion of a mixed jogged dislocation in the Peierls potential. We show the existence of a mixed-mode between the double-kink and jog-dragged motion domains that spans over a wide range of effective stress values.

8.1 INTRODUCTION

The dynamical properties of dislocations in silicon have been studied extensively since the first uniaxial tensile tests of [Patel 1963] revealed the characteristic yield drop of the flow stress upon dynamical straining of as-grown crystals. Initially believed to originate from dislocation unpinning from impurities, the yield phenomena has been attributed a couple of years later to the combined effect of low initial dislocation densities in as-grown intrinsic semiconductors, and of the weak stress dependence of their strongly thermally activated velocity. This behavior is a priori not limited to semiconductors but to any material presenting a deficit of mobile dislocations upon loading as discussed by [Estrin 1986]. Too few dislocations limited in their motion by the high Peierls potential of the diamond cubic lattice cannot accomodate the imposed strain rate, resulting in an apparent elastic behavior of the crystals until an explosive dislocation multiplication allows for relief of the flow stress and the occurence of a yield drop (for reviews see, e.g., [Alexander 1968, George 1987a, George 1987b]).

The properties of the yield region, also called stage o of deformation, have been studied extensively by several authors throughout the years ([Patel 1963, Yonenaga 1978, Omri 1987] to mention but a few). Its extent and intensity are enhanced at low temperatures, high strain rates

and low initial dislocation densities. The upper yield stress τ_{uy} is found very sensitive to sample prestraining and its surface state, whereas the lower yield stress τ_{ly} is almost solely determined by the temperature and strain rate, provided the initial dislocation density remains low enough to avoid disturbing effects from the forest as mentioned by [Yonenaga 1978, Suezawa 1979] and [Siethoff 1992]. The experimentally determined τ_{ly} depends on the applied strain rate $\dot{\gamma}$ and the temperature T following the equation ([Alexander 1968, Yonenaga 1978]):

$$\tau_{ly} = C\dot{\gamma}^{\frac{1}{m+2}} \exp\left(\frac{U_{ly}}{(m+2)k_bT}\right) \tag{8.1}$$

where C, U_{ly} and m are constant parameters depending on the semiconductor considered and $k_b = 8.617 \times 10^{-5}\,\text{eV.K}^{-1}$ is Boltzmann's constant.

The proper use of any physically-based constitutive model requires the derivation of the distribution of the mobile dislocation density as a function of its speed as discussed in [Sumino 1971]. A way to circumvent this difficulty is to rely on the *mean* velocity $\overline{v}$ of the *total* mobile dislocation density. Hence, an expression for the mean dislocation velocity is required.

The introduction of isolated dislocation loops in virgin silicon crystals is possible by, e.g., indentation or scratching followed by high-temperature expansion of the loops. Observation at high stresses has revealed very early their characteristic hexagonal shape betraying the strong Peierls potential keeping dislocation segments straight in the valleys (see Part i). In such a configuration two types of dislocations can be distinguished depending on their orientation with respect to the Burgers vector: either screws or 60° segments. The temperature- and stress dependencies of the dislocation velocities have been determined experimentally and are best given by an expression of the type:

$$v = v_0 \left(\frac{\tau}{\tau_0}\right)^{m_0} \exp\left(-\frac{U}{k_bT}\right) \tag{8.2}$$

where $\tau_0 = 1\,\text{MPa}$ is a normalizing stress, v_0 is the velocity prefactor, m_0 the stress exponent and U the apparent activation energy for dislocation motion. The three last parameters depend on the dislocation character, screws being slower than 60° segments.

Interestingly, the m and U parameters of Eqs. 8.1 and 8.2 are similar. This allows for the identification of the (microscopic) velocity parameters directly by observation of the (macroscopic) lower yield point. Such an approach adopted by, e.g., [Siethoff 1969] and [Siethoff 1999] yields excellent results in agreement with *in situ* observations. Note that Eq. 8.2 is valid as long as dislocation motion proceeds by nucleation and propagation of double kinks in a high Peierls potential. Diffusional effects at very high temperatures affect the velocity expression as reported by [Farber 1982]; however the occurence of this motion regime is not clearly understood yet. For example, [Yonenaga 1996] observes no change of the motion mechanisms at 1573 K.

We develop in this Chapter a model for dislocation velocity in *dislocated* silicon crystals. The standard case of a virgin lattice free from forest obstacles and impurities is very quickly reviewed, as more details have already been given in the previous Parts of this thesis.

The influence of dislocation pinning by forest interactions is introduced in Section 8.3 by calculating the time spent by dislocations waiting in a bowed configuration before unpinning.

If jogs are present at concentrations high enough on the dislocation line, then their drag can control dislocation velocity as discussed in Section 8.4. The mathematical aspects of the effect of jog dragging on the double kink mechanism and dislocation pinning are detailed in each respective Section.

Classical models for f.c.c. crystals (see, e.g., [Harder 1999]) rely on an expression of the type $\overline{v} \propto l_v/t_w$ to compute the mean dislocation velocity, where l_v is the mean free path swept after waiting a time t_w at an obstacle. Such models consider that the time of free flight t_f from one obstacle to the next can be disregarded as $t_f \ll t_w$. In covalent crystals a strong lattice motion opposes dislocation glide. Hence, in this work we account explicitely for t_f in the derivation of the mean dislocation velocity $\overline{v}$.

The use of Friedel statistics when t_f cannot be neglected requires the derivation of the stress-dependent mean free path as discussed by [Hiratani 2001], but for simplicity in this work we neglect this aspect. If v is the dislocation velocity in free flight then $t_f \simeq l_v/v$ and the mean velocity $\overline{v}$ reads:

$$\overline{v} = \frac{l_v}{t_w + l_v/v} \tag{8.3}$$

The objectives of this Chapter and the following are to derive expressions for v, t_w and l_v. If obstacles are neglected or $t_w \ll t_f$ then $\overline{v} = v$.

8.2 THE DOUBLE KINK MECHANISM

In a virgin lattice, that is in intrinsic crystals with no internal stress fields, dislocation motion proceeds at low stresses by thermally-activated nucleation and propagation of sharp double kinks over the primary and secondary Peierls barriers as detailed in Chapter 1. The primary barrier is due to the high Peierls potential of semiconductors, as motion of a dislocation from one valley to another requires the breaking of covalent bonds. The secondary barrier arises from core reconstruction ([Bulatov 2001]).

The model of [Hirth 1982] for motion of dislocations in a material with high Peierls valleys is believed to be the most relevant for silicon. Other models ([Celli 1963, Möller 1978]) relying solely on the presence of weak obstacles along the dislocation line have been shown inappropriate through the years. The influence of point defects both at the core and in the matrix on the secondary barrier associated to kink propagation along the dislocation line is however still unclear as discussed in [Nikitenko 1984, Farber 1993, Choudhury 2010]. Adaptations of the HL model to dissociated dislocations have been suggested by [Möller 1978, Caillard 2003]. The model for perfect dislocations is considered here.

The HL model predicts two motion regimes depending on the dislocation length X governed by the double kink mechanism. A length-independent motion mode sets in if $X \geq X_c$, with X_c a thermally activated critical dislocation length; the dislocation velocity is proportional to X otherwise. A general expression for the velocity v_{dk} is given by Eq. 8.4:

$$v_{dk} \propto \min(X, X_c)\, \tau \exp\left(-\frac{U_{LD}}{k_b T}\right) \tag{8.4}$$

with U_{LD} the effective activation energy for dislocation motion in the length-dependent regime. With X_c thermally activated the effective activation energy in the length-independent regime (see below), $U_{LI} < U_{LD}$. Similar expressions of dislocation velocity are obtained for dissociated dislocations by [Nunes 1998, Caillard 2003]. Values of the velocity parameters have been derived *in situ* by [Imai 1983] for both screw and 60° dislocation segments.

X_c is defined in Eq. 8.5, where l is the crystal periodicity along the dislocation line, shown by atomistic simulations to be $l = 2b$ on the 30° partial because of its reconstruction. Theoretical calculations (e.g., [Nunes 1998, Miranda 2003]) point towards the same periodicity along the 90° partial as well. $F_{kp}^{(c)}(\tau_{eff})$ is the stress-dependent critical energy barrier for the nucleation of a stable kink pair and the free energy for kink migration. More details are found in Chapter 1.

$$X_c = 2l \exp\left(\frac{F_{kp}^{(c)}(\tau_{eff})}{2k_b T}\right) \tag{8.5}$$

8.2.1 *Mean dislocation velocity in presence of internal stresses*

Dislocation motion is affected by the presence of internal stresses and the applied stress τ is reduced by the athermal internal stress field τ_{int}, leading to the definition of an effective stress $\tau_{eff} = \tau - \tau_{int}$. As discussed in Section 6.2, although the dislocation velocity locally reads $v_{dk} \propto \tau - \tau_{int}$ this remains also true for the mean velocity $\overline{v}$. With the mean effective stress $\overline{\tau}_{eff}$ usually written $\overline{\tau}_{eff} = \sqrt{(\tau - \tau_b)^2 - \tau_{max}^2}$, it can be shown that in a dynamical state $\tau_{max} \ll \tau_b$ and $\overline{\tau}_{eff} = \tau - \tau_b$.

Experiments performed by [Yamashita 1993] have detected no change of the apparent activation energy upon crossing the critical segment length. The model of [Maeda 1989] suggests that the dislocations always move in the length-dependent regime, the mean free path of kinks $X_{max} < X_c$ being limited by point defects along the line and independent on the temperature. This is the assumption we adopt in this work. Dislocation velocity is then given by Eq. 8.4 where X_c is replaced by an effective maximum kink mean free path X_{max}. The following approximation for v_{dk} given a dislocation length X moving by nucleation and propagation of double kinks is usually adopted:

$$\begin{cases} v_{dk} = v_0 \frac{X_{eff}}{L_0} \left(\frac{\tau_{eff}}{\tau_0}\right)^{m_0} \exp\left(-\frac{U}{k_b T}\right) \\ X_{eff} = \min(X,\, L_0),\; L_0 = \min(X_{max},\, X_c) \end{cases} \tag{8.6}$$

where $X_{max} = 10^{-7}$ m and $\tau_0 = 1$ MPa are used for normalizing purposes, v_0, m_0 and U are experimentally determined and depend on the dislocation character. If no obstacles limit the kink mean free path then $\overline{\tau}_{eff} = \tau_{eff}$ and Eq. 8.6 is exactly the widely-used Eq. 8.2.

8.2.2 *Continuous approximation of v_{dk}*

Such an expression for the dislocation velocity has the drawback of being piecewise defined as a function of X_{eff}. This might pose some numerical issues since its first derivative is not continuous, and complicate its integration. [Dour 2002] choose to approximate v_{dk} by a $\mathcal{C}^\infty$ function. We show in this Chapter that this step is not necessary, and using the exact velocity function is actually computationally more efficient.

We adopt the following equation to approximate the dislocation velocity by the double kink mechanism:

$$v_{dk} = v_0 \left(\frac{\tau_{eff}}{\tau_0}\right)^{m_0} \exp\left(-\frac{U}{k_b T}\right) \left[1 - \exp\left[-\left(\frac{X}{L_1}\right)^{m_1}\right]\right] \tag{8.7}$$

where $m_1 = 1.75$ and $L_1 = 6 \times 10^{-8}$ m are obtained by best fit. A drawback of such an equation is its high nonlinearity in X, that is be shown in the next Section to lead to high computational cost if it is to be integrated.

Since $m_0 = 1$, Eq. 8.7 can be written $v_{dk} = \lambda_{dk}(X, T)\, \tau_{eff}$ with λ_{dk} depending on the dislocation character. Fig. 8.1 compares the velocity given

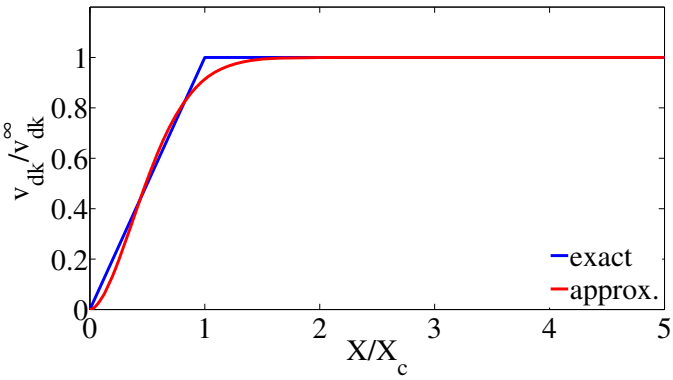

Figure 8.1: Comparison of dislocation velocity by the double kink mechanism given by the exact Eq. 8.6 and its approximation (Eq. 8.7). v_{dk}^{∞} is given by Eq. 8.6 with $X = L_0$.

by Eqs. 8.6 and 8.7. Note that the present formulation differs from the less accurate one adopted by [Dour 2002]. It is shown in Section 8.4 that the dislocation velocity in free flight can always be given by Eq. 8.7 even when jog dragging governs dislocation motion, provided that X is correctly computed.

8.3 INFLUENCE OF LOCALIZED OBSTACLES

8.3.1 *Preliminary discussion*

The presence of localized obstacles on the slip plane such as forest dislocations, impurities or small precipitates, can temporarily pin moving dislocations and delay their motion on the slip plane otherwise governed by the kink pair mechanism (see, e.g., [Rauch 1994, Baufeld 1998]). The present model for dislocation velocity in covalent crystals can be enhanced to account for localized obstacles.

We suggest in the following a model that differs significantly from the work of [Dour 2002]. The sole common point is the methodology chosen: in such a framework dislocations break free from forest obstacles when the cumulative unpinning probability reaches unity. Computation of this probability $P_{obs}(t)$ requires the derivation of the probability differential over an infinitesimal time step, or $\mathrm{d}P_{obs}/\mathrm{d}t$. The latter is defined thanks to the theory of dislocation dynamics as presented in, e.g., [Kocks 1975, Nagdornyi 1988].

Devil lies in the details, therefore the very equations adopted by [Dour 2002] are questionable.

- The authors adopt for dislocation velocity at high forest densities a power law (as a function of stress). The problem with such a law is that it is valid at stresses close to the critical unlocking stress only. It is actually an approximation at high stresses of Eq. 8.11. Unfortunately, we show in this Section that forest trees impede dislocation motion significantly at *low* stresses only, questioning hereby the validity of their choice.

- Another questionable point is that they consider the attack frequency (ν_{eff} in this Section) to be proportional to the inverse of the dislocation length L. The latter is assumed to behave as a vibrating chord. However, an unlocking attempt -the attack frequency- is a *local* process that is not concerned by the dislocation length. In our model the effective attack frequency is considered independent of L.

- Finally, [Dour 2002] adopt a rough estimate for the dislocation velocity v_{dk} as a function of the dislocation length. We show in the following that it is possible and preferable for numerical reasons to adopt the exact velocity expression, piecewise defined.

Let us consider an array of obstacles of density ρ_{obs} on the primary slip plane, leading to a mean distance between obstacles l_{obs} (see Section 9.5.1 for its derivation). At $t = 0$ a dislocation segment of length l_{obs} is pinned at its ends by two thermally overcomeable obstacles of height F_{obs}, and the tangent to the dislocation at one pinning point makes an initial angle with the velocity vector $\theta(t = 0) = \pi/2$ (see Fig. 8.2). As the central segment moves forward the cumulative unpinning probability increases, until it

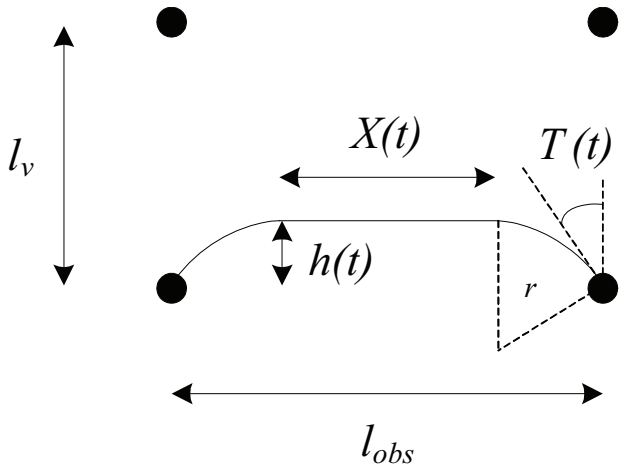

Figure 8.2: Model for dislocation slip through an array of obstacles.

reaches unity at $t = t_w$, or $\theta(t_w) = \theta_w$. The mean dislocation velocity in the presence of obstacles is then given by Eq. 8.3.

8.3.2 *Mathematical aspects*

Model definition

Let us consider Fig. 8.2. The straight central part of the segment of length $X(t)$ ruled by the double kink mechanism moves forward under an applied stress τ and a long-range internal stress τ_{int}, coming from, e.g., other dislocations on the primary plane, long-range stress component of the forest, etc. In the meantime, the segment ends bow as these are kept fixed by the obstacles. These curved parts are made up of an accumulation of kinks and their curvature radii r depends on the effective stress $\tau_{eff} = \tau - \tau_{int}$ (see [Gottschalk 1983a, Gottschalk 1983b]), assumed constant during the pinning-unpinning process (see Chapter 1):

$$r = \frac{\Gamma}{\tau_{eff} b} = \frac{\mu b}{2\tau_{eff}} \tag{8.8}$$

where Γ is the line tension, considered for simplicity to be constant with $\Gamma = \mu b^2/2$ ([Kocks 1975, Omri 1987]). Geometrical considerations yield (see Fig. 8.2):

$$X(t) = l_{obs} - \frac{\mu b}{\tau_{eff}} \cos\theta(t) \tag{8.9}$$

$$\begin{cases} h(t) = r\,(1 - \sin\theta(t)) \\ \dot{h}(t) = v_{dk} = -r\dot{\theta}\cos\theta \end{cases} \tag{8.10}$$

where v_{dk} is the velocity of the dislocation segment moving in a perfect lattice as derived[1] in Sec. 8.2.2.

Unpinning probability

GENERAL EXPRESSION Over an infinitesimal time increment $\mathrm{d}t$ the probability of breakaway from the pinning points reads:

$$\mathrm{d}P_{obs} = \nu_{eff} \exp\left(-\frac{\Delta G_{obs}(\tau_{eff})}{k_b T}\right) \mathrm{d}t \tag{8.11}$$

with ν_{eff} is the effective attempt frequency and $\Delta G_{obs} = F_{obs}\left(1 - \left(\tau_{eff}/\tau_c\right)^p\right)^q$ the activation energy, where τ_c is the athermal unlocking stress, $0 < p \leq 1$ and $1 \leq q \leq 2$ are exponents characterizing the obstacle energy barrier (see [Kocks 1975, Nagdornyi 1988, Kothari 1998]).

As the dislocation segment moves forward, the angle $\theta(t)$ decreases until the segment tears apart from its pinning points. The athermal unlocking stress is given as a function of the critical angle $\theta_c \geq 0$ with $\tau_c l_{obs} = \mu b \cos\theta_c$.

At a finite temperature, unpinning can take place at $\theta_w \geq \theta_c$ and $\tau_{eff} l_{obs} = \mu b \cos\theta_w$. Between $t = 0$ and t_w the unpinning probability reads:

$$P_{obs}(t_w) = \int_0^{t_w} \nu_{eff} \exp\left[-\frac{F_{obs}}{k_b T}\left(1 - \left(\frac{\cos\theta}{\cos\theta_c}\right)^p\right)^q\right] \mathrm{d}t \tag{8.12}$$

Unpinning takes place when $P_{obs}(\theta_w) = 1$. Eq. 8.12 must be solved for θ_w numerically for $\theta_w \leq \theta_c$ by decomposing the interval $[\pi/2, \theta_c]$ into n steps of individual length $\Delta\theta = (\pi/2 - \theta_c)/n$.

Once θ_w is determined, the waiting time t_w can be computed by using Eq. 8.10b. Free from the pinning points, the dislocation segment moves in a defect-free lattice at a velocity v_{dk} over a distance $l_v - h(t_w) \simeq l_v$, until it meets another pinning point. Use of Eq. 8.10b allows to write the cumulative probability as:

$$P_{obs}(\theta_w) = \int_{\theta_w}^{\pi/2} \nu_{eff} \exp\left[-\frac{F_{obs}}{k_b T}\left(1 - \left(\frac{\cos\theta}{\cos\theta_c}\right)^p\right)^q\right] \frac{r\cos\theta}{v_{dk}(\theta)} \mathrm{d}\theta \tag{8.13}$$

EFFECTIVE ATTACK FREQUENCY The effective attempt frequency at high stresses is given by $\nu_{eff} \simeq 10^{-2}\nu_D$ ([Nagdornyi 1988]). At low effective stresses the dislocation can attempt to jump back before the obstacle, consequently ν_{eff} becomes (see [Kocks 1975]):

$$\nu_{eff} = 10^{-2}\nu_D \left(1 - \exp\left(-\frac{\tau_{eff} b \mathcal{A}}{k_b T}\right)\right) \tag{8.14}$$

1 Here, it does not matter whether the exact velocity equation (defined piecewise as a function of X) or its approximation is used. The consequences of relying on a nonlinear approximation of v_{dk} are discussed below.

where $\mathcal{A} = 1/\rho_{obs}$ is the area swept by the dislocation between two obstacles.

Calculation of t_w

There are two ways to proceed with the computation of the cumulative probability. Either the exact dislocation velocity equation (Eq. 8.6) is used, or an approximation (Eq. 8.7) is relied upon. Mathematical details are introduced in the following with the latter option, since it is more straightforward and does not require to divide the θ interval into several subintervals, but the principle remains general. We assume that the influence of jogs can be disregarded. Then the integral to solve for θ_w is given by:

$$\int_{\theta_w}^{\pi/2} \exp\left[-\frac{F_{obs}}{k_b T}\left(1-\left(\frac{\cos\theta}{\cos\theta_c}\right)^p\right)^q\right] \frac{\cos\theta}{1-\exp\left[-\left(\frac{X_{obs}}{L_1}\right)^{m_1}\right]} \mathrm{d}\theta = \frac{2\tau_{eff}^2 v_0}{\mu b \nu_{eff} \tau_0} \exp\left(-\frac{U}{k_b T}\right) \tag{8.15}$$

with $X_{obs} = l_{obs} - \frac{\mu b}{\tau_{eff}} \cos\theta(t)$. A singularity shows up at $X_{obs} = 0$ and therefore the integration is performed down to $X_{min} = X(\theta_{min}) = 3b$ only, assumed to be the minimal segment length allowing for double kinks to nucleate ([Caillard 2003]). The time spent at $\theta_w > \theta_{min}$ is found by computing $t(\theta_w)$ using Eq. 8.10b:

$$t(\theta_w) = \frac{\mu b \tau_0}{2\tau_{eff}^2 v_0} \exp\left(\frac{U}{k_b T}\right) \int_{\theta_w}^{\pi/2} \frac{\cos\theta}{1-\exp\left[-\left(\frac{X_{obs}}{L_1}\right)^{m_1}\right]} \mathrm{d}\theta \tag{8.16}$$

If $P_{obs}(\theta_{min}) < 1$ then the dislocation waits in a completely bowed configuration, and

$$t_w = t(\theta_{min}) + t_B = \frac{\mu b \tau_0}{2\tau_{eff}^2 v_0} \exp\left(\frac{U}{k_b T}\right) \int_{\theta_{min}}^{\pi/2} \frac{\cos\theta}{1-\exp\left[-\left(\frac{X_{obs}}{L_1}\right)^{m_1}\right]} \mathrm{d}\theta + \frac{1-P_{obs}(\theta_{min})}{\nu_{eff} \exp\left[-\frac{F_{obs}}{k_b T}\left(1-\left(\frac{\cos\theta_{min}}{\cos\theta_c}\right)^p\right)^q\right]} \tag{8.17}$$

Accounting for the influence of jog dragging as introduced in Section 8.4 leads simply to alternative definitions of $X(t) = \min\left(X_j, X_{obs}\right)$ and $X_{min} = \min\left(3b, X_j\right)$ to insert in the above equations.

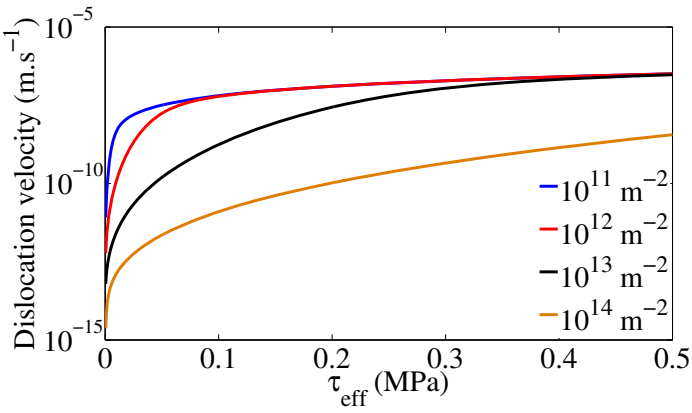

Figure 8.3: Mean screw dislocation velocity through a square array of forest obstacles of varying densities ρ_f. $T = 1073\,\mathrm{K}$, $F_{obs} = 4\,\mathrm{eV}$.

8.3.3 *Model results and discussion*

Parameter sensitivity

This model has been implemented and tested at various parameter values. The influence of jogs is neglected in the following for simplicity. The effective stress τ_{eff} is assumed equal to the applied stress τ, and the critical stress for athermal dislocation unpinning taken as $\tau_c = 0.35\mu b\sqrt{\rho_f}$. As discussed in Section 9.5.2 its actual expression is more complicated. Finally, both l_{obs} and l_v are set equal to $1/\sqrt{\rho_f}$ at first (i.e., dislocations glide through a square array of obstacles). The exact value of these model parameters is in the meantime not necessary in the following as we aim solely at identifying the qualitative properties of the velocity model.

Setting $F_{obs} = 4\,\mathrm{eV}$, the temperature to 1073 K and letting the forest density ρ_f vary, Figure 8.3 is obtained for $\overline{v}(\tau_{eff})$. The influence of F_{obs} at a fixed forest density $\rho_f = 10^{12}\,\mathrm{m}^{-2}$ is shown in Figure 8.4. The following conclusions can be drawn:

- Firstly, the lower the obstacle density ρ_f, the lower the effective stresses must be in order for the pinning-unpinning process to significantly affect dislocation velocity. In other words, the model correctly reproduces a progressive influence of the forest trees as their density increases.
- Secondly, the influence of F_{obs} on the simulated dislocation velocity is very important, and localized obstacles have no significant effect on dislocation motion for $F_{obs} \lesssim 3\,\mathrm{eV}$.

Figure 8.5 assesses the effect of Friedel statistics on the computed mean velocity. It can be seen that in this framework the influence of obstacles is even lower than modeling the obstacles array in a square configuration.

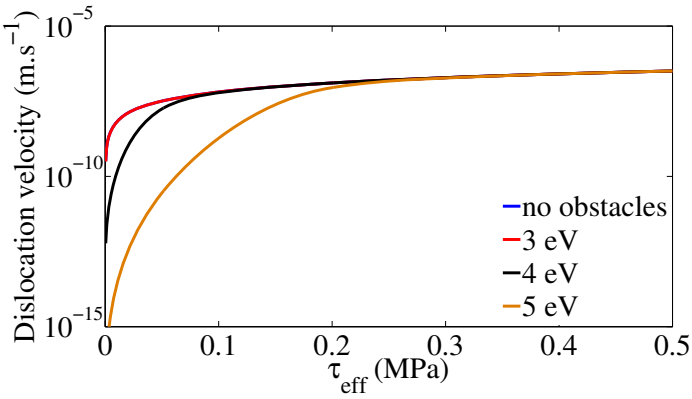

Figure 8.4: Mean screw dislocation velocity through a square array of forest obstacles for varying obstacle heights F_{obs}. $T = 1073\,\mathrm{K}$, $\rho_f = 10^{12}\,\mathrm{m}^{-2}$.

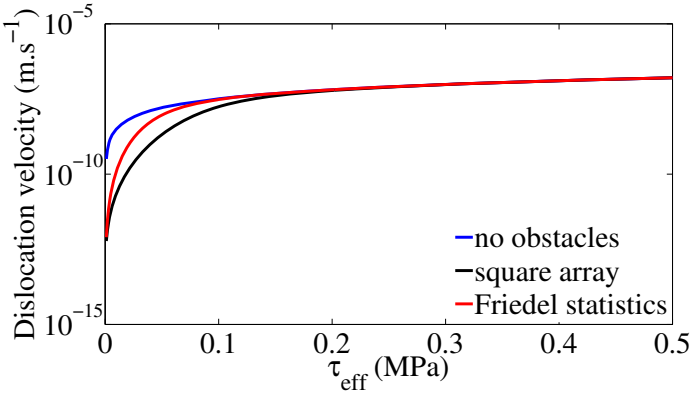

Figure 8.5: Comparison of the computed mean dislocation velocity through an array of localized obstacles using a square array or relying on Friedel statistics. $T = 1073\,\mathrm{K}$, $\rho_f = 10^{12}\,\mathrm{m}^{-2}$, $F_{obs} = 4\,\mathrm{eV}$.

Numerical aspects

An important issue stemming from the present model relying on Eq. 8.7 is that integration of the probability function (Eq. 8.13) requires a very fine discretization of the integration interval $[\pi/2, \theta_{min}]$ in order for the solution to be continuous. Figure 8.6 shows the computed dislocation velocity at various discretization widths, with $n = 10$, 100 or 1000. If motion is considered to take place in a square array of localized obstacles the precision required is still acceptable from a computational point of view ($n = 100$ giving satisfying results). However, if Friedel statistics are adopted and l_{obs} is made dependent on τ_{eff} (see Section 9.5.1) then a very small integration step (i.e., a large n) is necessary in order to minimize the occurence and magnitude of discontinuities.

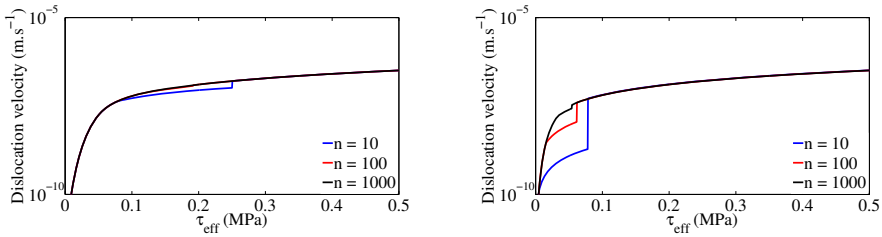

(a) Square array, approximate v_{dk}

(b) Friedel statistics, approximate v_{dk}

(c) Square array, exact v_{dk}

(d) Friedel statistics, exact v_{dk}

Figure 8.6: Influence of the integration step length $\Delta\theta$ onto the computed mean dislocation velocity $\bar{v}(\tau_{eff})$ in an array of obstacles, basing integration of the cumulative unpinning probability on Eq. 8.7. $T = 1073\,\mathrm{K}$, $\rho_f = 10^{12}\,\mathrm{m}^{-2}$, $F_{obs} = 4\,\mathrm{eV}$. Top figures: the dislocation velocity is approximated by Eq. 8.7. Bottom figures: the piecewise definition of v_{dk} (Eq. 8.6) is chosen.

The effect of n on the numerically derived mean dislocation velocity can be reduced by taking the exact (linear piecewise) expression for the dislocation velocity in free flight, namely Eq. 8.6, that is, by reducing the nonlinearity of $v_{dk}(X)$. This is shown in Figs. 8.6c and d.

Discussion

The main unknown is the value of F_{obs}. As discussed previously, as long as it remains below roughly $0.1\mu b^3$ (with $\mu b^3 \simeq 22\,\mathrm{eV}$ in Si) the obstacles likely do not play any significant role on the mean dislocation velocity as long as the forest density remains below roughly $10^{13}\,\mathrm{m}^{-2}$.

A way to estimate this parameter is to consider that forest interactions lead to the formation of atomic jogs on the intersecting dislocations. A low bound for F_{obs} is therefore $2F_{jog}$ with F_{jog} the jog formation free energy. Following [Hirth 1982] $2F_{jog}$ should not differ significantly from $2F_k$, or approximately 1 eV. Taking a large margin we can set $F_{obs} = 2.2\,\mathrm{eV}$.

As seen later on, the effect of obstacles on the simulated mechanical behavior of silicon materials is marginal as long as our model can tell, and can be neglected. We find on the other hand that jog dragging is a potentially better candidate to explain a change in the dislocation motion mechanisms when forest interactions gain in importance.

8.4 MOBILITY OF JOGGED MIXED DISLOCATIONS

8.4.1 *General expression for jog-dragging dislocation motion*

We show in the next Chapter that a change in the dislocation motion mechanisms is responsible both for the observed stress overshoot and a sustained decrease of the hardening rate in stage I. We suggest that this change stems from the dragging of sessile atomic jogs on secondary dislocations created by forest cutting throughout stage I. A model for motion of jogged dislocations in the diamond cubic structure is proposed in this Section.

Jogs on the screw component of a dislocation, with a mean spacing d_j, can affect dislocation motion if their drag becomes rate-limiting, owing to their sessile nature[2].

If dislocation bowing between jogs is neglected, the screw dislocation velocity v_{jog} reads (see [Hirth 1982, Messerschmidt 2010]):

$$v_{jog} \propto \frac{D_{sd}}{b} \sinh\left(\frac{\tau_{eff}\Omega d_j}{bk_bT}\right) \tag{8.18}$$

where $D_{sd} = 2175.4 \exp(-4.95/k_bT) + 2.3 \times 10^{-3} \exp(-3.6/k_bT)$ given in $cm^2.s^{-1}$ is the self-diffusion coefficient taken from [Shimizu 2007] and $\Omega = a^3$ the atomic volume, with $a = 5.43 \times 10^{-10}$ m. D_{sd} accounts for the transition between a vacancy and interstital self-diffusion mechanism around 1173 K. The prefactor is usually taken of the order of 4π (see, e.g. [Milevskii 1977]).

Accounting for the influence of jogs on dislocation velocity requires to distinguish explicitely between the dislocation populations based on their character, since screws are more susceptible to jog dragging than 60° segments. Jogs created on edge segments are indeed glissile.

8.4.2 *Interaction between jog dragging and the double kink mechanism in covalent crystals*

The combined effect of jogs and a high Peierls potential must be accounted for in order not to introduce discontinuities in the constitutive behavior at the transition between both motion modes. We detail here the methodology employed in order to compute the dislocation velocity v in free flight when jogs affect their motion that proceeds otherwise by the double kink mechanism (see Section 8.2). We consider here the steady-state motion of the dislocation only.

Jog dragging leads to the bowing out of dislocations in a similar way as pictured in Fig. 8.2, where l_{obs} must be replaced by d_j. The force exerted on jogs includes a contribution from the line tension Γ (the latter assumed to

2 Jogs on screw dislocations move nonconservatively as motion does not proceed in their glide plane. Their climb requires emission or absorption of point defects.

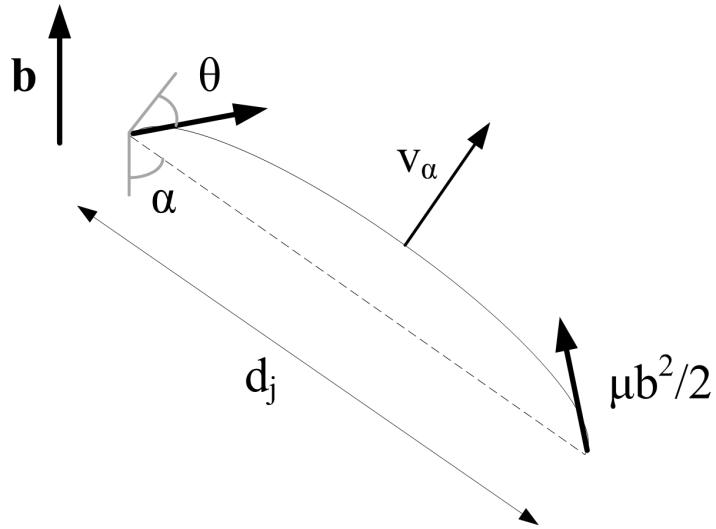

Figure 8.7: Model for jog dragging of a dislocation segment oriented at an angle α with respect to the Burger's vector.

be constant and of magnitude $\mu b^2/2$) in addition to the applied effective stress τ_{eff}.

Drag of a randomly oriented jogged dislocation

Let us consider a jogged dislocation segment having an $\alpha°$ orientation with the the Burgers vector such as depicted in Fig. 8.7. Sessile jogs are separated with a mean distance d_j. Our model makes the following assumptions:

- Climb of sessile jogs proceeds by emission of a point defect every jump of length b along the direction perpendicular to the Burger's vector.
- The energy barrier for point defect emission is similar for any random orientation α to the reference case of screw segments. What differs, however, is the work performed by various forces over the barrier length, as seen below.
- Dislocation bowing is similar on each side of the jogs. This approximation implies that jog sliding along the dislocation line is not possible, as long as mutual jog interaction is disregarded.

Geometrical considerations yield a total force acting on jogs due to the line tension and helping overcome the thermal barrier:

$$F = \mu b^2 \cos\theta \cos\alpha \tag{8.19}$$

where θ is defined as in Section 8.3 and Fig. 8.7. A $\cos\alpha$ factor is required since Γ helps overcome the thermal barrier only when the jog moves in a direction perpendicular to the Burger's vector.

For the same reason, the work performed by the line tension and the applied stress when the jogs climb over a length b includes a $\cos\alpha$ factor. This leads to a modified Eq. 8.18:

$$v_{jog} = \frac{4\pi D_{sd}}{b} \sinh\left(\frac{\left(\tau_{eff} d_j a b + \mu b^3 \cos\theta\right)\cos\alpha}{k_b T}\right) \tag{8.20}$$

Bowing out of the dislocation segment accelerates the jog dragging process because μb^3 is large in Si, delaying somehow the appearance the jog dragging-dominated motion regime. Changing the orientation of the dislocation segment from screw towards edge allows for less work to be performed by τ_{eff} and Γ, *increasing* hereby the tendency of jog drag to control dislocation motion[3].

Combining motion mechanisms

The dislocation velocity is determined by the rate-limiting motion mechanism. If $v_{jog}\,(\cos\theta = 0) \geqslant v_{dk}(d_j)$, the bowing out has no effect and $v = v_{dk}(d_j)$.

The whole dislocation moves at a speed $v \in]0, v_{dk}[$, and the velocity of the straight segment between jogs, of length $X_j = d_j - \mu b \cos\theta/\tau_{eff}$ (see Eq. 8.9) equals v_{jog}:

$$v_0 \left(\frac{\tau_{eff}}{\tau_0}\right)^{m_0} \left[1 - \exp\left[-\left(\frac{d_j - \mu b \cos\theta/\tau_{eff}}{L_1}\right)^{m_1}\right]\right] \exp\left(-\frac{U}{k_b T}\right) = \frac{4\pi D_{sd}}{b} \sinh\left(\frac{\left(\tau_{eff} d_j a b + \mu b^3 \cos\theta\right)\cos\alpha}{k_b T}\right) \tag{8.21}$$

where the continuous approximation of v_{dk} is chosen. Solving Eq. 8.21 for $\cos\theta$ under the constraint $X_j > 0$ and insertion into Eq. 8.20 yields the equilibrium X_j. The dislocation velocity is then given by Eq. 8.7 with $v = v_{dk}(X_j)$. The influence of segment orientation on the jog dragging-dominated motion domain is shown in Fig. 8.8.

Note that the present model does not rule out different rates of evolution for the d_j's depending on the dislocation character. Indeed, jogs on edge dislocations are glissile and $\lim_{\alpha\to\pi/2} v_{jog} = \infty$. Therefore, a complete model for drag of jogged mixed dislocations must include an evolution law for d_j that depends on the dislocation character and yields $\lim_{\alpha\to\pi/2} d_j = \infty$. This aspect is discussed in the next Chapter.

Discussion

MATHEMATICAL CONSIDERATIONS This approach yields a velocity law $v \in \mathcal{C}^\infty$. Adopting a more simple law for the motion of jogged dislocations

3 This remark is valid at a constant d_j.

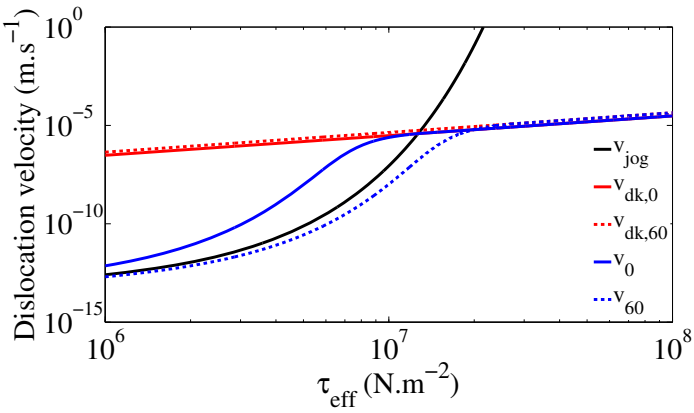

Figure 8.8: Computed velocities of different dislocation characters when sessile jogs are present along the line. $T = 1073\,\mathrm{K}$, $d_j = 10^{-7}\,\mathrm{m}$.

such as $v = \min\left(v_{jog}, v_{dk}\right)$ has the drawback of restraining continuity as in this case $v \in \mathcal{C}^0$ only, which poses numerical problems at the transition between both motion modes. Fig. 8.10 shows the computed screw dislocation velocity at $T = 1073\,\mathrm{K}$ at various d_j and τ_{eff}.

COMPUTATIONAL COST There is *a priori* no interest in choosing the exact, piecewise-defined velocity functon v_{dk} when deriving Eq. 8.21. An analytical function allows indeed to solve the nonlinear equation with a fast-converging algorithm such as a Newton-Raphson (NR) solver requiring the existence and continuity of the first derivative to perform correctly.

However, the constraint[4] imposed on $\cos\theta$ by the condition $X_j > 0$ is observed most often to be violated during the first iterations of the NR solver. It is therefore computationally more efficient to start readily with a solver exhibiting a linear convergence rate (e.g., the bisection method). In this case, adopting the highly nonlinear approximation for v_{dk} is not necessary and numerically risky, as a weak error on the converged X_j has then potentially large consequences on the dislocation velocity. The computed dislocation velocity v based on Eq. 8.6 is additionally indistinguishable from the one derived with Eq. 8.7, as seen in Fig. 8.9.

Combined with the discussion of Section 8.3.3, this shows that *using a nonlinear $\mathcal{C}^\infty$ approximation of v_{dk} is not necessary and should actually be avoided in order not to increase the computational cost of the model and divergence risks.*

EQUIVALENT JOG DENSITY The present model assumes that Eq. 8.18 is applicable for any dislocation character. At a given d_j, a dislocation with a strong edge component will see its velocity severly affected by sessile jogs. Disregarding the line tension contribution, Eq. 8.21 can be interpreted as if

4 It is equivalent to look for the solution in the interval $\left[0,\, d_j\tau_{eff}/\mu b\right[$, which exists by virtue of the intermediate value theorem.

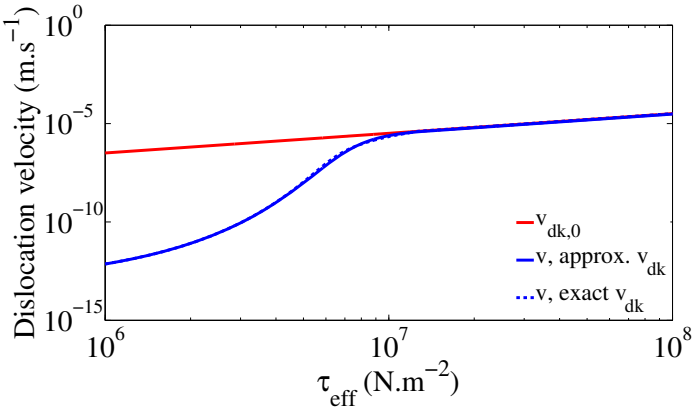

Figure 8.9: Screw dislocation velocity resulting from the combined effect of jog dragging and double kink mechanism: effect of the approximate v_{dk} function.

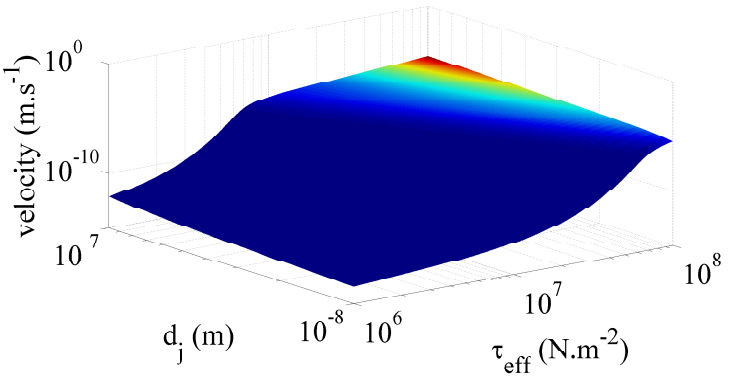

Figure 8.10: Screw dislocation velocity resulting from the combined effect of jog dragging and double kink mechanism.

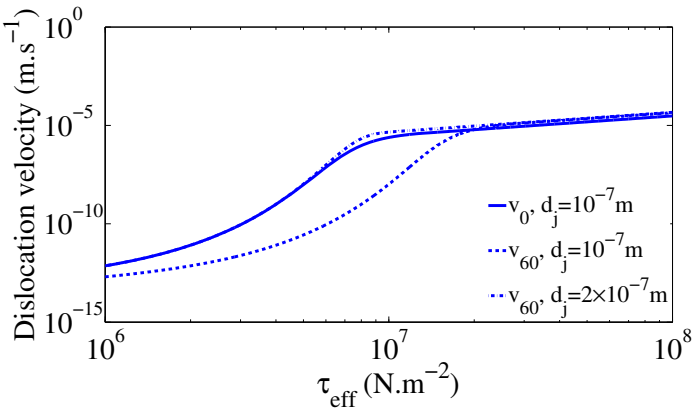

Figure 8.11: Comparison of screw and 60° dislocation velocities at $T = 1073\,\mathrm{K}$ for different d_j.

all dislocations were affected in a similar way by jogs, provided that d_j is modulated by a factor $\cos\alpha$. At a given τ_{eff}, this means that if $d_{j,60} = 2d_{j,s}$, then screws and 60° segments have approximately the same velocity, as shown in Fig. 8.11.

ALTERNATIVE SOLUTION An approximation of the solution shown in Fig. 8.10 can be obtained by searching for the solution to $v_{jog} = v_{dkm}$, reached for $\tau_{eff} = \tau_v$ given the mean jog spacing, and assuming the following expression for v:

$$v_{app} = v_{dkm}^{\min\left(\tau_{eff}/\tau_v,1\right)} \times v_{jog}^{1-\min\left(\tau_{eff}/\tau_v,1\right)} \tag{8.22}$$

This approximation is far from perfect as shown in Fig. 8.12, but yields results of the same order of magnitude as the exact solution over the whole stress and jog spacing range considered.

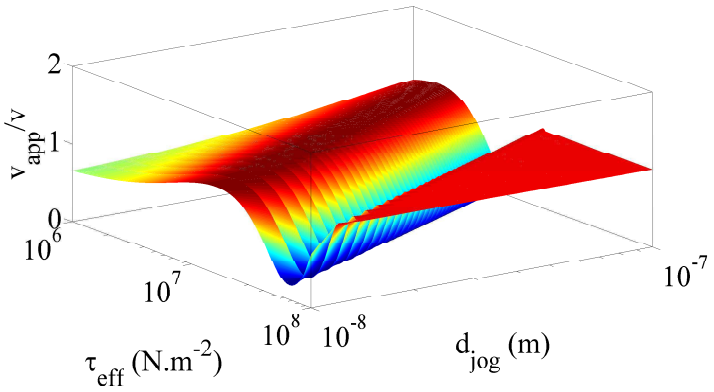

Figure 8.12: Ratio of dislocation velocity computed by the approximation of Eq. 8.22 to the exact one.

8.5 INFLUENCE OF IMPURITIES ON DISLOCATION MOBILITY

The influence of impurity atoms on the dislocation motion mechanisms depends on their nature, as they constitute additional thermally overcomable obstacles opposing dislocation motion.

They can ease kink nucleation if they are electrically active (e.g., dopants), affecting U by changing the defect density at the dislocation cores (see, e.g., [Heggie 1991, De Araujo 2004] and Chapter 3).

Instead of affecting directly the activation energy for dislocation motion the effect of dissolved electrically inactive impurities such as oxygen is generally modelled by the incorporation of an additional internal stress component stemming from their locking effect when present at the core (see Section 6.4); formation of a Cottrell atmosphere in the temperature range where plasticity actually takes place has been shown by [Sumino 1999] to be thermodynamically unlikely.

Only a fraction of the potentially mobile dislocations is actually set into motion upon loading, the remaining part representing the statistically locked segments [Yonenaga 1984, Petukhov 2004]. Modifications of the model for intrinsic crystals introduced in Chapter 6 give excellent results in the yield region as long as the concentration of dissolved impurities does not lead to their inhomogeneous distribution in the matrix.

8.6 CONCLUSION - MOTION OF DISLOCATIONS IN SEMICONDUCTORS

The constitutive parameters steering dislocation motion are given in Table 8.1, where those specific to screw and 60° segments are detailed.

The refinements brought throughout this Chapter to the standard velocity expression show that rate-limiting motion mechanisms in silicon, or more generally in semiconductors, differ significantly from those active in f.c.c. crystals. The most striking discrepancy lies in the absence of significant influence of localized obstacles on the mean dislocation velocity. This is understood by accounting for the strong lattice friction opposing dislocation motion in free flight. In f.c.c. crystals $t_f \ll t_w$; the opposite relationship is valid in semiconductors.

This is further strengthened by the low self-diffusion coefficient (or high self-diffusion activation energy), so that when jog dragging takes over from the double kink mechanism in free flight, the effect of localized obstacles on $\overline{v}$ shrinks even more and one gets in practice $\overline{v} \simeq v$.

Jog dragging is a possible controlling mechanism for dislocation motion, as the intrinsic constituent segments of any dislocation loop, screw and 60° orientations, both have a screw component. However, owing to the large μb^3 energy in semiconductors, the transition from the double kink to jog dragging mechanism is predicted by our model to be somehow delayed. In the mixed mode, segment bowing between the atomic jogs eases dislocation motion.

As seen in Fig. 8.8, the difference between the velocities of jogged screw and 60° segments at equal effective mean sessile jog spacing is quite significant, several orders of magnitude. This is explained by the smaller work performed by the effective stress and line tension in helping overcoming the thermal barrier of jog climbing when the dislocation is rotated towards an edge orientation. Note that the present model does *not* rule out different jog spacings on screws and 60° dislocations at a given deformation state.

	screws	60°/edge
v_0 (m.s^{-1})	3.5×10^4	10^4
τ_0 (MPa)	1	1
m_0	1	1
U (eV)	2.35	2.2
X_{max} (m)	10^{-7}	
F_{obs} (eV)	2.2	
p	2/3	
q	3/2	

Table 8.1: Model parameters related to dislocation velocity.

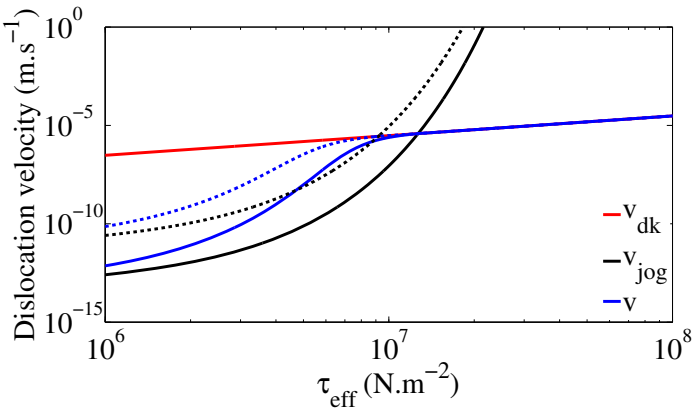

Figure 8.13: Screw dislocation velocity for the standard D_{sd} (plain curves) and a diffusion coefficient 100 times larger (dashed curves). $T = 1073\,\mathrm{K}$, $d_j = 10^{-7}\,\mathrm{m}$.

Our discussion has indeed shown that the evolution law for d_j *must* depend on the dislocation character.

The transition sharpness (that can be defined in mathematical terms as the maximum $\partial v/\partial \tau_{eff}\Big|_{d_j}$) can be reduced by increasing the self-diffusion coefficient D_{sd} in Eq. 8.18, as shown in Fig. 8.13. The presence of point defects close to or at the dislocation core, or a modification of the diffusion coefficient close to the core due to lattice distortion, could affect significantly this parameter and help smoothen the transition between both modes further. However, this aspect will not be discussed in this work.

Finally, we have shown that using a continuous analytical law for the dependency of v_{dk} on the dislocation length X leads to higher computational costs and instability risks, by increasing the nonlinearity of the function.

The remarks that closed Part ii mentioned that any attempt to improve the model of Alexander & Haasen should include the case of multiple slip, or in other words the effects of forest on dislocation motion and multiplication mechanisms. This Chapter has proposed a model for the former aspect. The next Chapter introduces a constitutive model for silicon monocrystals that incorporates the results derived here. It is shown that the simulated mechanical behavior of silicon is extremely dependent on the law chosen for dislocation velocity. Indeed, any approximation made in the derivation of $\overline{v}$ has a potentially important consequence on the stress-strain curves generated by a constitutive model.

9

A HOLISTIC CONSTITUTIVE MODEL FOR EXTRINSIC EG-SI MONOCRYSTALS

A physically-based constitutive model for silicon crystals is built from scratch. Owing to the physical processes we are aiming at reproducing, the total dislocation density on each of the twelve slip systems of the d.c. structure is divided between mobile and immobile dislocations. The former enter Orowan's law, while the latter contribute to the internal stress build-up. An additional refinement consists in distinguishing between screw and 60° dislocations for each population. All internal and critical stresses required for the derivation of the dislocation velocity are defined using the dislocation densities or impurity concentration as sole variables. Differential equations ruling the evolution of the model variables (dislocation densities, jog spacing, impurity concentration) are then proposed. Dislocation storage and annihilation processes as a function of the effective stress are modeled based on physical observations only, and are derived separately for screws and 60° dislocations. The present model is believed to constitute a significant step forward in modeling the mechanical behavior of semiconductors, albeit at a rather high complexity level.

INTRODUCTION

Our previous model introduced in Chapter 6 presents some limitations: the total dislocation density is underestimated, the share of mobile dislocations is much larger than experimentally estimated, and the model is not valid in stage II of hardening.

These shortcomings are solved in this Chapter, where a holistic constitutive model for silicon monocrystals is introduced. We aim at deriving a physically-based constitutive model, or *discrete dislocation slip model*, to use the formulation of Section A.2. The kinematical framework of crystal plasticity introduced in Annex A links the microscopic plastic strain rates to the macroscopic deformation gradient.

Such a model must be based on Orowan's law (derived in Section 9.1), that in turn requires the knowledge of the dislocation velocity (modeled in the previous Chapter). The latter requires calculation of the internal stress τ_{int} in order to obtain the effective stress: this is achieved in Section 9.2.

Evolution laws are then required for the dislocation densities (Section 9.3). Physical processes such as dipole formation and dislocation annihilations are modeled in Section 9.4; dislocation interactions are dealt with in Section 9.5 where parameters necessary to the computation of dislocation

velocity and multiplication are defined. The jog density evolution laws are derived in Section 9.6. Ultimately, the model for dislocation locking by impurities, similar to the one introduced in Chapter 6, is reminded in Section 9.7.

9.1 PLASTIC STRAIN RATE

Dislocation motion is not limited to a single slip plane and from now on we consider dislocation glide on each of the 12 slip systems of the glide set of the diamond cubic lattice of silicon. The systems are identified using Schmid & Boas notation, each plane being identified by a letter from A to D, the slip directions refered to by a number from 1 to 6 (see Fig. A.1 for system numbering). Let us consider as a generic object an hexagonal dislocation loop made up of screw and 60° segments, typically encountered at high effective stresses (see Chapter 1). For simplicity dislocations are considered as perfect. Under a finite effective stress the loop expands in a volume V, and its area $\mathcal{A}$ increases at a rate $\dot{\mathcal{A}}$, leading to the plastic strain rate:

$$\dot{\gamma}_p = \frac{b\dot{\mathcal{A}}}{V} \tag{9.1}$$

The loop expansion increases its perimeter as shown in Fig. 9.1. Both screw and 60° segments, of respective lengths l_s and l_{60}, are *a priori* affected. Geometrical considerations yield:

$$\frac{\mathrm{d}\mathcal{A}}{\mathrm{d}t} = \sqrt{3}\left(l_{60}\frac{\mathrm{d}l_s}{\mathrm{d}t} + (l_0 + l_{60})\frac{\mathrm{d}l_{60}}{\mathrm{d}t}\right) \tag{9.2}$$

where the factor $\sqrt{3}$ stems from the orientation of the 60° segments. The terms $\mathrm{d}l_s/\mathrm{d}t$ and $\mathrm{d}l_{60}/\mathrm{d}t$ are derived as:

$$\begin{cases} \frac{\mathrm{d}l_{60}}{\mathrm{d}t} = \frac{2\overline{v}_s}{\sqrt{3}} \\ \frac{\mathrm{d}l_s}{\mathrm{d}t} = \frac{2}{\sqrt{3}}\left(2\overline{v}_{60} - \overline{v}_s\right) \end{cases} \tag{9.3}$$

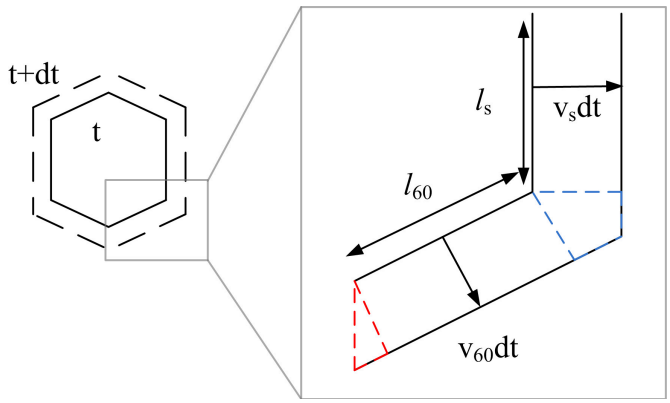

Figure 9.1: Calculation of $\dot{\gamma}_p$ from the expansion of a hexagonal dislocation loop.

where the computation of the mean screw (resp. 60°) dislocation velocity $\overline{v}_s$ (resp. $\overline{v}_{60}$) requires the derivation of the long-range internal stress $\tau_{int}^{(\alpha)}$ as discussed in the previous Chapter. Eq. 9.3 yields $\dot{\mathcal{A}} = 4\overline{v}_{60} l_{60} + 2\overline{v}_s l_s$. Considering the whole loop, the total screw and 60° lengths are given by[1] $L_s = 2l_s$ and $L_{60} = 4l_{60}$. With $\rho_{m,s} = L_s/V$ and $\rho_{m,60} = L_{60}/V$ screw and 60° mobile dislocation densities respectively, one gets Orowan's law on the slip system α:

$$\dot{\gamma}_p^{(\alpha)} = \dot{\gamma}_{p,s}^{(\alpha)} + \dot{\gamma}_{p,60}^{(\alpha)} = b\left(\rho_{m,s}^{(\alpha)}\overline{v}_s^{(\alpha)} + \rho_{m,60}^{(\alpha)}\overline{v}_{60}^{(\alpha)}\right)\text{sign}(\tau^{(\alpha)}) \tag{9.4}$$

Negative strain rates allowed by the introduction of $\text{sign}(\tau^{(\alpha)})$ representing slip in the direction of $-\mathbf{s}_0^{(\alpha)}$.

1 We neglect any possible velocity difference between the different 60° segments, that could be due to their different partial ordering (see Chapter 1).

9.2 INTERNAL AND CRITICAL STRESSES

9.2.1 *Intrinsic crystals*

Independently of the presence of obstacles on the slip plane, the exact expression of the internal stress entering into Eq. 8.7 is necessary for the derivation of the mean dislocation velocities $\overline{v}_s^{(\alpha)}$ and $\overline{v}_{60}^{(\alpha)}$. It has been shown in [Sumino 1974b, Suezawa 1979] that the constant component of the internal stress τ_b is made up of a contribution coming from the mobile dislocations and an additional term proportional to the hardening strain. The original works did not attempt to express explicitely the hardening component as a function of dislocation densities. [Sumino 1993] have generalized this equation to multiple slip systems and assume the direct additivity of the internal stress stemming from mobile dislocations, but these authors consider all dislocations to be mobile.

We distinguish in this work four dislocation populations, based on their character -screws or 60°- and mobility potential.

As dislocations move on their slip plane, they meet dislocations of opposite sign gliding on parallel planes. If their elastic interaction is strong enough as they pass each other, a dipole might form. This results in the statistical trapping of dislocations into a population that cannot carry plastic flow anymore, stored as dipolar or multipolar structures or as isolated debris (see Section 6.2). Both edge and screw dipoles can form *a priori*. We call these densities of stored dislocations the densities of *immobile* dislocations, written $\rho_{i,s}^{(\alpha)}$ and $\rho_{i,60}^{(\alpha)}$ depending on the dislocation character, with $\rho_i^{(\alpha)} = \rho_{i,s}^{(\alpha)} + \rho_{i,60}^{(\alpha)}$.

A similar equation applies to the density of mobile dislocations $\rho_m^{(\alpha)}$. The total dislocation density $\rho_t^{(\alpha)}$ is equal to $\rho_m^{(\alpha)} + \rho_i^{(\alpha)}$.

Note that a dipole might be destroyed if the applied stress is large enough; a given dislocation can consequently shift between mobile and immobile configurations before it is annihilated. Immobile dislocations differ from mobile dislocations at rest, since the latter can still carry plastic flow if the effective stress takes a finite value. Dipole and multipoles exhibit much weaker long-range stress fields than mobile dislocations do. It is consequently necessary to distinguish both populations in the estimation of the internal stress.

The model derived in this work is not limited to one slip plane, and dislocations are assumed to be present on all the slip systems. Latent hardening is accounted for by the introduction of constant interaction parameters $A_{\alpha\beta}$ and $B_{\alpha\beta}$ characterizing the intensity of the long-range elastic stress fields created by $\rho_m^{(\beta)}$ and $\rho_i^{(\beta)}$ respectively, onto dislocations belonging to the slip system α. These interaction coefficients are derived on

geometrical arguments only as discussed by [Zarka 1972] and the internal stress reads:

$$\tau_{int}^{(\alpha)} = \mu b \sum_{\beta=1}^{12} \left(A_{\alpha\beta} \sqrt{\rho_m^{(\beta)}} + B_{\alpha\beta} \sqrt{\rho_i^{(\beta)}} \right) \tag{9.5}$$

The effective stress reads:

$$\overline{\tau}_{eff}^{(\alpha)} = \left\langle \left| \tau^{(\alpha)} \right| - \mu b \sum_{\beta=1}^{12} \left(A_{\alpha\beta} \sqrt{\rho_m^{(\beta)}} + B_{\alpha\beta} \sqrt{\rho_i^{(\beta)}} \right) \right\rangle \tag{9.6}$$

with $\langle x \rangle = \max(x, 0)$. The absolute value of the resolved shear stress is considered in Eq. 9.6 as we do not consider forward and backward motion of dislocations on a slip system as two different slip mechanisms.

Finally, the critical stress $\tau_c^{(\alpha)}$ for athermal overcoming of the localized obstacles is required for the computation of the dislocation velocity (see Section 8.3). It incorporates both long-range and short-range components of the dislocation interactions, and includes all dislocation populations. The critical stress resulting from dislocations on several slip systems are not additive as demonstrated by [Franciosi 1982]:

$$\tau_c^{(\alpha)} = \mu b \sqrt{\sum_{\beta=1}^{12} a_{\alpha\beta} \rho_t^{(\beta)}} \tag{9.7}$$

The $a_{\alpha\beta}$ coefficients depend on the type of interaction between the slip systems α and β and are derived in Section 9.5. Table 6.1 gives an overview of the interactions between the 12 slip systems of silicon.

9.2.2 *Influence of electrically inactive impurities at the cores*

We consider in this work oxygen only as a model impurity. Dissolved oxygen atoms that have diffused at the dislocation cores at a concentration $c_O^{(\alpha)}$ exert an additional back stress $\tau_O^{(\alpha)}$ opposing dislocation motion. To set dislocations back into motion the applied stress must be large enough to surmount the internal stress now incorporating the effect of impurities. Because of the relatively weak interaction energy between an impurity and a dislocation, the formation of Cottrell atmosphere around dislocations is unlikely at the high temperatures of interest for plasticity [Sumino 1999]. The contribution of the Cottrell atmosphere to $\tau_O^{(\alpha)}$ is therefore disregarded and the internal stress reads:.

$$\tau_O^{(\alpha)} = f(T) c_O^{(\alpha)} \tag{9.8}$$

The temperature-dependent prefactor $f(T)$ depends linearly on the temperature as long as the impurity atoms at the core do not form aggregates or impurity clusters.

Aggregation by pipe diffusion is however favored at high temperatures, so a nonlinear dependency of $f(T)$ can be expected at the temperatures of interest in the present work. Experimental data is lacking on

this point but extrapolation of the data by [Senkader 2004] gives $f(T) = 9.44 \times 10^{-22} \exp(0.29/k_b T)$ (see Chapter 6).

Note that distinguishing 60° from screw dislocations implies independent oxygen concentrations and *a priori* different $\tau_O^{(\alpha)}$ on each dislocation character. It should follow different effective stresses. This complicates further the model, and for the sake of simplicity a single oxygen-generated back stress is considered, taken as the mean value of the $\tau_O^{(\alpha)}$'s on 60° and screw dislocations.

9.3 EVOLUTION OF DISLOCATION DENSITIES

The remaining components required in Orowan's law are the densities of mobile dislocations $\rho_{m,s}^{(\alpha)}$ and $\rho_{m,60}^{(\alpha)}$. These microstructural parameters are usually considered as constant in fcc crystals, and representing only a minor fraction of the total dislocation density $\rho_t^{(\alpha)}$ (see, e.g., [Kothari 1998]). Silicon materials are different as their very low as-grown dislocation content guarantees that all dislocations in the crystal are *initially* mobile. [Alexander 1968] consider this approximation remains true throughout deformation when deriving their model. This has been shown experimentally inaccurate. At the lower yield point immobile dislocations are estimated to make up a significant part of ρ_t, with their share increasing through stage I (see [Kojima 1971, Sumino 1974a, Yonenaga 1978, Oueldennaoua 1988]). A correct representation of the mechanical behavior of silicon monocrystals requires indeed the introduction of an additional population of immobile dislocations, those that are statistically trapped in dipolar, multipolar structures or bundles.

9.3.1 *Intrinsic crystals*

Multiplication of dislocations on their plane proceeds by means of the athermal activation of Frank-Read sources observed, e.g., by [Dash 1956] and modeled by [Moulin 1997]. The occurence of thermally activated double cross-slip events is also experimentally observed ([Vallino 2001]), although the extent of dislocation *multiplication* by this mechanism ought to be very limited at the temperatures considered in this work, especially if the crystallographic orientation of the samples favors single glide, as discussed by [Moulin 1997]. Dislocation *annihilation* by cross-slip of screw segments is however observed to proceed beyond the lower yield point, as witnessed by the predominance of edge segments in stage I (see, e.g., [Alexander 1968, Oueldennaoua 1988]).

Rate of generation of mobile dislocations

Different multiplication laws for intrinsic semiconductors in the absence of forest dislocations can be found in the literature. Eq. 9.9 makes use of a generic function $K_1(\tau_{eff}^{(\alpha)}, T, \dot{\gamma}_p^{(\alpha)})$. It can be proportional to $\tau_{eff}^{(\alpha)}$ as introduced by [Alexander 1968] following the empirical results of [Berner 1967], independent of $\tau_{eff}^{(\alpha)}$ ([Moulin 1997]) or proportional to $\sqrt{\tau_{eff}^{(\alpha)}}$ as derived by [Moulin 1999] by means of dislocation dynamics simulations[2]. A powerful

2 Note that if dislocation velocity is linear in τ_{eff} Orowan's law gives $\rho_m \propto \dot{\gamma}_p/\tau_{eff}$ and the multiplication law of [Moulin 1999] $\dot{\rho}_m \propto \sqrt{\tau_{eff}/\rho_m}\dot{\gamma}_p$ is strictly equivalent to the introduction of a strain rate dependency in the rate equation of [Alexander 1968] that reads $\dot{\rho}_m = \delta(\dot{\gamma}_p)\tau_{eff}\dot{\gamma}_p$ with $\delta \propto \dot{\gamma}_p^{-0.5}$. A negative strain rate power dependency of δ has been shown in [Cochard 2010b] to reproduce more accurately the yield drop.

definition of K_1 is proposed in Section 10.3. Dislocation multiplication by creation of Frank-Read sources on the microstructure is proportional to the inverse of the mean free path $l_{FR}^{(\alpha)}$ (see, e.g., [Stainier 2002]). The total generation rate reads:

$$\dot{\rho}_m^{(\alpha)} = \left(K_1(\tau_{eff}^{(\alpha)}, T, \dot{\gamma}_p^{(\alpha)}) + \frac{K_2(T, \dot{\gamma}_p^{(\alpha)})}{l_{FR}^{(\alpha)}} \right) \frac{\dot{\gamma}_p^{(\alpha)}}{b} \tag{9.9}$$

K_1 and K_2 are *a priori* dependent on temperature and strain rate. Note that at low effective stresses (for example at high temperatures or low strain rates) or high dislocation densities $K_1 \ll K_2$, showing that the first term in the multiplication law dominates mainly in the yield region and at low temperatures (resp. high strain rates). As mentioned above, cross-slip breeding is disregarded and we set $K_2 = 1$, the possible constant factors being aggregated into $l_{FR}^{(\alpha)}$ (see Section 9.5).

Considering the generation of screw and 60° segments separately, the dislocation generation rate reads

$$\begin{cases} \dot{\rho}_{m,s}^{(\alpha)} = \left(K_1 + \frac{0.5}{l_{FR}^{(\alpha)}} \right) \frac{\dot{\gamma}_p^{(\alpha)}}{b} \\ \dot{\rho}_{m,60}^{(\alpha)} = \left(K_1 + \frac{0.5}{l_{FR}^{(\alpha)}} \right) \frac{\dot{\gamma}_p^{(\alpha)}}{b} \end{cases} \tag{9.10}$$

For each population, the first term on the right-hand side of Eq. 9.10 refers to the increase in dislocation density due to the expansion of existing dislocation loops, whereas the second one is related to the generation of new loops as the segments meet obstacles on their slip plane.

Storage and annihilation rates of mobile dislocations

The derivation of the storage and annihilation rates of mobile dislocations requires the knowledge of the dislocation density distribution as a function of their sign. We assume that the density of positive dislocation segments equals the density of negative segments for each character.

MOBILE DISLOCATION STORAGE Dislocation storage by immobilization in dipolar, multipolar structures or bundles is considered in this work, a process involving dislocations on the same slip system only. For the sake of simplification we model only the formation of dipoles.

Let us consider only one dislocation character. A positive (or negative) dislocation segment moving at a velocity $\overline{v}$ meets $2h_{max} \times \rho_m/2 \times 2\overline{v}$ moving dislocations of opposite sign per unit time, potentially favorable for the formation of a dipole maximum height h_{max} ($2\overline{v}$ being their relative velocity, see Figure 9.2). This yields a storage rate $\dot{\rho}_{m,+} = \dot{\rho}_{m,-} = -2h_{max} \times (\rho_m/2)^2 \times 2\overline{v}$, and finally $\dot{\rho}_m = -2h_{max}\rho_m^2\overline{v}$ for each dislocation character.

The maximum dipole height depends on its nature and $h_{max,e} = \mu b/8\pi(1-\nu)\tau_{eff}$ for edge dipoles (assumed to form by storage of 60° dislocations). $h_{max,s} = \mu b/4\pi\tau_{eff}$ for screw dipoles. It is shown in Section 9.4 that the *effective* maximum dipole heights (serving as capture radii) are not increased by cross-slip or climb.

h_{min} is the minimum dipole height below which spontaneous annihilation takes place, considered equal for screws and edge characters.

MOBILE DISLOCATION ANNIHILATION Annihilation of a pair of mobile screw segments by thermally activated cross-slip leads to an additional sink for $\rho_{m,s}$. We make use of a capture radius $r_{a,m}^{(0)}$ to model this process, the derivation of which is detailed in Section 9.4. $r_{a,m}^{(0)}$ depends indirectly on temperature and strain rate through its nonlinear dependence on τ_{eff}. Following the same reasoning as above, the annihilation rate of screws is consequently $\dot{\rho}_{m,s} = -2r_{a,m}^{(0)}\rho_{m,s}^2\overline{v}_s$.

Annihilation of moving edge segments bypassing each other is shown below not to be enhanced by τ_{eff}, and this process occurs consequently at a constant capture radius equal to $r_{a,m}^{(90)} = h_{min}$.

Storage and annihilation of 60° segments is *a priori* more complex to model, as these dislocations exhibit both a screw and edge component. In order to simplify this treatment and setting $r_e = \max(h_{max,e}, h_{min})$ storage radius for edge segments, we define for a dislocation segment of random orientation α:

$$r_\alpha = r_s r_e / \sqrt{(r_e \cos\alpha)^2 + (r_s \sin\alpha)^2} \tag{9.11}$$

r_α is then by definition the polar equation of the ellipse centered on 0 having r_e and r_s as major and minor axis, respectively. This yields for $\alpha = \pi/3$:

$$r_{60} = \frac{r_s r_e}{\sqrt{\frac{1}{4}r_e^2 + \frac{3}{4}r_s^2}} \tag{9.12}$$

The storage and annihilation rates of mobile dislocations finally read:

$$\begin{cases} \dot{\rho}_{m,60}^{(\alpha)} = -2r_{60}\rho_{m,60}^{(\alpha)}\dfrac{\dot{\gamma}_{p,60}^{(\alpha)}}{b} \\ \dot{\rho}_{m,s}^{(\alpha)} = -2r_s\rho_{m,s}^{(\alpha)}\dfrac{\dot{\gamma}_{p,s}^{(\alpha)}}{b} \end{cases} \tag{9.13}$$

with $r_s = \max(h_{max,s}, r_{a,m}^{(0)})$, with obviously $r_{a,m}^{(0)} \geqslant h_{min}$.

Evolution of immobile dislocations

STORAGE OF IMMOBILE SEGMENTS The stored dislocations build up a density of immobile dislocations $\rho_i^{(\alpha)}$. Some of the dipoles formed annihilate readily by climb or cross-slip, so that r_e (resp. r_s) is reduced by h_{min} (resp. $r_{a,m}^{(0)}$). Following Eq. 9.11, this results in r_{60} being reduced by $r_{a,m}^{(60)} = r_{a,m}^{(0)}h_{min}/\sqrt{h_{min}^2/4 + 3r_{a,m}^{(0)2}/4}$.

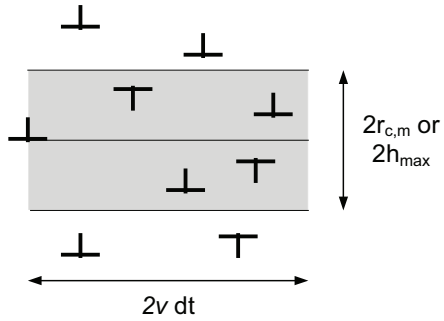

Figure 9.2: Trapping or annihilation of mobile dislocations resp. by formation of dipoles or by cross-slip. See text for details.

ANNIHILATION OF IMMOBILE SEGMENTS Annihilation of immobile dislocation segments is possible both by cross-slipping of a passing screw or climb of a passing edge. Such annihilations cause the loss of two segments while freeing the second dipole constituent. This process has consequently no net effect on ρ_m.

The capture radius $r_{a,i}^{(0)}$ for cross-slip is calculated in the next Section, where it is also shown that annihilation of edge dipoles by climb of by-passing mobile edge segments effectively takes place at a constant capture radius $r_{a,i}^{(90)} = h_{min}$. This gives $r_{a,i}^{(60)} = r_{a,i}^{(0)} h_{min} / \sqrt{h_{min}^2/4 + 3r_{a,i}^{(0)2}/4}$.

The rate of annihilation of mobile 60° segments with an immobile dipole component reads $\dot{\rho}_{m,60} = -2r_{a,i}^{(60)} \rho_{i,60} \rho_{m,60} \overline{v}_{60}$; annihilation of screw segments leads to $\dot{\rho}_{m,s} = -2r_{a,i}^{(0)} \rho_{i,s} \rho_{m,s} \overline{v}_s$. These processes free one mobile segment while annihilating an immobile and a mobile one, so these rates actually apply to immobile densities. Finally one gets:

$$\begin{cases} \dot{\rho}_{i,60}^{(\alpha)} = 2\left[\left(r_{60} - r_{a,m}^{(60)}\right)\rho_{m,60}^{(\alpha)} - r_{a,i}^{(60)}\rho_{i,60}^{(\alpha)}\right]\frac{\dot{\gamma}_{p,60}^{(\alpha)}}{b} \\ \dot{\rho}_{i,s}^{(\alpha)} = 2\left[\left(r_s - r_{a,m}^{(0)}\right)\rho_{m,s}^{(\alpha)} - r_{a,i}^{(0)}\rho_{i,s}^{(\alpha)}\right]\frac{\dot{\gamma}_{p,s}^{(\alpha)}}{b} \end{cases} \tag{9.14}$$

Total dislocation evolution rate

If no difference is made between the dislocation characters, with $K_1 \ll 1/l_{FR}^{(\alpha)}$ and assuming that $\rho_m^{(\alpha)} \ll \rho_i^{(\alpha)}$, one retrieves from the equations introduced above the classical rate equation for the evolution of dislocation density in metals which has been shown able to correctly reproduce the mechanical behavior of fcc crystals up into stage III (see, e.g., [Harder 1999]):

$$\dot{\rho}_t^{(\alpha)} \simeq \left(\frac{1}{l_{FR}^{(\alpha)}} - 2r\rho_t^{(\alpha)}\right)\frac{\dot{\gamma}_p^{(\alpha)}}{b} \tag{9.15}$$

9.3.2 *Alterations in the presence of impurities*

Effective density of mobile dislocations

The density of mobile dislocations $\rho_m^{(\alpha)}$ is replaced in the above rate equations by an effective density $\rho_{m,eff}^{(\alpha)} = \eta\left(\tau_O^{(\alpha)}\right)\rho_m^{(\alpha)}$ with $\eta \leq 1$ verifying $\eta(0) = 1$ and $\eta(\infty) = 0$.

This model aims at reproducing the experimental observations of the yield region of CZ-crystals by [Yonenaga 1984] and is supported by the theoretical calculations of [Petukhov 2004]. It has been shown in Chapter 6 that such a modification to the model for intrisinc crystals yields a successful representation of the increase of τ_{uy} at large oxygen concentrations if $\eta(\tau_O^{(\alpha)}) = \exp\left(-\tau_O^{(\alpha)}/\tau_O^{ref}\right)$ is used, where τ_O^{ref} is a reference stress. In the present work we adopt Eq. 9.16 for η:

$$\eta(\tau_O^{(\alpha)}) = \exp\left(-\frac{\left\langle \tau_O^{(\alpha)} - \tau_O^{min} \right\rangle}{\tau_O^{ref}}\right) \tag{9.16}$$

where τ_O^{min} is the minimum locking stress required for impurities to have a significant effect on the mobile dislocation density.

Dislocation multiplication

Impurities diffused at the dislocation cores likely create an additional energy barrier to overcome prior to dislocation multiplication by cross-slip as discussed in [Maroudas 1991c] and Section 6.4.3.

This effect is accounted for by reducing the dislocation multiplication function K_1, but in a different way than chosen by [Maroudas 1991c]. Instead of considering the activation volume to be dependent on the mean jog spacing, it is made function of the impurity mean spacing along the dislocations[3] $c_O/\rho_m^{(\alpha)}$. With Eq. 9.8 this yields:

$$K_O = K_1 \exp\left(-\frac{c_O^{(\alpha)} f(T) b^2}{k_b T}\right) \tag{9.17}$$

3 This choice seems physically more right. The additional obstacle compared to the intrinsic case where jogged dislocations cross-slip anyway is the impurites diffused at the core, and only them. As a sidenote, this complication of the constitutive model does not bring significant improvement of the simulated behavior, as seen in the next Chapter.

9.4 DIPOLE FORMATION AND DISLOCATION ANNIHILATION PROCESSES

We derive in this Section models for the capture radii ruling:

1. the formation of screw and edge dipoles (r_s and r_e),
2. the annihilation of mobile screw dislocations by cross-slip $r_{a,m}^{(0)}$,
3. the annihilation of mobile edge dislocations by climb $r_{a,m}^{(90)}$, and
4. the subsequent dipole annihilation by bypassing dislocations (respectively $r_{a,i}^{(0)}$ and $r_{a,i}^{(90)}$ for screw and edge dipoles).

These models are physically based, adapted to the case of silicon and do not require further calibration.

It is assumed that cross-slipping takes place in the stress field generated by isolated dislocations or screw dipole components, and that no obstacle prevents subsequent dislocation annihilation once cross-slip has been initiated, since distances much smaller than the mean obstacle spacing are considered for cross-slip. The same assumptions are taken for climb of edge segments.

9.4.1 *Annihilation of mobile screw dislocations*

We apply in the following the methodology of [Stainier 2002] and adapt it to the case of silicon. It is shown that the capture radius for dislocation annihilation by cross-slip is strongly affected by the high cross-slip activation energy in semiconductors.

Preliminary discussion

Let us consider a screw dislocation whose mobility is determined by the double kink mechanism over a segment length X, moving in the primary plane under an effective stress τ_{eff} at a velocity v determined as described in Chapter 8. This dislocation is at a distance r of an isolated screw dislocation of opposite sign. The force per unit length exerted on the incoming dislocation reads $f_r = K/r$ with $K \simeq \mu b^2/2\pi$ [Hirth 1982]. Both segments are assumed to cross-slip towards each other at a velocity v_{dk}. Neglecting in a first step the resolved shear stress and internal stresses on the cross-slip system, the *relative* velocity of the cross-slipping segments reads:

$$v_{CS} = 2\lambda_{dk,s}(X)\frac{K}{br} \tag{9.18}$$

where the function $\lambda_{dk,s}$ has been defined in Section 8.2.2. The time it takes for the dislocations to annihilate is given by:

$$t_{CS} = \int_{r_{a,m}}^{r_{min}} \frac{-\mathrm{d}r}{v_{CS}(r)} = \frac{b}{K\lambda_{dk,s}(X)}\frac{r_{a,m}^{(0)2} - r_{min}^2}{4} \tag{9.19}$$

with r_{min} a cut-off radius below which cross-slipping always takes place successfully, of the order of 10^{-9} m or a few b. We take $r_{min} = 2 \times 10^{-9}$ m $\simeq 5b$. The moving dislocation stays within the radius $r_{a,m}$ during a time $t \simeq r_{a,m}^{(0)}/v$. Consequently cross-slip is possible if $t_{CS} \leq r_{a,m}^{(0)}/v$. Including the effects of jogs on dislocation velocity this yields:

$$r_{a,m}^{(0)} \leq r_{a,m}^{(0,max)} = \frac{2\lambda_{dk,s}(X)K}{bv(X_j)} + \sqrt{\left(\frac{2\lambda_{dk,s}(X)K}{bv(X_j)}\right)^2 + r_{min}^2} \tag{9.20}$$

For $\tau_{eff} \to 0$ the critical radius for annihilation of mobile dislocations $r_{a,m}^{(0,max)}$ diverges. An upper bound can be taken as $1/\sqrt{\rho_t}$. Note that if jogs have no influence on dislocation motion $\lambda_{dk,s}/v = 1/\tau_{eff}$.

In the presence of internal stresses on the collinear system, derivation of the capture radius gives the same result as previously but adds a condition on $r_{a,m}^{(0)}$. The incoming dislocation cross-slips at a velocity:

$$v_{CS} = 2\lambda_{dk,s}(X)\left(\left|\tau^{(CS)}\right| + \frac{K}{br} - \tau_{int}^{(CS)}\right) \tag{9.21}$$

and cross-slip can occur only if $\left|\tau^{(CS)}\right| + K/br_{a,m}^{(0)} > \tau_{int}^{(CS)}$. If $\tau_{eff}^{(CS)} > 0$ this is always verified; otherwise one must have $r_{a,m}^{(0)} < K/\left(b(\tau_{int}^{(CS)} - \left|\tau^{(CS)}\right|)\right)$. Assuming this relation holds, integration of this Eq. 9.21 yields

$$t_{CS} = \frac{1}{2\lambda_s(X)\tau_{eff}^{(CS)}}\left[r_{a,m}^{(0)} - r_{min} - \frac{K}{b\tau_{eff}^{(CS)}}\ln\left(\frac{1 + r_{a,m}^{(0)}b\tau_{eff}^{(CS)}/K}{1 + r_{min}b\tau_{eff}^{(CS)}/K}\right)\right] \tag{9.22}$$

with $r_{a,m}^{(0)}b\tau_{eff}^{(CS)}/K \ll 1$ a second order Taylor expansion of the logarithmic term gives after simplification t_{CS} equal to Eq. 9.19 and the same $r_{a,m}^{(0)}$ as previously. Consequently, the upper bound for the critical radius $r_{a,m}^{(0)}$ for annihilation of two isolated dislocations by cross slip reads:

$$r_{a,m}^{(0,max)} = \min\left(\frac{1}{\sqrt{\rho_t}}, \frac{2\lambda_{dk,s}(X)K}{bv(X_j)} + \sqrt{\left(\frac{2\lambda_{dk,s}(X)K}{bv(X_j)}\right)^2 + r_{min}^2}, \frac{K}{b\left(\tau_{int}^{(CS)} - \left|\tau^{(CS)}\right|\right)}\right) \tag{9.23}$$

where the last term has to be considered only if $\tau_{int}^{(CS)} - \left|\tau^{(CS)}\right| > 0$. Note that because of latent hardening, $\tau_{int}^{(CS)} > 0$ is always verified. Eq. 9.23 is similar to the one derived by [Stainier 2002].

The case of silicon

A limitation of this model is that it considers cross-slip to take place as soon as the dislocations are close enough from each other, without accounting for the thermal barrier that must be overcome to initiate cross-slipping. This

micromechanism is not easy in semiconductors because constrictions are required for the dissociated dislocations to initiate their motion onto the collinear system. Consequently it is expected that $r_{a,m}^{(0)} < r_{a,m}^{(0,max)}$.

Integrating the effects of jog dragging on dislocation motion into this model, the dislocation velocity in its plane v is given by $v_{dk}(X_{j,s})$, with $X_{j,s}$ derived in Section 8.4. We assume that segments of length $X_s = \min\left(L_0, d_{j,s}\right)$ are cross-slipping. [Moulin 1997] chose a fixed value $L_0 \simeq 10^{-7}$ m similar to ours. We introduce the number of successful cross-slip events per unit time $P_{CS} = \nu_{CS} \exp\left(-\frac{U_{CS} - V_{CS}(\tau_{eff}^{(CS)} + K/br)}{k_b T}\right)$ with $U_{CS} = 6$ eV and $V_{CS} = X_s b^2$, respectively activation energy taken from [Möller 1979] and activation volume for cross-slip, and $\nu_{CS} = b\nu_D / X_s$ the attempt frequency. Owing to the large activation energy U_{CS}, P_{CS} remains extremely small except for small r.

The mean time for cross-slip to successfully initiate is $1/P_{CS}$. Cross-slip leads to dislocation annihilation when $r/v > 1/P_{CS}(r) + t_{CS}(r)$, that is, when the time spent in the capture area is larger than the mean time required for cross-slip to take place added to the time for the dislocations to annihilate. The equation to solve for $r_{a,m}^{(0)}$ is therefore:

$$r_{a,m}^{(0)} - \frac{b v_{dk,s}(X_{j,s})}{4K\lambda_{dk,s}(d_{j,s})}\left(r_{a,m}^{(0)2} - r_{min}^2\right) - \frac{v_{dk,s}(X_{j,s})}{\nu_{CS}} \exp\left(\frac{U_{CS} - V_{CS}(\tau_{eff}^{(CS)} + K/br_{a,m}^{(0)})}{k_b T}\right) = 0 \tag{9.24}$$

under the constraint $r_{a,m}^{(0)} < r_{a,m}^{(0,max)}$.

Numerical estimates of the solution to Eq. 9.24 at different temperatures and effective stresses are shown in Figure 9.3 for $d_{j,s} = 10^{-6}$ m. The solution is extremely weakly sensitive to the effective stress, jog dragging affecting the capture radius at low effective stresses only. Note that T does not affect significantly $r_{a,m}^{(0)}$. The absence of significant difference between the capture radii at 673 and 1673 K is due to the much larger velocity at high temperatures that offsets the increased cross-slip probability.

If the influence of jogs and of $\tau_{eff}^{(CS)}$ are neglected then $r_{a,m}^{(0)}$ can be approximated by:

$$r_{a,m}^{(0)} = 46.1 \left(\frac{\tau_{eff}^{(\alpha)}}{\tau_0}\right)^{-0.028} \tag{9.25}$$

9.4.2 *Annihilation of immobile screw dislocations*

Now let us turn to the similar case of attrition of the *immobile* screw dislocations, defined by the capture radius $r_{a,i}^{(0)}$. We consider in our work

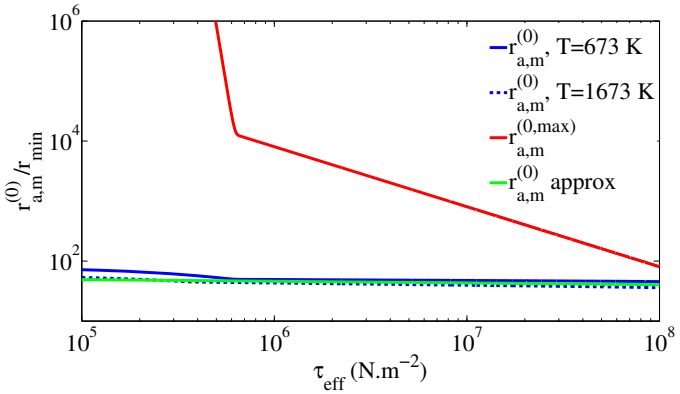

Figure 9.3: Annihilation of mobile screw dislocations: $r^{(0)}_{a,m}$ and $r^{(0,max)}_{a,m}$ from Eqs. 9.24 and 9.20 with $r_{min} = 2 \times 10^{-9}$ m and $d_{j,s} = 1\,\mu$m. The analytical approximation neglecting the presence of jogs (Eq. 9.25) is shown as well.

immobile dislocations stored in dipolar structures of mean height $h_{eff,s} = \sqrt{(e-1)\,h_{min,s}h_{max,s}}$ (see [Hähner 1996]), with $h_{max,s} = \mu b/4\pi\tau_{eff}$ and $h_{min,s} = r^{(0)}_{a,m}$ if $h_{max,s} > r^{(0)}_{a,m}$ and o otherwise.

The long-range force field per unit length created by a screw dipole of height $h_{eff,s}$ reads $f_r = K'/r^2$ with $K' = \mu b^2 h_{eff,s}/2\pi$. Following the same reasoning as previously, t_{CS} in the presence of internal stresses is approximated by:

$$t_{CS} = \frac{b}{K'\lambda_{dk,s}(X)} \frac{r^{(0)3}_{a,i} - r^3_{min}}{3} \tag{9.26}$$

and a first condition on $r^{(0)}_{a,i}$ reads, with $r^3_{min} \ll r^{(0)3}_{a,i}$:

$$r^{(0)}_{a,i} \leq r^{(0,max)}_{a,i} = \sqrt{\frac{3\lambda_{dk,s}(X)K'}{bv(X_j)}} \tag{9.27}$$

$r^{(0,max)}_{a,i}$ is indeed bounded by $1/\sqrt{\rho_t}$ and the presence of internal stresses on the collinear system leads to additional conditions on $r^{(0,max)}_{a,i}$:

$$r^{(0,max)}_{a,i} = \min\left(\frac{1}{\sqrt{\rho_t}}, \sqrt{\frac{3\lambda_{dk,s}(X)K'}{bv(X_j)}}, \sqrt{\frac{K'}{b\left(\tau^{(CS)}_{int} - \left|\tau^{(CS)}\right|\right)}}\right) \tag{9.28}$$

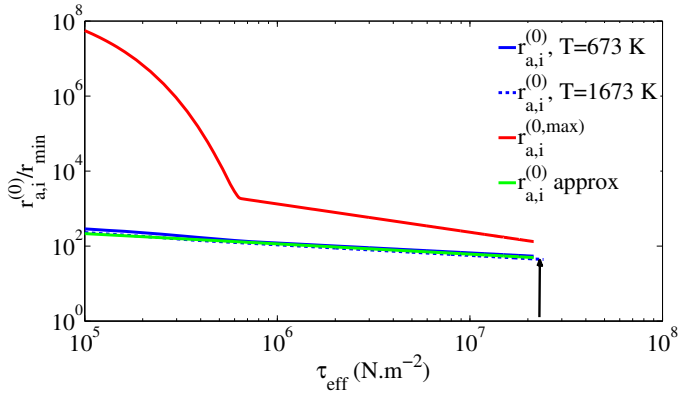

Figure 9.4: Annihilation of stored dislocations: $r^{(0)}_{a,i}$ and $r^{(0,max)}_{a,i}$ from Eqs. 9.29 and 9.27 with $r_{min} = 2 \times 10^{-9}$ m and $d_{j,s} = 1\,\mu$m. At large effective stresses $r^{(0)}_{a,i}$ is not defined as no dipole is created (indicated by an arrow). The analytical approximation in the absence of jogs (Eq. 9.30) is shown as well.

Insertion of the condition for a successful cross-slip, $r^{(0)}_{a,i}$ is given by solving:

$$r^{(0)}_{a,i} - \frac{b v_{dk,s}(X_{j,s})}{3K' \lambda_{dk,s}(d_{j,s})} \left(r^{(0)3}_{a,i} - r^{3}_{min} \right) - \frac{v_{dk,s}(X_{j,s})}{\nu_{CS}} \exp\left(\frac{U_{CS} - V_{CS}(\tau^{(CS)}_{eff} + K'/b r^{(0)2}_{a,i})}{k_b T} \right) = 0 \tag{9.29}$$

Figure 9.4 compares $r^{(0)}_{a,i}$ derived from Eq. 9.29 to $r^{(0,max)}_{a,i}$. Temperature has again a very marginal *direct* effect on $r^{(0)}_{a,i}$, and affects the capture radius mainly through τ_{eff}. Again, an approximation of the solution that neglects the presence of jogs and the effective stress on the collinear system reads:

$$r^{(0)}_{a,i} = 114.5 \left(\frac{\tau^{(\alpha)}_{eff}}{\tau_0} \right)^{-0.274} \tag{9.30}$$

9.4.3 *Formation of screw dipoles*

The constitutive model assumes that formation of screw dipoles is possible and relies on the maximum dipole height $h_{max,s} = \mu b / 4\pi\tau_{eff}$ to define the capture radius r_s. A fraction or all dislocations trapped in dipoles immediately annihilate by cross-slip. Screw dipoles are consequently formed by dislocations contained within the radii $h_{max,s}$ and $r^{(0)}_{a,m}$ (see Eq. 9.14).

The capture radius $h_{max,s}$ could be increased as dislocations initially too distant to form a dipole can still cross-slip as they pass by each other, eventually coming closer and below $h_{max,s}$ and triggering dipole formation.

In a material with a low U_{CS}, the actual capture radius $r_s^{(max)}$ would be given by Eq. 9.23 with r_{min} replaced by $h_{max,s}$. However it can be verified that in silicon $h_{max,s}$ is not increased, owing to the large U_{CS}. As seen in Fig. 9.4, at large effective stresses $h_{max,s} < r_{a,m}^{(0)}$, mobile screw dislocations readily annihilate and no screw dipole is created.

9.4.4 *Capture radii for edge dislocations and edge dipole annihilation*

A similar approach as previously can be adopted to compute the influence of climb on the capture radii for edge dipole formation and annihilation, respectively r_e, $r_{a,m}^{(90)}$ and $r_{a,i}^{(90)}$.

It is already known that the maximum dipole height $h_{max,e}$ at a given effective stress reads $h_{max,e} = \mu b/8\pi\,(1-\nu)\,\tau_{eff}$. Dislocations initially distant from each other by $h > h_{max,e}$ can *a priori* still capture each other, provided that they come closer by climb while passing by each other. Assuming that the attractive force remains constant in the vincinity of the dipole equilibrium configuration, the *relative* (diffusion-controlled) climb velocity v_{cl} in the absence of external stress reads:

$$v_{cl}(h) = \frac{D_{sd}\Omega}{bk_bT}\left(\frac{\mu b}{\pi\,(1-\nu)\,h}\right) = -\frac{\mathrm{d}h}{\mathrm{d}t} \tag{9.31}$$

The time t_{CL} necessary for dislocations to climb the distance $h - h_{max,e}$ is given by

$$t_{CL} = \frac{\pi\,(1-\nu)\,k_bT}{2D_{sd}\mu\Omega}\left(h^2 - h_{max,e}^2\right) = \frac{1}{2\beta}\left(h^2 - h_{max,e}^2\right) \tag{9.32}$$

As for screw dislocations, a condition for trapping to occur is for edge dislocations to verify $t_{CL} \leq r_e^{(max)}/v_{dk}$, or after simplification:

$$\begin{cases} r_e^{(max)} = \frac{\beta}{v_{dk}} + \sqrt{\left(\frac{\beta}{v_{dk}}\right)^2 + h_{max,e}^2} \\ \beta = \frac{D_{sd}\mu\Omega}{\pi(1-\nu)k_bT} \end{cases} \tag{9.33}$$

If climb is neglected ($D_{sd} = 0$) then $r_e^{(max)} = h_{max,e}$ is retrieved. Owing to the small values of β, the correction brought by Eq. 9.33 is marginal ($\beta/v_{dk} \ll h_{max,e}$) and can be neglected. The same remark is valid when a stress component normal to the glide plane of the edge dislocation is applied.

A similar method can be used to check that $r_{a,m}^{(90)} = r_{a,i}^{(90)} = h_{min}$. Our model shows that the capture radii for edge dipole formation and annihilation is not affected significantly by climb at the temperatures of interest.

Note that the diffusion coefficient close to edge dipoles is bound to increase because of the lattice distortion it creates. Consequently, climb velocity ought to increase at short interaction distances, potentially affecting the present conclusion.

9.5 DISLOCATION INTERACTIONS

9.5.1 *Obstacle density and mean free path*

Computation of the dislocation velocity in the presence of localized obstacles requires the knowledge of the effective forest spacing l_{obs} and mean free path l_v. A dislocation density $\rho_t^{(\beta)}$ belonging to a plane characterized by its normal unit vector $\mathbf{n}_0^{(\beta)}$ has a projected density on the system α given by $\rho_t^{(\beta)}\sqrt{1-\left(\mathbf{n}_0^{(\beta)}.\mathbf{n}_0^{(\alpha)}\right)^2}$. The obstacle density piercing the system α reads:

$$\rho_{obs}^{(\alpha)} = \sum_{\beta \in f_\alpha} \rho_t^{(\beta)} \sqrt{1-\left(\mathbf{n}_0^{(\beta)}.\mathbf{n}_0^{(\alpha)}\right)^2} \tag{9.34}$$

where f_α is defined as $f_\alpha = \left\{\beta,\, \mathbf{n}_0^{(\beta)}.\mathbf{n}_0^{(\alpha)} \neq 1\right\}$, and p_α such as $p_\alpha = \left\{\beta,\, \mathbf{n}_0^{(\beta)}.\mathbf{n}_0^{(\alpha)} = 1\right\}$. f_α and p_α are respectively the forest and coplanar systems relative to system α.

Mean free path of dislocation free flight

There can be two ways to derive the mean free path l_v of dislocations. If the derivation of l_{obs} follows from Friedel statistics (see, e.g., [Kocks 1975]) then this quantity depends on the effective stress as dislocations "see" more or less obstacles as the stress is varied:

$$l_{obs}^{(\alpha)} = \left(\frac{\mu b}{\rho_{obs}^{(\alpha)} \tau_{eff}^{(\alpha)}}\right)^{1/3} \tag{9.35}$$

and the mean free path is traditionally derived from the relationship $l_v = l_{obs}/\rho_{obs}$. The critical stress for dislocation unlocking τ_c is also affected by Friedel statistics:

$$\tau_{c,F}^{(\alpha)} = \sqrt{\frac{\tau_c^{(\alpha)3}}{\mu b \sqrt{\rho_{obs}^{(\alpha)}}}} \tag{9.36}$$

Another way of deriving l_v is to rely on dislocation dynamics simulations from [Kubin 2008a, Kubin 2008b]. These authors have computed by means of dislocation dynamics the mean free path of dislocations in fcc crystals moving through a forest and creating junctions with the trees:

$$\frac{1}{l_v^{(\alpha)}} \simeq \frac{1}{k_f} \frac{\sum_{\beta \in f_\alpha} \sqrt{a_{\alpha\beta}} \rho_t^{(\beta)}}{\sqrt{\sum_\beta a_{\alpha\beta} \rho_t^{(\beta)}}} + \frac{1}{k_c} \sum_{\beta \in p_\alpha} \sqrt{a_{\alpha\beta} \rho_t^{(\alpha)}} \tag{9.37}$$

where the density of junctions is neglected, k_f and k_c are coefficients related to f_α and p_α respectively. From this equation $l_{obs}^{(\alpha)}$ is retrieved from $l_v = l_{obs}/\rho_{obs}$.

It is physically more relevant to adopt the framework of Friedel statistics when confronted to dislocation motion in a random array of localized obstacles. As discussed in Section 8.3, combined with a potentially low F_{obs}, this results in a marginal influence of the forest trees on dislocation motion.

Mean free path for dislocation mutliplication

The mean free path derived from Eq. 9.35 or Eq. 9.37 is used in our model to compute $l_v^{(\alpha)}$ related to $\overline{v}$. However, the mean free path $l_{FR}^{(\alpha)}$ controlling dislocation generation by formation and activation of Frank-Read sources is determined only by the immobile forest dislocation densities, since fixed poles are required for such a source to be active. The dislocation densities $\rho_i^{(\beta)}$, $\beta \in f_\alpha$ are assumed to contribute to this generation mechanism. Neglecting the build-up of a junction density, the mean free path reads:

$$\frac{1}{l_{FR}^{(\alpha)}} \simeq \frac{1}{k_{FR}} \frac{\sum_{\beta \in f_\alpha} \sqrt{a_{\alpha\beta}} \rho_i^{(\beta)}}{\sqrt{\sum_\beta a_{\alpha\beta} \rho_t^{(\beta)}}} \tag{9.38}$$

Note that this formulation does not impose $k_{FR} = k_f$. The influence of forest dislocations is decisive on the mean free path and at high dislocation densities Eq. 9.38 can be approximated by $l_{FR}^{(\alpha)} \propto 1/\sqrt{\rho_{f_\alpha}}$, which is a well-known relationship (see, e.g., [Mecking 1981, Kocks 2003]).

9.5.2 *Interaction coefficients*

The $a_{\alpha\beta}$ used in Eq. 9.38 are the same as introduced previously for the definition of internal stresses, and depend nonlinearly on $\rho_t^{(\beta)}$ as given by [Devincre 2006, Kubin 2008b] if related to the junction-forming slip system combinations:

$$\sqrt{a_{\alpha\beta}} = \left[0.2 + 0.8 \frac{\log\left(1/2b\sqrt{a_{\alpha\beta}^{(ref)} \rho_t^{(\beta)}}\right)}{\log\left(1/2b\sqrt{a_{\alpha\beta}^{(ref)} \rho_{ref}}\right)} \right] \sqrt{a_{\alpha\beta}^{(ref)}} \tag{9.39}$$

where the constant line tension approximation $\Gamma = \mu b^2/2$ has been adopted for consistency with Chapter 1 and Section 8.3. $\rho_{ref} = 10^{12}\,\mathrm{m}^{-2}$ is a reference forest density. The first term of the right-hand side of Eq. 9.39 is related to elastic interactions, while the second one stems from line tension effects.

We are thus left with three parameter sets related to dislocation interactions to identify. To simplify the treatment of latent hardening[4], we assume

4 Note that the assumption made by [Alexander 2000] to derive the supposed $A_{\alpha\beta}$ coefficients from latent hardening tests, namely that the flow stress of the latent system stems from hardening by the *long-range* stress field of the primary dislocations, is in clear contradiction with theoretical and experimental results showing that $A_{\alpha\beta} \leq A_{\alpha\alpha}$ (see, e.g., [Zarka 1972, Nemat-Nasser 2004]). These relationships are obviously also valid for the $B_{\alpha\beta}$'s.

Interaction	Self	Copl	Col	HL	LL	GJ
$A_{\alpha\beta}$	$A_{\alpha\alpha}$	$A_{\alpha\alpha}/2$	$2A_{\alpha\alpha}/5$	$2A_{\alpha\alpha}/3$	$2A_{\alpha\alpha}/3$	$2A_{\alpha\alpha}/3$
$B_{\alpha\beta}$	$B_{\alpha\alpha}$	$B_{\alpha\alpha}/2$	$2B_{\alpha\alpha}/5$	$2B_{\alpha\alpha}/3$	$2B_{\alpha\alpha}/3$	$2B_{\alpha\alpha}/3$
$a_{\alpha\beta}^{(ref)}$	0.123	0.123	0.625	0.07	0.123	0.137

Table 9.1: Interaction coefficients for computation of the internal stress $\tau_b^{(\alpha)}$ coming from mobile dislocations, from immobile dislocations, and critical stress $\tau_c^{(\alpha)}$ (the anisotropy of the $A_{\alpha\beta}$ and $B_{\alpha\beta}$'s is taken from [Zarka 1972], the $a_{\alpha\beta}^{(ref)}$'s are adapted from [Kubin 2008b]).

that the ratios of long-range interaction coefficients $A_{\alpha\beta}/A_{\alpha\alpha}$ and $B_{\alpha\beta}/B_{\alpha\alpha}$ provided by [Zarka 1972] are valid (see Table 9.1). The $a_{\alpha\beta}^{(ref)}$ coefficients are adapted from [Kubin 2008b]. The self-interaction coefficient $a_{\alpha\alpha}^{(ref)} = 0.123$ is an equivalent one accounting for the influence of debris left in the collinear slip system generated during deformation ([Madec 2003, Devincre 2007]), observed in silicon crystals as well by [Yonenaga 1993]. Ultimately only two parameters are left to identify, $A_{\alpha\alpha}$ and $B_{\alpha\alpha}$.

9.6 JOG DENSITY EVOLUTION

Evaluation of the dislocation mobility requires the knowledge of the effective mean jog spacing $d_j^{(\alpha)}$ on the mobile dislocations belonging to the slip system α, which varies throughout deformation. The number of jogs per unit volume for the system α is defined as $n_j^{(\alpha)} = \rho_m^{(\alpha)}/d_j^{(\alpha)}$. The model derived in this Section for jog density evolution an extension of the one introduced by [Cuitiño 1997], here accounting for jog annihilation.

It is necessary to work with an *effective* jog density because, like for impurities, dynamic ageing of dislocations takes place. Freshly generated dislocations are less jogged than new ones and move consequently faster at a given effective stress. Working with a single dislocation population on each slip system, we cannot go into the details of dislocation density distribution as a function of its jogged state, and simplify the problem to a single n_j.

9.6.1 *Jog formation rate*

We assume jogs to form solely during dislocation junction unzipping events. Jog formation by double cross-slip is neglected. As is shown later on, this approximation yields satisfying results.

Junction formation and unzipping leads to the formation of atomic jogs on both interacting dislocations. The density of jog-producing obstacles on the slip plane is taken as $\rho_{obs}^{(\alpha)}$. The jog density increase rate reads then $\dot{n}_j^{(\alpha)} = \kappa_+^{(\alpha)} \rho_{obs}^{(\alpha)} \dot{\gamma}_p^{(\alpha)}/b$, where $\kappa_+^{(\alpha)}$ is a dimensionless parameter characterizing the effective jog density build-up.

The same number of jogs are created on the forest systems, so that for each dislocation character on a given slip system the total increase rate reads:

$$\dot{n}_j^{(\alpha)} = \kappa_+^{(\alpha)} \rho_{obs}^{(\alpha)} \frac{\dot{\gamma}_p^{(\alpha)}}{b} + \rho_m^{(\alpha)} \sum_{\beta \in f_\alpha} \sqrt{1 - \left(\mathbf{n}_0^{(\beta)}.\mathbf{n}_0^{(\alpha)}\right)^2}\, \kappa_+^{(\beta)} \frac{\dot{\gamma}_p^{(\beta)}}{b} \tag{9.40}$$

9.6.2 *Jog annihilation rate*

The higher the linear jog density $c_j = a/d_j$ along the dislocation line, the higher their annihilation rate. Our model assumes that the jog disappearance rate is proportional on the strain rate and makes use of an effective capture distance $d_c^{(\alpha)}$. The jog annihilation rate reads then $\dot{c}_j = -c_j d_c^{(\alpha)} \dot{\gamma}_p^{(\alpha)}/b$. After simplification this gives for n_j:

$$\dot{n}_j^{(\alpha)} = n_j^{(\alpha)} \left(\frac{\dot{\rho}_m^{(\alpha)}}{\rho_m^{(\alpha)}} - \frac{d_c^{(\alpha)}}{b} \dot{\gamma}_p^{(\alpha)} \right) \tag{9.41}$$

The net jog evolution rate is the sum of Eqs. 9.40 and 9.41. One evolution equation is required for each dislocation character, since we distinguish the jog spacings $d_{j,60}$ and $d_{j,s}$ on 60° and screw segments respectively.

9.6.3 *Discussion*

The present model remains simple, as jog annihilation has been shown in [Messerschmidt 1970, Messerschmidt 1971] to result from the density of point defects in the crystal. The evolution equations for the jog spacing and point defects concentration are then coupled, resulting in an additional complexity that we do not attempt to reproduce in the present work.

Writing $d_c^{(\alpha)} = \kappa_-^{(\alpha)} b$, the net jog evolution equation reads:

$$\begin{aligned}\dot{n}_j^{(\alpha)} =& \kappa_+^{(\alpha)} \rho_{obs}^{(\alpha)} \frac{\dot{\gamma}_p^{(\alpha)}}{b} + \rho_m^{(\alpha)} \sum_{\beta \in f_\alpha} \sqrt{1 - \left(\mathbf{n}_0^{(\beta)} . \mathbf{n}_0^{(\alpha)}\right)^2} \kappa_+^{(\beta)} \frac{\dot{\gamma}_p^{(\beta)}}{b} \\ &+ n_j^{(\alpha)} \left(\frac{\dot{\rho}_m^{(\alpha)}}{\rho_m^{(\alpha)}} - \kappa_-^{(\alpha)} \dot{\gamma}_p^{(\alpha)} \right)\end{aligned} \tag{9.42}$$

Eq. 9.42 can be used to derive the steady-state jog density on a given system α. Assuming that $\dot{\rho}_m^{(\alpha)} \ll \rho_m^{(\alpha)}$, the model predicts a steady-state value of $n_j^{(\alpha)}$ proportional to the ratio $\kappa_+^{(\alpha)} / \kappa_-^{(\alpha)}$. The ratio of the constitutive parameters defines the equilibrium density (all other things being equal), while their individual values affect the transition speed between two states. The model exposed in this Section yields an effective jog spacing at steady-state:

$$d_j^{(\alpha)} \simeq b \frac{\kappa_-^{(\alpha)}}{\kappa_+^{(\alpha)}} \frac{\rho_m^{(\alpha)} \dot{\gamma}^{(\alpha)}}{\rho_{obs}^{(\alpha)} \dot{\gamma}^{(\alpha)} + \rho_m^{(\alpha)} \sum_{\beta \in f_{(\alpha)}} \frac{\kappa_+^{(\beta)}}{\kappa_+^{(\alpha)}} \dot{\gamma}^{(\beta)}} \tag{9.43}$$

In particular, if $\dot{\gamma}^{(\alpha)} \gg \dot{\gamma}^{(\beta)}$, a situation typical of stage I, then Eq. 9.43 reduces to $d_j^{(\alpha)} \simeq b \kappa_-^{(\alpha)} \rho_m^{(\alpha)} / \kappa_+^{(\alpha)} \rho_{obs}^{(\alpha)}$.

Experiments and simulations show (see, e.g., [Karthikeyan 2004] and references therein) that jogs tend to annihilate with each other until their spacing reaches the equilibrium Orowan bowing value of $\mu b / \tau_{eff}$, that is, jog spacing is stress-dependent. It is therefore tempting to introduce a stress dependency into the constitutive parameters $\kappa_+^{(\alpha)}$ and $\kappa_-^{(\alpha)}$. This aspect is discussed in Section 10.4.2.

9.7 DIFFUSION OF IMPURITIES TO THE DISLOCATION CORES

The same model as introduced in Chapter 6 is presented here. Only a purely local diffusion phenomena is considered in this work, assuming that the impurity concentration at the core boundary is similar to the one in the bulk c_O^∞ and that the latter is not affected by impurity gettering. This approximation is justified by the absence of development of Cottrell atmosphere in the strain field of the dislocation at the high temperatures considered in this work. It simplifies tremendously the numerical treatment of the diffusion problem. Static diffusion follows the equation:

$$\dot{c}_O^{(\alpha)}\Big|_{\overline{v}^{(\alpha)}=0} = \frac{2D_O}{\pi r_0 b}\left(c_O^\infty - c_O^{(\alpha)}\exp\left(-\frac{\triangle G_O}{k_b T}\right)\right) \tag{9.44}$$

with D_O the effective diffusion coefficient of oxygen in the silicon matrix, r_0 the core radius taken as the lattice parameter $a = 5.43 \times 10^{-10}$ m, and $\triangle G_O$ the binding energy of oxygen to the dislocation. $\triangle G_O$ can be expressed as a function of the enthalpy change $\triangle H_O$ and entropy change $\triangle S_O$, as $\triangle G_O = \triangle H_O - T\triangle S_O$. Experimental observations by [Senkader 2002, Murphy 2006] give $\triangle S_O \simeq k_b$ and $\triangle H_O = 0.74$ eV above 923 K. The diffusion coefficient of oxygen to the dislocations D_O depends on the temperature and the concentration of dissolved oxygen in the crystal as different species exhibit affect D_O as shown by [Senkader 2001]. Above 973 K D_O is given by Eq. 9.45, expressed in $m^2.s^{-1}$ (see [Mikkelsen 1985]):

$$D_O = 0.13 \times 10^{-4}\exp\left(-\frac{2.53}{k_b T}\right) \tag{9.45}$$

Diffusion to a moving dislocation has been modeled by [Petukhov 1990, Petukhov 2003]:

$$\dot{c}_O^{(\alpha)}\Big|_{\overline{v}^{(\alpha)}>0} = \dot{c}_O^{(\alpha)}\Big|_{\overline{v}^{(\alpha)}=0} + \frac{\overline{v}^{(\alpha)}}{a}\left(\frac{r_0}{a}c_O^\infty - c_O^{(\alpha)}\exp\left(-\frac{a}{\overline{v}^{(\alpha)}t_m}\right)\right) \tag{9.46}$$

with $t_m = \lambda_O \frac{a^2}{D_O}\exp\left(-\Delta G_O/k_b T\right)$ the time of oxygen migration from the bulk back onto the dislocation core. The prefactor λ_O translates the effect of the lattice distortion close to the dislocation core and is taken as 10^2. Its influence on the mechanical behavior of extrinsic materials has been discussed in Chapter 6.

9.8 CONCLUSION: A NOVEL APPROACH TO MODELING SILICON

The model equations introduced in this Chapter enrich significantly the palette available for semiconductors. It has however a high numerical cost, as there exists no closed-form for the dislocation velocity law. The present model considers 24 systems of mobile dislocations, with two different populations of mobile segments; up to 24 nonlinear equations must be solved to determine their velocity only at each time increment.

The many insights provided by the novel constitutive equations, such as differentiating the evolution of screw and 60° segments according to their mobility, provide valuable information about the micromechanisms responsible for the peculiar plastic behavior of silicon.

Our constitutive model is not restricted solely to silicon materials. Its extension to other diamond cubic materials is quite straightforward, provided parameters such as the activation energies for cross-slip and double kink motion mechanism are known. Its applicability to f.c.c. materials can also be examined: the fundamental difference with semiconductors would lie in the rate-limiting role of localized obstacles. The influence of Peierls valleys on dislocation motion in the latter material class is namely negligible. Dislocation dynamics would be severely affected by a change in the velocity law. However, the evolution laws and expressions for internal stresses introduced in the present Chapter should be valid for f.c.c. metals as well.

The model is calibrated to experimental data and discussed in the next Chapter.

10

MODEL CALIBRATION AND RESULTS

The holistic constitutive model derived in the previous Chapter is calibrated to experimental data. Given the physical arguments relied on to establish the constitutive equations, a rather limited amount of parameters need to be identified by best fit. A self-multiplication law for the yield region of intrinsic silicon crystals is derived based on the absence of strain rate dependency of its constitutive parameter. It is shown to be accurate at the usual strain rates of interest. The model reproduces fairly well the increase of upper yield stress at large oxygen contents. Localized obstacles are shown to lead neither to significant hardening in stage II nor to experimentally observed overshoot. On the other hand, accounting for jog dragging allows the reproduction of these features. Finally, the performances and limitations of the model are discussed, and suggestions for future work given.

10.1 PRELIMINARY DISCUSSION

10.1.1 *FE model*

The model has been implemented in a VUMAT for ABAQUS/EXPLICIT only. The numerical details of the kinematics are given in Annex A and Chapter 6.

Yield region

A finite element model similar as previously is used in the following. The specimen design has been improved, however, to better reproduce the original samples[1], see Fig. 10.1.

Identification of the parameters related to the yield region is done by applying a constant velocity to the outer nodes of an elastic bounding block while keeping the second one fixed at its end.

Large strains

BOUNDING BLOCKS The study of large strains is done on the contrary by removing the bounding blocks and applying a constant velocity to the ends of the silicon specimen. This method is chosen because the relatively

1 The specimen used in Part ii have a fillet radius of 6 mm, whereas the actual tensile samples have a fillet radius of 3 mm. This difference has no noticeable effect on the study of small strains, but affects strongly deformation localization at large strains.

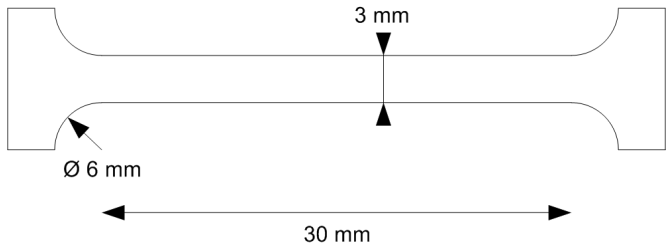

Figure 10.1: Sketch of the tensile specimen used for identification of the constitutive parameters of the constitutive model. The cross-section width is 2 mm.

low stiffness of the bounding blocks affects the stress-strain response at high hardening rates such as the ones met in stage II. In other words, the bounding blocks of $E_{block} \ll E_{Si}$ absorb significantly the energy when silicon is stiff, be it in the elastic range or in multiple slip situations.

Assuming that the bounding blocks always play a role at large strains yields a strain rate- and temperature-dependence of the hardening rate in stage II that is not detected experimentally. It can be concluded that the influence of the tensile apparatus discussed in Chapter 6 fades out for good from the upper yield point.

ELEMENT FORMULATION ABAQUS/EXPLICIT offers two types of linear brick elements (8 nodes), either with full or reduced integration. Choosing the former type gives poor results, as discussed in Annex C. Using C3D10M elements leads to very large computational times, owing to the mesh refinements necessary to study overshooting. Consequently, only first-order, reduced integration elements C3D8R are left available.

This requires in turn a careful study of hourglassing, as a sustained deformation in single glide and high strain rates propagates an instability upon activation of secondary systems, leading to element hourglassing and model instability. ABAQUS/EXPLICIT proposes several algorithms for hourglass treatment, and stable results could be obtained only using the integral viscoelastic approach (*relax stiffness* option).

For the study of overshoot some finer meshes are used, as shown in Fig. 10.2. A coarse mesh can still yield stable results if automatic remeshing is more affordable than the cost of a denser mesh. In practice, the mesh density requirements for the study of extreme overshoot cases are so large that it is numerically more efficient to opt for remeshing option.

10.1.2 *Model parameters to identify*

Analysis of the experimental data is made difficult by the strong influence of the tensile apparatus in the yield region, as discussed in Section 7.2. We show below that some of the unknown parameters and functions for

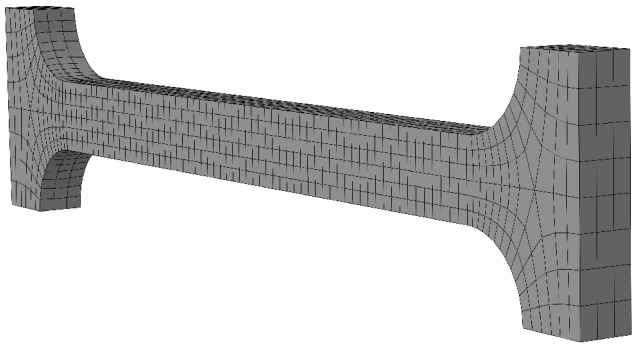

Figure 10.2: Example of finer mesh used for the study of stress overshoot. Here the gauge is discretized in $60 \times 6 \times 3$ elements, for a model total of 1656 C3D8R elements.

intrinsic crystals strongly affect a particular region of the stress-strain curve only and allow their relatively straightforward identification.

Owing to our particular model for dislocation storage and annihilation, only a limited amount of constitutive parameters has to be derived: formation of dipoles and dislocation annihilation are micromechanisms that do not need any particular calibration (see Section 9.4). Dislocation velocity parameters have been introduced in Table 8.1. The unknown parameters characterizing intrinsic crystals are the interaction coefficients $A_{\alpha\alpha}$ and $B_{\alpha\alpha}$ for the internal stress. k_{FR} and K_1 steer dislocation multiplication[2], and jog evolutions are defined by the κ_+ and κ_- parameters related to each dislocation character. Ultimately, 8 unknown parameters define the constitutive behavior of intrinsic crystals.

The case of oxygen-contaminated silicon crystals requires the identification of the reference stress τ_O^{ref} and threshold stress τ_O^{min}. λ_O is an unknown parameter as well.

Out of these 11 parameters, some can be estimated from the literature. In particular, we know that $A_{\alpha\alpha}$ is of the order of 0.3, and k_f is computed for fcc crystals to be roughly 8 (see [Kubin 2008b]). Owing to the similarities between fcc the diamond cubic crystals, this parameter is expected to be of the same order of magnitude for silicon.

Since jogs are likely to affect dislocation motion at large strains only, the remaining parameters for intrinsic crystals $A_{\alpha\alpha}$, $B_{\alpha\alpha}$ and the function K_1 can be identified by the sole study of the yield region, setting $n_j = 0$ for all systems and dislocation characters. This way, decoupling is achieved between those three parameters and the remaining κ coefficients that define the material behavior at large strains.

2 Two more parameters defining the mean free path, k_f and k_c, are required if Friedel statistics are not relied on and the influence of localized obstacles on dislocation motion is accounted for.

10.2 EXPERIMENTAL DATA AND INITIAL CONDITIONS

The experimental data sets used for calibration of the model parameters are the same ones as introduced in Part ii and taken from the extensive work of [Yonenaga 1978, Yonenaga 1981, Yonenaga 1984].

All tensile specimen are oriented in the $[\bar{1}\bar{2}3]$ direction, with the [111] axis in the width direction. This gives initial Euler angles in Bunge's notation of 169.1°, 54.7° and 45°, respectively (see Annex A).

Data sets *ds1*, *ds2* and *ds3* have been obtained on intrinsic, Float-Zone (FZ) grown silicon monocrystals. Experimental data set *ds4* deals with Czochralski extrinsic crystals of varying dissolved oxygen contents.

Initial dislocation densities

The initial dislocation densities $\rho_{0,\text{exp}}$ have been experimentally measured by etch-pit counting on the [111] surfaces. This means that the values provided in the works of Yonenaga *et al*. are the total densities of slip systems on planes A, C and D using Schmid & Boas notation[3] (see Fig. A.1).

In order to determine the initial dislocation densities on each of the twelve slip systems, the following method is adopted:

1. Determine the optimal value of the variable parameter in K_1 assuming all dislocations to be initially present on the primary slip system exclusively
2. Deform a virgin crystal (1173 K, $\dot{\gamma} = 1.2 \times 10^{-4}\,\text{s}^{-1}$) up to the lower yield point[4], extract the dislocation density percentages on each slip system, with respect to $\sum_\alpha \rho_m^{(\alpha)}$ and $\sum_\alpha \rho_i^{(\alpha)}$
3. Scale the densities so that $\sum_{A,C,D} \rho_t = \rho_{0,\text{exp}}$, by fixing the ratio of mobile to immobile dislocation densities
4. optimize K_1 to the yield region of experimental data sets, reiterate the algorithm until convergence.

A virgin crystal is defined as having initial mobile dislocation densities of $10^4\,\text{m}^{-2}$ on all slip systems, and null immobile densities. At the lower yield point, almost all dislocations (roughly 90 %) are immobile. How much of immobile dislocations annihilate upon annealing depends on the final density reached: the longer the annealing time, the lower the measured initial density and the larger its relative content of mobile dislocations.

3 The plane B is actually the cross-slip system, which is not activated in the uniaxial tensile test considered. Consequently, dislocation densities on this plane are negligible anyway.

4 The experimental prestrain is 10 %, into the early stage I. This leads to a larger immobile-to-mobile dislocation ratio before annealing than the one resulting from deformation up to the lower yield point.

However, the exact mobile-to-immobile density ratio has little impact on the results, and assuming that almost all dislocations (90 %) are mobile segments yields good results. Equal initial densities of screw and 60° segments are assumed on all slip systems.

The forest densities have on the contrary more impact. The algorithm described above shows that after prestraining, roughly 40 % of dislocations are on the primary plane only. This leaves a relatively large density of trees availabe for the generation of Frank-Read sources.

Temperature and strain rate

Temperature varies between 1073 and 1223 K by 50 K increments in *ds1* while the crosshead speed is set so that the shear strain rate is $\dot{\gamma} = 1.2 \times 10^{-4}\,\mathrm{s}^{-1}$. The shear strain rate spans a decade from 6×10^{-5} to $6 \times 10^{-4}\,\mathrm{s}^{-1}$ in *ds2* at a fixed temperature of 1173 K.

Extrinsic crystals

The deformation conditions for *ds4* are as follows: temperature 1073 K, shear strain rate $\dot{\gamma} = 1.1 \times 10^{-4}\,\mathrm{s}^{-1}$ and the initial total dislocation density $\rho_{0,\mathrm{exp}} = 10^{10}\,\mathrm{m}^{-2}$.

Jog density

The initial linear jog density on each slip system, when used, is set to $b \exp\left(1.1/k_b T\right)$, which is the jog density at thermal equilibrium assuming[5] that $F_{jog} = 1.1\,\mathrm{eV}$.

Experimental data sets

The experimental data sets are shown in Fig. 10.3. The force-time ($F - t$) simulation outputs are converted into shear strain-resolved shear stress curves ($\tau - \gamma$) to allow their comparison with the experimental data sets. The following equations are used (see [Yonenaga 1981]):

$$\varepsilon = \frac{v_{CH} t}{l_0} = \sqrt{\left(\gamma \cos\phi_0 + \cos\lambda_0\right)^2 + \sin^2\lambda_0} - 1 \tag{10.1}$$

$$\tau = \frac{F \cos\phi_0 \sqrt{\left(1+\varepsilon\right)^2 - \sin^2\lambda_0}}{\mathcal{A}_0 \left(1+\varepsilon\right)^2} \tag{10.2}$$

where ε is the engineering strain, v_{CH} is the constant crosshead speed, $l_0 = 30\,\mathrm{mm}$ and $\mathcal{A}_0 = 6\,\mathrm{mm}^2$ the initial gauge length and cross-section area.

5 The exact F_{jog} is not known, but this value is chosen because it does not affect dislocation motion in the early deformation stages, as is experimentally observed.

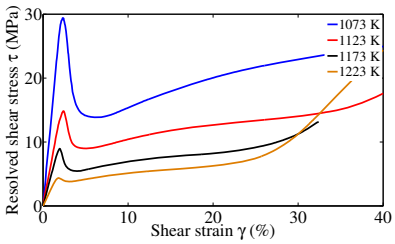

(a) *ds1*: FZ crystals, various T.

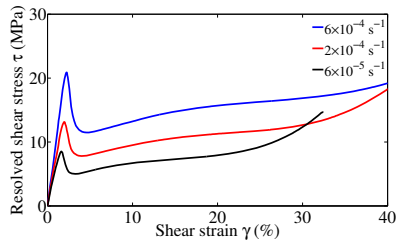

(b) *ds2*: FZ crystals, various $\dot{\gamma}$.

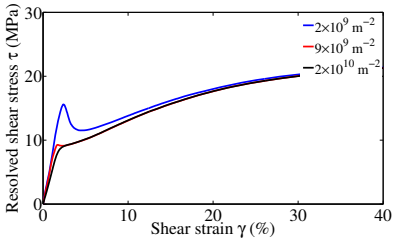

(c) *ds3*: FZ crystals, various $\rho_m^{(D4)}$.

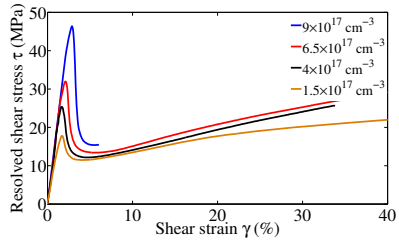

(d) *ds4*: CZ crystals, various c_O^∞.

Figure 10.3: Experimental data used for model calibration. See text for details.

ϕ_0 and λ_0 are the initial angles between the tensile direction and the primary slip normal and direction, respectively: $\cos\phi_0 = 4/\sqrt{42}$, $\cos\lambda_0 = 4/\sqrt{28}$ and $\sin\lambda_0 = \sqrt{3/7}$. Derivation of the experimental stress-strain curves from the force-time curves assume v_{CH} and $\dot{\varepsilon}$ constants. As discussed in Section 7.2, the latter assumption is not true in the yield region and proportionality between time and strain is not verified throughout deformation. However for readability all figures in the following assume $\varepsilon(t) \propto t$.

Preference is given for the study of the large strains to the force-time curves rather than to the resolved shear stress-shear strain because the methodology employed by the experimentalists to compute τ and γ looses accuracy at large strains.

10.3 MODELING THE YIELD REGION

10.3.1 *Intrinsic crystals*

For bounding blocks of length 5 mm, the Young's moduli E_{block} giving good fits with the experimental data are given in Tables 10.1 to 10.3.

Derivation of K_1, effect of temperature and strain rate

TRADITIONAL LAWS The yield region of silicon crystals sees a marginal increase in the forest density as noticed by [Yonenaga 1978]. All dislocation multiplication processes in the early stage 0 at intermediate temperatures can be assigned to the influence of K_1 as long as the forest obstacle density is not large. This function can consequently be identified by considering the upper yield point of *ds1* and *ds2*.

Once the dislocation density has increased on all active slip systems owing to K_1, generation from forest trees can take place, the intensity of which is steered by k_{FR}. Therefore, the yield drop is governed both by K_1 and k_{FR}. Let us in a first time set $k_{FR} = 16$ and assess the influence of the K_1 function on the yield region.

Writing $K_1 = \delta g(\tau_{eff})$, best fits of δ for various multiplication laws to *ds2* are given in Table 10.4, assuming δ constant and taking the optimum[6] $A_{\alpha\alpha}$ and $B_{\alpha\alpha}$ (see below).

Athermal dislocation multiplication from Frank-Read sources should lead to a constant δ, while multiplication by means of thermally activated mechanisms such as double cross-slip should at worse decrease with the strain rate. However δ is found to *increase* with the strain rate independently of the model considered. This behavior is physically unprobable. An increase of the cross-slip activity at large strain rates by the application of stress on the collinear system is not possible since the latter is null given the $[\overline{1}23]$ orientation of the tensile axis.

All three multiplication laws for the yield region considered until now in the literature do not fit correctly to experimental data at various strain rates, as has already been mentioned in Chapter 5.

EFFECT OF k_{fr} The influence of K_1 fades out through the yield drop as forest dislocations are generated on secondary systems owing to the large effective stresses applied in the yield region. As shown in Fig. 10.4, the intensity of the yield drop is strongly affected by k_{FR}.

6 These two parameters have an extremely weak influence on the upper yield stress.

T (K)	1073	1123	1173	1223
E_{block} (MPa)	750	360	250	140

Table 10.1: Best fits of E_{block} for *ds1*.

$\dot{\gamma}$ (s^{-1})	6×10^{-5}	2×10^{-4}	6×10^{-4}
E_{block} (MPa)	320	380	520

Table 10.2: Best fits of E_{block} for *ds2*.

$\rho_{0,exp}$ (10^9 m^{-2})	2	9	20
E_{block} (MPa)	400	340	250

Table 10.3: Best fits of E_{block} for *ds3*.

Given the multiplication law derived below, the yield drop is very well reproduced by setting $k_{FR} = 16$. Note that the optimal value is sensibly larger than the one derived by means of DD for fcc crystals (8), and is affected both by the hardening coefficients and the multiplication law chosen.

HARDENING COEFFICIENTS At the lower yield point the density of immobile dislocations is significant and contributes to τ_{ly}. Consequently, the magnitude of the lower yield stress is affected by both $A_{\alpha\alpha}$ and $B_{\alpha\alpha}$. These parameters are identified using the experimental data at $\dot{\gamma} = 2 \times 10^{-4}\,s^{-1}$ from *ds2* as a reference.

Observation of the hardening rate $\theta = d(\tau_{eff} + \tau_{int})/d\gamma$ beyond the lower yield point allows for the identification of $B_{\alpha\alpha}$. With ρ_m near the steady-state in stage I and $d\tau_{eff}/d\gamma$ determined by the velocity law, θ_I in early stage I is modulated solely by the increase of ρ_i through $B_{\alpha\alpha}$.

SELF-MULTIPLICATION LAW Observation of the strain rate dependency of the optimum δ parameter in Table 10.4 indicates that increasing the power relationship between K_1 and τ_{eff} reduces the span covered by δ. Based on this idea, the following multiplication law is found to represent very well the yield region at all strain rates considered in *ds2*, with a *strain rate independent* δ:

$$K_1 = \delta \tau_{eff}^{(\alpha)1.25} \tag{10.3}$$

The introduction of a superlinear dependence on $\tau_{eff}^{(\alpha)}$ relieves the need for adjusting δ to each experimental curve.

Inserting a proportionality to $1/\sqrt{\rho_m^{(\alpha)}}$ in Eq. 10.3 as would do [Moulin 1999] does not improve noticeably the model accuracy in the yield region. On the contrary, such a term delays the yield drop by slowing down the dislocation multiplication from the upper yield point.

Meanwhile, inserting a saturation term in the dislocation multiplication law, function of the mobile dislocation density, has been observed to stabilize the model output at large strains (see below). A square root dependency of this term as suggested by [Moulin 1999] is however *too sensitive* because of the marked yield drop delay that follows.

$\dot{\gamma}\,(s^{-1})$	6×10^{-5}	2×10^{-4}	6×10^{-4}
$K_1=\delta$	6×10^{2}	1.2×10^{3}	2.2×10^{3}
$K_1=\delta\sqrt{\tau_{eff}/\rho_m}$	6×10^{3}	1.2×10^{4}	2.2×10^{4}
$K_1=\delta\tau_{eff}$	1.2×10^{-4}	1.4×10^{-4}	1.6×10^{-4}

Table 10.4: Best fits of δ to *ds2* for classical dislocation multiplication laws for the yield region, assuming δ constant and $k_{FR}=16$.

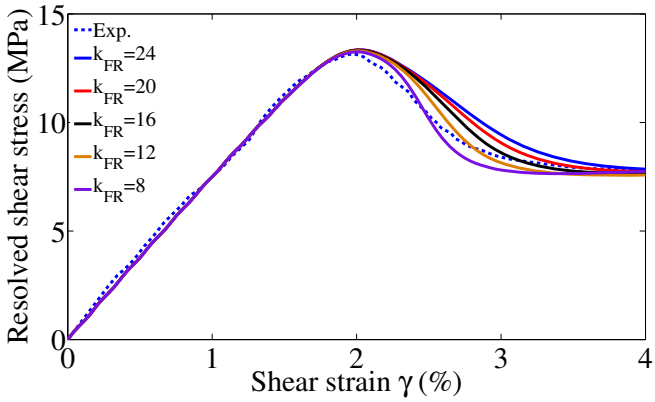

Figure 10.4: Experimental (dashed line) and simulated (plain lines) stress-strain curves in the yield region of the intrinsic crystal $\dot{\gamma}=2\times10^{-4}\,s^{-1}$ of *ds2* for various k_{FR} values.

A satisfying approximation of the yield region at all strain rates is then obtained by setting:

$$\begin{cases} A_{\alpha\alpha}=0.27 \\ B_{\alpha\alpha}=0.065 \\ \delta=2.5\times10^{-6} \end{cases} \tag{10.4}$$

Turning to *ds1*, we find that Eq. 10.3 still reproduces correctly the yield region at all temperatures with the same δ, as shown in Figure 10.5.

Figure 10.6 compares the simulated and experimental yield stresses of *ds1* and *ds2*. A very good agreement is reached at various strain rates, whereas some discrepancies appear as the temperature is changed. Inserting a temperature dependency into δ could improve further the simulation output in the yield region.

The simulated lower yield stresses of *ds1* and *ds2* can be fitted successfully by Eq. 8.1 with:

$$\begin{cases} m=1.1 \\ U_{ly}=2.19 \end{cases} \tag{10.5}$$

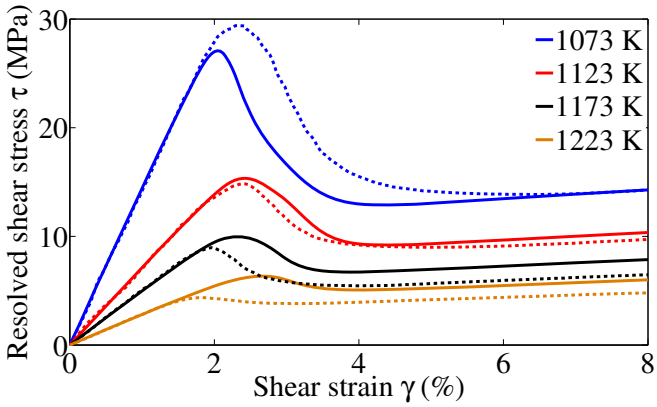

(a) *ds1*

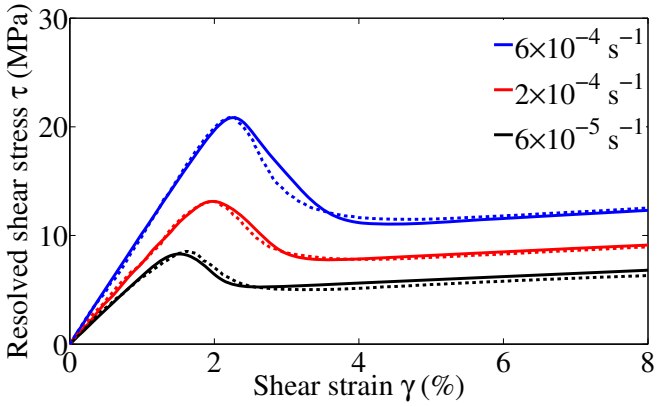

(b) *ds2*

Figure 10.5: Experimental (dashed lines) and simulated (plain lines) stress-strain curves in the yield region of intrinsic crystals.

which is in agreement with the values usually derived and shows that the constitutive model derived in this Part has the same ability as the AH model in predicting the yield stresses[7]. The upper yield stresses can be fitted by a similar law $\tau_{uy} \propto \dot{\gamma}^{1/n} \exp\left(U_{uy}/k_b T\right)$ with $n = 2.5$ and $U_{uy} = 1.08$. Both sets of parameters fall in the usual range found by experimentalists (see Table 1 in [Yonenaga 1978]).

High initial dislocation densities

Finally, the influence of large initial (forest) dislocation densities is simulated in Fig. 10.7. A fairly good agreement is reached between experimental results and simulations for what concerns the progressive disappearance of

7 It should be indeed no surprise that $m \simeq 1$ and $U \simeq 2.2$ are retrieved since the influence of jogs is neglected and all dislocation motion proceeds by the double kink mechanism.

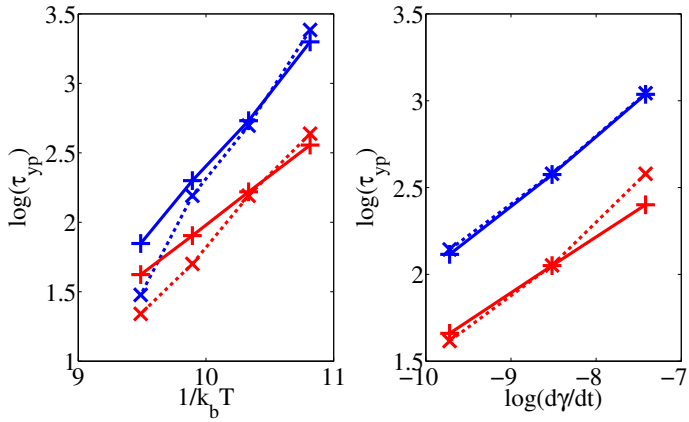

Figure 10.6: Comparison of experimental (dashed lines) and simulated (plain lines) upper and lower yield stresses, respectively in blue and red. Left: influence of temperature (*ds1*). Right: influence of strain rate (*ds2*).

the upper yield point with increasing initial dislocation density. However, marked discrepancies are observed between the experimental and simulated yield and flow stress values.

The delayed yielding is partially caused by the insertion of the saturation term in Eq. 10.5. At large initial ρ_m, the extent of self-multiplication is reduced and the sole influence of forest dislocations remains[8].

This points to a limitation of the present constitutive model, which is not able to reproduce *quantitatively* the evolution of the yield stresses at large initial dislocation densities. Such a large quantitative difference of output with respect to experimental data could be due to other factors related to the sample batch set, such as temperature stability: attempts to reproduce the stress-strain behavior at large initial dislocation densities with various multiplication laws have not been successful either.

An almost linear relationship between τ_{uy} and $\rho_{0,\text{exp}}$ is simulated. Writing $\tau_{uy} = a \log\left(\rho_{0,\text{exp}}/b\right)$, the simulated data of *ds3* can be well fitted by setting $a = -0.27 \times 10^7\,\text{N.m}^{-2}$ and $b = 10^{13}\,\text{m}^{-2}$. This departs strongly from the numerical values derived by [Yonenaga 1978], but shows that the influence of the initial dislocation density on the upper yield stress can still be approximated by a simple model.

10.3.2 *Extrinsic crystals*

DISLOCATION MULTIPLICATION We turn now to the case of oxygen-contaminated samples. Table 10.5 gathers the best fits of E_{blocks} to the experimental stress-strain curves from the data set *ds4*.

8 Extending the multiplication law by reducing the mean free path and using Eq. 9.37 instead of Eq. 9.38 does not improve qualitatively the results.

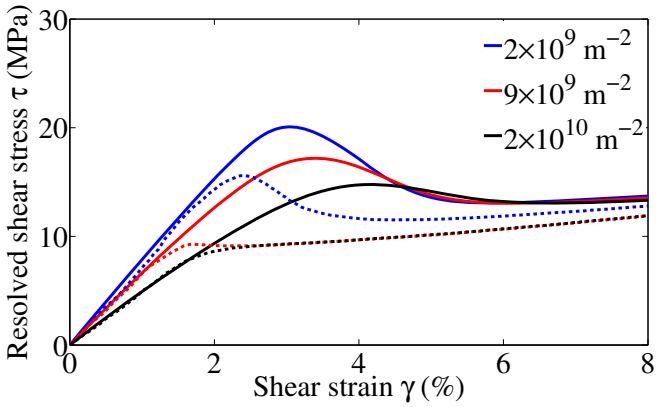

Figure 10.7: Experimental (dashed lines) and simulated (plain lines) stress-strain curves in the yield region of intrinsic crystals of set *ds3*.

c_O^∞ (10^{16} cm^{-3})	<1	1.5	4	6.5	9
E_{block} (MPa)	300	675	850	900	950

Table 10.5: Best fits of E_{block} for *ds4*.

However, as seen in Fig. 10.7 and discussed above, the present model underestimates the enhanced dislocation generation at high initial densities. This limitation is particularly relevant for the study of extrinsic crystals, as the simulated upper yield stress of the proxy FZ-Si sample ($\rho_{0,\text{exp}} = 10^{10}$ m^{-2}) is 75 % higher than the one experimentally observed.

If δ is increased in order to retrieve the experimental τ_{uy} on the intrinsic crystal, a multiplicative factor 10 is required[9]. Subsequent analysis shows that the effective mobile dislocation density $\rho_{m,eff}$ is then an extremely small fraction of ρ_m, at rather low oxygen contents. This is in clear contradiction with experimental observations of [Yonenaga 1984].

Instead of adjusting δ to the intrinsic crystal, we adopt the same methodology as in Section 7.2.4. Setting $\eta(1.5 \times 10^{17})$ to 20 %, $\delta = 6 \times 10^{-6}$ is derived.

PARAMETER IDENTIFICATION Table 10.6 shows the individual values of η giving an optimal simulated upper yield point. At the largest oxygen concentration no reasonable[10] value could be derived, with generation from forest sources systematically precipitating the sample yielding.

9 A similar discussion is valid for other multiplication laws.

10 η values leading to initial dislocation densities on the principal lower slip system lower than 1 m^{-2} are typically deemed unreasonable.

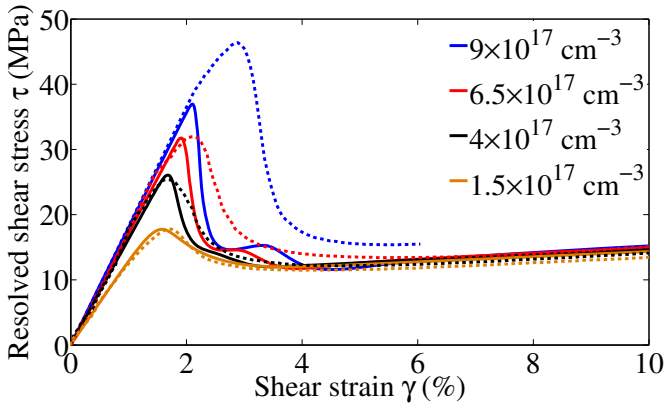

Figure 10.8: Experimental (dashed lines) and simulated (plain lines) stress-strain curves in the yield region of extrinsic crystals of set *ds4*.

c_O^∞ (10^{16} cm^{-3})	<1	1.5	4	6.5	9
η	1	0.2	10^{-3}	10^{-6}	-

Table 10.6: Individual best fits of η to *ds4*, with $\delta = 6 \times 10^{-6}$.

Given these data, Eq. 9.16 can be fitted by setting:

$$\begin{cases} \tau_O^{min} = 2.26\,\text{MPa} \\ \tau_O^{ref} = 0.97\,\text{MPa} \end{cases} \tag{10.6}$$

As for the extended AH model, the case of very large oxygen contents has been disregarded for the derivation of these parameters.

The resulting stress-strain curves are shown in Fig. 10.8. They are discussed in Section 10.5.

10.4 MODELING LATE DEFORMATION STAGES

No parameter fitting is immediately required to define stage I, as the physical processes of dislocation storage and annihilation are readily modeled. Activation of the secondary system A2 at large strains should follow from the rotation of the lattice with plastic flow.

Given that lattice rotation depends on the amount of plastic flow only and not on temperature or strain rate, the experimentally observed shift of secondary slip towards higher strains at large τ_{eff} betrays a peculiarity of semiconductors, especially when the very low stress sensitivity of the dislocation velocity in virgin materials is taken into account.

This stress overshoot is traditionally attributed to the pinning of secondary dislocations in solid solutions. However, intrinsic crystals only are considered here. In addition to a delayed onset, [Sumino 1971] detected a change in the activation energy for dislocation motion in stage II and mentioned high jog densities on the intersecting dislocations as a possible rate-limiting mechanism.

10.4.1 *Localized obstacles only*

We find that *it is impossible to reproduce the overshoot, keep a single slip system active in stage I and simulate a strong hardening rate in stage II if only the influence of localized obstacles is accounted for and jogs are disregarded*, as shown in Fig. 10.9.

The dislocation multiplication law adopted by our model leads to the simultaneous activation of the slip systems D4 and A2 all throughout what could be identified as stage I, characterized by a low hardening rate. Secondary systems C3 and D6 are also active up to intermediate strains, as seen in Fig. 10.10. This behavior is due both to the absence of obstacles strong enough to pin secondary dislocations in stage I (be it forest trees or jogs), and to the weak stress dependency of dislocation velocity in free flight ($m_0 = 1$) combined to a constant normalizing stress τ_0.

An attempt to magnify the effect of forest obstacles by increasing F_{obs} to 4.4 eV does not bring any significant improvement to the simulated behavior of silicon monocrystals: the simulated hardening rate in stage II is simply brought closer to the experimental one.

This could be expected from the analysis performed in Chapter 8, where it is shown that forest obstacles have only a minor effect on dislocation velocity (and therefore the potential variations of the effective stress), and then only at low τ_{eff}.

INITIAL YIELDING The shape of the yield region is due both to the very low initial dislocation contents and to the particular K_1 function chosen. No bounding block is included in the finite element model, so that all energy applied is absorbed by the tensile specimen only. The initial slope of the stress-strain curve is given by the elastic properties of silicon. Whatever

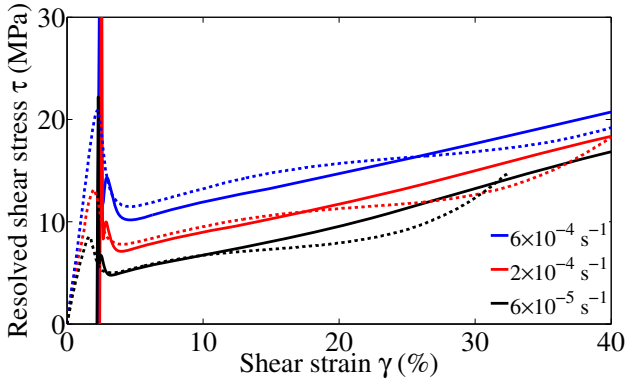

(a) $F_{obs} = 2.2\,\text{eV}$

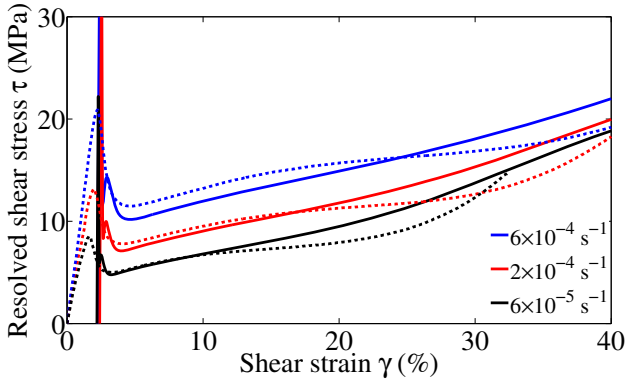

(b) $F_{obs} = 4.4\,\text{eV}$

Figure 10.9: Comparison of experimental and simulated stress-strain curves of *ds2*. Jog dragging is *not* accounted for, and only localized obstacles affect dislocation motion. The simulated curves are translated so the experimental and simulated lower yield points coincide.

the K_1 law, an initial stress peak at very high values and of extremely short duration is simulated. It is caused by a first yielding of the specimen, marked by an increase of the mobile dislocation density by a factor 100. A sharp drop follows the generation of this first dislocation burst. The total ρ_m available is then not large enough to sustain the applied strain rate, and a second, more regular yielding follows.

Choosing $K_1 \propto \tau_{eff}^{1.25}$ leads to a rather high stress sensitivity of the generation rate; dislocations are easily generated and the secondary yield drop is much lower than the one obtained if bounding blocks (the tensile apparatus) can absorb energy. Less immobile dislocations are generated and the resulting lower yield point is lower than the experimental one. Note that the yield stresses of Fig. 10.9 still follow Eq. 8.1 with the same n_{yp} and U_{yp}

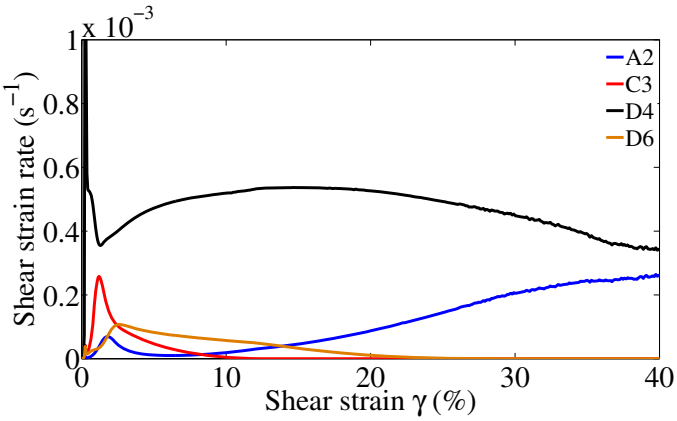

Figure 10.10: Shear strain rate on the primary (D4) and secondary (A2, C3 and D6) systems in the central elements of the specimen gauge. Only localized obstacles are accounted for and $F_{obs} = 2.2\,\text{eV}$. $\dot{\gamma} = 6 \times 10^{-4}\,\text{s}^{-1}$ from *ds2*.

parameters. Beyond the yield region, the experimental and simulated flow stresses evolve at the same rate.

Energy absorption by the tensile apparatus lowers τ_{eff} in the specimen gauge in the yield region, reducing hereby the mobile dislocation generation rate. No secondary yielding is detected in this case, but more immobile dislocations are generated during the yield drop. This explains the slight differences between the τ_{ly} simulated with and without elastic bounding blocks.

10.4.2 *Influence of jog dragging*

Preliminary discussion

A qualitatively good behavior is obtained if $n_j \neq 0$ and actually increases on latent systems. Jog dragging completely offsets any influence of the localized obstacles, as discussed in Section 8.6. The time of free flight t_f becomes much larger than the waiting time at obstacles t_w as long as F_{obs} remains in acceptable bounds for Friedel statistics to be valid ($< 0.2\mu b^3$, see [Kocks 1975]), and has reasonable values for a forest pinning obstacle type.

Two parameters control the jog evolution for each dislocation character, κ_+ and κ_-. Some requirements are set on them for the model to produce acceptable results.

- Primary dislocations must not be affected by jog dragging during stage I, as experimental evidence shows that the activation energy for their motion remains constant throughout easy glide and equal to the one measured on jog-free dislocations (see [Sumino 1971]). This either limits the magnitude of κ_+, or poses additional constraints on κ_-, that

must eventually compensate for a large generation rate. The results of Section 9.6.3 can provide with an estimate of the steady-state jog density reached on the primary system in stage I.

- In particular, this observation implies that mobile dislocations tend to have lower jog densities than immobile ones. This gives validity to our constitutive equations that assume jog annihilation when $\dot{\gamma} \neq 0$.

- Secondary dislocations must be significantly affected by jog dragging in order for overshoot to be detectable. Being at rest during stage I, κ_- has little or no influence on the jog density build-up of secondary dislocations. This implies a lower bound for κ_+.

- The magnitude of κ_- ultimately defines the mechanical behavior of the crystal at large strains, when both the primary and secondary dislocations move by jog-dragging. This strain domain sees additional microstructural changes such as cell formation, that our model cannot account for. It is therefore quite awkward to base the identification of κ_- on the study of late deformation stages.

  Rather, it can be considered that κ_- should be large enough for primary dislocations never to be affected by jog dragging in stage I, and small enough not to lead to model instabilities[11] at the transition between stage I and II.

- The model considers dislocation loops to be made up of two dislocation types, screw or 60°. Both have a screw component and are affected by jog-dragging as discussed in Chapter 8.

  It has been already emphasized that for physical reasons, the same parameters cannot be used in the jog density evolution laws of screw and 60° dislocations, i.e. one cannot have $d_{j,s} = d_{j,60}$ at any time.

  A simple model distinguishing mixed (oriented at an angle α from the Burger's vector) from screw dislocations could assume that only $\cos\alpha$ jogs created are sessile and impede dislocation motion. Jog annihilation relying on a capture radius and the actual jog density on the line, this process then takes place $1/\cos\alpha$ faster on mixed segments. This translates for 60° dislocations as:

$$\begin{cases} \kappa_{+,60} = \kappa_{+,s}/2 \\ \kappa_{-,60} = 2\kappa_{-,s} \end{cases} \tag{10.7}$$

  Generation of jogs on secondary 60° dislocations must still be large enough to prevent an early activation of the slip system. Note that this simple model yields an infinite effective sessile jog spacing on edge dislocations, which is the case.

11 Here, instability must be understood as a shift between the two motion modes. Upon activation of secondary dislocations associated to a peak in the resolved shear strain rate, a high κ_- could lead to a transition period during which the jog density is so low that their drag does not govern motion any longer.

These assumptions reduce the number of unknown parameters, and only the two κ related to screw dislocations are needed to define the behavior of silicon in multiple slip.

An additional factor influencing the simulated mechanical behavior of silicon in multiple slip is the actual value of the self-diffusion coefficient D_{sd}. As mentionned in Section 8.6, an increase of this parameter due to, e.g., the presence of point defects at or lattice distortion close to the dislocation cores, smoothens the transition between the velocity modes. We do not investigate this possibility here.

HOURGLASSING AND MESH EFFECTS Large $\kappa_{+,s}$ values imply that single slip is active over a larger strain range as dislocation motion on the secondary systems is more impeded. Deformation in single slip leads to significant element shearing. At large $\kappa_{+,s}$ the elements become very distorted upon "release" of the secondary systems, and hourglassing becomes a significant problem. ABAQUS/EXPLICIT responds by adding some hourglass stiffness, resulting in a facticious constitutive response of the model. Ultimately, the secondary system is activated too early and significant instabilities are propagated through the mesh.

A way to overcome this issue is to use the remeshing abilities of ABAQUS/EXPLICIT. Remeshing at frequent intervals guarantees that elements keep an acceptable shape and reduces the influence of hourglassing on the solution. However, this strategy increases significantly the computational cost and forbids the use of parallelization to speed up the calculations.

Constant κ's

Using constant jog evolution parameters allows the exploration of the basic abilities of the model. Strain rate and temperature both affect the effective stress necessary to set dislocations in motion, and experimental observations show that the severity of overshoot increases with τ_{eff}, but such a behavior is not correctly retrieved when using constant κ's.

The model of [Messerschmidt 1970] considers indeed that jog annihilation is thermally activated and depends both on the availability of point defects in the bulk (generated during deformation) and on the formation rate of jog pairs. The equations of the present model do not attempt to account for these phenomena.

Instead, we can assume an effective stress dependency of the jog generation parameter $\kappa_{+,s}$. This would insert an indirect strain rate and temperature dependency in the overshoot extent. A linear τ_{eff} dependency would yield a mean jog spacing inversely proportional to the effective stress (see Section 9.6.3).

Inserting a stress dependency into the annihilation parameter $\kappa_{-,s}$ only would not be sufficient, as jog annihilation takes place when $\dot{\gamma} > 0$.

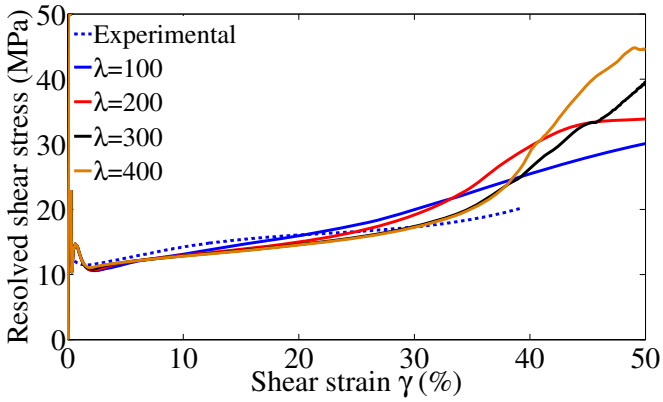

Figure 10.11: Stress-strain behavior at T=1173 K and $\dot{\gamma} = 6 \times 10^{-4}\,\mathrm{s}^{-1}$ for different $\kappa_{+,s} = \lambda \tau_{eff}/\mu$ and $\kappa_{-,s} = 100$.

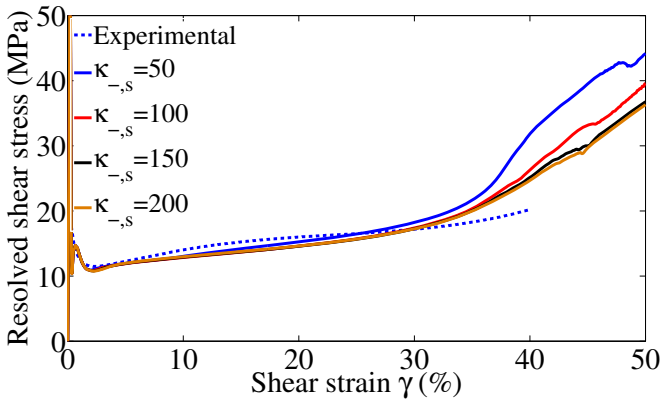

Figure 10.12: Stress-strain behavior at T=1173 K and $\dot{\gamma} = 6 \times 10^{-4}\,\mathrm{s}^{-1}$ for $\lambda = 300$ and different $\kappa_{-,s}$.

Stress-dependent κ_+'s

Let us rewrite:

$$\kappa_{+,s}^{(\alpha)} = \lambda \frac{\tau_{eff}^{(\alpha)}}{\mu} \tag{10.8}$$

and keep $\kappa_{-,s}$ constant. Letting λ vary, Fig. 10.11 is obtained. The influence of the jog annihilation parameter is then investigated in Fig. 10.12.

JOG GENERATION PARAMETERS The overshoot predicted by the constitutive model becomes significant above a threshold value of $\kappa_{+,s}$ and saturates at large jog generation rates: this is particularly visible in Fig. 10.11 where $\lambda = 100$ hardly leads to significant hardening in stage II; increas-

ing λ above 300 does not extend the overshoot but simply increases the unstabilities in the force outputs.

When simulated, the overshoot extent depends almost only on $\kappa_{+,s}$; this is clearly seen in Fig. 10.12. $\kappa_{-,s}$ affects the speed of transition between stage I and II. It can also be noticed that as a rule of thumb, increasing the annihilation parameter improves the stability of the result.

BEHAVIOR AT LARGE STRAINS Using high-order explicit solvers with substepping to integrate the constitutive equations has no effect on the solution stability. The unstabilities in the stress-strain curves noticed in the early stage II at large $\lambda/\kappa-,s$ ratios, e.g., for $\lambda = 400$ in Fig. 10.11, are rather mesh-induced. They can be reduced to some extent by increasing the amount of elements in the sample gauge and reducing the time increments. However, such refinements have a prohibitive numerical cost.

Model abilities

The force output cannot be trusted beyond the transition between stage I and II when strong mesh distortions are detected. Two aspects are therefore tackled separately in the following:

- agreement between the experimental and simulated hardening behavior in stage II, by simulations of uniaxial tensile tests of samples initially oriented for multiple slip.
- model ability to predict overshoot and its dependencies on strain rate and temperature

HARDENING RATE IN MULTIPLE SLIP It will be seen from Figs. 10.15 and 10.16 that the hardening rate in stage II predicted by the constitutive model is very close to the experimental one for $\kappa_{-,s} = 3\lambda = 1200$ and does not depend on the strain rate or on the temperature at large effective stresses. In order to derive the optimal $\kappa_{-,s}/\lambda$ ratio and λ value, experimental results from [Michel 1982] are used.

Tests performed on monocrystals loaded uniaxially along the [100] orientation indicate a hardening rate $\mathrm{d}\sigma/\mathrm{d}\varepsilon \simeq 1.4\,\mathrm{GPa}$. Various cases are studied in Fig. 10.13). The experimental slope is retrieved for $\kappa_{-,s}/\lambda \geq 3$. When this condition is satisfied, the exact value of λ has no influence on the output stress-strain curve whatsoever.

Setting $\kappa_{-,s}$ three times larger than λ provides a very good estimation of the hardening rate in multiple slip when samples are initially oriented in along [100]. Such a relationship actually leads to a small net jog generation rate on primary dislocations, whose motion then proceeds by the double kink mechanism.

Let us now turn to the model ability to reproduce the strain rate and temperature dependencies of overshoot.

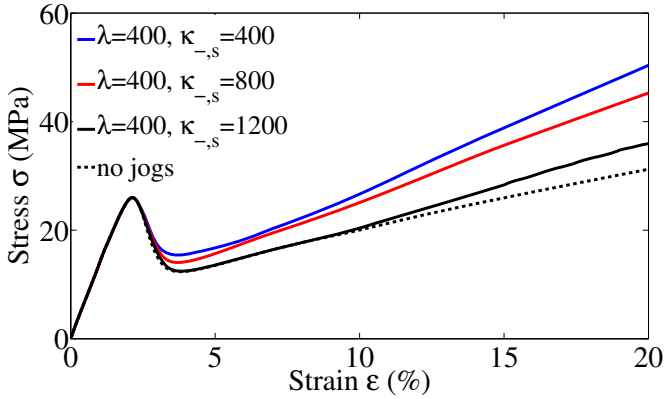

(a) Influence of $\kappa_{-,s}/\lambda$ ratio

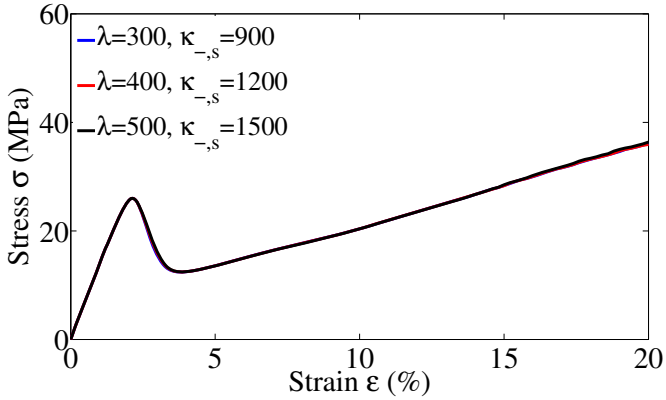

(b) Influence of λ value

Figure 10.13: Stress-strain behavior of [100] oriented samples at $\dot{\varepsilon} = 2 \times 10^{-3}\,\mathrm{s}^{-1}$, T=1095 K and $\rho_0 = 10^{10}\,\mathrm{m}^{-2}$ for various $\kappa_{-,s}/\lambda$ ratios and λ values. $E_{blocks} = 1\,\mathrm{GPa}$.

OVERSHOOT Keeping the ratio $\kappa_{-,s}/\lambda$ constant, Fig. 10.14 is obtained. At a given ratio, an overshoot saturation effect seems to develop as well, although mesh effects precipitating the transition into stage II cannot be ruled out at large λ's[12].

A first insight provided by Fig. 10.14 is that $\kappa_{-,s}$ has a slight but noticeable influence on the strain overshoot. As the $\kappa_{-,s}/\lambda$ ratio is increased, a larger λ is required for the simulated stage I to last longer. A second observation is the particular shape taken by the stress-strain curve into stage II at large $\kappa_{-,s}/\lambda$ ratios and low λ values.

Whatever the particular $\kappa_{-,s} - \lambda$ relationship imposed, as long as λ is large enough to prevent significant dislocation motion on the secondary slip systems in stage I, the model is able to reproduce overshoot.

Setting the jog parameters to $\kappa_{-,s} = 3\lambda$ for the reasons detailed on the previous paragraph, a correct hardening slope in stage II is retrieved for $\lambda = 400$, except at the largest temperature considered:

$$\begin{cases} \kappa_{+,s}^{(\alpha)} = 400\tau_{eff}^{(\alpha)}/\mu \\ \kappa_{-,s}^{(\alpha)} = 1200 \end{cases} \tag{10.9}$$

The influence of the strain rate on the simulated behavior is shown in Fig. 10.15. Interestingly, the model is able to reproduce the increasingly delayed activation of secondary systems. The strains at which stage II sets in are remarkably close to the experimental ones.

The effect of temperature on the stress-strain response is shown in Fig. 10.16. Overshoot increases as temperature is lowered, as is experimentally observed. The temperature dependency of the simulated overshoot follows qualitatively the experimental one.

INFLUENCE OF SAMPLE ORIENTATION To assess the model abilities in multiple slip conditions, uniaxial tensile tests are simulated for various crystallographic orientations.

A specimen of total initial dislocation density $\rho_0 = 10^{10}\,\mathrm{m}^{-2}$ is considered, 90 % of which being mobile, and equally distributed on the 12 slip systems. Deformation proceeds at a strain rate $\dot{\varepsilon} = 2 \times 10^{-3}\,\mathrm{s}^{-1}$ and a temperature of 1095 K. These conditions are similar to those used in Section 7.3.2.

The crystallographic orientations considered are [123] (single slip), [112] (double slip), [110] (4 slip systems active), [111] (6 slip systems) and [100] (8 slip systems). Elastic bounding blocks ($E_{block} = 1\,\mathrm{GPa}$) are included in order to smooth out the initial yield peak from the simulations.

Simulations are run for 50 s, theoretically leading to a tensile strain of $\varepsilon = 10\,\%$. Fig. 10.17 shows the results obtained with the present constitutive model, discussed in the next Section.

12 At the largest values tested, simulations actually crash because of excessive element distortion, and in spite of remeshing.

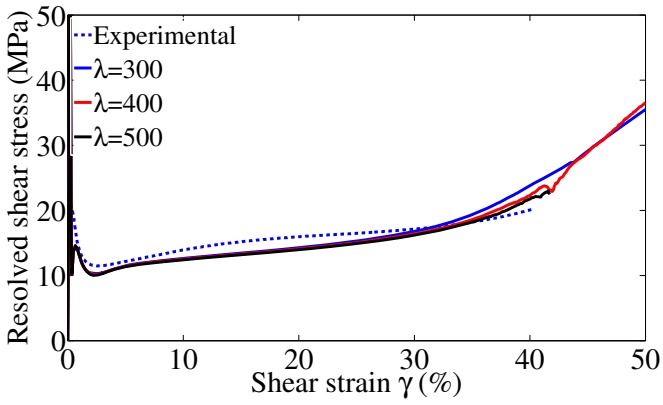

(a) $\kappa_{-,s} = \lambda$

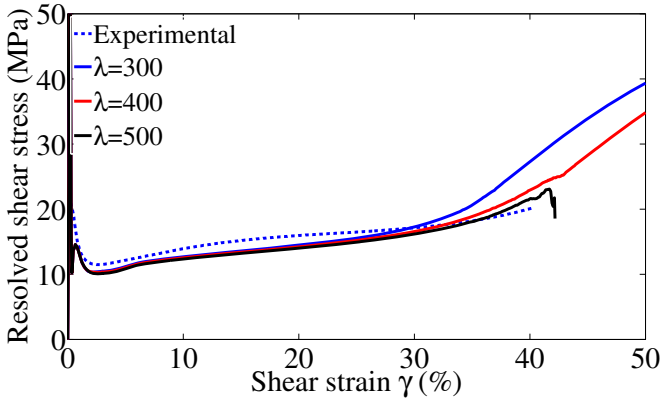

(b) $\kappa_{-,s} = 2\lambda$

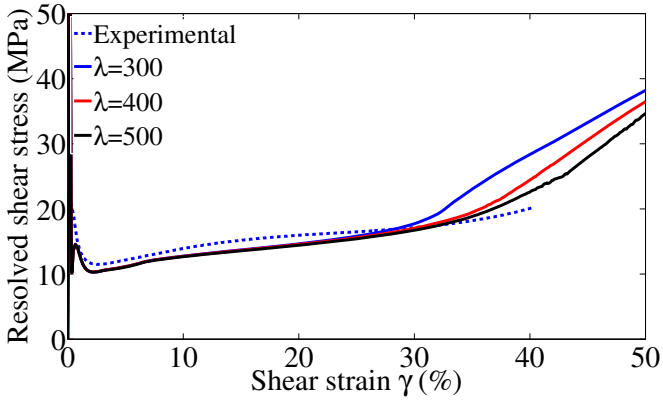

(c) $\kappa_{-,s} = 3\lambda$

Figure 10.14: Stress-strain behavior at T=1173 K and $\dot{\gamma} = 6 \times 10^{-4}\,\mathrm{s}^{-1}$ at a constant ratios $\kappa_{-,s}/\lambda$.

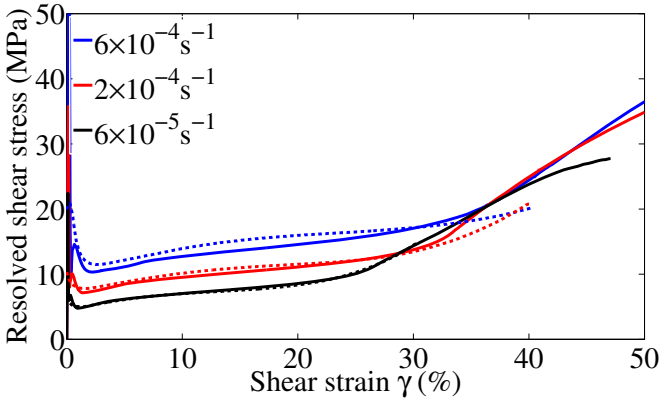

Figure 10.15: Stress-strain behavior at T=1173 K and various strain rates for $\kappa_{-,s} = 3\lambda$ and $\lambda = 400$.

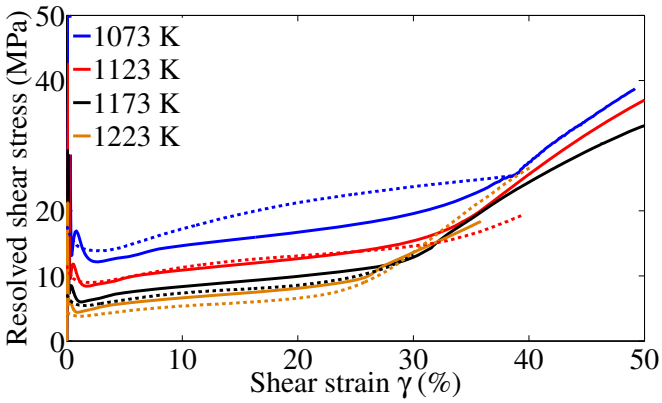

Figure 10.16: Stress-strain behavior at $\dot{\gamma} = 1.2 \times 10^{-4}\,\mathrm{s}^{-1}$ and various temperatures for $\kappa_{-,s} = 3\lambda$ and $\lambda = 400$.

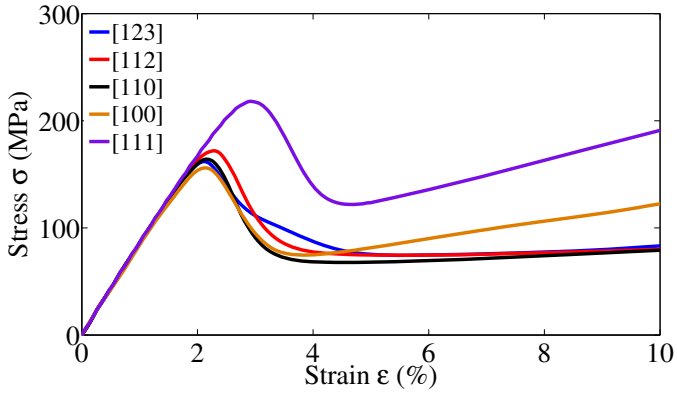

Figure 10.17: Influence of the specimen crystallographic orientation on the stress-strain behavior for $\dot{\varepsilon} = 2 \times 10^{-3}\,\mathrm{s}^{-1}$, T=1095 K and $\rho_0 = 10^{10}\,\mathrm{m}^{-2}$. $\lambda = 400$ and $\kappa_{-,s} = 1200$.

10.5 DISCUSSION AND CONCLUSION

10.5.1 *Constitutive equations and parameters*

Velocity law

The most important novelty of this model is the derivation of a velocity law coupling dislocation motion by the double-kink mechanism and jog-dragging. It has been shown that this mixed mode is the most likely reason for observing a high hardening rate in stage II of [123]-oriented tensile specimen, as well as overshoot.

In particular, the effect of localized obstacles on dislocation velocity is likely marginal in silicon, owing to the relatively low dislocation speed in free flight. The influence of point defects has been disregarded in this model, but could ease jog dragging and help explain some model shortcomings, as discussed below.

Breakdown of dislocation density

Apart from the velocity law, a particularity of this model is the distinction made between mobile and immobile dislocations on the one hand, and depending on their character on the other. This gives further insights and allows the correct reproduction of constitutive behavior at large strains.

Such a segmentation of the total dislocation density is made necessary by two factors: the strong variations of the mobile dislocation contents upon loading of as-grown silicon crystals on the one hand; and the different impacts jog dragging has on dislocations with various screw components on the other.

Dislocation evolution

SELF-MULTIPLICATION Remarks related to K_1 are discussed below.

FOREST MULTIPLICATION The model could be criticized for its choice of dislocation multiplication law from forest dislocations, relying on ρ_i rather than ρ_t (see Section 9.5.1).

In addition to the physical justification behind this choice, adopting such a law leads to severe model unstabilities at the transition between stage I and II, and to a very strong effective stress dependency of the hardening rate in stage II. Furthermore, such a law does not improve significantly the simulated behavior at large initial dislocation densities.

DISLOCATION STORAGE AND ANNIHILATION The capture radii for storage and annihilation of screw and 60° dislocations are entirely derived on physical arguments. Their accuracy is discussed in the next Section.

Internal stresses

The optimal hardening parameter $A_{\alpha\alpha}$ is very close to the values usually derived for the model of Alexander & Haasen. On the other hand, the $B_{\alpha\alpha}$ value derived by best fit is quite large. This was unexpected, since immobile dislocations are usually considered not to lead to the development of significant long-range internal stresses. With $B_{\alpha\alpha} \simeq 0.25 \times A_{\alpha\alpha}$, the influence of ρ_i on the total internal stress becomes quickly dominant.

Jog evolution

The most criticizable point of the model is the particular differential equations chosen to rule the evolution of jog densities on mobile dislocations. The influence of point defects generated during deformation, in particular, should affect jog dragging and lower the overwhelming dominance of this rate-limiting mechanism at large temperatures.

Additional jog annihilation mechanisms such as temperature-dependent pipe diffusion could as well play a role in inserting a potential stress dependency in the annihilation parameter.

Furthermore, the exact effects of jogs on 60° dislocations are not known; the set of equations 10.7 has been adopted for simplicity but poses some problems. No relevant model could be found in the literature about motion of jogged mixed dislocations.

Here it should be noted that leaving 60° dislocations jog-free leads to the disappearance of overshoot and a behavior closer to the one obtained with no jogs. This is due to the coupling between the mobile dislocation generation equations and the various dislocation characters (namely, motion of screws generates 60° dislocations, and vice-versa).

10.5.2 *Model outputs*

Yield region

INTRINSIC CRYSTALS The upper and lower yield stresses are very well reproduced by the constitutive model, in the temperature and strain ranges considered.

None of the numerous K_1 laws tested satisfying the requirement of strain rate independence of δ could follow the experimental disappearance of the upper yield point as the initial dislocation density is increased (set ds3).

Decreasing k_{FR} or even accounting for all forest dislocations in the multiplication law does not improve noticeably this aspect.

Multiplication from forest obstacles does not play any significant role at small strains, and *does not improve the (wrong) ordering of upper yield points compared to the extended AH model*, as seen by comparing Fig. 10.17 to Fig. 7.15.

On the other hand, it is observed that the self-multiplication law K_1 has a very strong influence on these results. *The variations of the upper yield*

stress with the sample orientation are mostly influenced by K_1 rather than k_{FR}, namely, the self-multiplication law has a significant impact on the simulated behavior in the yield region both for specimen oriented for single glide or in symmetrical orientations.

- The multiplication law K_1 has a critical role in determining the dependency of the yield stresses on the initial dislocation densities, as well as their variations with the crystallographic orientation

An additional point worth mentioning is the double yielding predicted by the constitutive model at high strain rates, especially visible in Fig. 10.17 and detectable in Fig. 10.5b. Its appearance is due both to the K_1 function chosen, and to the additional dislocation generation from forest densities through k_{FR}.

The combined effect of these two multiplication laws is self-reinforcing at large effective stresses: initial generation on all slip systems is facilitated by a non-saturating K_1, and further strengthened by k_{FR}. Accounting for jog dragging does not improve this aspect.

The appearance of secondary yield points at large strain rates can be avoided by the adoption of an alternative self-multiplication law K_1. If a saturation term is introduced, then a strain rate independency of δ is reached by setting:

$$K_1 = \delta \frac{\tau_{eff}^{(\alpha)1.5}}{\sqrt{\rho_m^{(\alpha)}}} \tag{10.10}$$

with $\delta = 1.5 \times 10^{-3}$, $A_{\alpha\alpha}$ and $B_{\alpha\alpha}$ remaining unchanged.

As shown in Fig. 10.18, the double yieldings disappear. A drawback of this formulation is a significantly delayed yield drop as the self-multiplication function is reduced upon multiplication of primary dislocations.

Adopting such a K_1 law also affects the yield region in various sample orientations, as shown in Fig. 10.19.

- Some combinations of multiplication law K_1 with dislocation generation from forest obstacles lead to the appearance of spurious secondary yield points at large effective stresses
- These remarks indicate that self-multiplication mechanisms are more complex than currently assumed
- In particular, additional mobile dislocation generation from sources on the primary slip system should be considered (e.g., a generation rate function of $\sqrt{\rho_i^{(\alpha)}}$)

EXTRINSIC CRYSTALS Double yield points are simulated because of the activation of secondary systems during the yield drop (see Fig. 10.8). These are not observed experimentally, but are likely due to the choice of K_1 law, as mentioned above.

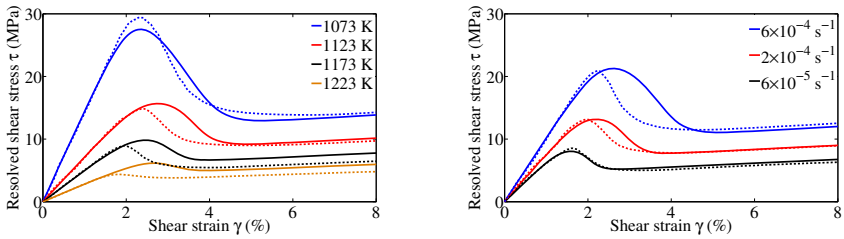

(a) *ds1* (b) *ds2*

Figure 10.18: Experimental (dashed lines) and simulated (plain lines) stress-strain curves in the yield region of intrinsic crystals, using a saturation term in K_1 (Eq. 10.10).

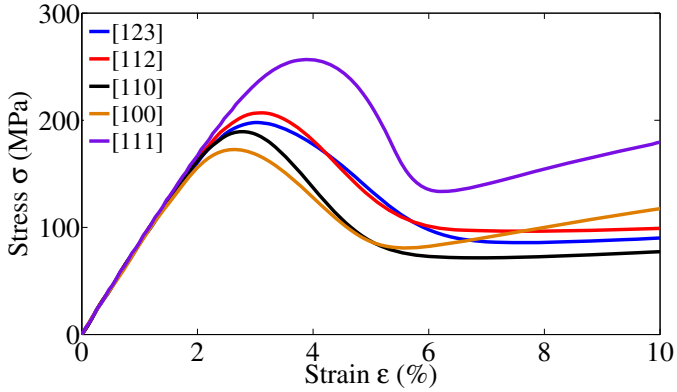

Figure 10.19: Influence of the specimen crystallographic orientation on the stress-strain behavior using Eq. 10.10 for K_1. $\dot{\varepsilon} = 2 \times 10^{-3}\,\mathrm{s}^{-1}$, T=1095 K and $\rho_0 = 10^{10}\,\mathrm{m}^{-2}$. $\lambda = 400$ and $\kappa_{-,s} = 1200$.

[Maroudas 1991c] reduce the dislocation multiplication parameter δ. This modification has been implemented in the present model, but improves noticeably neither the value of τ_{uy} nor the inactivation of secondary systems.

The influence of jogs on dislocation motion has *not* been inserted into the constitutive model for extrinsic crystals. It is not expected to play a significant role in the strain range considered, although it could to some extent hinder secondary dislocation motion and smoothen out the secondary yield points.

Stage I

Intrinsic crystals only are considered in the following.

FLOW STRESS The deactivation of the secondary slip system C3 at intermediate strains (see Fig. 10.20) results in the increase of the strain rate onto the primary system D4, and a subsequent increase of the flow stress,

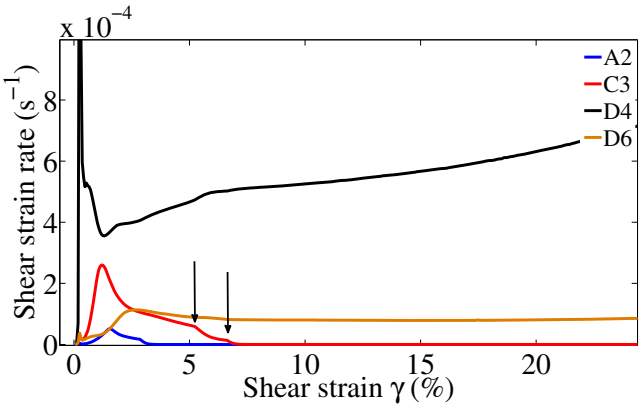

Figure 10.20: Shear strain rate on the primary (D4) and secondary (A2, C3 and D6) systems in the central elements of the specimen gauge. Jog dragging is accounted for. The change of rate-limiting motion mechanism of screws and 60° dislocations on C3 are indicated by arrows. $\dot{\gamma} = 6 \times 10^{-4}\,\mathrm{s}^{-1}$ from *ds2*.

particularly visible at high strain rates or low temperatures in Figs. 10.15 and 10.16.

This deactivation is due to the increase of jog density on the slip system, resulting in the particular shape of the strain rate curve from $\gamma \simeq 5\,\%$. The arrows in Fig. 10.20 point to the strains at which screws, then 60° dislocations on C3, change of rate-limiting mechanism from double kink to jog dragging.

The change of hardening rate noticed in the stress-strain curves at these strains is not observed experimentally. On the other hand, once plastic flow stops on C3, the hardening rate flattens out, as observed in the experimental curves before the onset of stage II.

This tends to indicate that in actual specimen, C3 is deactivated at large strains, but in a much smoother way than what simulations predict.

A smoother deactivation due to the progressive take-over of the motion mechanisms by jog dragging can be explained by two arguments:

1. The jog annihilation rate is actually larger than currently assumed
2. The dislocation generation rate is larger than currently assumed

Accounting for either of these remarks would lead to lower mean jog spacing on $\rho_m^{(C3)}$.

Given the previous discussion about the too weak dislocation self-multiplication law K_1 at large dislocation densities, the second point seems the most probable.

STEADY-STATE OF DEFORMATION The steady-state of the primary effective stress $\tau_{eff}^{(D4)}$ is determined by the magnitude of the capture radii expres-

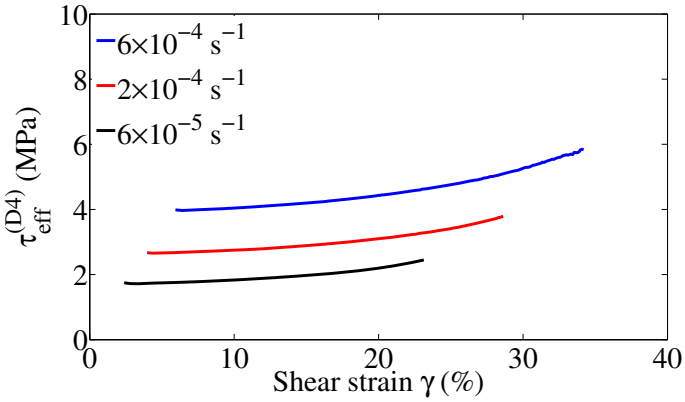

Figure 10.21: Effective shear stress τ_{eff} on the primary system in the central elements of the specimen gauge during stage I (conditions of *ds2*).

sions derived in Section 9.4. Its comparison with data from [Yonenaga 1978] allows consequently the validation of the physically derived capture radii.

Fig. 10.21 shows the evolution during stage I of $\tau_{eff}^{(D4)}$ in the central gauge elements of specimen from *ds2*. Note that the steady-state has been experimentally characterized by means of strain rate changes. A rigorous estimation of the simulated τ_{eff}^{*} should require the reproduction of such tests.

Still, the results indicate a rather good agreement between the simulations and experiments, with numerical values within a factor two from experimental data. Similar remarks are valid for the sample set *ds1*.

- This indicates that deriving the capture radii solely on physical arguments gives very satisfying results.

Disaggregation of the primary dislocation density according to the dislocation mobility and character gives interesting insights into the relative role played by screws and 60° segments. As seen in Fig. 10.22, the total mobile dislocation density ρ_m is roughly equally divided the two orientations. This could be expected from the similarity of the dislocation generation laws.

On the other hand, the immobile density is clearly dominated by 60° segments, owing to the very large capture radius for annihilation of screw segments. This result is in very good agreement with experimental observations pointing to an overwhelming majority of edge segments in stage I. The present model explains this tendency by the easy annihilation of screw dipoles by cross-slip, in spite of the relatively low temperatures considered.

The strength of the constitutive model derived in this Part lies in the limited amount of constitutive parameters left to identify by best fit. In particular, the behavior of primary dislocations in stage I is entirely defined by physically-based arguments.

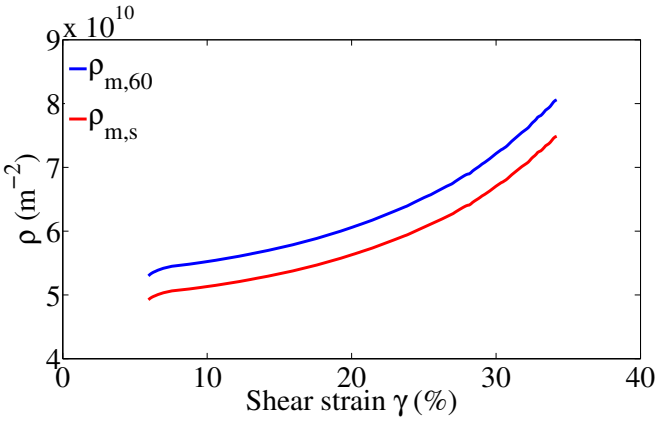

(a) $\rho_m^{(D4)}$

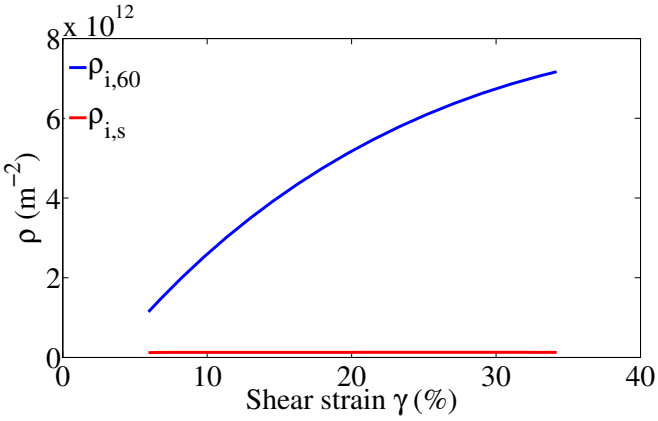

(b) $\rho_i^{(D4)}$

Figure 10.22: Breakdown of the total primary dislocation density $\rho_t^{(D4)}$ during stage I, according to dislocation character and mobility. $\dot{\gamma} = 6 \times 10^{-4}\,\mathrm{s}^{-1}$ from *ds2*.

SPECIMEN DESIGN As a side note, it has been observed that the extent of stage I is affected by the gauge length: the shorter the specimen, the less overshoot is observed. This aspect has not been investigated for time reasons.

Multiple slip and large strains

FROM STAGE I TO STAGE II *The model is able to reproduce overshoot and a high hardening rate in the subsequent stage II only when jog dragging is accounted for*. A critical outcome of the study is that *localized obstacles do not seem to influence dislocation motion strongly enough to explain the experimental observations*.

This remark is obviously unexpected, given the similarities between hardening mechanisms in f.c.c. crystals and intrinsic semiconductors. It stems directly from the particularly low dependency on τ_{eff} of the dislocation velocity in free flight in the latter material class, leading to much larger travelling times than waiting times.

The significant overshoot measured in *intrinsic* crystals must be caused by *intrinsic* defects affecting secondary dislocation motion. We have proposed jogs as a possible explanation. Such a model runs into several limitations, some of them already discussed above. Additional remarks related to multiple slip situations are tackled in the following paragraphs:

- Simulating overshoot by a change in dislocation motion mechanisms leads to severe numerical restrictions, given the explicit Finite Element solver and particular element type relied upon
- The hardening rate in stage II is slightly temperature dependent, and to a lower extent strain rate dependent, given the particular set of constitutive parameters derived
- Jogs do not seem to influence dislocation motion when the specimen is initially oriented for multiple slip

FEM ISSUES The first item imposes time constraints on the derivation of the model: a limited amount of constitutive equations and parameters can be studied. In spite of remeshing and time step reductions, unstabilities in the internal variables are systematically detected at the transition between stage I and stage II; this is particularly relevant for the shear strain rate evolution. They are due to a sudden activation of secondary systems throughout the specimen gauge, and are not reduced by using high-order explicit solvers with substepping to integrate the constitutive equations.

Working with second-order fully integrated brick elements could help in this respect. However, ABAQUS/EXPLICIT does not offer such an element type, and time limitations have not allowed the coding of C3D20 elements into a VUEL routine.

Another way of improving the model stability is to work with ABAQUS/STANDARD, which requires in turn the derivation of the consistent tangent moduli (CTM). The use of numerical methods to estimate the CTM would relieve its heavy derivation.

HARDENING OF [123] SPECIMEN As seen in Figs. 10.15, and especially 10.16, the model predicts a lower θ_{II} than experimentally observed at low effective stresses. This particular behavior is due partly to the relationship between the constitutive parameters $\kappa_{-,s} = 3\lambda$, and partly to the constitutive equations ruling the jog density evolution themselves.

θ_{II} is reduced at low effective stresses because the jog generation (proportional to τ_{eff}) is not large enough relative to the (constant) annihilation rate. As mentioned in the previous Section, using a constant $\kappa_{+,s}$ does not lead to a satisfying behavior either: if the constitutive equations of Section 9.6

are to be kept, then an effective stress dependency of the κ parameters is to be expected. This discussion can be summarized as follows: *Jogs must be accounted for to explain the mechanical behavior of* [123] *specimen, and their density on mobile dislocations should be larger than currently simulated at low* τ_{eff}.

HARDENING OF [100] SPECIMEN Another observation from Fig. 10.13 is that the simulated hardening rate of [100] samples is in agreement with experimental observations only if the $\kappa_{-,s}/\lambda$ ratio is large enough for primary dislocations not to be affected by jog dragging: *Jogs should not have a significant effect on dislocation motion in* [100] *samples*.

Relieving the contradiction lifted by the former two conclusions can be done by modifying the constitutive equations for the jog density evolution, possibly accounting for the influence of point defects generated during deformation: their number ought to be larger in [100] samples than [123] ones, resulting in an increase of the dragging velocity by reducing the self-diffusion coefficient U_{sd}.

INFLUENCE OF SPECIMEN ORIENTATION An important remark that can be made from Fig. 10.17 is that the simulated hardening rates in a [112] double slip and [110] quadruple orientations are not significantly different than in a [123] single slip one.

This seems to be in contradiction with experimental data, at least for the [110] orientation[13] (see Fig. 2.1), and might be due to the particular values of latent hardening coefficients $A_{\alpha\alpha}$ and $B_{\alpha\alpha}$.

Combining jog dragging and the influence of localized obstacles does *not* improve this point.

Meanwhile, the present model predicts better the hardening rate in multiple slip than the extended AH model introduced in Part ii. This can be seen by comparing Figs. 7.15 and 10.17.

LARGE STRAINS The model looses its validity at large strains because of the fundamental physical processes taking place during stage II and leading to the appearance of stage III, such as patterning and cell formation, are not included in the constitutive equations.

The decrease of the hardening rate at large strains simulated, e.g., for $\dot{\gamma} = 6 \times 10^{-5}\,\mathrm{s}^{-1}$ is due to a deformation localization phenomena. During stage I, plastic slip is initiated close to the specimen fillets, and propagates towards the central part of the gauge section. Into stage II, deformation spreads from the central part of the specimen and is rather homogeneously distributed in the gauge section.

However, the model predicts a progressive localization of deformation back to the specimen fillets at large strains, resulting in a reduced hardening

13 The case of Ge investigated by [Patel 1963] might differ from Si, but no data specific to silicon has been found.

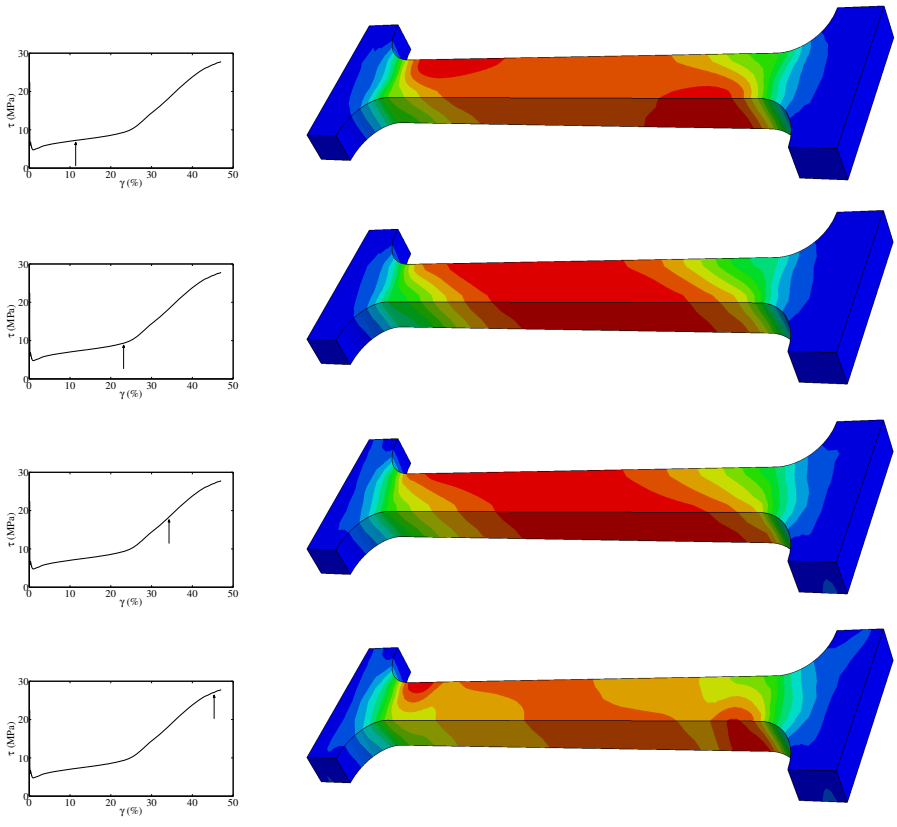

Figure 10.23: Contour plots of maximum principal deformation in the tensile specimen at various time points. The color scale is computed for each individual plot, in order to identify the regions of maximum deformation. $\dot{\gamma} = 6 \times 10^{-5}\,\mathrm{s}^{-1}$ from *ds2*.

rate θ_{II}. This localization effect is influenced by the constitutive parameters ruling the jog density, and indicates a rather weak limitation of the model[14]. Additional long-range internal stresses generated by cell formation could perhaps increase the flow stress at large strains and inhibit this localization tendency.

14 This is not a severe limitation since there is no practical need to study such large deformations.

11

ADAPTATION OF THE CONSTITUTIVE MODEL TO SOG-SI MONOCRYSTALS

The flexural strength of solar-grade silicon multicrystals has been experimentally determined at room temperature. Materials provided by Elkem Solar *and* SINTEF *have been tested. Only results related to the latter producer are introduced in the following. Given the brittle nature of silicon at low temperatures, the Weibull theory is relied on to fit the cumulative probability distribution as a function of the stress. Surface effects are investigated by comparing the strengths of grinded specimen to the one of chemically polished bars. The results presented here can be implemented into the constitutive models derived in the rest of this thesis.*

11.1 INTRODUCTION

Adaptation to Solar-grade materials deserves a particular discussion. What differs SoG-Si from EG-Si is the impurity and extrinsic defect content.

Dislocation locking by impurities can be dealt with as done in the previous Chapters. Electrically active species affect the activation energy for dislocation motion, and such a phenomena can be modeled as well (see Part i). SoG-Si contains high inclusion and precipitate densities, most often inhomogeneously distributed throughout the material block. How can we account for these inhomogeneities in a practical way?

It is worth remembering that the mechanical effects of inclusions is mainly local: acting as stress concentrators, they promote dislocation generation at high temperature and elastic stress increase at room temperature. A study of the stress and dislocation density distribution in a fictious mc-Si sample containing large inclusions is introduced in the next Part, but in the following we are concerned with the overall -averaged- influence of such contaminants. Furthermore, the effects of inclusions on plasticity is disregarded, as only the brittle behavior of silicon is considered.

A way to avoid modeling explicitely inclusions in a finite element model to study the fracture risk, a process that would be tedious and time-consuming, is to rely on statistical fracture properties derived from experimental results performed on SoG-Si materials. The knowledge of the cumulative fracture probability of a given material as a function of the

applied stress can be incorporated into the constitutive model introduced in the previous Chapters.

Fracture in Si materials takes usually place along the $\langle 111 \rangle$ planes. It is possible to extract from the stress tensor the maximum stress normal to all 4 such planes, and from that compute the fracture probability. Given the second Piola-Kirchoff stress tensor $\mathbf{S}^e$ in the CACS, its projection onto the four fracture planes identified by their normal $\mathbf{n}_0$ reads:

$$\tau_{\perp}^{(\alpha)} = \mathbf{S}^e : sym(\mathbf{F}^{eT}\mathbf{F}^e\mathbf{n}_0^{(\alpha)} \otimes \mathbf{n}_0^{(\alpha)}) \tag{11.1}$$

where $\mathbf{F}^{eT}\mathbf{F}^e$ can be approximated by the unity tensor as discussed in Annex A, and therefore $\tau_{\perp}^{(\alpha)} = \mathbf{S}^e : \mathbf{n}_0^{(\alpha)} \otimes \mathbf{n}_0^{(\alpha)}$.

Silicon is a brittle material at room temperature, and because of the fundamentally stochastic fracture process no definite strength (i.e. the stress at which fracture occurs) can be attributed. The reasons for a silicon material to break upon loading can be many: defects at the sample surface such as grooves and microcracks coming from the sample preparation, internal stresses left from the solidification process, or high stress localizations caused by the presence of inclusions in the silicon matrix.

This Chapter introduces experiments aiming at identifying the flexural strength of mc-Si bars deformed in a four-point bending (4PB) apparatus up to fracture. Although imperfect, this method allows for a relatively quick and straightforward identification of fracture parameters, namely the Weibull stress and exponent. Ultimately a cumulative fracture probability function $P(\sigma)$ is derived and implemented in the constitutive model to output $P(\max_\alpha(\tau_{\perp}^{(\alpha)}))$.

Experiments have been performed both on material provided by Elkem Solar and from SINTEF. All samples in a given test come from the same mc-Si ingot. The Young's modulus is computed from the recorded force-deflection data and is shown to vary, owing to the anisotropy of the single crystals constituting the multicrystalline bars. Two surface qualities have been tested for the purpose of strength analysis of Elkem's material: grinded and chemically etched. We show that mechanical processing of silicon samples leads to a lower average flexural strength and a lower dispersion in results than a chemical polishing. This is suggested to come from the dominance of surface defects over the internal stress concentrators for grinded specimen. Grinding being mechanically performed, the same defect size is expected on these specimen, leading to a tighter distribution. Chemical etching leads to results closer to the intrinsic strength of mc-Si silicon, limited by the amount and nature of internal defects in turn defined by the refining and solidification processes.

11.2 METHODOLOGY AND SAMPLE PREPARATION

11.2.1 *4-point bending tests description*

We used 4-point bending tests (4PBT) to characterize the flexural strength of mc-Si silicon. A schematic description of this method is presented in Figure 11.1. The mounted 4PB apparatus with a specimen ready for testing is shown in Figure 11.2. A force F is applied on the two upper rollers separated by a distance l. The external rollers have a span L. The deflection d is measured by three extensometers and is given with a precision of the order of the tenth of micrometer. This allows a precise determination of the Young's modulus of the specimen.

A 4PB apparatus creates a homogeneous moment in the specimen of thickness t and width w between the two internal rods. Fracture happens where the tensile stress is maximum, that is on the external, lower face of the specimen. In an isotropic homogeneous material the fracture probability is consequently the same on the external face between the outer rods. In mc-Si materials this is not true any longer, since any stress concentrator increases locally the stress level and the fracture probability. The inherent material anisotropy, enhanced by grain misorientation, complicates the picture further. As mentioned in the introduction, the aim of these experiments is not to determine what the *local* stress is at fracture, but rather at which level of *macroscopic* stress it does occur.

11.2.2 *Theoretical analysis*

Determination of Young's modulus

Analysis of the deformation of a rectangular-shaped bar loaded in a 4PB apparatus is done using the linear elasticity theory. Let us assume in addition that the material considered is homogeneous and isotropic. A bar having a moment of inertia along the z-axis I_z and made up of a material of Young's modulus E, submitted to a moment $M(x)$ will deform in pure bending (see Figure 11.3).

The displacement of the mid-fiber $v(x)$ along the y-axis is given by:

$$EI_z \frac{\mathrm{d}^2 v}{\mathrm{d}x^2} = -M(x) \tag{11.2}$$

The moment between the inner rollers in a 4PB apparatus is constant and equal to $M(x) = F(L-l)/2$ in this region. Integration of Eq. 11.2 gives two constants, one of which is determined by the condition that $\left.\frac{\mathrm{d}v}{\mathrm{d}x}\right|_{L/2} = 0$. This yields:

$$v(x) = \frac{1}{EI_z}\left(\frac{FL}{16}\left(x^2 - Lx\right) + C\right) \tag{11.3}$$

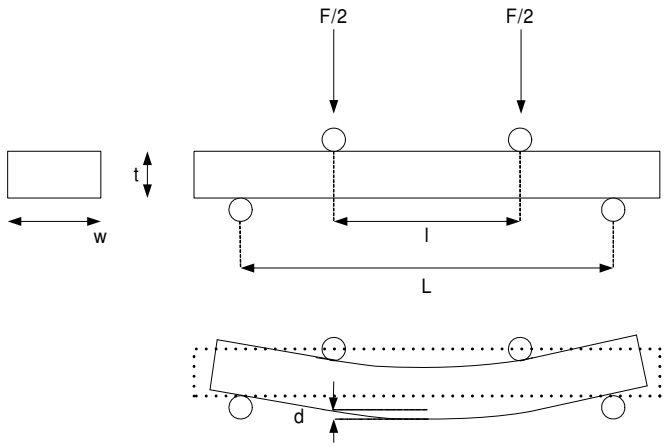

Figure 11.1: Schematic of the 4 point bending apparatus used in this work.

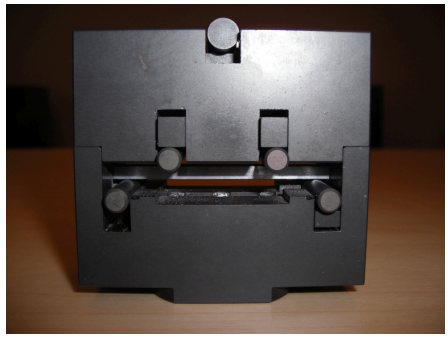

Figure 11.2: Mounted 4PB apparatus.

where the relationship $l = L/2$ has been used, and C is an integration constant. The experimental setup measures the deflection defined as the difference between $v(L/2)$ and $v(L/4)$:

$$d = v\left(\frac{L}{2}\right) - v\left(\frac{L}{4}\right) = \frac{FL^3}{256EI_z} \tag{11.4}$$

The moment of inertia of a rectangular bar of width w and thickness t is given by $I_z = wt^3/12$. We finally obtain:

$$d = \frac{3FL^3}{64Ewt^3} \tag{11.5}$$

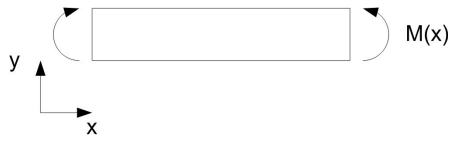

Figure 11.3: 4PB of a bar: definitions.

Recording F and d allows the determination of the Young's modulus E by inverting Eq. 11.5. The maximum stress in the sample is obtained using Eq. 11.6:

$$\sigma_{max} = \frac{3FL}{4wt^3} \tag{11.6}$$

Specimen strength

As mentioned in the introduction, no definite strength can be defined for brittle materials as fracture events follow the weakest link rule: the fracture probability varies with space as inclusions, grain misorientations and other defects lead to local stress concentrations in the material. Surface flaws such as microcracks might also play the role of stress concentrators and ease fracture. Once a crack opens at the weakest point complete fracture follows.

Given a stress level the probability of fracture depends on the amount, size and distribution of defects in the crystal. Weibull statistics allow a fairly good estimation of brittle fracture (see, e.g., [Lawn 1993]). The cumulative probability at a stress σ is:

$$P(\sigma) = 1 - \exp\left[-\left(\frac{\sigma}{\sigma_0}\right)^m\right] \tag{11.7}$$

with σ_0 a scaling stress and m the Weibull modulus. The fracture probability is given by:

$$f(\sigma) = \frac{\mathrm{d}P}{\mathrm{d}\sigma} = \frac{m\sigma^{m-1}}{\sigma_0^m} \exp\left[-\left(\frac{\sigma}{\sigma_0}\right)^m\right] \tag{11.8}$$

Weibull statistics predict a cumulative fracture probability of 66 % at the scaling stress σ_0, also called the Weibull stress. m and σ_0 are found by plotting $\ln\left[\ln\left(\frac{1}{1-P(\sigma)}\right)\right]$ vs $\ln(\sigma)$, the slope being m and the intersect $-m\ln(\sigma_0)$. A normal distribution can be adopted as well, although the Weibull approach traditionally yields better results for brittle materials. In this case, the relevant values are the average strength $\bar{\sigma}$ and its standard deviation α. The probability function reads then:

$$f(\sigma) = \frac{1}{\sqrt{2\pi}\alpha} \exp\left[-\frac{(\sigma-\bar{\sigma})^2}{2\alpha^2}\right] \tag{11.9}$$

11.2.3 *Specimen preparation*

Material provided by Elkem Solar

The ASTM standard C1211-98a [ASTM a] has been used to define sample size and surface state. Tracability has been kept of the location of the samples through the ingot. 100 bars of rectangular section and dimensions 4x3x50 mm have been cut, 61 of them have used for room-temperature testing. 30 bars have been etched with a CP4 solution for 60 seconds.

	Sample set 1: grinded	Sample set 2: grinded, CP_4 etched
Nr. of units	31	30
$R_a\ (\mu m)$	0.67	0.29

Table 11.1: Samples of Elkem Solar used for room temperature 4PB tests: amount and surface roughness.

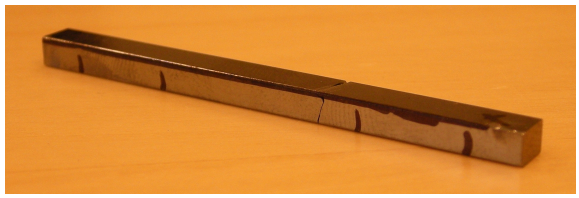

Figure 11.4: Etched specimen marked and tested. The vertical bars indicate the approximate position of the inner and external rollers and allow to validate the test.

This provides with two sets of samples of different surface qualities, see Table 11.1.

The surface roughness has been measured on one sample of each set, giving R_a values in the transversal direction of 0.76 μm for set 1 and 0.34 μm for set 2. Roughness in the longitudinal direction has been measured slightly lower than the transversal one, 0.67 and 0.29 μm respectively. No systematic roughness analysis has been done though, as the sole goal of roughness measurements has been to estimate the efficiency of the etching. Etching is seen to divide the roughness by a factor slightly larger than two.

The specimen have been marked at one corner to keep track of their orientation in the 4PB apparatus before breaking (see Figure 11.4). One edge has been marked black to ease reconstruction of specimen after fracture. The dimensions of the samples have been measured at both ends with an accuracy of 0.01 mm.

Material of SINTEF

A similar procedure has been adopted to prepare samples from a mc-Si block provided by SINTEF Materials & Chemistry. The block from which the samples have been cut was located in the middle part of a SoG-Si ingot cast at NTNU. A slightly different ASTM standard, C1161-02c [ASTM b], has been used to define the basic sample preparation[1]. The samples have been polished mechanically down to 1200μ before etching. This time, the effect of etching is seen to reduce the roughness by 75 % (see Table 11.2).

1 There is no significant difference between C1211 and C1161. The former is designed for high-temperature testing, while the latter is concerned with experiements performed at ambient temperatures. These standards differ solely by the roughness required after grinding (between 320 and 500 grit for C1211 and between 400 and 600 grit for C1161). C1211 gives naturally additional guidelines related to high temperature measurements.

	Sample set 1: grinded	Sample set 2: grinded, polished, CP_4 etched
Nr. of units	30	30
$R_a\ (\mu m)$	0.56	0.13

Table 11.2: Samples of SINTEF used for room temperature 4PB tests: amount and surface roughness.

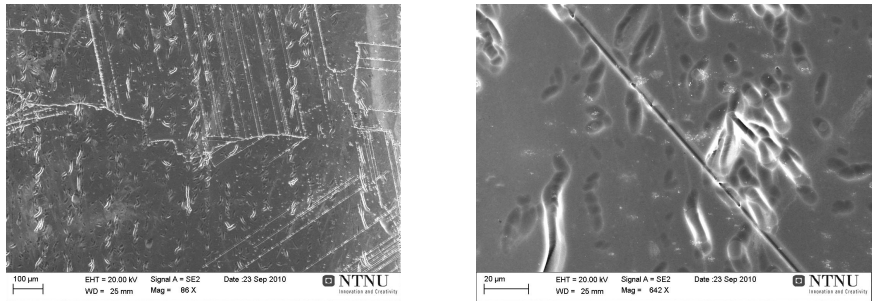

(a) Grain boundaries and remaining surface defects after CP_4 etching

(b) Close-up of remaining surface defects

Figure 11.5: SEM pictures of some surfaces after mechanical polishing and etching of samples from SINTEF.

The better surface state for this sample set is most certainly due to the better sample preparation prior to etching.

SEM pictures taken after mechanical polishing and etching (see Figure 11.5) show that traces from the grinding process are still left visible on some of the sample surfaces, as small ridges of low depth, but whose width has been increased by the etchant. Observation of polished samples under a light microscope reveals pointwise residual surface defects that ought to be at the origin of these ridges (see Figure 11.6). These shallow defects are not expected to play any significant role on the flexural strength of the samples as their depth and orientation relative to the loading direction are negligible compared to, e.g., microcracks and other stress concentrators.

Figure 11.6: Surface of a silicon bar after polishing seen through a light microscope. Some pointwise defects from the grinding process are still left.

11.3 EXPERIMENTAL

Specimen are numbered as follows: a letter identifying the material origin (E for ELKEM and S for SINTEF) followed by the sample number as provided by PREMATECH, the company that has been relied on to cut the specimen. Because of confidentiality agreements, only the experimental results of samples cut from the material of SINTEF are presented in the following.

11.3.1 *Experimental procedure*

The specimen are introduced in the 4PB apparatus and an initial load of maximum 1 N is applied. The rollers of the flexural apparatus are then checked to be parallel and correctly spaced. A constant velocity of 8.33 µm/s is then applied to the upper rollers, corresponding to the 0.5 mm/min recommended by the ASTM standard [ASTM a] to prevent any "slow crack growth" that could take place when testing ceramics. Slow crack growth is not a concern for silicon at room temperature, and any velocity could have been chosen. 8.33 µm/s has been taken for convenience.

The force-deflection data is recorded for extraction of the Young's modulus. The maximum applied force F_{max} is noted after fracture to calculate the sample strength with the help of Eq. 11.6. The samples are checked to have fractured between the inner rods. Upon difficulties to locate the crack initiation site the calculated sample strength is not accounted for in the statistical analysis.

11.3.2 *Results*

Young's modulus

The Young's modulus of a silicon monocrystal depends on its orientation because of the intrinsic anisotropy of the silicon lattice. Its lower and upper values are roughly 130 and 190 GPa respectively at room temperature [Wortman 1965]. In the case of multicrystals the overall Young's modulus is defined as the average of those of its constituent grains if their number is large enough. However, this is not the case of the specimen used in this study as their size usually limits the amount of grains in the transversal direction to a couple of units. The measured Young's modulus is therefore dictated by the one of the largest grain present between the inner rods.

This results in a distribution of the Young's modulus that depends on factors such as the sample location in the ingot and orientation with respect to the casting direction, preferred grain growth orientation, etc. It must be kept in mind that the measured Young's modulus corresponds to the one in the *transverse* direction of the grain growth. The Young's modulus of each sample k is determined using the derivative of the force-deflection slope:

$$E_k = \frac{3L^3}{64 w_k t_k^3} \left(\frac{\Delta F}{\Delta d} \right)_k \tag{11.10}$$

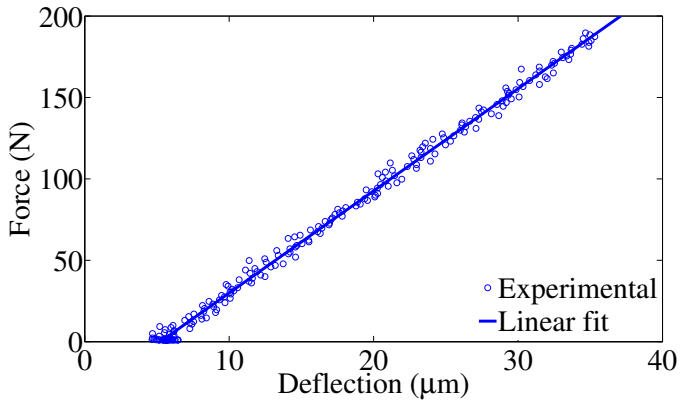

Figure 11.7: Example of force-deflection curve recorded during a 4PB test at room temperature up to fracture. Sample nr. S138: $E_{138} = 152\,\text{GPa}$, $\sigma_{max} = 150.5\,\text{MPa}$.

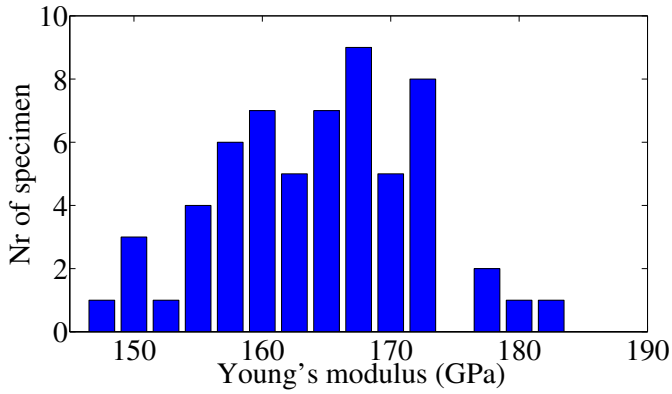

Figure 11.8: Distribution of the Young's moduli of the samples cut from the SINTEF mc-Si ingot.

where w_k and t_k are the average width and thickness of the sample k, respectively. The complete list of Young's moduli for each sample coming from SINTEF is given in Annex D. An example of recorded force-deflection curve used to derive E is shown in Figure 11.7. A distribution of the moduli of SINTEF silicon is shown in Figure 11.8: the average $\overline{E}$ is 166 GPa, with a standard deviation of 7.6 GPa. This falls well into the 130 to 190 GPa range mentioned earlier.

Flexural strength of grinded specimen

Specimen often broke at two or more different places, the elastic wave propagated by the first crack opening leading to secondary crack generally close to an inner roller. The higher the elastic energy stored at fracture (i.e.

Figure 11.9: Example of discarded sample, in which fracture took place too close from an inner roller (whose position is approximated by a vertical bar).

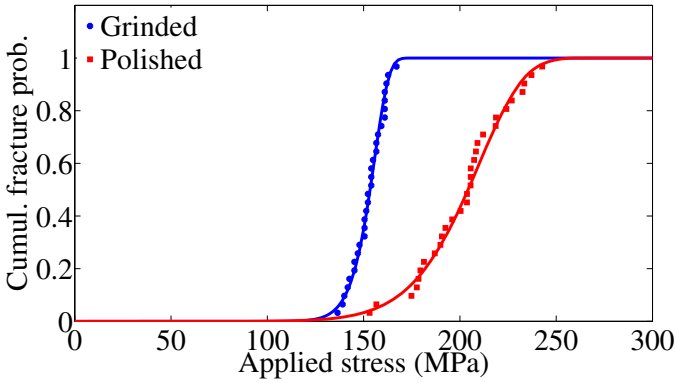

Figure 11.10: Experimentally measured cumulative fracture probability and approximations using the Weibull theory for SINTEF samples.

the higher the force fracture occurs at), the more the samples tend to break into numerous pieces. Fig. 11.9 shows an example of sample discarded for determination of the flexural strength, as fracture took place too close from an inner roller.

The average strength and standard deviation of the flexural strength of grinded specimen are:

$$\begin{cases} \overline{\sigma}_{gr} = 152\,\text{MPa} \\ \alpha_{gr} = 7.85\,\text{MPa} \end{cases} \tag{11.11}$$

The strength distribution shown in Fig. 11.10 is best fitted by setting the Weibull parameters as:

$$\begin{cases} \sigma_{0,gr} = 156\,\text{MPa} \\ m_{gr} = 21.5 \end{cases} \tag{11.12}$$

Flexural strength of chemically polished specimen

Chemical polishing smoothens the surface defects and leads to a much better surface quality. As a result, the dominance of surface flaws on the fracture behavior is reduced and the mechanical behavior of etched samples is believed to be more representative of the intrinsic properties of the material studied. The Weibull parameters are obviously affected by chemical

polishing, the scaling stress increasing by 30 % and m being more than halved:

$$\begin{cases} \overline{\sigma}_{et} = 202\,\text{MPa} \\ \alpha_{et} = 22.5\,\text{MPa} \end{cases} \tag{11.13}$$

The strength distribution shown in Fig. 11.10 is best fitted by setting the Weibull parameters as:

$$\begin{cases} \sigma_{0,et} = 212\,\text{MPa} \\ m_{et} = 9.82 \end{cases} \tag{11.14}$$

11.3.3 *Discussion: effect of surface treatment on the strength of SoG-Si*

Comparison of the experimental results exposed above gives interesting results. The average strength (or scaling stress) of the samples from batch 1 increases when chemically polished. This means that the dominant flaws leading to fracture of *grinded* specimen are located on the surface. The low dispersion of the results translates the homogeneity of the surface defects induced by the grinder: the large Weibull parameter m (or low strength deviation) indicates that the defects governing fracture have the same properties. This results in a material with predictable fracture properties. Internal defects play little role in the probability of fracture of grinded specimen at room temperature.

On the other hand, chemical etching removes the grinding traces and shifts the weakest link determining fracture from the sample surface to their inner part. This is translated by a heightened value of the Weibull stress. The lower Weibull modulus reveals instead a more random distribution of defects in the samples, much larger than the dispersion of the surface defect size left by grinding.

From an engineering point of view, grinded samples might be preferred because of the higher concentration of the strength around its average (or equivalently, of the fracture probability around the Weibull stress). Their lower strength can however be detrimental. The etched samples are believed to be more representative of the real strength of SoG-Si. The large result dispersion likely betrays large variations of defect density such as inclusions in the solidified ingots. The material strength is bound to vary with the position of the sample in the ingot, as it is known that defect density varies in space in directionally solidified mc-Si materials. Process parameters might also have an influence on the inclusion distribution, type and density. Given the small amount of samples tested in this study and the different surface qualities, there is no point in trying to map the strength over the mc-Si block and defining "weak" and "strong" regions. Such an analysis would require all samples to be chemically polished.

11.4 CONCLUSION

11.4.1 *Experimental results*

The Young's modulus of Solar-grade multicrystalline silicon material produced by SINTEF has been determined and is shown to depend on the specimen. This is due to the anisotropy of the multicrystalline bars stemming from the low amount of grains in the stressed region and their *a priori* random relative crystallographic orientation after solidification of the silicon ingot. The Young's modulus in the transversal direction of the grains seems however to follow a normal distribution centered on 166 GPa with a standard deviation of 7.6 GPa. The Young's modulus in the crystal growth direction has not been determined.

Statistical analysis of the fracture strength of two types of specimen having received different surface treatments shows that mechanical grinding alone leads to weaker specimen of Weibull stress 156 MPa, but evens the defect size at their surface, leading to a high Weibull modulus of 21.5. Chemically etched specimen exhibit a much larger strength at 212 MPa, but the results are more spread, as translated by a low Weibull modulus of 9.82. The latter specimen are thought to be more representative of the intrinsic behavior of SoG-Si multicrystals. More than 30 etched samples could have been tested to guarantee the accuracy of the cumulative probability distribution, as multiple flaw types are expected in SoG-Si (inclusion types and shapes, grain size and misorientation, microcracks, etc.).

11.4.2 *Implementation into a constitutive model*

The $P(\sigma)$ function as derived in this Chapter for etched specimen, assumed to represent the behavior of bulk material, can be interpreted as follows: *a macroscopically applied stress σ leads a local stress increase due to the material flaws nature and distribution, which in turn results in brittle fracture with a probability $P(\sigma)$*. Or equivalently, the likelihood of sample breakage at an applied stress σ is $P(\sigma)$.

Insertion of the results derived in this Chapter into any constitutive model based on RDCP is relatively straightforward. Using Eq. 11.1, the normal stresses are extracted on each of the 4 slip planes of the diamond cubic lattice. The maximum absolute value is then selected and $P(\tau_{\perp}^{(max)})$ is computed with the help of the Weibull parameters derived for etched specimen.

Adopting this methodology to assess fracture probability allows us to skip the local, microscopic representation of the material flaws leading to material breakage. This allows a mapping of the fracture probabilty distribution througout a given specimen. Examples of applications are given in the next Part.

CONCLUSION

NUMERICAL ASPECTS

This Part has concentrated on the derivation of a new and original constitutive model for silicon monocrystals. Entirely physically-based, its basic constitutive equations differ slighty from the extended AH model introduced in Part ii, with the addition of dislocation multiplication from forest trees.

Its fundamental difference lies in the dislocation velocity law, enriched to account for the possible effect of jog dragging on dislocations of random orientation. This requires in turn the derivation of differential equations for the evolution of the jog densities. The application of such a model to silicon is done by distinguishing between screw and 60° dislocation segments, following similar constitutive laws but with different constitutive parameters.

Table 11.3 gives a quick overview of the model pros and cons.

The following insights have been gained from the study of the model outputs:

- Localized obstacles seem to have a very limited effect on the mean dislocation velocity at the standard forest densities encountered in semiconductors, as opposed to the conventional case of f.c.c. crystals
- The experimentally observed stress overshoot and subsequent strong hardening in stage II of [123] tensile specimen is very likely due to jog dragging and cannot be reproduced otherwise

	Asset	Limitation
Kinematics	powerful	
Cost		expensive
Yield region	very good	double yieldings
Stage I	steady-state	
Multiple slip	yes	ordering of τ_{uy}
Extrinsic crystals	very good	double yieldings
Physical basis	yes	cost
Parameters	closed-form	

Table 11.3: Overview of the abilities of the model introduced in this Part.

- The experimental hardening rate in specimen initially oriented for multiple slip can be reproduced without accounting for jog dragging, provided enough slip systems are activated
- Deriving capture radii for dislocation storage and annihilation on physical arguments yields very satisfying results, with regards to the steady state of deformation and the evolution of individual dislocation densities, in agreement with experimental observations
- Self-multiplication laws K_1 traditionally used to model the yield region of intrinsic semiconductors systematically fail to reproduce quantitatively the variations of the upper yield stress at various initial dislocation contents
- When used in conjunction with dislocation generation from the forest trees, such laws often lead to a double yielding phenomena at high strain rates or very low temperatures
- The variations of the upper yield stress with the specimen orientation at constant temperature and strain rate are almost entirely due to the self-multiplication law K_1

Further work on constitutive models for silicon should therefore concentrate on three aspects:

1. Derive a multiplication law K_1 able to reproduce the yield region both at various strain rates and temperatures, but also at various initial dislocation densities and initial specimen orientation. A potential way of improving the model results is to consider an increase of dislocation sources with the build-up of the immobile density
2. Identify jog evolution laws that could lead to a better fit of the strain overshoot in various conditions on the one hand, and to a correct hardening rate in all situations on the other
3. Find a solution to stabilize the model at the transition between stage I and II, and to relieve the need for remeshing that increases significantly the computational cost.

INSERTION OF EXPERIMENTAL RESULTS

Relying on a powerful crystal plasticity framework for the implementation of the constitutive equations into a finite element software allows the incorporation of the experimentally derived cumulative fracture probability $P(\sigma)$ of SoG-Si materials.

The method used in this work relies on the derivation of $P(\sigma)$ from 4-point bending tests of multicrystalline SoG-Si bars at room temperature. A direct drawback is that the results do not give the *local* stress peak leading to fracture, but only the macroscopic one that could be derived assuming

the specimen to be homogeneous and isotropic. Consequently, further work is required to understand the local stress variations in mc-Si materials when subjected to a macroscopic force.

Simulations of various loading cases in the following Part give quantitative estimates of these local variations due either to the multicrystalline structure of the samples, or to the presence of inclusions in the silicon matrix.

BIBLIOGRAPHY

[Alexander 1968] *Dislocations and plastic flow in the diamond structure*, H. Alexander, P. Haasen, Solid State Physics, Vol. 22, pp. 27-158, 1968

[Alexander 2000] *Latent hardening of germanium crystals*, H. Alexander, J.L. Crawford, Physica Status Solidi (b), Vol. 222, No. 1, pp. 41-49, 2000

[Amirkhizi 2007] *A framework for numerical integration of crystal elasto-plastic constitutive equations compatible with explicit finite element codes*, A.V. Amirkhizi, S. Nemat-Nasser, International Journal of Plasticity, Vol. 23, pp. 1918-1937, 2007

[Arsenlis 2002] *Modeling the evolution of crystallographic dislocation density in crystal plasticity*, A. Arsenlis, D.M. Parks, Journal of the Mechanics and Physics of Solids, Vol. 50, pp. 1979-2009, 2002

[Asaro 1983] *Crystal plasticity*, R.J. Asaro, Journal of Applied Physics, Vol. 50, pp. 921-934, 1983

[ASTM a] *C1211-98a: Standard test method for flexural strength of advanced ceramics at elevated temperatures*, ASTM International, 1998

[ASTM b] *C1161-02c (reapproved 2008): Standard test method for flexural strength of advanced ceramics at ambient temperatures*, ASTM International, 2008

[Baufeld 1998] *Transition of mechanisms controlling the dislocation motion in cubic ZrO_2 below 700°C*, B. Baufeld, B.V. Petukhov, M. Bartsch, U. Messerschmidt, Acta Materialia, Vol. 46, No. 9, pp. 3077-3085, 1998

[Berner 1967] *Dislocation density and local slip in germanium single crystals*, K. Berner, H. Alexander, Acta Metallurgica, Vol. 15, No. 5, pp. 933-941, 1967

[Bulatov 2001] *Parameter-free modeling of dislocation motion: the case of silicon*, V.V. Bulatov, J.F. Justo, W. Cai, S. Yip, A.S. Argon, T. Lenosky, M. De Koning, T. Diaz de la Rubia, Philosophical Magazine A, Vol. 81, No. 5, pp. 1257-1281, 2001

[Burenkov 1974] *Temperature dependence of elastic constants in silicon*, Y.A. Burenkov, S.P. Nikaronov, Soviet Physics of Solid State, Vol. 16, No. 5, pp. 963-964, 1974

[Caillard 2003] *Thermally activated mechanisms in crystal plasticity*, D. Caillard, J.-L. Martin (ed. R.W. Cahn), Pergamon Materials Series, Pergamon, 2003

[Celli 1963] *Theory of dislocation mobility in semiconductors*, V. Celli, M. Kabler, T. Ninomiya, R. Thomson, Physical Review, Vol. 131, No. 1, pp. 58-72, 1963

[Chaudhri 1972] *Creep of germanium*, G. Chaudhri, P. Feltham, Journal of Materials Science, Vol. 7, pp. 1161-1167, 1972

[Cheong 2004] *Discrete dislocation density modelling of single phase FCC polycrystal aggregates*, K.-S. Cheong, E.P. Busso, Acta Materialia, Vol. 52, pp. 5665-5675, 2004-

[Choudhury 2010] *Molecular dynamics studies of the dissociated screw dislocation in silicon*, R. Choudhury, C. Gattinoni, G. Makov, A. De Vita, Journal of Physics: Condensed Matter, Vol. 22, pp. 074210-1/8, 2010

[Cochard 2010a] *Constitutive modeling of silicon monocrystals in single glide*, J. Cochard, I. Yonenaga, S. Gouttebroze, M. M'Hamdi, Z.L. Zhang, Journal of Applied Physics, Vol. 107, No. 3, pp. 033512-033520, 2010

[Cochard 2010b] *Constitutive modeling of intrinsic and oxygen-contaminated silicon monocrystals in easy glide*, J. Cochard, I. Yonenaga, S. Gouttebroze, M. M'Hamdi, Z.L. Zhang, Journal of Applied Physics, Vol. 108, No. 10, pp. 103524, 2010

[Cuitiño 1997] *A time-dependent deformation mechanism in metallic f.c.c. crystals*, A.M. Cuitiño, Acta Materialia, Vol. 45, No. 6, pp. 2509-2522, 1997

[Dash 1956] *Copper precipitation on dislocations in silicon*, W.C. Dash, Journal of Applied Physics, Vol. 27, No. 10, pp. 1193-1195, 1956

[De Araujo 2004] *Electronic charge effects on dislocation cores in silicon*, M.M. De Araujo, J.F. Justo, R.W. Nunes, Applied Physics Letters, Vol. 85, No. 23, pp. 5610-5612, 2004

[Devincre 2006] *Physical analyses of crystal plasticity by DD simulations*, B. Devincre, L. Kubin, T. Hoc, Scripta Materialia, Vol. 54, pp. 741-746, 2006

[Devincre 2007] *Collinear superjogs and the low-stress response of fcc crystals*, B. Devincre, L. Kubin, T. Hoc, Scripta Materialia, Vol. 57, pp. 905-908, 2007

[Dolling 1966] *The thermodynamic and optical properties of germanium, silicon, diamond and gallium arsenide*, G. Dolling, R.A. Cowley, Proceedings of the Physical Society, Vol. 88, pp. 463-494, 1966

[Dour 2002] *Dislocation motion in crystals with a high Peierls relief: a unified model incorporating the lattice friction and localized obstacles*, G. Dour, Y. Estrin, Journal of Engineering Materials and Technology, Vol. 124, No. 1, pp. 7-12, 2002

[Estrin 1986] *Local strain hardening and nonuniformity of plastic deformation*, Y. Estrin, L.P. Kubin, Acta Metallurgica, Vol. 34, No. 12, pp. 2455-2464, 1986

[Farber 1982] *Change of dislocation mobility characteristics in Si single crystals at elevated temperatures*, B.Ya Farber, V.I. Nikitenko, Physica Status Solidi (a), Vol. 73, pp. K141-143, 1982

[Farber 1993] *Barriers for the kink motion on dislocations in Si*, B.Ya Farber, Y.L. Iunin, V.I. Nikitenko, V.I. Orlov, H. Alexander, H. Gottschalk, P. Specht, Physica Status Solidi (a), Vol. 138, pp. 557-571, 1993

[Franciosi 1982] *Multislip in FCC crystals: a theoretical approach compared to experimental data*, P. Franciosi, A. Zaoui, Acta Metallurgica, Vol. 30, pp. 1627-1637, 1982

[Friedel 1974] *Dislocations*, J. Friedel, Pergamon Press, New York, 1974

[George 1972] *Velocities of screws and 60°dislocations in silicon*, A. George, C. Escaravage, G. Champier, W. Schröter, Physica Status Solidi (b), Vol. 53, No. 2, pp. 483-496, 1972

[George 1979] *Measurements of the dislocation velocities in silicon*, A. George, Journal de Physique Colloque, Vol. 40, No. 6, pp. C6/133-137, 1979

[George 1987a] *Dislocations and plasticity in semiconductors. I. Dislocation structures and dynamics*, A. George, J. Rabier, Revue de physique appliquée: supplément au Journal de Physique, Vol. 22, No. 9, pp. 941-966, 1987

[George 1987b] *Dislocations and plasticity in semiconductors. II. Relation between dislocation dynamics and plastic deformation*, A. George, Revue de physique appliquée: supplément au Journal de Physique, Vol. 22, No. 11, pp. 1327-1351, 1987

[Gottschalk 1983a] *Dislocation bends in high stress deformed silicon crystals*, H. Gottschalk, Journal de Physique Colloque, Vol. 44, No. 9, pp. C4/69-74, 1983

[Gottschalk 1983b] *On the motion of dislocation bends in terms of the kink model*, H. Gottschalk, Journal de Physique Colloque, Vol. 44, No. 9, pp. C4/475-477, 1983

[Gottschalk 1993] *Constricted dislocations and their use from TEM measurements of the velocities of edge and 60°dislocations in silicon*, H. Gottschalk, N. Hiller, S. Sauerland, P. Specht, H. Alexander, Physica Status Solidi (a), Vol. 138, pp. 547-555, 1993

[Harder 1999] *A crystallographic model for the study of local deformation processes in polycrystals*, J. Harder, International Journal of Plasticity, Vol. 15, pp. 605-624, 1999

[Hähner 1996] *The dynamics of dislocation dipoles during single glide*, P. Hähner, Scripta Materialia, Vol. 34, No. 3, pp. 435-441, 1996

[Heggie 1991] *Interaction of impurities with dislocation cores in silicon*, M. Heggie, R. Jones, A. Umerski, Philosophical Magazine A, Vol. 63, No. 3, pp. 571-584, 1991

[Hiratani 2001] *Combined model of dislocation motion with thermally activated and drag-dependent stages*, M. Hiratani, E.M. Nadgorny, Acta Materialia, Vol. 49, No. 20, pp. 4337-7346, 2001

[Hirsch 1981] *Relaxation of dislocations in deformed silicon*, P.B. Hirsch, A. Ourmazd, P. Pirouz, Proceedings of the 2nd Oxford Conference on Microscopy of Semiconducting Materials, pp. 29-34, 1981

[Hirth 1982] *Theory of Dislocations (2nd edition)*, J.P. Hirth, J. Lothe, Wiley, New York, 1982

[Hoc 2004] *Deformation stage I of FCC crystals: constitutive modelling*, T. Hoc, B. Devincre, L.P. Kubin, in Proceedings of the 25th Rise International Symposium on Materials Science, Gundlach et al. (eds.), pp. 43-59, 2004

[George 1999] A. George, in *Properties of crystalline silicon*, R. Hull (ed.), pp. 89-148, 1999

[Imai 1983] *In situ X-ray topographic study of the dislocation mobility in high-purity and impurity-doped silicon crystals*, M. Imai, K. Sumino, Philosophical Magazine A, Vol. 47, No. 4, pp. 599-621, 1983

[Jin 2010] *Computing transition rates of thermally activated events in dislocation dynamics*, C. Jin, W. Ren, Y. Xiang, Scripta Materialia, Vol. 62, pp. 206-209, 2010

[Jäger-Waldau 2010] *PV Status Report 2010: Research, Solar Cell Production and Market Implementation of Photovoltaics*, A. Jäger-Waldau, European Commission, DG Research Center, 2010

[Kalidindi 1994] *Macroscopic shape change and evolution of crystallographic texture in pre-texured fcc metals*, S.R. Kalidindi, L. Anand, Journal of the Mechanics and Physics of Solids, Vol. 42, No. 3, pp. 459-490, 1994

[Kalidindi 1998] *Incorporation of deformation twinning in crystal plasticity models*, S.R. KALIDINDI, Journal of the Mechanics and Physics of Solids, Vol. 46, No. 2, pp. 267-290, 1998

[Karthikeyan 2004] *Evaluation of the jogged-screw model of creep in equiaxed γ-TiAl: identification of the key substructural parameters*, S. KARTHIKEYAN, G.B. VISWANATHAN, M.J. MILLS, Acta Materialia, Vol. 52, No. 9, pp. 2577-2589, 2004

[Kocks 1975] *Thermodynamics and kinetics of slip*, U.F. KOCKS, A.S. ARGON, M.F. ASHBY, Progress in Materials Science, Vol. 19, 1975

[Kocks 2003] *Physics and phenomenology of strain hardening: the FCC case*, U.F. KOCKS, H. MECKING, Progress in Materials Science, Vol. 48, pp. 171-273, 2003

[Kojima 1971] *Strain-rate and temperature dependence of mechanical behaviour in germanium crystals*, K.I. KOJIMA, K. SUMINO, Crystal Lattice Defects, Vol. 2, No. 3, pp. 147-158, 1971

[Kolar 1996] *Observation of moving dislocation kinks and unpinning*, H.R. KOLAR, J.C.H. SPENCE, H. ALEXANDER, Physical Review Letters, Vol. 77, No. 19, pp. 4031-4034, 1996

[Kothari 1998] *Elasto-viscoplastic constitutive equations for polycrystalline metals: application to tantalum*, M. KOTHARI, L. ANAND, Journal of the Mechanics and Physics of Solids, Vol. 46, No. 1, pp. 51-83, 1998

[Kubin 2008a] *Toward a physical model for strain hardening in fcc crystals*, L. KUBIN, B. DEVINCRE, T. HOC, Materials Science and Engineering A, Vols. 483-484, No. 1, pp. 19-24, 2008

[Kubin 2008b] *Modeling dislocation storage rates and mean free paths in face-centered cubic crystals*, L. KUBIN, B. DEVINCRE, T. HOC, Acta Materialia, Vol. 56, pp. 6040-6049, 2008

[Lawn 1993] *Fracture of brittle solids - Second edition*, B. LAWN, Cambridge Solid State Science Series, Cambrigde University Press, Cambridge, 1993

[Lee 1969] *Elastic-plastic deformation at finite strains*, E.H. LEE, Journal of Applied Mechanics, Vol. 36, No. 1, pp. 1-6, 1969

[Li 2008] *A robust integration algorithm for implementing rate dependent crystal plasticity into explicit finite element method*, H.W. LI, H. YANG, Z.C. SUN, International Journal of Plasticity, Vol. 24, pp. 267-288, 2008

[Louchet 1981] *On the mobility of dislocations in silicon by in-situ straining in a high-voltage electron microscope*, F. LOUCHET, Philosophical Magazine A, Vol. 43, No. 5, pp. 1289-1297, 1981

[Madec 2003] *The role of collinear interaction in dislocation-induced hardening*, R. Madec, B. Devincre, L. Kubin, T. Hoc, D. Rodney, Science, Vol. 301, pp. 1879-1882, 2003

[Maeda 1989] *Kink formation and migration in covalent crystals*, K. Maeda, Y. Yamashita, Proceedings of the 6th International Symposium on Structure and Properties of Dislocations in Semiconductors, pp. 269-280, 1989

[Maroudas 1991a] *Model for dislocation locking by oxygen gettering in silicon crystals*, D. Maroudas, R.A. Brown, Applied Physics Letters, Vol. 58, No. 17, pp. 1842-1844, 1991

[Maroudas 1991b] *Constitutive modeling of the effects of oxygen on the deformation behavior of silicon*, D. Maroudas, R.A. Brown, Journals of Materials Research, Vol. 6, No. 11, pp. 2337-2352, 1991

[Maroudas 1991c] *Constitutive modeling of the effects of oxygen on the deformation behavior of silicon*, D. Maroudas, R.A. Brown, Journal of Materials Research, Vol. 6, No. 11, pp. 2337-2352, 1991

[Mecking 1981] *Kinetics of flow and strain-hardening*, H. Mecking, U.F. Kocks, Acta Metallurgica, Vol. 29, pp. 1865-1875, 1981

[Meissonnier 2001] *Finite element implementation of a generalized non-local rate-dependent crystallographic formulation for finite strains*, F.T. Meissonnier, E.P. Busso, N.P. O'Dowd, International Journal of Plasticity, Vol. 17, pp. 601-640, 2001

[Messerschmidt 1970] *Model of the temperature dependent part of stage I workhardening due to jog-dragging*, U. Messerschmidt, Physica Status Solidi, Vol. 41, No. 2, pp. 549-63, 1970

[Messerschmidt 1971] *Model of the temperature dependent part of stage I workhardening due to jog-dragging (II)*, U. Messerschmidt, Physica Status Solidi B, Vol. 48, No. 2, pp. 781-790, 1971

[Messerschmidt 2010] *Dislocation dynamics during plastic deformation*, U. Messerschmidt, Springer Series in Materials Science, Vol. 129, Springer, 2010

[Michel 1982] *Plastic deformation and surface investigations of <100> oriented silicon single crystals*, J.P. Michel, M. Omri, A. Oueldennaoua, A. George, Scripta Metallurgica, Vol. 16, pp. 677-682, 1982

[Mikkelsen 1985] *Diffusivity and solubility of oxygen in silicon*, J.C. Mikkelsen Jr., S.J. Pearton, J.W. Corbet, S.J. Pennycook, Materials Research Society, Proceedings of the Oxygen, Carbon, Hydrogen and Nitrogen in Crystalline Silicon conference, Boston, MA, USA, 1985 (Mater. Res. Soc, Pittsburgh, PA, USA), p. 19.

[Milevskii 1977] *Mechanism of dislocation motion in crystals having the diamond structure*, L.S. MILEVSKII, L. SMOLSKII, Soviet Physics of Solid State, Vol. 19, No. 5, pp. 772-774, 1977

[Miranda 2003] *Temperature effects on dislocation core energies in silicon and germanium*, C.R. MIRANDA, R.W. NUNES, A. ANTONELLI, Physical Review B, Vol. 67, No. 23, pp. 235201-1/8, 2003

[Moulin 1997] *Etude de la plasticité du silicium à une échelle mésoscopique par simulation numérique tridimensionnelle*, A. MOULIN, Ph.D. Thesis, Université Paris XI, 1997

[Moulin 1999] *Mesoscale modelling of the yield point properties of silicon crystals*, A. MOULIN, M. CONDAT, L.P. KUBIN, Acta Materialia, Vol. 47, No. 10, pp. 2879-2888, 1999

[Murphy 2006] *Oxygen transport in Czochralski silicon investigated by dislocation locking experiments*, J.D. MURPHY, S. SENKADER, R.J. FALSTER, P.R. WILSHAW, Materials Science and Engineering B, Vol. 134, pp. 176-184, 2006

[Musienko 2007] *Three-dimensional finite element simulation of a polycrystalline copper specimen*, A. MUSIENKO, A. TATSCHL, K. SCHMIDEGG, O. KOLEDNIK, R. PIPPAN, G. CAILLETAUD, Acta Materialia, Vol. 55, No. 12, pp. 4121-4136, 2007

[Möller 1978] *The movement of dissociated dislocations in the diamond-cubic structure*, H.J. MÖLLER, Acta Metallurgica, Vol. 26, No. 6, pp. 963-973, 1978

[Möller 1979] *Cross slip of single dissociated screw dislocations in silicon and germanium*, H.J. MÖLLER, H. EWALDT, P. HAASEN, Physica Status Solidi (a), 1979

[Nagdornyi 1988] *Dislocation dynamics and mechanical properties of crystals*, E.M. NAGDORNYI, Progress in Materials Science, Vol. 31, pp. 1-530, 1988

[Nemat-Nasser 2004] *Plasticity: a treatise on finite deformation of heterogeneous inelastic materials*, S. NEMAT-NASSER, Cambridge Monographs on Mechanics, Cambridge University Press, Cambridge, UK, 2004

[Nikitenko 1984] *Asymmetry of isolated dislocation mobility in silicon single crystals*, V.I. NIKITENKO, B.YA FARBER, E.B. YAKIMOV, Crystal Research and Technology, Vol. 19, No. 3, pp. 295-302, 1984

[Nunes 1998] *Atomic structure of dislocation kinks in silicon*, R.W. NUNES, J. BENNETTO, D. VENDERBILT, Physical Review B, Vol. 57, No. 17, pp. 10388-10397, 1998

[Omri 1987] *On the yield point of floating-zone silicon single crystals. I. Yield stresses and activation parameters*, M. Omri, C. Tete, J.-P. Michel, A. George, Philosophical Magazine A, Vol. 55, No. 5, pp. 601-616, 1987

[Oueldennaoua 1988] *On the yield point of floating-zone silicon single crystals. II. A quantitative analysis of the dislocation structure at the lower yield point*, A. Oueldennaoua, R. Allem, A. George, J.-P. Michel, Philosophical Magazine A, Vol. 57, No. 1, pp. 51-77, 1988

[Patel 1963] *Macroscopic plastic properties of dislocation-free germanium and other semiconductor crystals. I. Yield behavior*, J.R. Patel, A.R. Chaudhuri, Journal of Applied Physics, Vol. 34, No. 9, pp. 2788-2799, 1963

[Petukhov 1990] *The threshold for dislocation motion in impure semiconductors*, B.V. Petukhov, Soviet Physics: Technical Physics, Vol. 35, No. 10, pp. 1150-1153, 1990

[Petukhov 2003] *Different types of dislocation dynamics resulting from the dynamic aging of dislocations*, B.V. Petukhov, Technical Physics, Vol. 48, No. 7, pp. 880-884, 2003

[Petukhov 2004] *A theory of the effect of impurities on the yield stress of silicon crystals*, B.V. Petukhov, Semiconductors, Vol. 38, No. 4, pp. 369-375, 2004

[Rauch 1994] *The relation between forest dislocations and stress in BCC metals*, E.F. Rauch, Key Engineering Materials, Vols. 97-98, pp. 371-376, 1994

[Senkader 2001] *Oxygen-dislocation interactions in silicon below 700°C: dislocation locking and oxygen diffusion*, S. Senkader, P.R. Wilshaw, Journal of Applied Physics, Vol. 89, No. 9, pp. 4803-4808, 2001

[Senkader 2002] *On the dislocation-oxygen interactions in Czochralski-grown Si: oxygen diffusion and binding at low temperatures*, S. Senkader, A. Giannattasio, R.J. Falster, P.R. Wilshaw, Journal of Physics: Condensed Matter, Vol. 14, pp. 13141-13145, 2002

[Senkader 2004] *Dislocation locking in silicon by oxygen and oxygen transport at low temperatures*, S. Senkader, A. Giannattasio, R.J. Falster, P.R. Wilshaw, Solid State Phenomena, Vols. 95-96, pp. 43-52, 2004

[Shimizu 2007] *Experimental evidence of the vacancy-mediated silicon self-diffusion in single-crystalline silicon*, Y. Shimizu, M. Uematsu, K.M. Itoh, Physical Review Letters, Vol. 98, pp. 095901-1/4, 2007

[Siethoff 1969] *Yield points of Si and Si-Ge solutions*, H. Siethoff, Materials Science and Engineering, Vol. 4, Nos. 2-3, pp. 155-162, 1969

[Siethoff 1992] *The yield point of as-grown and pre-deformed semiconductors*, H. Siethoff, Philosophical Magazine Letters, Vol. 66, No. 1, pp. 1-7, 1992

[Siethoff 1999] *A regime of the yield point of silicon at high temperatures*, H. SIETHOFF, H.G. BRION, W. SCHRÖTER, Applied Physics Letters, Vol. 75, No. 9, 1234-1236, 1999

[Siethoff 2002] *Yield point and dislocation velocity of diamond and zincblende semiconductors in different temperature regimes*, H. SIETHOFF, Philosophical Magazine A, Vol. 82, No. 7, pp. 1299-1316, 2002

[Stainier 2002] *A micromechanical model of hardening, rate sensitivity and thermal softening in bcc single crystals*, L. STAINIER, A.M. CUITIÑO, M. ORTIZ, Journal of the Mechanics and Physics of Solids, Vol. 50, pp. 1511-1545, 2002

[Suezawa 1979] *Dislocation dynamics in the plastic deformation of silicon crystals. II. Theoretical analysis of experimental results*, M. SUEZAWA, K. SUMINO, I. YONENAGA, Physica Status Solidi (a), Vol. 51, pp. 217-226, 1979

[Sumino 1971] *Microdynamics of dislocations in plastic deformation of germanium crystals*, K. SUMINO, K.I. KOJIMA, Crystal Lattice Defects, Vol. 2, No. 3, pp. 159-170, 1971

[Sumino 1974a] *Dynamical state of dislocations in germanium crystals during deformation*, K. SUMINO, S. KODAKA, K.I. KOJIMA, Materials Science and Engineering, Vol. 13, No. 3, pp. 263-268, 1974

[Sumino 1974b] *A model for the dynamical state of dislocations in crystals during deformation*, K. SUMINO, Materials Science and Engineering, Vol. 13, No. 3, pp. 269-275, 1974

[Sumino 1993] *Dislocation dynamics and mechanical behavior of elemental and compound semiconductors*, K. SUMINO, I. YONENAGA, Physica Status Solidi (a), Vol. 138, pp. 573-581, 1993

[Sumino 1999] *Impurity reaction with dislocations in semiconductors*, K. SUMINO, Physica Status Solidi (a), Vol. 171, pp. 111-122, 1999

[Vallino 2001] *Dislocation multiplication during the very first stages of plastic deformation in silicon observed by X-ray topography*, F. VALLINO, J.P. CHÂTEAU, A. JACQUES, A. GEORGE, Materials Science and Engineering A, Vols. 319-321, pp. 152-155, 2001

[Wortman 1965] *Young's modulus, shear modulus, and Poisson's ratio in silicon and germanium*, J.J. WORTMAN, R.A. EVANS, Journal of Applied Physics, Vol. 36, No. 1, 1965

[Yamashita 1993] *Dislocation glide motion in heteroepitaxial thin films of $Si_{1-x}Ge_x/Si(100)$*, Y. YAMASHITA, K. MAEDA, K. FUJITA, N. USAMI, K. SUZUKI, S. FUKATSU, Y. MERA, Y. SHIRAKI, Philosophical Magazine Letters, Vol. 67, No. 3, pp. 165-171, 1993

[Yonenaga 1978] *Dislocation dynamics in the plastic deformation of silicon crystals. I. Experiments*, I. YONENAGA, K. SUMINO, Physica Status Solidi (a), Vol. 50, pp. 685-693, 1978

[Yonenaga 1981] PhD Thesis, I. YONENAGA, Tohuku University, 1981

[Yonenaga 1984] *Mechanical strength of silicon crystals as a function of the oxygen concentration*, I. YONENAGA, K. SUMINO, K. HOSHI, Journal of Applied Physics, Vol. 56, No. 8, pp. 2346-2350, 1984

[Yonenaga 1993] *Deformation-induced defects and their thermal stability in silicon*, I. YONENAGA, K. SUMINO, Physica Status Solidi (a), Vol. 137, pp. 611-617, 1993

[Yonenaga 1996] *Upper yield stress of Si crystals at high temperatures*, I. YONENAGA, Journal of the Electrochemical Society, Vol. 143, No. 8, pp. L176-L178, 1996

[Zarka 1972] *Généralisation de la théorie du potentiel plastique multiple en viscoplasticité*, P. ZARKA, Journal of the Mechanics and Physics of Solids, Vol. 20, No. 3, pp. 179-195, 1972

Part IV

APPLICATIONS OF THE EXTENDED A&H CONSTITUTIVE MODEL

INTRODUCTION

The preceding two Parts have introduced improvements of existing models and derivation of a new one for silicon materials. The present one aims at giving some examples of applications to macroscopic models. Both monocrystals and multicrystals are considered.

The simulations introduced in the following have been performed with the extended Alexander & Haasen model. Although of limited validity in multislip cases, this approach yields results interesting enough to provide an insight into the effects of a multicrystalline nature on the extent of hardening and dislocation generation at different positions within the grains.

Therefore, the results presented in this Part must be considered as indicative of the potential applications of the constitutive models derived in the course of this Ph.D. work.

Simulations are articulated as follows: first, the study of silicon monocrystals deformed in three-point or four-point bending tests is introduced in Chapter 12, allowing for the effects of orientation and stress gradients to be investigated. The case of a multicrystal deformed in a four-point bending apparatus is then proposed as a follow-up in Chapter 13.

Turing solely to multicrystals, the uniaxial tension of a small aggregate containing inclusions reveals the influence of grain misorientation and hard inclusions on the stress and dislocation density distribution throughout the material.

Finally, the extended AH model introduced in Chapter 6 is used in an implicit Finite Elements solver to study the potential effect of a multicrystalline structure on the stress state of a solidified SoG-Si ingot. Overall, the applications detailed in this Part are:

- 3 and 4-point bending of intrinsic and extrinsic silicon monocrystals of various crystallographic orientations
- 4-point bending of intrinsic and extrinsic silicon multicrystals
- uniaxial tension of a small multicrystal containing inclusions
- simulation of solidification and cooling of an intrinsic multicrystalline ingot

12

BENDING TESTS OF MONOCRYSTALS

The extended AH model is applied to bending tests of intrinsic and extrinsic silicon monocrystals. The effects of temperature, strain rate and crystallographic orientation on the stress, strain and dislocaton density distributions are studied. Comparison of model outputs with theoretical approaches reveals the extent of strain localization taking place at the specimen surfaces. Deformation propagation mechanisms are touched upon.

12.1 INTRODUCTION

This Chapter presents some results obtained by simulating bending tests, either 4-point or 3-point (written respectively 4PB and 3PB in the following). *Only intrinsic monocrystals are considered*. The goal of such simulations is twofold: firstly, assess the applicability of the extended AH model in other loading conditions than uniaxial tensile tests. This includes the study of the influence of various factors such as temperature, strain rate or crystal orientation on the simulated response. The particular stress fields generated by 3PB or 4PB tests are also of interest.

An additional motivation behind this choice of setup is that NTNU has the equipment required to perform 4PB tests at high temperature, as described in Chapter 11 and Annex D. Similarly, a 3PB apparatus is used to deform silicon monocrystals at Tohoku University by Professor I. Yonenaga. Comparing results from ongoing experimental tests to simulations provides valuable insights. The finite element models developed in this Chapter can obviously be used with various user-defined constitutive behaviors in the future, saving researchers the need to look for appropriate mesh refinements and model parameters.

The Finite Element models adopted in the following are replicas of the actual bending setups available in the Norwegian and Japanese labs. Section 12.2 provides with some details about the technical aspects of modeling, along with a discussion on the constitutive model used for the simulations. Results for various loading cases are then presented in Section 12.3.

12.2 FINITE ELEMENT MODELS

All simulations have been performed with ABAQUS/EXPLICIT. The actual samples and bending rods are modeled, using contact algorithms made available by the commercial FE package.

12.2.1 *4-point bending*

GENERAL CONSIDERATIONS The specimen are $4 \times 3 \times 45\,\text{mm}^3$ large, the dimensions suggested by [ASTM a, ASTM b] and actually used for room-temperature and high-temperature testing of mc-Si bars at NTNU. The half-rods are made of silicon carbide, modeled as an isotropic perfectly elastic material ($E = 410\,\text{GPa}$, $\nu = 0.14$). The contact between rods and the sample includes friction (with a coefficient taken as 0.6).

The boundary conditions imposed on the half rods are similar to the actual ones, with respect to their rotational degrees of freedom and displacement constraints. The inner and outer spacings are respectively 20 and 40 mm.

MESH PROPERTIES The elements relied upon are all C3D8R first-order bricks. Given the particular loading created by a 4PB test, going from tension at the bottom surface to compression at the top one, a fine discretization is required in the Z-direction (see Fig. 12.1). Mesh convergence is reached for 20 element layers. This high amount is required by the strong stress gradient through the thickness, and the subsequent material softening taking place in the yield region.

44 elements span the bar length (45 mm), and the width is meshed with 8 layers. This gives a rather dense mesh for the silicon bar, made up of 7040 elements. Each half-rod is discretized in roughly 14000 elements. The finite element model is shown in Fig. 12.1.

12.2.2 *3-point bending*

GENERAL CONSIDERATIONS 3PB tests create a particular bending distribution through the thickness and cross-section, that makes it difficult for the mesh to converge towards a satisfying solution in the case of silicon. Extreme stress concentrations are seen under the upper rod and at the opposite sample face.

This would not be a tremendous issue had virgin silicon crystals not exhibited a yield region. The instability the yielding phenomena represents is particularly tricky to handle in 3PB tests. Localization takes place and softening propagates throughout the thickness, preceded by a significant stress gradient owing to the upper yield stress being quickly reached at the interface of the strained area.

Specimen used for 3-point bending are bricks much thinner than those deformed in 4PB, 1.2 mm only. Their width is 3 mm and length 16 mm.

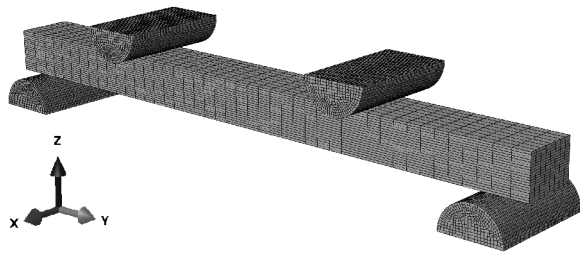

Figure 12.1: Finite element model for simulation of 4-point bending tests.

These dimensions and specimen geometry are similar to those provided by [Yonenaga 2009]. Furthermore, the position (12 mm outer span), size (3 mm diameter) and displacement degrees of freedom of the bending rods also respect those encountered in the original setup.

A different approach than previously is chosen to model the rods as shallow, half pipes. This allows to reduce the model size. Their stiffness is chosen such that their response to a radial loading at small strains is similar to the one of solid rods. This results in $E = 17.2 \times 10^{11}$ N.m^{-2} and $\nu = 0.14$.

As previously, contacts are defined between the rods and the sample. A friction coefficient of 0.6 is applied in order to avoid specimen sliding caused by twisting.

MESH PROPERTIES In spite of mesh refinements, the discontinuity at yielding cannot be completely smoothed, and 20 layers are found to produce rather good results. A fine mesh is also required in the longitudinal direction, unlike for 4PB specimen who see a rather homogeneous stress field develop between the inner rods. An element length and width of 0.25 mm is chosen. The sample is consequently made up of 19200 C3D8R elements, whereas the half-pipes are meshed with three element layers and end up at 600 elements each. Fig. 12.2 gives a snapshot of the FE mesh obtained.

12.2.3 *Constitutive model*

The only constitutive model used in this Chapter is the extended AH model, with temperature-dependent constitutive parameters only (see Chapter 6). Although of limited validity regarding its prediction of the flow stress in stage I, it reproduces satisfyingly the yield region and the effective

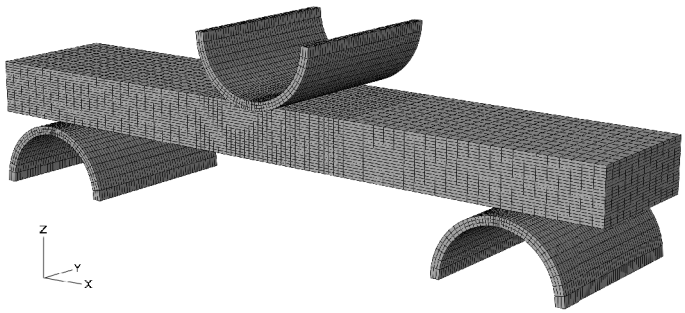

Figure 12.2: Finite element model for simulation of 3-point bending tests.

stress evolution. Its numerical cost is low enough to allow for a reasonable computational time, given the size of the models.

Another advantage of this version of the extended AH model is that it does not require any user-defined parameter, such as ζ_{sp} if strain rate variations are to be accounted for.

In order to reduce further the numerical cost of the constitutive model, a small strains approximation is implemented in the VUMAT. This allows a simplification of the kinematics without a significant loss of accuracy, since we are aiming at simulating low strains anyway (see Annex C for more details).

12.3 RESULTS AND DISCUSSION

12.3.1 *Cases studied*

4PB TESTS Only a limited amount of cases is considered: 4 temperatures and 3 strain rates. The temperatures considered are the same as in [Yonenaga 1978, Yonenaga 1981], from 1073 to 1223 K by 50 K increments.

Following [ASTM a] and assuming the sample to be homogeneous and isotropic, the strain rate[1] $\dot{\varepsilon}$ reads:

$$\dot{\varepsilon} = \frac{6tv}{L^2} \tag{12.1}$$

where t and L are the specimen thickness and outer span, and v the crosshead speed. We aim at studying three strain rates: 10^{-4}, 10^{-5} and $10^{-6}\,\mathrm{s}^{-1}$. This gives crosshead speeds ranging from 8.89×10^{-6} to $8.89 \times 10^{-8}\,\mathrm{m.s}^{-1}$, respectively. For numerical stability reasons, these crosshead speeds are applied progressively over 10 seconds. The simulations are run up to 0.5% deformation following Eq. 12.1.

Finally, 4 crystallographic orientations[2] are investigated: the standard [123] orientation promoting single slip, as well as [112], [110] and [111], favoring multiple slip. Table 12.1 summarizes the cases studied.

3PB TESTS The original goal of 3PB simulations was to investigate the possibility of double yield drop in silicon monocrystals, observed in certain temperature and strain rate ranges by [Yonenaga 2009]. However, in spite of the many cases investigated, no such effect could be retrieved. Aside from the standard temperature and strain rate variations studied, sample misplacement (rotation by a couple of degrees around the vertical axis) or weak parallelism do not yield any such result[3].

Therefore, only the effect of crystal orientation on the stress and dislocation density distribution are reported in the present work. The temperature considered is 1073 K, at an equivalent strain rate of $10^{-4}\ \mathrm{s}^{-1}$ and an initial homogeneous dislocation density set to $10^{8}\ \mathrm{m}^{-2}$ on each slip system. These conditions match those of cases 4-6 to 4-9, allowing a direct comparison of the stress-strain results between the bending types.

12.3.2 *Results*

4PB tests

STRESS DYNAMICS The force-time results are converted into stress-strain curves, assuming that time and strain at the center of the bottom surface

1 As discussed below, this relationship gives the *ideal* strain rate only, neglecting plastic localization effects.

2 The crystallographic orientation is defined with respect to the sample longitudinal axis.

3 This lack of evidence does not rule out intrinsic mechanical properties that the model do not reproduce. In particular, the effect of forest dislocations or point defects can be important in the particular loading situation considered. Some alternative explanations are given in later.

Case nr.	T (K)	$\dot{\gamma}$ (s^{-1})	$\rho_{m,0}$ (m^{-2})	orientation
4-1	1073	10^{-5}	10^8	[123]
4-2	1123	10^{-5}	10^8	[123]
4-3	1173	10^{-5}	10^8	[123]
4-4	1223	10^{-5}	10^8	[123]
4-5	1073	10^{-6}	10^8	[123]
4-6	1073	10^{-4}	10^8	[123]
4-7	1073	10^{-4}	10^8	[112]
4-8	1073	10^{-4}	10^8	[110]
4-9	1073	10^{-4}	10^8	[111]

Table 12.1: Simulated cases of 4PB tests. Initial dislocation density is per slip system.

Case nr.	T (K)	$\dot{\gamma}$ (s^{-1})	$\rho_{m,0}$ (m^{-2})	orientation
3-1	1073	10^{-4}	10^8	[123]
3-2	1073	10^{-4}	10^8	[112]
3-3	1073	10^{-4}	10^8	[110]
3-4	1073	10^{-4}	10^8	[111]

Table 12.2: Simulated cases of 3PB tests. Initial dislocation density is per slip system.

are proportional to time and relying on Eq. 12.2 to compute the stress (see [ASTM a]):

$$\sigma = \frac{3FL}{4wt^2} \tag{12.2}$$

With $L = 40\,\text{mm}$, $w = 4\,\text{mm}$ and $t = 3\,\text{mm}$ this yields $\sigma = 8.33 \times 10^5 F$.

As shown in Fig. 12.3a, a perfectly linear relationship between time and the maximum principal strain at the central elements on the tensile surface is not respected because of plasticity setting in from the yield region: Eq. 12.1 is only valid in the elastic domain. However, for simplicity in the following all strains are computed from Eq. 12.1.

Similarly, Eq. 12.2 gives accurate results in the elastic domain only. This is seen in Fig. 12.3b. Interestingly, the overall upper yield point observed from the force output is reached slightly later than the one on the outer element layer. As for the strain, we assume Eq. 12.2 to be valid all throughout deformation.

Figs. 12.4 to 12.6 show the stress-strain simulation results. The behavior as a function of temperature and strain rate is obviously qualitatively similar to the one obtained in tension specimen.

A limitation of the extended AH model in multiple slip already mentioned in Section 7.3.2 appears in Fig. 12.6, where lower upper yield stresses and higher lower yield stresses would be expected in symmetrical orienta-

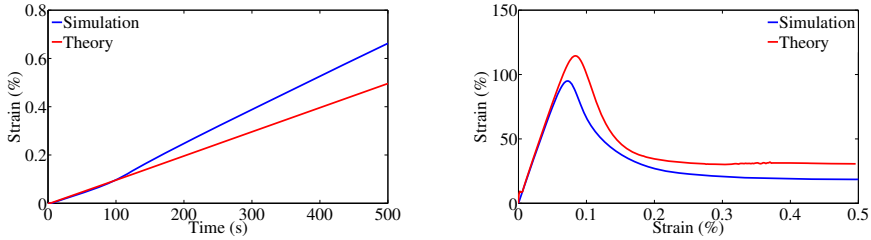

(a) Time-strain (b) Stress-strain

Figure 12.3: Comparison of 4PB simulation outputs with approximations given by [ASTM a] for case nr. 4-1.

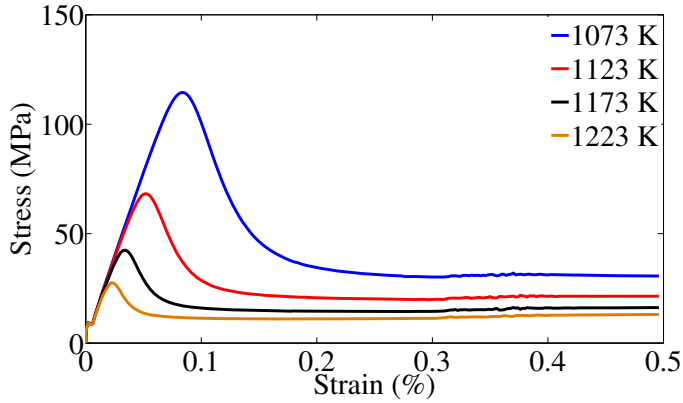

Figure 12.4: Stress-strain plots from 4PB simulations at different temperatures, respectively cases nr. 4-1 through 4-4 in Table 12.1.

tions. The ordering of the upper yield stresses is similar here as in Fig. 7.15.

Looking at a local scale, we can investigate how deformation propagates through the sample. Fig. 12.7 indicates the elements considered, spanning the sample in the X, Y and Z-directions. Only case nr. 4-1 is studied in the following.

As a homogeneous bending moment is applied between the inner rods, the central elements at the surface yield and softening takes place simultaneously in the Y-direction, propagating in the Z-direction. In the former case, all elements yields more or less simultaneously, owing to the same stress state at a given Z ordinate between the inner rods. The crystallographic orientation plays a slight role by affecting the yielding propagation in the X-direction. Fig. 12.8 shows the evolution of Von Mises stress σ_{VM} in all three directions.

A similar pattern is obviously observed for the mobile dislocation density, as shown in Fig. 12.9 for the Z-direction only.

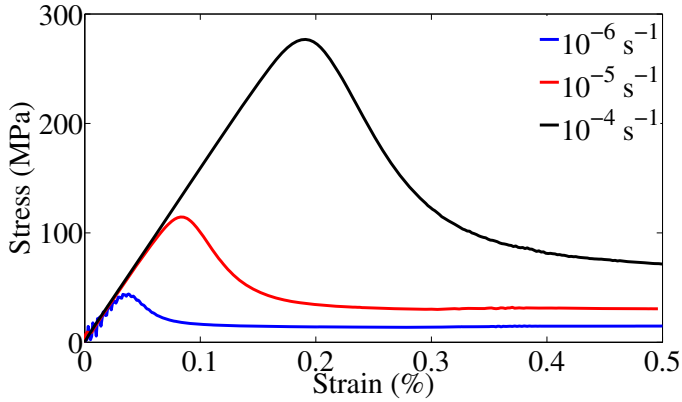

Figure 12.5: Stress-strain plots from 4PB simulations at different strain rates, cases nr. 4-1, 4-5 and 4-6 in Table 12.1.

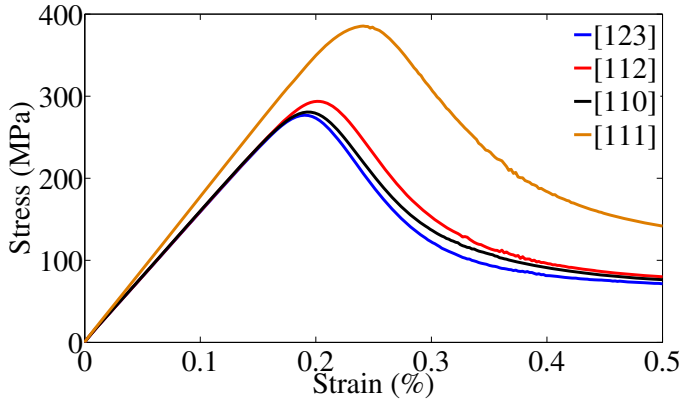

Figure 12.6: Stress-strain plots from 4PB simulations at different crystallographic orientations, cases nr. 4-6 to 4-9 in Table 12.1.

STRESS DISTRIBUTION AT $\varepsilon = 0.5\%$ Let us now turn to the deformation state at the end of the simulations. Figs. 12.10 to 12.12 show the distribution of σ_{VM} through the specimen as a function of temperature, strain rate or crystallographic orientation, respectively.

Interestingly, the stress distribution pattern as a function of, e.g., temperature, is not the same at all T considered. The final stress state in the specimen cannot be computed from a scaling of the values derived at a given reference temperature. The same remark is valid when the strain rate is varied. This can be understood as a direct consequence of the nonlinearity of the constitutive model in τ_{eff}.

Two bands of high stresses are formed towards close to the neutral axis in case 6 (Fig. 12.11c). This pattern is due to our choice of investigating the stress distribution at a given *strain* rather than at a given *deformation stage*.

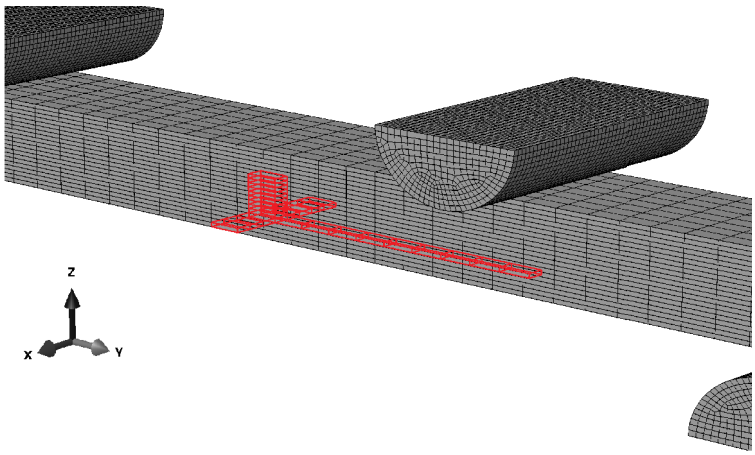

Figure 12.7: Elements considered for the study of the yielding propagation through the 4PB sample.

At $\varepsilon = 0.5\%$ all crystals have passed the lower yield point and are in stage I of hardening, whereas in case 4-6 the lower yield point is not yet reached at this strain.[4]

In this respect, it is interesting to consider the results of Fig. 12.12 since all three specimen reach their lower yield point in a very close time interval in spite of their different crystallographic orientations (see Fig. 12.6). The higher symmetry of the [111] orientation leads to the development of a finite σ_{VM} very close to the neutral axis and between the inner rods.

Further investigation reveals strong Schmid stress gradients through the neutral axis of the [111] sample, resulting from the merger of the two highly stressed regions propagating from the sample top and bottom surfaces towards the central part. At $\varepsilon = 0.5\%$ no significant dislocation generation has taken place in this central region (see Fig. 12.15).

MOBILE DISLOCATION DENSITY DISTRIBUTION AT $\varepsilon = 0.5\%$ Turning to the distribution of the total mobile dislocation density, defined as $\sum_\alpha \rho_m^{(\alpha)}$, Figs. 12.13 to 12.15 are obtained.

No particular remark can be done concerning the distributions, with no marked influence of temperature, strain rate or even crystallographic orientation on the dislocation pattern. Obviously the absolute densities depend strongly on the thermodynamical parameters, or on the number of active slip systems.

It can be noticed that shifting the crystallographic orientation from [123] to [111] in effect doubles the maximum value of the total dislocation density at a given strain.

4 The delayed appearance of the lower yield point at larger strain rates is partly due to the constitutive model used, that ignores the influence of forest dislocations on dislocation generation (and thus, strain hardening).

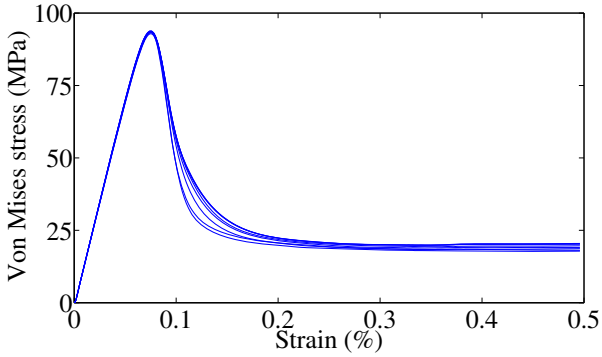

(a) X-direction

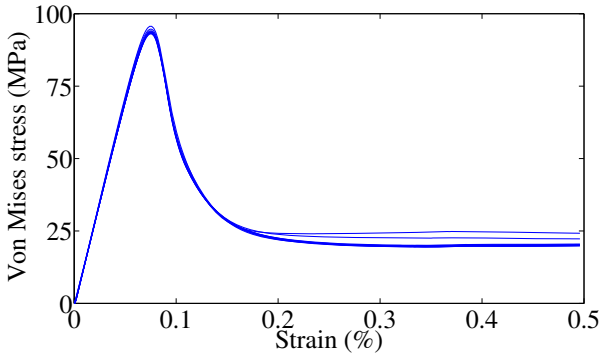

(b) Y-direction

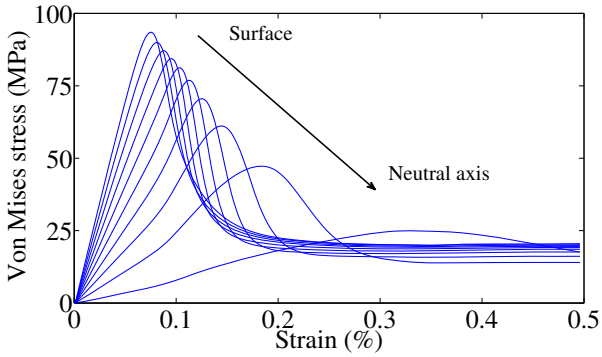

(c) Z-direction

Figure 12.8: Von Mises stress evolution throughout the sample in the X, Y and Z-directions (see Fig. 12.7 for definition), case 4-1.

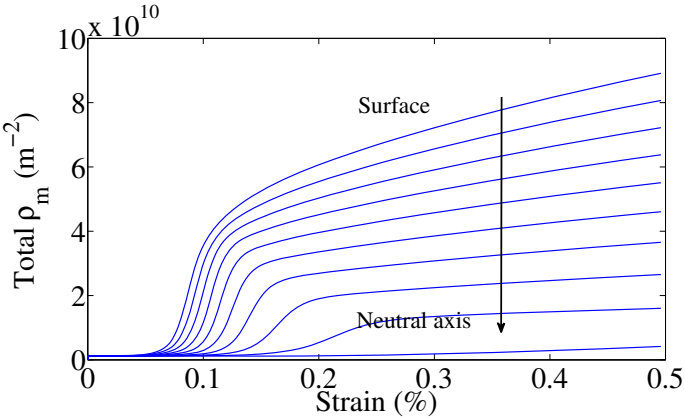

Figure 12.9: Evolution of the total mobile dislocation density through the sample half-thickness, case 4-1.

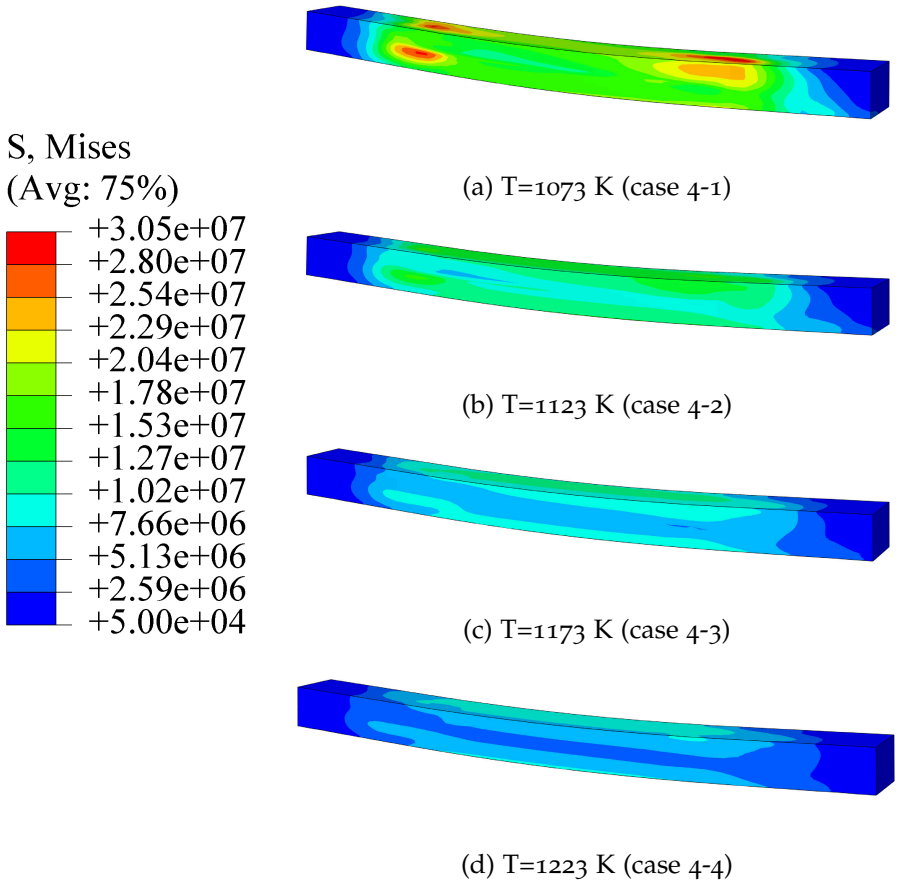

Figure 12.10: Effect of temperature on the Von Mises stress distribution at $\varepsilon = 0.5\%$.

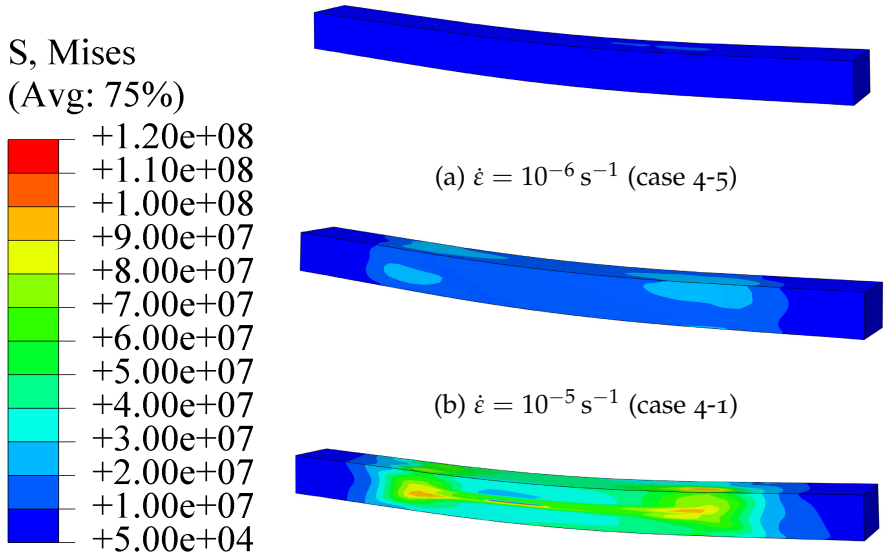

(a) $\dot{\varepsilon} = 10^{-6}\,\mathrm{s}^{-1}$ (case 4-5)

(b) $\dot{\varepsilon} = 10^{-5}\,\mathrm{s}^{-1}$ (case 4-1)

(c) $\dot{\varepsilon} = 10^{-4}\,\mathrm{s}^{-1}$ (case 4-6)

Figure 12.11: Effect of $\dot{\varepsilon}$ on the Von Mises stress distribution at $\varepsilon = 0.5\%$.

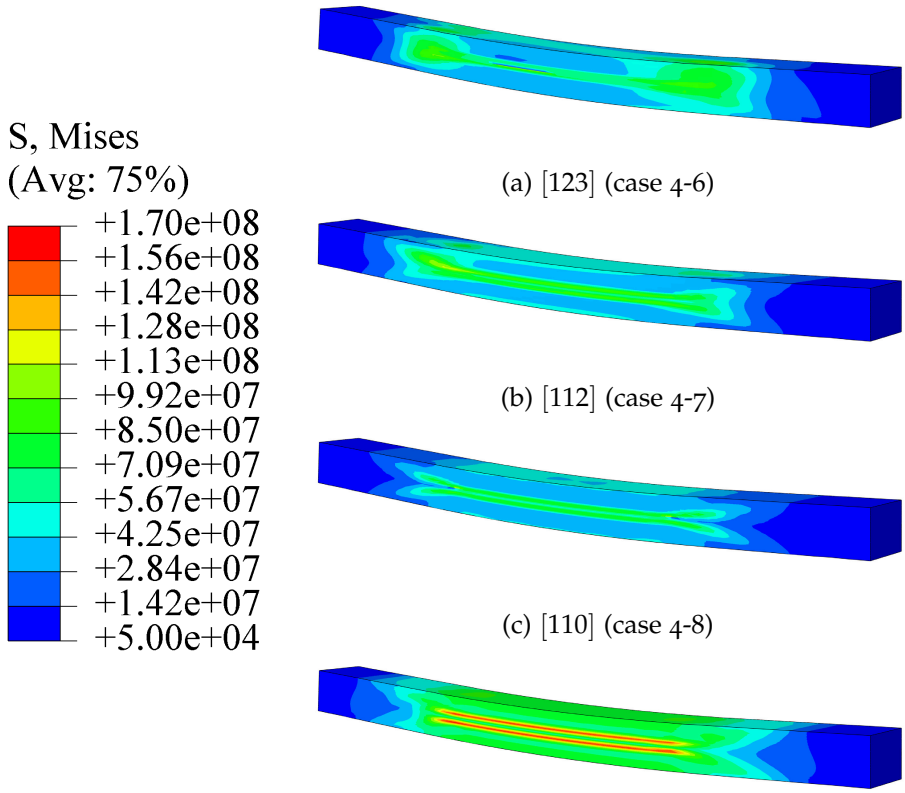

(a) [123] (case 4-6)

(b) [112] (case 4-7)

(c) [110] (case 4-8)

(d) [111] (case 4-9)

Figure 12.12: Effect of the crystallographic orientation on the Von Mises stress distribution at $\varepsilon = 0.5\%$.

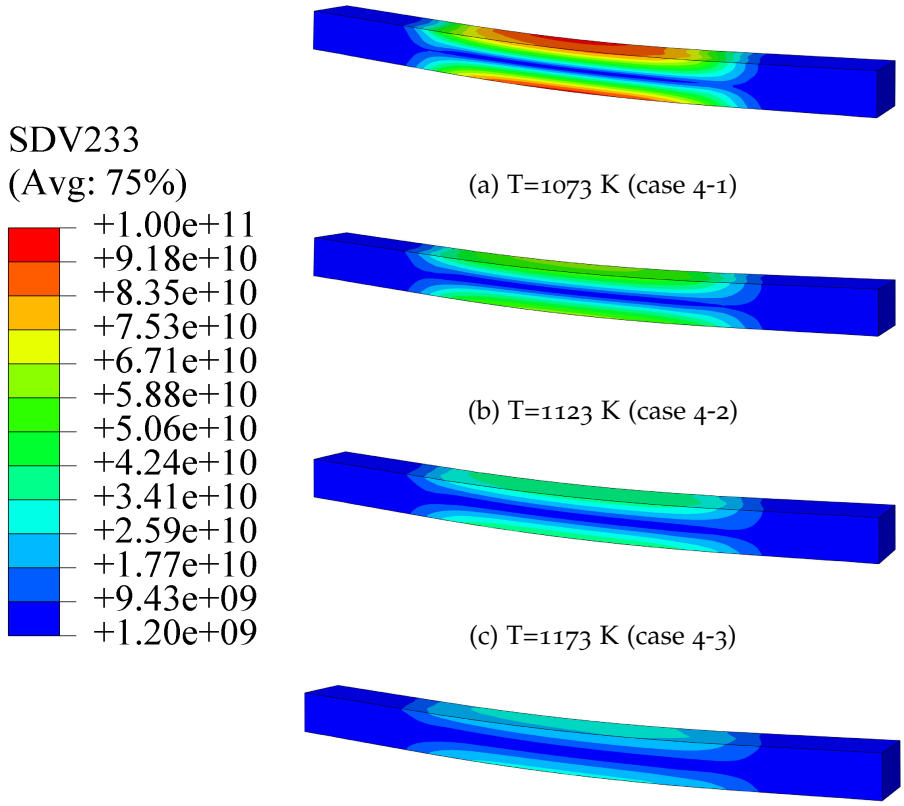

Figure 12.13: Effect of temperature on the total mobile dislocation density distribution at $\varepsilon = 0.5\%$.

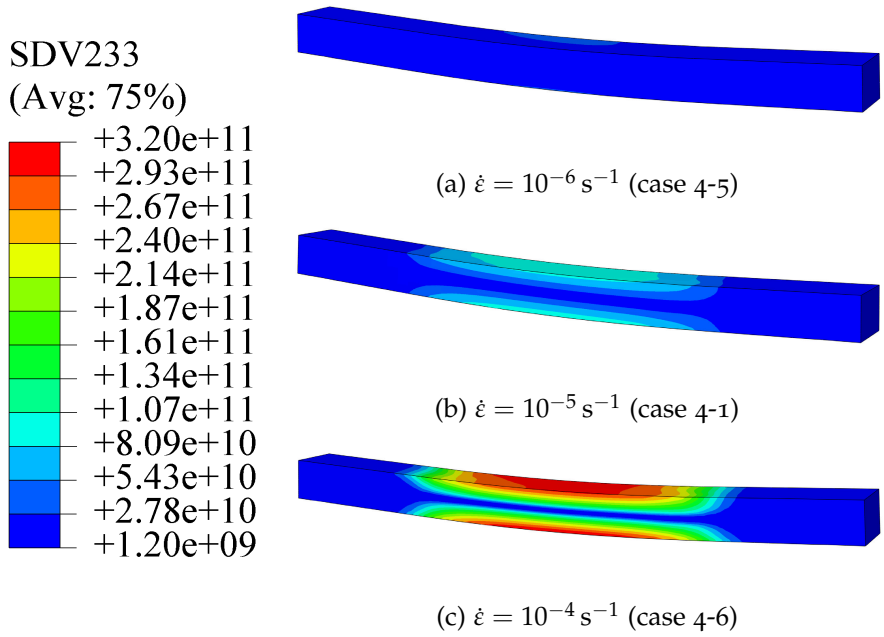

(a) $\dot{\varepsilon} = 10^{-6}\,\mathrm{s}^{-1}$ (case 4-5)

(b) $\dot{\varepsilon} = 10^{-5}\,\mathrm{s}^{-1}$ (case 4-1)

(c) $\dot{\varepsilon} = 10^{-4}\,\mathrm{s}^{-1}$ (case 4-6)

Figure 12.14: Effect of $\dot{\varepsilon}$ on the total mobile dislocation density distribution at $\varepsilon = 0.5\%$.

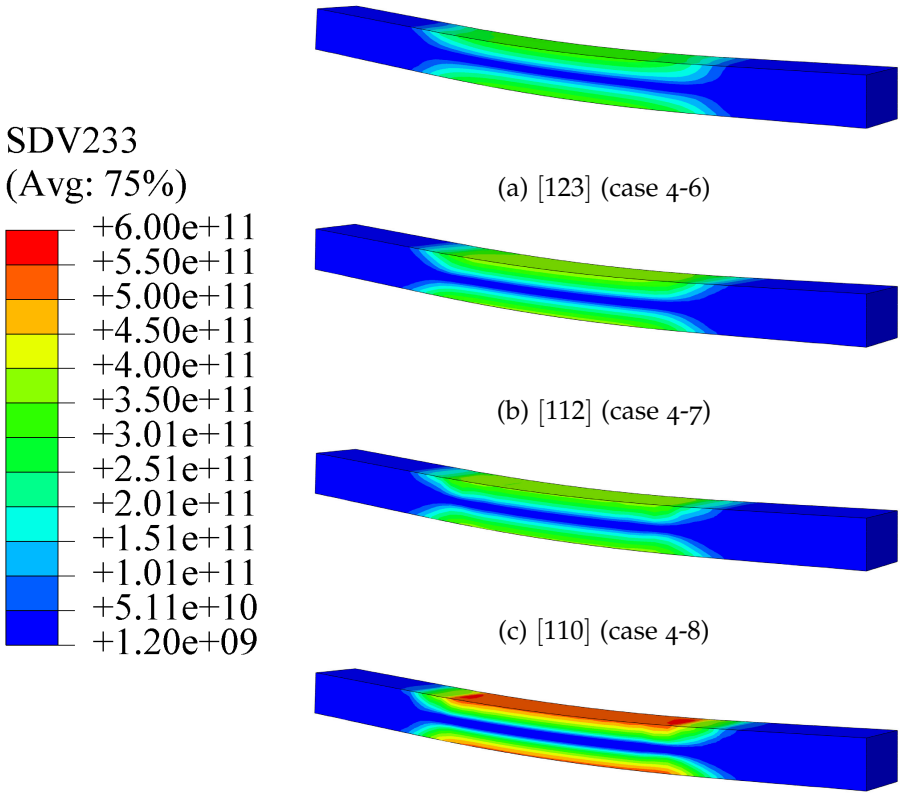

(a) [123] (case 4-6)

(b) [112] (case 4-7)

(c) [110] (case 4-8)

(d) [111] (case 4-9)

Figure 12.15: Effect of the crystallographic orientation on the total mobile dislocation density distribution at $\varepsilon = 0.5\%$.

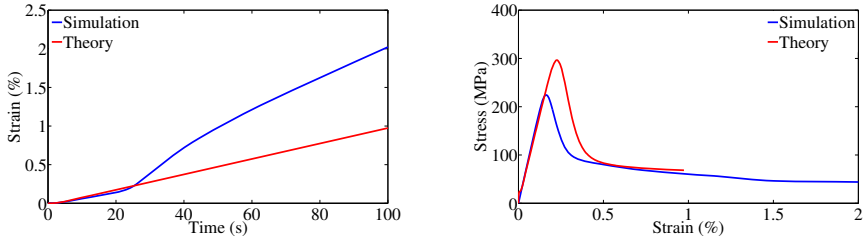

(a) Time-strain (b) Stress-strain

Figure 12.16: Comparison of 3PB simulation outputs with approximations given by [ASTM a] for case nr. 3-1.

3PB tests

Eq. 12.1 applies also to 3-point bending tests, and a target strain rate of $\dot{\varepsilon} = 10^{-4}\,\mathrm{s}^{-1}$ gives an upper rod velocity of $2 \times 10^{-6}\,\mathrm{m.s}^{-1}$. On the other hand, according to [ASTM a] Eq. 12.2 must be replaced by the following expression:

$$\sigma = \frac{3FL}{2wt^2} \tag{12.3}$$

A close examination of the simulation results shows that the total strain developing below the upper rod on the tensile surface is much larger than the one predicted by integration of Eq. 12.1. As seen in Fig. 12.16a at $t = 100\,\mathrm{s}$ the total strain is 2 % instead of the target 1 %. This has a direct consequence on the stress-strain plot at this location (Fig. 12.16b).

As previously, these discrepancies are left aside and Eqs. 12.1 and 12.3 are used to plot the stress-strain curves.

Fig. 12.17 compares the outputs from simulations 3-1 to 3-4. As for 4PB tests, the sample crystallographic orientation affects both its Young's modulus and yielding behavior.

Propagation of the upper yield stress and evolution of the total mobile dislocation density through the sample half-thickness are monitored in Figs. 12.18 and 12.19, respectively.

Owing to the linear increase of the bending moment along the specimen length and between the outer rods, stress and dislocation patterns during and at the end of simulations is of particular interest. Figs. 12.20 and 12.21 show the Von Mises stress and total dislocation density distribution at $\varepsilon = 1\,\%$, respectively.

These static views are complemented in Fig. 12.22 by a series of snapshots of the stress distribution in the sample oriented in the [110] direction, taken at different times during the simulation.

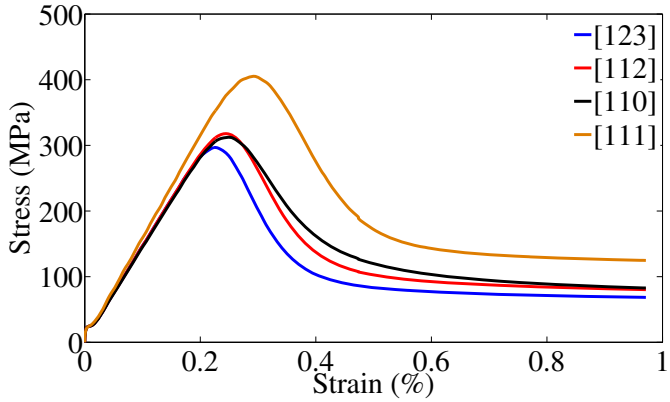

Figure 12.17: Influence of the specimen orientation on the simulated stress-strain behavior during a 3PB test, cases nr. 3-1 to 3-4.

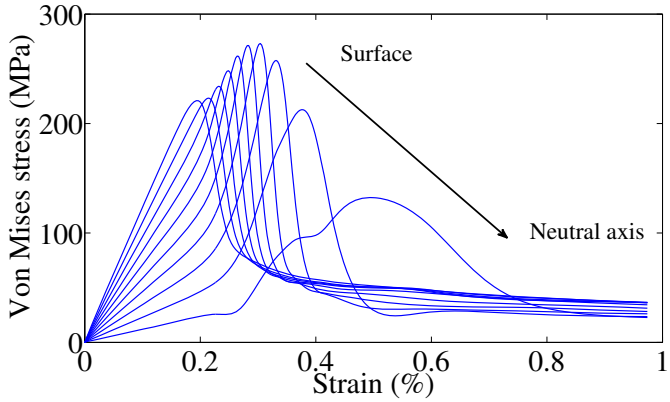

Figure 12.18: Evolution of the Von Mises stress through the sample half-thickness, case 3-1.

12.3.3 *Discussion*

Deformation homogeneity

The simulations performed in this Chapter confirm the smoothness of the stress distribution through the samples when deformed in bending. The 4-point bending configuration yields particularly smooth results that could be expected from the constant moment applied between the inner rods: at a given thickness, the stress state does not vary much along the longitudinal direction. The case of 3PB tests yields more irregularities at a given thickness, but this could be expected from the variations of the bending moment between the outer rods.

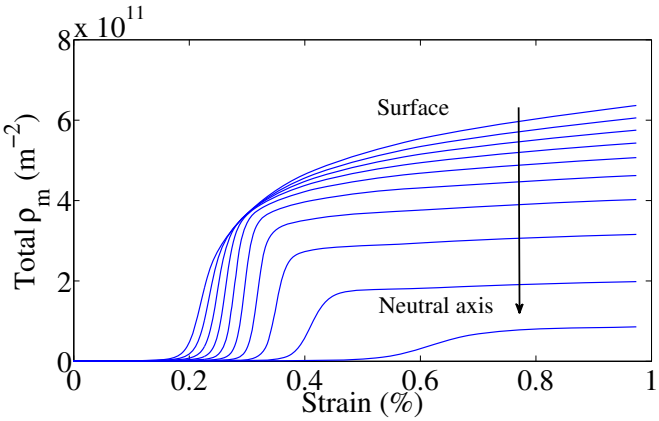

Figure 12.19: Evolution of the total mobile dislocation density through the sample half-thickness, case 3-1.

Strain and stress

GENERAL FEATURES Strain and stress patterning through the specimen do *not* depend qualitatively on the thermodynamic condition. The overall force-time behavior of the crystals is similar to the one of single crystals deformed in tension, in spite of the propagation of the yielding phenomena through the cross-section and towards the neutral axis (Figs. 12.8 and 12.18). Temperature and strain rate have the same influence on the yield region as well.

On the other hand, the pattern is significantly affected both qualitatively and quantitatively by the crystallographic orientation of the sample, as clearly shown in Figs. 12.12 and 12.20. Combined with the orientation dependency of the Young's modulus, this has potentially important consequences for industrial applications, as *loadings in highly symmetrical orientations lead to significantly different stresses than obtained on the basis of a classical* [123] *orientation*.

In both bending situations, the upper yield stress τ_{uy} increases by approximately 40 % when shifting from a [123] to a [111] orientation. This is in stark contrast with experimental data showing a *decrease* of the upper yield stress in symmetrical orientations. This discrepancy is due to the multiplication law for the yield region relied upon, as discussed in Part iii.

PLASTICITY It is worth noting that the upper yield point retrieved from the force-time records does not coincide with yielding of the tensile surface elements, but is slightly delayed, as seen in Figs. 12.3 and 12.16. This means that plasticity has developed locally when the overall behavior still seems elastic.

The onset of plastic deformation also puts an end to the validity of Eqs. 12.2 and 12.3. These equations fail to give the actual value of the maximum stress in the sample at a given time once plasticity has started

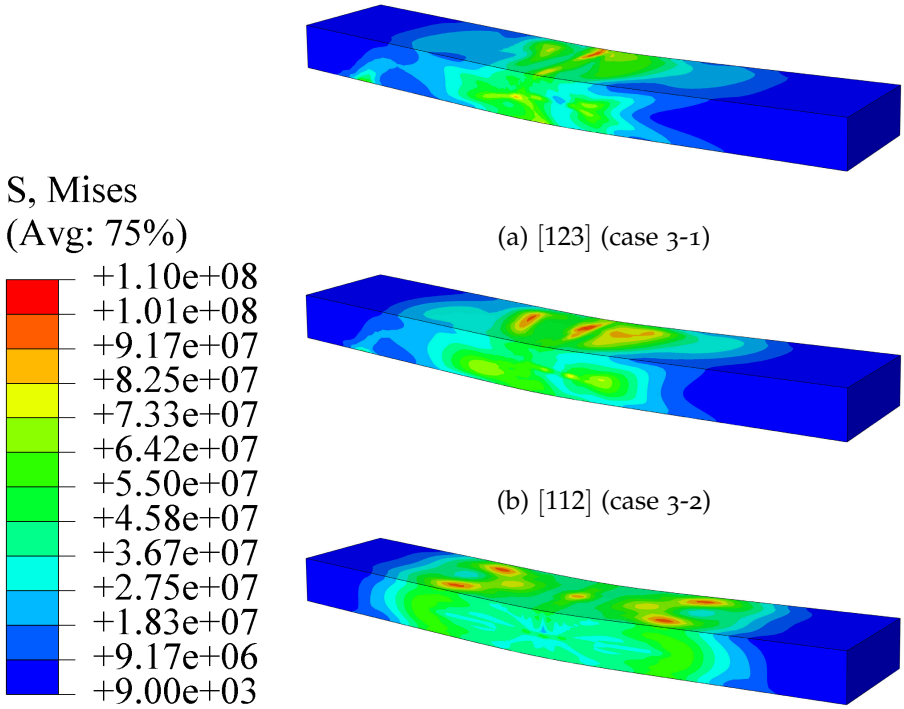

(a) [123] (case 3-1)

(b) [112] (case 3-2)

(c) [110] (case 3-3)

(c) [111] (case 3-4)

Figure 12.20: Effect of the crystallographic orientation on the Von Mises stress distribution at $\varepsilon = 1\,\%$.

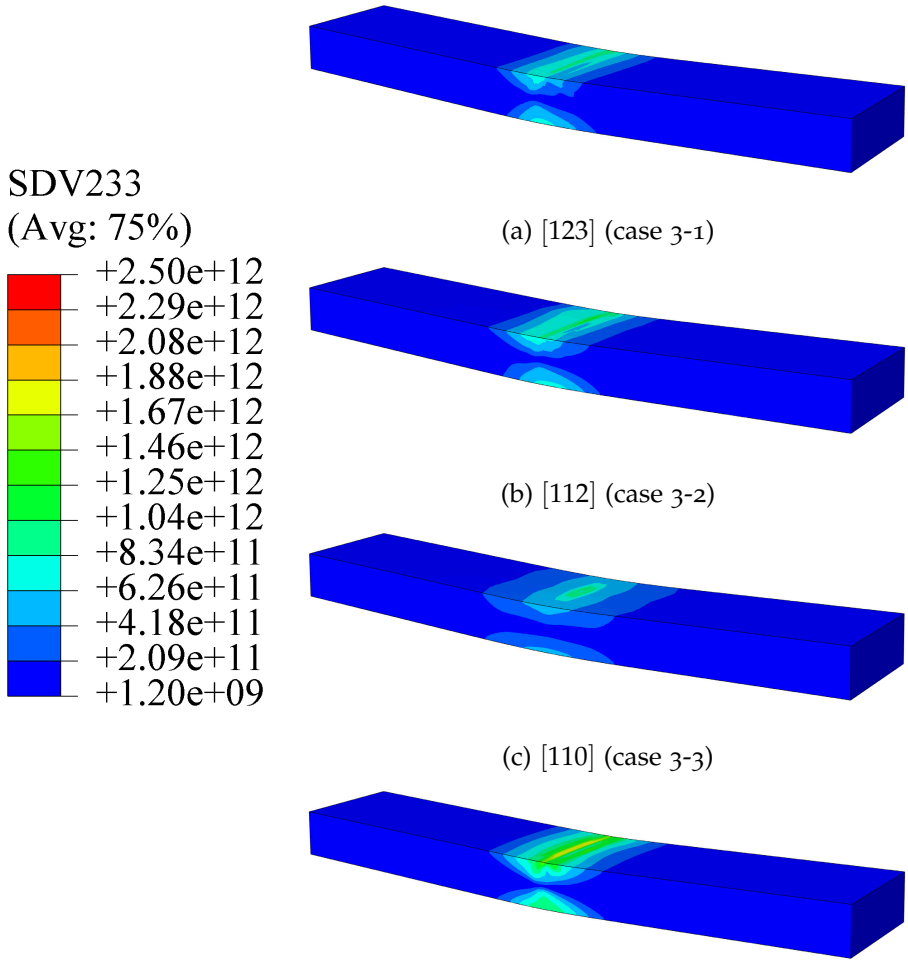

(a) [123] (case 3-1)

(b) [112] (case 3-2)

(c) [110] (case 3-3)

(c) [111] (case 3-4)

Figure 12.21: Effect of the crystallographic orientation on the total mobile dislocation density distribution at $\varepsilon = 1\,\%$.

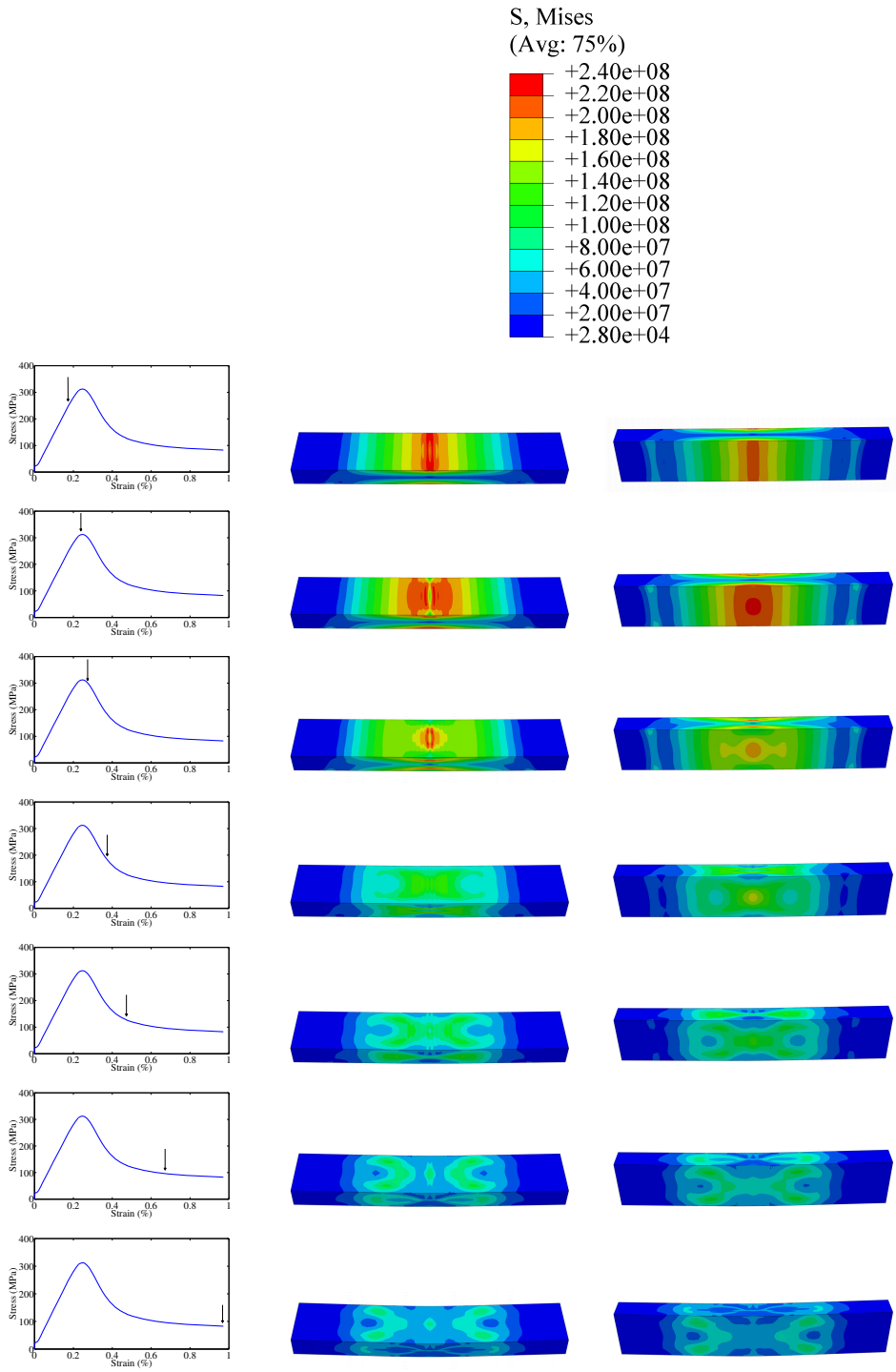

Figure 12.22: Snapshots of the Von Mises stress distribution through the 3PB specimen oriented in the [110] direction at different times, indicated by arrows on the stress-strain curves (left column). Views of the top (compressed) and bottom (stretched) surfaces are shown in the middle and right columns, respectively.

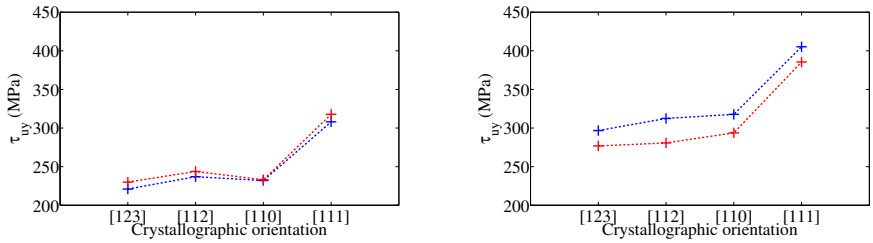

(a) From simulations (b) From [ASTM a]

Figure 12.23: Upper yield stress on the tensile surface from 3PB tests (in blue) and 4PB tests (in red) derived from (a) simulations or (b) using Eqs. 12.3 or 12.2.

to develop in the sample. In particular, the value of the local upper yield stress τ_{uy} extracted from simulations differs from the one calculated by the expressions of [ASTM a] by approximately 20 % for 4PB tests and 30 % for 3PB cases (see Fig. 12.23).

It can also be seen in Fig. 12.23a that at similar thermodynamic conditions and initial dislocation densities, the upper yield stress reached below the central rod on the tensile surface in 3PB tests is approximately the same as the one extracted from the surface of 4PB specimen. However, if Eqs. 12.2 and 12.3 are to be used, τ_{uy} would seem up to 10 % higher in 3PB than in 4PB.

UPPER YIELD STRESS PROPAGATION An interesting feature revealed by Figs. 12.8 and 12.18 is the difference of propagation of the upper yield stress through the sample thickness. In 4PB tests, once the surface has yielded the upper yield stress *decreases* as plastic deformation front propagates inwards and the element layers yield successively.

This is not the case during a 3PB test, and τ_{uy} *increases* from its surface value until its maximum is reached at one-third of the specimen depth, before decreasing towards the neutral axis. This can explain the larger delay between the surface yielding and maximum recorded force in 3PB simulations than in 4PB ones.

Constitutive model

The results derived in this Chapter are subject to caution, owing to the rather simple constitutive model relied on to simulate the mechanical response of the bending specimen. In particular, the effect of secondary systems on dislocation multiplication in multiple slip is expected to lead to lower upper yield stresses and enhance significantly the hardening behavior beyond the yield region.

Experimental results from 3PB tests [Yonenaga 2009] have revealed a double yielding of intrinsic and extrinsic dislocation-free silicon monocrystals. This phenomenon appears in a certain range of temperature and strain rate,

and in particular crystallographic orientations. Despite several attempts to reproduce this situation, it has been impossible to reproduce the experimental findings. Specimen misplacement with respect to the rods, deviation of the crystallographic orientation of a couple of degrees from the ideal one, and approximate face parallelism are some the factors investigated.

A possible explanation is the limited complexity of the constitutive model used. However, the main improvement brought by the holistic model introduced in Part iii lies in the incorporation of forest dislocations on the hardening mechanisms, that are unlikely to be of significance at small strains.

One of the most important outcomes from this Chapter is that the local stress-strain behavior is not necessarily reflected in the force-time curves, be it simultaneously or qualitatively. An example is the delay between the first yielding at the sample surface and the maximum force recorded. Another is the existence of a local double yielding in [110] samples that is not translated by a double upper yield point in the force-time data.

Local phenomena are consequently filtered before reaching the load cell of the bending apparatus.

A double yield point detected in the force-time records would then require an extended specimen volume to exhibit this feature. A possible explanation is that it finds its roots in the generation and propagation of Lüders bands from the specimen surface. Simulations show that when the first upper yield point is detected in the force-time curve, the surface layers have already yielded.

Lüders bands are observed to form in the yield region in tensile tests and to propagate from the most stressed regions inwards (see Section 2.4.1). Type G bands depicted in Fig. 2.10 actually lead to the appearance to a secondary yield drop, qualitatively similar to the one observed by [Yonenaga 2009]. The following mechanism is suggested:

- Upon loading, the outer layer yields while the overall specimen seems to be in the elastic region.
- Softening starts to propagate through the thickness, leading to a decreasing applied force;
- Lüders bands form at the surface and propagate through the thickness, leading to the appearance of a secondary upper yield point in the force-time curve.
- Once the unstability is overcome, homogeneous deformation resumes.

This model lacks experimental evidence for the time being. However, in light of simulations, it seems that the explanation to the double yielding phenomena must lie in local phenomena and cannot be found in macroscopic parameters.

12.4 CONCLUSIONS: BENDING OF INTRINSIC MONOCRYSTALS

We have shown in this Chapter the applicability of the extended AH model to bending of intrinsic monocrystals. Owing to the strong stress gradients through the sample thickness and, in the case of 3PB tests, along its length, rather fine meshes are required for the simulation results to converge. The increased computational time can be partly offset by parallelization. Input files for ABAQUS/EXPLICIT are available and can be used with any constitutive model for further investigation of the mechanical behavior of silicon materials in bending situations.

The results introduced in this work show that the overall behavior of silicon monocrystals loaded in bending exhibits the same features as in pure tension. This could indeed be expected. Of interest is the stress and dislocation density patterning that develops, especially in symmetrical loading situations such as [110] or [111]. The type of bending test does not affect significantly the upper yield stresses on the specimen surface at similar temperature, strain rate and initial dislocation density. On the other hand, it does modify significantly the stress distribution through the sample at a given strain level.

A conclusion drawn from the use of the extended AH model is that bending or uniaxial loadings along symmetrical orientations should be avoided in order to reduce the upper yield stress. An increase of τ_{uy} by roughly 40 % is simulated by switching from a [123] to a [111] orientation.

This conclusion is in apparent contradiction with experimental data, pointing to lower upper yield stresses in symmetrical orientations.

The local stress-strain behavior is not necessarily seen in the force-time record. The development of plastic strains can lead up to a doubling of the local maximum principal strain, relative to the value predicted by the linear elasticity theory.

We suggest that the double yield point phenomena experimentally recorded during 3PB tests in certain conditions could be due to local unstabilities such as Lüders bands propagating from the highly stressed sample surface inwards.

Next Chapter focuses on multicrystals and introduces results from various simulations performed not only on bending specimen, but also on small aggregates and mc-Si ingots.

13

EXTRINSIC MC-SI AGGREGATES

Simulations of multicrystals in various loading conditions are introduced. The comparison between 4-point bending tests on mono- and multicrystals reveals the fundamental differences between those two material types. Uniaxial tension of a small multicrystal containing hard inclusions allows for quantification of the stress increases taking place at various length scales and due to different factors. Finally, simulation of directional solidification of a mc-Si ingot gives an example of application of the extended AH model with the implicit version of the finite element software Abaqus/Standard.

13.1 INTRODUCTION

Until now only applications of the extended AH model to monocrystals have been discussed. The case of multicrystals follows naturally, and represents only additional finite element modeling tasks. Pushing further the model complexity, oxgyen-contaminated materials are studied as well. The present Chapter focuses on three cases.

Firstly, an actual 4PB specimen is modeled and deformed in Section 13.2. Different homogeneous dissolved oxygen concentrations are considered. Secondly, a small multicrystal containing isotropic perfectly elastic inclusions and exhibiting different mechanical properties than silicon is deformed in tension. This allows a careful study of the effect of grain misorientation and of inclusions on the local stress and strain fields in Section 13.3.

Finally, the simulation of solidification and cooling of a small mc-Si ingot is presented. This case requires the development of an additional constitutive model for the melt, relies on Abaqus/Standard for the computation and uses several modeling tricks described in Section 13.4.

13.2 4-POINT BENDING OF A MC-SI BAR

13.2.1 *Model properties*

The mc-Si bar model comes from a real mc-Si specimen whose surface has been analyzed by EBSD to determine the grain shape and orientation. Filtering out small grains and assuming the 11 remaining grains to be columnar, the whole sample is obtained by extruding the planar multigrain model. Fig. 13.1 shows the stereographic projections of the grain orientations.

The FE model is more complex and refined than the ones used in the previous Chapter, because the particular grain geometry poses some constraints on the geometrical discretization of the sample surface. The sample dimensions are still $4 \times 3 \times 45\,\mathrm{mm}^3$. C3D8R elements are kept, and 20 layers in the thickness are considered. Owing to the amount and size of grains, 5559 elements are used to mesh the specimen surface (see Fig. 13.2), leading to a total amount of elements slightly larger than 111000.

This heavy model is computationally expensive to run, therefore only a limited amount of simulations is considered here. The temperature is set to T=1073 K, the upper rod velocity constant and leading to a projected strain rate $\dot{\varepsilon} = 10^{-5}\,\mathrm{s}^{-1}$, and the initial dislocation density is considered homogeneous at $10^8\,\mathrm{m}^{-2}$ on each slip system. Three dissolved oxygen concentrations c_O^∞ are considered: intrinsic case, $c_O^\infty = 2.5 \times 10^{17}\,\mathrm{cm}^{-3}$ and $c_O^\infty = 5 \times 10^{17}\,\mathrm{cm}^{-3}$. The simulations last 500 s, up to a theoretical strain of 0.5 %. Table 13.1 summarizes the cases considered in this Section.

13.2.2 *Results and discussion*

Stress-strain and dislocation density

The force-time outputs are converted into stress-strain usingthe same assumptions as made in the previous Chapter, relying on Eqs. 12.1 and 12.2. These results are shown in Fig. 13.3. As expected, increasing the dissolved oxygen content raises the upper yield stress.

Stress-strain results of case 4-1 are also shown for comparison. The multicrystalline nature of the present specimen leads to a lower averaged Young's modulus relative to a single crystal oriented in the [123] direction.

Case nr.	T (K)	$\dot{\gamma}$ (s^{-1})	$\rho_{m,0}$ (m^{-2})	c_O^∞ (cm^{-3})
1	1073	10^{-5}	10^8	0
2	1073	10^{-5}	10^8	2.5
3	1073	10^{-5}	10^8	5

Table 13.1: Simulated cases of 4PB tests of mc-Si bars. Initial dislocation density is per slip system.

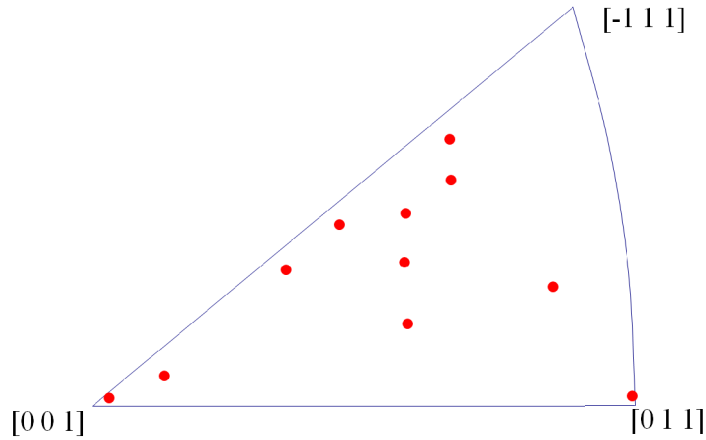

Figure 13.1: Stereographic projections of the mc-Si bar grain orientations.

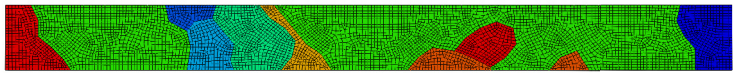

Figure 13.2: Finite Element mesh used for the study of a silicon multicrystal. Each grain is colored differently than its neighbours to help differentiating them.

In addition, the stress given by Eq. 12.2 is misleadingly lower than in the monocrystalline case, as discussed below.

Stress and total mobile dislocation density distributions in the mc-Si specimen are shown in Figs. 13.4 and 13.5. An interesting result is that increasing the oxygen content not only leads to higher peak stresses (+50 % between the FZ-Si and highly oxygen-contaminated CZ-Si bars), but also to stronger stress heterogeneities at a given specimen thickness and through the thickness. This remark is also valid for dislocation densities, albeit to a much lower extent.

Intrinsic crystals: comparison with the c-Si case

Comparison with the results of Chapter 12 shows that plastic deformation and the stress development take place in regions of approximately the same dimensions for both c-Si and mc-Si specimen.

Heterogeneities are best investigated by looking at the shape of isosurfaces. This is done for Von Mises stress and dislocation density in Figs. 13.6 and 13.7, respectively. Admittedly, the multicrystalline case adds a high degree of complexity to the stress state. High stress peaks and large dislocation densities are observed close to grain boundaries, both inside the bar and at its surfaces. However, it must be noted that highly stressed regions do *not* necessarily exhibit large dislocation densities.

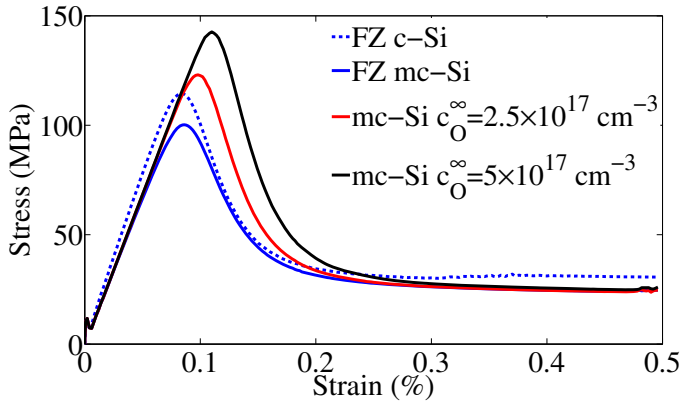

Figure 13.3: Stress-strain outputs from simulations of 4PB tests of mc-Si bars. The stress-strain results of case nr. 4-1 of Chapter 12 is also shown for comparison.

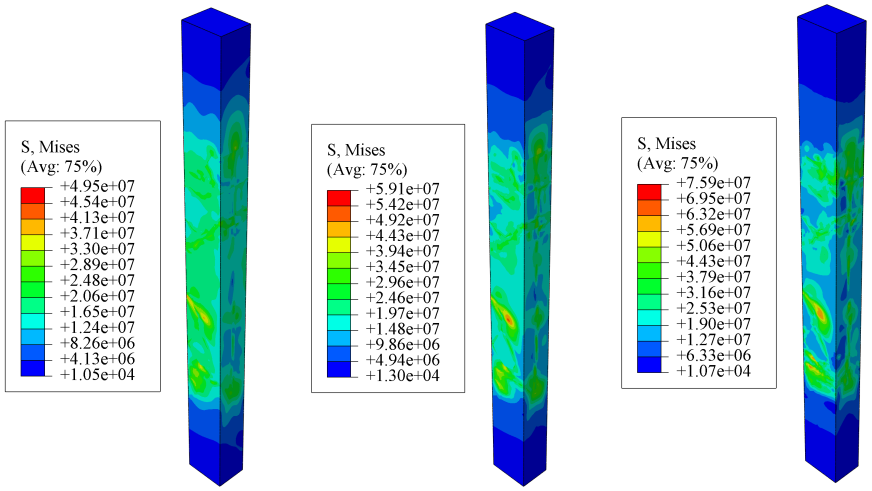

(a) FZ-Si (b) $c_O^\infty = 2.5 \times 10^{17}\,\mathrm{cm}^{-3}$ (c) $c_O^\infty = 5 \times 10^{17}\,\mathrm{cm}^{-3}$

Figure 13.4: Von Mises stress distribution in the 4PB mc-Si bars at ε=0.5 %.

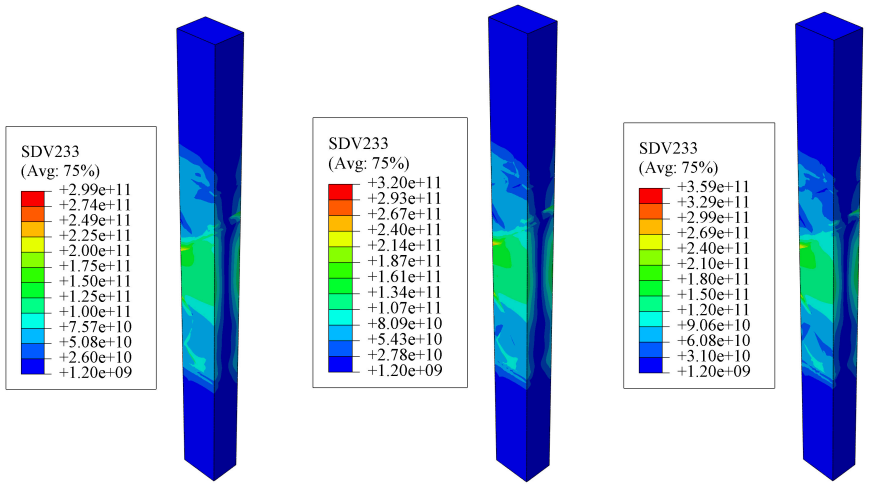

(a) FZ-Si (b) $c_O^\infty = 2.5 \times 10^{17}\,\mathrm{cm}^{-3}$ (c) $c_O^\infty = 5 \times 10^{17}\,\mathrm{cm}^{-3}$

Figure 13.5: Total mobile dislocation density distribution in the 4PB mc-Si bars at ε=0.5 %.

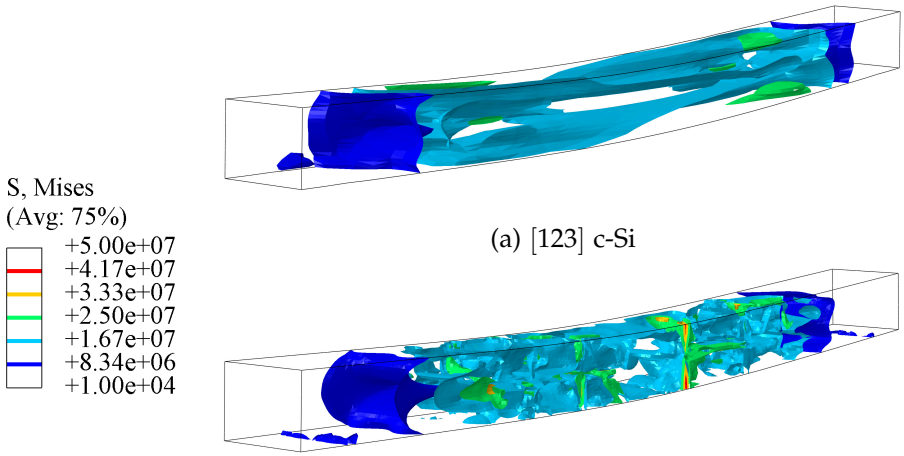

(a) [123] c-Si

(b) mc-Si

Figure 13.6: Isosurfaces of the Von Mises stress in intrinsic 4PB bars.

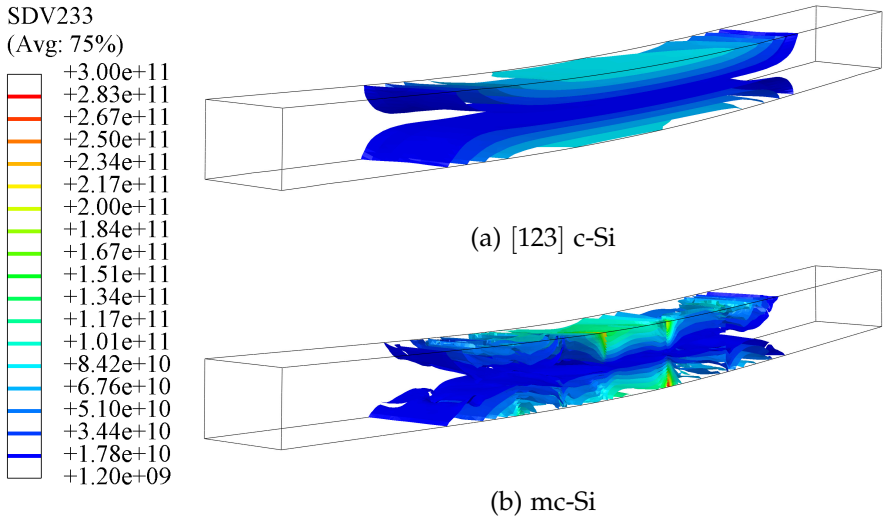

Figure 13.7: Isosurfaces of the total mobile dislocation density in intrinsic 4PB bars.

Table 13.2 provides some data for comparison between intrinsic monocrystalline and multicrystalline models: maximum values of the Von Mises stress, total mobile dislocation density and maximum principal strain are given at the end of the simulations.

Local vs. global behavior

COMPARISON WITH INTRINSIC C-SI The results indicate that the multicrystalline configuration considered in this Section leads to a tripling of the maximum dislocation density, more than a doubling of the maximum strain developing in the bar, and an increase of the maximum Von Mises stress by two-thirds, with respect to the homogeneous case of a [123]-oriented single crystal. These differences are slightly reduced when a [111] monocrystal is taken as reference[1].

NEED FOR A LOCAL APPROACH This shows that the conclusions reached in the previous Chapter concerning *the large discrepancy between the local and global behavior is even more accute in the case of multicrystals* and justify a multiscale approach to the problem.

Deformation heterogeneity associated to huge increases in the maximum values of stress, strain and dislocation density imply that the study of mc-Si materials cannot neglect the very crystallographic topography of its constituent grains. The most striking effect of introducing grain misorientations (and imposing kinematic compatibility at grain boundaries) is

1 The potential influence of the constitutive model on these results must be kept in mind, as the extended AH model does not correctly reproduce the strong stress and dislocation density increases taking place in multiple slip conditions.

	σ_{VM} (MPa)	$\varepsilon_{\max}$ (%)	$\sum \rho_m$ (10^{11} m^{-2})
[123] c-Si	30.5	0.71	0.95
[111] c-Si	38.7	0.56	1.45
mc-Si	50	1.74	3
from [123]	+64 %	+145 %	+215 %

Table 13.2: Maximum values of selected variables throughout intrinsic mono- and multicrystalline 4PB specimen deformed in the same conditions, at $\varepsilon = 0.5\,\%$.

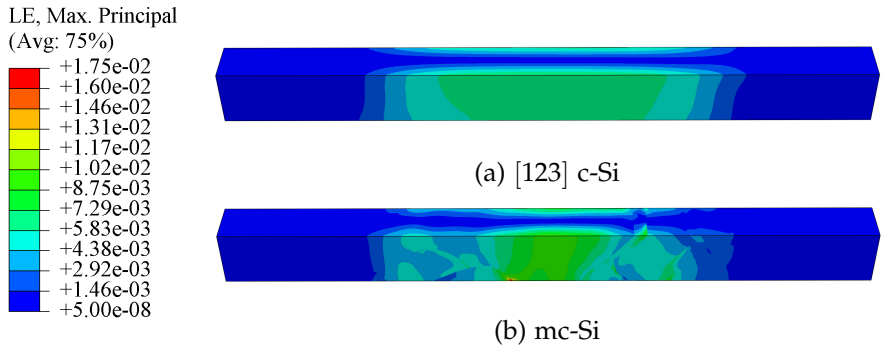

Figure 13.8: Distribution of the maximum principal strain in intrinsic 4PB bars at $\varepsilon = 0.5\,\%$.

the development of strong strain localizations[2] associated to strong plastic deformation, as shown in Fig. 13.8.

The presence of dissolved oxygen leads to the development of larger stresses, strains and dislocation densities than in the case of intrinsic crystals. Heterogeneities are similarly enhanced, calling further for the use of dedicated finite element models.

2 Mesh size effects can be expected at these localizations close to grain boundaries. No attempt to study mesh convergence at grain boundaries has been performed in this Section; therefore the maximum strain value given in, e.g., Table 13.2 is subject to caution.

13.3 ANALYSIS OF A MC-SI BLOCK WITH INCLUSIONS

This Section focuses on the study of a small multicrystal containing hard inclusions. Both the local effects of SiC particules and the overall anisotropy of the mc-Si aggregate are considered. The case of an oxygen-contaminated aggregate is also touched upon.

13.3.1 *Finite Element model*

Geometry and mesh

The mc-Si aggregate is made up of 7 columnar grains and contains 3 SiC inclusions, whose mechanical properties are assumed to be isotropic perfectly elastic ($E = 410\,\text{GPa}$, $\nu = 0.14$). The dimensions of the multicrystal are $6.6 \times 5 \times 5\,\text{mm}^3$. The inclusions are modeled as ellipsoids of length 0.6 mm and radius 0.1 mm. They are embedded into the silicon matrix and no separation is allowed at the Si/SiC interface.

Grain orientations are randomly generated and shown in Fig. 13.10 using the stereographic projection and the X-axis as the tensile one.

The matrix is meshed with roughly 142,000 C3D4 elements, while inclusions require 750 such elements each. This type of element is chosen in spite of its poor stress response because of its ability to mesh complex volumes and surfaces (see Annex C). No mesh convergence study has been attempted. Fig. 13.9 shows a grid view of the aggregate mesh. Figs. 13.11a and 13.11b show solid meshes of one grain and an inclusion, respectively.

Cases studied

All simulations are performed at a homogeneous and constant temperature of 1173 K, applying a unidirectional velocity on one of the specimen faces ensuring a strain rate $\dot{\varepsilon} = 10^{-5}\,\text{s}^{-1}$. The time-velocity function includes an acceleration phase of 10 s in order to limit oscillations in the force output of the explicit model. The displacements on the opposite face are constrained in the tensile direction, while nodes are free to move on the orthogonal plane. Simulations are run for 500 s, up to a tensile strain of 0.5 %.

The initial mobile dislocation density is set to $10^8\,\text{m}^{-2}$ on each slip system. For the CZ-Si case, a homogeneous dissolved oxygen concentration of $5 \times 10^{17}\,\text{m}^{-3}$ is chosen.

Anisotropic properties are studied on the FZ-Si sample only. Given the columnar nature of the grains, one natural direction to explore is the Y-axis "solidification" one. The two in-plane X and Z-axes orthogonal directions are then considered (see Fig. 13.9 for axis definition).

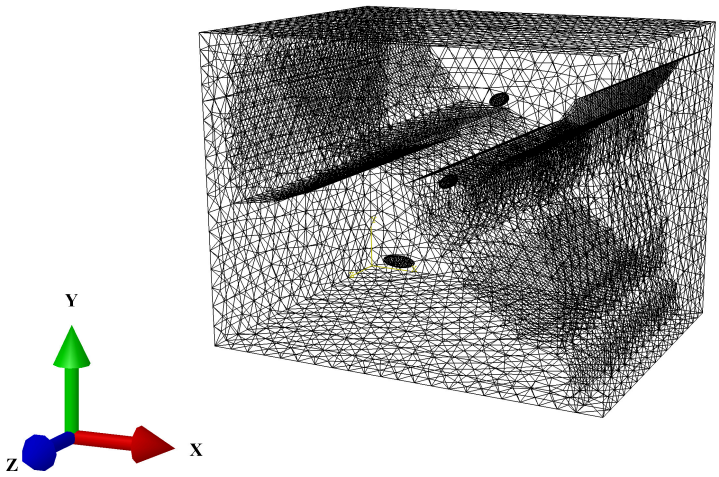

Figure 13.9: Grid view of the mesh used for study of a mc-Si block with inclusions.

13.3.2 *Results and discussion*

FZ-Si crystals

GLOBAL STRESS-STRAIN OUTPUTS The force-time simulation outputs are converted into stress-strain curves assuming small deformations. Fig. 13.12 shows the results obtained on the intrinsic aggregate. It can be seen that the randomly generated grain orientations do *not* lead to any particular anisotropic behavior, be it in the elastic or plastic deformation ranges. Overall, the multicrystal behaves like a single crystal, as was the case for bending specimen.

STRESS AND STRAIN DISTRIBUTIONS The global smooth force-time output hides local heterogeneous behavior. Fig. 13.13 shows the Von Mises stress distribution at the sample surfaces when deformed in all three directions considered. Looking at a local scale and inside the specimen, a view cut of the aggregate is selected for its ability to pass through all three inclusions. This gives us the ability to study both the effect of grain misorientation and of hard inclusions on the stress and strain levels inside the mc-Si block in Fig. 13.14.

Fig. 13.15 shows the view cut distribution of the maximum principal strain.

The maximum stress and strain reached in the silicon matrix at $\varepsilon = 0.5\,\%$ depend on the tensile axis, as shown in Table 13.3. Since mesh sensitivity has not been assessed, these values must be considered with caution. However, they point to a common pattern between simulations, namely that the maximum Von Mises stress (resp. strain) reached in the multicrystal is roughly 3 times (resp. 4 times) larger than the overall measured one.

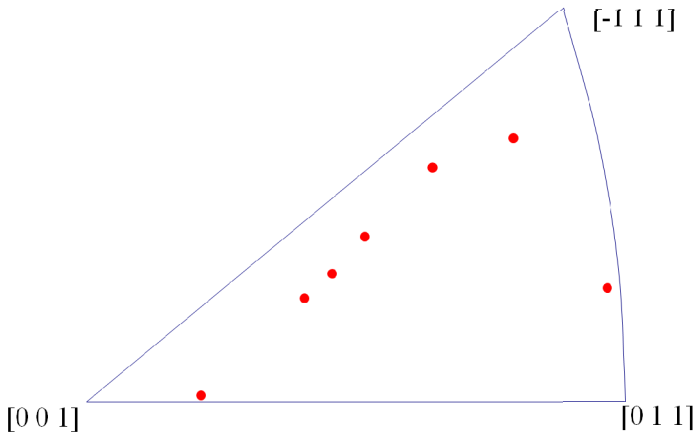

Figure 13.10: Stereographic projections of the orientation of the grains in the mc-Si block. The X-axis is considered as the tensile one.

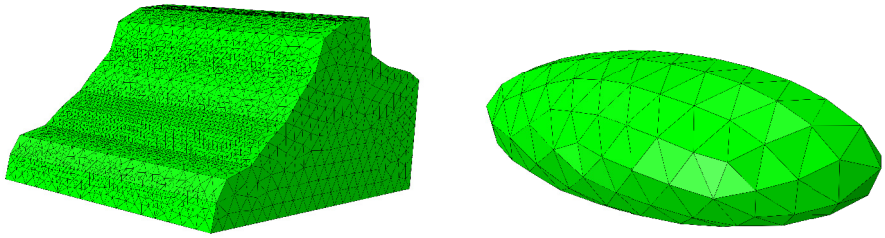

(a) One of the 7 grains (b) Inclusion

Figure 13.11: Solid views of instance meshes used in Section 13.3.

Stress heterogeneities are seen to develop principally at the sample surfaces and at grain boundaries, as is clearly seen in Fig. 13.14. This has a particular significance for small grains, as their grain boundary surface to volume ratio is larger than for big grains. This means that they are more prone to stress increases than their bigger neighbours.

DISTRIBUTION OF DISLOCATION DENSITY As could be expected, the distribution of the total mobile dislocation density $\sum_\alpha \rho_m^{(\alpha)}$ follows closely the strain distribution since deformation is mostly plastic[3]. As seen in Fig. 13.16, the density is quite homogeneous inside the grains, with clusters developing to some extent along some grain boundaries but especially at the inclusions.

3 This remark must be tempered by the time variations of the effective stress. The total plastic strain follows from the projection of the integrated shear strain rates $\dot{\gamma} \propto \rho_m \tau_{eff}$. Consequently, the final (plastic) strain is all the more correlated to the dislocation density when the effective stress remains constant throughout deformation.

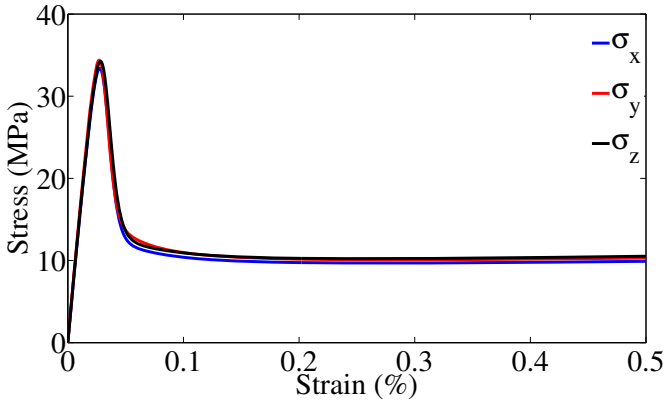

Figure 13.12: Stress-strain curves from uniaxial tensile deformation of the mc-Si block with inclusions along three orthogonal directions. Intrinsic crystals.

Tensile axis	X	Y	Z
σ_{VM} (MPa)	35	25	28
$\varepsilon_{\max}$ (%)	2.65	1.57	1.9

Table 13.3: Maximum values of the Von Mises stress and principal strain in the Si matrix of mc-Si blocks containing inclusions deformed at $\varepsilon = 0.5\,\%$.

THE EFFECT OF INCLUSIONS Inclusions have a very local effect, roughly over a region of the size of the inclusion itself. They participate in stress increase and are actually at the origin of the maximum Von Mises stress in all three cases considered here. The same remark is valid for dislocation densities: the clusters they generate exhibit densities 5 to 10 times the bulk ones.

The effect of inclusions is best seen in the strain distributions (Fig. 13.15). Grain boundaries do not have any significant effect on the strain heterogeneity as they do not lead to any noticeable discontinuity in the material properties. On the other hand, as inclusions behave perfectly elastically and no interface separation is allowed at the Si/SiC boundaries, the silicon lattice must accomodate plastically for the displacements imposed by the inclusions.

The elastic anisotropy of the silicon matrix leads to the development of strain lobes around inclusions, most visible in Fig. 13.15a. The dislocation density follows these patterns.

Note that the potential interaction between inclusions and free surfaces or grain boundaries has not been investigated. Adding kinematic constraints on the Si matrix elements ought to lead to further stress and strains developments. It is experimentally observed that inclusions tend to grow close

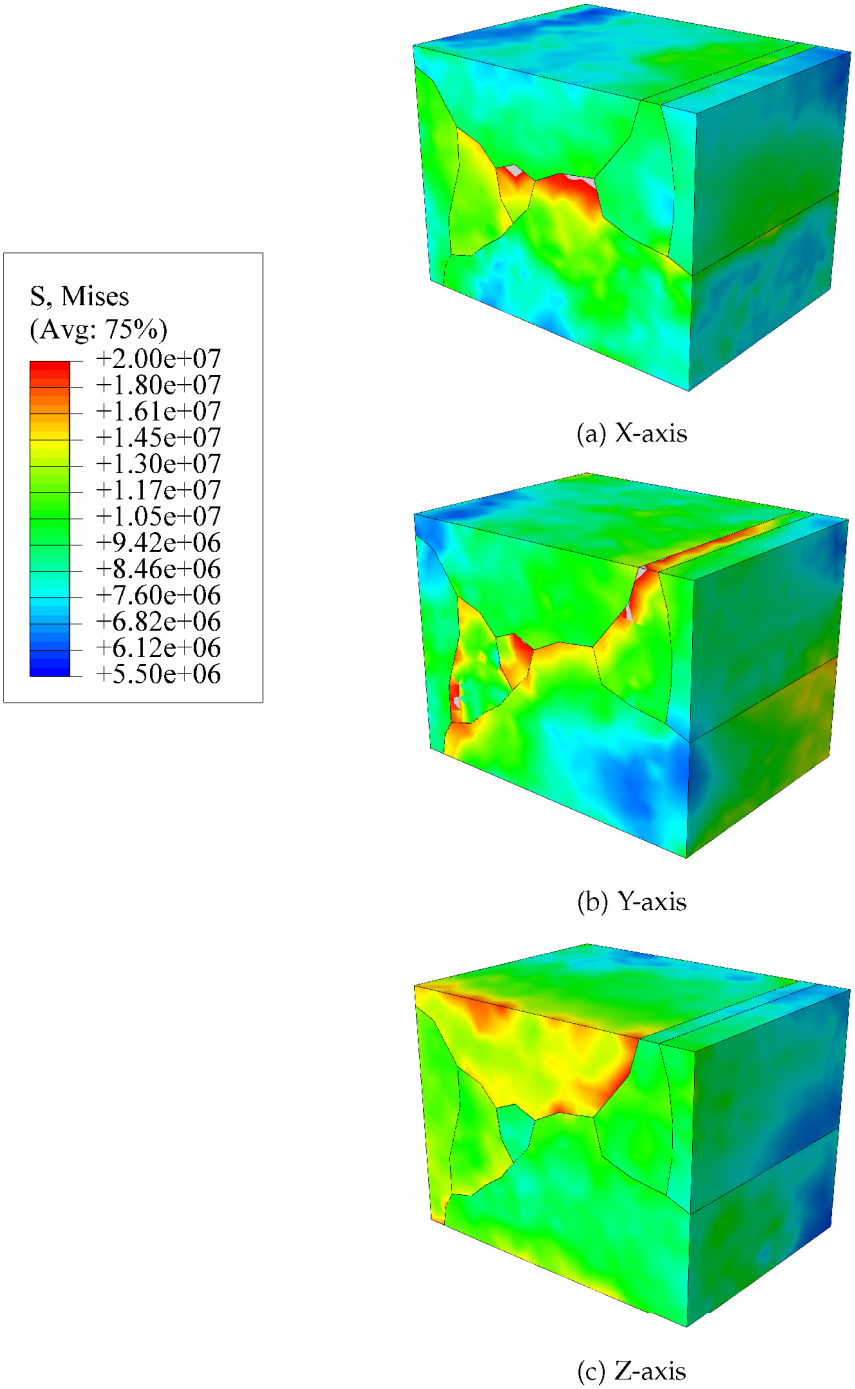

(a) X-axis

(b) Y-axis

(c) Z-axis

Figure 13.13: Stress distribution at the surface of the mc-Si aggregate after deformation up to $\varepsilon = 0.5\,\%$ along all 3 principal directions. The most visible surface is the (0,0,-1) one.

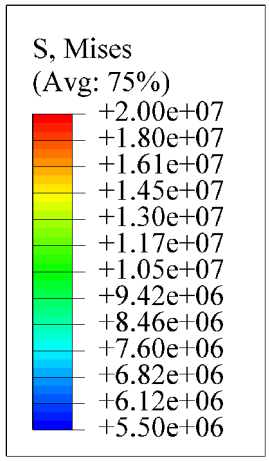

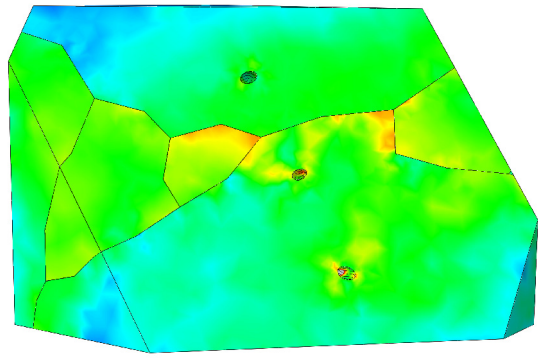

(a) X-axis

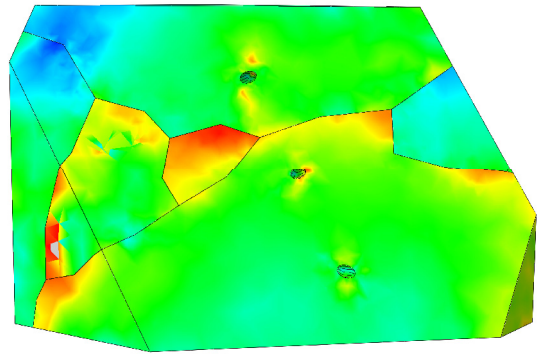

(b) Y-axis

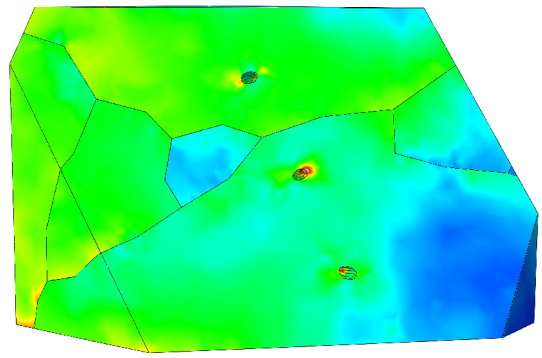

(c) Z-axis

Figure 13.14: Stress distribution in the mc-Si aggregate after deformation up to $\varepsilon = 0.5\,\%$ along all 3 principal directions (view cut).

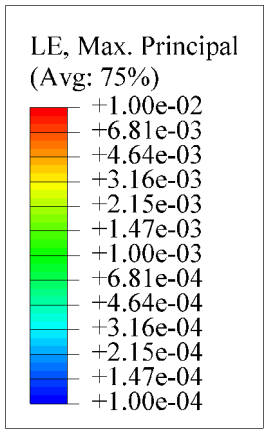

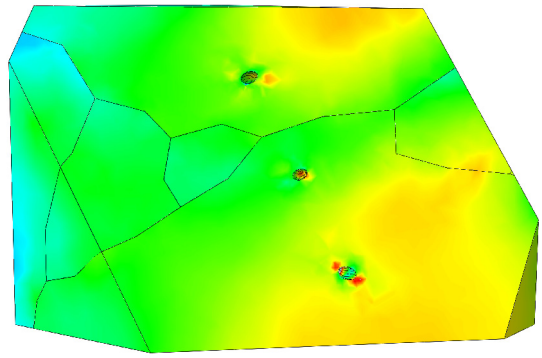

(a) X-axis

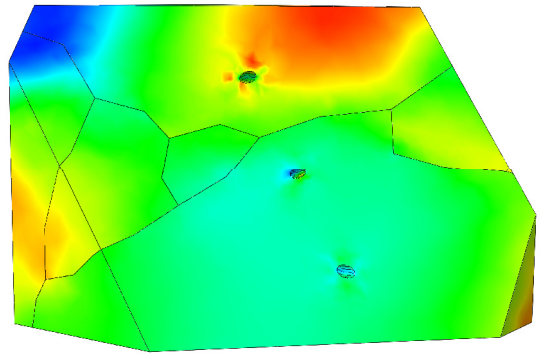

(b) Y-axis

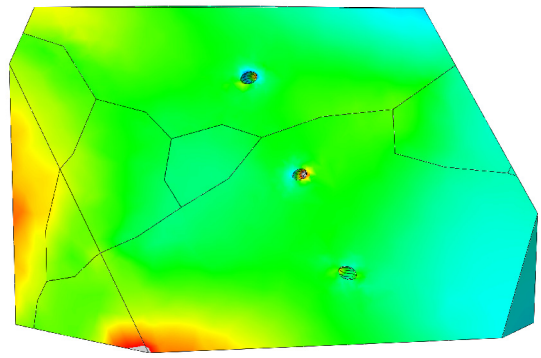

(c) Z-axis

Figure 13.15: Maximum principal strain distribution in the mc-Si aggregate after deformation up to $\varepsilon = 0.5\,\%$ along all 3 principal directions (view cut).

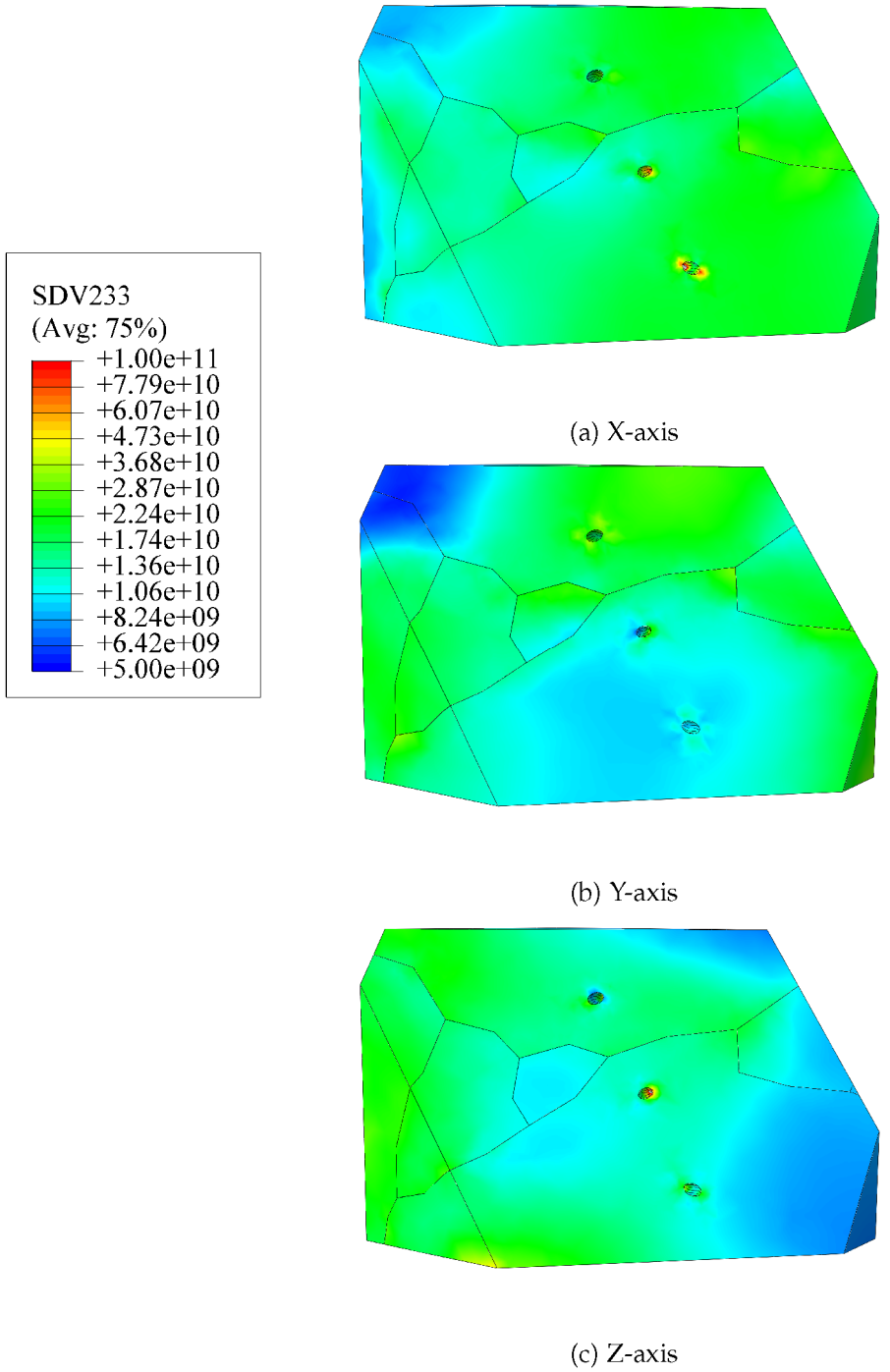

(a) X-axis

(b) Y-axis

(c) Z-axis

Figure 13.16: Distribution of the total mobile dislocation density in the mc-Si aggregate after deformation up to $\varepsilon = 0.5\,\%$ along all 3 principal directions (view cut).

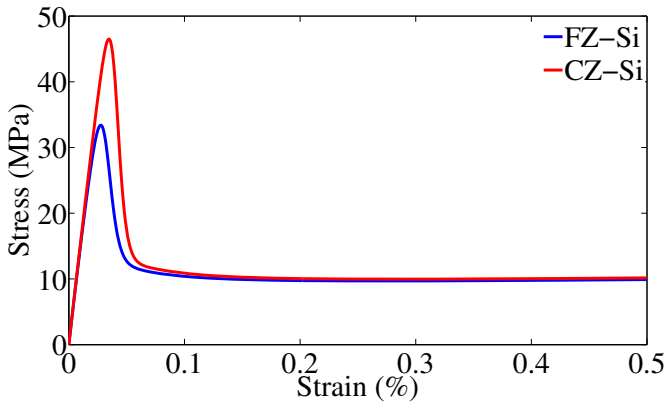

Figure 13.17: Stress-strain curves from uniaxial tensile deformation of the mc-Si block with inclusions along the X-axis direction: comparison between the intrinsic and extrinsic crystals.

to grain boundaries (see Part i), so such a study could prove valuable for industrial applications.

CZ-Si crystal

Comparison between the intrinsic and extrinsic cases gives results similar to those derived in the previous Section. The presence of dissolved oxygen raises the upper yield stress (Fig. 13.17), increases both the absolute Von Mises stress values and heterogeneities in the sample (Fig. 13.18).

Dislocation locking does not increase noticeably the maximum value reached in the sample at $\varepsilon = 0.5\,\%$, but extends the volume submitted to large stresses. On the other hand, at the upper yield point the maximum Von Mises stress in the silicon matrix increases by 32 % when oxygen is present.

Closing remarks

The stress-strain curves obtained from uniaxial tension of a small multicrystalline aggregate in reveal no noticeable anisotropic properties, be it in the elastic or plastic domains. From a *macroscopic* point of view, solar-grade mc-Si materials behave like monocrystals. However, simulations show that a multicrystalline structure leads to *mesoscopic* variations of stress, strain and dislocation densities, owing to kinematic compatibility requirements at the grain boundaries.

Hard inclusions embedded in the silicon matrix increase further the maximum values reached by these variables, and must be accounted for if the fracture behavior of mc-Si is to be correctly predicted.

Simulations of bending tests have revealed that the maximum local Von Mises stress in silicon monocrystals can be derived from a standard

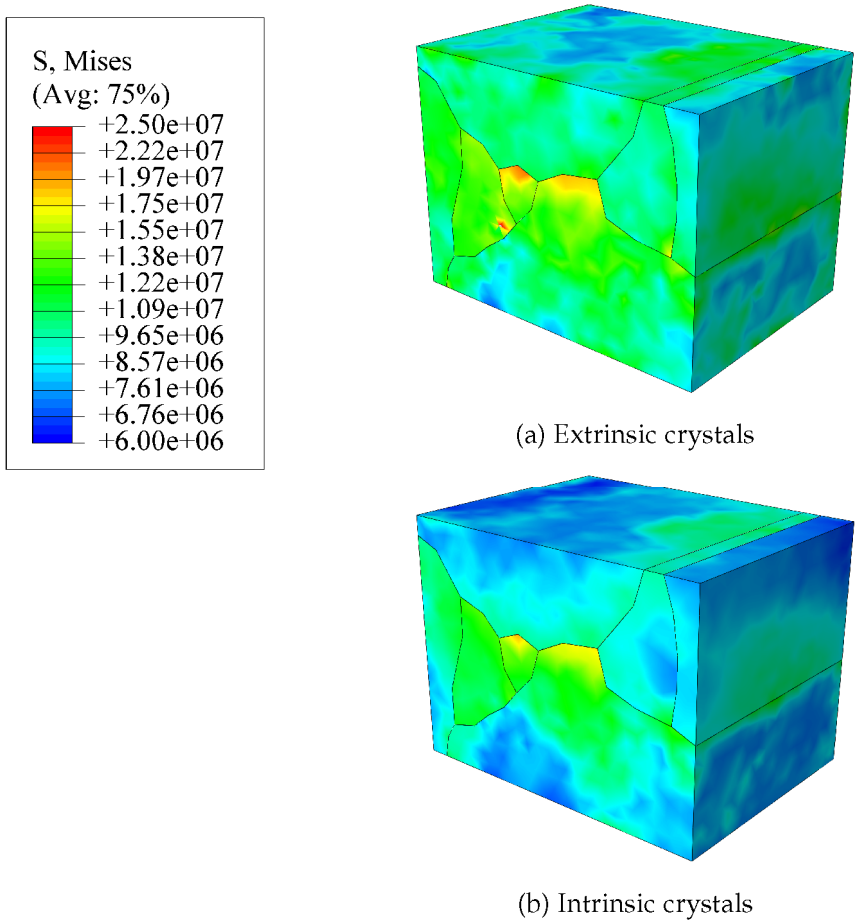

(a) Extrinsic crystals

(b) Intrinsic crystals

Figure 13.18: Von Mises stress distribution at the surface of the mc-Si aggregate after deformation up to $\varepsilon = 0.5\,\%$: comparison between the intrinsic and extrinsic cases. The most visible surface is the (0,0,-1) one.

approach, considering the macroscopic force-time records only. Shifting to a multicrystalline structure invalidates this approximation, leading roughly to a *doubling* of the maximum σ_{VM} with respect to the macroscopically-infered one. Inclusions have an even stronger effect on stress peaks, roughly *tripling* the macroscopic stress value[4].

Meanwhile, these stress increases are local in nature. Kinematic compatibility requirements at the grain boundaries affect the stress levels over a rather short distance, of the order of 0.1-0.2 mm. This means that small grains are particularly prone to significant stress enhancements. Stress peaks generated by inclusions are even more local, developing at the Si/SiC

4 Note that temperature could affect significantly these multiplicative factors, as stress relief by plastic deformation is hindered by lower temperatures.

interface and fading out in the silicon matrix over a distance shorter than 0.01 mm.

13.4 SOLIDIFICATION AND COOLING OF A MC-SI INGOT

13.4.1 *Finite element model*

Geometry and mesh

The previous model applications were concerned with relatively small multicrystalline aggregates. We turn now to the modeling of solidification and cooling of a cylindrical mc-Si ingot, of height 8 cm, diameter 20 cm and made up of 34 columnar grains. The ingot is supported by a stiff perfectly elastic plate, so that friction between the ingot and what could be identified as the bottom of the mould can be included (friction coefficient 0.6). No sticking at the ingot bottom is allowed: all nodes can separate freely from the supporting plate.

The ingot is meshed with slightly more than 90,000 C3D8R elements, and 680 elements are used for the plate (see Fig. 13.19). The grain orientations are generated randomly. Fig. 13.20 shows their stereographic projection with respect to the solidification direction.

Constitutive model and implementation

The simulation of directional solidification poses several problems. Firstly, simulated times are very large as real solidification processes can take several dozens of hours, so using an explicit finite element software is not a reliable solution as the propagated error ought to be large after several millions of time increments, not to mention the time it takes to complete the simulation given the complex constitutive model used.

Therefore, ABAQUS/STANDARD is relied on for the purpose of this simulation. This requires in turn the derivation of the constitutive tangent modulus (CTM) to ensure rapid convergence of the solver iterations at each time increment. This is done in Annex B for the temperature-dependent extended AH model.

The potentially large increments could lead to errors in the integration of the constitutive equations. To remedy this problem, a second order explicit solver with substepping is chosen (see Annex A).

Secondly, directional solidification means that molten silicon is present above the solidified part of the ingot, with the solidification front (the interface between the molten and solid silicon) advancing slowly. The possibility offered by ABAQUS/STANDARD for modeling fluids are inexistent. A solution is to consider that all nodes at temperatures above the melting temperature behave as a soft, perfectly elastic solid[5]. The constitutive behavior of this material is also implemented into the UMAT (see Annex B).

This allows a tremendous simplification of the problem, with the drawback of inducing a discontinuity of the material properties at the solidifica-

5 The constitutive equations are solved at integration points located at the center of the C3D8R elements, where the temperature is interpolated from its values at the nodes.

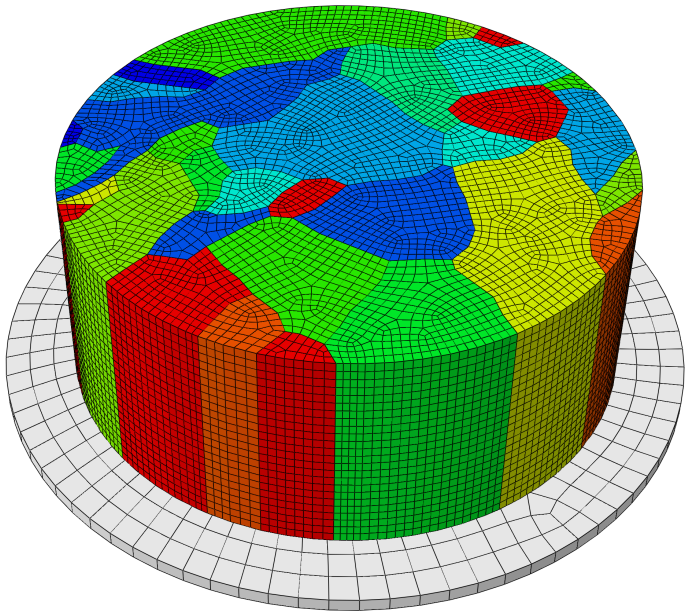

Figure 13.19: Mesh of the mc-Si ingot and supporting plate for simulation of directional solidification. The grains are colored according to their crystallographic orientation.

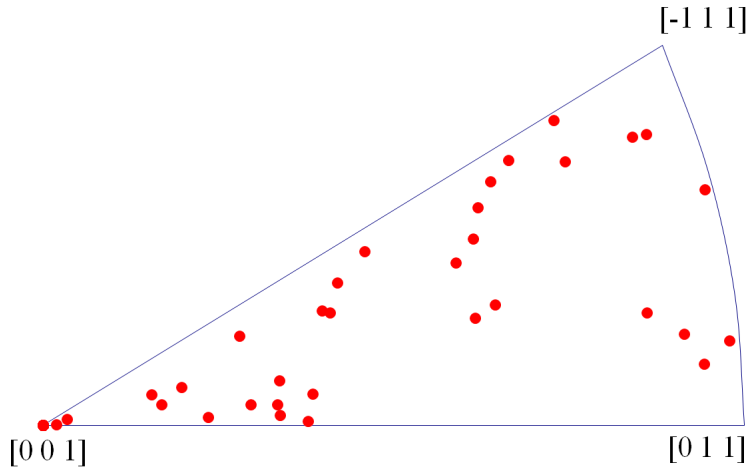

Figure 13.20: Stereographic projection of the 34 grains forming the mc-Si ingot studied in Section 13.4.

tion front. This means that the time steps have to be sufficiently small for the solution to converge correctly at the liquid/solid interface.

13.4.2 *Case studied*

The case considered here is an extremely simplified solidification and cooling process, with a flat solidification front moving upwards at a constant velocity of 1 mm/s. Once solidified, silicon cools down at a rate of 10 K/s. No temperature homogeneization stage is included when the whole ingot is solidified.

These values are extreme, compared to the industrial baseline. However, such choices are made solely to demonstrate the feasability of the simulation and the potential application of a constitutive model to a real multicrystal. With 24 elements in the vertical direction, the temperature interpolation at the integration points is still quite rough and leads to discontinuities in the material properties, that can be resolved by reducing the time increment. Significant simulation times result from this limitation, and only one case is shown in this work.

The initial dislocation density is set to $10^7\ \mathrm{m}^{-2}$ on each slip system.

13.4.3 *Results and discussion*

General observations

TIME INCREMENTS The rather coarse vertical discretization of the mc-Si ingot into 24 finite elements layers, combined with the discontinuity of the constitutive behavior at the melting temperature, has a direct effect on the increment size used by ABAQUS. The "solidification" of an additional layer stiffens the concerned elements, leading to a stress increase that propagates downwards into the solidified material, until relieved by plastic deformation. Each layer solidification requires the use of smaller time increments for convergence to be reached.

It is believed that using a finer vertical discretization can help smoothen this stiffening effect, and could allow the finite element solver iterations to converge more easily.

Once all the ingot has solidified, the time increments increase significantly, even if plasticity is *a priori* still active in the model, pointing to the bottleneck posed by the liquid-to-solid transition.

ABSENCE OF ANNEALING No annealing or temperature homogeneization step is included in the simulations. This means that once solidified, a layer cools down at a constant rate of 10 K/s, until reaching room temperature. The strain gradients that result from the strong temperature gradient in the ingot can be relieved by plastic deformation at rather high temperatures. Below roughly 1073 K, plasticity is much less likely to take place

and the ingot contraction due to the finite thermal expansion coefficient of silicon lead to elastic stress developments.

Once the bottom layer has cooled down to 293 K, it basically stops contracting while the others still do. Behaving mostly elastically at this point, buckling of the ingot follows, during which very high stresses are reached as shown in Fig. 13.21.

Stress and dislocation densities

Fig. 13.22 shows the evolution of the Von Mises stress and total dislocation density in the ingot at different time points. A view cut of the ingot along its diameter is chosen to give more insights about variable distribution inside the block.

STRESS EVOLUTION The Von Mises stress remains very low all throughout the solidification phase, since dislocation generation allows for plastic relief of the stress developments at the liquid/solid interface. Only unidirectional temperature gradients have been imposed in the model, whereas in real cases the solidification front takes a bowed shape that induces additional temperature gradients in the radial direction[6]. These would lead to the development of additional elastic stresses, most likely dampened by dislocation generation.

As could be expected, stresses develop mainly during the cooling step, when silicon behaves elastically.

Disregarding the buckling event, the Von Mises stress remains below 7 MPa and develops mainly at the ingot surfaces. Its distribution follows somehow the grain shapes, with larger values at the boundaries than in the bulk (with a factor 3 to 5 at room temperature). This is particulary visible in Fig. 13.23, showing snapshots of the Von Mises stress at various ingot heights both at the end of the solidification and cooling phases.

Note that the final stress state, with the largest stresses at the top ingot surface, differs from the one simulated after solidification (in which case the highest stresses are recorded at the ingot bottom). This ought to be due to the buckling above-mentioned.

DISLOCATION DENSITY Dislocations are generated at very high temperatures only: most of the increase of $\sum_\alpha \rho_m^{(\alpha)}$ takes place right after solidification of each element layer. This explains why the density pattern does not vary through the solidification phase, as seen in Fig. 13.22.

Interestingly, the model predicts the formation of a columnar structure of dislocation densities, which is in agreement with experimental observations (see Figs. 13.24 and 13.25). This can be understood by noticing that all layers are submitted to approximately the same loading, with the exception of

6 Accounting for them could be rather easily done by providing to ABAQUS the time-temperature evolution for each element. However, mesh issues are bound to appear then.

those close to the surfaces. It is therefore not surprising that the dislocation density distribution stays very stable in the central part of the ingot[7].

Fracture probability

NO MOULD STICKING When the ingot is let free to separate from the supporting plate, the bottom surface quickly takes a bowed shape, leaving the ingot to rest on its outer elements (see Fig. 13.26). The contact between the ingot and the mould is therefore stress-free. Since the crystals are intrinsic, the elastic stress development remains small during solidification and cooling. Even accounting for the buckling phase, the fracture probability remains extremely small, practically null.

THE IMPORTANCE OF BOUNDARY CONDITIONS A simulation has been run in the same conditions, but fixing four regions onto the supporting plate. Fig. 13.27 is obtained; the stresses generated at the sticking elements are so large that material chipping should have occured before the end of the simulation. The regions whose displacements are constrained also see large increases of the dislocation densities.

This simple case shows that boundary conditions and especially any potential sticking with the mould could be severly detrimental to the ingot integrity. The quality of the coating is therefore critical to any attempt to produce low-stress mc-Si materials.

Conclusions

The extended AH model has been implemented in ABAQUS/STANDARD. This requires the derivation of the CTM in order to reach a quadratic convergence of the FE solver iterations. This model can be used to simulate the solidification and cooling of mc-Si ingots. Molten silicon is then modeled as an extremely soft material. Such a choice is relatively straightforward to implement, but has the drawback of leading to discontinuities in the constitutive behavior of the elements, resulting in longer simulation times.

Being able to activate each element layer as the solidification front propagates upwards, or to remesh the solidified material accounting for the liquid/solid interface shape would constitute elegant solutions to this issue, improve the solution accuracy and hopefully reduce the computational cost.

Simulation of directional solidification of an intrinsic mc-Si ingot (34 columnar grains) using an extremely simplified temperature profile shows that dislocations are generated almost exclusively at the solidification front, and develop in columns of increasing density as the front propagates

7 More accurately, all layers are submitted to the same temperature history, and the grains are perfectly columnar. This remark would not be valid if grain growth does not take place in the vertical direction.

towards the top surface. Very low densities are found at the bottom surface, provided the ingot does not stick to the mould.

The multicrystalline structure of the ingot leads to stress and dislocation density heterogeneities, in a way similar to the other cases studied in this Chapter. Grain boundaries see a slight stress increase compared to the bulk.

The temperature homogeneization step is crucial if ingot "buckling" and its associated large stresses are to be avoided. The simulations run in the framework of this PhD work show that the fracture probability in mc-Si materials remains extremely small if boundary conditions to not lead to additional, strong kinematic constraints.

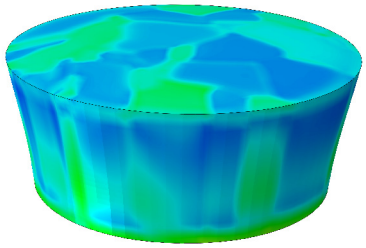

(a) 100 % solidified

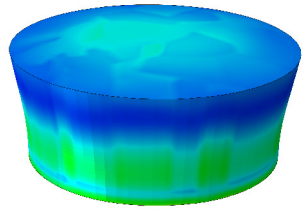

(b) Bottom layer at 293 K

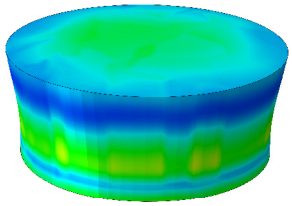

(c) Propagation of 293 K layer

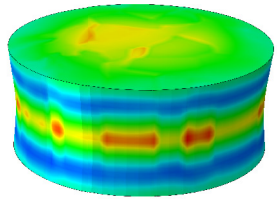

(d) 293 K layer at half-height

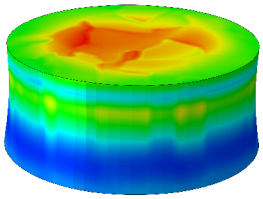

(e) Propagation (cont.)

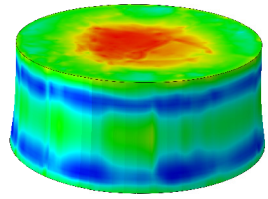

(f)Final state

Figure 13.21: Influence of lack of temperature homogeneization step on the mc-Si ingot deformation and Von Mises stress evolution during the cooling phase. Ingot buckling takes place when the 293 K layer has reached half its height on Fig. (d). Deformations magnified 50 times.

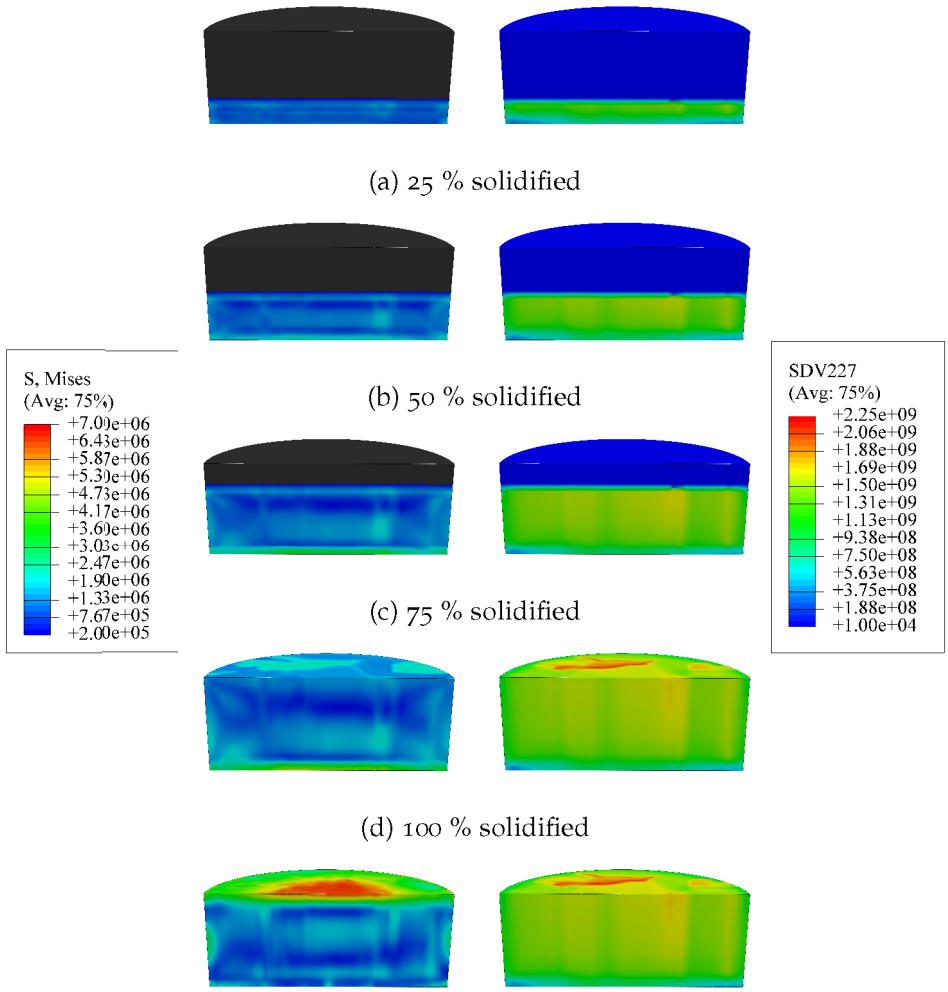

Figure 13.22: (Left-hand side column) Von Mises stress and (right-hand side) total dislocation density distributions at (a) to (d) different stages of the solidification step and (e) after cooling.

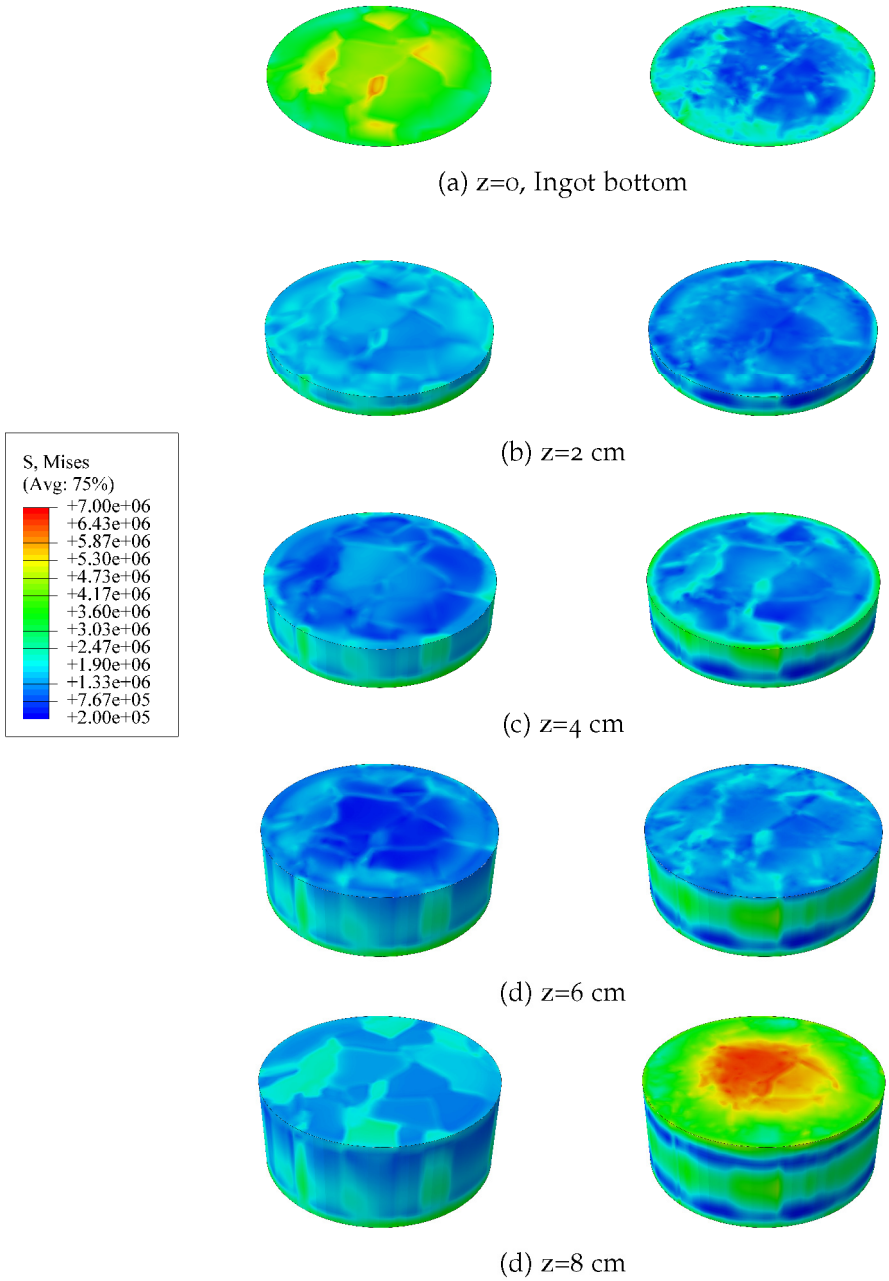

Figure 13.23: Von Mises stress distribution in the ingot at (Left-hand side column) the end of solidification and (right-hand side) after cooling. View cuts at different ingot heights are shown.

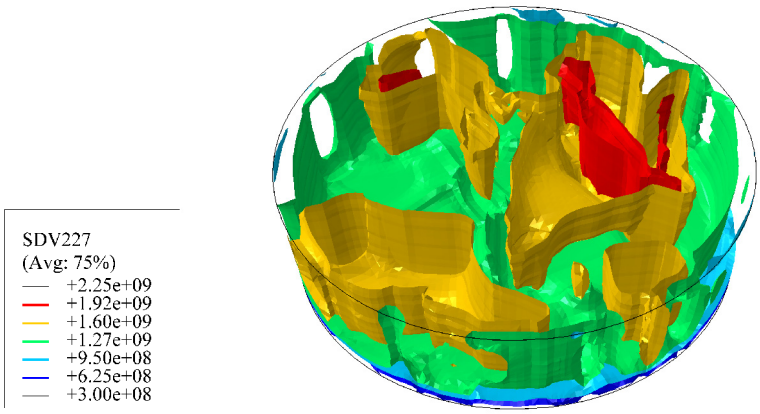

Figure 13.24: Total dislocation density isosurfaces in the solidified mc-Si ingot. Notice the columnar development of dislocation densities.

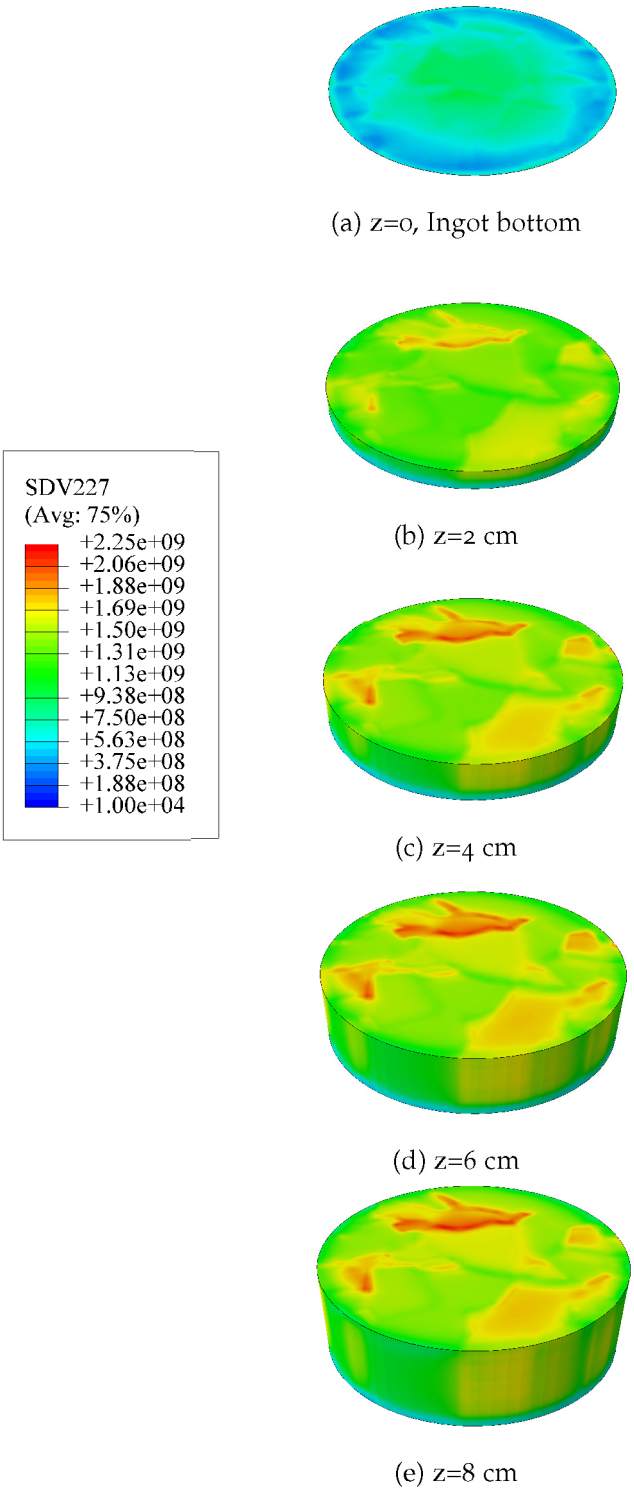

Figure 13.25: Total dislocation density distribution in the ingot at the end of the cooling step. View cuts at different ingot heights are shown.

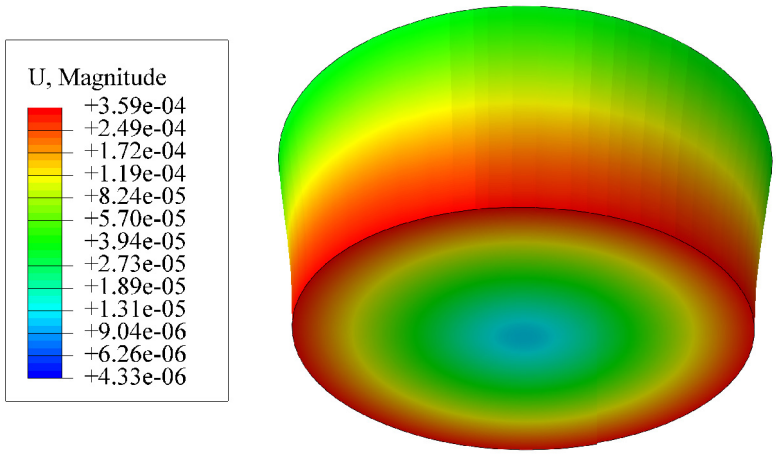

(a) Displacements

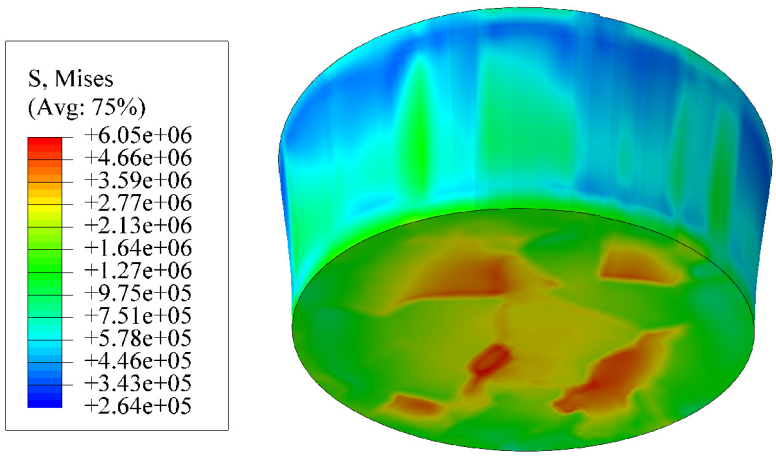

(b) Von Mises stress

Figure 13.26: Displacement magnitude and Von Mises stress in the lower part of the ingot at hte end of solidification, no sticking with the mould.

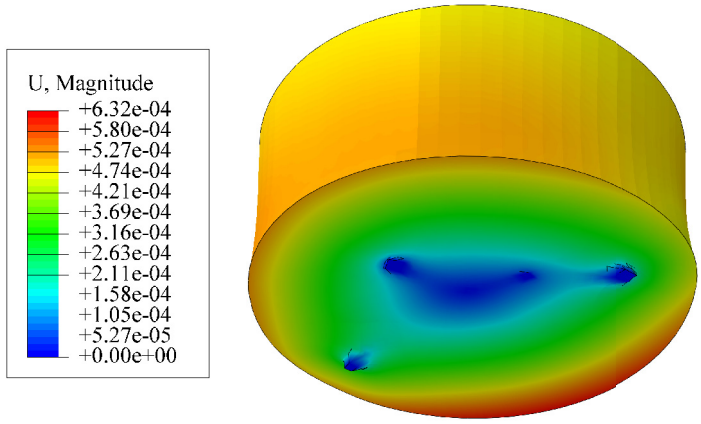

(a) Displacements

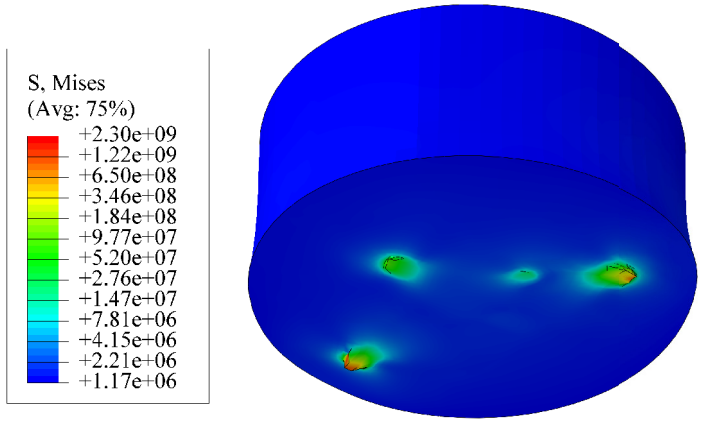

(b) Von Mises stress

Figure 13.27: Displacement magnitude and Von Mises stress in the lower part of the ingot at hte end of solidification. Several regions are constrained in order to simulate sticking with the mould.

CONCLUSION

The extended model of Alexander & Haasen has been used to study the deformation of mono- and multicrystals in various loading situations.

MONOCRYSTALS

Reproductions of 3-point and 4-point bending tests actually performed at NTNU and Tohoku University have shown the influence of the sample crystallographic orientation on the recorded force-time curves. It is seen that the stress-strain derived from standard formulas do not account for plastic localization at the specimen surfaces.

The plastic front propagation mechanisms have been studied, and exhibit noticeable differences depending on the bending test of interest. The location of the maximum stress when plastic deformation has set in varies with time, and can be located inside the bending specimen.

Temperature, strain rate and crystal orientation all affect the stress level and magnitude of dislocation density at a given strain. A striking feature of orientations such as [110] is the inhomogeneous stress distribution they create, exhibiting symmetrical patterns. Such "hard" orientations are simulated to have higher upper yield stresses than a classical [123] one would, although this is in contradiction with experimental results (see Section 2.1). This discrepancy is due to the limitations of the constitutive model in multiple slip situations.

MULTICRYSTALS

Simulations of bending tests and uniaxial tensile testing of multicrystals have revealed two features:

1. There is no significant difference between the recorded force-time curves of tests performed on single or multicrystals. In particular, no secondary upper yield stress is detected in the latter case, and the multicrystal considered does not show any specific anisotropic property.

2. This macroscopic mechanical behavior seemingly similar to the case of single crystals hides strong stress and dislocation density heterogeneities on smaller length scales. These are due to various factors such as relative differences of grain crystallographic orientations and the presence of hard inclusions embedded in the silicon matrix.

These heterogeneities lead to local stress peaks where fracture is more likely to occur. Their intensity and location hav been determined for the

cases studied in this work. The main outcome of these case studies is *the imperative need for a multiscale approach when deformation of multicrystals is considered*. This can be achieved by the modeling of random multicrytals given the statistical properties of the material considered, such as mean grain size and its standard variation, prefered crystallographic orientation, distribution of dislocation density, etc.

APPLICATION TO INDUSTRIAL PROBLEMS

The constitutive model has been implemented into ABAQUS/EXPLICIT and ABAQUS/IMPLICIT, respectively in VUMAT and UMAT user subroutines. The former is well-suited to the study of small specimen loaded during short times, such as bending tests. The latter fits better the requirements posed by simulations of long processes, such as directional solidification of SoG-Si ingots. The last Section of Chapter 13 has shown the applicability of the extended AH constitutive model to such an industrially-relevant problem.

The model outputs agree qualitatively with experimental observations: stresses develop mostly close to the ingot surfaces, and regions of high dislocation densities grow in columns, following the solidification front.

Boundary conditions have a considerable influence on the fracture probability of mc-Si ingots. Ingot sticking most likely leads at best to the growth of dislocation clusters and at worst to local material chipping, which has the potential to tunr into a large-scale ingot fracture if the cracks spread inwards.

Such boundary conditions have a much larger influence on the final stress state than the multicrystalline nature of cast ingots.

FUTURE WORK

Future simulations of bending tests should aim at comparing numerical results with experimental ones. Comparing the results given by various constitutive models could also be of high interest; in particular the influence of forest hardening in multiple slip conditions could be studied with the help of the model derived in Part iii.

The study of bicrystals could shed some light on the influence of the *relative* grain orientations on plastic deformation. The conditions necessary for the development of strong discontinuities in the dislocation densities across a grain boundary could be investigated.

Hard inclusions have a local effect on stress increases and dislocation cluster generation, ans so do grain boundaries, albeit to a lower extent. The combined influence of both factors should be studied as well, by creating a model of bicrystal with several inclusions close to the grain boundary.

Finally, simulation of directional solidification using a real temperature history should be done. This is indeed the ultimate goal of the DESA

project. However, the objective of this Ph.D. was to derive constitutive models only; their application to ingot solidification and cooling is the task of another subgroup. Using a in-house developed finite element code would provide more freedom and better tools to deal with the shape of the solidification front and the fundamental problem of modeling the liquid/solid interface. To this date, ABAQUS does not offer the ability to deal with phase transformation.

BIBLIOGRAPHY

[ASTM a] *C1211-98a: Standard test method for flexural strength of advanced ceramics at elevated temperatures*, ASTM International, 1998

[ASTM b] *C1161-02c (reapproved 2008): Standard test method for flexural strength of advanced ceramics at ambient temperatures*, ASTM International, 2008

[Yonenaga 1978] *Dislocation dynamics in the plastic deformation of silicon crystals. I. Experiments*, I. Yonenaga, K. Sumino, Physica Status Solidi (a), Vol. 50, pp. 685-693, 1978

[Yonenaga 1981] PhD Thesis, I. Yonenaga, Tohuku University, 1981

[Yonenaga 1984] *Mechanical strength of silicon crystals as a function of the oxygen concentration*, I. Yonenaga, K. Sumino, K. Hoshi, Journal of Applied Physics, Vol. 56, No. 8, pp. 2346-2350, 1984

[Yonenaga 2009] Private communication, I. Yonenaga, 2009

CONCLUSION

BRIDGING THE LENGTH SCALES

This thesis has been written on the idea that macroscopic characteristics of the plastic behavior of silicon find their origins in the microscopic processes taking place at dislocations, and that a successful constitutive model should account for them.

Hence, all the constitutive models introduced in this book are based on the very physical mechanisms of plastic deformation, namely dislocation glide on discrete slip systems.

On the other hand, there is no real alternative to such a choice because of the particularly low initial dislocation densities encountered in as-grown semiconductors: reproducing the yield region and its high sensitivity on thermodynamic conditions without relying on the concepts of mobile dislocation density and an analytical velocity law is hardly feasible.

As shown in Part iii, relying on standard dislocation velocity models for fcc metals does not yield satisfying results for silicon at large dislocation densities; in other words, the mechanical behavior of semiconductors cannot be satisfyingly reproduced if the physics of plastic deformation typical of this material class are overlooked.

A multiscale approach is then required: building a dislocation velocity law knowing the rate-limiting mechanisms, deriving rate equations for the evolution of the dislocation densities, and finally linking the microscopic, physically-based internal variables of the model to the macroscopic plastic strain rate through Orowan's law and a relevant kinematic framework.

COMPARISON OF CONSTITUTIVE MODELS FOR SILICON MONOCRYSTALS

Part i has concentrated on exposing the current knowledge we have of silicon mechanics and the physics of its plastic deformation. It has introduced the standard constitutive models available for the study of the yield region of silicon; they have been analyzed in depth in the early Part ii. The following remarks have been made:

1. all models are based on four building blocks:
    a) a stress- and temperature-dependent dislocation velocity law
    b) a rate equation for the evolution of the dislocation density
    c) a definition of the effective stress actually setting dislocations into motion

   d) Orowan's law, allowing the transition from physically-based internal variables to the macroscopic kinematic framework

2. The kinematics into which the constitutive equations are traditionally implemented inherently limit their range of application, either because the model is a scalar one assuming a perfectly controlled crystallographic orientation, homogeneous state of deformation, or because the three-dimensional J_2 approach assumes plasticity to develop isotropically on one single slip system only.

Kinematics

The kinematics have been fixed by adopting a rate-dependent crystal plasticity (RDCP) framework. Accounting for the 12 different slip systems onto which dislocations can actually move and multiply, RDCP also allows couplings between these systems through the constitutive equations. In other words, RDCP enables a correct modeling of latent hardening and forest interactions.

Constitutive equations

Analysis of experimental observations in the yield region and early stage I has revealed the limited validity of assumptions commonly made when deriving constitutive equations. In particular, considering all dislocations to carry plastic flow is the most troublesome point.

EXTENDED AH MODEL Accounting for the build-up of a density of immobile dislocations allows the extended model of Alexander & Haasen introduced in Chapter 6 to predict correctly the effective stress in the steady-state of deformation. Introducing temperature and strain rate dependencies in the dislocation multiplication law increases the model accuracy in the yield region in a wide range of conditions.

EXTRINSIC CRYSTALS Turning to extrinsic crystals, the definition of an effective density of mobile dislocations depending on the concentrations of oxygen at the dislocation cores has enabled the correct reproduction of the upper yield stress dependency on the dissolved oxygen concentration.

A NEW APPROACH Distinguishing between screw and 60° dislocations and accounting for the influence of jog dragging on dislocation motion mechanisms has proved crucial to the success of a novel constitutive model derived in Part iii.

- Although of a high complexity, this model has few unkown parameters requiring identification by comparison with experimental data, most of them being derived on physical principles

- The high model accuracy in the yield region is reinforced by the absence of explicit temperature or strain rate dependency of the dislocation multiplication law
- Stress overshoot, single glide and a strong linear hardening rate in stage II are all retrieved when the rate-limiting action of jogs is accounted for
- The most striking characteristic of plasticity mechanisms in semiconductors is that forest obstacles do not seem to play any significant role in delaying dislocation glide
- The model introduced in Part iii is based on physical processes commonly encountered in materials and can thus be applied to, e.g., fcc crystals, provided the dislocation velocity law in free flight and constitutive parameters are adapted to the material considered

NEW INSIGHTS

The various constitutive models studied in the course of this Ph.D. thesis have been calibrated on uniaxial tensile tests. Other loading cases are investigated in Part iv, relevant to research or industrial applications: three- and four-point bendings of intrinsic and extrinsic mono- and multicrystals, influence of a multicrystalline structure and of hard inclusions on local stress developments, directional solidification of a mc-Si ingot.

The main outcome of the study of multicrystals with a RDCP framework is the ability to quantify the local stress variations due to incompatibility at the grain boundaries and to other factors such as inclusions. All cases reviewed have shown that nothing in the force-time records distinguishes a mono from a multicrystal; the differences are visible on a local scale only and can be revealed by numerical methods.

The models are physically based on dislocation generation and annihilation processes, and can therefore be used to estimate the dislocation density distribution in real samples. This is of high industrial relevance since regions with high dislocation densities typically exhibit low electrical performance.

Finally, coupling of the models with experimental characterization of the fracture strength of silicon materials can yield the evolution of the fracture probability distribution through a given specimen during loading.

FUTURE WORK

This thesis is concluded by some guidelines for future work. The following ideas complement the comments and discussions made at the end of each Part.

Constitutive model

The work introduced in Part iii has shown that dislocation from forest obstacles does not improve the ordering of the upper yield stress as a function of the sample orientation. Further work should therefore concentrate in priority on deriving a more accurate law for the yield region.

The differential equations ruling the evolution of the jog density on dislocations should be improved as well. In particular, the influence of jog dragging on segments of random orientation should be investigated further.

Macroscopic use of models

ADDITIONAL APPLICATIONS Future work should concentrate on applying the constitutive models to various cases. In particular, simulations of ingot casting should be performed considering various thermal histories. The rather large variations of dislocation density across certain grain boundaries, with one grain more dislocated than its neighbour, could be als systematically investigated with the novel constitutive model.

A dozen of multicrystalline bars have been prepared for 4-point bending tests, analyzed by EBSD and PVscan to determine the grain shapes, orientations, and dislocation densities. An interesting task would be to deform them at high temperatures up to large strains and compare the experimental results with the predictions of the advanced constitutive model.

ABAQUS ROUTINE CODING Coding a bilinear continuum brick element (C3D20) into a user-defined element routine (VUEL) for ABAQUS/EXPLICIT could help improve the stability and accuracy of simulations of uniaxial tensile tests at large deformations when jog dragging is accounted for, as it would relieve the user from using computationally heavy remeshing methods to avoid hourglassing.

An alternative solution would be to derive or approximate the constitutive tangent moduli of the complete constitutive model in order to allow its use with ABAQUS/STANDARD.

Theoretical aspects

GRAIN BOUNDARIES The influence of grain boundaries on dislocation generation and annihilation has been neither considered nor reviewed. Therefore, any further attempt to model multicrystals should include a discussion about their possible role in deformation mechanisms.

In particular, grain boundary sliding has been observed to take place at very high temperatures. It is indeed possible that plastic deformation proceeds by other means than dislocation glide at temperatures closer to the melting point; this aspect is worth investigating.

NUMERICAL METHODS Mc-Si materials have rather large grains, so the effect of grain boundaries might not always dominate over bulk hardening mechanisms. However, it could be interesting to estimate intragranular hardening by implementing a nonlocal crystal plasticity framework, or strain gradient crystal plasticity, by the introduction of Geometrically Necessary Dislocations (GNDs). Although of theoretical interest, the relevance of this enrichement for industrial applications ought to be low.

Part V

APPENDIX

A

CRYSTAL PLASTICITY

Numerical tools this thesis relies on are detailed. The mathematical framework of rate dependent crystal plasticity (RDCP) is introduced. Kinematics are derived both at small and finite strains. Some algorithms for explicit integration of the constitutive equations at each integration point are then detailed. The performances of a classical J_2 plastic flow formulation are compared to the ones of a RDCP model. The constitutive equations of Alexander and Haasen are considered at a single integration point, subjected to an isochoric or plane strain deformation. It is shown that RDCP gives far more insight into the deformation mechanisms than a J_2 framework does.

A.1 INTRODUCTION

The constitutive models introduced previously are perfectly suited for an implementation into a standalone routine that considers the deformation in the crystal to be homogeneous and the resolved shear strain rate to be known on the single active slip system. In other words, the models of Chapter 5 are concerned mainly with the micromechanisms of plasticity, the bridge with macroscopic deformation and stress being done simply by introducing the equivalent shear modulus μ^*. The crystallographic orientation of the specimen relative to the tensile (or compressive) axis is in addition known and considered constant throughout deformation.

However, in real cases deformation is most likely not homogeneous; several slip systems can be activated simultaneously and interact with each other, the applied strain rate might vary with time, the lattice might rotate upon straining, etc. Crystal Plasticity (CP) is a mathematical framework allowing the user to account for the real physics of plastic deformation involving dislocation mechanisms. The principle of this framework can traced back to the work of [Taylor 1938], followed by [Bishop 1951]. The underlying idea follows from observation of deformed crystals exhibiting typical patterns: deformation proceeds by gliding along certain directions. This forms slip lines, aggregated in bands of various thickness. Plastic deformation of single crystals proceeds therefore along discrete directions only, whose amount is limited. In the case of face-centered cubic or diamond cubic crystals for example, twelve such slip systems are available, three directions on four planes.

The kinematics of crystal plasticity usually suppose to work with large deformations, although some models adapted to small deformations have been introduced in the literature. The originality of CP is that each slip system can interact with the other ones provided the constitutive equations account for such interaction mechanisms. The determination of the "activated" systems in the original rate *independent* CP formulation follows from computation of the resolved shear stresses on each slip system according to Schmid's law. The system subjected to the highest resolved shear stress is checked against the yield condition for slip (physically meaning, the onset of dislocation motion). If several slip systems are potentially activated, then undetermination can arise because of the normality rule at apexes of the yield surface: which ones are actually active? Adopting a rate *dependent* formulation levels off this undertermination by smoothing the yield surface, as will be exposed later on.

This Annex is organized as follows. Both the rate independent and rate dependent crystal plasticity frameworks are introduced in Section A.2. Two ways of deriving constitutive models are discussed, either based on physically-based internal variables such as dislocation densities, or on phenomenological variables (e.g., the integrated plastic strain). Kinematics of finite deformations and related issues are derived in Section A.3 as large deformations are relied on when implementing new constitutive models in this Thesis. High order explicit algorithms for the integration of the constitutive equations are introduced in Section A.4. Finally, the advantages of adopting a RDCP formulation when complex loadings are considered are shown in Section A.5.

We adopt here Einstein's notation if not stated otherwise: if the same indice is repeated twice in the same equation, then it has be summed over all its possible values.

Numbering and notation of slip systems

Reference is often made in this Thesis to the notation of Schmid & Boas for the denomination of the slip systems and slip planes. Dislocation slip in silicon crystals is allowed on twelve slip systems, the <111> directions on each of the four (111) slip planes. Figure A.1 illustrates the nomenclature used. A letter is associated to each plane, a number to each slip direction, identified in the undeformed fcc lattice respectively by their unit normal vector $\mathbf{n}_0$ and unit unit colinear vector $\mathbf{s}_0$. Table A.1 gives the complete list of systems with their respective numbering from 1 to 12.

Vectors such as $\mathbf{n}_0$, $\mathbf{s}_0$ or the tensile axis are defined in the lattice coordinate system having for basis the ([001], [010], [001]) vectors, each one representing a translation of one basis atom in the lattice (of length a, the lattice parameter).

α - S&B notation	$\mathbf{n}_0^{(\alpha)}$	$\mathbf{s}_0^{(\alpha)}$
1 - A2	$\left(-\frac{1}{\sqrt{3}}\ \frac{1}{\sqrt{3}}\ \frac{1}{\sqrt{3}}\right)$	$\left(0\ -\frac{1}{\sqrt{2}}\ \frac{1}{\sqrt{2}}\right)$
2 - A3	$\left(-\frac{1}{\sqrt{3}}\ \frac{1}{\sqrt{3}}\ \frac{1}{\sqrt{3}}\right)$	$\left(\frac{1}{\sqrt{2}}\ 0\ \frac{1}{\sqrt{2}}\right)$
3 - A6	$\left(-\frac{1}{\sqrt{3}}\ \frac{1}{\sqrt{3}}\ \frac{1}{\sqrt{3}}\right)$	$\left(\frac{1}{\sqrt{2}}\ \frac{1}{\sqrt{2}}\ 0\right)$
4 - B2	$\left(\frac{1}{\sqrt{3}}\ \frac{1}{\sqrt{3}}\ \frac{1}{\sqrt{3}}\right)$	$\left(0\ -\frac{1}{\sqrt{2}}\ \frac{1}{\sqrt{2}}\right)$
5 - B4	$\left(\frac{1}{\sqrt{3}}\ \frac{1}{\sqrt{3}}\ \frac{1}{\sqrt{3}}\right)$	$\left(-\frac{1}{\sqrt{2}}\ 0\ \frac{1}{\sqrt{2}}\right)$
6 - B5	$\left(\frac{1}{\sqrt{3}}\ \frac{1}{\sqrt{3}}\ \frac{1}{\sqrt{3}}\right)$	$\left(-\frac{1}{\sqrt{2}}\ \frac{1}{\sqrt{2}}\ 0\right)$
7 - C1	$\left(-\frac{1}{\sqrt{3}}\ -\frac{1}{\sqrt{3}}\ \frac{1}{\sqrt{3}}\right)$	$\left(0\ \frac{1}{\sqrt{2}}\ \frac{1}{\sqrt{2}}\right)$
8 - C3	$\left(-\frac{1}{\sqrt{3}}\ -\frac{1}{\sqrt{3}}\ \frac{1}{\sqrt{3}}\right)$	$\left(\frac{1}{\sqrt{2}}\ 0\ \frac{1}{\sqrt{2}}\right)$
9 - C5	$\left(-\frac{1}{\sqrt{3}}\ -\frac{1}{\sqrt{3}}\ \frac{1}{\sqrt{3}}\right)$	$\left(-\frac{1}{\sqrt{2}}\ \frac{1}{\sqrt{2}}\ 0\right)$
10 - D1	$\left(\frac{1}{\sqrt{3}}\ -\frac{1}{\sqrt{3}}\ \frac{1}{\sqrt{3}}\right)$	$\left(0\ \frac{1}{\sqrt{2}}\ \frac{1}{\sqrt{2}}\right)$
11 - D4	$\left(\frac{1}{\sqrt{3}}\ -\frac{1}{\sqrt{3}}\ \frac{1}{\sqrt{3}}\right)$	$\left(-\frac{1}{\sqrt{2}}\ 0\ \frac{1}{\sqrt{2}}\right)$
12 - D6	$\left(\frac{1}{\sqrt{3}}\ -\frac{1}{\sqrt{3}}\ \frac{1}{\sqrt{3}}\right)$	$\left(\frac{1}{\sqrt{2}}\ \frac{1}{\sqrt{2}}\ 0\right)$

Table A.1: Slip system numbering and Schmid & Boas notation.

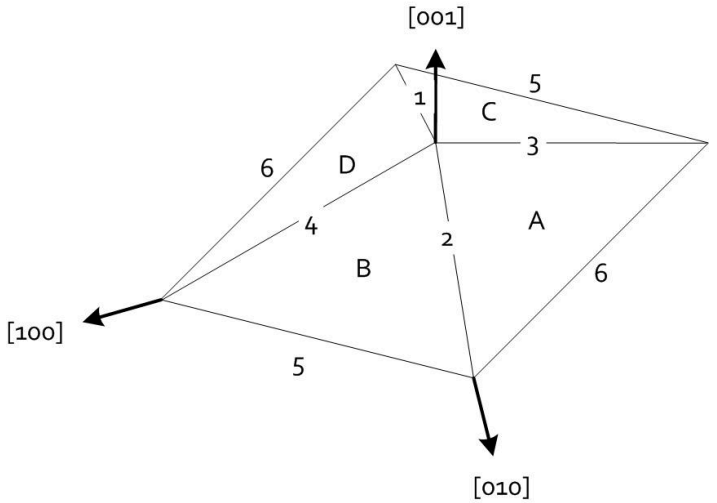

Figure A.1: Schmid & Boas notation.

A.2 PRINCIPLES OF CRYSTAL PLASTICITY

A.2.1 *rate independent formulation*

Because of its historical importance, we introduce first the rate dependent formulation. This formulation is characterized by a relatively heavy implementation cost due to the undetermination of active slip systems in the case of multiple slip, and by the approximative physical assumptions underlying it (materials have in fact a rate dependent behaviour, as observed experimentally especially for silicon).

Mathematical background

Simultaneously to [Mandel 1965], [Hill 1966] published the fundaments for polycrystal plasticity and the basic set of equations governing the slip mechanisms. The interactions between slip systems affect directly the formulation of plasticity. Let us consider for example a classical yield function $f(\sigma, \chi_k) \leq 0$, σ being the second-order stress tensor and χ_k, $0 \leq k \leq N$ the internal variables. If the loading is elastic, then the internal variables will not change, not being affected by a purely elastic loading of the considered system. On the contrary, when the yield surface $f = 0$ is reached, then the internal variables follow evolution law that translate hardening mechanisms.

This yield function remaining unchanged upon purely elastic loading would also hold if the plastic deformation on the slip systems did not affect each other, being perhaps ruled by different yield conditions. Koiter exposed initially such a theory, but its obvious limitations, not taking into account latent hardening, have led to further developments that will be exposed in the following. The amount of glide on slip system α defined by its normal $\mathbf{n}^{(\alpha)}$ and the slip direction $\mathbf{s}^{(\alpha)}$ (vectors in the reference coordinate system), is noted $\gamma^{(\alpha)}$. In the reference coordinate system[1] and using a small deformations formulation, the plastic strain rate reads

$$\dot{\varepsilon}^p = \mathbf{P}^{(\alpha)} \dot{\gamma}^{(\alpha)} \tag{A.1}$$

$$\mathbf{P}^{(\alpha)} = \frac{1}{2} \left(\mathbf{s}^{(\alpha)} \otimes \mathbf{n}^{(\alpha)} + \mathbf{n}^{(\alpha)} \otimes \mathbf{s}^{(\alpha)} \right) \tag{A.2}$$

In the formalism established by [Mandel 1965], glide occuring on the same slip system but in opposite directions is considered as two different mechanisms. For face-centered cubic crystals for example, we have 12 slip *systems*, yielding 24 different slip *mechanisms*. A yield function is defined for each such mechanism, as in the usual plasticity formulation, in function of the stress state and the amount of slip *on all* the mechanisms. For example,

1 The choice of the reference coordinate system is not obvious at first: in addition to the plastic deformation by glide, elastic distortions of the lattice add to the complexity. [Hill 1966] suggested to use the coordinate system co-rotating, but not deforming with the lattice. The objective stress measure chosen is the Cauchy stress on the current configuration.

the yield function of mechanism $\alpha \in [1, 24]$ reads $f_\alpha(\sigma, \gamma^{(\beta)}) \leq 0$, $\beta \in [1, 24]$. In the following, the amount of mechanisms is not limited to 24 and taken as N. Moreover, "mechanisms" is considered as equivalent to "slip systems", keeping in mind that in our formalism, glide on the same physical slip system but in two opposite directions is considered as two different mechanisms. This implies that the relations $\gamma^{(\alpha)} \geq 0$ and $\dot{\gamma}^{(\alpha)} \geq 0$ always hold.

Glide occurs for the mechanism α if $f_\alpha = 0$, the elastic domain in the stress space of six dimensions being defined as the intersection of all the regions that verify $f_\alpha(\sigma, \chi_\beta) \leq 0$. At time t, the mechanism α can be elastic or plastic:

- if $f_\alpha < 0$, the loading is elastic
- if $f_\alpha = 0$ and $\dot{f}_\alpha = 0$, the loading is plastic and stays plastic at $t + \Delta t$
- if $f_\alpha = 0$ and $\dot{f}_\alpha < 0$, elastic unloading from the plastic state occurs at $t + \Delta t$.

Writing f_α as a function of the stress tensor and the internal variables (the amount of slip on the systems), its derivative with respect to time can be written

$$\dot{f}_\alpha = \frac{\partial f_\alpha}{\partial \sigma} : \dot{\sigma} + \frac{\partial f_\alpha}{\partial \gamma_\beta} \dot{\gamma}^{(\beta)} \tag{A.3}$$

and in the following, the hardening matrix $(H_{\alpha\beta})_{1 \leq \alpha, \beta \leq N}$ is used, its coefficients being defined as

$$H_{\alpha\beta} = -\frac{\partial f_\alpha}{\partial \gamma^{(\beta)}} \tag{A.4}$$

The case of plastic loading ($f_\alpha = 0$ and $\dot{f}_\alpha = 0$) is then written for the mechanism α . Combining Equations A.3 and A.4 gives

$$\begin{cases} \frac{\partial f_\alpha}{\partial \sigma} \dot{\sigma} - H_{\alpha\beta} \dot{\gamma}^{(\beta)} = 0 \\ f_\alpha = 0 \\ \dot{\gamma}^{(\alpha)} \geq 0 \end{cases} \tag{A.5}$$

Among the N systems, let us consider n arbitrary that are on their yield surfaces. This leads to C_N^n loading possibilities for this loading case; finally the number of loading cases is

$$\sum_{n=1}^{N} C_N^n = 2^N$$

The principle of maximum work still applies, but a fundamental difference with the classical plasticity formulation is that we do not longer have $\dot{\sigma} : \dot{\varepsilon}^p > 0$. Here, the sign is undetermined and depends on the coefficients of $(H_{\alpha\beta})_{1 \leq \alpha, \beta \leq N}$. The existence of solutions to the equation system and their eventual unicity depends on the properties of the hardening matrix

-if it is symmetric and positive definite for example. For more details, the reader is refered to [Mandel 1965].

This formulation has several implications that are characteristic of the crystal plasticity framework. The most important point might be that the evolution of the yield surface on any slip system α depends on what happens on the other systems β through the $H_{\alpha\beta}$ row, even if the system α is not active. Then, the limiting plane in the stress space for plastic evolution is no longer determined by the relation $\frac{\partial f}{\partial \sigma} : \dot{\sigma} = 0$, since the new formulation implies to take into account the influence of the inverse of $H^{(\nu_1 \ldots \nu_n)}$, assuming it exists:

$$\left(H^{(\nu_1 \ldots \nu_n)}\right)^{-1}_{\beta\alpha} \frac{\partial f_\alpha}{\partial \sigma} : \dot{\sigma} = 0 \tag{A.6}$$

where $(\nu_1 \ldots \nu_n)$ is the set of active systems.

Case of Schmid's law

In the case of crystals ruled by Schmid's law, the yield condition on each system α is expressed in function of the resolved shear stress $\tau^{(\alpha)}$ given by Equation A.7:

$$\tau^{(\alpha)} = \sigma : \mathbf{P}^{(\alpha)} \tag{A.7}$$

The yield function follows (Eq. A.8), and the time derivative of f_α can be derived (Eq. A.9):

$$f_\alpha = \tau^{(\alpha)} - g\left(\gamma_1 \ldots \gamma_N\right) \tag{A.8}$$

$$\dot{f}_\alpha = \mathbf{P}^{(\alpha)} : \dot{\sigma} - \frac{\partial g_\alpha}{\partial \gamma^{(\beta)}} \dot{\gamma}^{(\beta)} \tag{A.9}$$

And we obtain the relation $H_{\alpha\beta} = \frac{\partial g_\alpha}{\partial \gamma^{(\beta)}}$. Using Eqs. A.7 and A.9 for the case of plastic loading ($f_\alpha = 0$ and $\dot{f}_\alpha = 0$), we get Eq. A.10[2], where the hardening matrix now takes its full signification as the link between the slip rate and the stress variation on each slip system. It is reminded that the hardening matrix coefficients vary with deformation.

$$\dot{\tau}^{(\alpha)} = H_{\alpha\beta} \dot{\gamma}^{(\beta)} \tag{A.10}$$

Determination of the active systems among the potentially active ones (those that fulfill the relation $f_\alpha = 0$) is not a trivial exercise. Assuming Schmid's law to be valid, plastic flow then occurs on the system α only if the resolved shear stress reaches a critical value $\tau^{(\alpha)} = \tau_c^{(\alpha)}$, although this is not a sufficient condition to enable plasticity on these *potentially* active systems. The determination of the actual active systems requires the use of an energetic criterion. The method has been exposed in [Franciosi 1982]

2 Here we have assumed that $\dot{\mathbf{P}}^{(\alpha)} = 0$, which is valid in the case of small deformations only. The case of large deformations is introduced further.

and relies on a maximization problem among the ensemble of kinematically admissible stress and strain rates. In order to solve the optimization problem it is required to know the values of the hardening coefficients $H_{\alpha\beta}$ that depend on the amount of plastic deformation.

Determining which set of glide systems are activated and the corresponding amount of glide requires the previous knowledge of the matrix of instantaneous hardening moduli $H_{\alpha\beta}$. They represent the mutual interactions between slip systems on hardening.

Ordering relations between hardening moduli

It has been postulated that latent hardening coefficients, meaning hardening on a slip system caused by the *other* systems, were larger than the self-hardening coefficients (diagonal terms) [Franciosi 1982]. However, experimental observations by [Wu 1991, Bassani 1991] and theoretical investigations (see, e.g., [Zarka 1972]) have led to the opposite conclusion, as well as the establishement of fundamental relations ruling the evolution of the hardening coefficients with the extent of deformation.

These opposing views are due to different uses of the hardening coefficients. [Franciosi 1982] considers the threshold stress determined by relatively short-range elastic interactions between primary dislocations and the forest, leading to the formation of junctions. On the other hand, [Zarka 1972] considers long-range elastic interactions only. In other words, latent hardening by long-range elastic stresses is always weaker than self-hardening; however significant plastic flow on secondary systems sets in only when the applied stress (possibly reduced by latent hardening) reaches the threshold stress.

The rules derived by [Wu 1991, Bassani 1991] are reminded here.

- The total hardening on any latent secondary system is lower than the total hardening coefficient on the primary system. This is valid at least up to the activation of secondary systems.

$$H_{\alpha\beta}(\gamma^{(\alpha)}, 0...0) < H_{\alpha\alpha}(\gamma^{(\alpha)}, 0...0)$$

- The *cumulated* effect of slip on all the systems has a stronger influence on the hardening coefficient than slip on the considered system alone.

$$H_{\alpha\alpha}(\gamma^{(\alpha)}, 0...0) < H_{\alpha\alpha}(\gamma^{(\alpha)}, \gamma^{(\beta)}, ...)$$

- The activation of a secondary slip system leads to larger hardening on this newly activated one, compared to hardening on the primary systems, for low amount of glide on the secondary one.

$$H_{\alpha\alpha}(\gamma^{(\alpha)}, \gamma^{(\beta)}, ...) \ll H_{\beta\beta}(\gamma^{(\alpha)}, \gamma^{(\beta)}, ...) \text{ if } \gamma^{(\beta)} \ll \gamma^{(\alpha)}$$

Some explanations have been given to the different conclusions reached through time by research groups on the ordering of the instantaneous

moduli. The size of the tested samples has an influence on the measured hardening coefficients, because it can favor special glide orientations. Therefore, using the same aspect ratio neutralizes this effect and yields the preceding results. In addition, the different postulates concerning the ordering of the hardening moduli are due to different ways of measuring the yield stress when the secondary systems are activated. Usually a backward extrapolation from the stress-strain curve is used, which does not take into consideration the rapid and large hardening taking place upon reloading due to the existence of forest dislocations on the secondary systems created during the first loading stage. This gives artificially high flow stresses for secondary systems.

Analytical expressions of the instantaneous hardening moduli

From experiments on copper single crystals, [Wu 1991, Bassani 1991] determined a general expression for the off-diagonal components of the hardening matrix $\left(H_{\alpha\beta}\right)_{1\leq\alpha,\beta\leq m}$, considering them to be proportional to the associated diagonal moduli: $H_{\alpha\beta} = qH_{\alpha\alpha}$, $\alpha \neq \beta$, $0 \leq q < 1$. They showed moreover that the behaviour of such crystals was satisfactorily described using $q = 0$, meaning that the hardening matrix was diagonal in their case. Even if this formulation is adapted for easy glide, it is believed to hold for further hardening stages. They give the following expression for the instantaneous hardening moduli:

$$\begin{cases} H_{\alpha\alpha} = F(\gamma^{(\alpha)})G(\{\gamma^{(\beta)}\ \beta \neq \alpha\}) \\ H_{\alpha\beta} = qH_{\alpha\alpha},\ \alpha \neq \beta,\ 0 \leq q < 1 \end{cases} \tag{A.11}$$

Multiplicative decomposition is assumed, that allows a distinction between influence of primary and latent slip on self-hardening moduli. Other expressions of the hardening matrix have been suggested in the literature.

One must be aware that these moduli are expressed as functions of the total plastic deformation on each slip sytem $\gamma^{(\alpha)}$, obtained by integration of the glide rates throughout the crystal history. This formulation is called a *continuum slip model* by [Rice 1971]. It is worth reminding that the plastic strains are *not* state variables. Physically relevant variables would be for example dislocation densities (leading to a *discrete dislocation slip model* according to the same author). On the other hand, choosing to express the hardening moduli as a function of the dislocation densities requires additional equations describing their evolution, the glide rates being obtained directly from the solution to the minimization problem described above. Other expressions of hardening moduli can be found for instance in [Asaro 1983, Bronkhorst 1992].

[Zarka 1972] gives the expression of the yield function for the monocrystal as a function of the densities of dislocations on the systems, using his results derived from theoretical calculations to obtain the critical resolved

shear stress (see Section 6.3.2), from which the hardening matrix can be expressed as a function of the dislocation densities:

$$f = \sum_{\alpha} f_{\alpha} = \sum_{\alpha} K_{\alpha} \frac{\rho_m^{(\alpha)}}{\rho_f^{(\alpha)}} (\tau^{(\alpha)} - \tau_{int}^{(\alpha)})^2 \tag{A.12}$$

A.2.2 *Rate dependent materials*

The mechanical behaviour of most materials is rate dependent. The hardening laws for such materials differ from the examples given above. In particular, the numerical treatment of the model is lighter because there is no more need to look for the set of active slip systems. In the rate dependent framework, all systems follow the same evolution law whatever the conditions. In particular, undetermination of the active slip systems is no longer an issue, the apexes of the yield surface being smoothened. The only requirement is to find an evolution law for the slip rates that depends on the resolved shear stress as well as other internal variables. Several models have been introduced in the literature. Some examples are introduced below.

Thermally activated glide

An interesting model accounting for changes of temperature can be mentioned from the work of [Harder 1999], who considers the case of thermally activated slip rate (Eq. A.13). The effective stress $\tau_{eff}^{(\alpha)}$ accounts for kinematic hardening. More general models of thermally activated glide are available in the literature (see, e.g., [Kocks 1975, Nemat-Nasser 2004]).

$$\dot{\gamma}^{(\alpha)} = \dot{\gamma}_0^{(\alpha)} \left(\frac{\left| \tau_{eff}^{(\alpha)} \right|}{\mu} \right)^n \exp\left(-\frac{\Delta F}{k_b T} \left(1 - \frac{\left| \tau_{eff}^{(\alpha)} \right|}{\tau_{ref}^{(\alpha)}} \right) \right) sign\left(\tau_{eff}^{(\alpha)} \right) \tag{A.13}$$

Power law

The derivation of a power law for dislocation velocity and accordingly the strain rate is a particular case of the more general expression for dislocation velocity moving through thermally overcomable obstacles, as discussed in [Kocks 1975]. In this case, the slip rate on a given system α is expressed as a power function of the flow stress, normalized by a reference stress $\tau_{ref}^{(\alpha)}$, typically the internal stress (Eq. A.14), originally developped by [Hutchinson 1976] and adopted by several authors (see for example [Peirce 1983, Bronkhorst 1992, Zikry 1996]). The evolution of the reference stress can depend for example on the internal variables of all slip systems through an interaction matrix H similar to the hardening matrix introduced above. As in Section A.2, the internal variables can be the total strain or

the dislocation densities on the slip systems. An example of such a reference stress is given in Equation A.15 for the case of a continuum slip model [Peirce 1983] and Equation A.16 for a discrete dislocation slip model [Zikry 1995, Zikry 1996].

$$\dot{\gamma}^{(\alpha)} = \dot{\gamma}_0^{(\alpha)} \left(\frac{\tau^{(\alpha)}}{\tau_{ref}^{(\alpha)}} \right) \left| \frac{\tau^{(\alpha)}}{\tau_{ref}^{(\alpha)}} \right|^{n-1} \tag{A.14}$$

$$\begin{cases} \tau_{ref}^{(\alpha)} = \tau_0^{(\alpha)} + \int_0^t \dot{\tau}_{ref}^{(\alpha)} \\ \dot{\tau}_{ref}^{(\alpha)} = \sum_\beta H_{\alpha\beta} \left| \dot{\gamma}^{(\beta)} \right| \end{cases} \tag{A.15}$$

$$\tau_{ref}^{(\alpha)} = \tau_y^{(\alpha)} + a_1 \mu b \sqrt{\rho_{im}^{(\alpha)}} + a_2 \mu b \sqrt{\rho_{im}^{(\beta)}},\ \beta \neq \alpha \tag{A.16}$$

The strain rate prefactor $\dot{\gamma}_0^{(\alpha)}$ comes from Orowan's law and should be depending on the density of mobile dislocations that carry plastic flow, although in practice it is considered to remain constant [Nemat-Nasser 2004]. This is actually justified as the density of mobile dislocations quickly saturates to reach a steady-state value in easy glide.

The stress exponent n is usually very high to guarantee that the slip rates remain extremely small at low applied stresses. On the other hand, as soon as it comes closer to the reference stress the strain rate increases quickly. Negative strain rates are allowed by such a law, reducing the amount of systems required by the model.

Isotropic and kinematic hardening

It is also possible to take into account isotropic and kinematic hardening, see Eq. A.17, as done by [Meric 1991, Barbe 2001a, Barbe 2001b]. There, $k^{(\alpha)}$ translates the kinematic hardening, while $i^{(\alpha)}$ represents isotropic hardening. Of course, these variables follow evolution laws depending on for example the dislocation interactions and other internal variables. This model represents satisfactorily the Bauschinger effect and can be used e.g. for cyclic loadings.

$$\dot{\gamma}^{(\alpha)} = \left\langle \frac{\left| \tau^{(\alpha)} - k^{(\alpha)} \right| - i^{(\alpha)}}{\tau_{ref}^{(\alpha)}} \right\rangle^n sign\left(\tau^{(\alpha)} - k^{(\alpha)} \right) \tag{A.17}$$

Several models for rate dependent materials are available in the literature. They all express the strain rate on the slip systems as a function of the applied stress and a set of internal variables. It must be noted that these models might be extremely nonlinear and difficult to integrate implicitely. Section A.4 introduces high-order explicit solvers that can be used for this purpose.

The mathematical framework described above has been derived in the small strains approximation. If the constitutive equations are updated in the current configuration, the stress and strain increments are likely to be small enough to justify a local use of small strain, provided that the lattice spin due to plastic slip is accounted for and correctly sent to the global solver. It is however possible to express the whole problem in finite strains, a formulation that is useful, e.g., to identify the model parameters from uniaxial tensile tests of single crystals loaded in single glide, as secondary slip then sets in at very large strains.

A.3 LARGE DEFORMATIONS

The obvious limitations of the small strains formulation when applied to real cases (for example, metal forming) have been overcome by using large deformations and a multiplicative decomposition of the displacement gradient tensor [Lee 1969, Rice 1971]. It is then assumed that the total deformation gradient can be decomposed into a purely plastic term, translating glide on the slip systems and an intermediate stress-free configuration, whereas lattice rotation, rigid body rotations and other additional effects are gathered into the thermoelastic part of the gradient. It is also possible to extract the thermal part of the latter.

A.3.1 *Kinematics*

For a comprehensive review of the mathematic formulation of the large deformations in the context of crystal plasticity, the reader is refered for example to [Asaro 1983]. The basics are detailed here.

Consider the transformation $\mathbf{u}(\mathbf{X}, t)$ that maps at each time t a material point $\mathbf{X}$ in the inital configuration $\mathcal{C}_0$ into a material point $\mathbf{x}$ in the current configuration $\mathcal{C}_t$ (Eq. A.18). The deformation gradient $\mathbf{F}$ is defined as in Eq. A.19.

$$\mathbf{u} : \mathbf{X} \in \mathcal{C}_0 \longrightarrow \mathbf{x} = \mathbf{u}(\mathbf{X}, t) \in \mathcal{C}_t \tag{A.18}$$

$$\mathbf{F} = \boldsymbol{\nabla}\mathbf{u}(\mathbf{X}, t) = \frac{\partial \mathbf{u}(\mathbf{X}, t)}{\partial \mathbf{X}} \tag{A.19}$$

It is assumed that the material is deformed plastically *solely through slip mechanisms*, meaning that deformation mechanisms such as twinning or dislocation climb are not taken into account, although they could be implemented as well. The associated plastic (or inelastic) deformation gradient tensor is noted $\mathbf{F}^p$, and represents an intermediate stress-free configuration. Slip leaves the *lattice* unrotated and unstressed, but induces a rotation of the *material point* that can be identified by polar decomposition of $\mathbf{F}^p$.

In addition to slip, the lattice undergoes elastic deformations and rigid-body rotations embedded into the elastic deformation gradient $\mathbf{F}^e$, the ultimate deformation gradient tensor being given by Eq. A.20, see Figure A.2. This definition implies that plastic deformation is isochoric, meaning that $\det \mathbf{F}^p = 1$ and $\det \mathbf{F} = \det \mathbf{F}^e > 0$.

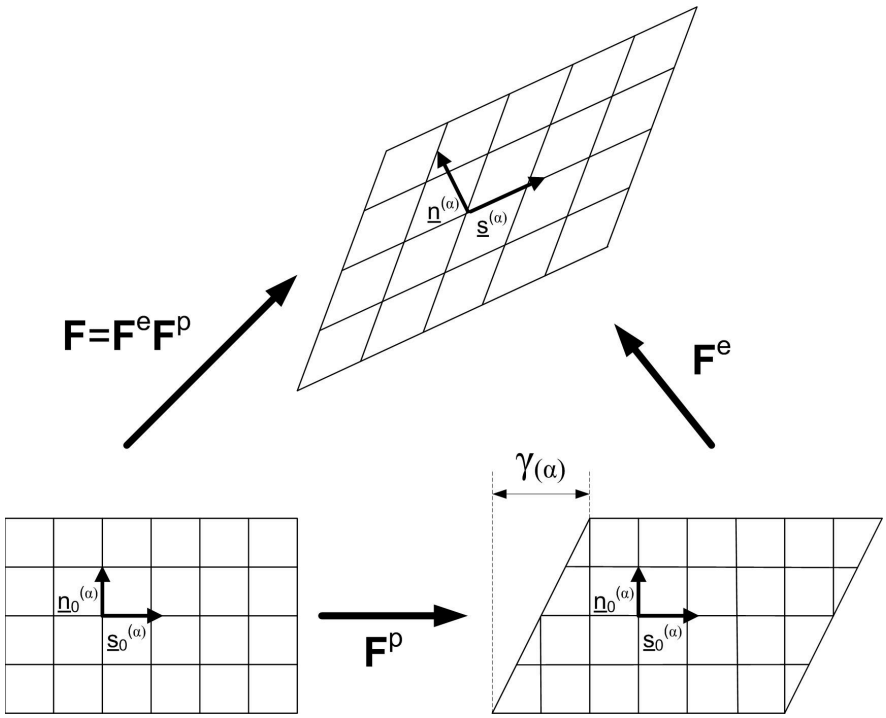

Figure A.2: Kinematics of deformation of a solid. The multiplicative decomposition of the displacement gradient tensor is shown.

$$\mathbf{F} = \mathbf{F}^e\mathbf{F}^p \tag{A.20}$$

The slip direction $\mathbf{s}_0^{(\alpha)}$ of a glide system α in the undeformed configuration becomes upon application of $\mathbf{F}$, $\mathbf{s}^{(\alpha)} = \mathbf{F}^e\mathbf{s}_0^{(\alpha)}$. The direction normal to the slip plane becomes $\mathbf{n}^{(\alpha)} = \mathbf{F}^{e-1}\mathbf{n}_0^{(\alpha)}$. This is because plastic deformation by pure slip does not affect the slip directions and the normal to the slip planes: for example, $\mathbf{F}^p\mathbf{s}_0^{(\alpha)} = \mathbf{s}_0^{(\alpha)}$. These vectors in the current configuration are still orthogonal, but no longer *unit* vectors. The velocity gradient $\mathbf{L}$ is equal to

$$\mathbf{L} = \dot{\mathbf{F}}\mathbf{F}^{-1} = \dot{\mathbf{F}}^e\mathbf{F}^{e-1} + \mathbf{F}^e\dot{\mathbf{F}}^p\mathbf{F}^{p-1}\mathbf{F}^{e-1} = \mathbf{L}^e + \mathbf{L}^p = (\mathbf{D}^e + \mathbf{\Omega}^e) + (\mathbf{D}^p + \mathbf{\Omega}^p) \tag{A.21}$$

The tensors $\mathbf{D}$ and $\mathbf{\Omega}$ are the rates of stretching and spin tensors, respectively, defined in the spatial coordinates by

$$\begin{cases} \mathbf{D} = \frac{1}{2}\left(\boldsymbol{\nabla}\mathbf{v} +^t \boldsymbol{\nabla}\mathbf{v}\right) = \mathbf{D}^e + \mathbf{D}^p \\ \mathbf{\Omega} = \frac{1}{2}\left(\boldsymbol{\nabla}\mathbf{v} -^t \boldsymbol{\nabla}\mathbf{v}\right) = \mathbf{\Omega}^e + \mathbf{\Omega}^p \end{cases} \tag{A.22}$$

with $\mathbf{v}(\mathbf{x}, t) = \frac{\partial \mathbf{u}}{\partial t}$. Since we assume that plastic deformation happens by slip only, the plastic velocity gradient can be decomposed in the sum of the amount of plastic strain rate on all slip systems defined relative to the reference state lattice:

$$\mathbf{L}^p = \mathbf{D}^p + \mathbf{\Omega}^p = \mathbf{F}^e\dot{\mathbf{F}}^p\mathbf{F}^{p-1}\mathbf{F}^{e-1} = \sum_\alpha \dot{\gamma}^{(\alpha)}\mathbf{s}^{(\alpha)} \otimes \mathbf{n}^{(\alpha)} \tag{A.23}$$

The $\dot{\gamma}^{(\alpha)}$ are defined so that:

$$\dot{\mathbf{F}}^p\mathbf{F}^{p-1} = \sum_\alpha \dot{\gamma}^{(\alpha)}\mathbf{s}_0^{(\alpha)} \otimes \mathbf{n}_0^{(\alpha)} \tag{A.24}$$

Physically, they are the slip rates on the different slip systems. Eq. A.24 can be used to update the plastic deformation gradient. The introduction of two additional tensors $\mathbf{P}^{(\alpha)}$ and $\mathbf{W}^{(\alpha)}$ (Eq. A.25) leads to the expression of the plastic stretching and spinning tensors as sole functions of the $\dot{\gamma}^{(\alpha)}$'s (Eq. A.26):

$$\begin{cases} \mathbf{P}^{(\alpha)} = \frac{1}{2}\left(\mathbf{s}^{(\alpha)} \otimes \mathbf{n}^{(\alpha)} + \mathbf{n}^{(\alpha)} \otimes \mathbf{s}^{(\alpha)}\right) \\ \mathbf{W}^{(\alpha)} = \frac{1}{2}\left(\mathbf{s}^{(\alpha)} \otimes \mathbf{n}^{(\alpha)} - \mathbf{n}^{(\alpha)} \otimes \mathbf{s}^{(\alpha)}\right) \end{cases} \tag{A.25}$$

$$\begin{cases} \mathbf{D}^p = \sum_\alpha \mathbf{P}^{(\alpha)}\dot{\gamma}^{(\alpha)} \\ \mathbf{\Omega}^p = \sum_\alpha \mathbf{W}^{(\alpha)}\dot{\gamma}^{(\alpha)} \end{cases} \tag{A.26}$$

A.3.2 *Stress update*

Two approaches are available to integrate the stress: either the solution is found on the actual configuration, or a pull-back is imposed. The latter method is more convenient from a computational point of view, but both ways are introduced in the following.

Incremental update on the current configuration

The constitutive law in large deformations requires the choice of an objective stress rate and of a stress measure. We choose here the Jaumann rate of Kirchhoff stress, since the Kirchhoff stress is the work conjugate of the strain field $\mathbf{D}$ defined previously. The Kirchhoff stress $\boldsymbol{\tau}$ is related to the Cauchy stress $\boldsymbol{\sigma}$ by the determinant J of the deformation gradient:

$$\begin{aligned} J &= \det \mathbf{F} = \det \mathbf{F}^e \\ \boldsymbol{\tau} &= J\boldsymbol{\sigma} \end{aligned} \tag{A.27}$$

The Jaumann rate is defined by:

$$\overset{\circ}{\boldsymbol{\tau}} = \dot{\boldsymbol{\tau}} - \boldsymbol{\Omega}\boldsymbol{\tau} + \boldsymbol{\tau}\boldsymbol{\Omega} \tag{A.28}$$

We introduce the fourth order tensor of elastic moduli $\boldsymbol{\mathcal{C}}$ so that $\overset{\circ}{\boldsymbol{\tau}}^e = \boldsymbol{\mathcal{C}} : \mathbf{D}^e$. The difference between the rates of the purely elastic and the total Kirchhoff stress is written with the help of a second-order tensor $\boldsymbol{\beta}^{(\alpha)}$, see Eq. A.29. This yields the expression of the material Jaumann stress rate (Eq. A.30):

$$\overset{\circ}{\boldsymbol{\tau}}^e - \overset{\circ}{\boldsymbol{\tau}} = \sum_\alpha \boldsymbol{\beta}^{(\alpha)} \dot{\gamma}^{(\alpha)},\ \boldsymbol{\beta}^{(\alpha)} = \mathbf{W}^{(\alpha)}\boldsymbol{\tau} - \boldsymbol{\tau}\mathbf{W}^{(\alpha)} \tag{A.29}$$

$$\overset{\circ}{\boldsymbol{\tau}} = \boldsymbol{\mathcal{C}} : \mathbf{D} - \sum_\alpha \left(\boldsymbol{\mathcal{C}} : \mathbf{P}^{(\alpha)} + \boldsymbol{\beta}^{(\alpha)} \right) \dot{\gamma}^{(\alpha)} \tag{A.30}$$

Finally, the Schmid stress (or resolved shear stress) $\tau^{(\alpha)}$ on the slip system α is defined to be the work conjugate of $\dot{\gamma}^{(\alpha)}$:

$$\begin{cases} \boldsymbol{\tau} : \mathbf{D}^p = \sum_\alpha \tau^{(\alpha)} \dot{\gamma}^{(\alpha)} \\ \tau^{(\alpha)} = \mathbf{P}^{(\alpha)} : \boldsymbol{\tau} \end{cases} \tag{A.31}$$

Since the $\mathbf{P}^{(\alpha)}$ vary with the lattice and are not constant with respect to time, the time derivative of the Schmid stress reads $\dot{\tau}^{(\alpha)} = \dot{\mathbf{P}}^{(\alpha)} : \boldsymbol{\tau} + \mathbf{P}^{(\alpha)} : \dot{\boldsymbol{\tau}}$, which can be written in different forms, using the Jaumann rate.

Derivation on the initial configuration

An alternative framework has been suggested, where another stress and stress measure pair is chosen (see for example [Bronkhorst 1992, Kalidindi 1992]). Adopting the strain measure of Green-Lagrange and considering only the elastic part of the displacement gradient tensor that creates stresses, it follows

$$\mathbf{E}^e = \frac{1}{2}\left(\mathbf{F}^{eT}\mathbf{F}^e - \mathbf{I} \right) \tag{A.32}$$

its work conjugate is the second Piola-Kirchhoff stress (2PK) (Eq. A.33) which is assumed in the case of a hyperelastic material to be related to the

strain by a fourth-order elastic tensor $\mathcal{L}$ (Eq. A.34). This linear approximation coming from a Taylor expansion of the 2PK stress is valid for small *elastic* strains only, which is usually the case for metals.

$$\mathbf{S}^e = \mathbf{F}^{e-1}(J\sigma)\mathbf{F}^{e-T} \tag{A.33}$$

$$\mathbf{S}^e = \mathcal{L} : \mathbf{E}^e \tag{A.34}$$

As previously, the plastic deformation gradient is given by Eq. A.24, and the definition of the resolved shear stress follows from the plastic stress power per unit volume associated to $\mathbf{L}^p$:

$$\tau^{(\alpha)} = \mathbf{S}^e : sym(\mathbf{F}^{eT}\mathbf{F}^e\mathbf{s}_0^{(\alpha)} \otimes \mathbf{n}_0^{(\alpha)}) \tag{A.35}$$

In the case where elastic deformations are small, $\mathbf{C}^e = \mathbf{F}^{eT}\mathbf{F}^e$ can be approximated by the identity tensor, giving equation A.36 for the Schmid stress, expressed as a function of the lattice vectors in the initial configuration only.

$$\tau^{(\alpha)} = \mathbf{S}^e : sym(\mathbf{s}_0^{(\alpha)} \otimes \mathbf{n}_0^{(\alpha)}) \tag{A.36}$$

The use of such an integration scheme on the initial configuration is attractive since the stresses are related uniquely to the elastic part of the deformation gradient. Given the updated total deformation gradient $\mathbf{F}$ and by integration of its plastic part $\mathbf{F}^p$ by virtue of eq. A.24, $\mathbf{F}^e$ is directly found by using the multiplicative decomposition of $\mathbf{F}$.

A.3.3 *Thermal expansion*

We have until now assumed an isothermal framework. Temperature variations and gradients lead nonetheless to strain build-up through the thermal expansion coefficients and the stiffness anisotropy of the materials. In the case of large deformations, it is possible to consider the related displacement gradient tensor $\mathbf{F}^\theta$. The total deformation gradient reads[3]:

$$\mathbf{F} = \mathbf{F}^e\mathbf{F}^p\mathbf{F}^\theta \tag{A.37}$$

where it is assumed that plastic deformation takes place on the thermally expanded *unstressed* configuration. Figure A.2 is no longer valid and should hence be replaced by Figure A.3. The lattice unit vectors $\mathbf{s}_0^{(\alpha)}$ and $\mathbf{n}_0^{(\alpha)}$ defined above are affected by the thermal expansion and plastic glide takes place on the intermediate (unstressed) configuration characterized by the vectors $\mathbf{F}^\theta\mathbf{s}_0^{(\alpha)}$ and $\mathbf{F}^{\theta-1}\mathbf{n}_0^{(\alpha)}$, as depicted in Figure A.3. The lattice orientation remains nonetheless unchanged by the application of both the thermal and plastic parts of the deformation gradient, the elastic part still being the only responsible for stress development.

3 We use in this section the symbol θ to denote temperature instead of T, since the latter is also used to transpose a tensor.

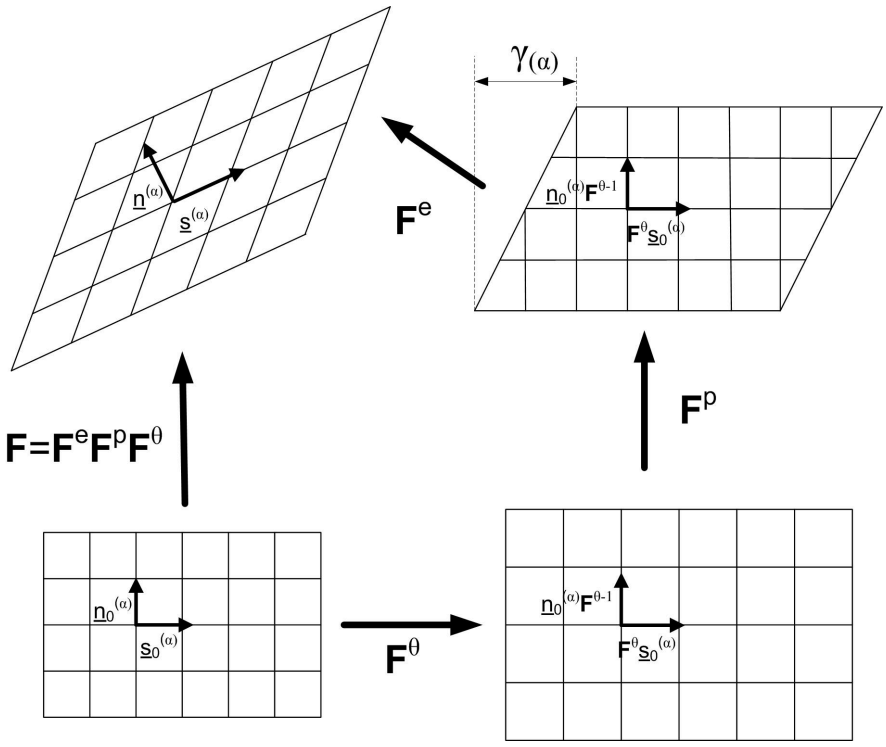

Figure A.3: Kinematics of deformation of a solid in the case of non-isothermal conditions. The multiplicative decomposition of the displacement gradient tensor is shown.

It is also possible to consider an alternative decomposition of the deformation gradient by applying first the inelastic deformations, followed by the thermal expansion. The deformation gradient reads in this case $\mathbf{F} = \mathbf{F}^e\mathbf{F}^\theta\mathbf{F}^p$, but such a formulation is less physically meaningful because plastic strains are not allowed to be applied on the actual relaxed configuration of the lattice. The choice of Eq. A.37 allows plastic slip to depend on temperature. $\mathbf{F}^\theta$ is given by Eq. A.38 for the most general case, where $\boldsymbol{\alpha}$ is the tensor of thermal expansion coefficients and θ_0 a reference temperature [Meissonnier 2001]. This expression can be derived with respect to time in the case of temperature-independent thermal expansion coefficients to obtain Eq. A.39 [McHugh 1993].

$$\mathbf{F}^\theta = \exp\left(\boldsymbol{\alpha}(\theta - \theta_0)\right) \tag{A.38}$$

$$\dot{\mathbf{F}}^\theta\mathbf{F}^{\theta-1} = \dot{\theta}\boldsymbol{\alpha} \tag{A.39}$$

Since the thermal expansion coefficients of silicon are temperature-dependent and we are aiming at covering a large temperature span we will use the exact derivation of Eq. A.38, leading to:

$$\dot{\mathbf{F}}^\theta\mathbf{F}^{\theta-1} = \dot{\theta}\left(\boldsymbol{\alpha} + (\theta - \theta_0)\frac{\partial\boldsymbol{\alpha}}{\partial\theta}\right) \tag{A.40}$$

The numerical treatment of the equations is similar to previously, writing $\mathbf{F}^e = \mathbf{F}(\mathbf{F}^p\mathbf{F}^\theta)^{-1}$. Therefore, once the plastic and thermal parts of the deformation gradient are integrated (using Eqs. A.24 and A.40 respectively) the elastic part can easily be obtained.

$$\mathbf{L} = \dot{\mathbf{F}}\mathbf{F}^{-1} = \mathbf{L}^e + \mathbf{L}^p + \mathbf{L}^\theta \tag{A.41}$$

$$\mathbf{L}^\theta = \mathbf{F}^e\mathbf{F}^p\left(\dot{\mathbf{F}}^\theta\mathbf{F}^{\theta-1}\right)(\mathbf{F}^e\mathbf{F}^p)^{-1} \tag{A.42}$$

A.4 INTEGRATION OF THE CONSTITUTIVE EQUATIONS

Chapter 5 exposes the limitations of the models currently available for the study of the mechanical behaviour of silicon single crystals, inherent both to their kinematical framework and to their constitutive equations: limitation to small strains and to uniaxial, zero-dimensional straining cases sollicitating crystals along one slip system only, the secondary systems being completely ignored. This Section aims at detailing the numerical methods used to update the internal variables of the constitutive equations, independently on the kinematical framework and plasticity formulations adopted by the user (that is, using RDCP at small or finite strains, or a J_2 framework, etc.). We focus in the following on the implementation of models onto a single integration point: the strain rate tensor $\dot{\boldsymbol{\varepsilon}}$ (or velocity gradient $\mathbf{L}$), the time increment and set of internal variables at the end of the last increment are given as inputs. Implementation of a crystal plasticity framework into a commercial Finite Element package is detailed in Chapter 6. We are concerned in this Annex by the update of internal variables and stress state. This procedure is not straightforward because of the potentially high degrees of nonlinearity and coupling between the internal variables. Different solvers are introduced.

A.4.1 *Generic algorithm*

Definition of coordinate systems and Euler angles

In order to ease the comprehension of the numerical procedures, we introduce in this Section a generic algorithm. Let us consider a fictious f.c.c. (or diamond cubic) crystal located in a laboratory, the latter being characterized as a Galilean referential and an orthogonal coordinate system[4] $\mathfrak{C}_0$, defined by unit vectors $(\boldsymbol{x}_0, \boldsymbol{y}_0, \boldsymbol{z}_0)$. The coordinate system linked to the crystal lattice and its orientations $\langle 100\rangle$, $\langle 010\rangle$, $\langle 001\rangle$ is written $\mathfrak{C}_{lat}$. Instead of the traditional crystallographic denominations the unit vectors are written $(\boldsymbol{x}, \boldsymbol{y}, \boldsymbol{z})$. This coordinate system is co-rotating with the lattice during deformation.

The relative orientation of $\mathfrak{C}_{lat}$ with respect to $\mathfrak{C}_0$ can be defined by three successive rotations to which we associate the three Euler angles (ψ, θ, ϕ),

4 This coordinate system will also be called in the following *global* system, in opposition the crystallographic, or *local* system.

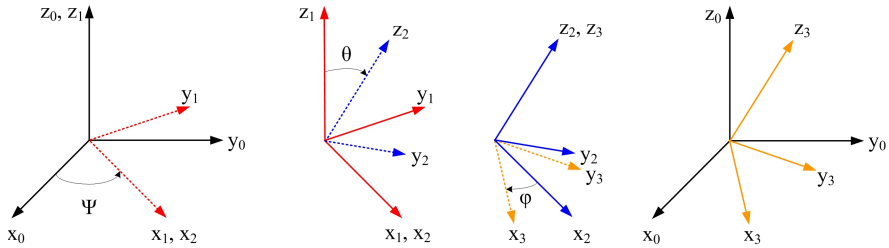

Figure A.4: Definition of the Euler angles (ψ, θ, ϕ)

see Figure A.4 [Kocks 1998]. Adopting the Bunge notation, the angles become (ϕ_1, θ, ϕ_2), with $\phi_1 = \psi + \frac{\pi}{2}$, $\phi_2 = \frac{\pi}{2} - \phi$. The matrix allowing for coordinate transformation from the global to the lattice system is written $Q(\phi_1, \theta, \phi_2)$ (Eq. A.43). The component $e_i^{(lat)}$ of a vector $\mathbf{e}^{(lat)}$ in the lattice coordinate system is expressed with the help of Q from its coordinates in the global system $e_j^{(global)}$:

$$Q(\phi_1, \theta, \phi_2) = \begin{bmatrix} \cos\phi_1 \cos\phi_2 - \sin\phi_1 \cos\theta \sin\phi_2 & \sin\phi_1 \cos\phi_2 + \cos\phi_1 \cos\theta \sin\phi_2 & \sin\theta \sin\phi_2 \\ -\cos\phi_1 \sin\phi_2 - \sin\phi_1 \cos\theta \cos\phi_2 & -\sin\phi_1 \sin\phi_2 + \cos\phi_1 \cos\theta \cos\phi_2 & \sin\theta \cos\phi_2 \\ \sin\phi_1 \sin\theta & -\cos\phi_1 \sin\theta & \cos\theta \end{bmatrix} \tag{A.43}$$

$$e_i^{(lat)} = Q_{ij} e_j^{(global)} \tag{A.44}$$

Consequently, a tensor $\boldsymbol{T}_0$ expressed in $\mathfrak{C}_0$ can be expressed into $\mathfrak{C}_{lat}$ with the help of Q as follows:

$$\mathbf{T}_{lat} = \mathbf{Q} \boldsymbol{T}_0 \mathbf{Q}^T \tag{A.45}$$

Formulation of the problem

For convenience, the problem treated here is formulated in the approximation of small deformations, but the treatment remains general and its extension to finite strains is relatively straightforward. Because of the incremental form of the constitutive equations, the experiment duration time t_{tot} is discretized into n_{steps} equal finite time increments of length Δt, with $t_{tot} = n_{steps} \Delta t$. Let us consider a displacement field $\mathbf{u}(\boldsymbol{x}, t)$ applied to a material point positioned at $\boldsymbol{x}$. Then the strain tensor is given by the symmetrical part of the gradient of $\mathbf{u}(\boldsymbol{x}, t)$ also called the deformation gradient

$\boldsymbol{\nabla u} = \mathbf{F}$, see Eq. A.46. The strain rate is the time derivative of the strain tensor:

$$\boldsymbol{\varepsilon} = \frac{1}{2}\left(\boldsymbol{\nabla}\mathbf{u} + {}^{t}\boldsymbol{\nabla}\mathbf{u}\right), \varepsilon_{ij} = \frac{1}{2}\left(\frac{\partial u_i}{\partial x_j} + \frac{\partial u_j}{\partial x_i}\right) \tag{A.46}$$

$$\dot{\varepsilon}_{ij} = \frac{\partial \varepsilon_{ij}}{\partial t} \tag{A.47}$$

Assume that we apply the given displacement field $\mathbf{u}(\boldsymbol{x}, t)$ to the whole volume of the crystal. Using Eq. A.46, we can derive the corresponding strain tensor. For convenience, the strain rate tensor at time t is assumed constant during each time step and given by $\dot{\varepsilon}_{ij} = \frac{\varepsilon_{ij}(t+\Delta t) - \varepsilon_{ij}(t)}{\Delta t}$. This approximation assumes that the time steps shall be small enough to guarantee a satisfying approximation of the actual strain evolution with time. The problem to solve is then to find the stress tensor $\boldsymbol{\sigma}$ and the set of internal variables that satisfy the incremental equation $\dot{\boldsymbol{\sigma}} = \boldsymbol{\mathcal{L}} : (\dot{\boldsymbol{\varepsilon}} - \dot{\boldsymbol{\varepsilon}}_p)$, with $\dot{\boldsymbol{\varepsilon}}_p$ the plastic strain rate tensor that follows a given constitutive law introducing k internal variables $(y_i)_{1 \leq i \leq k}$, and $\boldsymbol{\mathcal{L}}$ is the linear, fourth-order stiffness tensor that might depend on temperature.

In the more general case of large deformations, instead of applying a strain rate we would need the velocity gradient $\mathbf{L}$ given by Eq. A.21, rotated into the lattice referential with Eq. A.44 and from which the current total displacement gradient $\mathbf{F}$ can be found by integration. Once the updated plastic strain (or displacement gradient) and internal variables are found, the tensors are rotated back into the global system, the Euler angles updated if necessary[5], and the next time step is processed. The complete procedure is shown in Algorithm A.1. Note that the variables are updated on the current configuration.

The critical part of the programs is clearly the solver. How to get the updated internal variables determining the plastic part of the deformation? Next Section describes the different strategies available to achieve this goal.

A.4.2 *Explicit solvers*

Because different explicit solvers can be used in the routines, their principles are exposed in the following. Let us consider a system of k coupled first-order differential equations: $\{y_i' = f_i\left(t, y_j(t)\right), y_i(t_0) = y_{i,0}, 1 \leq i, j \leq k\}$. For convenience, derivation with respect to time only is considered, and we write $\frac{\partial y_i}{\partial t} = y_i' = \dot{y}_i$. In our problem, these functions (resp. their first-order derivatives) would be the internal variables (resp.

5 The Euler angles are updated after each step only if finite strains are used. The small strains approximation assumes that the initial and current configuration are the same, there is consequently no lattice rotation.

Algorithm A.1 Generic solving procedure for an assumed strain problem. The framework can be either small strains approximation or finite strains.

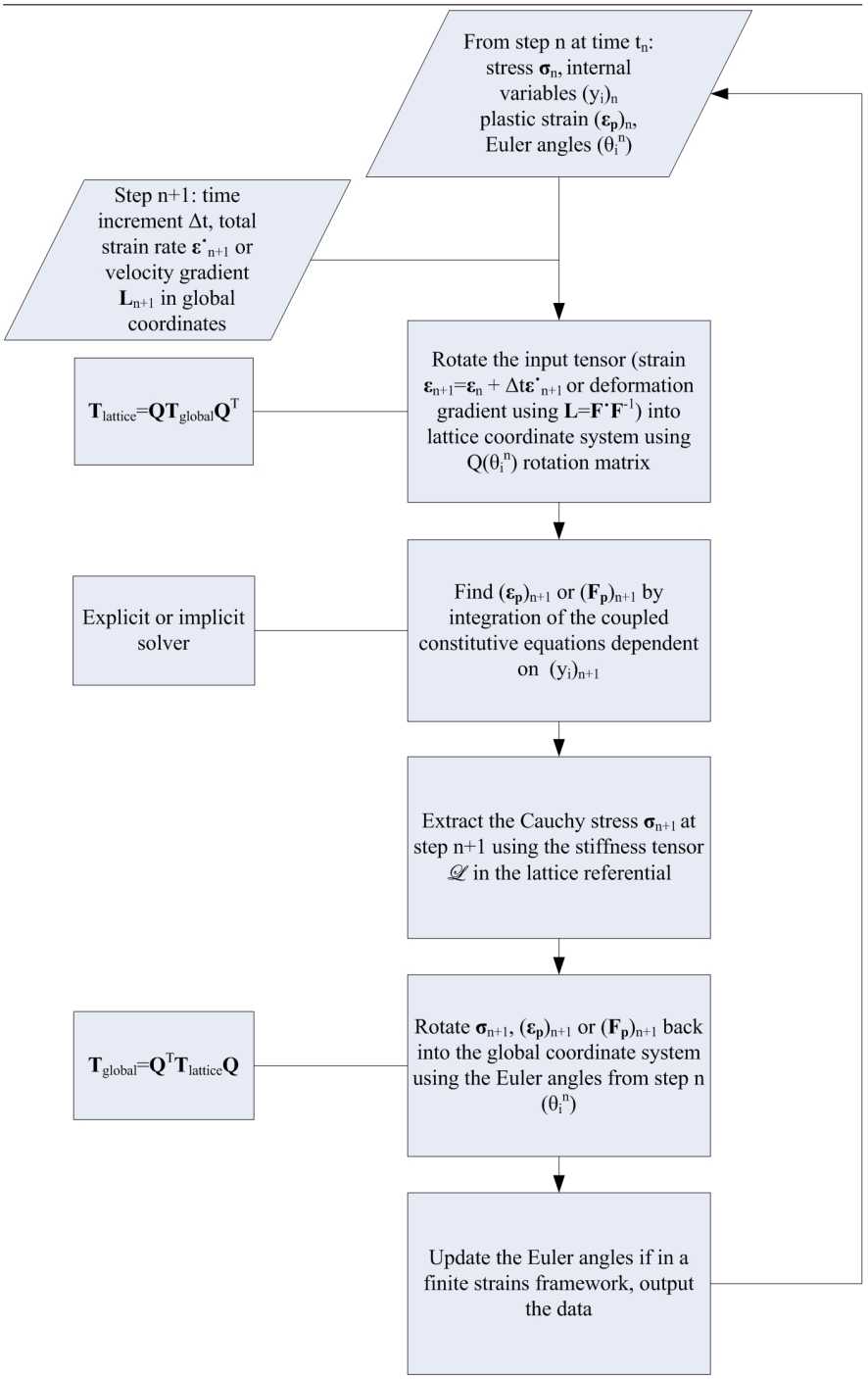

their evolution rates) that determine for instance the value of the plastic strain and dislocation velocity at each step. The continuous equations read:

$$\begin{cases} \dot{y}_i(t) = f_i\left(t, y_j(t)\right) \\ y_i(t_0) = y_{i,0} \\ 1 \leq i, j \leq k \end{cases}$$

with $y_{i,0}$ the initial values of the problem required to solve it. Time discretization into time steps of length $\Delta t_n = t_{n+1} - t_n$ allows to write the derivatives of the functions as in Eq. A.48, where the choice of α determines the type of the solver.

$$f_i\left(t_n, y_j(t_n)\right) = \frac{\alpha y_i(t_{n+1}) + (1-\alpha) y_i(t_n)}{\Delta t_n} \tag{A.48}$$

For $\alpha = 0$, the formulation is fully explicit and the time derivative of the functions y_i for step n are taken as the derivatives at the beginning of the step. On the other hand, if α is taken as unity, then the solver is fully implicit, and the (usually) non-linear equation system to solve might require the use of a Newton-Raphson iteration scheme. Let us call $\overline{y_i}(t_{n+1})$ the exact solution to the problem. Then the error of any solver reads:

$$\text{err} = \overline{y_i}(t_{n+1}) - y_i(t_{n+1}) \tag{A.49}$$

A Taylor expansion of the solution at t_{n+1} gives Eq. A.50, and the order of a solver is simply given by the order of magnitude of the remaining terms minus 1.

$$\overline{y_i}(t_{n+1}) = y_i(t_n) + \Delta t_n \dot{y}_i(t_n) + \frac{(\Delta t_n)^2}{2}\ddot{y}_i(t_n) + \ldots + \frac{(\Delta t_n)^k}{k!} y_i^{(k)}(t_n) + \ldots \tag{A.50}$$

Forward Euler method

The easiest and straightforward integration method is of course to consider the explicit method at each time step n, since the rates $\dot{y}_i(t_n)$ are known from the functions y_j derived at previous step. The forward Euler method uses the Taylor development of the solution up to the first derivative. Then the set of equations reads in its discretized form:

$$\begin{cases} y_i(t_{n+1}) = y_i(t_n) + \Delta t_n\, \dot{y}_i\left(t_n, y_j(t_n)\right) \\ 1 \leq i, j \leq k \end{cases} \tag{A.51}$$

Such a solution is of first order, meaning that the error of the solution is one order of magnitude higher than the time step chosen.

$$\text{err}_{FE} = \mathcal{O}\left((\Delta t_n)^2\right) \tag{A.52}$$

Euler-Cauchy method

It seems therefore interesting to increase the order p of the solver, since the final error after n steps of equal length Δt reads $\text{err}_n = \mathcal{O}\left(n(\Delta t)^{p+1}\right)$. Equation A.50 shows that it is possible to refine the approximate solution $y_i(t_{n+1})$ by using terms of higher order in the Taylor expansion. For example, the second derivative can itself be approximated by a first order development, giving the Euler-Cauchy method, namely

$$\left\{\begin{array}{c} y_i(t_{n+1}) = y_i(t_n) + \frac{\Delta t_n}{2}\left(\dot{y}_i\left(t_n, y_j(t_n)\right) + \dot{y}_i\left(t_{n+1}, y_j(t_n)\right.\right. \\ \left.\left. + \Delta t_n \dot{y}_j\left(t_n, y_l(t_n)\right)\right)\right) \\ 1 \leq i, j, l \leq k \end{array}\right. \tag{A.53}$$

Such an approach is easily implemented into an algorithm since it is based on the explicit derivation of expressions at successive iterations. For example, the Euler-cauchy method can be written

$$\left\{\begin{array}{c} y_i(t_{n+1}) = y_i(t_n) + \frac{1}{2}(k_1 + k_2) \\ k_1 = \Delta t_n\, \dot{y}_i\left(t_n, y_j(t_n)\right) \\ k_2 = \Delta t_n\, \dot{y}_i\left(t_n + \Delta t_n, y_j(t_n + k_1)\right) \end{array}\right. \tag{A.54}$$

where k_1 and k_2 are the solutions given by the forward Euler method at t_n and t_{n+1} respectively, using the former solutions as the initial values for the second iteration. The Euler-Cauchy method is of order 2, since the term of order 2 in Equation A.50 has been integrated into the approximation, leaving third derivatives.

$$\text{err}_{EC} = \mathcal{O}\left((\Delta t_n)^3\right) \tag{A.55}$$

Higher order Runge-Kutta methods

A simple fourth order method requires four evaluations of the derivatives and the functions at different times. The solution reads:

$$\left\{\begin{array}{c} y_i(t_{n+1}) = y_i(t_n) + \frac{1}{6}(k_1 + 2k_2 + 2k_3 + k_4) \\ k_1 = \Delta t_n\, \dot{y}_i\left(t_n, y_j(t_n)\right) \\ k_2 = \Delta t_n\, \dot{y}_i\left(t_n + \frac{\Delta t_n}{2}, y_j(t_n) + \frac{k_1}{2}\right) \\ k_3 = \Delta t_n\, \dot{y}_i\left(t_n + \frac{\Delta t_n}{2}, y_j(t_n) + \frac{k_2}{2}\right) \\ k_4 = \Delta t_n\, \dot{y}_i(t_n + \Delta t_n, y_j(t_n) + k_3) \end{array}\right. \tag{A.56}$$

$$\text{err}_{RK} = \mathcal{O}\left((\Delta t_n)^5\right) \tag{A.57}$$

Such a solver is attractive for nonlinear problems that would otherwise require extremely small time steps to ensure stability. Of course the numerical treatment of the solution is quite heavy, and it might be more effective to use a lower order solver.

A.4.3 *Substepping algorithm*

This Section describes a substepping algorithm for integration of differential equations that guarantees accuracy of the solution. Because the solvers exposed above are all explicit, they require small time steps to ensure a minimal propagated error and stability. If an explicit Finite Elements software is used to solve the elliptic boundary value problem, then small time steps are readily imposed to ensure stability of the global solver, and the use of a forward Euler scheme to integrate the constitutive equations *might* suffice.

If the constitutive model is implemented into an implicit Finite Element solver, the time increments imposed to solve the displacement problem might be large enough to generate significant errors in the update of the internal variables, and consequently of the stress state. A way to avoid this issue is to rely on the use of substepping algorithms that divide the global time step Δt imposed at the increment n into k substeps of variable lengths $(\Delta t_{s,1}...\Delta t_{s,k})$ so that $\Delta t = \sum_{i=1,k} \Delta t_{s,i}$ [Fellin 2002]. The length of each substep is determined from a convergence criterion on the error of the solver. This is typically achieved by comparing the solution given by a solver of order i to the one yielded by the use of a solver of order i-1.

If the substep k has converged, the next substep length $\Delta t_{s,k+1}$ is imposed to be larger than the successful $\Delta t_{s,k}$ by a factor $\alpha_2 > 1$ and the differential equations with updated variables are sent for solving at $t_{s,k+1} = t_{s,k} + \Delta t_{s,k}$; otherwise a new attempt is made at substep k of reduced size $\Delta t_{s,k} = \alpha_1 \Delta t_{s,k}$ with $\alpha_1 < 1$. The substepping algorithm decides automatically the substep length based on the errors and tolerance as follows:

$$\begin{cases} \alpha_1 = \max\left(0.9\sqrt{\frac{tol}{err}}, 0.2\right) \\ \alpha_2 = \min\left(0.9\sqrt{\frac{tol}{err}}, 5\right) \end{cases} \tag{A.58}$$

Algorithm A.2 gives an overview of the procedure described in this Section.

Substepping algorithms can consequently be based on the comparison between the results given by, e.g., a forward Euler and an Euler-Cauchy solver. If one desires to use higher order solvers instead, it is possible to base substepping on a set of 4^{th} and 5^{th} order Runge-Kutta schemes, or so-called embedded Runge-Kutta formulae [Dormand 1980].

A basic drawback from using high order explicit solvers is that it requires more than one function evaluation, increasing thereby the computational time. A fifth order embedded RK solver requires for example six such evaluations. Using substepping is therefore not always wanted as it multiplies further the computation requirements.

Algorithm A.2 Substepping algorithm. The exact expression of the substep size actuators α_1 and α_2 are given in Eq. A.58.

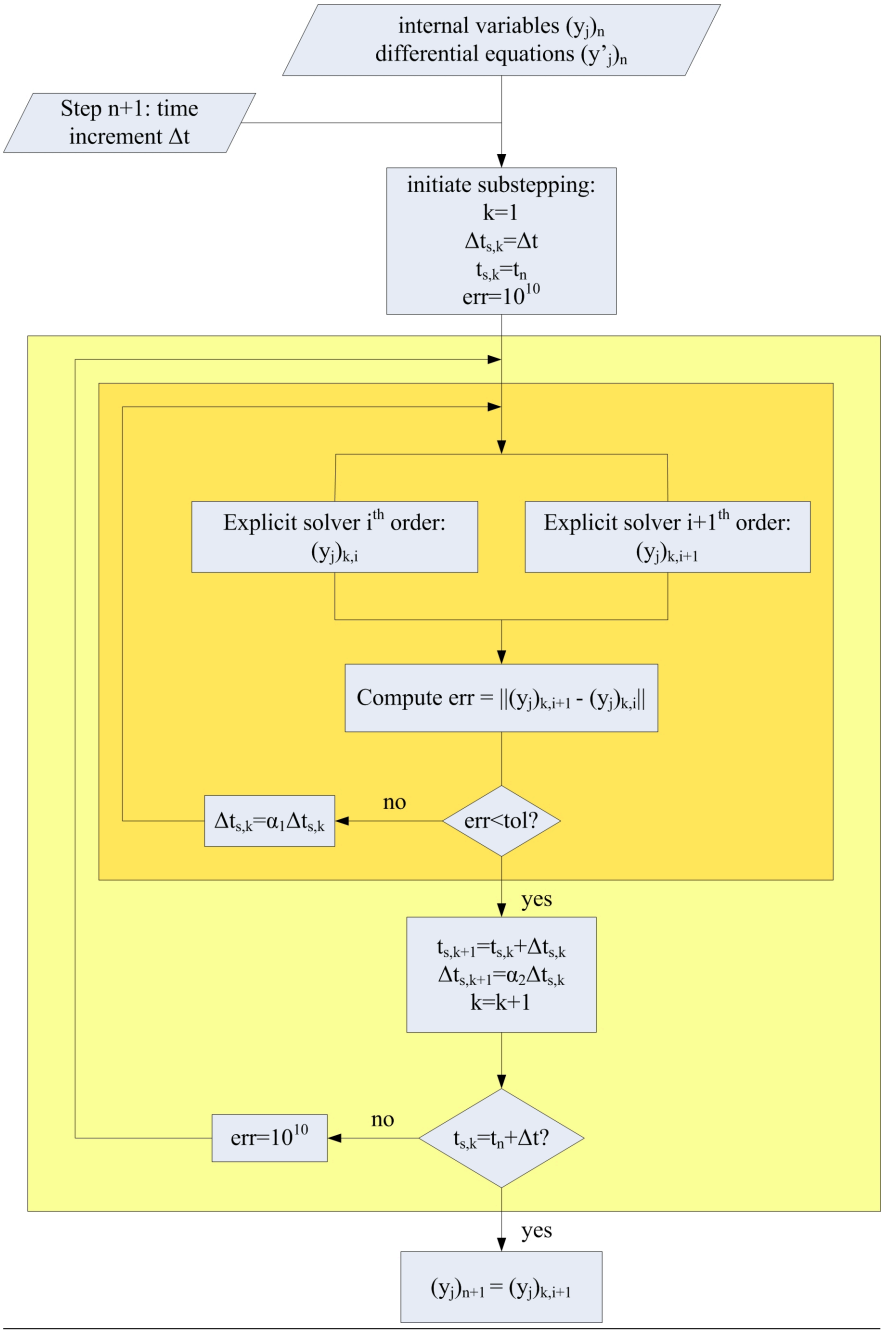

A.5 COMPARISON OF MODELING STRATEGIES: THE CASE OF SILICON

Two possibilities are offered to model plasticiy. Either plastic deformation is considered to be able to proceed along any spatial direction (as assumed by the model of [Dillon 1986] relying on small strains approximation and a J_2-plasticity formulation), or the physically more realistic case of discrete plastic slip is chosen by adopting a crystal plasticity framework described previously. Both methods are studied and compared in the following.

Throughout this Section, the material modeled is a pure silicon crystal, without impurities or dopants. Considering the standard model of Alexander & Haasen (model 1) only, we show that a crystal plasticity routine provides with far more insight into the deformation processes than a J_2-plasticity code does. In particular, the plastic anisotropy and projection of strain rates onto the "slip systems" are much more accurate with the former method. Complex, three-dimensional loadings lead to peculiar stress responses that can be effectively captured only by the discretization of plastic deformation that crystal plasticity provides.

The differences between two modeling approaches are studied using stand-alone programs, considering a single integration point to be representative of the whole specimen. The user must provide the routines with the strain rate or velocity gradient as inputs at each time increment. In particular, such an approach does *not* allow for simulation of purely uniaxial tensile tests, since the latter do not impose known displacements on the free surfaces. Those need to be derived using for instance the finite element method. Nonetheless, this preliminary study gives interesting insights into the overwhelming abilities of crystal plasticity modeling. The results of this Section have been presented in [Cochard 2008].

A.5.1 *Kinematics and constitutive equations*

Small strains: J_2-plasticity

The framework introduced here comes directly from the work of [Dillon 1986, Kim 1987]. The resolved shear stress is approximated by $\sqrt{J_2}$, where J_2 is computed from the deviatoric part $\mathbf{S}$ of the stress tensor σ:

$$\mathbf{S} = \sigma - \frac{1}{3}\mathrm{tr}(\sigma)\mathbf{I} \tag{A.59}$$

$$J_2 = \frac{1}{2}\mathbf{S} : \mathbf{S} \tag{A.60}$$

The strain rate is additively decomposed into a plastic and elastic part. The plastic strain rate is expressed as a linear function of $\mathbf{S}$, the prefactor f playing the role of Orowan's law in a fictious crystal with one slip sytem having no specific plane or direction:

$$\begin{cases} \dot{\boldsymbol{\sigma}} = \boldsymbol{\mathcal{L}} : (\dot{\boldsymbol{\varepsilon}} - \dot{\boldsymbol{\varepsilon}}^p) \\ \dot{\boldsymbol{\varepsilon}}^p = f\mathbf{S} \\ f = \frac{1}{\sqrt{J_2}}\rho b v \end{cases} \tag{A.61}$$

Note that this model does not account for multiple slip cases and neglects totally the interactions between the 12 slip systems. In particular, no evolution of the dislocation densities on the "latent" systems is predicted by these constitutive equations. This approximation presents the advantage of being easy and numerically efficient to compute. Nevertheless, as we will see its drawback is a wrong estimation of the actual resolved shear strain rate upon complex loading conditions. The effective stress acting on the fictious and only slip system is obtained using the classical approach of Alexander & Haaasen (Eq. 5.5), by substracting from the applied stress $\tau = \sqrt{J_2}$ the internal stress τ_{int}.

Algorithm A.3 summarizes the method used for integration of the J_2-plasticity model in a small strains approximation, given a strain rate tensor $\dot{\boldsymbol{\varepsilon}}_n$ at each time step n of length Δt_n. The solver used to derive the internal variables at each step in case of plastic loading can be either explicit or implicit. Algorithm A.3 uses model 1 to calculate the internal stress and the dislocation density evolution rate. This simple case allows for easy derivation of the Jacobian matrix if an implicit solver is chosen. The routine has been implemented into MATLAB and different solvers have been tested: first order explicit forward Euler, second order explicit Euler-Cauchy, fourth order explicit Runge-Kutta, or fully implicit Euler backward solver.

Finite strains: crystal plasticity

This framework requires to bridge the gap between the macroscopic (displacement or velocity gradient) and the microscopic (slip systems) scales. This is done using Eq. A.24. Algorithm A.4 describes briefly the different steps needed to overcome this multiscaling difficulty, in the case of a simple Euler forward integration scheme. The stand-alone routine has been written in FORTRAN 95, since compilation of the code allows for rapid execution of the algorithm. The explicit solvers introduced previously have been implemented.

Equations and parameters of the constitutive models

The model of Alexander & Haasen is used in the following on each slip system[6] α. The set of parameters used is as follows: the dislocation velocity $v^{(\alpha)} = v_0 \left(\frac{\tau_{eff}^{(\alpha)}}{\tau_0} \right)^{m_0} \exp\left(-\frac{U}{k_b T} \right)$ is obtained with $v_0 = 3.5 \times 10^4\,\mathrm{m.s^{-1}}$, $\tau_0 =$ 1 MPa, $m_0 = 1$ and $U = 2.35\,\mathrm{eV}$. The effective stress reads $\tau_{eff}^{(\alpha)} = \tau^{(\alpha)} -$

6 Note that for the case of J_2-plasticity only one slip system is considered.

Algorithm A.3 Solving procedure for a J_2-plasticity small strains problem, given the strain rate tensor at each time step.

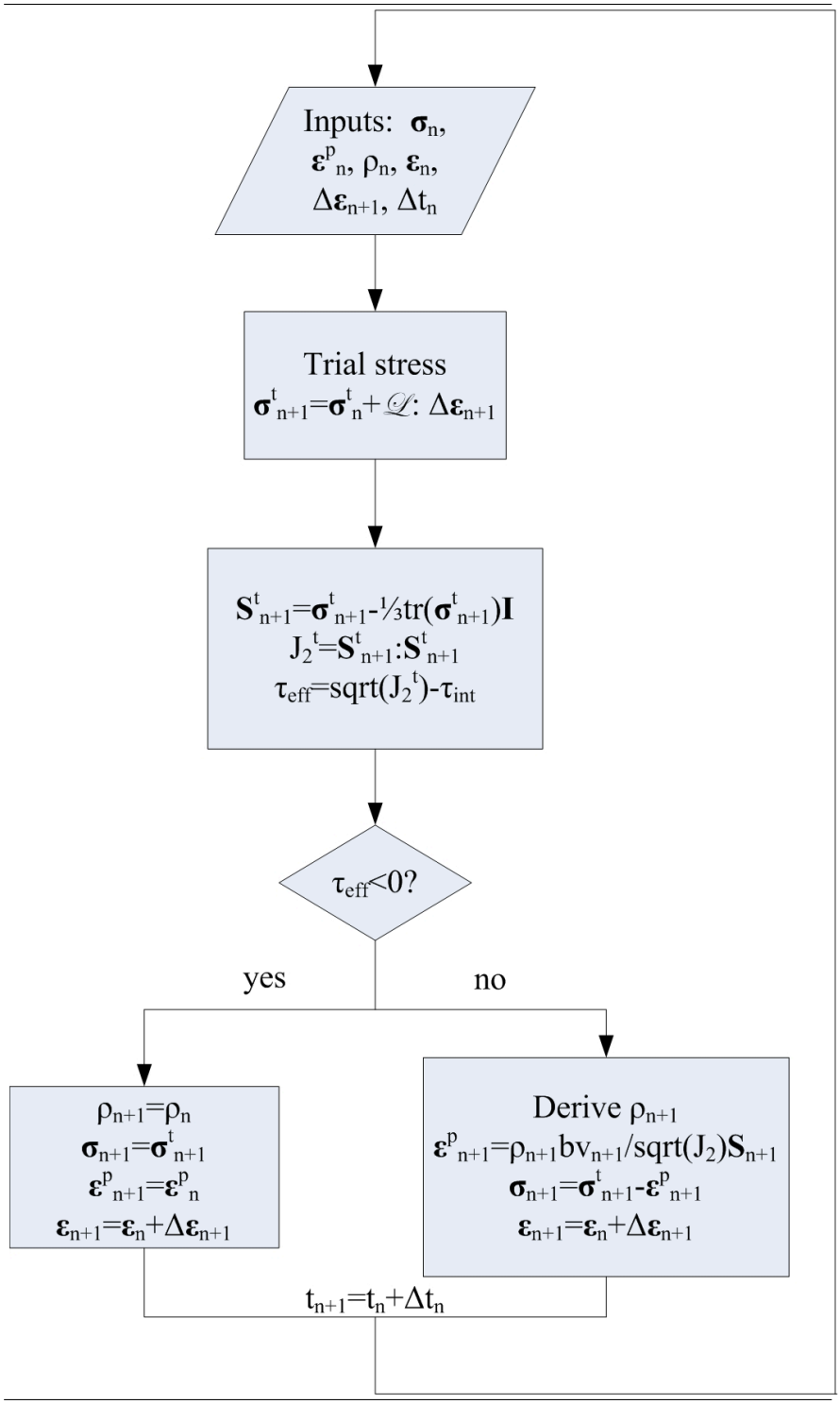

Algorithm A.4 Solving procedure for a crystal plasticity problem in finite strains, given the deformation gradient tensor at each time step.

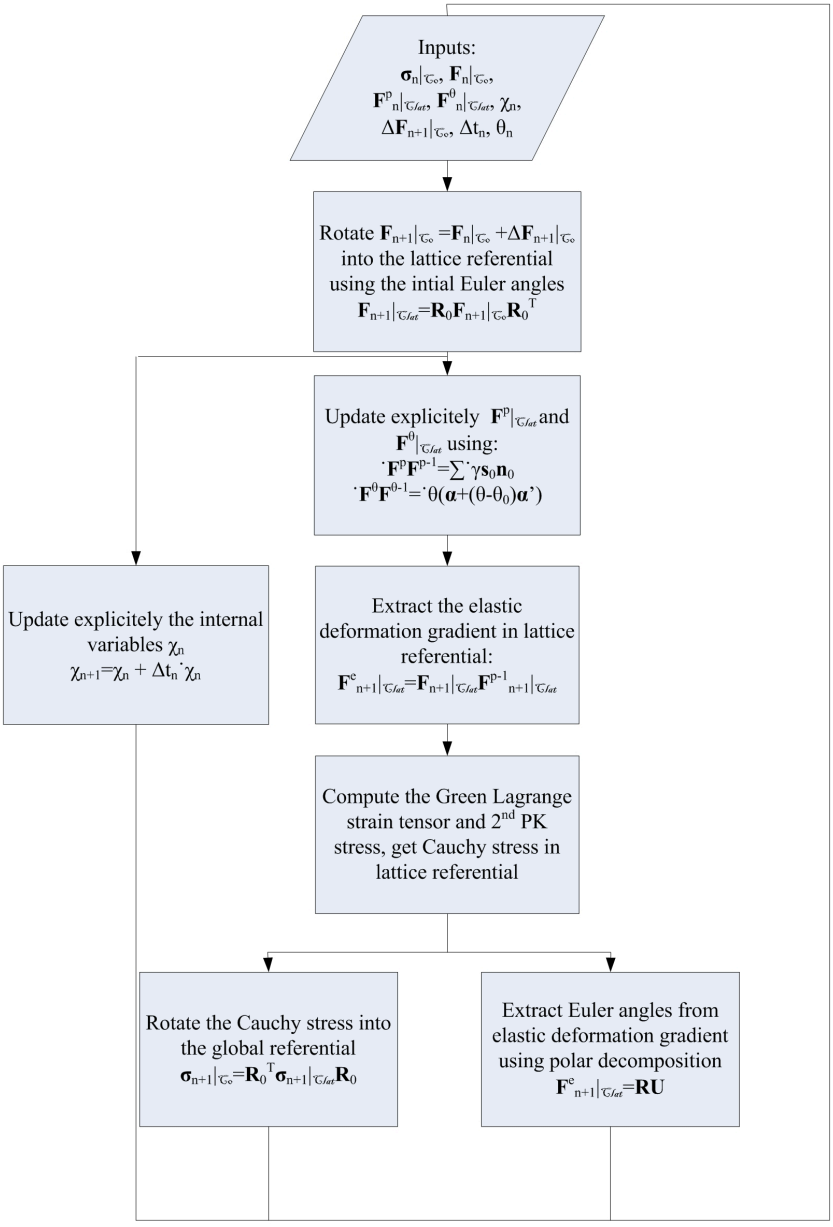

$\tau_{int}^{(\alpha)}$. Finally, the dislocation multiplication $\dot{\rho}^{(\alpha)} = \delta_{AH}\tau_{eff}^{(\alpha)}\rho^{(\alpha)}v^{(\alpha)}$ uses a prefactor $\delta_{AH} = 3.1 \times 10^{-4}$. Note that the exact value of the parameters is not important in as much as we are aiming at comparing qualitatively more than quantitatively the models.

$$\begin{cases} v^{(\alpha)} = v_0 \left(\frac{\tau_{eff}^{(\alpha)}}{\tau_0} \right)^{m_0} \exp\left(-\frac{U}{k_b T} \right) \\ \dot{\rho}^{(\alpha)} = \delta_{AH}\tau_{eff}^{(\alpha)}\rho^{(\alpha)}v^{(\alpha)} \end{cases} \tag{A.62}$$

Crystal plasticity can take into account interactions between slip systems and can include latent hardening effects by the introduction of a matrix of hardening coefficients $\left(a_{\alpha\beta}\right)_{1\leq\alpha,\beta\leq 12}$:

$$\tau_{int}^{(\alpha)} = \mu b\sqrt{\sum_\beta a_{\alpha\beta}\rho^{(\beta)}} \tag{A.63}$$

Setting the off-diagonal parameters in the interaction matrix $\left(a_{\alpha\beta}\right)_{1\leq\alpha,\beta\leq 12}$ to zero allows for self-hardening only. The only case considered in the following is where the diagonal coefficients are set to $\sqrt{a_{ii}} = 0.3$ and the off-diagonal to null: latent hardening is absent and the constitutive law on each slip system is similar to the one of the original AH model. On the other hand, the J_2 model working with one system only relies on the classical expression for the internal stress:

$$\tau_{int} = \mu b A\sqrt{\rho} \tag{A.64}$$

with $A = 0.3$.

A.5.2 *Isochoric loadings*

All simulations are performed[7] at a temperature of 1073 K and an initial dislocation density of $10^8\,\mathrm{m}^{-2}$ on each slip system. The initial dislocation density in the J_2 model is taken as $10^8\,\mathrm{m}^{-2}$. The three Euler angles are taken initially as (15°, 20°, 15°). The boundary conditions are given by the strain rate or velocity gradient tensor. The loadings considered in this Section are tensile in the $\mathbf{e}_1$ direction (in the lab referential) and isochoric. The tensors read therefore:

$$\dot{\boldsymbol{\varepsilon}} = \dot{\varepsilon}_{11}\mathbf{e}_{11}\otimes\mathbf{e}_{11} - \frac{\dot{\varepsilon}_{11}}{2}\left(\mathbf{e}_{22}\otimes\mathbf{e}_{22} + \mathbf{e}_{33}\otimes\mathbf{e}_{33}\right) \tag{A.65}$$

$$\mathbf{L} = \mathrm{L}_{11}\mathbf{e}_{11}\otimes\mathbf{e}_{11} - \frac{\mathrm{L}_{11}}{2}\left(\mathbf{e}_{22}\otimes\mathbf{e}_{22} + \mathbf{e}_{33}\otimes\mathbf{e}_{33}\right) \tag{A.66}$$

Simulations are performed up to 1 % strain in the tensile direction, the time step being chosen small enough to reach convergence of the results. A strain rate $\dot{\varepsilon}_{11} = 10^{-2}\,\mathrm{s}^{-1}$ or $\mathrm{L}_{11} = 10^{-2}\,\mathrm{s}^{-1}$ is taken.

7 This set of conditions is refered to as "reference conditions" in this Section.

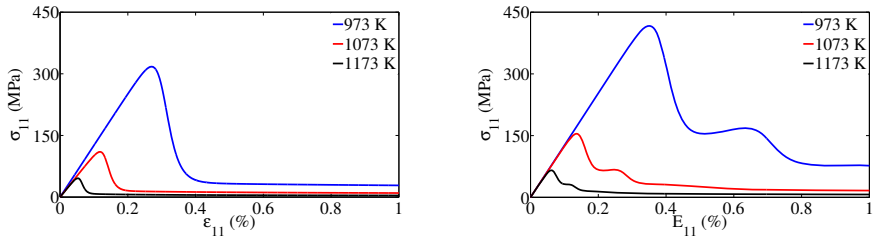

(a) (b)

Figure A.5: Influence of temperature on the simulated mechanical behavior of silicon using (a) the J_2 continuum formulation of [Dillon 1986] and (b) finite strains RDCP. The strain and stress plotted are the components of the tensors along the tensile direction.

Results - response to deformation conditions

Both modeling approaches reproduce the variations of mechanical response of silicon to different temperatures, strain rates and initial dislocation densities. Nonetheless, two significant discrepancies are the magnitude of the upper yield point, roughly 25 % higher with the crystal plasticity model, and the presence of secondary yield drops that the continuum formulation does not reveal. Figure A.5 allow for comparison of the simulated stress-strain behaviors at various temperatures.

Analysis of discrepancies between the models

The origin of the multiple yield drops is the successive activation of slip systems. Each explosion of dislocation density leads to softening of the crystal, translated by a yield drop in the stress-strain curve. The three dimensional isochoric loading requires the activation of more than one slip system for the virtual crystal to accomodate the imposed deformation. Plotting the evolution of the six principal systems as a function of strain clearly illustrates the series of explosions (see Figure A.6). The rate of growth of dislocation densities during their explosion is not the same for all systems. This is due to the different values of the resolved shear stresses that influence the magnitude of the effective stress, and in turn the rate of multiplication of the densities. A clear correlation between the yield drop in the stress-strain curve and the sudden increase of the total dislocation density coming from the activation of secondary systems can be seen in Figure A.7.

A higher upper yield point follows from a larger resolved shear strain rate projected onto the primary system. The J_2 formulation namely considers that the plastic strain rate is given by $\dot{\varepsilon} = \frac{\mathbf{S}}{\sqrt{\frac{1}{2}\mathbf{S}:\mathbf{S}}}\rho b v$ if $\sqrt{J_2} = \sqrt{\frac{1}{2}\mathbf{S}:\mathbf{S}} > \mu b A \sqrt{\rho}$. This Von Mises criteria, with the yield surface evolving with deformation, would be adapted to the case where the mechanical behavior

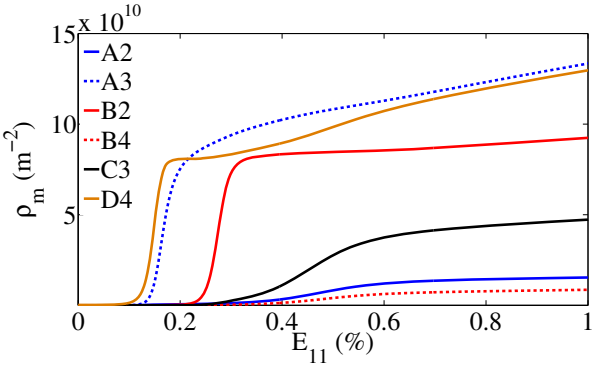

Figure A.6: Evolution of the dislocation densities on the six principal slip sytems during deformation in reference conditions, using RDCP.

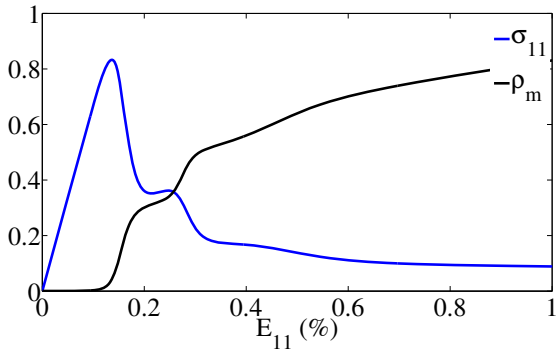

Figure A.7: Normalized stress (σ_{11} component) and total dislocation density evolutions with strain in reference conditions, using RDCP.

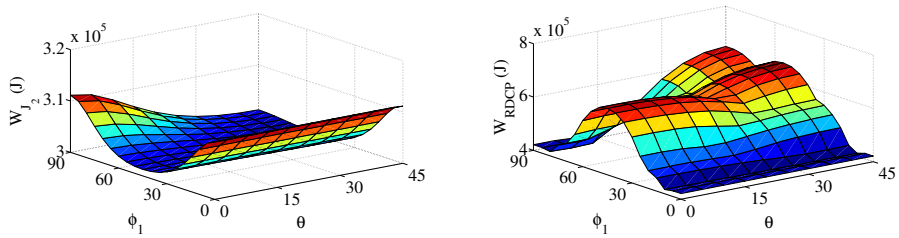

(a) (b)

Figure A.8: Mechanical work required to deform a fictious silicon monocrystal, as computed by (a) a J_2 formulation and (b) a RDCP framework, as a function of the two first Euler angles. Isochoric deformation, maximum principal strain 1 %.

of the specimen is an average over a large amount of grains. Such a choice of model is valid for polycrystals that exhibit a rather isotropic behavior. Silicon materials being made of a small amounts of grains, it is not possible to consider a mean average of the aggregates, and the choice of a J_2 formulation of plasticity poses some problems.

Anisotropy of the plastic deformation

The discretization of the crystal into twelve slip systems induces an anisotropic behavior of the plastic deformation of silicon. In order to evaluate the ability of the models to account for such an aspect, different simulations have been performed in the reference conditions but considering different initial Euler angles. The third angle being fixed to 0°, the total mechanical work up to 1 % deformation is calculated using Eq. A.67 or A.68 depending on the formulation.

$$W_{J_2} = \int \boldsymbol{\sigma} : \dot{\boldsymbol{\varepsilon}} dt \tag{A.67}$$

$$W_{RDCP} = \int \mathbf{P} : \dot{\mathbf{E}} dt \tag{A.68}$$

Figure A.9 shows the variations ratio of mechanical works $r_W(\phi_1, \theta) = W_{RDCP}(\phi_1, \theta)/W_{J_2}(\phi_1, \theta)$ with the first two Euler angles[8]. The discrepancy between both methods is quite large, a J_2-formulation taking into account anisotropy solely through the coefficients of the stiffness matrix and therefore neglecting anisotropy of plastic deformation. In other words, a RDCP framework enriches the results by adding plastic anisotropy to the elastic one. Introducing latent hardening in the crystal plasticity routine increases further the ratio r_W.

8 Due to the symmetry of the diamond cubic lattice, it is sufficient to study the variations of $r_W(\phi_1, \theta)$ for $0 \leq \phi_1 \leq \frac{\pi}{2}$ and $0 \leq \theta \leq \frac{\pi}{4}$.

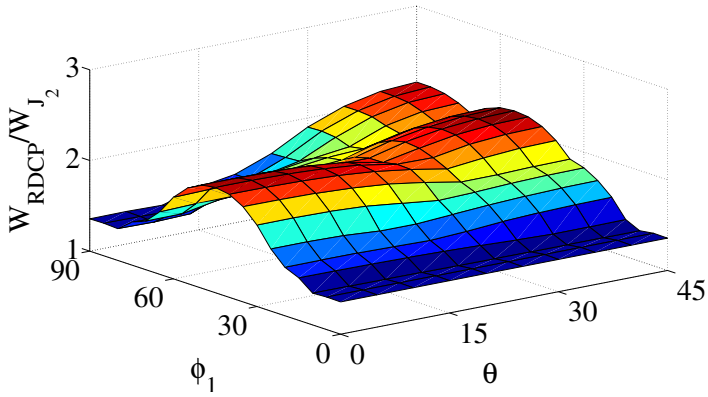

Figure A.9: Ratio of mechanical work computed with RDCP to the J_2-model at 1 % deformation, as a function of the first two Euler angles and in reference conditions. No latent hardening is accounted for in the crystal plasticity case.

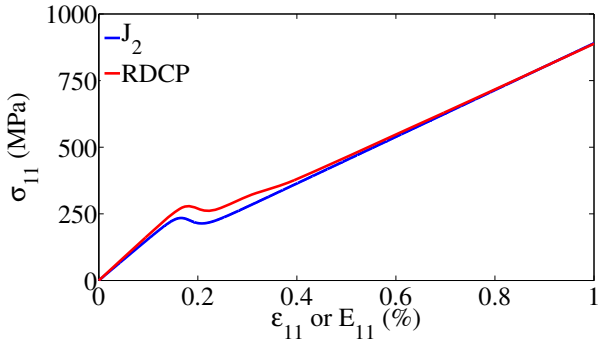

Figure A.10: Simulated stress-strain curves of plane strain loadings, in reference conditions

A.5.3 *Plane strain loadings*

In order to check the influence of the velocity gradient tensor components, other simulations have been run using plane strain conditions:

$$\mathbf{L} = L_{11}\mathbf{e}_{11} \otimes \mathbf{e}_{11} \tag{A.69}$$

Such loadings impose event more constrains on the crystals. This can be seen in Figure A.10 where the stress does not seem to reach a steady state value towards large strains. The secondary yield peaks are much less visible than in the case of constant volume loadings.

A.5.4 *Conclusions*

Limitations of a continuum approach

Adopting a J_2-plasticity formulation limits the ability of accounting for the discretization of slip mechanisms in monocrystals. Plastic deformation is assumed isotropic. A direct consequence is a "projection" of the strain rate onto the deviatoric space that is too low compared to the more realistic projections performed by crystal plasticity. This results in significantly lower upper yield stresses than obtained with RDCP. In addition, the absence of secondary systems from the J_2 framework forbids the incorporation of latent hardening and activation of additional systems upon complex loading situations. The former limitation was already mentioned by [Dillon 1986].

Performance of crystal plasticity

Crystal plasticity has several advantages but costs much more than the former approach. Firstly, twelve systems must be treated instead of one. Secondly, the finite strains framework chosen in this work implies numerically heavy matrix operations. The adoption of crystal plasticity is consequently limited to relatively small problems with a limited amount of Gauss points (where the constitutive equations must be integrated). The following Chapter is dedicated to the implementation of an advanced model into ABAQUS/EXPLICIT and the calibration of its parameters at finite strains.

Applicability of crystal plasticity to silicon single crystals

[Moon 2002] used a crystalline formulation with different constitutive laws depending on the temperature range to simulate the mechanical behaviour of silicon single crystals. These authors used the creep law derived by [Myshlyaev 1969] for high temperatures above a critical dislocation density. However, this law is valid for high strains and represents fairly well the later stages of hardening of silicon, albeit without being able to relate the dislocation density with the strain state. It is therefore not interesting for us to consider this case.

[Cacho 2007] also used such a rate dependent crystal plasticity formulation for single crystal silicon and noticed the fundamental difference in predicting the plastic domains with the continuum formulation. Such a multislip formulation has also been used to model nanoindentation of silicon surfaces, and to study the initiation of cracking in the material under varying hydrostatic pressures, although the parameters used for the $(a_{\alpha\beta})$ interaction matrix might not be relevant for silicon, its coefficients being obtained from latent hardening experiments on copper single crystals [Yoshino 2001].

The case of polycrystalline aggregates

The work achieved by Cailletaud and his team provides us with examples of what can be done with a crystal plasticity formulation adapted to the modeling of polycrystals (see, e.g., [Barbe 2001a, Barbe 2001b, Diard 2005]). They start by considering a representative volume element (RVE) of a high number of grains generated randomly. The texture (crystallographic orientation of the grains with respect to a reference coordinate system) is defined either randomly or according to a given computational pattern. The cubic polycrystal studied is considered to be a RVE when the finite element simulations match the homogeneized equations. Such numerical simulations allow for investigation at the level of a phase (all the grains having the same crystallographic orientation), meaning the intergranular level, or at the level of a single grain (intragranular variations). In addition to the differences in orientations that lead to different macroscopic stress-strain responses, the existence of compatibility requirements between the grains lead to increased plastic activity at the grain boundaries and highly inhomogeneous strain distributions within the grains. This is believed to be a crucial starting point to investigate intergranular fracture.

Important results are that the intergranular and intragranular behaviors present a large scatter of answers to a given loading. Some grains work in tension, others in compression, and within grains the discrepancies seem to be even higher. These strong heterogeneities cannot be captured by the current models used for process modeling and can bring new insights into the mechanical state of directionally solidified silicon ingots.

B

CONSISTENT TANGENT MODULI FOR ABAQUS/STANDARD

B.1 CASE OF THE EXTENDED AH MODEL

Note: we do not use Einstein's notation here. If an indices is repeated twice in the same equation there is no summation unless specified otherwise. This section is concerned with the exact derivation of the consistent tangent moduli for the extended model of Alexander and Haasen with temperature-dependent constitutive parameters, in the small strains approximation. The evolution of the stress reads:

$$\dot{\boldsymbol{\sigma}} = \boldsymbol{\mathcal{C}} : \dot{\boldsymbol{\varepsilon}}^e = \boldsymbol{\mathcal{C}} : \left(\dot{\boldsymbol{\varepsilon}} - \dot{\boldsymbol{\varepsilon}}^p - \dot{\boldsymbol{\varepsilon}}^T \right) \tag{B.1}$$

with the plastic strain rate as a function of the plastic slip rates on the slip systems α:

$$\dot{\boldsymbol{\varepsilon}}^p = \frac{1}{2} \sum_{\alpha} \dot{\gamma}^{(\alpha)} \left(\mathbf{s}_0^{(\alpha)} \otimes \mathbf{n}_0^{(\alpha)} + \mathbf{n}_0^{(\alpha)} \otimes \mathbf{s}_0^{(\alpha)} \right) = \sum_{\alpha} \dot{\gamma}^{(\alpha)} \mathbf{P}_0^{(\alpha)} \tag{B.2}$$

$$\mathbf{P}_0^{(\alpha)} = \frac{1}{2} \left(\mathbf{s}_0^{(\alpha)} \otimes \mathbf{n}_0^{(\alpha)} + \mathbf{n}_0^{(\alpha)} \otimes \mathbf{s}_0^{(\alpha)} \right)$$

The thermal strain rate reads:

$$\dot{\boldsymbol{\varepsilon}}^T = \dot{T} \boldsymbol{\vartheta}(T)$$

with $\boldsymbol{\vartheta}(T)$ the temperature-dependent, second-order tensor of thermal expansion coefficients. The case of a coupled thermal-stress analysis requires the computation of $\frac{\partial \dot{\boldsymbol{\sigma}}}{\partial T}$ as discussed in the next section. The elastoplastic consistent tangent moduli (CTM) $\boldsymbol{\mathcal{C}}_{ep}$ reads in rate form:

$$\boldsymbol{\mathcal{C}}_{ep} = \frac{\partial \dot{\boldsymbol{\sigma}}}{\partial \dot{\boldsymbol{\varepsilon}}} = \boldsymbol{\mathcal{C}} - \sum_{\alpha} \boldsymbol{\mathcal{C}} : \mathbf{P}_0^{(\alpha)} \frac{\partial \dot{\gamma}^{(\alpha)}}{\partial \dot{\boldsymbol{\varepsilon}}} \tag{B.3}$$

or in an incremental form:

$$\boldsymbol{\mathcal{C}}_{ep} = \frac{\partial \Delta \boldsymbol{\sigma}}{\partial \Delta \boldsymbol{\varepsilon}} = \boldsymbol{\mathcal{C}} - \sum_{\alpha} \boldsymbol{\mathcal{C}} : \mathbf{P}_0^{(\alpha)} \frac{\partial \Delta \gamma^{(\alpha)}}{\partial \Delta \boldsymbol{\varepsilon}} \tag{B.4}$$

The latter equation considers the variations of the increments of stress $\Delta\sigma_{ij}$ with respect to the ones of strain $\Delta\varepsilon_{ij}$, upon perturbation of the system over a time increment Δt:

$$t \to t + \Delta t$$
$$\boldsymbol{\varepsilon} \to \boldsymbol{\varepsilon} + \Delta\boldsymbol{\varepsilon}$$
$$\boldsymbol{\chi} \to \boldsymbol{\chi} + \Delta\boldsymbol{\chi}$$
$$\boldsymbol{\sigma} \to \boldsymbol{\sigma} + \Delta\boldsymbol{\sigma}$$

where $\boldsymbol{\chi}$ is the vector of internal variables. The increments of amount of slip $\Delta\gamma^{(\alpha)}$ are obtained as functions of the $(\chi)_i$ and $(\chi + \Delta\chi)_i$'s.

Care must be taken to express all tensors in the same (global) coordinate system. The incremental expression (Eq. B.4) is used to derive the CTM. Calligraphic terms are used to represent fourth-order (symmetric) tensors. Bold capital letters are second-order tensors. Latin or greek characters in bold represent vectors. Symmetric second-order tensors can be written as 6-components columns while symmetric fourth-order tensors can be compressed down to 6x6 matrices. The double dot contraction of two symmetric second-order tensors $\mathbf{A} : \mathbf{B} = \sum_{i,j} A_{ij}B_{ij}$ is equal to the dot product between two vectors as follows: $\mathbf{A} : \mathbf{B} \equiv \mathbf{a}.\mathbf{b}$, but care must be taken to correctly account for the nondiagonal terms. Typically the vectorial representation of a symmetric second order tensor reads in this case $\mathbf{a} = \left(A_{11}\, A_{22}\, A_{33}\, \sqrt{2}A_{12}\, \sqrt{2}A_{13}\, \sqrt{2}A_{23}\right)^T$. In case of contraction between the fourth-order stiffness tensor and a symmetric second-order tensor (e.g., $\boldsymbol{\sigma} = \boldsymbol{\mathcal{C}} : \boldsymbol{\varepsilon}^e$), the vector representation of the latter reads $\boldsymbol{\varepsilon}^e = \left(\varepsilon^e_{11}\, \varepsilon^e_{22}\, \varepsilon^e_{33}\, 2\varepsilon^e_{12}\, 2\varepsilon^e_{13}\, 2\varepsilon^e_{23}\right)^T$, since the engineering notation is used by ABAQUS/STANDARD.

As shown in Eq. B.4, finding the CTM amounts to deriving the 12 second order tensors $\frac{\partial\Delta\gamma^{(\alpha)}}{\partial\Delta\boldsymbol{\varepsilon}}$. This implies a dependency of the CTM on the very constitutive law adopted for the material. Two integration algorithms can be considered to determine the $\Delta\gamma^{(\alpha)}$'s: either explicit forward, or explicit with use of the midpoint rule, namely a Euler-Cauchy solver.

Euler forward integration of the amount of plastic slip

If a first order, forward explicit solver is used, the plastic slip increments do not depend on $\Delta\boldsymbol{\varepsilon}$, and the CTM is simply equal to $\boldsymbol{\mathcal{C}}$. Note that this case is not the ideal one since stability of the integration scheme is not guaranteed, and small time increments are required. In these conditions it might be more relevant to consider the use of an explicit finite element solver.

Euler-Cauchy integration of the amount of plastic slip

The amount of slip on each system is updated at each increment following $\Delta\gamma^{(\alpha)} = \Delta t \left((1-\Theta)\, \dot{\gamma}^{(\alpha)}\Big|_t + \Theta\, \dot{\gamma}^{(\alpha)}\Big|_{t+\Delta t} \right)$, and consequently $\frac{\partial\Delta\gamma^{(\alpha)}}{\partial\Delta\boldsymbol{\varepsilon}} =$

$\Theta\Delta t\frac{\partial\dot{\gamma}^{(\alpha)}\big|_{t+\Delta t}}{\partial\Delta\varepsilon}$. If $\Theta=0$ the integration is fully explicit, if $\Theta=1$ it is fully implicit. Using Orowan's law one and dropping the $|_{t+\Delta t}$ for enhanced readability, one gets

$$\begin{aligned}\frac{\partial\Delta\gamma^{(\alpha)}}{\partial\Delta\varepsilon} &= \Theta b\Delta t\frac{\partial\left(\rho_m^{eff(\alpha)}v^{(\alpha)}\right)}{\partial\Delta\varepsilon} \\ &= \Theta b\Delta t\left(\rho_m^{eff(\alpha)}\frac{\partial v^{(\alpha)}}{\partial\Delta\varepsilon}+v^{(\alpha)}\frac{\partial\rho_m^{eff(\alpha)}}{\partial\Delta\varepsilon}\right)\end{aligned} \tag{B.5}$$

where the dislocation densities, velocities and their derivatives are taken at the end of the increment. The dislocation velocity depends solely on the effective stress acting on dislocations. Assuming the stress exponent to be unity:

$$\frac{\partial v^{(\alpha)}}{\partial\Delta\varepsilon}=\frac{v_0}{\tau_0}\exp\left(-\frac{U}{k_bT}\right)\frac{\partial\tau_{eff}^{(\alpha)}}{\partial\Delta\varepsilon} \tag{B.6}$$

the derivative of the effective mobile dislocation density with respect to the strain rate is more complicated. At $t+\Delta t$ the dislocation density is found by using the same integration scheme as for $\Delta\gamma^{(\alpha)}$'s so that:

$$\begin{aligned}\rho_m^{eff(\alpha)}\Big|_{t+\Delta t} &= \rho_m^{eff(\alpha)}\Big|_t+\Delta\rho_m^{eff(\alpha)} \\ &= \rho_m^{eff(\alpha)}\Big|_t+\Delta t\left(\left(1-\Theta\right)\dot{\rho}_m^{eff(\alpha)}\Big|_t+\Theta\,\dot{\rho}_m^{eff(\alpha)}\Big|_{t+\Delta t}\right)\end{aligned} \tag{B.7}$$

Its derivative is equal to:

$$\frac{\partial\rho_m^{eff(\alpha)}}{\partial\Delta\varepsilon}=\frac{\partial\Delta\rho_m^{eff(\alpha)}}{\partial\Delta\varepsilon}=\Theta\Delta t\frac{\partial\,\dot{\rho}_m^{eff(\alpha)}\Big|_{t+\Delta t}}{\partial\Delta\varepsilon} \tag{B.8}$$

the constitutive law gives the evolution of the density of mobile dislocations as $\dot{\rho}_m^{eff(\alpha)}=\left(K_1\exp\left(-\frac{f(T)c_O^{(\alpha)}}{\tau_O}\right)\tau_{eff}^{(\alpha)}-2y_c\rho_m^{eff(\alpha)}\right)\rho_m^{eff(\alpha)}v^{(\alpha)}$ and K_1 a parameter depending on temperature only. After calculation of its derivative and simplification one gets, using $\theta=\Theta\Delta t\frac{v_0}{\tau_0}\exp\left(-\frac{U}{k_bT}\right)$ and $K_O=K_1\exp\left(-\frac{f(T)c_O^{(\alpha)}}{\tau_O}\right)$,

$$\begin{cases}\frac{\partial\rho_m^{eff(\alpha)}}{\partial\Delta\varepsilon_j}=\left(\lambda_{m,\Delta\varepsilon_j}^{(\alpha)}+\lambda_{O,\Delta\varepsilon_j}^{(\alpha)}\right)\frac{\partial\tau_{eff}^{(\alpha)}}{\partial\Delta\varepsilon_j} \\ \lambda_{m,\Delta\varepsilon_j}^{(\alpha)}=\frac{2\theta\left(K_O\tau_{eff}^{(j,\alpha)}-y_c\rho_m^{eff(j,\alpha)}\right)\rho_m^{eff(j,\alpha)}}{1-\theta\left(K_O\tau_{eff}^{(j,\alpha)}-4y_c\rho_m^{eff(j,\alpha)}\right)\tau_{eff}^{(j,\alpha)}} \\ \lambda_{O,\Delta\varepsilon_j}^{(\alpha)}=-\theta\frac{f(T)}{\tau_O}\varphi_{O,\Delta\varepsilon_j}^{(\alpha)}K_O\rho_m^{eff(\alpha)}\tau_{eff}^{(\alpha)2}\end{cases} \tag{B.9}$$

where it is emphasized that the $\boldsymbol{\lambda}_{m,\Delta\varepsilon_j}$ and $\boldsymbol{\lambda}_{O,\Delta\varepsilon_j}$ vectors depend on the component of the strain increment $\Delta\varepsilon_{1\leq j\leq 6}$ considered: the vectors of effective stresses $\boldsymbol{\tau}_{eff}$ and dislocation densities $\boldsymbol{\rho}_m$ are evaluated at $t+\Delta t$ after

application of $\Delta\varepsilon_j$ and depend on j because of the anisotropy of plastic deformation. A useful relationship is the derivative of the oxygen concentration at $t+\Delta t$ with respect to the strain increment, assuming that $v^{(\alpha)} \neq 0$:

$$\begin{aligned}\frac{\partial c_O^{(\alpha)}}{\partial \Delta\varepsilon_j} &= \frac{\frac{\theta}{a}\left(c_O^{\infty} - c_O^{(\alpha)} \exp\left(-\frac{a}{t_m v^{(\alpha)}}\right)\left(1+\frac{a}{t_m v^{(\alpha)}}\right)\right)}{1+\Theta\Delta t\left(D_{eff}\exp\left(-\frac{\Delta G}{k_b T}\right)+\frac{v^{(\alpha)}}{a}\exp\left(-\frac{a}{t_m v^{(\alpha)}}\right)\right)}\frac{\partial \tau_{eff}^{(\alpha)}}{\partial \Delta\varepsilon_j} \\ &= \varphi_{O,\Delta\varepsilon_j}^{(\alpha)}\frac{\partial \tau_{eff}^{(\alpha)}}{\partial \Delta\varepsilon_j}\end{aligned}$$

If the velocity at $t+\Delta t$ is null, $\varphi_{O,\Delta\varepsilon_j}^{(\alpha)} = \frac{\theta\frac{c_O^{\infty}}{a}}{1+\Theta\Delta t D_{eff}\exp\left(-\frac{\Delta G}{k_b T}\right)}$.

Similarly, one can obtain a linear dependency of the variation of the total dislocation densities $\rho_t^{(\alpha)}$ with the strain increment as a

$$\begin{cases} \frac{\partial \rho_t^{(\alpha)}}{\partial \Delta\varepsilon_j} = \left(\lambda_{t,\Delta\varepsilon_j}^{(\alpha)} + \lambda_{O,\Delta\varepsilon_j}^{(\alpha)}\right)\frac{\partial \tau_{eff}^{(\alpha)}}{\partial \Delta\varepsilon_j} \\ \lambda_{t,\Delta\varepsilon_j}^{(\alpha)} = \theta K_1 \tau_{eff}^{(j,\alpha)}\left(2\rho_m^{eff(j,\alpha)} + \tau_{eff}^{(j,\alpha)}\left(\lambda_{m,\Delta\varepsilon_j}^{(j,\alpha)} + \lambda_{O,\Delta\varepsilon_j}^{(j,\alpha)}\right)\right) \end{cases} \tag{B.10}$$

In the following we will work on the j$^{\text{th}}$ column of the consistent tangent moduli yielded by $\Delta\varepsilon_j$, j$^{\text{th}}$ component of the strain increment vector. The variation of the plastic slip rate with respect to the strain rate (Eq. B.5) is proportional to the quantity $\frac{\partial \tau_{eff}^{(\alpha)}}{\partial \Delta\varepsilon_j}$ as follows:

$$\frac{\partial \Delta\gamma^{(\alpha)}}{\partial \Delta\varepsilon_j} = b\theta\left(\rho_m^{eff(j,\alpha)} + \left(\lambda_{m,\Delta\varepsilon_j}^{(\alpha)} + \lambda_{O,\Delta\varepsilon_j}^{(\alpha)}\right)\tau_{eff}^{(j,\alpha)}\right)\frac{\partial \tau_{eff}^{(\alpha)}}{\partial \Delta\varepsilon_j} \tag{B.11}$$

and the derivation of the CTM is equivalent to the determination of the $\frac{\partial \tau_{eff}^{(\alpha)}}{\partial \Delta\boldsymbol{\varepsilon}}$ terms. Writing $\tau_{eff}^{(\alpha)} = \tau^{(\alpha)} - \tau_{int}^{(\alpha)}$ and $\tau^{(\alpha)} = \boldsymbol{\sigma} : \mathbf{P}_0^{(\alpha)}$ one immediately obtains

$$\frac{\partial \tau_{eff}^{(\alpha)}}{\partial \Delta\boldsymbol{\varepsilon}} = \frac{\partial \Delta\boldsymbol{\sigma}}{\partial \Delta\boldsymbol{\varepsilon}} : \mathbf{P}_0^{(\alpha)} - \frac{\partial \tau_{int}^{(\alpha)}}{\partial \Delta\boldsymbol{\varepsilon}} \tag{B.12}$$

The internal stress is a function of the dislocation densities on all the slip systems and its derivative with respect to the strain increments reads:

$$\frac{\partial \tau_{int}^{(\alpha)}}{\partial \Delta\boldsymbol{\varepsilon}} = \mu b\sum_{\beta}\frac{A_{\alpha\beta}}{2\sqrt{\rho_m^{(j,\beta)}}}\frac{\partial \rho_m^{(\beta)}}{\partial \Delta\boldsymbol{\varepsilon}} + \mu b\sum_{\beta}\frac{a_{\alpha\beta}}{2\sqrt{\sum_{\kappa} a_{\alpha\kappa}\rho_t^{(j,\kappa)}}}\frac{\partial \rho_t^{(\beta)}}{\partial \Delta\boldsymbol{\varepsilon}} + f(T)\frac{\partial c_O^{(\alpha)}}{\partial \Delta\varepsilon_j} \tag{B.13}$$

Using the linear expressions derived previously (Eqs. B.9 and B.10) and considering individual tensorial components, Eq. B.13 is equivalent to:

$$\begin{aligned}\frac{\partial \tau_{int}^{(\alpha)}}{\partial \Delta\varepsilon_j} = & \left[\frac{\mu b}{2}\sum_{\beta}\left(\frac{A_{\alpha\beta}\left(\lambda_{m,\Delta\varepsilon_j}^{(\beta)}+\lambda_{O,\Delta\varepsilon_j}^{(\beta)}\right)}{\sqrt{\rho_m^{(j,\beta)}}}+\frac{a_{\alpha\beta}\left(\lambda_{t,\Delta\varepsilon_j}^{(\beta)}+\lambda_{O,\Delta\varepsilon_j}^{(\beta)}\right)}{\sqrt{\sum_\kappa a_{\alpha\kappa}\rho_t^{(j,\kappa)}}}\right)\right. \\ & \left.+\delta_{\alpha\beta}f(T)\varphi_{O,\Delta\varepsilon_j}^{(\alpha)}\right]\frac{\partial \tau_{eff}^{(\beta)}}{\partial \Delta\varepsilon_j}\end{aligned} \tag{B.14}$$

Let us define $\mathcal{A}_{\Delta\varepsilon_j}$, a 12x12 matrix depending on the jth component of the strain increment $\Delta\boldsymbol{\varepsilon}$ through the values of the internal variables:

$$\begin{aligned}\left(\mathcal{A}_{\Delta\varepsilon_j}\right)_{\alpha\beta} = \delta_{\alpha\beta}\left(1+f(T)\varphi_{O,\Delta\varepsilon_j}^{(\alpha)}\right)+\frac{\mu b}{2}\left(\frac{A_{\alpha\beta}\left(\lambda_{m,\Delta\varepsilon_j}^{(\beta)}+\lambda_{O,\Delta\varepsilon_j}^{(\beta)}\right)}{\sqrt{\rho_m^{(j,\beta)}}}\right. \\ \left.+\frac{a_{\alpha\beta}\left(\lambda_{t,\Delta\varepsilon_j}^{(\beta)}+\lambda_{O,\Delta\varepsilon_j}^{(\beta)}\right)}{\sqrt{\sum_\kappa a_{\alpha\kappa}\rho_t^{(j,\kappa)}}}\right)\end{aligned} \tag{B.15}$$

Insertion of Eq. B.14 into Eq. B.12 yields a linear system of equations linking the $\frac{\partial \tau_{eff}^{(\beta)}}{\partial \Delta\boldsymbol{\varepsilon}}$'s to the resolved shear stresses:

$$\sum_{\beta}\left(\mathcal{A}_{\Delta\varepsilon_j}\right)_{\alpha\beta}\frac{\partial \tau_{eff}^{(\beta)}}{\partial \Delta\varepsilon_j} = \frac{\partial \Delta\boldsymbol{\sigma}}{\partial \Delta\varepsilon_j}.\mathbf{P}_0^{(\alpha)} \tag{B.16}$$

Then one gets by solving this linear equation system:

$$\frac{\partial \tau_{eff}^{(\alpha)}}{\partial \Delta\varepsilon_j} = \frac{\partial \Delta\boldsymbol{\sigma}}{\partial \Delta\varepsilon_j}.\sum_{\beta}\left(\mathcal{A}_{\Delta\varepsilon_j}^{-1}\right)_{\alpha\beta}\mathbf{P}_0^{(\beta)} \tag{B.17}$$

Insert Eq. B.17 into Eq. B.11, which now reads:

$$\frac{\partial \Delta\gamma^{(\alpha)}}{\partial \Delta\varepsilon_j} = b\theta\left(\rho_m^{eff(j,\alpha)}+\left(\lambda_{m,\Delta\varepsilon_j}^{(\alpha)}+\lambda_{O,\Delta\varepsilon_j}^{(\alpha)}\right)\tau_{eff}^{(j,\alpha)}\right)\frac{\partial \Delta\boldsymbol{\sigma}}{\partial \Delta\varepsilon_j}.\sum_{\beta}\left(\mathcal{A}_{\Delta\varepsilon_j}^{-1}\right)_{\alpha\beta}\mathbf{P}_0^{(\beta)}$$

Replace now $\frac{\partial \Delta\boldsymbol{\sigma}}{\partial \Delta\varepsilon_j}$ by its expression (from Eq. B.4):

$$\begin{aligned}\frac{\partial \Delta\gamma^{(\alpha)}}{\partial \Delta\varepsilon_j} = & \; b\theta\left(\rho_m^{eff(j,\alpha)}+\left(\lambda_{m,\Delta\varepsilon_j}^{(\alpha)}+\lambda_{O,\Delta\varepsilon_j}^{(\alpha)}\right)\tau_{eff}^{(j,\alpha)}\right)\left(\sum_{\beta}\left(\mathcal{A}_{\Delta\varepsilon_j}^{-1}\right)_{\alpha\beta}\left(\boldsymbol{\mathcal{C}}.\mathbf{P}_0^{(\beta)}\right)_j\right. \\ & \left.-\sum_{\pi}\frac{\partial \Delta\gamma^{(\pi)}}{\partial \Delta\varepsilon_j}\sum_{\beta}\left(\mathcal{A}_{\Delta\varepsilon_j}^{-1}\right)_{\alpha\beta}\mathbf{P}_0^{(\beta)}.\left(\boldsymbol{\mathcal{C}}.\mathbf{P}_0^{(\pi)}\right)\right)\end{aligned}$$

The $\frac{\partial \Delta\gamma^{(\alpha)}}{\partial \Delta\varepsilon_j}$'s are obtained by solving the equation system:

$$\mathcal{Q}_{\Delta\varepsilon_j}.\mathbf{x}_j = \mathbf{r}_j \tag{B.18}$$

where $\left(\mathbf{x}_j\right)_{1\leq\alpha\leq12} = \frac{\partial\Delta\gamma^{(\alpha)}}{\partial\Delta\varepsilon_j}$ and

$$\left(\mathbf{r}_j\right)_{1\leq\alpha\leq12} = \sum_{\beta}\left(\mathcal{A}^{-1}_{\Delta\varepsilon_j}\right)_{\alpha\beta}\left(\boldsymbol{\mathcal{C}}.\mathbf{P}_0^{(\beta)}\right)_j \tag{B.19}$$

$$\begin{aligned}\left(\mathcal{Q}_{\Delta\varepsilon_j}\right)_{\alpha\pi} =& \frac{\delta_{\alpha\pi}}{b\theta\left(\rho_m^{eff(j,\alpha)} + \left(\lambda^{(\alpha)}_{m,\Delta\varepsilon_j} + \lambda^{(\alpha)}_{O,\Delta\varepsilon_j}\right)\tau^{(j,\alpha)}_{eff}\right)} \\ &+ \sum_{\beta}\left(\mathcal{A}^{-1}_{\Delta\varepsilon_j}\right)_{\alpha\beta}\mathbf{P}_0^{(\beta)}.\left(\boldsymbol{\mathcal{C}}.\mathbf{P}_0^{(\pi)}\right)\end{aligned} \tag{B.20}$$

Finally, the $\frac{\partial\Delta\gamma^{(\alpha)}}{\partial\Delta\varepsilon_j}$'s can be inserted into Eq. B.4 and the j$^{\text{th}}$ column of the consistent tangent moduli is obtained:

$$\boldsymbol{\mathcal{C}}^{ep}_{,j} = \boldsymbol{\mathcal{C}}_{,j} - \sum_{\alpha}\left(\boldsymbol{\mathcal{C}}.\mathbf{P}_0^{(\alpha)}\right)\left(\mathcal{Q}^{-1}_{\Delta\varepsilon_j}.\mathbf{r}_j\right)_{\alpha} \tag{B.21}$$

In practice, derivation of the complete CTM requires six evaluations of the internal variables and stresses following the application of the strain increments $\Delta\varepsilon_j$ over a time length Δt. Each time the equation systems B.16 and B.18 must be solved.

- at the end of increment i (i.e. at $t_i + \Delta t_i$), the initial internal variables, strain and stresses (at t_i) are sent to the routine `tangentmoduli` for derivation of the CTM. The time step used is Δt_i.
- `tangentmoduli` computes the CTM following Eq. B.21, that is, one column at a time. Each column is obtained by perturbating the system at t_i, imposing $(\Delta\boldsymbol{\varepsilon})_i = \delta_{ij}\Delta\varepsilon_j$ for $1 \leq j \leq 6$.
- For each component $\Delta\varepsilon_j$:
  - a second order Euler-Cauchy solver without substepping[1] is used to compute $\left(\rho_m^{(j,\alpha)}, \rho_t^{(j,\alpha)}, \tau^{(j,\alpha)}_{eff}\right)_{1\leq\alpha\leq12}$.
  - the vectors $\boldsymbol{\lambda}_{m,\Delta\varepsilon_j}$ and $\boldsymbol{\lambda}_{t,\Delta\varepsilon_j}$ are then formed (resp. Eqs. B.9 and B.10)
  - the $\mathcal{A}_{\Delta\varepsilon_j}$ matrix is built and inversed to derive $\mathcal{Q}_{\Delta\varepsilon_j}$ (Eqs. B.15 and B.20). The $\mathbf{r}_j$ vector is calculated as well.
  - $\mathcal{Q}_{\Delta\varepsilon_j}$ is inversed and the j$^{\text{th}}$ colum of the CTM formed.
- Note that the construction of the $\mathcal{Q}_{\Delta\varepsilon_j}$ matrices and $\mathbf{r}_j$ vectors require the use of $\boldsymbol{\mathcal{C}}.\mathbf{P}_0^{(\alpha)}$ vectors that can be built at the beginning of the routine. This implies the use of a rotation matrix allowing the transformation of coordinates between the local (crystal lattice) and the global

1 no improvement of the convergence properties is detected by the use of substepping with error control and direct integration is numerically less expensive, therefore prefered. Convergence is slower as the global time increment is increased upon strong softening of the material (in the yield region).

systems, since $\mathcal{C}$ and the $\mathbf{P}_0^{(\alpha)}$'s are typically known in the former one whereas the CTM must be expressed in the global system.

- Assuming the dislocation velocity law independent on the constitutive model, each constitutive model is characterized by a choice of (1) internal stress $\tau_{int}^{(\alpha)}$ depending on the internal variables, in the present case dislocation densities $\rho^{(\alpha)}$, and (2) first order differential equations ruling the evolution of these very internal variables, ultimately depending on the internal stresses. The derivation of the CTM must be adapted to each change in any of these components of the constitutive model, by correcting the $\boldsymbol{\lambda}_{\Delta\varepsilon_j}$ vectors and the components of the $\mathcal{A}_{\Delta\varepsilon_j}$ matrices.

CONVERGENCE OF THE NEWTON-RAPHSON ITERATIONS

The material is rate-dependent and its mechanical behavior extremely temperature sensitive (exponential dependency of the velocity and multiplication parameters). Therefore the convergence properties will depend sensitively on the global time increment and on the temperature. The element size might as well play a role by setting a length scale in the model.

B.2 DERIVATION OF DDSDDT FOR COUPLED THERMOMECHANICAL ANALYSES

This Section is concerned with the derivation of the DDSDDT required by Abaqus/Standard in the case of coupled mechanical-thermal analyses. Note that it has not been used in our work, but its derivation is proposed here for future reference.

Efficient convergence properties in the case of nonisothermal loadings in a fully coupled thermal-stress analysis require the precise definition of the variations of the stress increment with respect to those of the temperature increments, $\frac{\partial \Delta \boldsymbol{\sigma}}{\partial \Delta T}$, that reads:

$$\frac{\partial \Delta \boldsymbol{\sigma}}{\partial \Delta T} = \frac{\partial \boldsymbol{\mathcal{C}}}{\partial \Delta T} : \Delta \boldsymbol{\varepsilon}^e + \boldsymbol{\mathcal{C}} : \frac{\partial \Delta \boldsymbol{\varepsilon}^e}{\partial \Delta T} \tag{B.22}$$

Computation of $\frac{\partial \Delta \boldsymbol{\sigma}}{\partial \Delta T}$ is not required in the standard case of decoupled temperature-stress analysis. The first term is computed by writing $\boldsymbol{\mathcal{C}}(T + \Delta T) \simeq \boldsymbol{\mathcal{C}}(T) + \Delta T \frac{\partial \boldsymbol{\mathcal{C}}}{\partial T}$ and $\frac{\partial \boldsymbol{\mathcal{C}}}{\partial \Delta T} = \left.\frac{\partial \boldsymbol{\mathcal{C}}}{\partial T}\right|_T$. This approximation is valid since $\Delta T \ll T$ is always valid in practice, and the components of the stiffness tensor ar weakly dependent on the temperature. $\Delta \boldsymbol{\varepsilon}^e$ is computed by perturbating the system at the end of the increment, by applying a temperature change $\Delta T = \left.\dot{T}\right|_t \Delta t$ over a time increment Δt:

$$\begin{aligned} t &\to t + \Delta t \\ T &\to T + \Delta T \\ \boldsymbol{\chi} &\to \boldsymbol{\chi} + \Delta \boldsymbol{\chi} \\ \boldsymbol{\sigma} &\to \boldsymbol{\sigma} + \Delta \boldsymbol{\sigma} \end{aligned}$$

The total strain increment is here imposed to be null, so that $\Delta \boldsymbol{\varepsilon}^e = -\Delta \boldsymbol{\varepsilon}^p - \Delta \boldsymbol{\varepsilon}^T$. Let us consider as previously the solutions yielded by different choices of integration scheme. For simplicity the influence of osygen is disregarded in the following.

Euler forward explicit solver

The increment of thermal strains is calculated following: $\Delta \boldsymbol{\varepsilon}^T = \Delta t \dot{T} \boldsymbol{\vartheta}(T) = \Delta T \boldsymbol{\vartheta}(T)$, temperatures and parameters being taken at t. Consequently $\frac{\partial \Delta \boldsymbol{\varepsilon}^T}{\partial \Delta T} = \boldsymbol{\vartheta}(T)$. Similarly, $\frac{\partial \Delta \boldsymbol{\varepsilon}^p}{\partial \Delta T} = \mathbf{0}$ and the stress increment varies with the temperature increment as

$$\frac{\partial \Delta \boldsymbol{\sigma}}{\partial \Delta T} = \left.\frac{\partial \boldsymbol{\mathcal{C}}}{\partial T}\right|_T : \Delta \boldsymbol{\varepsilon}^e + \boldsymbol{\mathcal{C}} : \boldsymbol{\vartheta}(T) \tag{B.23}$$

Midpoint rule

As previously, an explicit solver of second order without substepping is used to derive the components of $\Delta \varepsilon^e$ and to update the vector of internal

variables χ. The second term of Eq. B.22 is harder to derive than the first one.

Variation of thermal strain increment with the temperature increment

Let us first consider the thermal strains: $\dot{\boldsymbol{\varepsilon}}^T = \dot{T}\boldsymbol{\vartheta}(T)$. In the lattice coordinate system, this reads:

$$\begin{aligned}\boldsymbol{\vartheta}(T) &= \vartheta(T)\,(1,\,1,\,1,\,0,\,0,\,0)^T = \vartheta(T)\mathbf{I}\\ \vartheta(T) &= 3.725\times\left(1-\exp\left(-5.88\times10^{-3}\,(T-124)\right)\right)\\ &\quad +5.548\times10^{-4}\,T\,\left(10^{-6}\,\mathrm{K}^{-1}\right)\end{aligned}$$

Adopting an Euler-Cauchy updating algorithm for computation of the thermal strain increment over a time Δt (i.e. setting $\Theta = 0.5$), one gets $\frac{\partial\Delta\boldsymbol{\varepsilon}^T}{\partial\Delta T} = \frac{\Delta t}{2}\left(\dot{T}\big|_t\,\boldsymbol{\vartheta}(T) + \dot{T}\big|_{t+\Delta t}\,\boldsymbol{\vartheta}(T+\Delta T)\right)$

$$\frac{\partial\Delta\boldsymbol{\varepsilon}^T}{\partial\Delta T} = \frac{\boldsymbol{\vartheta}(T)}{2} + \frac{\Delta t}{2}\,\dot{T}\big|_{t+\Delta t}\,\frac{\partial\boldsymbol{\vartheta}\,(T+\Delta T)}{\partial\Delta T}$$

and the thermal expansion coefficient vector at $T+\Delta T$ reads, assuming $\Delta T \ll T$:

$$\boldsymbol{\vartheta}\,(T+\Delta T) \simeq \boldsymbol{\vartheta}\,(T) + \Delta T\,\left.\frac{\partial\boldsymbol{\vartheta}}{\partial T}\right|_T$$

$$\frac{\partial\vartheta}{\partial T} = 2.19\times10^{-2}\exp\left(-5.88\times10^{-3}\,(T-124)\right) + 5.548\times10^{-4}\,\left(10^{-6}\,\mathrm{K}^{-2}\right)$$

Finally, the variation of the thermal strain increment with respect to the temperature increment reads:

$$\frac{\partial\Delta\boldsymbol{\varepsilon}^T}{\partial\Delta T} = \frac{\boldsymbol{\vartheta}(T)}{2} + \frac{\Delta T}{2}\,\left.\frac{\partial\boldsymbol{\vartheta}}{\partial T}\right|_T$$

where we assume that $\dot{T}\big|_{t+\Delta t} = \dot{T}\big|_t$.

Variation of plastic strain increment with the temperature increment

Derivation of $\frac{\partial\Delta\boldsymbol{\varepsilon}^p}{\partial\Delta T}$ is more intricated. The same method as for the CTM will be adopted in the following.

$$\begin{aligned}\frac{\partial\Delta\gamma^{(\alpha)}}{\partial\Delta T} &= \frac{\Delta t}{2}b\frac{\partial\left(\rho_m^{(\alpha)}v^{(\alpha)}\right)}{\partial\Delta T}\\ &= \frac{\Delta t}{2}b\left(\rho_m^{(\alpha)}\frac{\partial v^{(\alpha)}}{\partial\Delta T} + v^{(\alpha)}\frac{\partial\rho_m^{(\alpha)}}{\partial\Delta T}\right)\end{aligned}$$

where we assume the magnitude of the Burgers vector not to be affected by temperature, the dislocation densities and velocities are taken at $t + \Delta t$, i.e. $T + \Delta T$.

$$\begin{aligned}\frac{\partial v^{(\alpha)}}{\partial \Delta T} &= \frac{v_0}{\tau_0}\exp\left(-\frac{U}{k_b\left(T+\Delta T\right)}\right)\left(\frac{U}{k_b\left(T+\Delta T\right)^2}\tau_{eff}^{(\alpha)}+\frac{\partial \tau_{eff}^{(\alpha)}}{\partial \Delta T}\right)\\ &= v^{(\alpha)}\left(\frac{U}{k_b\left(T+\Delta T\right)^2}+\frac{1}{\tau_{eff}^{(\alpha)}}\frac{\partial \tau_{eff}^{(\alpha)}}{\partial \Delta T}\right)\end{aligned} \tag{B.24}$$

$$\begin{aligned}\frac{\partial \rho_m^{(\alpha)}}{\partial \Delta T} &= \frac{\left(U_{K_1}+U\right)K_1\tau_{eff}^{(\alpha)}-2\left(U_{y_c}+U\right)y_c\rho_m^{(\alpha)}}{\frac{2}{\Delta t}-K_1\tau_{eff}^{(\alpha)}v^{(\alpha)}+4y_c\rho_m^{(\alpha)}v^{(\alpha)}}\frac{\rho_m^{(\alpha)}v^{(\alpha)}}{k_b\left(T+\Delta T\right)^2}\\ &+\frac{2\rho_m^{(\alpha)}v^{(\alpha)}\left(K_1+\frac{y_c\rho_m^{(\alpha)}}{\tau_{eff}^{(\alpha)}}\right)}{\frac{2}{\Delta t}-K_1\tau_{eff}^{(\alpha)}v^{(\alpha)}+4y_c\rho_m^{(\alpha)}v^{(\alpha)}}\frac{\partial \tau_{eff}^{(\alpha)}}{\partial \Delta T}\end{aligned} \tag{B.25}$$

where the expressions $K_1 = A_{K_1}\exp\left(-\frac{U_{K_1}}{k_bT}\right)$ and $y_c = A_{y_c}\exp\left(-\frac{U_{y_c}}{k_bT}\right)$ have been used, yielding e.g. $\frac{\partial K_1}{\partial T} = \frac{U_{K_1}}{k_bT^2}K_1$. Eq. B.25 can be written, with $\theta = \Delta t\frac{v_0}{\tau_0}\exp\left(-\frac{U}{k_b(T+\Delta T)}\right)$,

$$\begin{cases}\frac{\partial \rho_m^{(\alpha)}}{\partial \Delta T} = \nu_{m,\Delta T}^{(\alpha)}+\lambda_{m,\Delta T}^{(\alpha)}\frac{\partial \tau_{eff}^{(\alpha)}}{\partial \Delta T}\\ \nu_{m,\Delta T}^{(\alpha)} = \frac{\theta\rho_m^{(\alpha)}\tau_{eff}^{(\alpha)}}{2k_b(T+\Delta T)^2}\frac{\left(U_{K_1}+U\right)K_1\tau_{eff}^{(\alpha)}-2\left(U_{y_c}+U\right)y_c\rho_m^{(\alpha)}}{1-\frac{\theta}{2}\left(K_1\tau_{eff}^{(\alpha)}-4y_c\rho_m^{(\alpha)}\right)\tau_{eff}^{(\alpha)}}\\ \lambda_{m,\Delta T}^{(\alpha)} = \frac{\theta\left(K_1\tau_{eff}^{(\alpha)}-y_c\rho_m^{(\alpha)}\right)\rho_m^{(\alpha)}}{1-\frac{\theta}{2}\left(K_1\tau_{eff}^{(\alpha)}-4y_c\rho_m^{(\alpha)}\right)\tau_{eff}^{(\alpha)}}\end{cases} \tag{B.26}$$

Similarly one can derive for the total dislocation densities:

$$\begin{cases}\frac{\partial \rho_t^{(\alpha)}}{\partial \Delta T} = \nu_{t,\Delta T}^{(\alpha)}+\lambda_{t,\Delta T}^{(\alpha)}\frac{\partial \tau_{eff}^{(\alpha)}}{\partial \Delta T}\\ \nu_{t,\Delta T}^{(\alpha)} = \frac{\theta}{2}K_1\tau_{eff}^{(\alpha)2}\left(\rho_m^{(\alpha)}\frac{U_{K_1}+U}{k_b(T+\Delta T)^2}+\nu_{m,\Delta T}^{(\alpha)}\right)\\ \lambda_{t,\Delta T}^{(\alpha)} = \frac{\theta}{2}K_1\tau_{eff}^{(\alpha)}\left(2\rho_m^{(\alpha)}+\lambda_{m,\Delta T}^{(\alpha)}\tau_{eff}^{(\alpha)}\right)\end{cases} \tag{B.27}$$

The variations of the plastic slip increments are given by

$$\frac{\partial \Delta\gamma^{(\alpha)}}{\partial \Delta T} = \frac{b\theta}{2}\left(\tau_{eff}^{(\alpha)}\left(\rho_m^{(\alpha)}\frac{U}{k_bT^2}+\nu_{m,\Delta T}^{(\alpha)}\right)+\left(\rho_m^{(\alpha)}+\lambda_{m,\Delta T}^{(\alpha)}\tau_{eff}^{(\alpha)}\right)\frac{\partial \tau_{eff}^{(\alpha)}}{\partial \Delta T}\right) \tag{B.28}$$

As in the case of the CTM, linear relationships are found between the derivatives of the dislocation densities and the one of the effective stress.

$$\frac{\partial \tau_{eff}^{(\alpha)}}{\partial \Delta T} = \frac{\partial \Delta\boldsymbol{\sigma}}{\partial \Delta T}.\mathbf{P}_0^{(\alpha)}-\frac{\partial \tau_{int}^{(\alpha)}}{\partial \Delta T}$$

Following Eq. B.13, the internal stresses derivatives can be expressed as a linear function of the effective stress derivatives:

$$\begin{aligned}\frac{\partial \tau_{int}^{(\alpha)}}{\partial \Delta T} =& \frac{\mu b}{2} \sum_{\beta} \left(\frac{A_{\alpha\beta} \nu_{m,\Delta T}^{(\beta)}}{\sqrt{\rho_m^{(\beta)}}} + \frac{a_{\alpha\beta} \nu_{t,\Delta T}^{(\beta)}}{\sqrt{\sum_{\kappa} a_{\alpha\kappa} \rho_t^{(\kappa)}}} \right) \\ &+ \left(\frac{A_{\alpha\beta} \lambda_{m,\Delta T}^{(\beta)}}{\sqrt{\rho_m^{(\beta)}}} + \frac{a_{\alpha\beta} \lambda_{t,\Delta T}^{(\beta)}}{\sqrt{\sum_{\kappa} a_{\alpha\kappa} \rho_t^{(\kappa)}}} \right) \frac{\partial \tau_{eff}^{(\beta)}}{\partial \Delta T}\end{aligned} \tag{B.29}$$

As previously, the effective stress variations on the slip systems are obtained by solving the linear system

$$\sum_{\beta} \left(\mathcal{A}_{\Delta T} \right)_{\alpha\beta} \frac{\partial \tau_{eff}^{(\beta)}}{\partial \Delta T} = \frac{\partial \Delta \boldsymbol{\sigma}}{\partial \Delta T} . \mathbf{P}_0^{(\alpha)} - \frac{\mu b}{2} \sum_{\beta} \left(\frac{A_{\alpha\beta} \nu_{m,\Delta T}^{(\beta)}}{\sqrt{\rho_m^{(\beta)}}} + \frac{a_{\alpha\beta} \nu_{t,\Delta T}^{(\beta)}}{\sqrt{\sum_{\kappa} a_{\alpha\kappa} \rho_t^{(\kappa)}}} \right) \tag{B.30}$$

with $\mathcal{A}_{\Delta T}$ a 12x12 matrix having a similar shape as the $\mathcal{A}_{\Delta \varepsilon_j}$'s:

$$\left(\mathcal{A}_{\Delta T} \right)_{\alpha\beta} = \delta_{\alpha\beta} + \frac{\mu b}{2} \left(\frac{A_{\alpha\beta} \lambda_{m,\Delta T}^{(\beta)}}{\sqrt{\rho_m^{(\beta)}}} + \frac{a_{\alpha\beta} \lambda_{t,\Delta T}^{(\beta)}}{\sqrt{\sum_{\kappa} a_{\alpha\kappa} \rho_t^{(\kappa)}}} \right) \tag{B.31}$$

$$\begin{cases} \frac{\partial \tau_{eff}^{(\alpha)}}{\partial \Delta T} = \frac{\partial \Delta \boldsymbol{\sigma}}{\partial \Delta T} . \sum_{\beta} \left(\mathcal{A}_{\Delta T}^{-1} \right)_{\alpha\beta} \mathbf{P}_0^{(\beta)} - \kappa^{(\alpha)} \\ \kappa_{\Delta T}^{(\alpha)} = \frac{\mu b}{2} \sum_{\beta} \left(\mathcal{A}_{\Delta T}^{-1} \right)_{\alpha\beta} \sum_{\pi} \left(\frac{A_{\beta\pi} \nu_{m,\Delta T}^{(\pi)}}{\sqrt{\rho_m^{(\pi)}}} + \frac{a_{\beta\pi} \nu_{t,\Delta T}^{(\pi)}}{\sqrt{\sum_{\kappa} a_{\beta\kappa} \rho_t^{(\kappa)}}} \right) \end{cases} \tag{B.32}$$

Insert this result into Eq. B.28 and then use Eq. B.22 to solve for the $\frac{\partial \Delta \gamma^{(\alpha)}}{\partial \Delta T}$'s:

$$\begin{aligned}\frac{2}{b\theta} \frac{\partial \Delta \gamma^{(\alpha)}}{\partial \Delta T} =& \tau_{eff}^{(\alpha)} \left(\rho_m^{(\alpha)} \frac{U}{k_b \left(T + \Delta T \right)^2} + \nu_{m,\Delta T}^{(\alpha)} \right) - \left(\rho_m^{(\alpha)} + \lambda_{m,\Delta T}^{(\alpha)} \tau_{eff}^{(\alpha)} \right) \\ & \left(\left(\frac{\partial \Delta \boldsymbol{\varepsilon}^T}{\partial \Delta T} + \sum_{\beta} \frac{\partial \Delta \gamma^{(\beta)}}{\partial \Delta T} \mathbf{P}_0^{(\beta)} \right) . \sum_{\beta} \left(\mathcal{A}_{\Delta T}^{-1} \right)_{\alpha\beta} \boldsymbol{\mathcal{C}} . \mathbf{P}_0^{(\beta)} + \kappa_{\Delta T}^{(\alpha)} \right)\end{aligned}$$

or under a friendlier form:

$$\mathcal{Q}_{\Delta T} . \mathbf{x} = \mathbf{r}_{\Delta T} \tag{B.33}$$

where $\left(\mathbf{x} \right)_{1 \leq \alpha \leq 12} = \frac{\partial \Delta \gamma^{(\alpha)}}{\partial \Delta T}$ and

$$\begin{aligned}\left(\mathbf{r}_{\Delta T} \right)_{1 \leq \alpha \leq 12} =& \tau_{eff}^{(\alpha)} \left(\rho_m^{(\alpha)} \frac{U}{k_b \left(T + \Delta T \right)^2} + \nu_{m,\Delta T}^{(\alpha)} \right) - \left(\rho_m^{(\alpha)} + \lambda_{m,\Delta T}^{(\alpha)} \tau_{eff}^{(\alpha)} \right) \\ & \left(\kappa_{\Delta T}^{(\alpha)} + \frac{\partial \Delta \boldsymbol{\varepsilon}^T}{\partial \Delta T} . \sum_{\beta} \left(\mathcal{A}_{\Delta T}^{-1} \right)_{\alpha\beta} \boldsymbol{\mathcal{C}} . \mathbf{P}_0^{(\beta)} \right)\end{aligned} \tag{B.34}$$

$$(\mathcal{Q}_{\Delta T})_{\alpha\pi} = \frac{2\delta_{\alpha\pi}}{b\theta} + \left(\rho_m^{(\alpha)} + \lambda_{m,\Delta T}^{(\alpha)} \tau_{eff}^{(\alpha)}\right) \sum_{\beta} \left(\mathcal{A}_{\Delta T}^{-1}\right)_{\alpha\beta} \mathbf{P}_0^{(\beta)} . \left(\boldsymbol{\mathcal{C}} . \mathbf{P}_0^{(\pi)}\right) \quad \text{(B.35)}$$

Once the $\mathcal{Q}_T$ matrix has been inversed the solution is given by:

$$\frac{\partial \Delta\gamma^{(\alpha)}}{\partial \Delta T} = \sum_{\beta} \left(\mathcal{Q}_{\Delta T}^{-1}\right)_{\alpha\beta} (\mathbf{r}_{\Delta T})_{\beta}$$

Finally, the solution reads:

$$\frac{\partial \boldsymbol{\sigma}}{\partial \Delta T} = \left.\frac{\partial \boldsymbol{\mathcal{C}}}{\partial T}\right|_T . \Delta\boldsymbol{\varepsilon}^e - \boldsymbol{\mathcal{C}} . \left(\frac{\boldsymbol{\vartheta}(T)}{2} + \frac{\Delta T}{2} \left.\frac{\partial \boldsymbol{\vartheta}}{\partial T}\right|_t + \sum_{\alpha} \sum_{\beta} \left(\mathcal{Q}_{\Delta T}^{-1}\right)_{\alpha\beta} (\mathbf{r}_{\Delta T})_{\beta} \mathbf{P}_0^{(\alpha)} \right)$$

B.3 VON MISES PLASTICITY FOR MELT

The consistent tangent modulus for the "silicon melt" is derived in the following. This liquid is assumed to behave like a very soft solid. It is used in a later Part of this Thesis, when simulating the solidification and cooling of a small multicrystalline ingot.

The melt is represented by an elastic-perfectly plastic material using Von Mises plasticity flow rule:

$$f = \sigma_{eq} - \sigma_y \leq 0,\ \dot{f} = 0 \,\text{if}\, f = 0 \tag{B.36}$$

$$\sigma_{eq} = \sqrt{\frac{3}{2}\mathbf{S} : \mathbf{S}} = \sqrt{\frac{3}{2}}\,\|\mathbf{S}\| \tag{B.37}$$

The deviator $\mathbf{s}$ is derived from the stress tensor:

$$\mathbf{S} = \boldsymbol{\sigma} - \frac{1}{3} tr\,(\boldsymbol{\sigma})\,\mathbf{I} \tag{B.38}$$

The increment of stress reads as usually:

$$\dot{\boldsymbol{\sigma}} = \boldsymbol{\mathcal{C}} : (\dot{\boldsymbol{\varepsilon}} - \dot{\boldsymbol{\varepsilon}}^p) \tag{B.39}$$

Associated plasticity gives:

$$\dot{\boldsymbol{\varepsilon}}^p = \dot{\lambda}\frac{\partial f}{\partial \boldsymbol{\sigma}} = \frac{3}{2}\dot{\lambda}\frac{\mathbf{S}}{\sigma_{eq}} = \sqrt{\frac{3}{2}}\dot{\lambda}\frac{\mathbf{S}}{\|\mathbf{S}\|} \tag{B.40}$$

Determination of the plastic strain increment is equivalent to the derivation of $\Delta\lambda$.

Return mapping algorithm

At t a strain increment $\Delta\boldsymbol{\varepsilon}$ is applied to the system initally at $(\boldsymbol{\sigma},\ \boldsymbol{\varepsilon})$, leading to the definition of a trial test $\boldsymbol{\sigma}^t = \boldsymbol{\sigma} + \boldsymbol{\mathcal{C}} : \Delta\boldsymbol{\varepsilon}$. If $f\,(\boldsymbol{\sigma} + \boldsymbol{\mathcal{C}} : \Delta\boldsymbol{\varepsilon}) \leq 0$ then the increment is elastic and the solution $\boldsymbol{\sigma}_{t+\Delta t} = \boldsymbol{\sigma}_t + \boldsymbol{\mathcal{C}} : \Delta\boldsymbol{\varepsilon}$ is accepted. If not, then plasticity sets in during the increment and the plastic strain correction $\Delta\boldsymbol{\varepsilon}^p$ must be derived, so that $f\,(\boldsymbol{\sigma} + \boldsymbol{\mathcal{C}} : (\Delta\boldsymbol{\varepsilon} - \Delta\boldsymbol{\varepsilon}^p)) = 0$. Eq. B.40 gives $\Delta\boldsymbol{\varepsilon}^p = \frac{3}{2}\Delta\lambda\frac{\mathbf{S}}{\sigma_{eq}}$, so that

$$\begin{aligned}\boldsymbol{\sigma} + \Delta\boldsymbol{\sigma} &= \boldsymbol{\sigma} + \boldsymbol{\mathcal{C}} : \Delta\boldsymbol{\varepsilon} - \boldsymbol{\mathcal{C}} : \frac{3}{2}\Delta\lambda\frac{\mathbf{S}}{\sigma_{eq}} \\ &= \boldsymbol{\sigma}^t - \Delta\lambda\left(\frac{3}{2\sigma_{eq}}\boldsymbol{\mathcal{C}} : \mathbf{S}\right)\end{aligned} \tag{B.41}$$

Taking the deviatoric part of this equations yields:

$$\mathbf{S} = \mathbf{S}^t - \Delta\lambda\frac{3}{2\sigma_{eq}} dev\,(\boldsymbol{\mathcal{C}} : \mathbf{S}) \tag{B.42}$$

Isotropic materials

If the material isotropic, the stiffness matrix reads:

$$\boldsymbol{\mathcal{C}} = \begin{bmatrix} C_{11} & C_{12} & C_{12} & & & \\ C_{12} & C_{11} & C_{12} & & 0 & \\ C_{12} & C_{12} & C_{11} & & & \\ & & & \frac{C_{11}-C_{12}}{2} & & \\ & 0 & & & \frac{C_{11}-C_{12}}{2} & \\ & & & & & \frac{C_{11}-C_{12}}{2} \end{bmatrix}$$

and $dev(\boldsymbol{\mathcal{C}} : \mathbf{S}) = \boldsymbol{\mathcal{C}} : \mathbf{S} = (C_{11} - C_{12})\,\mathbf{S}$. Therefore Eq. B.41 is simplified to:

$$\mathbf{S}^t = \mathbf{S}\left(1 + \Delta\lambda \frac{3\,(C_{11} - C_{12})}{2\sigma_{eq}}\right) \tag{B.43}$$

showing that $\mathbf{S}$ and $\mathbf{S}^t$ are colinear. For isotropic materials, an additional relationship is consequently obtained as $\frac{\mathbf{S}}{\|\mathbf{S}\|} = \frac{\mathbf{S}^t}{\|\mathbf{S}^t\|}$. Then Eq. B.40 can be written $\dot{\boldsymbol{\varepsilon}}^p = \frac{3}{2}\dot{\lambda}\frac{\mathbf{S}^t}{\sigma^t_{eq}}$, which simplifies tremendously the derivation of $\Delta\lambda$. Equivalently, one can derive:

$$\mathbf{S} = \mathbf{S}^t\left(1 - \Delta\lambda \frac{3\,(C_{11} - C_{12})}{2\sigma^t_{eq}}\right) \tag{B.44}$$

At $t + \Delta t$ the stress state should be on the plastic yield surface:$f = 0$, or $\sqrt{\frac{3}{2}\mathbf{S} : \mathbf{S}} - \sigma_y = 0$. This is equivalent to or $\sigma^t_{eq}\left(1 - \Delta\lambda\frac{3(C_{11}-C_{12})}{2\sigma^t_{eq}}\right) - \sigma_y = 0$ and

$$\Delta\lambda = \frac{2f(\boldsymbol{\sigma}^t)}{3(C_{11} - C_{12})} \tag{B.45}$$

The case of ideal plasticity of isotropic materials gives therefore the plastic strain increment directly from the trial state.

Perfect plasticity is characterized by a constant yield stress σ_y, therefore when $f = 0$,

$$\dot{f} = \dot{\sigma_{eq}} = \frac{\partial f}{\partial \boldsymbol{\sigma}} : \dot{\boldsymbol{\sigma}} = \frac{3}{2}\frac{\dot{\boldsymbol{\sigma}} : \mathbf{S}}{\sigma_{eq}} = 0 \tag{B.46}$$

This consistency condition gives for $\dot{\lambda}$, using Eqs. B.39 and B.40:

$$\dot{\lambda} = \frac{\boldsymbol{\mathcal{C}} : \mathbf{S}}{\frac{3}{2\sigma_{eq}}\mathbf{S} : \boldsymbol{\mathcal{C}} : \mathbf{S}} : \dot{\boldsymbol{\varepsilon}} \tag{B.47}$$

with $\boldsymbol{\mathcal{C}} : \mathbf{S} = (C_{11} - C_{12})\,\mathbf{S}$ and $\sigma_{eq} = \sigma_y$, the expression for the plastic strain rate reads for isotropic materials:

$$\dot{\boldsymbol{\varepsilon}}^p = \frac{3}{2\sigma_y^2}\mathbf{S} \otimes \mathbf{S} : \dot{\boldsymbol{\varepsilon}} \tag{B.48}$$

The consistent tangent moduli reads, when plasticity is developing,

$$\boldsymbol{\mathcal{C}}_{ep} = \boldsymbol{\mathcal{C}} \left(\boldsymbol{\mathcal{I}} - \frac{3}{2\sigma_y^2} \mathbf{S} \otimes \mathbf{S} \right) \tag{B.49}$$

and $\boldsymbol{\mathcal{C}}_{ep} = \boldsymbol{\mathcal{C}}$ otherwise.

Anisotropic materials

The case of anisotropy does not allow such simplifications as previously. For example, the increment $\Delta\lambda$ cannot be obtained in closed-form as in Eq. B.45 and it must be derived numerically by solving the equation $\sqrt{\frac{3}{2}\mathbf{S} : \mathbf{S}} - \sigma_y = 0$. Insertion of Eq. B.42 into the yield condition at the end of the increment (that is, when $\sigma_{eq} = \sigma_y$) gives:

$$\begin{aligned} 0 = &\left(\frac{27}{8\sigma_y^2} dev(\boldsymbol{\mathcal{C}} : \mathbf{S}) : dev(\boldsymbol{\mathcal{C}} : \mathbf{S}) \right) (\Delta\lambda)^2 \\ &- \left(\frac{9}{2\sigma_y} \mathbf{S}^t : dev(\boldsymbol{\mathcal{C}} : \mathbf{S}) \right) \Delta\lambda + \left(\sigma_{eq}^t \right)^2 - \sigma_y^2 \end{aligned} \tag{B.50}$$

which can be solved easily by a Newton-Raphson scheme in combination with Eq. B.40 to update the deviatoric stress $\mathbf{S}$ at each iteration. Once $\Delta\lambda$ and $\mathbf{S}$ have been updated, the consistent tangent moduli can be derived by using Eq. B.47:

$$\boldsymbol{\mathcal{C}}_{ep} = \boldsymbol{\mathcal{C}} \left(\boldsymbol{\mathcal{I}} - \mathbf{S} \otimes \frac{\boldsymbol{\mathcal{C}} : \mathbf{S}}{\mathbf{S} : \boldsymbol{\mathcal{C}} : \mathbf{S}} \right) \tag{B.51}$$

C

COMPUTATIONAL ASPECTS OF FE ANALYSES

Some remarks related to the computational aspects of the thesis are gathered in this Annex. Annex A provides with a deepened insight of computational strategies to integrate the equations of the constitutive model. This Annex focuses exclusively on issues related to the implementation of the models into a Finite Element package. In a first step, the accuracy of a small strain formulation is assessed by comparison with the outputs of a finite strain framework. Secondly, the efficiency of parallelization is evaluated. Finally, the effect of element type on the solution is studied.

C.1 SMALL VS. FINITE STRAINS KINEMATICS

We consider in this Section the finite element model of tensile specimen as used in Chapter 10. The elastic bounding blocks are not included. The mesh is dense enough to guarantee converged results. The extended AH constitutive model is chosen for the purpose of simplicity.

The initial Euler angles are set so that the sample is loaded in the $[\bar{1}\bar{2}3]$ direction. A constant velocity is applied to one sample end while the other is kept fixed, so that the resolved shear strain rate acting on the primary slip plane is $10^{-4}\,s^{-1}$. Simulations are run during 400 s, up to a tensile strain $\varepsilon \simeq 2$ %.

Time and force are converted into strain and stress using Eqs. 10.1 and 10.2, respectively. Fig. C.1 shows that the final stress differs by 6 % at a shear strain of 4 %, which is more than acceptable. The Von Mises stress and maximum principal strain distributions through the specimen at the end of the simulation are also extremely similar, as shown in Figs. C.2 and C.3, respectively.

This shows that adopting a small strains approximation does not lead to significant errors at the strains considered in the applications of the constitutive model. A computational time gain of 12.5 % has been obtained by shifting to the lighter, less calculation intensive small strains framework.

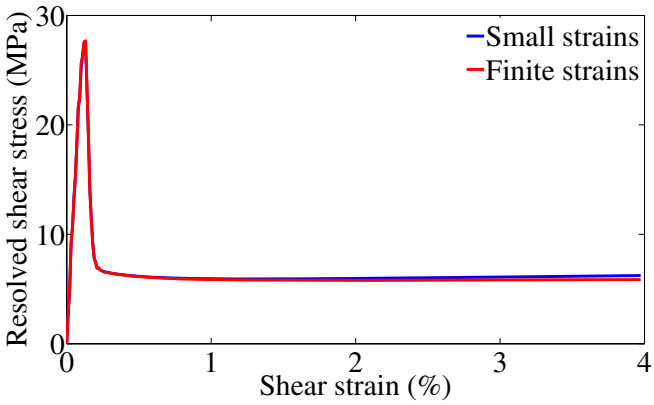

Figure C.1: Comparison of the stress-strain curves obtained using finite strains or a small strains approximation.

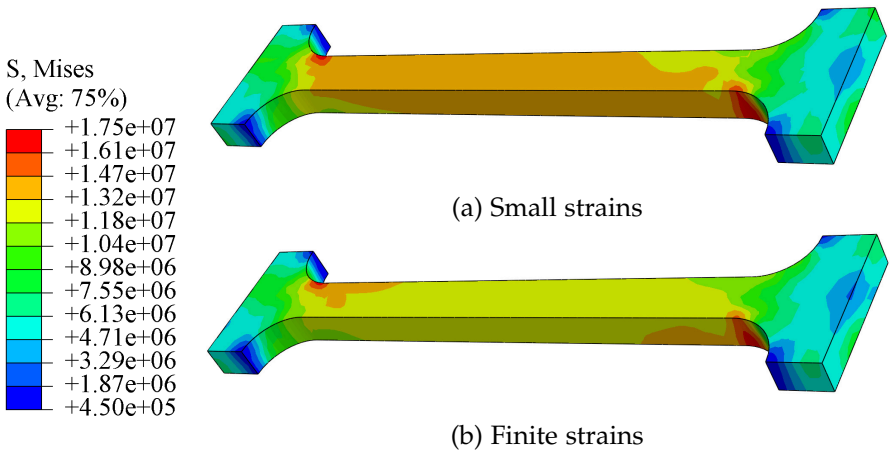

Figure C.2: Comparison of the Von Mises stress field at $t = 400\,\mathrm{s}$ using a small strains approximation or finite strains. The apparently different stress state in the gauge section is due to the scale discretization.

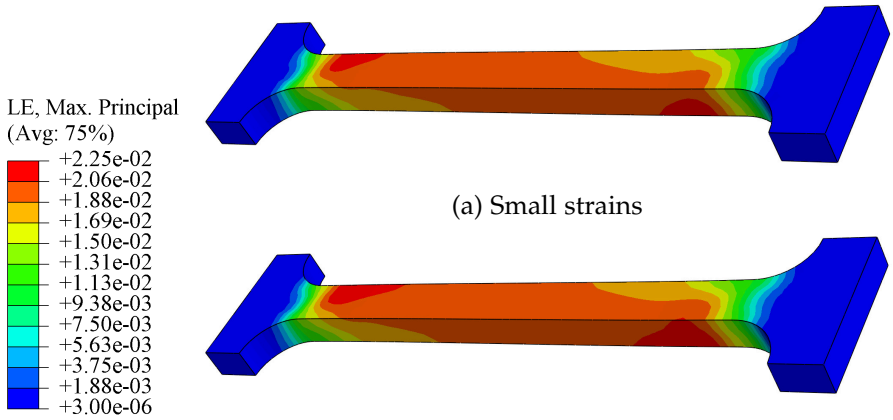

(a) Small strains

(b) Finite strains

Figure C.3: Comparison of the strain field at $t = 400\,\mathrm{s}$ using a small strains approximation or finite strains.

C.2 PARALLELIZATION GAINS

The benefits from parallel computation are investigated in this Section. The FE model considered here is similar to the previous one. Both finite and small strains are considered. The baseline is defined as the time necessary to complete a simulation with finite strains kinematics on one CPU. Fig. C.4 is obtained. Given the model size, parallelization yields significant computational time gains. Note that this would not be the case with smaller FE models, where a saturation of the simulation time is observed.

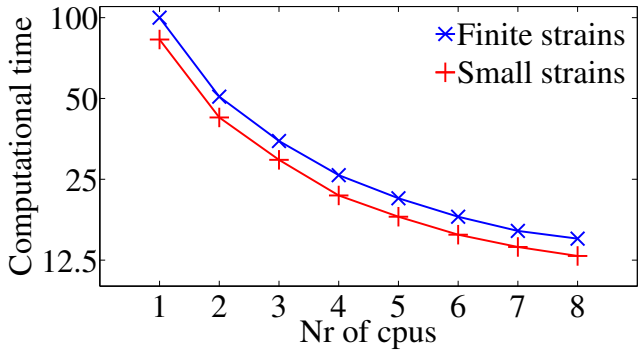

Figure C.4: Computation time using the parallelization possibilities offered by ABAQUS/EXPLICIT. Index 100: time for solving the finite strains problem with one cpu.

C.3 ELEMENT TYPE

Objective and strategy

The effect of element type on the simulation outputs is studied in this Section. ABAQUS/EXPLICIT proposes a limited amount of element types for analysis of 3-dimensional problems. We assess here the ability of the elements C3D8, C3D8R, C3D4and C3D10M to simulate a uniaxial tensile test of a silicon monocrystal oriented for single glide. The specimen geometry is a cube of 1 mm side length. A constant velocity is applied at one of its ends so that $\dot{\varepsilon} = 10^{-4}\,\mathrm{s}^{-1}$, while the displacement degrees of freedom of the nodes on the opposite face are prohibited in all directions as shown in Fig. C.5.

For each element type the cube is meshed with only one element through each cube edge. The output from a converged mesh of $5 \times 5 \times 5$ C3D8R elements is also shown as a reference. The duration of simulations is 100 s, and the extended constitutive model of Alexander & Haasen derived in Chapter 6 is used in conjunction with a finite strains framework.

Results

As seen in Fig. C.6, C3D4 elements yield the poorest results. This could be expected as this element type generally requires a high mesh density in order to produce converged results. Using C3D10M elements gives very good results, being of second order and therefore correctly accounting for the displacement possibilities left at the free surfaces of the cube.

The force output is similar for the C3D8 and C3D8R elements. A shallow secondary yield point can be detected in the corresponding curves of Fig. C.6, due to the lack of displacement degrees of freedom on the specimen edges and faces. Such mesh-induced kinematic constraints are relieved by

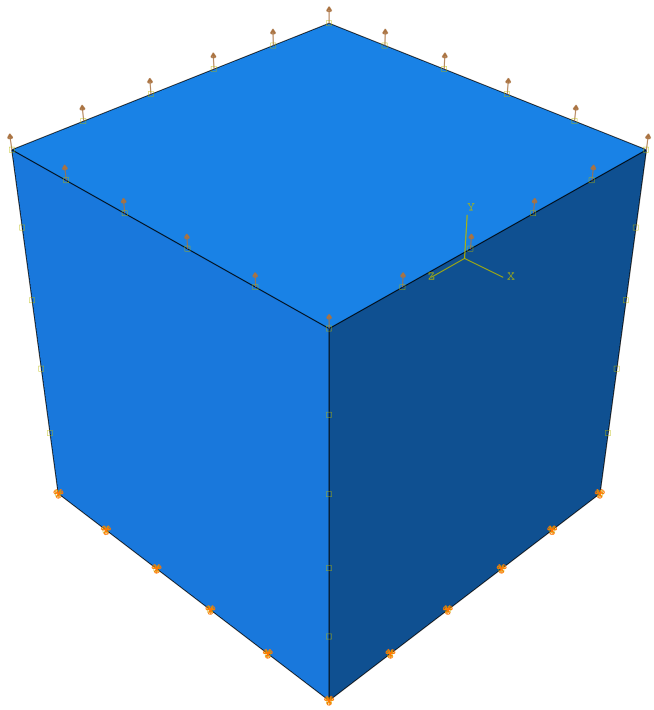

Figure C.5: Model used to study the effect of element types.

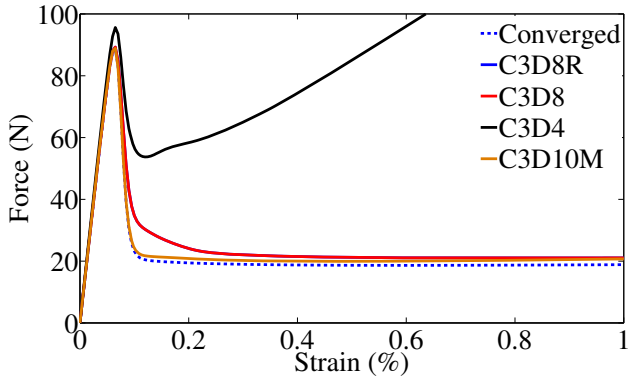

Figure C.6: Force output from a finite element model of a cube, using different element types.

the constitutive model through activation of secondary slip systems. This in turn generates additional dislocation density explosions and ultimately several upper yield points. Refining the C3D8R mesh indeed allows for one single slip system to accomodate for the applied deformation, and the correct force-time output is obtained.

The case of C3D8 elements

It is of high interest to consider the limitations induced by C3D8 elements. Such an element can be considered as equivalent to the aggregation of 8 C3D8R elements onto which additional kinematic constraints are added to neutralize the extra nodes. As seen previously, a severe drawback arising by restraining the degrees of freedom of a finite element model is the activation of additional slip systems in order for the additional constraints to be accomodated for.

Applying a purely uniaxial tension on a fully integrated, first-order element such as C3D8 does *not* yield the actual behavior of a monocrystal with free surfaces. Owing to the crystal plasticity-based constitutive model, this results in the spurious activation of slip systems. This problem of overstiffness is already widely known in the literature (see, e.g., [Liu 2003]), and has severe impacts when applied to nonlinear RDCP constitutive models.

An important consequence of this analysis is that *in the most general case, first-order fully integrated elements should not be used with a crystal plasticity framework*.

If brick elements are to be used to mesh a geometrical model, then only reduced integration can yield reliable results. This in turn may lead to element distortion by activation of hourglassing modes. Alternatively, C3D10M elements might provide with accurate solution, albeit at the price of a higher computational cost, each element having three Gauss points at which the constitutive equations must be solved.

D

EXPERIMENTAL DATA

This Annex gathers experimental data obtained on solar-grade silicon multicrystals during this PhD work, both at room temperature for flexural strength determination and at high temperature. All experiments performed are four-point bending tests.

D.1 ROOM TEMPERATURE EXPERIMENTS

Details about the experimental setup, analysis methods and results processing are given in Chapter 11. For confidentiality reasons, only results relative to the material provided by SINTEF are introduced below. 4PB tests yield two results: a Young's modulus can be extracted from the force-displacement data, and the maximum force reached before fracture gives an indication of the flexural strength of the sample.

Young's moduli

The Young's modulus of a sample does not depend on its surface state, but for readability the results of sets 1 and 2 are separated and shown in Table D.1 and D.2 respectively.

A histogram can be plotted given these data, and shows that the distribution of Young's moduli is not totally random but follows roughly a normal law. For more details, refer to Chapter 11.

Sample nr.	E	Sampl nr.	E (GPa)
S128	180	S145	157
S129	175	S146	164
S130	175	S147	161
S131	172	S149	162
S132	175	S150	173
S133	171	S151	171
S134	178	S152	170
S135	183	S153	168
S136	172	S154	169
S137	158	S155	168
S138	162	S156	167
S139	164	S157	166
S140	157	S158	167
S143	157	S159	166
S144	160	S160	165

Table D.1: Young's modulus of mc-Si bars from SINTEF material, set 1.

Sample nr.	E	Sampl nr.	E (GPa)
S161	159	S179	153
S162	171	S180	158
S163	173	S181	164
S164	179	S182	169
S165	167	S183	158
S168	170	S184	159
S169	164	S188	160
S170	168	S189	163
S172	173	S190	150
S173	174	S193	156
S174	169	S195	162
S175	151	S196	162
S176	152	S197	173
S177	169	S198	161
S178	152	S200	166

Table D.2: Young's modulus of mc-Si bars from SINTEF material, set 2.

D.2 HIGH TEMPERATURE EXPERIMENTS

Preliminary discussion

The goal of high temperature experiments (above 1073 K) is to assess whether the mechanical behavior of SoG-Si multicrystals resembles the one of monocrystals. Several factors make this assessment difficult, and the restricted amount of results presented in the following only reflects the consequences of the remarks below.

- A first issue is the grain size, large with respect to the standard sample dimensions imposed by the testing apparatus. Ideally, one would like to have as many grains as possible in the cross-section, so that the observed behavior (force-displacement record) results from the averaging of each individual response of the grains to the mechanical load. However, the experimental setup sets a limit on the size of samples that can be tested, with an inner span of 20 mm only. This brings the maximum number of grains in the longitudinal direction between the inner rods down to a dozen.

- Another factor to remember is that the particular loading created by the 4PB apparatus sollicitates the sample along one direction only. Consequently, any anisotropy introduced during ingot crystallization cannot be observed since all samples have been cut along the same orientation.

- More than that, the very crystallographic topography and properties of the samples are unknown: grain size, orientation, shape, initial dislocation density, chemical composition, etc.

- The most severe drawback encountered comes from the maximum allowed heating rate, 200 K per hour. Such a limit is set by the mechanical properties of the oven components. This means that heating up from room temperature to the target one takes several hours, during which many annealing and diffusion processes can take place without giving the operator any control over them.

  Dislocation annihilation and stress relief in the material are to be expected, as well as diffusion of locking impurities such as nitrogen and oxygen. It is consequently not surprising to observe mechanical behaviors similar to those of monocrystals. The validity of the results is consequently extremely limited.

- Finally, security purposes require the operator to be present in the lab during all the heating step[1].

The results presented in this Section have not been used for model calibration for the reasons exposed above: too much uncertainty on the

1 This is obviously a personal observation that does not influence the validity of the results but rather weights significantly in the decision to perform more tests.

Sample nr.	T (K)	$\dot{\varepsilon}$ (s^{-1})
E77	1073	10^{-6}
E78	1073	10^{-6}
E76	1073	5×10^{-6}
E75	1073	5×10^{-6}
E73	1073	10^{-5}
E74	1073	10^{-5}
E80	1173	5×10^{-6}
E79	1173	10^{-5}
E40	1173	10^{-5}

Table D.3: High-temperature testing conditions.

thermodynamical state of the samples when loading starts, unknown grain size and orientation, etc. Note that a dozen of samples have been analyzed by EBSD and PVscan for future test and modeling.

D.2.1 *Sample preparation and experimental conditions*

The mc-Si bars have been cut following the ASTM standard C1211-98a [ASTM a]. The samples E79 and E80 have been polished and etched on the tensile side, following the same procedure as room-temperature samples of set 2 (see Chapter 11).

The factors above-mentioned limit severly the amount of samples tested. Only two temperatures (1073 and 1173 K) and a limited range of strain rates (from 10^{-6} to $10^{-5}\,s^{-1}$) are explored. The latter are calculated assuming the samples to be isotropic homogeneous materials. Following [ASTM a], the strain rate is given by:

$$\dot{\varepsilon} = \frac{6ts}{L^2} \tag{D.1}$$

where t is the specimen thickness, s the cross-head speed and L the outer span. Knowing t, L and the target strain rate, s can be calculated and applied to the specimen.

Temperature is monitored continuously by thermocouples at two positions in the oven, close to the sample and outside the 4PB apparatus. The temperature is kept accurate during the experiments within less than 1 K. All experiments are performed in an argon atmosphere after the chamber is flushed and filled with argon four to five times. The heating rate is set to 200 K per hour. Table D.3 gives the details of the experimental conditions considered[2].

2 Sample E78 has been tested but the data has been subsequently lost due to a manipulation error.

Sample nr.	T (K)	E (GPa)
E77	1073	138
E78	1073	-
E76	1073	146
E75	1073	146
E73	1073	152
E74	1073	162
E80	1173	117
E79	1173	114
E40	1173	119

Table D.4: Young's modulus of samples tested at high temperatures.

D.2.2 *Results*

The force-deflection records are converted into stress-strain results assuming small deformations and isotropic homogeneous materials. The total elastic strain can be obtained by dividing Eq. 11.6 by Eq. 11.5 and identifying the elastic strain ε_e as $\sigma = E\varepsilon_e$:

$$\varepsilon_e = \frac{16td}{L} \tag{D.2}$$

The samples are deformed either up to fracture or when the tensile apparatus reaches its maximum allowed load cell displacement. The results obtained at 1173 K are not presented.

Young's modulus

The Young's modulus of each sample can be computed as well, using the same method as described in Chapter 11. Table D.4 shows the calculated values. As expected, the Young moduls decreases with temperature.

Stress-strain curves

Figure D.1 shows the results measured at 1073 K. As mentioned earlier, the mechanical behavior of the samples likens the one of monocrystals: an upper yield point is followed by a sharp yield drop, and a quasi-linear hardening rate sets in beyond the lower yield point.

Some points are worth mentioning:

- Strain rate has the same effect on the yield region of multicrystals than it has on single crystals, by increasing the upper yield stress. However, the lower yield stress evolution is not strictly enforced for SoG-Si, as impurities likely influence its magnitude.
- Reproducability is not guaranteed, especially when it comes to the lower yield stress and flow stress. Of particular interest are the two

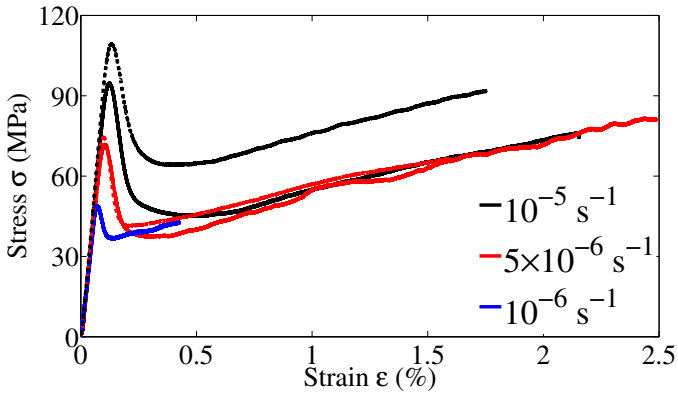

Figure D.1: Experimental results obtained by 4PB deformation of SoG-Si multicrystals produced by Elkem Solar. Temperature 1073 K.

curves obtained at $10^{-5}\,s^{-1}$. Impurities and different grain orientations could be reasons for the discrepancy.

- On the other hand, the samples deformed at $5 \times 10^{-6}\,s^{-1}$ exhibit the same behavior in the yield region, but stage I is affected for one specimen by what could be identified as diffusion of impurities to the dislocations, resulting in a wavy force response.

The specimen deformed at 1173 K follow the same pattern, and exhibit lower yield stresses than those deformed at 1073 K, as could be expected.

D.2.3 *Discussion*

Overall, these few experiments allow to draw only qualitative conclusions: the average response of small SoG-si multicrystalline aggregates is like the one of monocrystals when it comes to the existence of a yield region and the influence of thermodynamic conditions on the yield points. The hardening rate beyond the lower yield points is always low, suggesting that the majority of the stressed volume deforms in single glide[3].

In addition to the initial dislocation density, impurity type and concentration that vary both between and within samples, grain misorientation limit the reproducability of the stress-strain curves at given temperature and strain rate.

It is in the meantime very tricky, to draw quantitative conclusions based on these experimental data. No sample is like another both because of their constituent crystals which vary in size, shape and orientation, and because their respective thermomechanical histories have led to different dislocation

3 This remark does not rule out *local* deformation in multiple slip, particularly close to the grain boundaries. Sample fracture observed at very low strains and stresses is most likely due to local stress concentrators that do not have any effect in the global force records.

density and impurity distributions. This last remark is strengthened by the fact that our experimental apparatus restrics severly the heating rate; annealing and diffusional effects cannot be ruled out and make any parameter identification almost impossible.

Additional tests have been performed during the completion of this thesis by a private company. The specimen were then much larger and tested in a much wider temperature and strain rate range. The same conclusions as derived in this Section hold.

BIBLIOGRAPHY

[Asaro 1983] *Crystal plasticity*, R.J. Asaro, Journal of Applied Mechanics, Vol. 50, No. 4b, pp. 921-934, 1983

[Barbe 2001a] *Intergranular and intragranular behavior of polycrystalline aggregates. Part 1: F.E. model*, F. Barbe, L. Decker, D. Jeulin, G. Cailletaud, International Journal of Plasticity, Vol. 17, pp. 513-536, 2001

[Barbe 2001b] *Intergranular and intragranular behavior of polycrystalline aggregates. Part 2: Results*, F. Barbe, S. Forest, G. Cailletaud, International Journal of Plasticity, Vol. 17, pp. 537-563, 2001

[Bassani 1991] *Latent hardening in single crystals. II. Analytical characterization and predictions*, J.L. Bassani, T.-Y. Wu, Proceedings of the Royal Society of London A, Vol. 435, pp. 21-41, 1991

[Bishop 1951] *A theoretical derivation of the plastic properties of a polycrytalline face-centered metal*, J.F.W. Bishop, R. Hill, Philosophical Magazine, Vol. 42, pp. 1298-1307, 1951

[Bronkhorst 1992] *Polycrystalline plasticity and the evolution of crystallographic texture in FCC crystals*, C.A. Bronkhorst, S.R. Kalidindi, L. Anand, Philosophical Transactions of the Royal Society of London A, Vol. 341, pp. 443-477, 1992

[Cacho 2007] *A constitutive single-crystal model for the silicon mechanical behaviour: applications to the stress induced by silicided lines and STI in MOS technologies*, F. Cacho, S. Orain, G. Cailletaud, H. Jaouen, Microelectronics Reliability, Vol. 47, pp. 161-167, 2007

[Cochard 2008] *A multicrystal model for the viscoplastic deformation of silicon at high temperature*, J. Cochard, S. Gouttebroze, S. Dumoulin, M. M'Hamdi, Z.L. Zhang, Proceedings of the 23rd European Photovoltaic Solar Energy Conference (EUPVSEC), Valencia, Spain, 2008

[Diard 2005] *Evaluation of finite element based analysis of 3D crystalline aggregates plasticity. Application to crystal plasticity model identification and the study of stress and strain fields near grain boundaries*, O. Diard, S. Leclercq, G. Rousselier, G. Cailletaud, International Journal of Plasticity, Vol. 21, pp. 691-722, 2005

[Dillon 1986] *Dislocation dynamics during the growth of silicon ribbon*, O.W. Dillon, C.T. Tsai, R.J. De Angelis, Journal of Applied Physics, Vol. 60, No. 5, pp. 1784-1792, 1986

[Dormand 1980] *A family of embedded Runge-Kutta formulae*, J.R. Dormand, P.J. Prince, Journal of Computational and Applied Mathematics, Vol. 6, No. 1, pp. 19-26, 1980

[Fellin 2002] *Consistent tangent operators for constitutive rate equations*, W. Fellin, A. Ostermann, International Journal for Numerical and Analytical Methods in Geomechanics, Vol. 26, pp. 1213-1233, 2002

[Franciosi 1982] *Multislip in FCC crystals: a theoretical approach compared to experimental data*, P. Franciosi, A. Zaoui, Acta Metallurgica, Vol. 30, pp. 1627-1637, 1982

[Harder 1999] *A crystallographic model for the study of local deformation processes in polycrystals*, J. Harder, International Journal of Plasticity, Vol. 15, pp. 605-624, 1999

[Hill 1966] *Generalized constitutive relations for incremental deformation of metal crystals by multislip*, R. Hill, Journal of the Mechanics and Physics of Solids, Vol. 14, No. 2, pp. 95-102, 1966

[Hutchinson 1976] *Bounds and self-consistent estimates for creep of polycrystalline materials*, J.W. Hutchinson, Proceedings of the Royal Society of London A, Vol. 348, pp. 101-127, 1976

[Kalidindi 1992] *Crystallographic texture evolution in bulk deformation processing of FCC crystals*, S.R. Kalidindi, C.A. Bronkhorst, L. Anand, Journal of the Mechanics and Physics of Solids, Vol. 40, No. 3, pp. 537-569, 1992

[Kim 1987] *Dislocation motion and multiplication during the growth of silicon ribbon*, Y.K. Kim, R.J. De Angelis, C.T. Tsai, O.W. Dillon, Acta Metallurgica, Vol. 35, No. 8, pp. 2091-2099, 1987

[Kocks 1975] *Thermodynamics and kinetics of slip*, U.F. Kocks, A.S. Argon, M.F. Ashby, Progress in Materials Science, Vol. 19, 1975

[Kocks 1998] *Texture and anisotropy*, U.F. Kocks, C.N. Tomé, H.-R. Wenk (Eds.), Cambridge University Press, 1998

[Lee 1969] *Elastic-plastic deformation at finite strains*, E.H. Lee, Journal of Applied Mechanics, Vol. 36, No. 1, pp. 1-6, 1969

[Liu 2003] *The finite element method - a practical course*, G.R. Liu, S.S. Quek, Butterworth-Heinemann, Elsevier, 2003

[Mandel 1965] *Généralisation de la théorie de plasticité de Koiter*, J. Mandel, International Journal of Solids and Structures, Vol. 1, pp. 273-295, 1965

[McHugh 1993] *Computational modeling of metal matrix composite materials - I. Isothermal deformation patterns in ideal microstructures*, P.E. McHugh, R.J. Asaro, C.F. Shih, Acta Metallurgica et Materialia, Vol. 41, No. 5, pp. 1461-1476, 1993

[Meissonnier 2001] *Finite element implementation of a generalised non-local rate-dependent crystallographic formulation for finite strains*, F.T. Meissonnier, E.P. Busso, N.P. O'Dowd, International Journal of Plasticity, Vol. 17, pp. 601-640, 2001

[Meric 1991] *Single crystal modeling for structural calculations: Part I - Model presentation*, L. Meric, P. Poubanne, G. Cailletaud, Journal of Engineering Materials and Technology, Vol. 113, pp. 162-170, 1991

[Moon 2002] *A constitutive model for the mechanical behavior of single crystal silicon at elevated temperatures*, H.-S. Moon, L. Anand, S.M. Spearing, Materials Science of MEMS Devices IV, Symposium proceedings, Vol. 687, pp. 279-284, 2002

[Myshlyaev 1969] *Dislocation structure and macroscopic characteristics of plastic deformation at creep of silicon crystals*, M.M. Myshlyaev, V.I. Nikitenko, V.I. Nesterenko, Phys. stat. sol. (a), Vol. 36, pp. 89-96, 1969

[Nemat-Nasser 2004] *Plasticity: a treatise on finite deformation of heterogeneous inelastic materials*, Sia Nemat-Nasser, Cambridge Monographs on Mechanics, pp. 440-501, 2004

[Peirce 1983] *Material rate dependence and localized deformation in crystalline solids*, D. Peirce, R.J. Asaro, A. Needleman, Acta Metallurgica, Vol. 31, No. 12, pp. 1951-1976, 1983

[Rice 1971] *Inelastic constitutive relations for solids: an internal-variable theory and its application to metal plasticity*, J.R. Rice, Journal of the Mechanics and Physics of Solids, Vol. 19, No. 6, pp. 433-455, 1971

[Taylor 1938] *Plastic strain in metals*, G.I. Taylor, Institute of Metals - Journal, Vol. 62, No. 1, pp. 307-324, 1938

[Wu 1991] *Latent hardening in single crystals. I. Theory and experiments*, T.-Y. Wu, J.L. Bassani, C. Laird, Proceedings of the Royal Society of London A, Vol. 435, pp. 1-19, 1991

[Yoshino 2001] *Finite element simulation of plane strain plastic-elastic indentation on single-crystal silicon*, M. Yoshino, T. Aoki, N. Chandrasekaran, T. Shirakashi, R. Komanduri, International Journal of Mechanical Sciences, Vol. 43, pp. 313-333, 2001

[Zarka 1972] *Généralisation de la théorie du potentiel plastique multiple en viscoplasticité*, P. Zarka, Journal of the Mechanics and Physics of Solids, Vol. 20, No. 3, pp. 179-195, 1972

[Zikry 1995] *Large-scale crystal plasticity computations of microstructural failure modes*, M.A. Zikry, M. Kao, Computing systems in Engineering, Vol. 6, No. 3, pp. 225-240, 1995

[Zikry 1996] *Dislocation based multiple slip crystalline constitutive formulation for finite-strain plasticity*, M.A. Zikry, M. Kao, Scripta Materialia, Vol. 34, No. 7, pp. 1115-1121, 1996

LIST OF PUBLICATIONS AT THE DEPARTMENT OF STRUCTURAL ENGINEERING

Reliability Analysis of Structural Systems using Nonlinear Finite Element Methods, C. A. Holm, 1990:23, ISBN 82-7119-178-0

Uniform Stratified Flow Interaction with a Submerged Horizontal Cylinder, Ø. Arntsen, 1990:32, ISBN 82-7119-188-8

Large Displacement Analysis of Flexible and Rigid Systems Considering Displacement-Dependent Loads and Nonlinear Constraints, K. M. Mathisen, 1990:33, ISBN 82-7119-189-6

Solid Mechanics and Material Models including Large Deformations, E. Levold, 1990:56, ISBN 82-7119-214-0, ISSN 0802-3271

Inelastic Deformation Capacity of Flexurally-Loaded Aluminium Alloy Structures, T. Welo, 1990:62, ISBN 82-7119-220-5, ISSN 0802-3271

Visualization of Results from Mechanical Engineering Analysis, K. Aamnes, 1990:63, ISBN 82-7119-221-3, ISSN 0802-3271

Object-Oriented Product Modeling for Structural Design, S. I. Dale, 1991:6, ISBN 82-7119-258-2, ISSN 0802-3271

Parallel Techniques for Solving Finite Element Problems on Transputer Networks, T. H. Hansen, 1991:19, ISBN 82-7119-273-6, ISSN 0802-3271

Statistical Description and Estimation of Ocean Drift Ice Environments, R. Korsnes, 1991:24, ISBN 82-7119-278-7, ISSN 0802-3271

Properties of concrete related to fatigue damage: with emphasis on high strength concrete, G. Petkovic, 1991:35, ISBN 82-7119-290-6, ISSN 0802-3271

Turbidity Current Modelling, B. Brørs, 1991:38, ISBN 82-7119-293-0, ISSN 0802-3271

Zero-Slump Concrete: Rheology, Degree of Compaction and Strength. Effects of Fillers as Part Cement-Replacement, C. Sørensen, 1992:8, ISBN 82-7119-357-0, ISSN 0802-3271

Nonlinear Analysis of Reinforced Concrete Structures Exposed to Transient Loading, K. V. Høiseth, 1992:15, ISBN 82-7119-364-3, ISSN 0802-3271

Finite Element Formulations and Solution Algorithms for Buckling and Collapse Analysis of Thin Shells, R. O. Bjærum, 1992:30, ISBN 82-7119-380-5, ISSN 0802-3271

Response Statistics of Nonlinear Dynamic Systems, J. M. Johnsen, 1992:42, ISBN 82-7119-393-7, ISSN 0802-3271

Digital Models in Engineering. A Study on why and how engineers build and operate digital models for decisison support, J. Høyte, 1992:75, ISBN 82-7119-429-1, ISSN 0802-3271

Sparse Solution of Finite Element Equations, A. C. Damhaug, 1992:76, ISBN 82-7119-430-5, ISSN 0802-3271

Some Aspects of Floating Ice Related to Sea Surface Operations in the Barents Sea, S. Løset, 1992:95, ISBN 82-7119-452-6, ISSN 0802-3271

Modelling of Cyclic Plasticity with Application to Steel and Aluminium Structures, O. S. Hopperstad, 1993:7, ISBN 82-7119-461-5, ISSN 0802-3271

The Free Formulation: Linear Theory and Extensions with Applications to Tetrahedral Elements with Rotational Freedoms, G. Skeie, 1993:17, ISBN 82-7119-472-0, ISSN 0802-3271

Høyfast betongs motstand mot piggdekkslitasje. Analyse av resultater fra prøving i Veisliter'n, T. Tveter, 1993:62, ISBN 82-7119-522-0, ISSN 0802-3271

A Nonlinear Finite Element Based on Free Formulation Theory for Analysis of Sandwich Structures, O. Aamlid, 1993:72, ISBN 82-7119-534-4, ISSN 0802-3271

The Effect of Curing Temperature and Silica Fume on Chloride Migration and Pore Structure of High Strength Concrete, C. J. Hauck, 1993:90, ISBN 82-7119-553-0, ISSN 0802-3271

Failure of Concrete under Compressive Strain Gradients, G. Markeset, 1993:110, ISBN 82-7119-575-1, ISSN 0802-3271

An experimental study of internal tidal amphidromes in Vestfjorden, J. H. Nilsen, 1994:39, ISBN 82-7119-640-5, ISSN 0802-3271

Structural analysis of oil wells with emphasis on conductor design, H. Larsen, 1994:46, ISBN 82-7119-648-0, ISSN 0802-3271

Adaptive methods for non-linear finite element analysis of shell structures, K. M. Okstad, 1994:66, ISBN 82-7119-670-7, ISSN 0802-3271

On constitutive modelling in nonlinear analysis of concrete structures, O. Fyrileiv, 1994:115, ISBN 82-7119-725-8, ISSN 0802-3271

Fluctuating wind load and response of a line-like engineering structure with emphasis on motion-induced wind forces, J. Bogunovic Jakobsen, 1995:62, ISBN 82-7119-809-2, ISSN 0802-3271

An experimental study of beam-columns subjected to combined torsion, bending and axial actions, A. Aalberg, 1995:66, ISBN 82-7119-813-0, ISSN 0802-3271

Scaling and cracking in unsealed freeze/thaw testing of Portland cement and silica fume concretes, S. Jacobsen, 1995:101, ISBN 82-7119-851-3, ISSN 0802-3271

Damping of water waves by submerged vegetation. A case study of laminaria hyperborea, A. M. Dubi, 1995:108, ISBN 82-7119-859-9, ISSN 0802-3271

The dynamics of a slope current in the Barents Sea, Sheng Li, 1995:109, ISBN 82-7119-860-2, ISSN 0802-3271

Modellering av delmaterialenes betydning for betongens konsistens, Ernst Mørtsell, 1996:12, ISBN 82-7119-894-7, ISSN 0802-3271

Bending of thin-walled aluminium extrusions, Birgit Søvik Opheim, 1996:60, ISBN 82-7119-947-1, ISSN 0802-3271

Material modelling of aluminium for crashworthiness analysis, Torodd Berstad, 1996:89, ISBN 82-7119-980-3, ISSN 0802-3271

Estimation of structural parameters from response measurements on submerged floating tunnels, Rolf Magne Larssen, 1996:119, ISBN 82-471-0014-2, ISSN 0802-3271

Numerical modelling of plain and reinforced concrete by damage mechanics, Mario A. Polanco-Loria, 1997:20, ISBN 82-471-0049-5, ISSN 0802-3271

Nonlinear random vibrations - numerical analysis by path integration methods, Vibeke Moe, 1997:26, ISBN 82-471-0056-8, ISSN 0802-3271

Numerical prediction of vortex-induced vibration by the finite element method, Joar Martin Dalheim, 1997:63, ISBN 82-471-0096-7, ISSN 0802-3271

Time domain calculations of buffeting response for wind sensitive structures, Ketil Aas-Jakobsen, 1997:148, ISBN 82-471-0189-0, ISSN 0802-3271

A numerical study of flow about fixed and flexibly mounted circular cylinders, Trond Stokka Meling, 1998:48, ISBN 82-471-0244-7, ISSN 0802-3271

Estimation of chloride penetration into concrete bridges in coastal areas, PER EGIL STEEN, 1998:89, ISBN 82-471-0290-0, ISSN 0802-3271

Stress-resultant material models for reinforced concrete plates and shells, JAN ARVE ØVERLI, 1998:95, ISBN 82-471-0297-8, ISSN 0802-3271

Chloride binding in concrete. Effect of surrounding environment and concrete composition, CLAUS KENNETH LARSEN, 1998:101, ISBN 82-471-0337-0, ISSN 0802-3271

Rotational capacity of aluminium alloy beams, LARS A. MOEN, 1999:1, ISBN 82-471-0365-6, ISSN 0802-3271

Stretch Bending of Aluminium Extrusions, ARILD H. CLAUSEN, 1999:29, ISBN 82-471-0396-6, ISSN 0802-3271

Aluminium and Steel Beams under Concentrated Loading, TORE TRYLAND, 1999:30, ISBN 82-471-0397-4, ISSN 0802-3271

Engineering Models of Elastoplasticity and Fracture for Aluminium Alloys, ODD-GEIR LADEMO, 1999:39, ISBN 82-471-0406-7, ISSN 0802-3271

Kapasitet og duktilitet av dybelforbindelser i trekonstruksjoner, JAN SIEM, 1999:46, ISBN 82-471-0414-8, ISSN 0802-3271

Etablering av distribuert ingeniørarbeid; Teknologiske og organisatoriske erfaringer fra en norsk ingeniørbedrift, LARS LINE, 1999:52, ISBN 82-471-0420-2, ISSN 0802-3271

Estimation of Earthquake-Induced Response, SÍMON ÓLAFSSON, 1999:73, ISBN 82-471-0443-1, ISSN 0802-3271

Coastal Concrete Bridges: Moisture State, Chloride Permeability and Aging Effects, RAGNHILD HOLEN RELLING, 1999:74, ISBN 82-471-0445-8, ISSN 0802-3271

Capacity Assessment of Titanium Pipes Subjected to Bending and External Pressure, ARVE BJØRSET, 1999:100, ISBN 82-471-0473-3, ISSN 0802-3271

Validation of Numerical Collapse Behaviour of Thin-Walled Corrugated Panels, HÅVAR ILSTAD, 1999:101, ISBN 82-471-0474-1, ISSN 0802-3271

Strength and Ductility of Welded Structures in Aluminium Alloys, MIROSLAW MATUSIAK, 1999:113, ISBN 82-471-0487-3, ISSN 0802-3271

Thermal Dilation and Autogenous Deformation as Driving Forces to Self-Induced Stresses in High Performance Concrete, ØYVIND BJØNTEGAARD, 1999:121, ISBN 82-7984-002-8, ISSN 0802-3271

Some Aspects of Ski Base Sliding Friction and Ski Base Structure, DAG ANDERS MOLDESTAD, 1999:137, ISBN 82-7984-019-2, ISSN 0802-3271

Electrode reactions and corrosion resistance for steel in mortar and concrete, ROY ANTONSEN, 2000:10, ISBN 82-7984-030-3, ISSN 0802-3271

Hydro-Physical Conditions in Kelp Forests and the Effect on Wave Damping and Dune Erosion. A case study on Laminaria Hyperborea, STIG MAGNAR LØVÅS, 2000:28, ISBN 82-7984-050-8, ISSN 0802-3271

Random Vibration and the Path Integral Method, CHRISTIAN SKAUG, 2000:39, ISBN 82-7984-061-3, ISSN 0802-3271

Buckling and geometrical nonlinear beam-type analyses of timber structures, TROND EVEN EGGEN, 2000:56, ISBN 82-7984-081-8, ISSN 0802-3271

Structural Crashworthiness of Aluminium Foam-Based Components, ARVE GRØNSUND HANSSEN, 2000:76, ISBN 82-7984-102-4, ISSN 0809-103X

Measurements and simulations of the consolidation in first-year sea ice ridges, and some aspects of mechanical behaviour, KNUT V. HØYLAND, 2000:94, ISBN 82-7984-121-0, ISSN 0809-103X

Kinematics in Regular and Irregular Waves based on a Lagrangian Formulation, SVEIN HELGE GJØSUND, 2000-86, ISBN 82-7984-112-1, ISSN 0809-103X

Self-Induced Cracking Problems in Hardening Concrete Structures, DANIELA BOSNJAK, 2000-121, ISBN 82-7984-151-2, ISSN 0809-103X

Ballistic Penetration and Perforation of Steel Plates, TORE BØRVIK, 2000:124, ISBN 82-7984-154-7, ISSN 0809-103X

Freeze-Thaw resistance of Concrete. Effect of: Curing Conditions, Moisture Exchange and Materials, TERJE FINNERUP RØNNING, 2001:14, ISBN 82-7984-165-2, ISSN 0809-103X

Structural behaviour of post tensioned concrete structures. Flat slab. Slabs on ground, STEINAR TRYGSTAD, 2001:52, ISBN 82-471-5314-9, ISSN 0809-103X

Slipforming of Vertical Concrete Structures. Friction between concrete and slipform panel, KJELL TORE FOSSÅ, 2001:61, ISBN 82-471-5325-4, ISSN 0809-103X

Some numerical methods for the simulation of laminar and turbulent incompressible flows, JENS HOLMEN, 2002:6, ISBN 82-471-5396-3, ISSN 0809-103X

Improved Fatigue Performance of Threaded Drillstring Connections by Cold Rolling, STEINAR KRISTOFFERSEN, 2002:11, ISBN: 82-421-5402-1, ISSN 0809-103X

Deformations in Concrete Cantilever Bridges: Observations and Theoretical Modelling, Peter F. Takâcs, 2002:23, ISBN 82-471-5415-3, ISSN 0809-103X

Stiffened aluminium plates subjected to impact loading, Hilde Giæver Hildrum, 2002:69, ISBN 82-471-5467-6, ISSN 0809-103X

Full- and model scale study of wind effects on a medium-rise building in a built up area, Jónas Thór Snæbjørnsson, 2002:95, ISBN82-471-5495-1, ISSN 0809-103X

Evaluation of Concepts for Loading of Hydrocarbons in Ice-infested water, Arnor Jensen, 2002:114, ISBN 82-417-5506-0, ISSN 0809-103X

Numerical and Physical Modelling of Oil Spreading in Broken Ice, Janne K. Økland Gjøsteen, 2002:130, ISBN 82-471-5523-0, ISSN 0809-103X

Diagnosis and protection of corroding steel in concrete, Franz Pruckner, 20002:140, ISBN 82-471-5555-4, ISSN 0809-103X

Tensile and Compressive Creep of Young Concrete: Testing and Modelling, Dawood Atrushi, 2003:17, ISBN 82-471-5565-6, ISSN 0809-103X

Rheology of Particle Suspensions. Fresh Concrete, Mortar and Cement Paste with Various Types of Lignosulfonates, Jon Elvar Wallevik, 2003:18, ISBN 82-471-5566-4, ISSN 0809-103X

Oblique Loading of Aluminium Crash Components, Aase Reyes, 2003:15, ISBN 82-471-5562-1, ISSN 0809-103X

Utilization of Ethiopian Natural Pozzolans, Surafel Ketema Desta, 2003:26, ISSN 82-471-5574-5, ISSN:0809-103X

Behaviour and strength prediction of reinforced concrete structures with discontinuity regions, Helge Brå, 2004:11, ISBN 82-471-6222-9, ISSN 1503-8181

High-strength steel plates subjected to projectile impact. An experimental and numerical study, Sumita Dey, 2004:38, ISBN 82-471-6282-2 (printed version), ISBN 82-471-6281-4 (electronic version), ISSN 1503-8181

Alkali-reactive and inert fillers in concrete. Rheology of fresh mixtures and expansive reactions, Bård M. Pedersen, 2004:92, ISBN 82-471-6401-9 (printed version), ISBN 82-471-6400-0 (electronic version), ISSN 1503-8181

On the Shear Capacity of Steel Girders with Large Web Openings, Nils Christian Hagen, 2005:9 ISBN 82-471-6878-2 (printed version), ISBN 82-471-6877-4 (electronic version), ISSN 1503-8181

Behaviour of aluminium extrusions subjected to axial loading, Østen Jensen, 2005:7, ISBN 82-471-6873-1 (printed version), ISBN 82-471-6872-3 (electronic version), ISSN 1503-8181

Thermal Aspects of corrosion of Steel in Concrete, Jan-Magnus Østvik, 2005:5, ISBN 82-471-6869-3 (printed version), ISBN 82-471-6868 (electronic version), ISSN 1503-8181

Mechanical and adaptive behaviour of bone in relation to hip replacement. A study of bone remodelling and bone grafting, Sébastien Muller, 2005:34, ISBN 82-471-6933-9 (printed version), ISBN 82-471-6932-0 (electronic version), ISSN 1503-8181

Analysis of geometrical nonlinearities with applications to timber structures, Lars Wollebæk, 2005:74, ISBN 82-471-7050-5 (printed version), ISBN 82-471-7019-1 (electronic version), ISSN 1503-8181

Pedestrian induced lateral vibrations of slender footbridges, Anders Rönnquist, 2005:102, ISBN 82-471-7082-5 (printed version), ISBN 82-471-7081-7 (electronic version), ISSN 1503-8181

Initial Strength Development of Fly Ash and Limestone Blended Cements at Various Temperatures Predicted by Ultrasonic Pulse Velocity, Tom Ivar Fredvik, 2005:112, ISBN 82-471-7105-8 (printed version), ISBN 82-471-7103-1 (electronic version), ISSN 1503-8181

Behaviour and modelling of thin-walled cast components, Cato Dørum, 2005:128, ISBN 82-471-7140-6 (printed version), ISBN 82-471-7139-2 (electronic version), ISSN 1503-8181

Behaviour and modelling of selfpiercing riveted connections, Raffaele Porcaro, 2005:165, ISBN 82-471-7219-4 (printed version), ISBN 82-471-7218-6 (electronic version), ISSN 1503-8181

Behaviour and Modelling og Aluminium Plates subjected to Compressive Load, Lars Rønning, 2005:154, ISBN 82-471-7169-1 (printed version), ISBN 82-471-7195-3 (electronic version), ISSN 1503-8181

Bumper beam-longitudinal system subjected to offset impact loading, Satyanarayana Kokkula, 2005:193, ISBN 82-471-7280-1 (printed version), ISBN 82-471-7279-8 (electronic version), ISSN 1503-8181

Control of Chloride Penetration into Concrete Structures at Early Age, Guofei Liu, 2006:46, ISBN 82-471-7838-9 (printed version), ISBN 82-471-7837-0 (electronic version), ISSN 1503-8181

Modelling of Welded Thin-Walled Aluminium Structures, Ting Wang, 2006:78, ISBN 82-471-7907-5 (printed version), ISBN 82-471-7906-7 (electronic version), ISSN 1503-8181

Time-variant reliability of dynamic systems by importance sampling and probabilistic analysis of ice loads, Anna Ivanova Olsen, 2006:139, ISBN 82-471-8041-3 (printed version), ISBN 82-471-8040-5 (electronic version), ISSN 1503-8181

Fatigue life prediction of an aluminium alloy automotive component using finite element analysis of surface topography, Sigmund Kyrre Ås, 2006:25, ISBN 82-471-7791-9 (printed version), ISBN 82-471-7791-9 (electronic version), ISSN 1503-8181

Constitutive models of elastoplasticity and fracture for aluminium alloys under strain path change, Dasharatha Achani, 2006:76, ISBN 82-471-7903-2 (printed version), ISBN 82-471-7902-4 (electronic version), ISSN 1503-8181

Simulations of 2D dynamic brittle fracture by the Element-free Galerkin method and linear fracture mechanics, Tommy Karlsson, 2006:125, ISBN 82-471-8011-1 (printed version), ISBN 82-471-8010-3 (electronic version), ISSN 1503-8181

Penetration and Perforation of Granite Targets by Hard Projectiles, Chong Chiang Seah, 2006:188, ISBN 82-471-8150-9 (printed version), ISBN 82-471-8149-5 (electronic version), ISSN 1503-8181

Deformations, strain capacity and cracking of concrete in plastic and early hardening phases, Tor Arne Hammer, 2007:234, ISBN 978-82-471-5191-4 (printed version), ISBN 978-82-471-5207-2 (electronic version), ISSN 1503-8181

Crashworthiness of dual-phase high-strength steel: Material and Component behaviour, Venkatapathi Tarigopula, 2007:230, ISBN 82-471-5076-4 (printed version), ISBN 82-471-5093-1 (electronic version), ISSN 1503-8181

Fibre reinforcement in load carrying concrete structures, Åse Lyslo Døssland, 2008:50, ISBN 978-82-471-6910-0 (printed version), ISBN 978-82-471-6924-7 (electronic version), ISSN 1503-8181

Low-velocity penetration of aluminium plates, Frode Grytten, 2008:46, ISBN 978-82-471-6826-4 (printed version), ISBN 978-82-471-6843-1 (electronic version), ISSN 1503-8181

Robustness studies of structures subjected to large deformations, Ørjan Fyllingen, 2008:24, ISBN 978-82-471-6339-9 (printed version), ISBN 978-82-471-6342-9 (electronic version), ISSN 1503-8181

Constitutive modelling of morsellised bone, Knut Birger Lunde, 2008:92, ISBN 978-82-471-7829-4 (printed version), ISBN 978-82-471-7832-4 (electronic version), ISSN 1503-8181

Experimental Investigations of Wind Loading on a Suspension Bridge Girder, Bjørn Isaksen, 2008:131, ISBN 978-82-471-8656-5 (printed version), ISBN 978-82-471-8673-2 (electronic version), ISSN 1503-8181

Cracking Risk of Concrete Structures in The Hardening Phase, Guomin Ji, 2008:198, ISBN 978-82-471-1079-9 (printed version), ISBN 978-82-471-1080-5 (electronic version), ISSN 1503-8181

Modelling and numerical analysis of the porcine and human mitral apparatus, Victorien Emile Prot, 2008:249, ISBN 978-82-471-1192-5 (printed version), ISBN 978-82-471-1193-2 (electronic version), ISSN 1503-8181

Strength analysis of net structures, Heidi Moe, 2009:48, ISBN 978-82-471-1468-1 (printed version), ISBN 978-82-471-1469-8 (electronic version), ISSN1503-8181

Numerical analysis of ductile fracture in surface cracked shells, Espen Berg, 2009:80, ISBN 978-82-471-1537-4 (printed version), ISBN 978-82-471-1538-1 (electronic version), ISSN 1503-8181

Subject specific finite element analysis of bone for evaluation of the healing of a leg lengthening and evaluation of femoral stem design, Sune Hansborg Pettersen, 2009:99, ISBN 978-82-471-1579-4 (printed version), ISBN 978-82-471-1580-0 (electronic version), ISSN 1503-8181

Evaluation of fracture parameters for notched multi-layered structures, Lingyun Shang, 2009:137, ISBN 978-82-471-1662-3 (printed version), ISBN 978-82-471-1663-0 (electronic version), ISSN 1503-8181

Modelling of Dynamic Material Behaviour and Fracture of Aluminium Alloys for Structural Applications, Yan Chen, 2009:69, ISBN 978-82-471-1515-2 (printed version), ISBN 978-82 471-1516-9 (electronic version), ISSN 1503-8181

Nanomechanics of polymer and composite particles, Jianying He, 2009:213, ISBN 978-82-471-1828-3 (printed version), ISBN 978-82-471-1829-0 (electronic version), ISSN 1503-8181

Mechanical properties of clear wood from Norway spruce, Kristian Berbom Dahl, 2009:250, ISBN 978-82-471-1911-2 (printed version) ISBN 978-82-471-1912-9 (electronic version), ISSN 1503-8181

Modeling of the degradation of TiB2 mechanical properties by residual stresses and liquid Al penetration along grain boundaries, Micol Pezzotta 2009:254, ISBN 978-82-471-1923-5 (printed version) ISBN 978-82-471-1924-2 (electronic version) ISSN 1503-8181

Effect of welding residual stress on fracture, Xiabo Ren, 2010:77, ISBN 978-82-471-2115-3 (printed version) ISBN 978-82-471-2116-0 (electronic version), ISSN 1503-8181

Pan-based carbon fiber as anode material in cathodic protection system for concrete structures, Mahdi Chini, 2010:122, ISBN 978-82-471-2210-5 (printed version) ISBN 978-82-471-2213-6 (electronic version), ISSN 1503-8181

Structural Behaviour of deteriorated and retrofitted concrete structures, Irina Vasililjeva Sæther, 2010:171, ISBN 978-82-471-2315-7 (printed version) ISBN 978-82-471-2316-4 (electronic version) ISSN 1503-8181

Prediction of local snow loads on roofs, Vivian Meløysund, 2010:247, ISBN 978-82-471-2490-1 (printed version) ISBN 978-82-471-2491-8 (electronic version) ISSN 1503-8181

Behaviour and modelling of polymers for crash applications, Virgile Delhaye, 2010:251, ISBN 978-82-471-2501-4 (printed version) ISBN 978-82-471-2502-1 (electronic version) ISSN 1503-8181

Blended cement with reducted CO2 emission utilizing the Fly Ash-Limestone Synergy, Klaartje De Weerdt, 2011:32, ISBN 978-82-471-2584-7 (printed version) ISBN 978-82-471-2584-4 (electronic version) ISSN 1503-8181

Chloride induced reinforcement corrosion in concrete - Concept of critical chloride content - methods and mechanisms, Ueli Angst, 2011:113, ISBN 978-82-471-2769-9 (printed version) ISBN 978-82-471-2763-6 (electronic version) ISSN 1503-8181

A thermo-electric-Mechanical study of the carbon anode and contact interface for Energy savings in the production of aluminium, Dag Herman Andersen, 2011:157, ISBN 978-82-471-2859-6 (printed version) ISBN 978-82-471-2860-2 (electronic version) ISSN 1503-8181

Structural Capacity of Anchorage Ties in Masonry Veneer Walls Subjected toEarthquake. The implications of Eurocode 8 and Eurocode 6 on a typical Norwegain veneer wall, Ahmed Mohamed Yousry Hamed, 2011:181, ISBN 978-82-471-2911-1 (printed version) ISBN 978-82-471-2912-8 (electronic version) ISSN 1503-8181

Work-hardening behaviour in age-hardenable Al-Zn-Mg(-Cu) alloys, Ida Westermann, 2011:247, ISBN 978-82-471-3056-8 (printed version) ISBN 978-82-471-3057-5 (electronic version) ISSN 1503-8181

Behaviour and modelling of selfpiercing riveted connections using aluminium rivets, Nguyen-Hieu Hoang, 2011:266, ISBN 978-82-471-3097-1 (printed version) ISBN 978-82-471-3099-5 (electronic version) ISSN 1503-8181 ISSN 1503-8181.